

IMAGING NETWORK ONTARIO

PROCEEDINGS OF THE 12th ImNO SYMPOSIUM • MARCH 24 - 25, 2014 • TORONTO

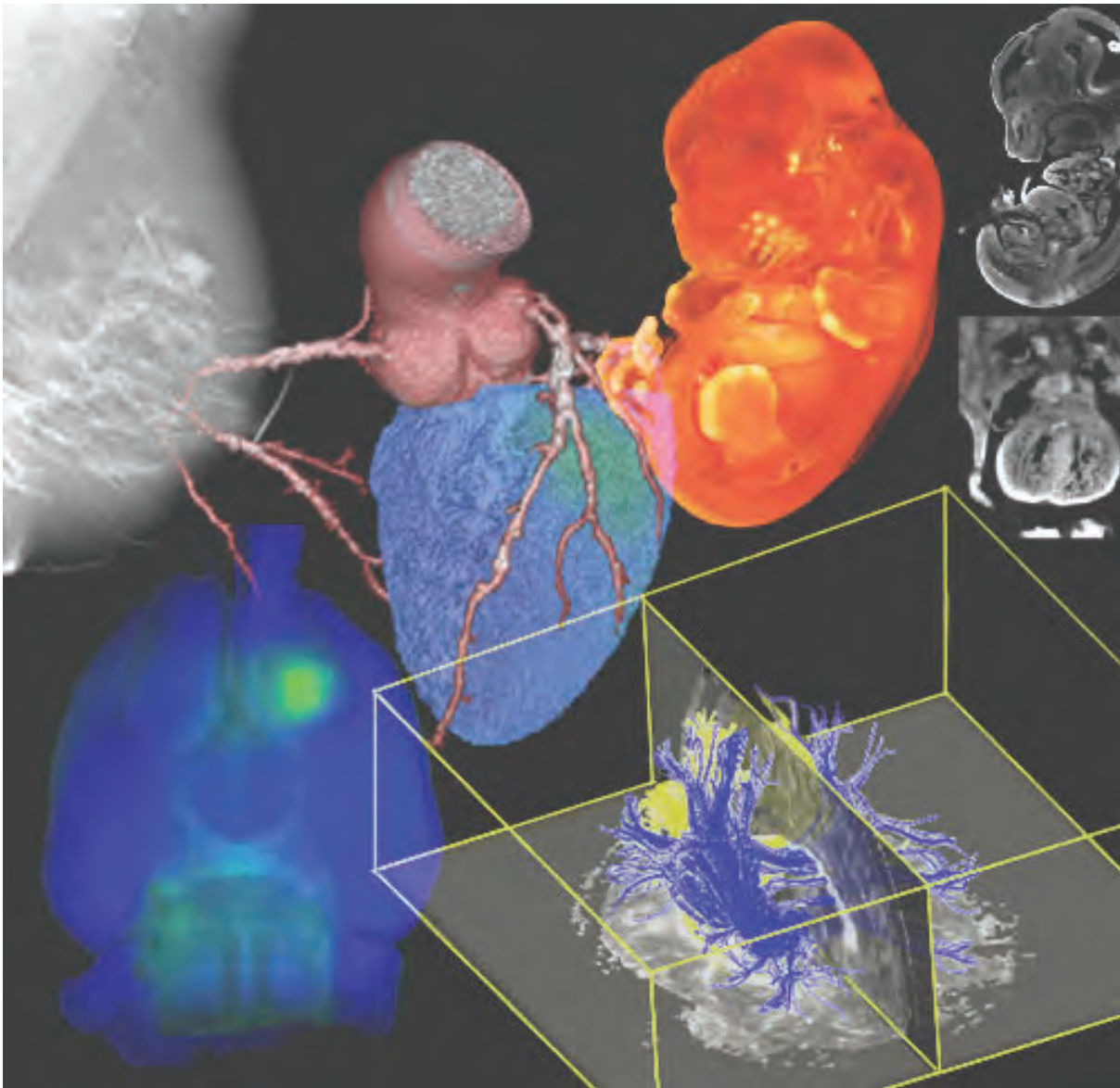


Table of Contents

Symposium Committee

Scientific Committee.....	ii
Organizing Committee.....	ii
Poster Competition Committee.....	ii

Acknowledgements.....iii

Program

March 24, 2014.....	1
March 25, 2014.....	4

Keynote Speakers7

Commercialization Session Speaker9

Commercialization Session Panel Members.....9

Oral Presentations and Poster Session Abstracts

Canadian Atherosclerosis Imaging Network	11
Cancer Imaging Network of Ontario	17
Medical Imaging Trial Network of Canada	47
Ontario Consortium for Adaptive Interventions in Radiation Oncology	59
Ontario Consortium in Imaging for Cardiovascular Therapeutics	91
OICR Imaging Translation Program	113
OICR Smarter Imaging Program	135
Ontario Preclinical Imaging Consortium	171

Abstract and Biography Index.....201

Symposium Committees

Scientific Committee

Jerry Battista, CINO
Aaron Fenster, OICR ITP
Stuart Foster, OPIC
Richard Frayne, CAIN and MITNEC
Stewart Gaede, OCAIRO
David Jaffray, OCAIRO
Frank Prato, OCICT
Tom Purdie, OCAIRO
Giles Santyr, OPIC
Aaron Ward, OICR ITP
Graham Wright (chair), OCICT
Martin Yaffe, OICR SIP

Organizing Committee

Alison Cheung, OICR ITP
Paolina Corsaro, OICR ITP
Dwayne Dickey, CAIN and MITNEC
Connie Marano, CINO
Carol Richardson, OICR ITP
Jean Rookwood, OCICT
Mary Wong, OCAIRO
Yulia Yerofeyeva, OICR SIP

Poster Competition Committee

Tom Purdie, OCAIRO
Aaron Ward, OICR ITP
Yulia Yerofeyeva, OICR SIP

Acknowledgements

We would like to thank our government and private sector partners, the Canadian Institutes of Health Research, the Ministry of Research and Innovation, the Ministry of Health and Long-Term Care, the Ontario Institute for Cancer Research, the Department of Medical Biophysics at the University of Toronto, and Cancer Care Ontario for their contributions to, and their participation in, the following consortia:

Canadian Atherosclerosis Imaging Network

Cancer Imaging Network of Ontario

Medical Imaging Trial Network of Canada

Ontario Consortium for Adaptive Interventions in Radiation Oncology

Ontario Consortium in Imaging for Cardiovascular Therapeutics

OICR Imaging Translation Program

OICR Smarter Imaging Program

Ontario Pre-Clinical Imaging Consortium

The Centre for Imaging Technology Commercialization (CIMTEC) sponsored the ImNO 2014 commercialization session and provided secretariat support for the 12th ImNO Symposium.

Abstract Reviewers and Poster Judges

We would also like to thank the volunteer abstract reviewers and poster judges.

CAIN/MITNEC

Herald Becher
Benjamin Chow
Dwayne Dickey
Humphrey Fonge
Therese Heinonen
Mike Kovacs

CINO

Gabor Fichtinger
Michael Sharpe
Alex Vitkin

OCAIRO

Stewart Gaede
Chris McIntosh
Tom Purdie

OCICT

Robert deKemp
Terry Peters
Marshall Sussman
Christopher Macgowan

OICR ITP

Rob Bartha
Aaron Fenster
Ting Lee
James Mainprize
Anne Martel
Tim Scholl
Aaron Ward

OICR SIP

Alison Cheung
Paula Foster
Martin Yaffe

OPIC

Giles Santyr
Timothy Scholl
John Sled
Greg Stanisz

MARCH 24, 2014

- 7:00 – 8:00** **REGISTRATION & BREAKFAST (FOYER & BALLROOM WEST)**
- 8:00 – 8:10** **OPENING REMARKS (BALLROOM CENTRAL & EAST)**
Graham Wright, Sunnybrook Research Institute
- 8:10 – 9:00** **COMPUTER AIDED DIAGNOSIS AND INTERVENTION OF PROSTATE CANCER**
Henkjan Huisman, Radboud University Medical Centre
- 9:00 – 9:50** **FUSED DIAGNOSTICS: A NEW PARADIGM FOR PERSONALIZED MEDICINE IN THE 21ST CENTURY**
John Tomaszewski, School of Medicine and Biomedical, University of Buffalo
- 9:50 – 10:35** **POSTER VIEWING & BREAK (GIOVANNI ROOM, ARMOURY & BALLROOM WEST)**
- 9:55 – 10:15** Poster judging for presenters with last names starting with A-K
- 10:15 – 10:35** Poster judging for presenters with last names starting with L-Z

<p>10:35 - 12:05 SESSION 1 (BALLROOM CENTRAL)</p> <p>PERFUSION, METABOLIC AND HYPOXIA IMAGING Chair: Frank Prato Lawson Health Research Institute</p> <p><i>10:35 Translational Imaging of Coronary Vascular Reactivity with Myocardial Perfusion PET</i> Rob deKemp, University of Ottawa Heart Institute</p> <p><i>10:50 Poor Correlation Between Noninvasive Cardiac Imaging and Fractional Flow Reserve in Patients with Multi-vessel Coronary Artery Disease</i> Marie-Jean Bertrand, Montreal Heart Institute</p> <p><i>11:05 Simultaneous Assessment of Myocardial Ischemia and Edema and Viability with a Single Bolus of Contrast Injection and CT Acquisition</i> Aaron So, Lawson Health Research Institute</p> <p><i>11:20 18F-FAZA-PET Imaging in Colon, Rectal and Pancreatic Patient-derived Xenografts recapitulates the Hypoxic Microenvironment: Validation with Autoradiography and Immunofluorescence</i> Trevor McKee, Princess Margaret Cancer Centre</p> <p><i>11:35 Model Based Reconstruction for Simultaneous [1-13C]Pyruvate and Lactate Imaging</i> Benjamin Geraghty, University of Toronto</p> <p><i>11:50 Real-time Imaging of Live Cells During Fluid Shear: Design and Fabrication of a Novel Platform</i> Daniel Lorusso, Western University</p>	<p>10:35 - 12:05 SESSION 2 (BALLROOM EAST)</p> <p>IMAGE-GUIDED ADAPTIVE THERAPIES Chair: Stewart Gaede London Regional Cancer Program</p> <p><i>10:35 The Accuracy and Reproducibility of Computer-Assisted Surgical Plane Resections in Orthopaedic Oncology</i> Aidin Kashigar, University Health Network</p> <p><i>10:50 MRI-Guided Prostate Focal Laser Ablation Therapy using a Mechatronic Needle Guidance System: Initial Experience and Future Directions</i> Jeremy Cepek, Western University</p> <p><i>11:05 Development of a Novel Functional Orthopaedic Implant for Use in a Rodent Model of Partial Hip Replacement</i> Adam Paish, Western University</p> <p><i>11:20 MRI Characterizes the Evolution of Brain Metastasis and Response to Radiotherapy in a Brain Metastatic Breast Cancer Model</i> Donna Murrell, Western University</p> <p><i>11:35 Augmenting the Parametric Response Map For Guidance of Locally Adaptive Radiotherapy in The Presence of Image Registration Error</i> Anthony Lausch, Western University</p> <p><i>11:50 Inverse Planning for Single Needle Radiofrequency Ablation in Liver Cancer Treatment Using Approximation</i> Shefali Kulkarni-Thaker, University of Toronto</p>
--	---

12:05 – 1:05 **LUNCH (BALLROOM WEST)**

MARCH 24, 2014 CONTINUED**1:05 – 2:35 SESSION 3 (BALLROOM CENTRAL)****ANIMAL IMAGING MODELS**

Chair: Giles Santyr
Hospital for Sick Children

1:05 Novel Contrast Agent for Dual-Energy Micro-CT to Characterize Bone Vasculature
Justin Tse, Western University

1:20 Multi-modality Neuroimaging in a Porcine Model of Endothelin-1 Induced Cerebral Ischemia
Christopher d'Esterre, University of Calgary

1:35 Contrast-Enhanced CT Reveals the Early Hemodynamic Changes of Focal Cerebral Ischemia and Amyloid Protein Toxicity in a Rat Model
Jun Kevin Yang, Western University

1:50 Application of 3D Echocardiography and Gated Micro-CT to assess Cardiomyopathy in a Duchenne Muscular Dystrophy Mouse Model
Andrew Bondoc, Lawson Health Research Institute

2:05 Three-Dimensional Imaging of the Mouse Heart and Vasculature Using Micro-CT and Whole-Body Perfusion of Iodine of Phosphotungstic Acid
Sarah Detombe, Western University

2:20 3D Histology Reconstruction for Microvasculature Quantification in Preclinical Studies
Yiwen Xu, Western University

1:05 - 2:35 SESSION 4 (BALLROOM EAST)**QUANTITATIVE IMAGING**

Chair: Jerry Battista
Medical Biophysics, Western University

1:05 Preliminary Clinical Study of a True Elastography Method for Prostate Cancer Assessment
Seyed Reza Mousavi, Western University

1:20 High Resolution Cardiac T1 Maps of Chronic Fibrosis Correlate with Collagen Content*
Mihaela Pop, Sunnybrook Research Institute

1:35 Quantification of Total Adipose Tissue in Fetal Guinea Pigs Subjected to Suboptimal in Utero Conditions Using Water-Fat MRI
Kevin Sinclair, Western University

1:50 Correlation of Quantitative MRI and Histology of Surgical Specimens in Drug-Resistant Focal Epilepsy
Maged Goubran, Western University

2:05 Characterizing Magnetic Susceptibility Changes of Human Brain in Normal Aging Using Quantitative Susceptibility
Armin Eilaghi, University of Calgary

2:20 Dynamic Contrast Enhanced MRI Parameter Map Sensitivity to Imaging Temporal Resolution in the Prostate
Thomas Hrinivich, Western University

2:35 – 3:20 POSTER VIEWING & BREAK (GIOVANNI ROOM, ARMOURY & BALLROOM WEST)

2:40 – 3:00 Poster judging for presenters with last names starting with A-K

3:00 – 3:20 Poster judging for presenters with last names starting with L-Z

MARCH 24, 2014 CONTINUED

<p>3:20 – 5:05 SESSION 5 (BALLROOM CENTRAL)</p> <p>TARGETED PROBE DEVELOPMENT AND BIOMARKERS Chair: Martin Yaffe Sunnybrook Research Institute/Centre for Imaging Technology Commercialization</p> <p><i>3:20 Nanodroplet Imaging of Liver Cancer</i> Peter Burns, Sunnybrook Research Institute</p> <p><i>3:35 MagA Reporter Gene Expression for MRI</i> Donna Goldhawk, Lawson Health Research Institute</p> <p><i>3:50 High Relaxivity Gd-free T1 MRI Contrast Agents</i> Weiran Cheng, University of Toronto</p> <p><i>4:05 PK11195-Cryptophane-A as a Contrast Agent in 129XE Hyper-CEST Studies for Enhanced Hyper-CEST Efficiency</i> Krista Dowhos, Lakehead University</p> <p><i>4:20 Magnetic Resonance Imaging of 5-Fluorouracil: A Preliminary Study for Monitoring Drug Resistance</i> Jordan Lovis, Thunder Bay Regional Research Institute</p> <p><i>4:35 Freehand Fluorescence Diffuse Optical Tomography for Head & Neck Surgery</i> Michael Daly, Princess Margaret Hospital</p> <p><i>4:50 Cancer Immunotherapy: Dendritic Cell Tracking using Fluorine-19 with a 9.4T MRI</i> Jeff Gaudet, Western University</p>	<p>3:20 – 5:05 SESSION 6 (BALLROOM EAST)</p> <p>VISUALIZATION AND IMAGE ANALYSIS Chair: Aaron Ward Western University</p> <p><i>3:20 Groupwise Conditional Random Forest Learning for Automated Region Of Interest Classification and Quality Assurance in Radiotherapy Planning</i> Chris McIntosh, Princess Margaret Cancer Centre</p> <p><i>3:35 Toward prostate cancer contouring guidelines for focal therapy on MRI: assessment of target volume dominant lesion coverage via accurate histology fusion</i> Eli Gibson, Western University</p> <p><i>3:50 Elastic Registration of Prostate MR Images Based on Estimation of Deformation States</i> Bahram Marami, Western University</p> <p><i>4:05 Design of Mobile Image Overlay System for Image-Guided Interventions</i> Manjunath Anand, Queen's University</p> <p><i>4:20 Target localization in MRI-guided prostate biopsy</i> Helen Xu, Queen's University</p> <p><i>4:35 Magnetic Resonance Imaging-Targeted, 3D Transrectal Ultrasound-Guided Fusion Biopsy for Prostate Cancer: Quantifying the Impact of Needle Delivery Error on Diagnosis</i> Peter Martin, Western University</p> <p><i>4:50 Robust 3D MRI Segmentation of Femoral Artery for Morphological Analysis of Peripheral Arterial Disease Plaque Burden</i> Eranga Ukwatta, Western University</p>
---	--

5:05 – 7:00 POSTER SESSION & RECEPTION (GIOVANNI ROOM, ARMOURY AND BALLROOM WEST)**5:10 – 5:30** Poster judging for presenters with last names starting with A-K**5:30 – 5:50** Poster judging for presenters with last names starting with L-Z

MARCH 25, 2014

- 7:00 – 8:00** **REGISTRATION & BREAKFAST (FOYER & BALLROOM WEST)**
- 8:00 – 8:10** **OPENING REMARKS (BALLROOM CENTRAL & EAST)**
Graham Wright, Sunnybrook Research Institute
- 8:10 – 9:00** ***BIOMOLECULAR ENGINEERING FOR NON-INVASIVE IMAGING OF BIOLOGICAL FUNCTION***
Mikhail Shapiro, California Institute of Technology
- 9:00 – 9:50** ***CARDIAC CT FOR STABLE ANGINA - BEYOND STENOSIS***
Jonathon Leipsic, St. Paul's Hospital, University of British Columbia
- 9:50 – 10:35** **POSTER VIEWING & BREAK (GIOVANNI ROOM, ARMOURY & BALLROOM WEST)**
- 9:55 – 10:15** Poster judging for presenters with last names starting with A-K
- 10:15 – 10:35** Poster judging for presenters with last names starting with L-Z

10:35 – 12:05 COMBINED SESSION 7 & 8 (BALLROOM CENTRAL & EAST)**COMMERCIALIZATION**

Chairs: Raphael Ronen, Sunnybrook Health Sciences Centre
Michael Waterston, Centre for Imaging Technology Commercialization

10:35 – 11:20 PLENARY KEYNOTE

FACULTY ENTREPRENEURSHIP: DO'S AND D'OOH'S
Rock Mackie, University of Wisconsin-Madison

11:20 – 12:05 PANEL

FROM RESEARCH TO STARTUP AND BEYOND

Panel Members:

Mike Bronskill, Profound Medical Inc.
Aaron Fenster, Western University, Centre for Imaging Technology Commercialization
Rock Mackie, University of Wisconsin-Madison
Don Plewes, Sentinelle

12:05 – 1:05 Lunch (Ballroom West)

MARCH 25, 2014 CONTINUED**1:05 – 2:35 SESSION 9 (BALLROOM CENTRAL)****IMAGING BIOMARKERS - LUNG**

Chair: Mitch Albert

Thunder Bay Regional Research Institute

1:05 Sex, Airways Disease and Emphysema in Ex-smokers with and Without Airflow Limitation

Damien Pike, Western University

1:20 Hyperpolarized 3He MRI Ventilation Abnormalities of Cystic Fibrosis and Non-Cystic Fibrosis Bronchiectasis

Gregory Paulin, Western University

1:35 In Vivo Regional Ventilation Mapping by Using Fluorinated Gas MRI

Alexei Ouriadov, Thunder Bay Regional Research Institute

1:50 Pulmonary Functional Imaging of Bronchiectasis: A First Look at Ventilation Abnormalities and their Relationship with Pulmonary Function and Symptoms

Sarah Svenningsen, Western University

2:05 Early Prediction of Lung Cancer Recurrence After Stereotactic Radiotherapy Using Second-Order Texture Statistics

Sarah Mattonen, Western University

2:20 Ultra-short Echo Time (UTE) MRI and CT of Bronchiectasis and Emphysema: Tissue Density Measurements and Relationship to Pulmonary Function Tests

Khadija Sheikh, Western University

1:05 – 2:35 SESSION 10 (BALLROOM EAST)**INSTRUMENTATION**

Chair: Aaron Fenster

Western University/Centre for Imaging Technology Commercialization

1:05 Image-based 3D replication in metal alloys

David Holdsworth, Western University

1:20 Tracking a 6F catheter under MRI using a controllable susceptibility device: a new tracking mechanism

William Dominguez-Viqueira, Sunnybrook Research Institute

1:35 Multifrequency Intravascular Ultrasound for Imaging of Coronary Plaque

Chelsea Munding, University of Toronto

1:50 Design of a tracked ultrasound calibration phantom made of LEGO® bricks

Marie Soehl, Queen's University

2:05 Fully MRI-Compatible Dynamic Motion Stage

Ali Mohamed Tavallaei, Western University

2:20 Robust Intra-operative Ultrasound Probe Tracking Using a Monocular Endoscopic Camera

Uditha Jayarathne, Western University

2:35 – 2:50 Afternoon Break (Giovanni Room, Armoury & Ballroom West)

MARCH 25, 2014 CONTINUED**2:50 – 4:20 SESSION 11 (BALLROOM CENTRAL)****3D VISUALIZATION**

Chair: Gabor Fichtinger
Queens University

2:50 Construction of an Attenuation map for mMR Breast coil

John Patrick, London Regional Cancer Program

3:05 In Vivo Validation of a 3D Ultrasound System for Imaging the Lateral Ventricles of Neonates

Jessica Kishimoto, Western University

3:20 A Novel Technology for Teaching Ultrasound-Guided Intrathecal Needle Insertion with Perk Tutor

Tamas Ungi, Queen's University

3:35 Software Development for Image Guidance on the Magnetic Resonance-Guided Radiation Therapy (MRgRTTM) System

Wenyao Xia, Princess Margaret Hospital

3:50 Improvements in SlicerRT, the Radiation Therapy Research Toolkit for 3D Slicer

Andras Lasso, Queen's University

4:05 Three-Dimensional Non-Rigid MR-TRUS Registration Using Duality-Based Optimization Method

Yue (Joy) Sun, Western University

2:50 – 4:20 SESSION 12 (BALLROOM EAST)**CLINICAL**

Chair: Richard Frayne
University of Calgary

2:50 Prominence of vein on susceptibility-weighted MRI indicates the severity of small vessel disease

Farhang Jalilian, Sunnybrook Health Sciences Centre

3:05 Cerebra-WML: A Stand-Alone Application for Quantification of White Matter Lesion

Qian Lu, University of Calgary

3:20 [18F]-fluorodeoxyglucose is a Stronger Correlate of Intraplaque Inflammatory Burden in Human Carotid Plaque than C-Reactive Protein: A Sub-study of the Canadian Atherosclerosis Imaging Network (CAIN)

Myra Cocker, University of Calgary

3:35 Dynamic Carotid MR Imaging for Distensibility Assessment

Mari Boesen, University of Calgary

3:50 IMAGE-CAD Pilot Study Assessment of Patients with Suspected Coronary Artery Disease (CAD): What is the best initial imaging strategy? Cardiac Computed Tomographic Angiography (CCTA) vs Stress Echocardiography (SE) vs Single-Photon Emission Computed Tomography (SPECT)

Victoria Sarban, Mazankowski Alberta Heart Institute

4:05 Medical Imaging Trials Network of Canada (MITNEC) - Project C6 - Amyloid and glucose PET Imaging in Alzheimer and Vascular Cognitive Impairment patients with significant White Matter Disease

Sandra Black, Sunnybrook Health Sciences Centre

4:30 – 4:50 POSTER AWARDS (BALLROOM CENTRAL)

Aaron Fenster, Western University/Centre for Imaging Technology Commercialization

4:50 – 5:00 CLOSING REMARKS (BALLROOM CENTRAL)

Aaron Fenster, Western University/Centre for Imaging Technology Commercialization

The Medical Imaging Trials Network of Canada (MITNEC) will record a number of the presentations at the 2014 ImNO meeting. These will be combined with animated slides and made into podcasts. By the fall of 2014, these podcasts will be available on the MITNEC-funded KT web site – imagingkt.ca. MITNEC acknowledges the support of the CIHR for these activities.

Keynote Speakers' Biographies

Henkjan J. Huisman, PhD

Assistant Professor Radboud University Medical Centre

Dr. Henkjan Huisman received his PhD in quantitative medical ultrasound in 1998 at the Radboud University Medical Center, Nijmegen, The Netherlands. He continued his research in quantitative MR and ultrasound in breast and prostate resulting in several publications, clinical applications and a patent on a Pharmacokinetic DCEMR processing. He started a research group in 2004 on Computer Aided Diagnosis and Intervention of prostate cancer focussing on computerized support systems for interpretation of multiparametric MR and MRL as well as image guided biopsy and intervention. Since 2011 he is also product manager of a CE certified prostate MR workstation in DIAGTechnologies (TM). He has published over a 100 papers and book chapters, and has co-organized several workshops / challenges on prostate MR image analysis.

Jonathon A. Leipsic, MD

Vice-Chair Research, Department of Radiology, Faculty of Medicine, University of British Columbia

Jonathan Leipsic is the Chairman of the Department of Radiology for Providence Health Care and the Vice Chairman of Research for the UBC Department of Radiology. He is the Assistant Professor of Radiology and is also appointed in the Division of Cardiology with the University of British Columbia. He acts as the co-director of Advanced Cardiac Imaging for the Providence Health Care Heart Centre at St. Paul's Hospital. Dr. Leipsic is actively involved in cardiac CT and MR research with prior involvement in a multi-centre trial evaluating coronary CT angiography vs. QCA. Dr. Leipsic has over 50 peer reviewed manuscripts in press or in print and over 100 scientific abstracts. These include, but are not limited to, diagnostic performance and radiation reduction as well as CT to guide minimally invasive valve intervention. He speaks internationally on a number of cardiovascular imaging subjects. He is currently sitting on the education, programs, and international regional committees for the Society of Cardiovascular CT as well as the board of directors. He also chairs the Canadian International Regional Committee for the SCCT. Dr Leipsic serves as a reviewer for numerous cardiac imaging journals and is also the director for the Advanced Cardiac Imaging fellowship at the Heart Centre at St. Paul's Hospital in Vancouver.

Mikhail G. Shapiro, PhD

Assistant Professor of Chemical Engineering, California Institute of Technology

Mikhail Shapiro is an Assistant Professor of Chemical Engineering at the California Institute of Technology. His research is focused on developing molecular technologies to image and control biological function non-invasively in living organisms. To achieve this goal, the Shapiro Lab adapts, evolves and engineers proteins and other biological structures into non-invasive reporters for imaging with MRI and ultrasound and control using magnetic, acoustic and thermal energy. Dr. Shapiro received his PhD in Biological Engineering from the Massachusetts Institute of Technology and a BSc in Neuroscience from Brown. He conducted post-doctoral research in biophysics at the University of Chicago and was a Miller Fellow at the University of California, Berkeley. Dr. Shapiro has been awarded the Hertz, Soros, Miller and Life Science Research Foundation fellowships, the Hertz PhD Thesis Prize and the Burroughs Wellcome Career Award at the Scientific Interface. The Technology Review has recognized him as one of the world's top 35 innovators under age 35. More information about the Shapiro Lab can be found online at shapirolab.caltech.edu.

John Tomaszewski, MD

Department of Pathology and Anatomical Sciences, School of Medicine and Biomedical Sciences, University of Buffalo

A native of Philadelphia, Dr. Tomaszewski received his MD from the University of Pennsylvania School of Medicine. He did his residency and fellowships in pathology at the Hospital of the University of Pennsylvania. After joining the faculty of UPenn in 1983 as an Assistant Professor of Pathology and Laboratory Medicine, he rose through the ranks to Professor and held many leadership positions. He joined the faculty at SUNY at Buffalo as Professor and Chair of Pathology and Anatomical Sciences in 2011.

Dr Tomaszewski's long-term research interests lie in the fields of genitourinary pathology. He has a strong interest in quantitative imaging and computational modeling in support of an evolving paradigm of "integrated diagnostics".

Dr. Tomaszewski's work has resulted in over 280 peer-reviewed publications. He is recognized nationally and internationally in his field. He is Chair of the APC Advocacy Committee and the past -President of the American Society for Clinical Pathology

Commercialization Session Speaker's Biography

Thomas “Rock” Mackie, PhD

Director of Medical Devices, Wisconsin Institutes for Discovery, University of Wisconsin-Madison

Chairman, co-founder and co-inventor of TomoTherapy, Inc. and a University of Wisconsin-Madison professor of medical physics at the School of Medicine and Public Health and biomedical engineering in the College of Engineering, the focus of Rock Mackie’s area is to explore and build medical devices with the potential to treat or cure medical conditions in patients and to improve the movement of new devices from research lab to clinical use. This area will be the most closely integrated with UW-Madison and in many ways its translational emphasis has been modeled on the successful Coulter Foundation Program at the university’s department of biomedical engineering. Mackie’s plans include a facility for rapid prototyping and the launch of a medical devices consortium through partnerships with companies and academia.

Commercialization Session Panel Members' Biographies

Michael Bronskill, PhD

NexGen Medical Systems Inc.

Dr. Michael Bronskill, PhD is a Co-founder and Advisor of NexGen Medical Systems, Inc. Dr. Bronskill co-founded Profound Medical Inc., in 2008. Dr. Bronskill is a medical physicist, with unparalleled expertise in medical imaging using MRI. He is a Senior Scientist Emeritus at Sunnybrook Health Sciences Centre and a Professor of Medical Biophysics at the University of Toronto. He served as Director of Imaging Research at Sunnybrook Health Sciences Centre in Toronto from 1990 to 2004. He served as a Director of Profound Medical Inc. He is an internationally known authority on magnetic resonance imaging and interventional, image-guided techniques, and holds several patents related to imaging technologies. He has published over 140 peer-reviewed papers, mainly on MRI techniques and their applications in biophysics and medicine. He holds five patents and has several applications pending. Dr. Bronskill received his BSc degree in Mathematics and Physics from the University of Toronto in 1966, and MSc and PhD degrees in Medical Biophysics from the University of Toronto in 1968 and 1970, respectively.

Aaron Fenster, PhD, FCCPM

CIMTEC Chief Scientific Officer and Centre Director

Dr. Aaron Fenster received his PhD degree in 1976 from the Department of Medical Biophysics of the University of Toronto. In 1987, he moved to London and became a scientist and founding Director of the Imaging Research Laboratories (IRL) at the Robarts Research Institute and Professor in Radiology at the University of Western Ontario (UWO). Under his leadership, the IRL has grown to a staff of 250.

Dr. Fenster is the Director of the Biomedical Imaging Research Centre at Western University and continues as the Director of the IRL. In addition, he is the founder and Associate Director of the new interdisciplinary graduate program in Biomedical Engineering at Western and Chair of the Division of Imaging Sciences in the Department of Medical Imaging. This Division combines the strengths in imaging research across London’s institutions, making the London medical imaging research community one of the largest in North America with more than 350 staff and students and \$100M in research equipment.

Dr. Fenster is the Program Director of the Imaging Translation Program for the Ontario Institute for Cancer Research (OICR), as well as the Co-Program Director of OICR's Smarter Imaging Program. In 2010, he became the Chief Scientific Officer, Centre Director and acting CEO of the Centre for Imaging Technology Commercialization (CIMTEC) – a federally funded Centre of Excellence in Commercialization and Research.

Currently, he holds a Tier 1 Canada Research Chair in Medical Imaging. He is the first recipient of the Premier’s (Ontario) Discovery Award for Innovation and Leadership (2007), and has been awarded Western's Hellmuth

Prize for Achievement in Research(2008) and the Canadian Organization of Medical Physicists (COMP) Gold Medal Award (2010). In 2011 he was inducted into the Canadian Academy of Health Sciences.

Fenster's research has resulted in 250 papers in peer reviewed journals, 37 patents (27 awarded and 10 pending) and the formation of four London-based companies. In addition, his patents have been licensed to 13 companies which have commercialized them for world-wide distribution.

In 2013, the International Organization of Medical Physics named Fenster one of the top 50 Medical Physicists in the world who have made outstanding contributions to the advancement of medical physics and healthcare through research, clinical developments, education and training activities over the last 50 years.

Donald B. Plewes, PhD

Professor Emeritus, University of Toronto

Dr. Donald Plewes is a Professor Emeritus in the Department of Medical Biophysics at the University of Toronto. His career has been devoted to the physics of medical imaging and has conducted research in x-ray/CT imaging, ultrasound and magnetic resonance imaging with clinical applications related to cardiovascular disease and cancer. His work has explored the use of phase MRI methods for the evaluation of flow characteristics in cardiovascular applications and tissue biomechanical based on MR Elastography. Using similar methods, he presented the first visualization of biomedical ultrasound fields based on MR imaging which allowed absolute non-invasive measurement of the pressure distribution of the ultrasound field. More recently his group has been devoted to devising novel technologies for breast MRI which include pulse sequence and instrumentation development for DCE-MR, breast intervention and co-registration methods. Starting in 1997, Dr. Plewes was the co-PI of a large, 12 year clinical trial aimed at measuring the efficacy of DCE-MRI for the surveillance of breast cancer in BRCA1 and BRCA2 mutation carriers. That study demonstrated the superiority of breast MRI in the early detection of breast cancer with MRI with a 2.5 fold increase in sensitivity compared to that by mammography or ultrasound. This seminal study helped lead to recent recommendations by various cancer agencies throughout North American, Europe and Asia for the use of breast MRI for high risk breast screening. In 2004, Dr. Plewes, in conjunction with Cameron Piron and Christopher Luginbuhl, both previous students in Dr. Plewes' laboratory, founded Sentinelle Medical to commercialize technologies developed in Dr. Plewes' laboratory. The company sells breast MRI equipment and software compatible with MRI systems from General Electric, Siemens and Toshiba throughout the world.

Canadian Atherosclerosis Imaging Network CAIN

Oral Presentation and Poster Abstracts

[18F]-fluorodeoxyglucose is a Stronger Correlate of Intraplaque Inflammatory Burden in Human Carotid Plaque than C-Reactive Protein: A Sub-study of the Canadian Atherosclerosis Imaging Network (CAIN)

Myra S Cocker, Univ of Ottawa Heart Inst, Ottawa, ON, Canada; J David Spence, Western Univ, Robarts Res Inst, London, ON, Canada; Robert Hammond, Western Univ and London Health Sciences Ctr, London, ON, Canada; Brian Mc Ardle, Jordan Bernick, Rob deKemp, Univ of Ottawa Heart Inst, Ottawa, ON, Canada; Cheemun Lum, The Ottawa Hosp, Ottawa, ON, Canada; George Youssef, Univ of Ottawa Heart Inst, Ottawa, ON, Canada; Yulia Yerofeyeva, Tigran Karavardanyan, Adebayo Adeeko, Sunnybrook Res Inst, Toronto, ON, Canada; Andrew Hill, Sudhir Nagpal, The Ottawa Hosp, Ottawa, ON, Canada; Grant Stotts, The Ottawa Hosp Inst, Ottawa, ON, Canada; Jennifer Renaud, Cathy Kelly, Joanne Brennan, Linda Garrard, Univ of Ottawa Heart Inst, Ottawa, ON, Canada; Murad Alturkustani, Western Univ and London Health Sciences Ctr, Ottawa, ON, Canada; Laura Hammond, Western Univ and London Health Sciences Ctr, London, ON, Canada; Jean DaSilva, Univ of Ottawa Heart Inst, Ottawa, ON, Canada; Jean-Claude Tardif, Montreal Heart Inst, Montreal, QC, Canada; Rob Beanlands, Univ of Ottawa Heart Inst, Ottawa, ON, Canada

Background and Purpose:

Inflammation triggers and contributes to the progression of atherosclerosis. C-reactive protein (CRP), a circulating marker of inflammation, is a putative risk factor for cardiovascular disease, but this is not borne out in Mendelian randomization studies. Inflammation in carotid arteries can be imaged with hybrid [18F]-fluorodeoxyglucose (18FDG) positron emission tomography (PET) computed tomography (CT) imaging.

In this investigation, circulating levels of CRP and 18FDG uptake in carotid vasculature were directly compared with intraplaque inflammatory burden, using macrophage-specific CD68 immunohistology.

Methods:

Nineteen prospectively recruited patients (66 ± 11 years, 15 male) scheduled for carotid endarterectomy underwent 18FDG-PET and CT angiography of carotids. CRP levels were assessed. Maximum 18FDG uptake in both internal carotids was quantified and normalized to blood (tissue:blood ratio, TBR). Following endarterectomy, excised plaque was fixed, sectioned and immunostained for CD68. CD68 expression was quantified.

Results:

Carotid endarterectomy was performed in 19 patients; one received a 2nd carotid endarterectomy due to bilateral disease. The direct burden of inflammation, as quantified by CD68 immunohistology, correlated with maximum 18FDG uptake ($r=0.716$, $p<0.001$). There was no evidence of a correlation between CRP and CD68 ($r=0.159$, $p=0.50$), nor with maximum 18FDG uptake ($r=0.238$, $p=0.31$). Furthermore, 18FDG and CRP are different correlations where FDG is more strongly correlated with CD68 than CRP ($p=0.02$, Hotelling Williams test).

Conclusion:

18FDG uptake is more strongly related to the extent of inflammatory burden within high-risk carotid plaque than CRP. CRP may not be an accurate criterion for assessing vulnerable carotid plaque (based on histopathology nor 18FDG uptake). Prospective outcomes-based trials are needed to establish 18FDG as a direct biomarker of vulnerable carotid plaque.

Characterizing Magnetic Susceptibility Changes of Human Brain in Normal Aging Using Quantitative Susceptibility Mapping

A. Eilaghi^{1,2}, D.A. McLean^{2,3}, D.G. Gobbi^{2,3}, M.E. MacDonald^{1,2}, M.L. Lauzon^{1,2}, M. Salluzzi^{2,3}, and R. Frayne^{1,2,3}

¹Department of Radiology and Clinical Neurosciences, Hotchkiss Brain Institute, University of Calgary, Calgary, Alberta, Canada ²Seaman Family MR Centre, Foothills Medical Centre, Calgary, Alberta, Canada, ³Calgary Image Processing and Analysis Centre, Calgary, Alberta, Canada.

Research Supervisor: Richard Frayne

Background and Purpose: Magnetic susceptibility changes in white matter and deep nuclei due to demyelination and iron deposition are an important characteristic of aging in brain. [1] These spatial and temporal variations can be identified and measured using quantitative susceptibility mapping (QSM). [2] In this study we use QSM to quantify susceptibility changes in white matter (WM), caudate nucleus (C), putamen (P), and globus pallidus (GP), previously suggested to be the most sensitive regions [3] to normal aging. Specifically, we compare susceptibility values between young and elderly normal subjects.

Methods: Four young (age = 22.2 ± 4.0) and four elderly (age = 76.3 ± 3.9) individuals were imaged on a 3-T scanner (Discovery 750; GE Healthcare). Exclusion criteria included a) history of neurological disorder, b) MR incompatibility, c) claustrophobia, d) composite score below 27 on the Montreal Cognitive Assessment (MoCA). Image acquisition parameters were multi-echo gradient recalled sequence: $TE_1 = 2.1$ ms; $\Delta TE = 2.4$ ms; $TR = 22$ ms; voxel = 1mm^3 ; matrix = $256 \times 256 \times 128$. QSM images underwent skull stripping [4], 3D phase unwrapping [5] and dipole fitting. [2] The magnetic field was calculated using phase data and the background field was removed using RESHARP technique. [6] Finally, truncation deconvolution method was utilized to generate QSM data. The International Consortium of Brain Mapping (ICBM) brain parcellation atlas (Figure 1-a) was registered to each patient's native space and used to anatomically segment the QSM data. [7] Regional QSM data were compared between young and elderly patients and between different regions using Mann-Whitney and Kruskal-Wallis tests, respectively.

Results: Magnetic susceptibility was significantly different for all regions of interest in all patients ($p < 0.001$). Globus pallidus and white matter showed highest and minimum mean susceptibility, respectively. Different regions were ranked in terms of magnetic susceptibility as follows: 1) globus pallidus, 2) putamen, 3) caudate, and 4) white matter. Whole brain analysis showed that elderly group had higher average susceptibility ($p = 0.04$). Also, magnetic susceptibility was significantly higher in the elderly within each of the four regions of interest, consistent for all regions of interest ($p < 0.001$).

Conclusions: QSM highlighted spatial susceptibility differences in all regions of interest due to normal aging. Quantification and location of susceptibility variation characterizes iron deposition in deep nuclei and demyelination in white matter, and may help better understanding of age- and disease-related functional and cognitive decline.

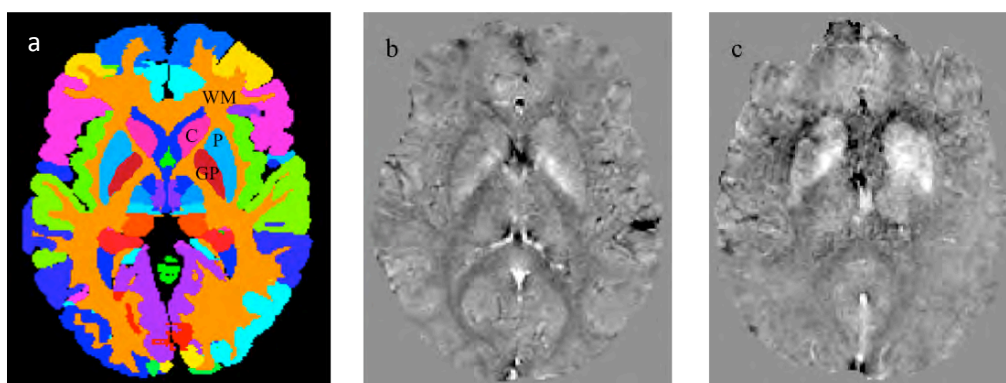


Figure 1. a) ICBM brain parcellation atlas on which caudate (C), putamen (P), globus pallidus (GP) and white matter (WM) are indicated. QSM maps of a 20-year old (b) and 79-year old (c) normal subjects.

References: [1] Li W, et al. Hum Brain Mapp, 2013, doi: 10.1002/hbm.22360. [2] De Rochefort L, et al. Magn Reson Med, 2010, 63: 194-206. [3] Bilgic B, et al. NeuroImage, 2012, 59: 2625-35. [4] Smith SM, Hum Brain Mapp, 2002, 17: 143-55. [5] Jenkinson M, Magn Reson Med, 2003, 49:193-7. [6] Sun H, et al. Magn Reson Med, 2013, doi: 10.1002/mrm.24765. [7] Avants BB, NeuroImage, 2011, 54:2033-44.

Prominence of vein on susceptibility-weighted MRI indicates the severity of small vessel disease

Farhang F Jalilian^{a,b}, David E Crane^a, FuQiang Gao^a, Sandra E Black^{a,c,d} & Bradley J MacIntosh^{a,b}

^aHeart and Stroke Foundation Canadian Partnership for Stroke Recovery, Sunnybrook Research Institute, Toronto, ON, ^bMedical Biophysics, University of Toronto, Toronto, ON, ^cDivision of Neurology, Department of Medicine, University of Toronto, Toronto, ON, ^dBrain Sciences Research Program, Sunnybrook Research Institute, Toronto, ON

Research Supervisor: Bradley J MacIntosh

Introduction: Cerebral Small Vessel Disease (SVD) is the most prevalent neurological condition among elderly adults and is associated with an increased risk of stroke and dementia [1]. SVD manifests as regions of white matter hyperintensity (WMH) on fluid attenuated inversion recovery (FLAIR) images. While SVD is thought to be a vascular problem and ischemic in nature, very little is known about the role of venous vasculature in this condition. Some argue that collagen builds up in veins as SVD progresses [2], which could restrict perfusion to upstream white matter tissue. Among venography techniques, susceptibility-weighted magnetic resonance imaging (SWI) has gained popularity over the past decade [3] and may be useful in the context of assessing SVD severity. The ability of SWI to enable visualization of deep medullary venule in the periventricular white matter has received special attention in a number of clinical applications such as multiple sclerosis and hypoxic-ischemic disorders [4, 5]. To our knowledge, no SWI study to date has investigated SVD. The aim of the current study is to examine the role that SWI can play in understanding SVD by developing an automated and quantitative procedure that can isolate venous anatomy. We hypothesize that the number of veins detected on SWI, which may reflect widening related to venous wall pathology will correlate positively to periventricular SVD lesion volume.

Materials and Methods: 32 subjects (mean age 70.7 ± 11.3 years) were scanned on a Philips 3.0T Achieva MRI system at the Sunnybrook Research Institute. They had moderate to severe SVD, either as spontaneous WMHs in the elderly or as Cerebral Autosomal-Dominant Arteriopathy with Subcortical Infarcts and Leukoencephalopathy (CADASIL) in middle-aged individuals. T1-weighted, FLAIR and SWI images were obtained for tissue segmentation, WMHs quantification and venous segmentation, respectively. FLAIR images were acquired with TE/TR=125/9000ms, flip angle=90° and voxel dimensions of $1 \times 1.1 \times 3 \text{ mm}^3$. Imaging parameters for SWI were: TE/TR=41/29 ms, flip angle=15° and voxel dimensions of $0.48 \times 0.48 \times 2.8 \text{ mm}^3$. FLAIR images were automatically segmented using the Fuzzy Lesion EXtractor algorithm to delineate the WMH lesions [6]. SWI images were used to segment veins. This procedure was implemented in MATLAB using a 2-D multiscale vessel-enhancement filtering algorithm [7] that enhanced the vessel-like structures. This was followed by a global thresholding to obtain binary images of venous structures in each axial slice of the SWI images. Lastly, T1-weighted images were segmented to obtain white matter (WM), grey matter (GM) and cerebrospinal fluid masks using FMRIB's Automated Segmentation Tool [8]. The WM region of interest (ROI) was subdivided into normal appearing white matter (NAWM) and WMHs. The periventricular WMH lesion volumes were calculated for each individual and normalized to take into account the periventricular brain volumes. The vein fraction was calculated as the number of vein voxels in an ROI divided by the volume of the ROI.

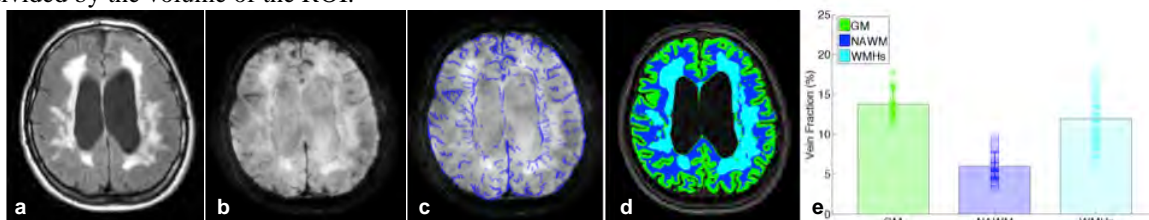


Figure 1: a: Representative FLAIR image co-registered to the SWI space showing WMHs, an indication of small vessel disease. b: The SWI image for the same participant showing the venous anatomy. c: Segmented venous structures overlaid on the SWI image. d: Tissue segmentation delineating GM (green), NAWM (blue) and WMHs (light blue). e: Vein fraction in different tissue ROIs.

Results: Lesion burden is reported as the percentage of the ROI that contains WMHs. An ROI analysis shows a higher vein fraction in the WMH lesion compared to NAWM as seen in Fig. 1.e ($p < 0.001$). The vein fraction in the periventricular WM shows a positive correlation ($p < 0.05$) (Fig. 2).

Discussion and Conclusion: Our findings highlight the importance of investigating the venous vasculature in SVD. The higher vein fraction in WMHs compared to NAWM suggests the possible involvement of the venous vasculature in the etiology of the SVD. In fact, a limited number of pathological studies have identified the involvement of venous vasculature pathologies in WMHs [2, 9 & 10]. The positive correlation between the prominence of vein of the WM and the lesion load confirms our hypothesis and further supports the ischemic nature of SVD.

References: [1] Thompson & Hakim, Stroke, 40(5), 2009 [2] Brown & Thore, Neuropathol Appl Neurobiol, 37(1), 2011. [3] Haacke et al., AJNR, 30(2), 2009. [4] Ge et al., JMRI, 29(5), 2009. [5] Arrigoni et al., AJNR, 32(11), 2011. [6] Gibson et al., JMRI, 31(6), 2010. [7] Frangi et al., MICCAI, 1496, 1998. [8] Zhang et al., IEEE Trans Med Imag, 20(1), 2001. [9] Moody et al., Radiology, 194(2), 1995. [10] Black et al., Stroke, 40(3 Suppl), 2009.

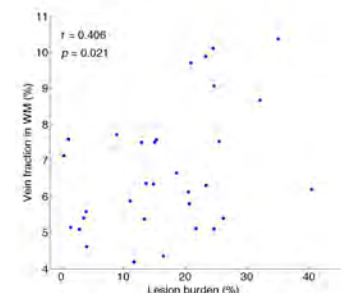


Figure 2: Vein fraction vs. Lesion burden.

Cerebra-WML: A Stand-Alone Application for Quantification of White Matter Lesion

Qian Lu¹, David G. Gobbi¹, Richard Frayne^{2,3}, Marina Salluzzi¹

¹Calgary Image Processing and Analysis Centre (CIPAC), ²Seaman Family MR Research Centre, and ³Department of Radiology and Clinical Neurosciences, Hotchkiss Brain Institute, University of Calgary, Calgary, Alberta, Canada

Background and Purpose

Cerebra white matter lesions (WML) that are commonly observed on T2 MR images of adults are considered to be highly associated with cerebrovascular disease and cognitive impairment [1-2]. To date, although many algorithms have been developed for semi- or fully-automated segmentation of WML [3], there is a need for a robust and practical tool to quantify WML. We have designed and developed a stand-alone GUI application, called Cerebra-WML (Figure 1) that leads the user through a brain segmentation workflow to evaluate brain structures and to quantify WMLs.

Methods

The image-processing pipeline in Cerebra-WML combines information from T1-weighted and fluid-attenuated inversion recovery (FLAIR) images. From the T1-weighted images, the skull is stripped by an implementation of the BET algorithm [4] and the result is corrected and optimized by using a registered atlas [5]. Then the cerebrospinal fluid (CSF) is removed from the brain tissue by using a region-growing method with interactive threshold selection. Both the brain extraction and CSF removal results can be manually edited based on an automatically generated contour. After applying a nonuniformity correction by using N4 bias field correction algorithm [6], the brain tissue is then segmented into gray matter (GM) and white matter (WM) by implementing a K-means classifier. The WML detection can be done through either an automated or a manual process. The automated segmentation method is based on an automatically determined threshold from the histogram of the FLAIR images [7], whereas the manual segmentation method is based on a seeded region-growing algorithm. Segmented WMLs are labeled and lesions within 7 mm of the ventricles are classified as periventricular lesions, others are labeled as subcortical lesions [8]. Different types of lesions are displayed in different colors. Finally, the application automatically generates a quantitative analysis report of the segmented WMLs in a PDF format. The overall processing time for analysis of one brain takes less than 20 minutes if no or little manual adjustments to the segmentation results are required.

The application is implemented entirely in C++. Most algorithms developed in this project are based on or inherit from the Visualization Toolkit (VTK) and the Insight segmentation and registration (ITK) libraries, and the graphical user interface (GUI) implementation is based on Qt toolkit libraries.

Discussion

We have developed a robust application for quantifying WMLs in research trials that allows for reproducibility and traceability of the results. In addition, it generates a standardized report of the processing results. The architectural concept of Cerebra-WML is based on an extensible and reusable approach. Each newly developed algorithm in the software is implemented and tested separately which can be easily reused by other applications. The software was made extensible by integration of GUI widgets with data structure changes. The efficiency and usability of the application were evaluated in a black-box software testing study. A thorough validation of the software is in process.

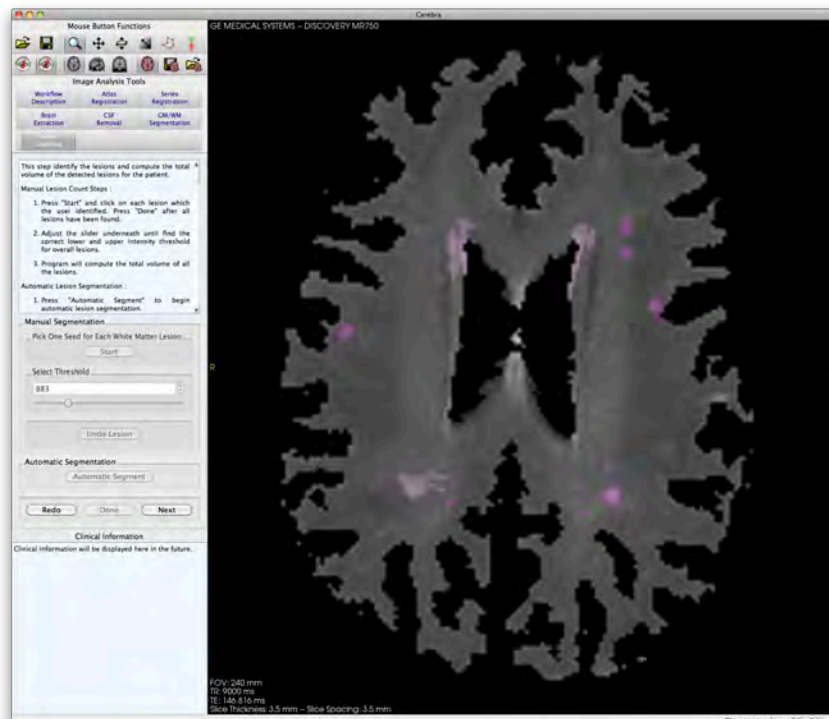


Figure 1: Manual segmentation of WMLs with auto-labeled periventricular lesions (pink) and subcortical lesions (purple).

Keywords

WML, T1-weighted, FLAIR, image processing, software application, algorithm, ITK, VTK, Qt

References

1. V. Srikanth, et al., Stroke 40, 175–180, 2009
2. H. Koga, et al., J. Stroke Cerebrovasc. Dis. 18, 32–37, 2009.
3. J. Ramirez, et al., NeuroImage 54, 963-973, 2011.
4. S.M. Smith, et al., Hum. Brain Mapp. 17, 143-155, 2002.
5. V. Popescu, et al., NeuroImage 61, 1484-1494, 2012.
6. N.J. Tustison, et al., IEEE Trans. Med. Imaging 29, 1310-1320, 2010.
7. R. de Boer, et al., NeuroImage 45, 1151-1161, 2009.
8. F. van der Lijn, et al., NeuroImage 59, 3901-3908, 2012.

Robust 3D MRI Segmentation of Femoral Artery for Morphological Analysis of Peripheral Arterial Disease Plaque Burden

Eranga Ukwatta^{ac}, Jing Yuan^{ac}, Wu Qiu^{ac}, Martin Rajchl^{ac}, Bernard Chiu^d, Aaron Fenster^{abc}

^aBiomedical Engineering Graduate Program, ^bDepartment of Medical Biophysics,

^cRobarts Research Institute, Western University, London, ON

^dDepartment of Electronic Engineering, City University of Hong Kong, Hong Kong

PURPOSE: With the advent of fast and non-invasive 3D black-blood MRI sequences such as, the 3D motion-sensitized driven equilibrium (MSDE) prepared rapid gradient echo sequence (3D MERGE), superficial femoral artery (SFA) vessel wall can be evaluated up to 50 cm coverage (see Fig. 1) for generating morphological measurements of peripheral arterial disease (PAD) plaque burden. This study aims develop and evaluate a fast and precise algorithm for segmentation of the femoral artery outer wall and lumen from 3D MR images.

METHOD AND MATERIALS: Using multi-planar reformatting software, the observer chooses approximate mid points on transverse cross-sections of the artery with an inter-slice distance of 30 mm. The user selected points are then connected using the live-wire algorithm to find the rest of the points on the medial axis. The 3D image is reoriented using the medial axis of the artery obtained. A novel algorithm was then applied to jointly delineate the femoral artery lumen and outer wall surfaces from 3D black-blood MR images in a global optimization manner, while enforcing the spatial consistency of the reoriented MR slices along the medial axis of the femoral artery. Our data set comprised of 650 2D slices extracted from 20 3D MERGE images from 12 subjects. Seven of these subjects were symptomatic with intermittent claudication.

RESULTS: The implementation of the algorithm was parallelized using graphics processing units (GPU), thus required only 1.8 min of total time to segment a 3D MR image compared to 70-80 min of observer time for the manual segmentation. The accuracy of the algorithm is evaluated with respect to the manual segmentation (see Fig. 2) and the algorithm yielded Dice similarity coefficients of $90.9 \pm 5.1\%$ and $87.7 \pm 6.9\%$ and mean absolute distance errors of 0.37 ± 0.2 mm and 0.35 ± 0.2 mm, and maximum absolute distance errors of 0.90 ± 0.3 mm and 0.87 ± 0.5 mm for both the femoral outer wall and lumen. The algorithm also yielded Pearson correlation coefficient of 0.89 (see Fig. 3) for generating vessel wall volume. The reproducibility of the algorithm is computed using repeated segmentations and the algorithm yielded intra-class correlation coefficient of 0.95 and coefficient of variation of 6.69% for generating vessel wall area.

CONCLUSION: The algorithm requires only 1-2% of the time required for manual segmentation, which significantly alleviates measurement burden of observers while maintaining high accuracy and reproducibility.

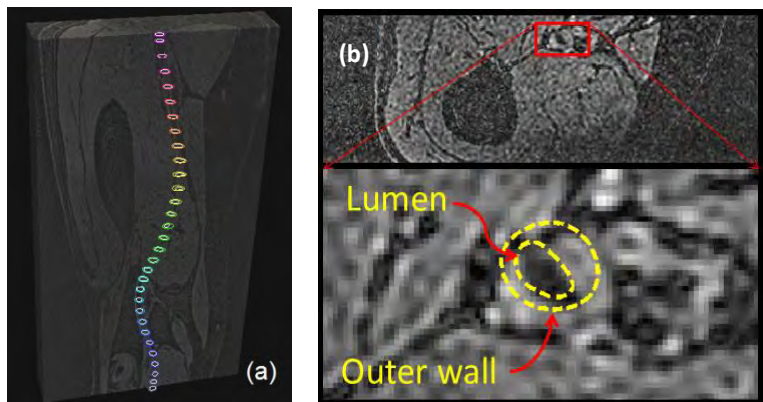


Fig. 1. An example 3D femoral MR image with manual delineations. (a) Longitudinal view and (b) transverse view.

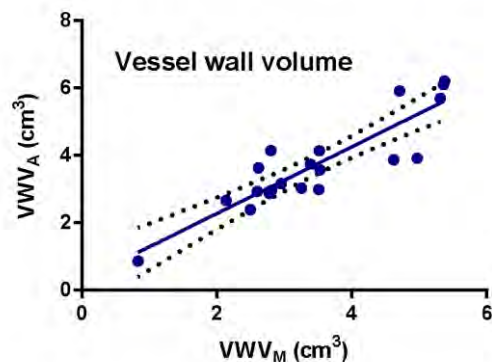


Fig. 3. Correlation plot for the of manual and algorithm-generated vessel wall volume.

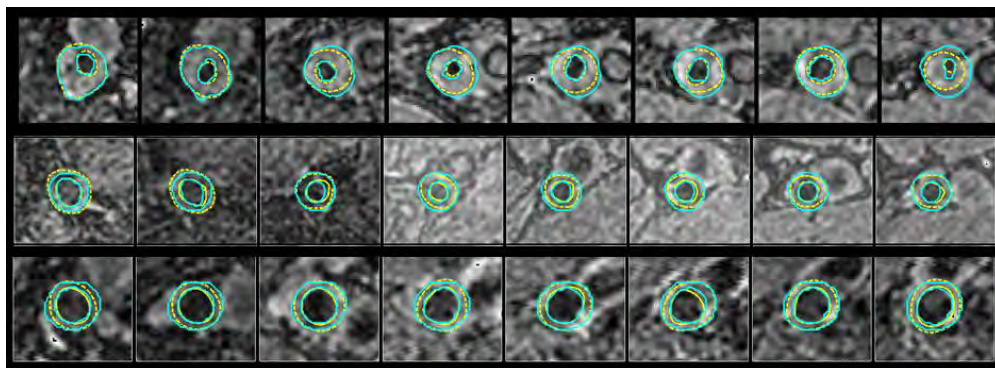


Fig. 2. Slice-wise comparison of the algorithm results (cyan) to manual segmentation (yellow) for the femoral artery wall and lumen boundaries for three 3D MR images. The displayed slices are extracted from the algorithm-generated 3D surface at 30 mm from each other.

Cancer Imaging Network of Ontario CINO

Oral Presentation and Poster Abstracts

Design of Mobile Image Overlay System for Image-Guided Interventions

M. Anand¹, F. King¹, T. Ungi¹, A. Lasso¹, J. Rudan², J. Jayender³, J. Fritz⁴, J. A. Carrino⁴, F. A. Jolesz³, G. Fichtinger^{1,4}

¹Laboratory for Percutaneous Surgery, Queen's University, Canada; ²Department of Surgery, Kingston General Hospital, Canada;

³Surgical Planning Laboratory, Harvard Brigham and Women's Hospital, USA; ⁴Department of Radiology, Johns Hopkins University, USA

Research supervisor: Gabor Fichtinger

BACKGROUND: Static image overlay system was previously proposed [1] to provide accurate transverse image guidance for musculoskeletal interventions of the shoulder, hip and spine [2]. The lack of dynamic tracking resulted in increased calibration time and prone to misalignments due to structural deformation or unintended physical contact with the device. Also the static mounting over the CT/MR [1] imaging system or on floor-mounted-frame over the patient table [2] resulted in limited access to the patient and excluded clinically relevant ranges of motion to the device and the physician. To overcome those limitations, we propose the Mobile Image Overlay System (MIOS).

OBJECTIVES: The aim of the project is to design and develop dynamically tracked mobile image overlay system (MIOS). The design activities include hardware design and prototyping, developing 3D visualization module and integration of optical tracking system for dynamic experimental validation of the system accuracy.

METHODS: MIOS (Fig.1) consists of mirror-monitor configuration called as viewbox similar to [1] and attached to a floor mounted articulated counter-balanced system. The hardware design of the system was done using CREO2.0 CAD tool, MIOS 3D visualization module was developed in Slicer and MicronTracker was the optical tracking system used. Workspace analysis study was conducted [3] to determine the optimal mirror-monitor configuration between 60° and 90° system configurations. Direct and indirect calibration methods [3] were studied for determining the pose of image overlay plane w.r.t physical reference upon the viewbox. Laser source is used to indicate the physical location of image overlay plane and used for guidance of needle insertion [1, 2]. The optical alignment and dynamically tracked alignment were the two solutions studied for laser plane alignment. Slicer 3D visualization module was developed to display the image slice upon the extended monitor depending upon the pose determined using MicronTracker. Passive optical markers are mounted on front and side of the viewbox. Few donut type CT markers are attached upon the patient surface and a passive optical marker is placed beside the patient attached to the patient table. The CT volume of the patient is registered to the passive optical markers using customized optically tracked stylus and the donut type CT markers upon the patient. Optical marker displayed on the monitor is reflected through the semi-transparent mirror forming the virtual marker in the image overlay plane which is directly recognized by the MicronTracker. The pose of the image overlay plane w.r.t physical markers upon the side of the viewbox is determined. The image overlay plane pose w.r.t patient is determined by obtaining the transform between markers attached upon the side of the viewbox and marker beside the patient. Customized phantom using spot type and donut type CT markers were designed for experimental accuracy validation of MIOS.

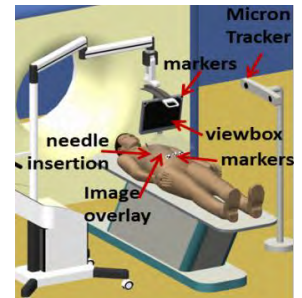


Fig. 1: MIOS concept

DISCUSSION: The optimal configuration for MIOS is i.) 90° mirror-monitor configuration (Fig.2) [3], ii.) direct calibration using MicronTracker [3] (Fig.3) and iii.) dynamically tracked laser alignment method (Fig. 4). The first prototype developed for MIOS is shown in Fig.5. Validation phantom designed for accuracy validation experiment is shown in Fig.6. Based on successful pre-clinical testing of the static image overlay system [2], MIOS promises to become an even more useful tool for image-guided surgical navigations. The next step is to complete the experimental accuracy validation by performing the needle insertion with phantom developed. The potential applications of MIOS are musculoskeletal needle injections, parathyroidectomy, percutaneous nephrolithotomy and percutaneous access to blood vessel.

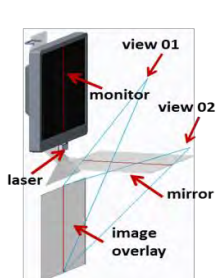


Fig.2: 90° configuration

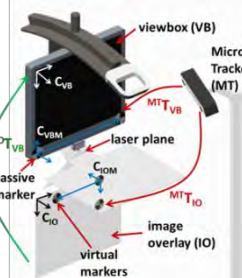


Fig.3 : Direct calibration

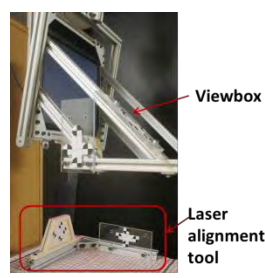


Fig.4: Laser alignment

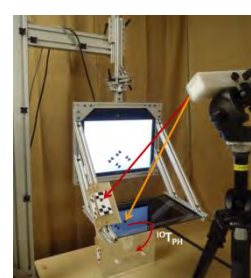


Fig.5: MIOS prototype

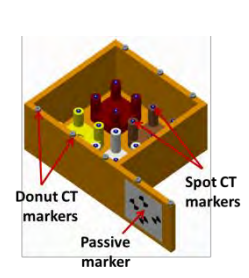


Fig.6: Validation phantom

This work was in part funded by Cancer Care Ontario through Applied Cancer Research Unit and Research Chair in Cancer Imaging grants. This work was funded by the NIH grant number R01 CA118371, USA. The Discovery Grant of NSERC, Canada. National Center for Research Resources and National Institute of Biomedical Imaging and Bioengineering of the NIH USA, through grant numbers P41EB015898 and P41RR019703.

REFERENCES: [1]. Fichtinger et al. "Image overlay guidance for needle insertion in CT scanner," IEEE Transactions on Biomedical Engineering, (52:8), 2005, pp. 1415-1424. [2]. Fritz et al. "Augmented Reality Visualization with Use of Image Overlay Technology for MR Imaging-guided Interventions: Assessment of Performance in Cadaveric Shoulder and hip orthography at 1.5 T," Radiology (265:1), 2012, pp. 254-259. [3]. Anand et al. "Workspace Analysis and Calibration Method for Mobile Image Overlay System used for Image-Guided Interventions," The Hamlyn Symposium on Medical Robotics – 2013.

Proposed Feasibility Analysis of Low Cost Inertial Freehand Ultrasound Position Tracking

Ryan Anderson¹, Andras Lasso², Keyvan Hashtrudi-Zaad¹, Gabor Fichtinger²

¹Department of Electrical and Computer Engineering, Queen's University, Kingston, ON

²School of Computing, Queen's University, Kingston, ON

Background: Ultrasound is a popular medical imaging modality due to its low cost, safety and simplicity of use and setup. Combining ultrasound imaging with 3D tracking technology enables its use for tool guidance, volumetric image reconstruction, and other procedures. Current tracking technology is mainly divided into optical and magnetic trackers. Inertial tracking, common in the aerospace industry, offers another potential tracking solution. Low cost micro-electro-mechanical system (MEMS) based inertial measurement units (IMUs) can potentially provide tracking at costs an order of magnitude below current technology. Few pure MEMS based position tracking solutions exist however, due to inaccuracy and long term drifts in position and orientation estimates from pure MEMS solutions. While MEMS based orientation tracking is accurate and widely used, accurate position tracking requires intermittently updating the position estimate with a ground truth value.

Objectives: Volumetric reconstruction typically requires under 1-3 mm positional accuracy over a couple of seconds, while tool guidance requires this accuracy be maintained at least for several minutes. The aim of this work is to determine IMU position and orientation tracking performance required to meet these needs, and to determine the amount of estimation correction required to maintain accurate long term position estimation.

Methodology: Freehand motion data of volume reconstruction procedures were collected with high accuracy optical position tracker as seen in Figure 1 and a very low cost commercial MEMS-based IMU (1044 PhidgetSpatial 3/3/3, Phidgets, Inc., Calgary, AB). Two tests were performed to determine expected sensor performance. For position tracking with minimal rotation, a static test was performed. Integrating accelerometer data while motionless gives a best case scenario of expected position estimation accuracy over time. The second motion path was a rotation along one axis with minimal translation, typical motion used in a 3D volumetric scan. This case gives a comparison of orientation estimation performance, and can allow for position estimation if the distance from sensor to rotation point is known.

We used a simple motion trajectory and noise model to estimate sensor performance. If a trajectory is analytically chosen, applying the expected noise of a sensor to the acceleration and angular rate of that trajectory and then estimating position and orientation from samples of the noisy data can give an estimation of sensor performance and how quickly it would diverge from useful estimations. A basic test of the validity of this method was tested with the Phidget Spatial sensor. The standard deviation of the Phidget accelerometer sensors was measured. The sensor was kept in a stationary position and white Gaussian noise was used as the noise model. Comparing the accumulation of position error from simulated data created with the noise model to the actual measured error accumulation was used to test the validity of this method.

Orientation sensing was tested with a single axis rotation with minimal translational movement, a typical volumetric reconstruction tool trajectory. Tool orientation was estimated with an algorithm which corrects for gyroscope drift via magnetic and gravitation field measurements, and also by simply integrating the gyroscope measurements.

Results: Preliminary results show that even basic noise modelling matches measured sensor error within an order of magnitude. It does still underestimate noise, which is likely due to the actual sensor noise not falling in a Gaussian distribution. Figure 2 shows error accumulation for a static test over a long time period, which shows the inability of IMUs to maintain long term position estimates. Figure 3 however shows that over the course of a few seconds error does remain within the sub centimeter range. In Figure 4 the orientation estimation error for two methods are shown. While they both suffer from errors, for the test data shown the gyroscope only estimation had a mean error of only 0.1 degrees with standard deviation of 0.5 degrees for the first five seconds.

Conclusions: From the preliminary results, low cost sensors show promise for position and orientation estimation provided an intermittent correction to the position and orientation can be provided at least every 3-5 seconds. Modelling sensor noise show promise for characterization of expected performance. Further work will focus on using improved noise models such as auto-regressive models, and integrating models of corrective measurements to compensate for drift in position and orientation.

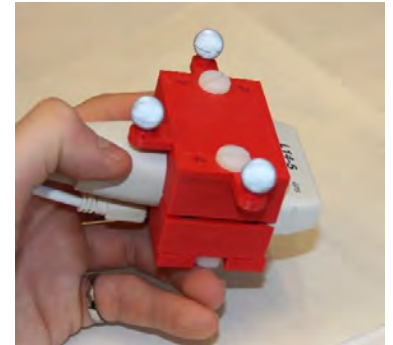


Fig. 1: Optical and Inertial Tracking for Ultrasound

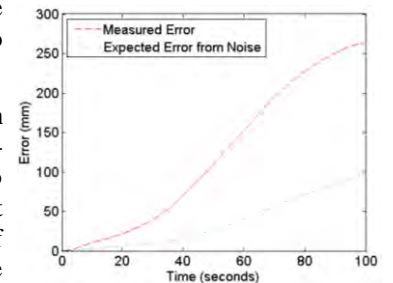


Fig. 2: Long Term Position Error Accumulation

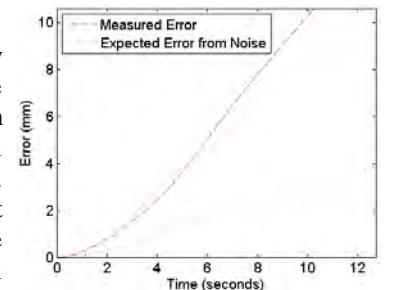


Fig. 3: Short Term Position Error Accumulation

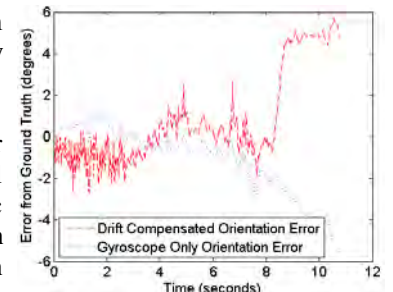


Fig. 4: Orientation Estimation Error for Single Axis Rotation

Effective Dose of Dental Scanning Protocols Using the Sirona Galileos Cone Beam CT Scanner

David Chambers¹, Linada Kaci², Richard Bohay¹, Jerry Battista^{2,3}, Rob Barnett³

¹ *Schulich School of Medicine & Dentistry, Western University, Ontario, Canada*

² *London Regional Cancer Program, London, Ontario, Canada*

³ *Department of Medical Biophysics, Western University, Ontario, Canada*

Introduction: Cone Beam Computed Tomography (CBCT) imaging is now more prevalent in dentistry yet much is unknown with regard to how radiation dose varies between different CBCT scanners and imaging protocols. Establishing the effective dose associated with available imaging protocols will aid in determining the appropriate settings for each patient when considered in the context of image quality sufficient for diagnosis, treatment planning and treatment.

Purpose: To determine the effective dose for a range of imaging protocols using the Sirona GALILEOS Comfort CBCT scanner. These protocols were chosen as a representative sample of those available and include those most often used.

Materials and Methods: Calibrated InLight nanoDot optically stimulated luminescent (OSL) dosimeters (Landauer, Glenwood, Ill) were placed at 26 select sites in the head and neck of a modified, human tissue-equivalent RANDO phantom. These sites represent tissues and organs known for their sensitivity to radiation. Effective dose was calculated using the measured local absorbed doses, accounting for the fractional volume of tissue exposed, and applying the 2007 ICRP tissue weighting factors. In total, 12 different scanning protocols were investigated varying the field of view, mAs, contrast and resolution parameters. One protocol was repeated on three occasions to investigate variability of measurement between identical protocols.

Results: The effective dose calculated for a full maxillomandibular scan at maximum (42) mAs was 141 μ Sv with repeated protocols demonstrating a high degree of reproducibility.

Protocol	Field of View	mAs	Contrast	Resolution	Effective Dose (μ Sv) (2007 ICRP)	Equivalent Days of per Capita Background Radiation
1	Full	14	High	High	48	7
2		28	High	High	95	14
3		42	High	High	142	22
3		42	High	High	140	21
3		42	High	High	141	22
4		42	High	Normal	142	22
5	Maxillary	42	Standard	High	142	22
6		42	Standard	Normal	140	21
7		14	High	High	36	5
8		28	High	High	69	11
9		42	High	High	100	15
10		Mandibular	14	High	High	37
11	28		High	High	74	11
12	42		High	High	107	16

Table 1: Effective Dose (μ Sv)

Conclusions: This study quantifies the effective doses obtained with various CBCT protocols using the Sirona GALILEOS CBCT scanner. Changes to mAs and beam collimation have a significant influence on effective dose. Effective dose varies linearly with mAs as expected; changing mAs from 14 to 42 results in a three-fold increase in effective dose. Collimating to obtain a maxillary or mandibular scan decreases effective dose by approximately 28% and 23% respectively, as compared to a full maxillomandibular scan. Changes to contrast and resolution settings had little influence on effective dose. These parameters likely process the same acquired raw projection data. This study demonstrates the importance of setting individualized patient exposure protocols in order to minimize patient dose from ionizing radiation used for diagnostic or treatment planning tasks in dentistry. The effective doses, however, are considerably lower than those obtained by general diagnostic CT scanning of the head and neck.

Freehand Fluorescence Diffuse Optical Tomography for Head & Neck Surgery

Michael J. Daly,^{1,2} Nidal Muhanna,³ Harley Chan,² Jimmy Qiu,² Robert Weersink,²

Brian C. Wilson,^{2,4} Jonathan C. Irish,^{3,4} and David. A. Jaffray^{1,2,4,5}

¹Institute of Medical Science, University of Toronto, Toronto ON

²TECHNA Institute, University Health Network, Toronto ON

³Department of Surgical Oncology, Princess Margaret Cancer Centre, Toronto ON

⁴Ontario Cancer Institute, Princess Margaret Cancer Centre, Toronto ON

⁵Department of Radiation Physics, Princess Margaret Cancer Centre, Toronto ON

A freehand, non-contact diffuse optical tomography (DOT) system has been developed for multimodal imaging with intraoperative cone-beam CT (CBCT) during minimally-invasive cancer surgery. This translational research system is under investigation for clinical applications in head-and-neck surgery including oral cavity tumour resection, lymph node mapping, and free-flap perforator assessment. The DOT system is configured for fluorescence imaging with indocyanine green (ICG) using a collimated 780 nm laser diode (Thor Labs) and a near infrared CCD camera (PCO Pixelfly-USB). Depending on the intended surgical application, the camera is coupled to either a rigid endoscope (Karl Storz 10-mm) or a compact lens (Edmund Optics 25-mm). A prototype flat-panel CBCT C-Arm acquires low-dose 3D images with sub-mm spatial resolution. A 3D mesh is extracted from CBCT for finite element DOT implementation in NIRFAST (Dartmouth College), with the capability for soft/hard imaging priors (e.g., segmented lymph nodes). A stereoscopic optical camera (NDI Polaris) provides real-time 6D localization of reflective spheres mounted to the laser and camera. Camera calibration combined with tracking data is used to estimate intrinsic (focal length, principal point, non-linear distortion) and extrinsic (translation, rotation) lens parameters. Source/detector boundary data is computed from the tracked laser/camera positions using radiometry models. Target registration errors (TRE) between real and projected boundary points are <2 mm for typical acquisition geometries. Pre-clinical studies using tissue phantoms and small animals are presented to characterize 3D imaging performance as a function of inclusion size, depth, and concentration.

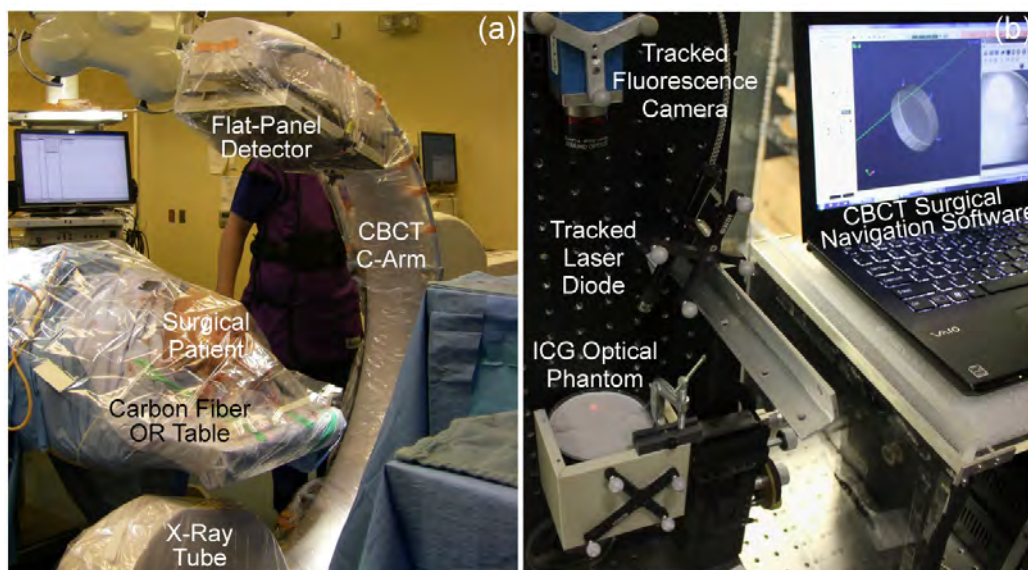


Figure 1. (a) Mobile C-Arm for intraoperative cone-beam CT (CBCT) implemented in a clinical study in head and neck cancer surgery. (b) Benchtop fluorescence diffuse optical tomography (fDOT) system incorporating stereoscopic optical tracking of the laser source and fluorescence camera.

***In-vivo* imaging and signal processing of early radiobiological responses in irradiated tissues by optical coherence tomography**

Valentin Demidov^a and I. Alex Vitkin^{a,b}

^aDept. of Medical Biophysics, ^bDept. of Radiation Oncology, University of Toronto, 610 University Avenue, Toronto, ON M5G 2M9, Canada

Despite the recent major advances in radiation therapy (RT) for cancer treatment, this widely-used treatment has some drawbacks. These include the damage to adjacent normal tissues, numerous side effects, incomplete tumor regression, and variability of outcome. This is compounded by the fact that outcome of therapy is often not known for significant time after the treatment (weeks/months). If some technique for “early” (1-3 weeks) radiation response assessment could be developed, the standard multi-fraction radiotherapy treatment course could be individualized, potentially resulting in more optimal outcomes. Clearly, a need for such a pre-clinical/clinical *in-vivo* imaging method sensitive to RT-induced tissue changes (at clinically relevant dose levels of a few Gy or less) exists, is important and is currently unmet [1].

I have joined the Biophotonics Laboratory (Medical Biophysics, University of Toronto) as a PhD student this fall, and am developing a sensitive OCT-based method to image early radiobiological changes in irradiated tissues. The functional optical coherence tomography (OCT) approach is an emerging non-invasive imaging modality for visualizing subsurface tissue details *in-vivo* at resolutions approaching histology and blood flow details at the microcirculation level. OCT holds promise for detecting functional radiobiological tissue changes induced by RT; indeed, recent initial results from our lab based on OCT speckle analysis support this promise [2, 3].

In OCT, speckle characteristics contain information (related to tissue type, cellularity, response to therapeutic insult) that is not directly visible nor spatially resolved on the images (caused by coherent superposition of light waves scattered by object features that are smaller than the OCT spatial resolution). OCT speckle patterns may indeed be related to underlying tissue viscosity and thus tissue microvasculature visualization (as revealed by its temporal statistics [3, 4]) and to cellular/subcellular tissue microstructure (via its spatial statistics [5] and fractal dimension analysis [6]).

Thus, this study is devoted to development of an objective and quantitative method for analysis of OCT speckle textural properties, suitable for detection of subtle early radiobiological changes present in the image (but otherwise not directly discernible). The preliminary results show that early tissue microstructural and functional (microvascular, compositional) changes induced by ionizing radiation, while not directly visible in *in-vivo* OCT images, may nevertheless be detected by analyzing their textural speckle features.

References

- [1] Yoo DS et al. The role of adaptive and functional imaging modalities in radiation therapy: approach and application from a radiation oncology perspective. (2010) *Semin Ultrasound CT MR*. 31: 444-61.
- [2] Lindenmaier AA et al. Texture analysis of optical coherence tomography speckle for characterizing biological tissues *in vivo*. (2013) *Opt Lett* 38: 1280-2.
- [3] Conroy L et al. Quantifying microvasculature with speckle variance OCT (2012) *Opt Lett* 37: 3180-2.
- [4] Mariampillai A et al. Optimized speckle variance OCT imaging of microvasculature. (2010) *Opt Lett* 35: 1257-9.
- [5] Gossage KW et al. Texture analysis of speckle in optical coherence tomography images of tissue phantoms. (2006) *Phys Med Biol* 51: 1563-75.
- [6] Sullivan AC et al. Fractal analysis for classification of breast carcinoma in optical coherence tomography. (2011) *J Biomed Opt* 16: 066010-6.

A New Three-Component Signal Model to Objectively Select Power Doppler Wall Filter Cut-Off Velocity for Quantitative Microvascular Imaging

Mai Elfarnawany^{1,3,4} and James C. Lacefield^{1,2,3,4}

¹ Biomedical Engineering Graduate Program, ² Departments of Electrical and Computer Engineering and Medical Biophysics, ³ Robarts Research Institute, and ⁴ Biomedical Imaging Research Centre,

Western University

The wall-filter selection curve (WFSC) method was developed to automatically select cut-off velocities for high-frequency power Doppler imaging. Selection curves are constructed by plotting colour pixel density (CPD) as a function of wall filter cut-off velocity. A new three-component mathematical model is developed to guide the design of an online implementation of the method for *in vivo* imaging. The model treats Doppler imaging as a signal detection task in which the scanner must distinguish intravascular pixels from perivascular and extravascular pixels and includes a cost function to identify the optimum cut-off velocity that provides accurate vascular quantification and minimizes the effect of colour pixel artefacts on visualization of vascular structures. The goodness of fit of the three-component model to flow-phantom data is significantly improved compared to a previous two-component model (F test, $p < 0.005$). The improved fit of the new model to the experimental flow phantom data is illustrated in Fig. 1. Simulations using the new model indicate that selection curves should be sampled using at least 100 cut-off velocities to ensure robust performance of the automated WFSC method and determine an upper bound on CPD variability that ensures reliable vascular quantification accuracy, defined as CPD within 5% of the reference vascular volume fraction. Results of the simulations also provide evidence that limiting the selection of the cut-off velocity to a binary choice between the middle and right end of the characteristic interval is sufficient to meet the quantification accuracy goal. The model provides an intuitive, empirical description of the relationship between system settings and blood-flow detection performance in power Doppler imaging.

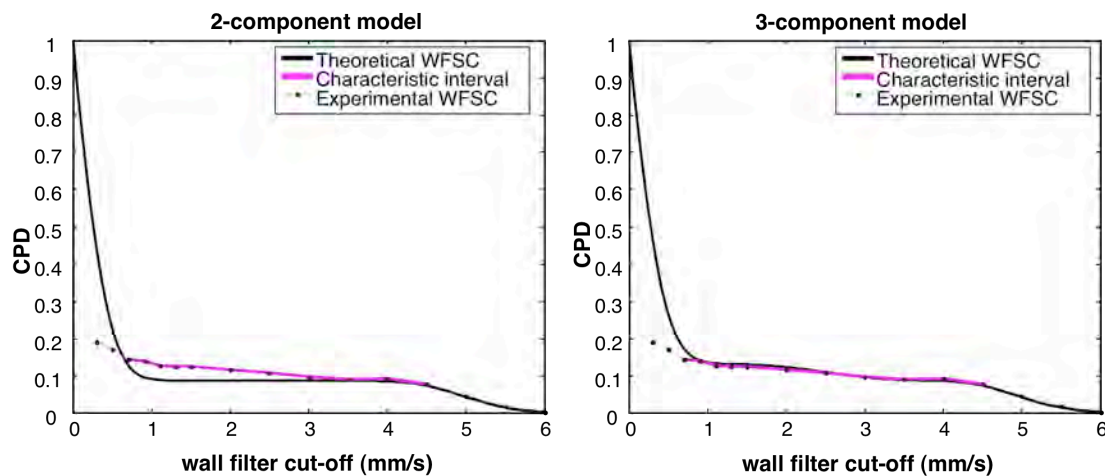


Figure 1. Theoretical wall-filter selection curves (solid lines) fitted to experimental multiple-vessel flow-phantom data (dashed lines) using: (a) original 2-component model and (b) new 3-component model. The detected characteristic intervals are highlighted in violet. The 3-component model fits the sloped interval in the flow-phantom WFSC significantly better than the 2-component model.

Three Dimensional CryoViz™ Cry-Imaging as a Validation Tool for Medical Imaging Modalities

Amanda M. Hamilton, Paula J. Foster, Terry M. Peters

Robarts Research Institute, London, ON, Canada

The CryoViz™ instrument is a cryo-imaging system for three dimensional (3D), microscopic imaging of large samples including whole mice or excised organs. Originally developed in collaboration between BioInVision Inc and Case Western Reserve University, the only unit in operation in Canada is housed at the Robarts Research Institute. Cryo-imaging fills the gap between multiple modalities of whole animal *in vivo* imaging and endpoint histology. By alternating between tissue sectioning and imaging, the instrument generates high-resolution, large field-of-view microscopic images that can be rendered into a representative 3D volume. With both brightfield and fluorescence imaging capabilities, the CryoViz™ can simultaneously collect images of true-colour anatomy and fluorescent entities, thereby enabling both the imaging of anatomic anomalies and the precise localization of fluorescent protein reporters or imaging agents.

Tissue preparation: Whole mice or excised organs are frozen embedded in optimal cutting temperature (OCT) medium by liquid nitrogen freezing. Samples can either be fixed and cryoprotected in increasing concentrations of sucrose (10-30%) or fresh flash frozen. Samples as large as 25 x 11 x 5 cm³ can be imaged in an individual session.

Cryo-imaging: The CryoViz™ system consists of a modified brightfield/fluorescence microscope, a robotic imaging positioner and a motorized cryostat. The microscope is capable of in plane resolutions between 2.4-17.5 μm and cryosectioning can be performed at thicknesses ranging between 5-40 μm. Sectioning and imaging is programmable such that images can be collected for every tissue section or at programmed increments.

Image processing: The CryoViz™ preprocessor software stitches together images corresponding to individual sections to generate large meshed tiff files. Meshed tiff files can be used for registration with 2D images from other image modalities. In addition, the CryoViz™ preprocessor software also aligns the meshed tiffs to generate lda files that can be used to manipulate 3D volumes in two BioInVision-developed, Amira-based software programs.

To date the CryoViz™ instrument at Robarts has been used in the evaluation of animal models, novel imaging techniques and treatment strategies in multiple disease states including cardiovascular disease, obesity and cancer.

Example: Validation of MRI using CryoViz™ imaging: Human JIMT1-BR3-eGFP+ breast carcinoma brain metastases in mouse brain

Green fluorescent protein (GFP)-positive JIMT1-BR3 (human breast carcinoma) cells were injected into the left ventricle of a female nude mouse to enable direct cell delivery to the brain. At approximated one-month post cell injection the mouse was imaged on a 3 Tesla MRI system using a balance steady state free precession (bSSFP) sequence. The mouse was sacrificed post-imaging and the excised brain was fresh flash frozen in OCT. The brain was sectioned and imaged every 20 μm with an in plane resolution image of 6.5 x 6.5 μm². Brightfield and fluorescent images were generated.

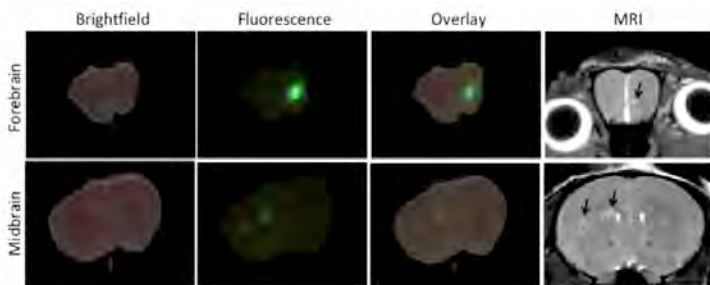


Figure 1: JIMT1-BR3 brain tumours imaged by bSSFP MRI were detected as GFP positive growths in CryoViz™ images.

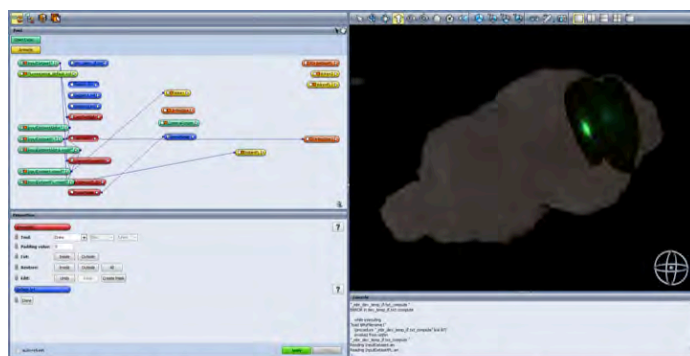


Figure 2: 3D volume datasets can be viewed and manipulated in BioInVision amira-based software programs

In *in vivo* bSSFP MR images, tumours were evident as hyperintense regions within the mouse brain parenchyma (Figure 1, black arrows). When the excised mouse brain was sectioned and imaged by the CryoViz™, JIM1-BR3 tumours were seen as GFP positive regions in fluorescence images (examples in figure 1). Based on the brain morphology evident in brightfield images, GFP positive regions corresponded well to the hyperintense regions seen in bSSFP MR images, thereby validating the MRI technique. An advantage of the cryo-imaging method is that, like the MRI technique, the entire mouse brain volume can be assessed for tumour burden within one imaging session. The time required to accomplish this with traditional sectioning and imaging methods generally necessitates a subsampling of the examined tissue.

Hyperpolarized Xenon-129 MRI for Evaluation of a Continuous Negatively-Applied Pressure (CNAP) Approach for Recruitment of Atelectasis in a Rat Model

Elaine Hegarty¹, Doreen Engelberts², Trevor Wade¹, Krzysztof Wawrzyn¹, Ozkan Doganay¹, Brian Kavanagh², Giles Santyr^{1,2}

¹Robarts Research Institute, London, Ontario ²The Hospital for Sick Children, Toronto, Ontario, Canada

Rationale:

Hyperpolarized noble gas (helium-3 and xenon-129) Magnetic Resonance Imaging (MRI) has been used for anatomical and functional imaging of the lungs [1]. In particular, regions not ventilated with hyperpolarized gas, referred to as defects, can be attributed to unventilated lung. Ventilation defects have been observed in chronic obstructive pulmonary disease, asthma and cystic fibrosis, but have not as yet been used to investigate lung injury, specifically atelectasis resulting from ventilator-induced lung injury (VILI) and subsequent recruitment using ventilation strategies [2]. In this work, a hyperpolarized xenon-129 MRI approach is presented which is compatible with a continuous negatively-applied pressure (CNAP) device and used to investigate the recruitment of lung in a rat model of atelectasis.

Methods:

All procedures followed animal use protocols approved by Western University's Animal Use Subcommittee and were consistent with the guidelines written by the Canadian Council on Animal Care (CCAC). Tracheostomized and anesthetized Sprague Dawley rats were used for this study. Rats were then placed within the MRI system and mechanically ventilated using an MR-compatible ventilator with a tidal volume of approximately 3 mL and 60 breaths per minute. The abdomen of the rat, up to the xyphoid process, was placed within a negative-pressure chamber in order to allow constant negative pressure to be applied. The CNAP device consisted of a plastic vessel forming a tight seal with the rat skin and connected to a negative pressure ventilator (Pegaso V, Dima Italia, Bologna Italy). MRI of the lungs was performed using a two-dimensional fast gradient echo pulse sequence (8 cm FOV, 64x64 matrix, +/- 2kHz BW, 10 Nex, acquired using a variable flip angle) following ventilation using five breaths of hyperpolarized xenon-129.

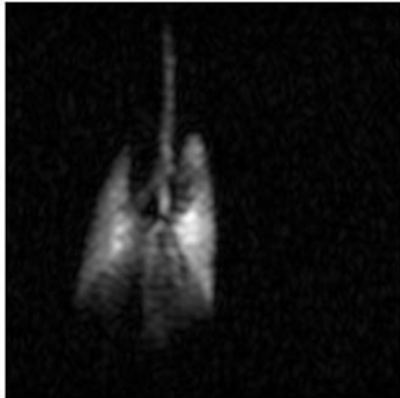


Figure 1: 2D coronal projection image of rat lungs during application of CNAP.

Results and Discussion:

All rats tolerated the MRI and CNAP procedures with no ill effects. Figure 1 shows a representative 2D coronal projection image of rat lungs during application of CNAP. The lack of any significant defects confirms that the rat lungs were well ventilated and image quality is acceptable with the CNAP device in place. The application of this technique to atelectasis and subsequent recruitment of lung using CNAP will be demonstrated and discussed using the methodology described.

References:

- [1] Ouriadov, A. et al., MRM, 2013.
- [2] Chierichetti, M. et al., CCM, 2012.

Acknowledgements: This work was supported by CIHR, NSERC and OPIC.

Linear Object Registration: A Registration Algorithm using Points, Lines, and Planes

Matthew S. Holden, Gabor Fichtinger

Laboratory for Percutaneous Surgery, School of Computing, Queen's University, Kingston, Canada

PURPOSE: Image-guided interventions require medical images to be expressed in the same coordinate frame as physical anatomy. The process of determining the transformation between the image and anatomy coordinate frames is registration. Registration is typically performed using landmarks points with known correspondence and positions known or collected in both coordinate frames [1]. Unfortunately, many devices which must be registered do not have landmark points manufactured on them, so cannot be registered by typical methods; however, most devices have points, lines, or planes on them due to engineering constraints. We propose a registration algorithm which uses points, lines, and/or planes (which we call linear objects) and is guaranteed to converge to a solution close to the global optimum if a unique solution to the registration exists.

METHODS: The proposed algorithm uses the following pipeline: (1) find linear object correspondences between the two coordinate frames using distances to a set of reference points; (2) determine the least-squares centroid of the set of linear objects in each coordinate frame; (3) project the centroid onto each linear object in the coordinate system; (4) use the projected centroids and direction vectors to do traditional point-set registration; (5) use an iterative closest point algorithm to converge to the optimal solution. This algorithm was validated using simulated data and for practical phantom registrations (Fig. 1) where point-set registration results were used as ground-truth. It is implemented as a practical tool for phantom registration in the PLUS software library [2].

RESULTS: The proposed algorithm performs sufficiently well in both simulated and real phantom registrations. With simulated data noise at 1.4mm (the root-mean-square noise associated with our tool tracking system) the algorithm exhibited average rotational error of 0.085° and translational error of 0.21mm, both of which are acceptable in practical scenarios. For real phantom registrations with an ultrasound calibration phantom and a lumbar puncture phantom, the average rotational deviation was 0.66° and the average translational deviation was 1.99mm.

CONCLUSION: The proposed algorithm provides an alternative method for phantom registration if landmark points are unavailable. The algorithm also has potential application to image registration problems, though its efficacy has not been tested for this. Current work involves improving the matching component of the algorithm and optimizing its implementation.

ACKNOWLEDGEMENT: This work was in part funded by Cancer Care Ontario through Applied Cancer Research Unit and Research Chair in Cancer Imaging grants.

[1] Horn, B. K. P., "Closed-form solution of absolute orientation using unit quaternions", Journal of the Optical Society of America, vol. 4, pp. 629-642, Apr. 1987.

[2] PLUS: Public Software Library for Ultrasound Imaging Research, <http://www.plustoolkit.org/>.

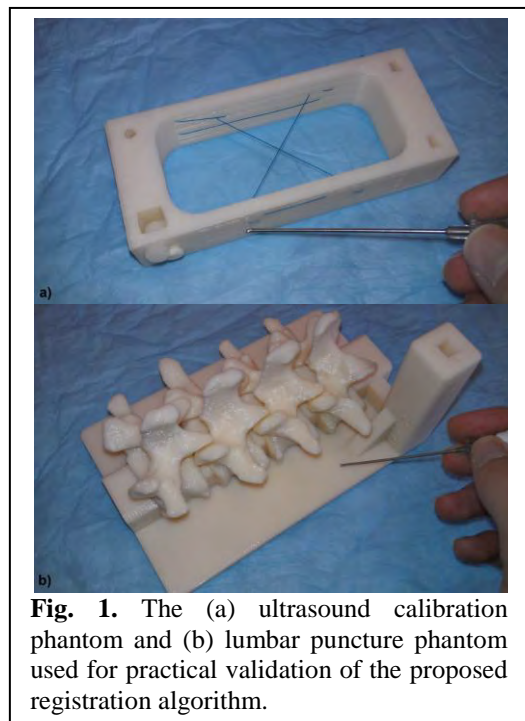


Fig. 1. The (a) ultrasound calibration phantom and (b) lumbar puncture phantom used for practical validation of the proposed registration algorithm.

Image-based 3D replication in metal alloys

David W. Holdsworth,^{1,2,3} Matthew G. Teeter,^{1,2,3} Hristo N. Nikolov,^{2,3} Maria Drangova^{1,2,3}

¹Department of Medical Biophysics, Western University, London, ON

²Imaging Research Laboratories, Robarts Research Institute, London, ON

³Schulich School of Medicine and Dentistry, Western University, London, ON

Introduction: Recent advances in micro-imaging – combined with new techniques for 3D fabrication using additive manufacturing – have provided the opportunity to create complex objects in 3D, which have been previously impossible to build.¹ Micro-computed tomography (micro-CT) devices offer the routine capability for scanning objects with spatial resolution between 50 and 150 μm , and commercially available software utilities provide the capability in post-processing to create 3D computer-aided design (CAD) models directly from the 3D image data. This combination of technologies comes close to realizing the science-fiction concept of the “replicator”, and also can be used to modify, scale, or enhance objects after they have been scanned. We describe the implementation of 3D micro-replication, using a slip-ring micro-CT scanner and a 3D metal printer.

Objectives: The objective of this project is to demonstrate the capability of state-of-the-art 3D fabrication techniques to create complex objects directly from 3D image data. Example micro-CT data has been acquired from a live mouse and post-processed to determine the 3D geometry, in a format that is compatible with rapid prototyping. As a demonstration of capabilities, the skeleton of a mouse is reproduced to scale in solid stainless steel, using selective laser melting (SLM).

Materials and Methods: Image data was acquired from a live mouse (C57Bl6) under isoflurane anesthesia. The micro-CT image was acquired with a high-speed slip-ring scanner (eXplore Ultra, GE Medical Systems) using exposure parameters of 80 kVp and 40 mA during a 16 s acquisition.² This scan protocol provides 3D image data with isotropic 150 μm voxel spacing, over an axial extent of 95 mm. The entire mouse was included within one scan volume, and reconstructed using a conebeam reconstruction algorithm. After reconstruction, grey-scale segmentation was used to select the mineralized skeleton, using a threshold of 300 HU. Post-processing in dedicated 3D acquisition software (Microview 2.2, GE Medical Systems) was used to create a surface model of the skeleton, using a modified marching-cubes algorithm. The 3D surface data was saved as a stereolithographic format file (STL) and imported into a 3D design program (Geomagic) for refinement and correction of erroneous elements. The corrected 3D surface data was then exported to a dedicated 3D fabrication program (Marcam) for preparation of fabrication instructions using SLM.

Fabrication was carried out using a selective-laser melting system (DM 125, 3D Systems), which is capable of manufacturing in a range of metals, including stainless steel, cobalt chrome, titanium, and aluminum alloys.

With this approach, objects are built one layer at a time within an inert argon-atmosphere chamber, using fine metal powder (~40 μm grain size) that is deposited in a 50 μm layer and then fused in place by a 200 W laser with a nominal beam focal spot of 30 μm . The maximum build size for fabrication with this system is 120 x 120 x 125 mm.

Results: The 3D micro-CT image data was acquired with sufficient signal-to-noise ratio to allow automatic greyscale segmentation of the skeleton (Fig. 1a). The resulting STL CAD data was compatible with rapid-prototyping design software, providing layer-by-layer instructions for laser fusion. Fabrication in stainless-steel alloy (316L) resulted in full-scale replication of the original skeleton, with features as fine as 200 μm (Fig. 1b). The finished component contained 16.8 g of metal and required approximately five hours of printing time. Total cost was estimated at approximately \$300 in this case, including materials, operator time and the hourly cost of the SLM printer.

Conclusions: We have demonstrated that it is possible to determine complex 3D geometries using non-destructive micro-imaging and subsequently use this data to produce high-resolution structures directly in metal, using additive manufacturing. Although the object created in this case (a metal murine skeleton) is for demonstration purposes only, it serves to illustrate the complexity of object that can be fabricated, including the possibility of internal channels and manifolds. Applications in medical research include: the creation of complex objects as instructional aids; “reverse-engineering” of complex structures, subsequent to non-destructive evaluation; scaling or modification of physical objects to create functional metal prototypes, such as surgical tools and implants; and the generation of detailed CAD models, based on clay or plastic models. The advent of routine 3D additive manufacturing has enhanced a natural linkage between 3D micro-imaging and rapid fabrication of working prototypes.

1. Stamp R, Fox P, O'Neill W, Jones E, Sutcliffe C. The development of a scanning strategy for the manufacture of porous biomaterials by selective laser melting. *J Mater Sci Mater Med.* 2009; 20:1839-1848.

2. Du LY, Umoh J, Nikolov HN, Pollmann SI, Lee TY, Holdsworth DW. A quality assurance phantom for the performance evaluation of volumetric micro-CT systems. *Physics in Medicine and Biology.* 2007; 52:7087-7108.

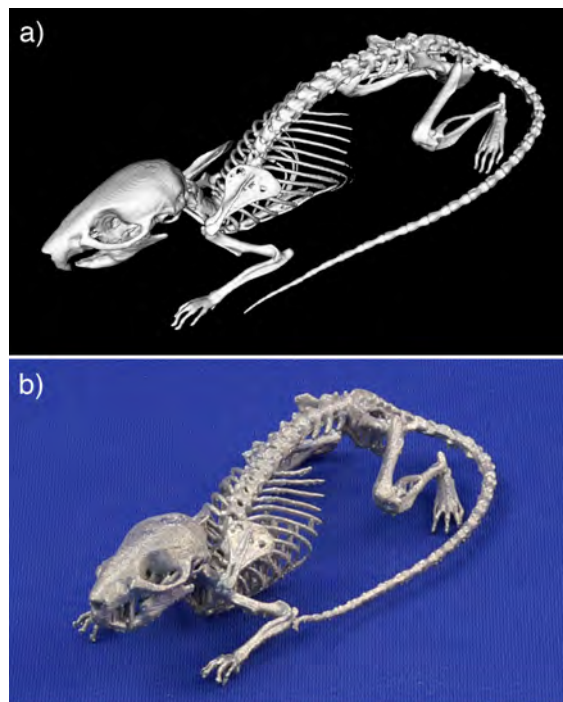


Figure 1: (a) The 3D surface of an adult mouse skeleton, derived from micro-CT image data. (b) the final replicated skeleton, fabricated to scale in stainless steel, using selective laser melting.

Characterization of Prostate Cancer Using RF Time Series Spectrum

F. Imani¹, P. Abolmaesumi², M. Ramezani², S. Nouranian², E. Gibson³, A. Khojaste¹, M. Gaed³, M. Moussa^{3,4}, J.A. Gomez-Lemus^{3,4}, C. Romagnoli^{3,4}, D.R. Siemens⁵, M. Leviridge⁵, S. Chang⁶, A. Fenster³, A.D. Ward³, and P. Mousavi¹

¹Queen's university, Kingston, ON, Canada, farhad@cs.queensu.ca, ²University of British Columbia, Vancouver, BC, Canada, ³Western University, London, ON, Canada, ⁴London Health Science Centre, London, ON, Canada, ⁵Kingston General Hospital, Kingston, ON, Canada, ⁶Vancouver General Hospital, Vancouver, BC, Canada

BACKGROUND: Prostate cancer (PCa) is the most common cancer among men in North America. According to the American and Canadian Cancer Societies, about 262,000 new cases are diagnosed and 33,600 die of PCa annually in North America. Accurate diagnosis and staging of PCa increases the appropriate treatment options including surgery, radiotherapy, cryo- and thermal ablation therapies. The current procedure for PCa diagnosis involves ultrasound-guided core needle biopsy; however, the biopsy procedure is not scaled to individual patients due to the lack of sensitivity and specificity of conventional ultrasound images. Recently our group has proposed a tissue typing approach that uses ultrasound RF time series acquired from a stationary transducer and tissue position over a few seconds. This method has been successfully and effectively used to characterize PCa in *ex vivo* and *in vivo* experiments [Imani'13]. A challenge of this approach has been to exhaustively search for the best combination of features of RF time series that results in high classification accuracies of cancerous regions in the prostate.

PURPOSE: We propose a new approach based on independent component analysis (ICA) to characterize *in vivo* PCa, using RF time series data, without the need for exhaustive search in the feature space.

METHODS: Our method applies ICA to the spectrum of RF time series prior to characterizing PCa. We decompose the spectrum of RF time series to three uncorrelated components; we then use a support vector machine to classify between cancerous and normal tissue regions in a leave-one-patient-out evaluation. RF time series data is collected *in vivo* from seven patients prior to prostatectomy. The gold standard for evaluating the results of PCa characterization is whole-mount histology contoured and graded by a clinician under the advisement of two genitourinary pathologists, all blinded to the *in vivo* imaging. Deformable registration is employed to align the RF time series information with the reference standard histologic contours for every patient. We show that characterization of cancer from a selected group of patients can be effectively extended to an unseen patient using the three independent components of RF time series and support vector machines as a classifier.

RESULTS: The ROC curves for seven leave-one-patient-out evaluations are shown in Fig. 1. The areas under the ROC (AUC) curves using three independent components from ICA for seven subjects, are 0.87, 0.78, 0.91, 0.91, 0.55, 0.79, and 0.84, respectively with an average of 0.81.

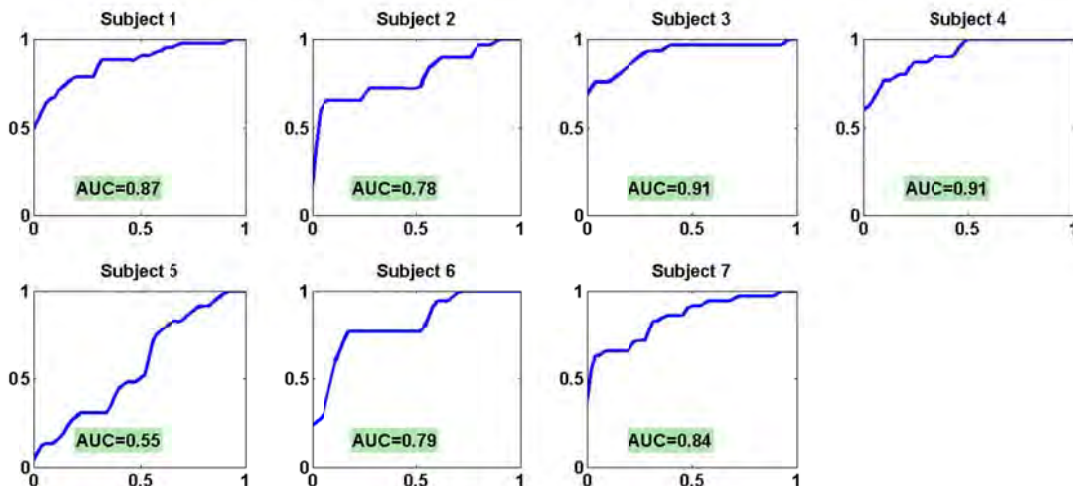


Fig. 1. ROC curves and AUC for seven leave-one-patient-out evaluations.

CONCLUSION: The proposed approach demonstrates the clinical relevance of RF time series for *in vivo* characterization of cancer.

REFERENCES: [Imani'13] F. Imani, P. Abolmaesumi, E. Gibson, A. Khojaste, M. Gaed, M. Moussa, J.A. Gomez, C. Romagnoli, D.R. Siemens, M. Leviridge, S. Chang, A. Fenster, A.D. Ward, P. Mousavi "Ultrasound-Based Characterization of Prostate Cancer: An *in vivo* Clinical Feasibility Study", *MICCAI*, Japan, 2013.

Robust Intra-operative Ultrasound Probe Tracking Using a Monocular Endoscopic Camera

Uditha L. Jayarathne^{1,2}, A. Jonathan McLeod^{1,2}, Terry M. Peters^{1,2}, and Elvis C.S. Chen¹

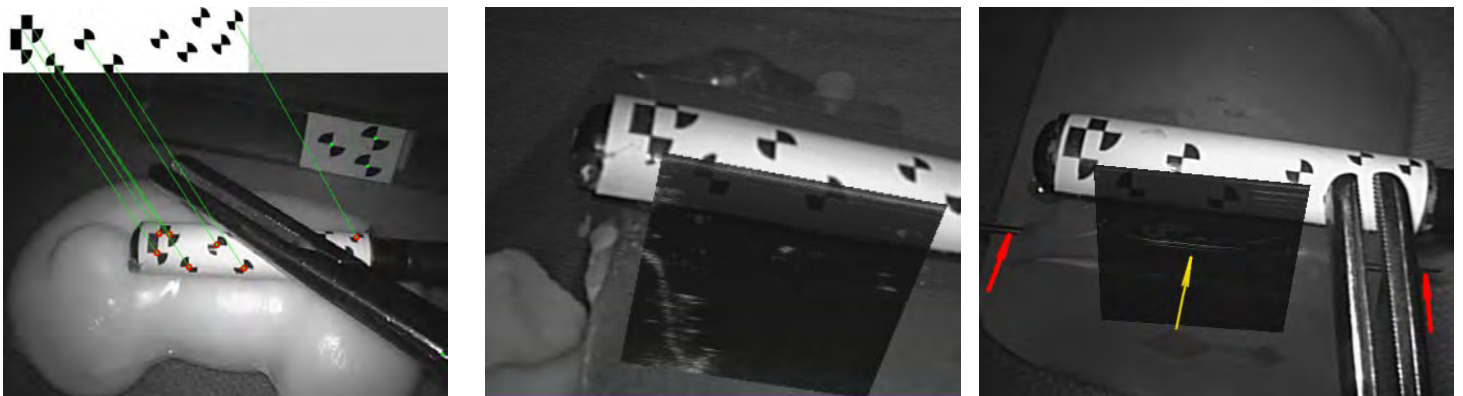
¹Robarts Research Institute, London, Ontario, Canada

²Western University, London, Ontario, Canada

During laparoscopic surgery surgeons use a monocular camera to view the organ surface and intra-operative ultrasound to visualize structures within. In a typical surgical configuration, the endoscopic video and the ultrasound video are displayed to the surgeon separately and in 2D. Therefore, the surgeon has to perform spatial reasoning to mentally map the US image onto the video which may introduce unnecessary risks for critical surgical tasks such as tumor margin delineation.

Navigated endoscopy incorporates a spatial tracking system to infer the pose of the US probe relative to the camera, allowing the US image to be registered to and fused with the video, resulting in an intuitive visualization of US image data. To solve the problem of spatially tracking the US probe with respect to the monocular endoscopic camera, we propose a vision based method that is robust to endoscopic lighting conditions and partial feature occlusions. This approach requires only cosmetic modification to the ultrasound probe, hence it can seamlessly be integrated to the existing OR workflow. The method uses an Extended Kalman Filter based framework to solve both the feature correspondence and pose estimation problems simultaneously in near real-time.

The tracking capability is demonstrated by performing an ultrasound calibration of the visually tracked US probe, using a standard endoscopic camera. Ultrasound calibration resulted in a mean TRE of 2.3 ± 1 mm and the comparison with an external optical tracking system demonstrated a mean FRE of 4.4 ± 3.3 mm between the two tracking systems. The experimental results are comparable to the results one would obtain using a magnetic tracking system.



(a)

(b)

(c)

(a) The proposed method solves for 2D-3D point correspondence even in the presence of spurious and missing features (b) US overlay showing a continuous contour of the outline of the spine phantom (c) US overlay showing the alignment of a needle seen in the US image (in yellow) with its protruding ends (in red).

Unique metabolic and functional profiles in mild and moderate cervical myelopathy

Izabela Kowalczyk, BHSc^{1,2}, Neil Duggal, MD, MSc, FRCS(C)^{2,3}, Robert Bartha, PhD^{1,2}

¹Department of Medical Biophysics, Western University, London, Ontario, Canada

²Centre for Functional and Metabolic Mapping, Robarts Research Institute, Western University, London, Ontario, Canada

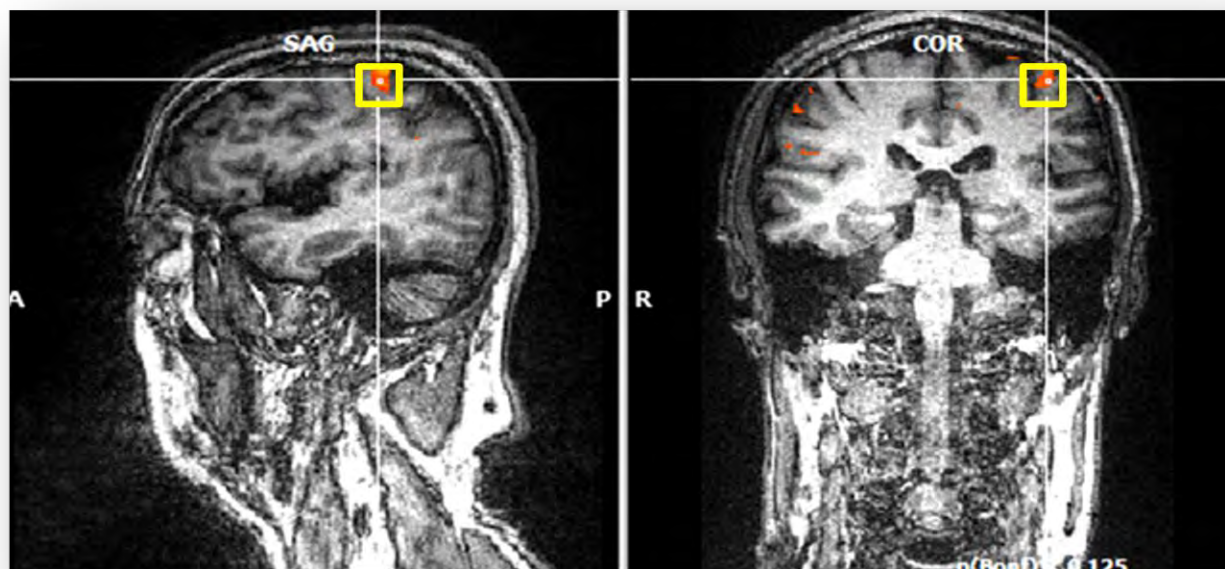
³Department of Clinical Neurological Sciences, University Hospital, London Health Sciences Centre, London, Ontario, Canada

Objective: The management of cervical myelopathy (CM) is guided by severity of symptoms, neurological findings and pre-op imaging studies. The goal of this study was to use proton magnetic resonance spectroscopy (¹H-MRS) and functional MRI (fMRI) to assess the heterogeneity of this unique population and determine whether there are distinct metabolic and functional profiles in the mild and moderate CM groups. We also evaluated how surgical intervention affects the CM groups and their neurological recovery following surgery.

Methods: Twenty-eight patients with CM (15 mild CM and 13 moderate CM) had two separate MRI scans that included MRS and fMRI on a 3.0 Tesla Siemens Magnetom Tim Trio MRI before and six months following surgery. Ten healthy controls underwent two MRI scans six months apart. A spectroscopy voxel was localized on the contralateral side of the greater deficit side in the patient group and on each side of the motor cortex in controls. Patients and controls completed a finger-tapping paradigm with their right and left hand. Volumes of activation (VOA) maps were created and analyzed using BrainVoyager QX. Neurological and functional disability was measured with modified Japanese Orthopaedic Association (mJOA) questionnaires.

Results: There are two important distinctions between mild and moderate CSM groups. Mild CSM had a much lower pre-operative NAA/Cr ratio (1.55 ± 0.46) compared to moderate CSM (1.94 ± 0.27 ; $p=0.02$) which was similar to that of controls. Following surgery, the NAA/Cr in the moderate group dropped to be of similar value as the NAA/Cr in the mild group. The metabolic profile of the motor cortex did not recover, despite significant clinical improvement. The mild group had a larger VOA than controls and moderate CM prior to surgery. Following surgery, the VOA in the mild group decreased while the moderate Cm group showed increases in the VOA in the hand motor area of the cortex. Moderate CM patients show a trend for a correlation between the change in NAA/Cr ratio and the change in clinical myelopathy scores.

Conclusion: NAA and VOA in the motor cortex discriminate between mild and moderate CM patients. It is a possible tool for prediction of recovery in moderate CM. Together with clinical improvement following surgery, these results suggest brain reorganization and recruitment of surrounding cortex as the primary modality for clinical recovery.



The EDoF Method for Improved Linear Contrast-Enhanced Ultrasound Perfusion Quantification via Analysis of First-Order Speckle Statistics

Matthew R. Lowerison,^{1,4,5} M. Nicole Hague,⁶ Ann F. Chambers,^{1,2,5,6} and James C. Lacefield^{1,3,4,5}

Departments of ¹Medical Biophysics, ²Oncology, and ³Electrical & Computer Engineering, ⁴Robarts Research Institute, and ⁵Biomedical Imaging Research Centre, Western University, and ⁶London Regional Cancer Program

CCO - Cancer Imaging Network of Ontario (CINO)

Contrast-enhanced ultrasound (CEUS) serves oncology by imaging tumor blood supply to enable quantification of longitudinal vascular changes and monitoring of treatment responses. Unfortunately, the linear subtraction methods commonly used for preclinical imaging are susceptible to registration errors and motion artifacts that lead to reduced contrast-to-tissue ratios. This presentation proposes a new approach to linear contrast-enhanced ultrasound (CEUS) based on analysis of the temporal dynamics of the speckle statistics during wash-in of a bolus injection of microbubbles. In the proposed method, the speckle signal is approximated as a mixture of temporally varying random processes representing the microbubble signal superimposed onto tissue backscatter in multiple subvolumes within the region of interest. A wash-in curve is constructed by plotting the effective degrees of freedom (EDoF) of the speckle signal as a function of time; the proposed method is therefore named the EDoF method. Images acquired at 18 MHz from a murine mammary fat pad breast cancer xenograft model were processed using gold-standard nonlinear amplitude modulation, conventional linear subtraction, and the proposed statistical method (Fig. 1). The EDoF method of wash-in curve analysis shows promise for improving the robustness of linear CEUS based on reduced frame-to-frame variability compared to conventional linear subtraction time-intensity curves (Fig. 2). The EDoF method also demonstrated higher correlation to nonlinear CEUS for area under curve and three perfusion indices (mean transit time, relative blood flow, and relative blood volume) as well as reduced Bland-Altman bias for the perfusion indices. The conceptual basis of the statistical method implies that EDoF wash-in curves should carry information about vascular complexity that could provide valuable new imaging biomarkers for cancer research.

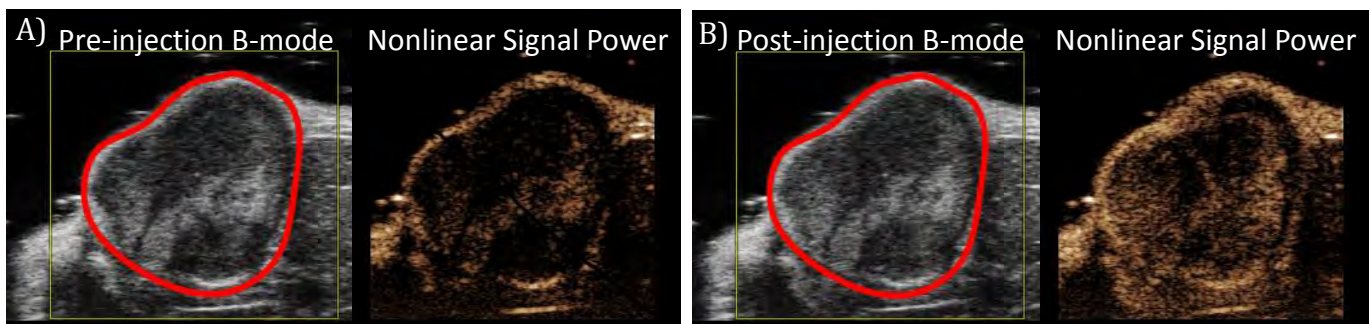


Fig. 1: Sample images of a tumor (35 days post inoculation) taken (a) before and (b) after a bolus of microbubbles

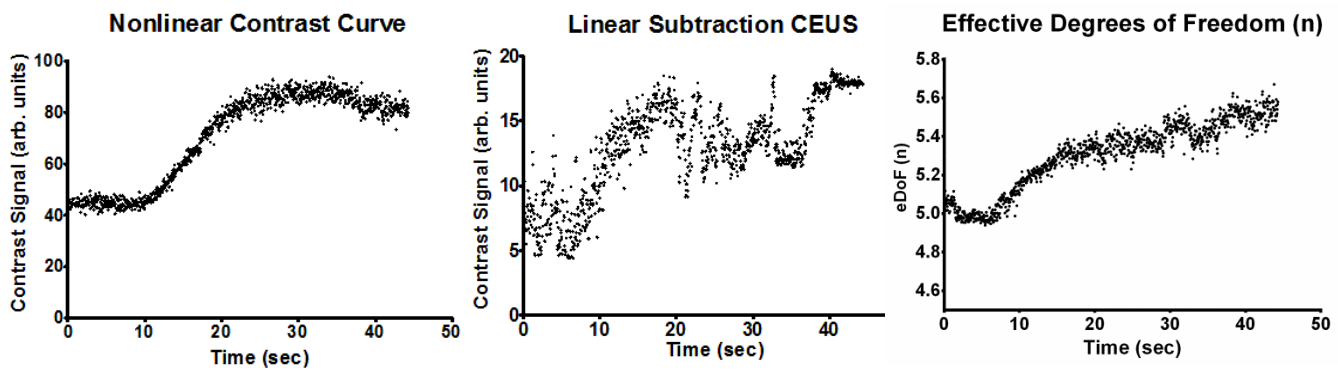


Fig. 2: EDoF processing demonstrates reduced frame-to-frame variability over conventional linear subtraction

Polymeric nanoparticles as a self-regulated drug delivery system to target chemotherapeutic agents to human cancer – preparation and characterization

Amirul I Mallick¹, Jonathan Shloush², Eleonora Bolewska-Pedyczak³ and Jean Gariepy⁴

^{1,3,4} Physical Science Discipline, Sunnybrook Research Institute,
Sunnybrook Health Science Centre,

² Department of Pharmaceutical Science
University of Toronto, Toronto, Ontario, Canada

Polymeric nanoparticles have attracted much interest as multimodal delivery systems as therapeutic and diagnostic agents for targeting human cancers. Their ability to respond and change their physical properties in response to external stimuli, such as changes in temperature, surface charges and pH provide a potential strategy to better target and control release of drugs in the tumour microenvironment. We report the construction and characterization of a self-regulated multimodal nanoparticles consisting of Poly-(N-Isopropylacrylamide) (pNIPAM) co-polymerized with Chitosan to target drugs to human cancers. Chitosan is used as a co-polymer to modulate release of drug as well as the LCST (Lower Critical Solution Temperature) of the composite nanoparticles above normal body temperature to prevent premature release of entrapped molecules. We used Chitosan, (CS) as a naturally occurring biodegradable, pH-sensitive polysaccharide as a co-polymer to ensure the biocompatibility of the present form of nanoparticle. The thermo responsive behavior of pNIPAM -Chitosan nanoparticles exhibit a sharp phase transition in aqueous media above a critical temperature (37°C to 41°C) in which swollen gel particles, collapse and release their contents into the surrounding environment. We speculate that pNIPAM based nanoparticles in their shrunken state would enhance the release of drugs around the tumour neo-vasculature. Our study demonstrates that co-polymerization of pNIPAM with increasing proportion of CS can effectively modulate particle size and net surface charge, enhance the water holding capacity, and effectively entrap and regulate the release of water and macromolecules such as proteins. Further, the *in vitro* kinetics of positively charged pNIPAM-CS based nanoparticle was investigated for targeted delivery. In order to determine the *in vitro* cell uptake, we labeled CS with FAM (fluorescein) to synthesize pNIPAM-CS composite nanoparticles, and incubated with HeLa cells at 4°C and 37°C for 0-4 hrs. Confocal microscopy and FACS analysis clearly show that pNIPAM-CS nanoparticles can effectively enter into the cells at 37°C, suggesting that pNIPAM-CS based nano-particles uptake is energy dependent. Altogether, thermo responsive nature and efficient cellular uptake of present nanoparticles formulation may prove to be a useful tool for temperature guided cancer therapy or diagnostic approach.

Key words: Polymeric nanoparticles, Poly(*N*-isopropylacrylamide), Chitosan, EPR, biocompatible.

Magnetic resonance imaging-targeted, 3D transrectal ultrasound-guided fusion biopsy for prostate cancer: quantifying the impact of needle delivery error on diagnosis

Peter R. Martin¹, Derek W. Cool^{2,4}, Cesare Romagnoli², Aaron Fenster^{1,2,4}, Aaron D. Ward^{1,3}

Departments of ¹Medical Biophysics, ²Medical Imaging, ³Oncology; ⁴Robarts Research Institute; The University of Western Ontario

Background: Magnetic resonance imaging (MRI)-targeted, 3D transrectal ultrasound (TRUS)-guided “fusion” prostate biopsy intends to reduce the ~23% false negative rate [1] of clinical 2D TRUS-guided sextant biopsy. Although it has been reported to double the positive yield [2], magnetic resonance imaging (MRI)-targeted biopsies continue to yield false negatives [3]. Therefore, we propose optimization of biopsy planning, according to the clinician’s desired probability of sampling each tumour. This optimizes needle target positions within each tumour and accounts for uncertainties due to guidance system errors, image registration errors, and irregular tumour shapes. By assuming that the overall RMS needle delivery error (*RMSE*) can be modeled using a Gaussian distribution, we added the measured uncertainties of the guidance system in quadrature and considered an estimated *RMSE* = 3.5 mm for contemporary MRI-targeted fusion biopsy systems.

Objectives: To (1) estimate the probability of obtaining a tumour sample in one biopsy, given total system needle delivery error; (2) investigate the effect of spherical tumour assumptions on estimated probabilities; and (3) investigate the effect of axial-direction error on perceived tumour burden.

Methods: T2-weighted, dynamic contrast-enhanced T1-weighted, and diffusion-weighted prostate MRI and 3D TRUS images were obtained from 49 patients. A radiologist and radiology resident contoured 81 suspicious regions, yielding 3D tumour surfaces that were registered to the 3D TRUS images using an iterative closest point prostate surface-based method to yield 3D binary images of the suspicious regions in the TRUS context. The probability *P* of obtaining a sample of tumour tissue in one biopsy core was calculated by integrating a 3D Gaussian distribution over each suspicious region domain. As previous work in this problem domain has been conducted under the assumption of spherical tumour shape [4], we repeated the procedure using equal-volume spheres corresponding to each tumour sample, and compared results with those obtained using real tumour contour shapes. We also investigated the effect of probe-axis-direction error on measured tumour burden by studying the relationship between the RMS error and estimated percentage of an 18 mm biopsy core that would contain tumour tissue. This experiment was performed on the 55 tumours that would produce a percentage core involvement $\geq 50\%$ with ideal targeting, hence making these tumours candidates for treatment by the Johns Hopkins criteria [5]. We determined the number of tumours that would incorrectly have an observed percentage core involvement $< 50\%$ for a range of different values of axial error, leading to potential misclassifications as candidates for active surveillance.

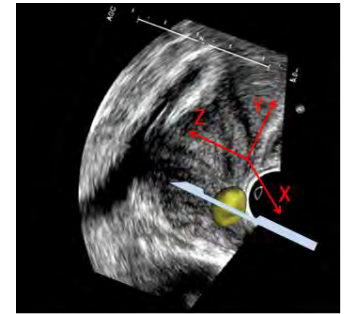


Fig. 1: MRI-defined tumour registered to 3D TRUS, showing simulated positioning of the biopsy needle at the centre of the tumour volume.

Results and discussion: An MRI-defined prostate tumour illustrating simulated positioning of the biopsy needle is shown in Fig. 1. We calculated *P* for each tumour, for *RMSE*s of 1 to 6 mm (Fig. 2 left). We observed that given a 3.5 mm *RMSE* for contemporary fusion biopsy systems, $P \geq 95\%$ for 21 out of 81 tumours. We determined that for a biopsy system with 3.5 mm *RMSE*, *one cannot expect to sample tumours of approximately 1 cm³ or smaller with 95% probability with only one biopsy core.* Similarly, we determined that *a biopsy system would need to have a RMS needle delivery error of no more than 1.6 mm in order to sample 95% of tumours with one core.* Fig. 2 (middle) shows that an assumption of spherical tumour shape led to a consistent overestimation of tumour sampling probabilities. Our experiments indicated that the effect of axial-direction error on the measured tumour burden was mitigated by the 18 mm core length for $RMSE \leq 4$ mm, but more than half are misclassified for $RMSE \geq 5.5$ mm as depicted in Fig. 2 (right).

Conclusions: These observations support our perspective that some tumours of clinically significant sizes may require more than one biopsy attempt in order to be sampled during the first biopsy session. Optimized planning of within-tumour targets for MRI-3D TRUS fusion biopsy could support earlier diagnosis of prostate cancer while it remains localized to the gland and curable.

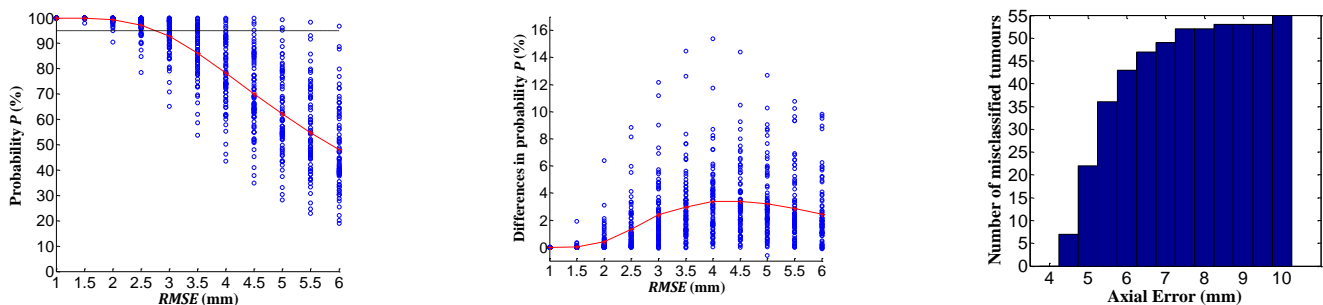


Fig. 2: (Left) Probability of sampling each tumour in one biopsy attempt vs. overall RMS error of biopsy system, red curve is the mean of *P*, dashed line indicates $P = 95\%$. (Middle) Probabilities of a positive core sample with no spherical tumour assumption, subtracted from the probabilities of a positive core sample under the spherical assumption; red curve is the mean difference. (Right) Histogram of tumours incorrectly classified as $< 50\%$ core involvement due to axial error in biopsy needle delivery.

[1] Rabbani, F. et al., J Urol 159(4), 1998

[2] Cool, D. et al., LNCS 6963, 2011

[3] Engehausen, D. et al., TSWJ, DOI: 10.1100/2012/975971, 2012.

[4] van de Ven, W.J. et al., Eur Radiol 23(5), 2013

[5] Epstein, J.I., J Urol 186(3), 2011

Construction of an Attenuation map for mMR Breast coil

John C. Patrick^{1,2,4}, Aaron So^{2,5}, John Butler², Terry Thompson^{1,2}, Frank Prato^{1,2}, Stewart Gaede^{1,2,4}.

(1) Department of Medical Biophysics, Western University, (2) Imaging, Lawson Health Research Institute,

(3) Diagnostic Imaging St Joseph's Health Care London (4) London Regional Cancer Program

(5) Imaging Laboratories - Robarts Research Institute

Research Supervisor: Dr. Stewart Gaede

Breast cancer is a complex disease that will affect 1 in 9 Canadian women during their lifetime. It is estimated that in 2013, around 23000 Canadian women and 200 Canadian men will be diagnosed with breast cancer. Of those, an estimated 55 men and 5100 women will die from it. Thanks to improvements in screening, detection and treatment the 5 year survival rate for men is about 80% and 88% for women. Using the sensitivity of MRI with the selectivity of PET, PET/MRI combines anatomical and functional information within the same scan and could help with early detection in high-risk patients. Breast imaging with MRI requires a breast radiofrequency coil for transmitting energy and receiving signal but they attenuate PET signal. To correct for this PET attenuation, a mapping of material densities or a μ -map of the breast coil must be created and incorporated into the PET reconstruction process. Siemens' four channel breast coil for the Biograph mMR is built on a rigid frame and fixed to the patient bed. This allows us to link a hardware μ -map to a position relative to the patient bed location for PET reconstruction. Several methods have been proposed for building hardware attenuation μ -maps including conventional CT and Dual energy CT. These methods can produce high resolution images based on the electron densities of materials that can be converted into mappings of linear attenuation coefficients. However, imaging hardware containing metal components with photons in the kV range is susceptible to metal artifacts. These artifacts can compromise the accuracy of the resulting μ -map and PET reconstruction. We propose a method for calculating hardware μ -maps based on megavoltage imaging with a 6MV linear accelerator that has been detuned for imaging with a mean photon energy of 1.5MV. In this study bottles of a known geometry with an even distribution of F18 were placed in the breast coil for imaging. Then a comparison of signal homogeneity between reconstructions based on the different hardware μ -map construction methods was made. Preliminary results from PET reconstructions with our method show a possible 6% improvement when compared to the existing conventional CT-based reconstructions currently available.

Development and Evaluation of a Needle Deflection Estimation Method

Hossein Sadjadi^{1,2}, Keyvan Hashtrudi-Zaad², Gabor Fichtinger¹

¹Laboratory for Percutaneous Surgery, Queen's University, Kingston, Canada

²BioRobotics Research Laboratory, Queen's University, Kingston, Canada

Purpose: Many diagnostic and therapeutic interventions require accurate needle placement. However, complex behavior of the needle within biological tissue poses a major challenge, particularly when deflection of the needle exacerbates targeting error. Accurate estimation of needle deflection can help compensate for placement errors before and during insertion. Numerous mechanical models have been proposed to estimate needle deflection in soft tissue. However, these models perform rather poorly in clinical circumstances, as they demand precise prior quantification of the deflection model parameters, including tissue properties, which is not feasible in clinical settings. We suggest that the effect of parameter quantification uncertainty can be mitigated by integrating limited additional position measurements taken directly from the needle [1]. We investigate the accuracy of this approach through extensive simulation and phantom experiments.

Methods: We use Kalman filters to combine a kinematic needle deflection model with the position measurements of the needle base and tip taken by electromagnetic trackers. One position sensor is installed on the needle base and estimates the needle tip position indirectly using the kinematic needle deflection model. Another position sensor is installed on the needle tip and estimates the needle tip position through direct, but noisy and imprecise measurements. Kalman filters are then employed to fuse the position measurements with the deflection model to provide an accurate real-time estimate of the needle tip position [2]. The experiments use prostate brachytherapy needle insertion procedures to explore the capabilities of the deflection estimation approach. A total of 21 beveled tip, 18 ga, 200 mm needles were manually inserted at various speeds through a template and towards different targets distributed within 3 deformable soft tissue mimicking PVC prostate phantoms with varying stiffness (soft, standard, and rigid) representing inter-patient variability [3]. The needle deflection was modeled as a kinematic quadratic polynomial. Parameters of the deflection model were identified and perturbed to simulate uncertainties in model parameters. The tracked positions of both the needle tip and base were then fused recursively with the deflection model using a Kalman filter (KF) and an extended Kalman filter (EKF) to improve on the needle tip position estimation accuracy. The estimation results were subsequently validated using ground truth obtained from C-arm fluoroscopy images.

Results: During the experiments, the manual insertion speed ranged from 8 to 34 mm/s, the needle deflections ranged from 5 to 8 mm at an insertion depth of 76 mm, and the elastic modulus of the soft tissue ranged from 50 to 150 kPa. The reliability and robustness of the estimation method was verified within these ranges. Furthermore, compared to the standard phantom, it was observed that on average, needles deflected 23.61% less in the soft phantom and 9.72% more in the hard phantom. When compared to purely model-based estimation, we observed a reduction of needle tip estimation error by $52 \pm 17\%$ (mean \pm standard deviation) and the cumulative deflection error (CDE) by $57 \pm 19\%$ in the 21 insertions.

Conclusion: In general, estimation methods based exclusively on needle deflection models normally include some degree of uncertainty due to the error in the model parameter quantification. Similarly, direct observations of the needle tip contain some degree of uncertainty due to the measurement noise. As a result, statistical sensor fusion techniques, such as Kalman filters can help improve the estimation accuracy. The results of this work demonstrate significant improvement in needle deflection estimation and suggest potential clinical applicability in the guidance of needle placement medical interventions. We will therefore continue to examine the performance of this method using alternative needle deflection models and expand the experimental validation to a wider range of clinical applications.

[1] H. Sadjadi, K. Hashtrudi-Zaad and G. Fichtinger, "Needle deflection estimation using fusion of electromagnetic trackers," EMBC, 2012.

[2] H. Sadjadi, K. Hashtrudi-Zaad and G. Fichtinger, "Fusion of electromagnetic trackers to improve needle deflection estimation: simulation study," TBME, 2013.

[3] H. Sadjadi, K. Hashtrudi-Zaad and G. Fichtinger, "Needle Deflection Estimation: Brachytherapy Phantom Experiments," IJCARS, submitted for publication.

This work was in part funded by Cancer Care Ontario through Applied Cancer Research Unit and Research Chair in Cancer Imaging grants.

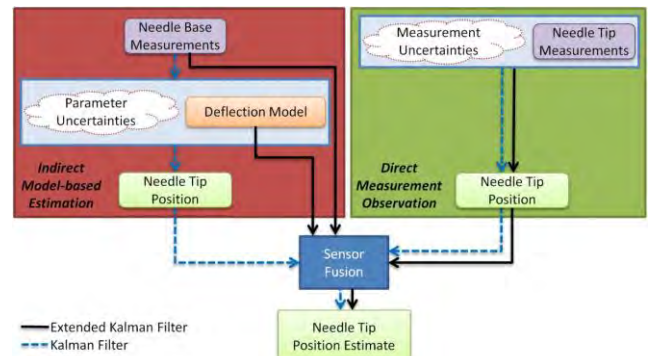


Fig. 1: To accurately estimate the needle tip position, KF fuses the direct needle tip observations with the model-based tip estimations, whereas EKF combines the deflection model with both the needle base and tip observations.

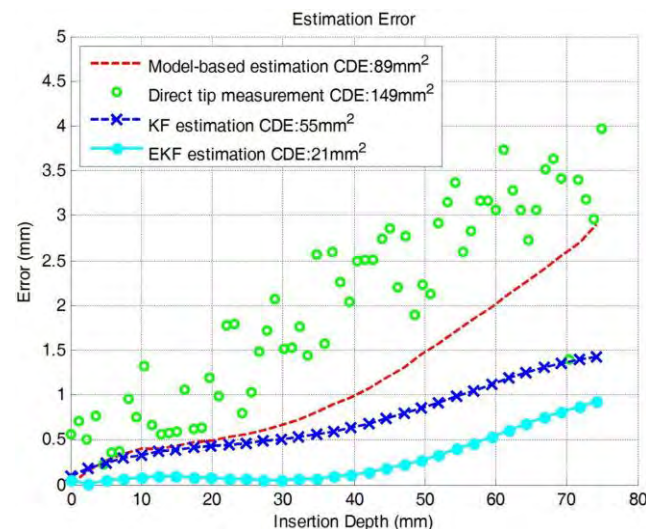


Fig. 2: Comparison of needle deflection estimation errors at various insertion depths during a sample insertion.

Accuracy and variability of tumour burden measurement on multi-parametric MRI

Mehrnoush Salarian¹⁹, Eli Gibson^{1,2}, Maysam Shahedi^{1,2,9}, Mena Gaed³, José A. Gómez³, Madeleine Moussa³, Cesare Romagnoli⁴, Derek W. Cool^{2,4}, Matthew Bastian-Jordan⁴, Joseph L. Chin^{5,7}, Stephen Pautler^{5,7}, Glenn S. Bauman^{5,8,9}, and Aaron D. Ward^{1,5,8,9}
¹Biomedical Engineering Graduate Program, ²Robarts Research Institute, ³Departments of Pathology, ⁴Medical Imaging, ⁵Oncology, ⁶Surgery, ⁷Urology, ⁸Medical Biophysics, The University of Western Ontario; ⁹London Regional Cancer Program, London, Canada

Purpose: Prostate tumour volume (TV) can inform prognosis and treatment selection, including an assessment of the suitability and feasibility of focal therapy [1]. Multi-parametric magnetic resonance imaging (MPMRI) is showing promise for prostate cancer detection. We investigated the accuracy and inter-sequence variability of TV estimation via separate contouring of 3-Tesla T2-weighted (T2W), dynamic contrast-enhanced (DCE), and apparent diffusion coefficient (ADC) images using a histologic reference standard.

Methods: Three observers assessed the MPMRI from 10 patients and delineated lesions separately on the T2W, DCE, and ADC images. A clinician under the supervision of two genitourinary pathologists, all blinded to the MRI, contoured and graded all lesions on each histology image. On MPMRI, TV was calculated as the number of voxels within each region, multiplied by the voxel volume (mm^3). On histology, the tumour volumes were measured by a typical planimetric technique (multiplying the cross-sectional area of each tumour by the inter-slide spacing). Based on our previous work [2], we linearly adjusted these TVs (Fig. 1a) to reflect TVs enclosed by smoother surfaces (Fig. 1b) determined by a level set-based interpolation; such surfaces may better agree with 3D tumour contours (Fig. 1c).

Results: The aggregate measurements of MPMRI tumour volume for each tumour are shown in Fig. 2. Note that there was a different number of observer-detected tumours for each pulse sequence (horizontal axes of Fig. 2). Overall, the MPMRI tumour volumes were overestimates of the histology tumour volumes, with the ADC maps providing the closest estimates and the DCE volumes providing the best correlation with histology volumes. The overall inter-sequence variability (standard deviation of volume) given by pooling all of the observers was 30 cm^3 ; detailed results are given in Fig. 3 for the six tumours that were detected on all sequences by all observers. With the exception of one tumour, the average volume estimates on DCE were lower than those for T2W and ADC.

Conclusions: Prostate TVs estimated based on MPMRI consistently overestimated histological reference TVs. We speculate this may be due to surrounding cancer-mimicking confounders such as prostatic intraepithelial neoplasia; further investigation is required in this area. TV estimates on DCE MRI and the ADC maps provided the lowest inter-observer variability and the lowest volume estimation error, respectively.

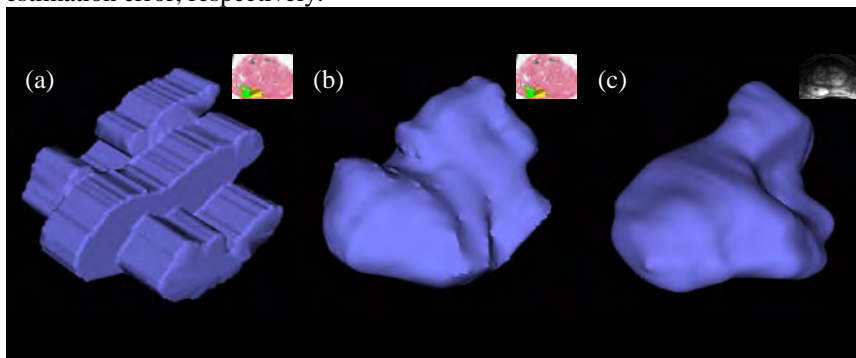


Fig. 1: Histologic tumour volume determined by (a) planimetric and (b) level set-based interpolation techniques. (c) Corresponding tumour surface from MRI contours.

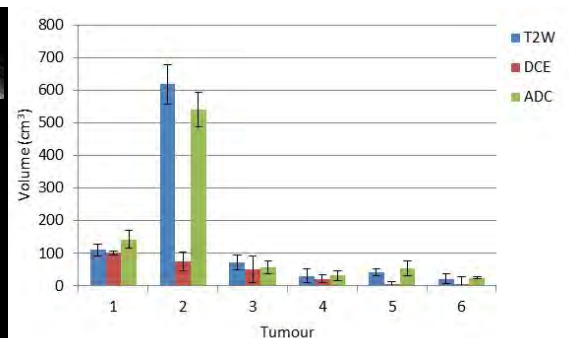


Fig. 3: Mean \pm std. tumour volume across all observers for each sequence.

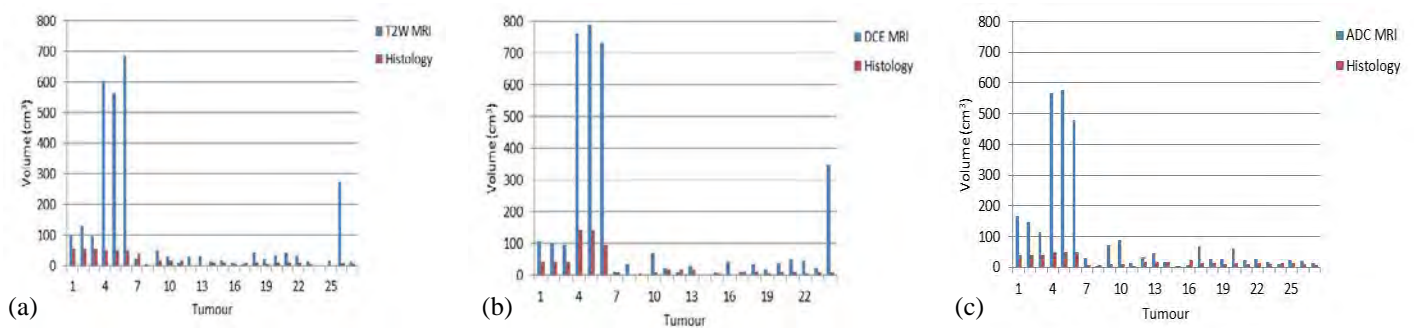


Fig. 2: MPMRI and histology tumour volume estimates for (a) T2W, (b) DCE, (c) ADC.

[1] Egevad L *et al.*, *Mod Pathol* 24(1), 2011.

[2] Salarian M *et al.*, *SPIE Medical Imaging*, 2014.

Quantifying the Relationship between Optical Coherence Tomography Speckle Decorrelation Time and Temperature in Tissue-Mimicking Suspension Phantoms

Subaagari Seevaratnam¹, Mashal Farid¹, Amitpal Bains¹, Golnaz Farhat^{2,3}, Michael C. Kolios^{1,2} and Beau A. Standish¹

¹Department of Electrical and Computer Engineering, Ryerson University, Canada

²Department of Medical Biophysics, University of Toronto, Canada

³Imaging Research, Sunnybrook Health Sciences Centre, Canada

There are a number of cancer therapies that induce temperature changes in benign and malignant tumors to trigger cell death. However, lack of feedback with respect to the local temperature of treated tumor regions poses a limitation in the efficiency of such procedures. Advancements in optical technology, such as: optical coherence tomography (OCT) and fiber Bragg gratings (FBG), demonstrate the capability of measuring the local temperature of these treated tumor regions. Temperature studies were conducted on phantoms fabricated with polystyrene microsphere (average diameter of 0.7 μm) and glycerin, which mimic the optical properties of tissue. OCT images within the vicinity of the FBG temperature monitored regions were obtained for temperature conditions ranging from 25°C to 60°C at 5°C intervals (generated via ~ digital hot plate). The pixel intensity fluctuation in the OCT images for duration of time was monitored within a region of interest. The corresponding autocorrelation function was computed and their respective speckle decorrelation time were also measured and quantified to detect the polystyrene microspheres' response to temperature changes. The preliminary results are promising in establishing a predictable temperature-response trend and in the future these techniques will be extended to monitor temperatures changes in tissue during therapy. Clinical benefit can be achieved once these optical techniques are used to evaluate the temperature-derived biological response of tissue and provide a feedback mechanism to improve treatment efficacy.

Tracked ultrasound calibration studies with a phantom made of LEGO® bricks

Marie Soehl, Ryan Walsh, Adam Rankin, Andras Lasso, Gabor Fichtinger
Laboratory for Percutaneous Surgery, Queen's University, Kingston, ON, Canada
Consortium research supervisor: Gabor Fichtinger

PURPOSE: Real-time tracked ultrasound imaging is a non-invasive and safe approach to facilitate needle-based interventions such as biopsy, drug delivery and surgical ablation. These procedures require a degree of accuracy maintained by an accurate and consistent spatial and temporal calibration that relates the image pixels of the ultrasound to the coordinate system of the tracked probe. In this study, spatial calibration of tracked ultrasound was compared by using a calibration phantom made of LEGO® bricks [1] and two 3-D printed N-wire phantoms [2].

METHODS: The accuracy and variance of calibrations were compared under a variety of operating conditions. Twenty trials were performed using an electromagnetic tracking device with a linear probe and three trials were performed using varied probes, varied tracking devices and the three aforementioned N-wire phantoms shown in figure 1. The accuracy and variance of spatial calibrations found through the standard deviation and error of the 3-D image reprojection were used to compare the calibrations produced from the phantoms.

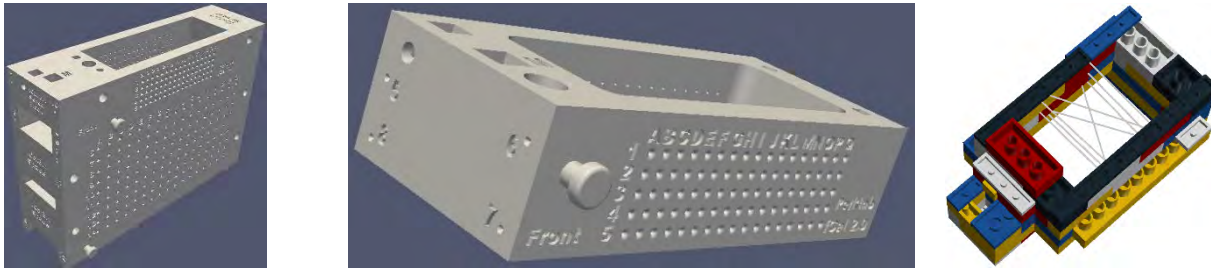


Figure 1. LEFT: fCal-3.1 calibration phantom (Carbajal *et al.* 2013). MIDDLE: fCal-2.0 calibration phantom (Carbajal *et al.* 2013). RIGHT: LEGO® calibration phantom (Walsh *et al.* in review).

RESULTS: This study found no significant difference between the measured variables of the calibrations. The average standard deviation of multiple 3-D image reprojections with the highest performing printed phantom and those from the phantom made of LEGO® bricks differed by 0.05 mm and the error of the reprojections differed by 0.13 mm [3].

CONCLUSION: Given that the phantom made of LEGO® bricks is significantly less expensive, more readily available, and more easily modified than precision-machined N-wire phantoms, it prompts to be a viable calibration tool especially for quick laboratory research and proof of concept implementations of tracked ultrasound navigation.

ACKNOWLEDGEMENTS: This project was supported by Natural Sciences and Engineering Research Council of Canada (NSERC) and Cancer Care Ontario (CCO). Marie Soehl was supported by Queen's University Summer Work Experience Program. Ryan Walsh was supported by NSERC. Gabor Fichtinger was funded as a CCO Research Chair. "LEGO®" is a trademark of the LEGO® group of companies which does not sponsor, authorize or endorse this publication.

REFERENCES

1. R. Walsh, M. Soehl, A. Rankin, A. Lasso, G. Fichtinger, "Design of a tracked ultrasound calibration phantom made of LEGO® bricks," SPIE Medical Imaging MI104, 2013 (accepted).
2. Carbajal, G., Lasso, A., Gómez, Á., Fichtinger, G., "Improving N-Wire Phantom-based Freehand Ultrasound Calibration," International Journal of Computer Assisted Radiology and Surgery, (2013).
3. M. Soehl, R. Walsh, A. Rankin, A. Lasso and G. Fichtinger, "Tracked ultrasound calibration studies with a phantom made of LEGO® bricks," SPIE Medical Imaging MI104, 2013 (accepted).

Tracked ultrasound snapshots improve the performance of novices in simulated percutaneous nephrostomy

Tamas Ungi¹, Darren Beiko², Michael Fuoco¹, Franklin King¹, Matthew Holden¹, Robert Siemens², Gabor Fichtinger¹

¹Laboratory for Percutaneous Surgery, Queen's University, Kingston, ON, Canada

²Department of Urology, Queen's University, Kingston, ON, Canada

Research supervisor: Gabor Fichtinger

Introduction. Urinary tract drainage is one of the most common image-guided minimally invasive interventions. It is performed in a number of conditions, including blocked urine passage by a tumor or kidney stone. Although this procedure is considered relatively safe, a number of factors make it challenging for inexperienced operators. The needle should be placed between the anterior and posterior blood supply region of the kidney, through the relatively poorly vascular watershed zone. Only the outer third of the kidney should be punctured to reduce the chance of bleeding in the central part from the renal vein or artery. The outer part of the kidney also has thicker parenchyma to seal the catheter. Two possible issues in ultrasound-guided nephrostomy may be the inability to clearly visualize the target area inside the kidney, and inability to visualize the needle during attempted access [1]. Tracked ultrasound snapshot guidance was shown to improve the success rate and reduce the procedure time in ultrasound-guided spinal facet joint injections compared to freehand ultrasound guidance as performed by residents [2]. Ultrasound snapshots improve the procedural performance of novice operators by decoupling ultrasound scanning and needle insertion, so the operator can focus their attention to one tool at any time. We tested if tracked ultrasound snapshots improve the performance of urology residents in percutaneous nephrostomy on a phantom model.

Methods. Six residents participated in this study as operators, who had no prior experience in ultrasound-guided nephrostomy. They received an introductory presentation of ultrasound-guided nephrostomy and a live demonstration of the technique by an instructor (Figure 1). Then each operator performed two procedures with conventional ultrasound guidance, and two procedures with ultrasound snapshot guidance, in an alternating pattern on a kidney simulation manikin. Conventional ultrasound guidance served as the control method in our comparative study. Three operators started with ultrasound-only guidance and two started with ultrasound snapshot guidance to balance the experience gained during the study. The software of the navigation system consists of two components, both available as open-source applications. The Public Software Library for Ultrasound Research (PLUS) is responsible for the communication with the ultrasound machine and tracking hardware. PLUS provides the calibration and synchronization methods for accurately tracking the needle tip and the ultrasound image [3]. The needle navigation display was generated using the SlicerIGT (www.slicerigt.org) software. SlicerIGT is a downloadable extension of 3D Slicer, a widely used software platform for image processing and image-guided interventions research.

Results. All nephrostomy procedures were successfully carried out by the residents, as confirmed by fluid backflow after removal of the stylet from the needle. The maximum number of needle insertion attempts in one procedure was 5 using conventional ultrasound guidance, while 2 using TUSS guidance. Needle path length measured inside the phantom tissue was significantly lower in the ultrasound snapshots group (310.9 ± 33.0 mm, average \pm SEM) compared to the control group (940.4 ± 192.1 , $p = 0.02$). This was associated with significantly lower number of needle insertion attempts in the ultrasound snapshots group (average 1.17 vs 2.92, $p = 0.01$). The total procedure time and the needle insertion time were also lower in the ultrasound snapshots group.

Conclusion. Tracked ultrasound snapshots may improve the performance of novice operators in percutaneous nephrostomy. The presented navigation system is reproducible due to commercially available hardware and open-source software components.

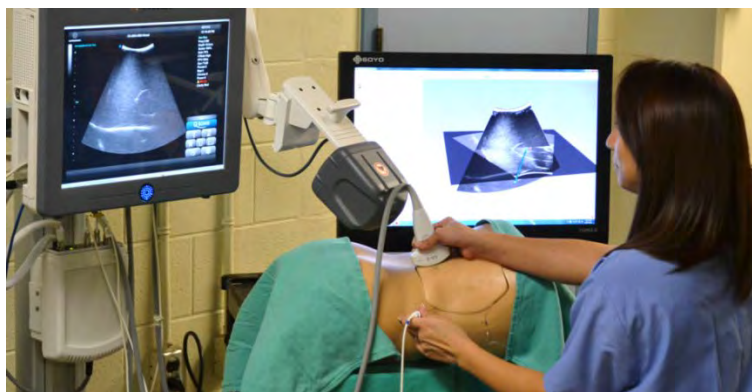


Figure 1. Tracked ultrasound snapshot guided nephrostomy procedure on a phantom model. The display on the right side provides a real-time 3D view of the ultrasound snapshot, the live ultrasound, and the needle position.

Acknowledgement. This work was in part funded by Cancer Care Ontario through Applied Cancer Research Unit and Research Chair in Cancer Imaging grants. The authors thank Dr. Caitlin T. Yeo for her assistance with the experiments.

[1] Uppot RN. Emergent nephrostomy tube placement for acute urinary obstruction. *Tech Vasc Interv Radiol.* 2009 Jun;12(2):154-61.

[2] Ungi T, Sargent D, Moulton E, Lasso A, Pinter C, McGraw RC, Fichtinger G. Perk Tutor: an open-source training platform for ultrasound-guided needle insertions. *IEEE Trans Biomed Eng.* 2012 Dec;59(12):3475-81.

[3] Lasso A, Heffter T, Pinter C, Ungi T, Fichtinger G. Implementation of the PLUS open-source toolkit for translational research of ultrasound-guided intervention systems. *The MIDAS Journal - Medical Imaging and Computing.* <http://hdl.handle.net/10380/3363> (2012)

A novel technology for teaching ultrasound-guided intrathecal needle insertion with Perk Tutor

Zsuzsanna Keri, MD¹, Devin Sydor, MD², Tamas Ungi, MD, PhD¹, Matthew Holden, MSc¹, Robert McGraw, MD³, Dan Borschneck MD⁴, Melanie Jaeger, MD², Gabor Fichtinger, PhD¹

¹Laboratory for Percutaneous Surgery, School of Computing, Queen's University, Kingston, ON, Canada

²Department of Anesthesiology and Perioperative Medicine, Queen's University, Kingston, ON, Canada

³Department of Emergency Medicine, Queen's University, Kingston, ON, Canada

⁴Department of Surgery, Queen's University, Kingston, ON, Canada

Research supervisor: Gabor Fichtinger

Introduction: Lumbar puncture is a procedure in which a needle is placed into the subarachnoid space surrounding the spinal cord at the lumbar spine level. Cerebrospinal fluid can be collected for diagnostic purposes or medication can be administered for the purpose of anesthesia or cytostatic therapy. Using ultrasound imaging to assist in lumbar puncture is increasingly used in clinical practice, particularly when the patient has spinal abnormalities, degenerative spine deformation or the bony landmarks are not palpable. The main disadvantage is the long learning curve required to gain competence in this ultrasound guided technique [1]. To facilitate the training of ultrasound-guided intrathecal needle insertion, the Perk Tutor training platform [2] has been developed and tested. We proposed that Perk Tutor would help learners gain skill in ultrasound image interpretation, needle coordination, and to achieve success in challenging cases with abnormal spinal anatomy.

Methods: Twenty resident volunteers from anesthesia and surgery programs were randomly assigned to one of two groups: the Perk Tutor group had access to the 3D display of the Perk Tutor (Figure 1) along with conventional ultrasound imaging during the training session and the Control group had access only to the conventional ultrasound image. Both groups were only allowed the conventional ultrasound during the testing phase. A commercial lumbar puncture phantom (Lumbar Puncture Simulator II, Kyoto Kagaku, Kyoto, Japan) was used as a low fidelity part-task trainer for the simulated procedure (Figure 2). Computed tomography (CT) images of three real patients were used to create three custom spine inserts for the simulator. The first spine model represented healthy and normal anatomy, the second had severely narrowed intervertebral spaces and mild scoliosis, and the third had severe scoliosis with narrowed intervertebral spaces. The first and the second model were used for training; testing occurred on the third model. We measured potential tissue damage (calculated from the area that the needle swept inside the tissue model), total procedure time and needle path during a test lumbar puncture on the third spine model.

Results: Needle trajectory analysis revealed that potential tissue damage was significantly greater in the Control Group than in the Perk Tutor group (173.2 cm^2 vs. 39.7 cm^2 , $p=0.01$). Needle path inside the tissue also trended lower in the Perk Tutor group (233.0 mm vs. 630.0 mm), as did total procedure time (151.3 sec vs. 254.3 sec), however these values did not reach statistical significance at our sample size.

Conclusion: We have demonstrated that learning ultrasound-guided lumbar puncture in pathological spine models may be improved by augmented reality 3-D visualization (Perk Tutor).

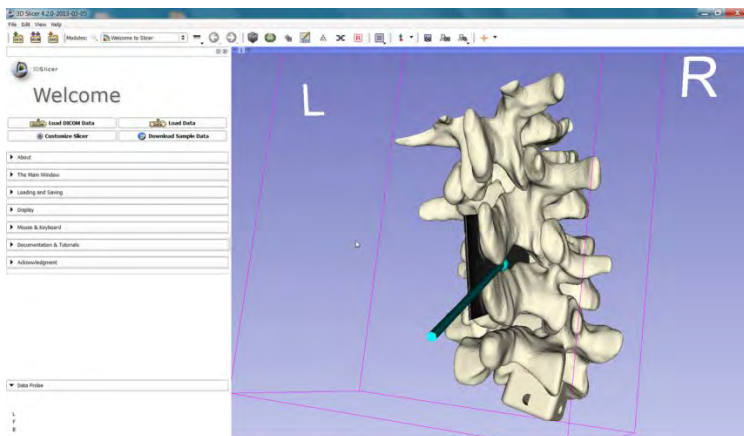


Figure 1. 3D view of the Perk Tutor display



Figure 2. Training session using Perk Tutor and the lumbar puncture simulator phantom.

Acknowledgement. This work was in part funded by Cancer Care Ontario through Applied Cancer Research Unit and Research Chair in Cancer Imaging grants. Financial support was also received from the Southeastern Ontario Academic Medical Organization (SEAMO), Educational Innovation and Research Fund.

[1] Chen CPC, Lew HL, Tsai W-C, Hung Y-T, Hsu C-C: Ultrasound-guided injection techniques for the low back and hip joint. *Am J Phys Med Rehabil* 2011;90:860Y867.

[2] Ungi T, Sargent D, Moulton E, Lasso A, Pinter C, McGraw RC, Fichtinger G. Perk Tutor: an open-source training platform for ultrasound-guided needle insertions. *IEEE Trans Biomed Eng.* 2012 Dec;59(12):3475-81.

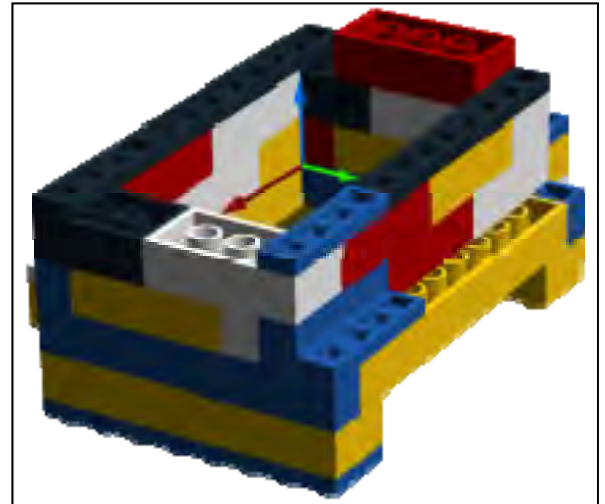
Design of a tracked ultrasound calibration phantom made of LEGO® bricks

Ryan Walsh, Marie Soehl, Adam Rankin, Andras Lasso, Gabor Fichtinger

Laboratory for Percutaneous Surgery, Queen's University, Kingston, ON, Canada

PURPOSE: Tracked ultrasound imaging is an inexpensive, safe and non-invasive method for providing augmented reality for interventionalists. However, tracked ultrasound imaging systems require an accurate spatial calibration between a reference tracking sensor and the ultrasound image [1]. For one method of tracked ultrasound calibration, a phantom is registered to a tracker sensor using a calibrated tracked stylus and landmark points on the phantom. Since the positions of the landmarks are precise and the margin of error for tracked ultrasound calibration is less than 1.0 mm, the phantom must be built with high precision. Currently such a phantom is often produced by rapid prototyping (*i.e.*, 3D printing). However, 3D printing is not available everywhere, typically takes several days and is expensive. Therefore, a more accessible, faster and lower cost method of building a phantom was desired

METHODS: We propose a low cost, available N-wire phantom for tracked ultrasound calibration made from LEGO® bricks. A phantom constructed from widely available materials allows a lower cost, more available and modifiable model that can be built in less time compared to 3D printed phantom models. Ultrasound calibrations using the phantom were expected to have a calibration error less than 1.0 mm. The phantom was required to be inexpensive and available worldwide. We produced a phantom for freehand tracked ultrasound calibration, by using LEGO® bricks and cotton yarn string, as shown in the image [2]. The phantom was rebuilt and used for tracked ultrasound calibration ten times to affirm its performance. To affirm the phantom's reproducibility and build time, ten builds were done by first-time users. The phantoms were used for a tracked ultrasound calibration by an experienced user. The success of each user's build was determined by the lowest root mean square (RMS) wire reprojection error of three calibrations.



RESULTS: The brick phantom was successfully built by all ten first-time users in an average time of 18.8 minutes. The longest build was 26.2 minutes with 18.5 minutes spent threading the N-wires. The required LEGO® bricks cost \$10.60 CAD. Repeated calibrations resulted 0.68 mm root mean square (RMS) wire reprojection error. Only one of ten trials produced a calibration with a RMS error above 1 mm. A separate study showed that these ultrasound calibrations maintain the precision of those done with 3D printed phantoms [3]. The results of these trials show that the phantom can be built by any user and produce a valid ultrasound calibration. The brick phantom can be assembled in less time and at a one third the cost of similar 3D printed phantoms.

CONCLUSION: It was found that the brick phantom could be reproduced more easily, was one third the cost, more accessible and faster to build than similar 3D printed models. The brick phantom was found to be capable of producing equivalent calibrations to 3D printed phantoms. The brick phantom is sufficiently reproducible, fast to build, inexpensive and accessible to allow any user to perform tracked ultrasound calibration. Owing to the popularity of LEGO® bricks, many users could possess the new phantom for tracked ultrasound calibration.

ACKNOWLEDGEMENTS: This project was supported by Natural Sciences and Engineering Research Council of Canada (NSERC) and Cancer Care Ontario (CCO). Ryan Walsh was supported by NSERC. Marie Soehl was supported by Queen's University Summer Work Experience Program. Gabor Fichtinger was funded as a CCO Research Chair. "LEGO®" is a trademark of the LEGO® group of companies which does not sponsor, authorize or endorse this publication.

REFERENCES

1. R. W. Prager, A. Gee and L. Berman, "Stradx: Real-time acquisition and visualization of freehand three-dimensional ultrasound," *Medical Image Analysis*, vol. 3, pp. 129-40, 1999.
2. R. Walsh, M. Soehl, A. Rankin, A. Lasso, G. Fichtinger, Design of a tracked ultrasound calibration phantom made of LEGO® bricks, *SPIE Medical Imaging MI104*, 2013 (accepted).
3. M. Soehl, R. Walsh, A. Rankin, A. Lasso and G. Fichtinger, "Tracked ultrasound calibration studies with a phantom made of LEGO® bricks," *SPIE Medical Imaging MI104*, 2013 (accepted).

Temporal Analysis of Optical Coherence Tomography to Measure Glucose Levels in Blood

Andrew Weatherbee

University of Toronto, Princess Margaret Hospital, Supervisor: Dr. Alex Vitkin

Hypothesis: It is hypothesized that Optical Coherence Tomography combined with Dynamic Light Scattering techniques can be used to accurately determine glucose levels in blood.

Rationale: Diabetes is a common disease in which patients experience dramatic swings in blood glucose concentrations. These swings can lead to both acute emergencies and long-term complications. Currently there are over 350 million people worldwide with diabetes, with over 3.5 million deaths per year from consequences of high blood sugar. Patients are required to prick their finger at least three times daily to determine their blood glucose level, and report significant levels of discomfort with this invasive method. Despite the high clinical need, a non-invasive method to quantify blood glucose levels does not exist.

The development of a non-invasive method to monitor blood glucose levels has the potential to improve the quality of life of diabetic patients and ultimately reduce the impact the disease has on their daily life activities.

Methods: Dynamic light scattering (DLS) is a useful tool for measuring translational and rotational dynamics of scattering microparticles in suspension. The phase and amplitude of the scattered light field are modulated by the dynamics of scattering particles. Recoding the resulting intensity fluctuations as a function of time using a photo-detector can yield certain physical properties of the scattering particles (their effective sizes / diameters) and the suspending fluid (its viscosity).

In an optically dilute suspension, light scatters only once, and detailed information about the sample, such as effective scatterer diameter or viscosity, can be obtained. In optically dense samples such as most biological tissues, however, some of the light scatters multiple times before detection, causing significant information loss. Therefore, it is desirable to have an optical technique that can separate singly from multiply scattered light, thus permitting detailed medium characterization even within optically dense media. Optical Coherence Tomography (OCT) is one such optical technique. OCT uses an interferometric set-up to discriminate between singly and multiply scattered light.

Using OCT along with DLS theory, we expect to be able to monitor glucose concentrations in blood non-invasively. Red blood cells (RBC) are the dominant optical scatterers in blood. If the size and shape of the RBCs are known, we expect to be able to infer the viscosity, and hence the glucose concentration, of the blood plasma.

The success attained previously in this lab in using OCT to quantify glucose levels in non-flowing phantoms and whole blood has already demonstrated the powerful potential of technique.

Conclusion: OCT is often used for high-resolution structural and functional imaging of tissues. Investigating the temporal dependence of the OCT signal, as proposed in this study, is less common but can also yield useful biophysical information (e.g., speckle variance imaging of vasculature). Specifically, analysis of the time-dependent properties of the OCT signal from the perspective of DLS theory is a different approach that has been used to obtain useful information about the dynamics of biological scatterers. In the context of diabetes, analyzing RBC scattering dynamics can yield quantification of blood viscosity, and thus potentially glucose concentration in a non-invasive manner.

Accuracy analysis in MRI-guided robotic prostate biopsy

H. Xu¹, A. Lasso¹, P. Guion², A. Krieger³, A. Kaushal², A.K. Singh⁴, P.A. Pinto⁵, J. Coleman⁶,
R.L. Grubb III⁷, J.B. Lattouf⁸, C. Menard⁹, L.L. Whitcomb¹⁰, G. Fichtinger^{1,11}

¹ Queen's University, School of Computing, Kingston, Canada, ² National Institutes of Health, Radiation Oncology, Bethesda, USA, ³ Children's National Medical Center, Sheikh Zayed Institute, Washington, USA, ⁴ Rosewell Park Cancer Institute, Department of Radiation Medicine, New York, USA, ⁵ National Institutes of Health, Urologic Oncology, Bethesda, USA, ⁶ Memorial Sloan-Kettering Cancer Center, Department of Surgery, New York, USA, ⁷ Washington University in St. Louis, Department of Surgery, Missouri, USA, ⁸ Centre Hospitalier de L'Universite de Montreal, Department of Surgery, Montreal, Canada, ⁹ Princess Margaret Hospital, Department of Radiation Oncology, Toronto, Canada, ¹⁰ Johns Hopkins University, Department of Mechanical Engineering, Baltimore, USA, ¹¹ Johns Hopkins University, Department of Computer Science, Baltimore, USA

Keywords: prostate biopsy, accuracy validation, MRI-guidance, image registration

Purpose

Needle biopsy the most definitive diagnosis for prostate cancer, the most prominent form of cancer for men in developed countries. The superior soft tissue imaging quality of magnetic resonance imaging (MRI) allows for image-guided target-specific biopsy of suspicious cancerous regions identified on the images. Due to confined physical space in the scanner and the length of the procedure, the Access to Prostate Tissue under MRI (APT-MRI) system [3] was developed and has been used for prostate biopsy at the U.S. National Cancer Institute for over six years. In addition to patient motion, the prostate itself can deform and dislocate upon needle insertion. However, the current system does not take into consideration of these factors, yet the biopsies still need to be sufficiently accurate to hit the intended target. We report a retrospective quantitative evaluation of the biopsy accuracy for the APT-MRI robotic biopsy system.

Methods

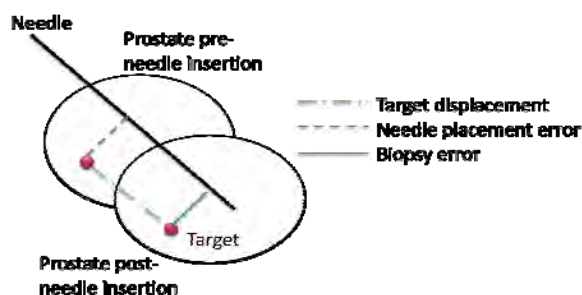
Series of 2D transverse volumetric MR image slices of the prostate both pre- and post-needle insertions were used to evaluate biopsy accuracy. The images were first pre-processed to decrease intensity non-uniformity in homogeneous tissue using N4ITK (Nick's N3 Insight Toolkit) implementation for MRI bias field correction. Next, a three-stage registration algorithm consisting of an initial rigid alignment of the whole image, followed by another rigid step and a B-spline deformable transform using only the prostate as region of interest was developed to capture prostate motion during biopsy. The algorithm was implemented using ITK in C++. The target displacement (distance between planned and actual biopsy target), needle placement error (distance from planned biopsy target to needle trajectory), and biopsy error (distance from actual biopsy target to needle trajectory) were calculated as accuracy assessment (Figure 1). The registrations were validated by performing image overlays and evaluating the prostate contour alignment between the resulting volumes and its corresponding fixed volume.

Results

A total of 90 biopsies from 24 patients were studied. The registrations were validated by checking prostate contour alignment using image overlay, and the results were accurate to within 2 mm. A signed rank test has shown that the results from rigid and deformable registrations were significantly different ($p \approx 0$). However, rigid registrations recovered the majority (88%) of the transformations. The mean target displacement, needle placement error, and clinical biopsy error were 5.2 mm (range: 0.9-18 mm, standard deviation: 3.5 mm), 2.5 mm (range: 0.1-10.7 mm, standard deviation: 1.6 mm), and 4.3 mm (range: 0.2-12 mm, standard deviation: 2.9 mm), respectively.

Conclusion

The targeting accuracy of the APT-MRI system is considered acceptable, since its needle placement error (mean: 2.5 mm) is less than the radius a clinically significant tumor (radius: 5 mm). This implies that the robotic device was accurate enough to place the needle at the intended biopsy target assuming no prostate movement. However, the prostate did dislocate and deform during the procedure, and this resulted in a mean biopsy error of 4.3 mm. Furthermore, 28% of the biopsies have an error greater than 5 mm, and this error is higher for cases with large patient motion. The biopsy error reported suggests that quantitative imaging techniques for prostate registration and motion compensation may improve prostate biopsy targeting accuracy.



Acknowledgements

This work is supported by: U.S. NIH 5R01CA111288-04 and 5R01EB002963-05, Canadian Ontario Graduate Scholarship (OGS) and Cancer Care Ontario.

This paper is published in *Int J Comput Assist Radiol Surg.*, vol. 8, no. 6, 2013.

Fig. 1 Illustration of the prostate dislocation during needle insertion and the parameters used in biopsy accuracy analysis.

Target Localization in MRI-guided Transperineal Prostate Biopsy using Multi-Slice-to-Volume Registration

Helen Xu¹, Andras Lasso¹, Andriy Fedorov², Clare Tempany², and Gabor Fichtinger¹

¹ Queen's University, School of Computing, Kingston, Canada

² Brigham and Women's Hospital, Boston, USA

Keywords: Prostate biopsy, target localization, MRI-guidance, registration.

Purpose:

Prostate needle biopsy is a commonly performed procedure since it is the most definitive form of cancer diagnosis. However, needle placements are often inaccurate due to intra-operative prostate motion and the lack of motion compensation techniques. Our previous study found a mean prostate centroid motion of 8.7 mm (range: 0.2-34.7 mm) during magnetic resonance imaging (MRI)-guided transperineal biopsies based on 538 images. Out of these cases, 19% have a biopsy error (orthogonal distance between target and the needle) greater than 5 mm, which corresponds to the radius of a clinically significant tumor (0.5 cc). It is important to incorporate motion compensation techniques into the clinical procedure in order to improve the overall needle targeting accuracy. We propose a method to track the biopsy target location in presence of prostate motion and deformation during MRI-guided biopsy.

Method:

The images used in the target localization method were multi-slice axial volumetric scans of the prostate (pre-operative planning volume) and image slices of the prostate in axial, sagittal, and coronal plane (intra-operative orthogonal image slices) acquired immediately before needle insertion (Figure 1). All images were first pre-processed to correct for non-uniform intensity caused by field inhomogeneities using N4ITK (Nicks N3 Insight Toolkit) implementation for MRI bias field correction. A multi-slice-to-volume registration algorithm was then developed to align the pre-operative planning volume with the three intra-operative orthogonal image slices of the prostate. Since each of the three orthogonal image slices needs to be registered to the planning volume, the mutual information metric was modified so that it calculates the sum of these three metrics. The algorithm consists of an initial rigid transformation of the whole image followed by a B-spline deformable step using only the prostate as the region of interest.

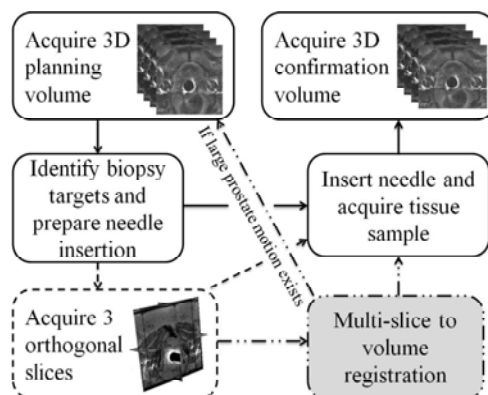
Simulated intra-operative orthogonal slices were generated from the planning volume to validate the algorithm using ground truth. Target reconstruction errors (TRE) for both rigid and deformable registrations were calculated. In addition, volume-to-volume registration between the needle confirmation volumes and the planning volumes was compared with the multi-slice-to-volume registration.

Results:

A total of 14 biopsies from 10 patients were studied. Based on prostate contour alignment of the clinical images, the registrations were accurate to within 2 mm. The mean execution times for rigid and deformable registrations were 7.6 and 45.4 seconds, respectively. With regards to validation using simulated images, the mean TREs for rigid and deformable registration were 0.1 mm (range: 0-0.9 mm) and 0.5 mm (range: 0.1-1.6 mm), respectively. Furthermore, the differences between multi-slice-to-volume and volume to volume registration were all less than 2.6 mm.

Conclusion:

The registration results from both clinical and simulated images demonstrated that our algorithm was able to recover initial rigid misalignments and correct for prostate deformation with less than 2 mm accuracy, which is under the diameter of a biopsy needle (3 mm). In addition, the fact that our multi-slice-to-volume registration was able to produce results similar to that of the volume-to-volume registration further indicates the reliability of our algorithm. The execution time for registration fulfills the clinical time requirement of 1 minute. In conclusion, we demonstrated feasibility of intra-operative target localization for MRI-guided prostate biopsy.



Acknowledgements:

This work was supported by: Canadian Ontario Graduate Scholarship (OGS), Cancer Care Ontario, U.S. NIH R01CA111288 and P41EB015898. The authors would like to thank Janice Fairhurst, MR technologist at Brigham and Women's Hospital for the image data collection.

Figure 1. Clinical work-flow of the image acquisitions during MRI-guided prostate biopsy. The solid lines indicate the standard biopsy procedure, and the dashed lines represent the additional orthogonal image slice acquisition specific to our study. The grey box is the motion compensation registration method we propose to incorporate.

3D histology reconstruction for microvasculature quantification in preclinical studies

Yiwen Xu¹, J. Geoffrey Pickering^{*1,2}, Zengxuan Nong², Eli Gibson², Aaron Ward^{*1,3} * Research Supervisor

1. Department of Medical Biophysics, 2. Robarts Research Institute, 3. Department of Oncology, University of Western Ontario

Introduction: In contrast to imaging modalities such as MRI and micro-CT, histology reveals multiple stained tissue components at high resolution (0.25 $\mu\text{m}/\text{pixel}$). Conventional 2D histology detects structural microvascular abnormalities, which can lead to vessel deterioration. However, 2D visualization challenges spatial interpretation, which is crucial to the comprehension of tissue components. In cancer research, high-accuracy reconstructions could facilitate 3D visualization and quantification of oncoproteins, receptors, tumour cell architecture, and microvasculature. In order to maintain vascular geometry and topology (Fig. 1), features used for registration should be chosen to avoid forcing curved or non-section-orthogonal structures to be straight and orthogonal after registration. Our objective was to perform an accurate and automatic 3D reconstruction of mouse hindlimb and cardiac tissue.

Materials and Methods: We performed a 3D reconstruction of three tibialis anterior (TA) muscle samples (Samples 1–3, Sample 3 after hind limb ischemia) and one heart (Sample 4), taken from wild type C57BL/J6 mice. Pairwise rigid registrations were performed on paraffin-embedded serial sections, 5 μm thick in the TA and 4 μm thick in the heart, all digitized at 0.25 $\mu\text{m}/\text{pixel}$. The TA was stained with hæmatoxylin and immunostained for smooth muscle α -actin using 3,3'-Diaminobenzidine (DAB), and the cardiac tissue was stained with the conventional hæmatoxylin and eosin stain. We initialized using a low-resolution intensity-based registration and refined using both a high-resolution intensity-based registration and a nucleus landmark-based registration (for comparison). Cell nucleus landmarks appearing on at most two adjacent sections were automatically extracted and corresponded across adjacent sections. These small landmarks were chosen to avoid registrations which incorrectly force structures to be straight and section-orthogonal (Fig. 1). We measured pairwise target registration error (TRE) across adjacent sections and accumulated TRE propagated throughout the 3D reconstructions, and compared the TREs to a typical murine microvessel diameter of 10 μm .

Results: The median pairwise and accumulated TREs were both significantly different ($p < 0.01$) between the intensity- and nucleus-based refined registrations for each sample (Table 1). The nucleus-based approach provided TREs $< 10 \mu\text{m}$ in Samples 2 and 3 (95% confidence interval on the median, Table 1). We observed concordant qualitative differences between the reconstructed volumes, with superior through-section vasculature continuity in the nucleus-based registration (Fig. 2). The 95% confidence intervals on the median observed fiducial registration errors suggest that non-rigid registration may improve registration error by less than 10 μm , when nuclei are accurately corresponded.

Discussion and Conclusions: Registration based on automatic extraction and correspondence of small, homologous landmarks spanning not more than two tissue sections may support accurate 3D histology reconstruction, avoiding the well-known “banana-into-cylinder” effect where conventional methods optimize the pairwise alignment of large, salient structures, forcing them to be section-orthogonal. However, a limitation is the need for corresponding nuclei to be within a defined distance for accurate correspondences and accurate registration. With further validation, this approach may provide a valuable tool for scientists conducting preclinical studies requiring high-accuracy 3D histology reconstructions for analysis of 3D microvasculature and surrounding tissue components in small animal models.

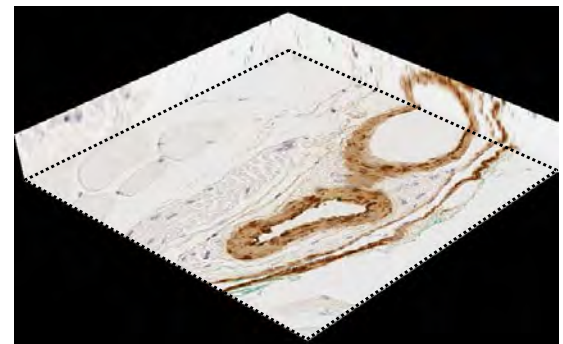
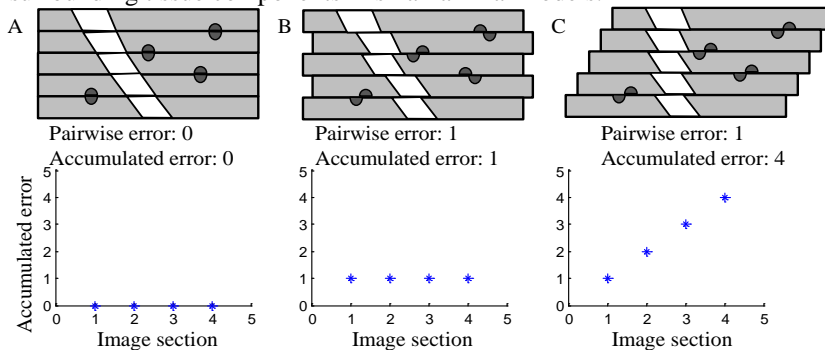


Figure 1: Comparison of the alignment of bisected nuclei when measuring the pairwise and accumulated registration error. (A) The ideal error-free reference reconstruction. (B) Shifted tissue sections misalign the nucleus landmarks, but vessel topology and geometry are mostly conserved. (C) Registration intended to optimize pairwise alignment of salient structures such as the vessel cross sections preserves vessel topology but not geometry; this is captured by the accumulated error but not the pairwise error, which is the same as in (B).

Figure 2: A tri-planar view of the nucleus-based 3D reconstructions of Sample 1, which consists of 5 μm thick serial sections stained with α -actin DAB immunostain to visualize the vessels in brown, and hæmatoxylin counter stain to visualize the nuclei in blue.

Table 1: Pairwise and accumulated TRE values (μm) of the intensity-based and nucleus-based landmark registration

	Sample 1 (n = 775, 10 sections)			Sample 2 (n = 781, 9 sections)			Sample 3 (n = 959, 12 sections)			Sample 4 (n = 416, 15 sections)		
	Median	IQR	95% CI	Median	IQR	95% CI	Median	IQR	95% CI	Median	IQR	95% CI
Pairwise TRE												
Intensity-based (low resolution)	19.5	23.6	[18.4,21.1]	9.5	9.6	[8.6,10.2]	9	8.6	[8.5,9.5]	32.5	52.7	[29.7,37.6]
Intensity-based (high resolution)	31	41.4	[28.8,34.6]	9.4	12.5	[8.7,10.1]	6.1	5.7	[5.7,6.4]	16.8	21.1	[15.2,18.1]
Nucleus-based	10.1	14.9	[9.3,11.2]	4.9	4.2	[4.6,5.2]	5.6	5.4	[5.3,5.8]	15.8	17.4	[14.1,17.2]
Accum. TRE												
Intensity-based (low resolution)	44.7	83.6	[37.9,49.6]	8.4	10.5	[8.0,8.9]	34.6	46.1	[32.7,37.5]	137.1	263.0	[123.5,244.8]
Intensity-based (high resolution)	77.8	147.4	[64.3,96.4]	23	18.6	[22.4,23.6]	11.3	11.2	[10.8,11.9]	36.0	27.7	[34.3,37.7]
Nucleus-based	29.2	14.8	[27.8,30.0]	5	5.9	[4.6,5.3]	4.2	4.9	[3.7,4.7]	95.7	173.5	[82.3,119.0]

Medical Imaging Trial Network of Canada MITNEC

Oral Presentation and Poster Abstracts

POOR CORRELATION BETWEEN NONINVASIVE CARDIAC IMAGING AND FRACTIONAL FLOW RESERVE (FFR) IN PATIENTS WITH MULTIVESSEL CORONARY ARTERY DISEASE

Marie-Jeanne Bertrand MD MSc¹, Philippe L.-L'Allier MD¹, Clifford Ekwempe², Marie-Claude Guertin PhD²,

Jean-Claude Tardif MD¹

¹Montreal Heart Institute, Montreal, Quebec, ²Montreal Heart Innovations Coordinating Centre (MHICC), Montreal, Quebec

Research supervisor: Philippe L.-L'Allier MD

Background: Noninvasive cardiac imaging is recommended to stratify ischemia and guide percutaneous coronary intervention (PCI), although it may underestimate the true ischemic burden, particularly in multivessel disease (MVD) patients.

Methods: We retrospectively identified patients who had undergone noninvasive cardiac imaging (SPECT sestaMIBI or Thallium-MPI (78% of patients), stress echocardiography, CMR or CCTA) prior to angiography with invasive FFR measurement in at least 1 coronary artery over a 2-yr period (n=110). We sought to determine the ability of noninvasive cardiac imaging to identify all ischemic segments in MDV patients by comparing these modalities to invasive fractional flow reserve (FFR) measurements (used as gold standard) according to matched vascular territories (anterior-apical, inferior and lateral). Sensitivity, specificity, positive predictive value (PPV), negative predictive value (NPV) and accuracy were calculated.

Results: Mean age was 66±10 years, 22% of patients were female, 35% were diabetics and 73% had previous CAD. Poor correlations between noninvasive cardiac imaging and invasive FFR were obtained when data were analyzed per vascular territories. Noninvasive cardiac imaging had an overall PPV of 41.5% and a NPV of 56.3%, a sensitivity of 43.5%, a specificity of 54.2% and a diagnostic accuracy of 49.7% when compared with a FFR≤0.80. Of those patients with any FFR derived ischemia, 90.3% had ischemia in at least one vascular territory identified by noninvasive cardiac imaging.

Conclusion: These results suggest that the diagnostic accuracy of noninvasive cardiac imaging (mostly nuclear perfusion scans) to detect all relevant ischemia is poor in patients with MDV and that invasive FFR is a relevant tool to identify ischemia on a per segment basis to guide proper revascularization.

Medical Imaging Trials Network of Canada (MITNEC) - Project C6 - Amyloid and glucose PET Imaging in Alzheimer and Vascular Cognitive Impairment patients with significant White Matter Disease

Sandra E. Black¹, Anoop Ganda¹, Christopher J.M. Scott¹, Gary Wang¹, Eric E. Smith², Richard Frayne³, Frank S. Prado⁴, Stephen C. Strother⁵, Demetrios J. Sahlas⁶, Ging-Yuek R. Hsiung⁷, Curtis E. Caldwell⁸, Jean-Claude Tardif⁹.

¹L.C. Campbell Cognitive Neurology Research Unit, Sunnybrook Research Institute, University of Toronto, Toronto, Ontario, ²University of Calgary, Calgary, Alberta, ³Departments of Radiology and Clinical Neurosciences, Hotchkiss Brain Institute, University of Calgary, Calgary, Alberta, ⁴Lawson Health Research Institute, St Joseph's Health Care, Medical BioPhysics Department, Western University, London, Ontario, ⁵Rotman Research Centre, Baycrest Medical Biophysics, University of Toronto, Toronto, Ontario, ⁶Division of Neurology, Department of Medicine, McMaster University, Hamilton, Ontario, ⁷UBC Hospital Clinic for Alzheimer and Related Disorders and St. Paul's Hospital, Vancouver, British Columbia, ⁸Sunnybrook Research Institute, Departments of Medical Imaging and Medical Biophysics, University of Toronto, Toronto, Ontario, ⁹Montreal Heart Institute, Université de Montréal, Montreal, Québec.

The prevalence of both Alzheimer's Disease (AD) and stroke doubles each decade over 65. Both are major causes of dementia, currently estimated to cost \$15B annually in Canada, and with population aging, the number of Canadians suffering from dementia is expected to double to over a million within a generation with annual costs increasing to \$150B¹. Additionally, in population studies elders over 65 years, "covert" cerebral small vessel disease appears on MRI scans as silent lacunar infarcts in 25%² as Microbleeds in 10%, and as focal or diffuse 'incidental' white matter disease (WMD) in 95%³. WMD is extensive in 20%, with a clinical threshold effect around 10cc²⁴. Small vessel disease is even more common in dementia, often coexisting with AD and independently contributing to cognitive decline and progression to dementia^{5,6}. Longitudinal imaging using cerebral amyloid labeling opens a new opportunity to understand the additive/interactive effects of small vessel disease and AD.

The design of this study includes recruitment of two cohorts, including 75 Mild Cognitive Impairment (MCI) and/or early Alzheimer Disease subjects from memory clinics and 75 subjects with strokes/TIA from stroke prevention clinics. Inclusion criteria include the presence of extensive white matter disease, eg. Fazekas score of 3, as determined by previous MR or CT, > 60 years of age, Mini-Mental Status Exam (MMSE) scores ≥ 20 . Subjects will undergo 3T structural MRI (including T1, PD/T2, FLAIR, GRE, DTI, and resting state fMRI), glucose PET, amyloid PET (using florbetapir) and neuropsychological testing, as well as blood sampling. Repeat imaging and neuropsychological testing will be conducted at twelve months. The imaging portion is designed to closely parallel the Alzheimer's Disease Neuroimaging Initiative (ADNI) in order to benefit from the availability of both cognitively normal controls (NC), MCI and Alzheimer's disease subjects with minimal WMD.

The primary outcomes aim to compare subjects with significant peri-ventricular WMH at baseline and follow-up on brain uptake of florbetapir, FDG, structural MRI and neuropsychological assessment. One of several specific hypotheses to be investigated is that patients who have high burden of pvWMH volumes will show more increase in amyloid deposition over one year, after accounting for appropriate covariates (eg. baseline scores, age and education, ApoE e4 status), as well as a decrease in cognition (especially speeded tasks and executive functions), instrumental function, and greater atrophy and glucose hypometabolism in the signature areas described in AD. It is expected that 60-80% of AD subjects will show a "positive" amyloid scan (Am+), while only 20-40% of stroke/TIA subjects will be positive for the presence of amyloid. Further subgroup analysis will aim to compare and contrast Am+ and Am- subjects from each cohort as well as comparing all of these subjects to ADNI AD subjects with minimal WMD, MCI's and NC's.

Recruitment is set to begin in late 2013, with all baseline subjects recruited by mid-2014.

References:

1. Alzheimer Society of Canada. Rising Tide: The Impact of Dementia on Canadian Society. 2010. Alzheimer Society of Canada. Ref Type: Report
2. W. T. Longstreth et al., "Lacunar Infarcts Defined by Magnetic Resonance Imaging of 3660 Elderly People: the Cardiovascular Health Study," *Archives of Neurology* 55, no. 9 (1998): 1217-1225.
3. W. T. Longstreth, Jr. et al., "Clinical Correlates of White Matter Findings on Cranial Magnetic Resonance Imaging of 3301 Elderly People. The Cardiovascular Health Study," *Stroke*. 27, no. 8 (1996): 1274-1282.
4. C. DeCarli et al., "The Effect of White Matter Hyperintensity Volume on Brain Structure, Cognitive Performance, and Cerebral Metabolism of Glucose in 51 Healthy Adults," *Neurology* 45, no. 11 (1995): 2077-2084.
5. O. Carmichael et al., "Longitudinal Changes in White Matter Disease and Cognition in the First Year of the Alzheimer Disease Neuroimaging Initiative," *Archives of Neurology* 67, no. 11 (2010): 1370-1378.
6. E. E. Smith et al., "Magnetic Resonance Imaging White Matter Hyperintensities and Brain Volume in the Prediction of Mild Cognitive Impairment and Dementia," *Arch Neurol*. 65, no. 1 (2008): 94-100.

Dynamic Carotid MR Imaging for Distensibility Assessment

Mari E Boesen,^{1,2} Alexandra Pulwicki,^{2,3} Luis A Souto Maior,^{2,4} Jerome Yerly,^{2,5} R Marc Lebel,^{2,6} and Richard Frayne^{2,7}

¹Biomedical Engineering, University of Calgary, AB, ²Seaman Family MR Research Centre, Calgary, AB, ³Physics & Astronomy, University of Calgary, AB, ⁴Universidade Federal de Campina Grande, PB, Brazil, ⁵CardioVascular MR Research Center, Centre d'Imagerie BioMedicale, Lausanne, Switzerland, ⁶Applied Sciences Laboratory, GE Healthcare, ⁷Radiology & Clinical Neuroscience, Hotchkiss Brain Institute, University of Calgary, AB

Background: The elasticity of the arteries serves to cushion pulsatile flow from the heart. Arterial elasticity can be measured as the distensibility coefficient $DC = 2(d_s - d_d)/d_d(\Delta P)$ where d_s and d_d are systolic and diastolic vessel diameters and ΔP is the pulse pressure. A decrease in arterial elasticity can have adverse effects on cardiovascular health and increase stroke risk.[1] While decreased distensibility is a part of normal aging,[2] it is also observed with atherosclerotic plaque presence.[3] As a primary site of atherosclerosis, the carotid arteries are an ideal location for arterial distensibility assessment. Currently, reported carotid DC values vary widely: from $41.6 \pm 9 \text{ MPa}^{-1}$ [4] to $56 \pm 22 \text{ MPa}^{-1}$. [5] A sensitive and reliable measurement of distensibility could provide a standard indicator of cardiovascular health as well as an indication of plaque stability and stroke risk.

Methods: We performed a series of three dynamic MR imaging techniques on ten normal subjects: prospectively gated fast spin echo (pFSE), retrospectively gated fast spin echo (cineFSE), and retrospectively gated gradient recalled echo (cineGRE). Imaging parameters are shown in Table 1. Each sequences provided temporally resolved axial images of the common carotid arteries. Brachial blood pressure was obtained *in situ* immediately prior to each acquisition. Three reviewers manually traced the cross sectional area of the left common carotid artery three times over on all cardiac phases for each sequence (Figure 1). Mean cross sectional areas (converted to effective diameters) and pulse pressure (ΔP) were used to calculate DC values for each subject.

	cineGRE	cineFSE	pFSE
Blood signal, reconstruction, cardiac phases	Bright blood, retrospective, 16 phases	Black blood, retrospective, 16 phases	Black blood, prospective, 4 phases
Flip Angle/TR/TE	30°/17 ms/6.1 ms	90°/1.2*RR/13 ms	90°/2*RR/13 ms
FOV, acquisition matrix, slice thickness	160 mm ² /256 x 256/3 mm	160 mm ² /256 x 252/3 mm	160 mm ² /256 x 256/3 mm

Table 1 – Imaging parameters

RR interval = average cardiac cycle duration

Results: Cross-sectional areas were comparable on the black blood images ($28 \pm 0.2 \text{ mm}^2$ on dFSE and $27.9 \pm 0.3 \text{ mm}^2$ on pFSE) but varied significantly from the area on bright blood images ($35.8 \pm 0.4 \text{ mm}^2$, $p < 0.01$). Of the three sequences, the cineFSE had the lowest minimum detectable difference in cross-sectional area (5.8 mm^2). Mean DC (Figure 2) was also comparable on the FSE based sequences ($p = 0.12$) and significantly different between cineFSE and cineGRE ($p < 0.01$). Calculated DC values varied largely across the healthy subjects (22.6 to 74.6 MPa^{-1}) and imaging sequence (mean DC of 39.6 ± 4.1 , 49.8 ± 4.9 , $61.8 \pm 6.0 \text{ MPa}^{-1}$ on cineFSE, pFSE, and cineGRE, respectively).

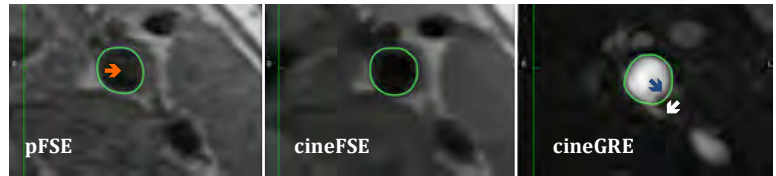


Figure 1 – Example manual tracing of the carotid artery on each sequence type. Arrows indicate areas of artifact that may affect cross sectional area measurement.

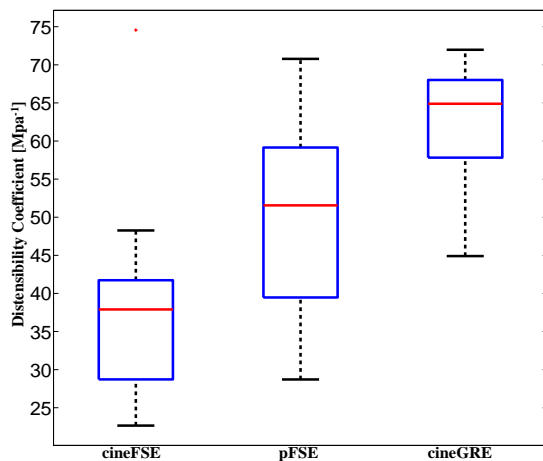


Figure 2 – Box plot of mean distensibility coefficients over all subjects by type of MR imaging sequence.

Discussion and Conclusion: The three MR distensibility measurement techniques investigated here reflect the wide range in DC values reported in the literature using MR imaging ($41.6 \pm 9 \text{ MPa}^{-1}$) and ultrasound ($41.3 \pm 7.4 \text{ MPa}^{-1}$). [4] A need for a standardized DC measurement and population characterization is apparent. MR imaging offers cross sectional visualization of the carotid arteries and may provide a more sensitive measure of distensibility as well as information on regional changes in DC with plaque presence. Of these techniques, the cine FSE sequence best suppresses motion and flow artifacts while visualizing the vessel wall.

References:

- [1] G. Tsigoulis, *et al. Eur J Neurol*, 2006; 13: 475.
- [2] D. Vaidya, *et al., J Womens Health*, 2012; 21: 516.
- [3] N. M. van Popele, *et al., Stroke*, 2001; 32:454.
- [4] A. Harloff, *et al., Eur Radiol*, 2009; 19: 1470.
- [5] Y. L. Liang, *et al., Clin Sci (Lond)*, 1998; 95:669.

Conventional non-contrast MRI of Ventilation Abnormalities in Bronchiectasis: New Tools and Measurements for an old Disease

Dante Capaldi^{1,2}, Khadija Sheikh^{1,2}, Gregory Paulin^{1,2}, Sarah Svenningsen^{1,2}, Harvey O Coxson³, David G McCormack⁴, and Grace Parraga^{1,2}

¹Imaging Research Laboratories, Robarts Research Institute; ²Department of Medical Biophysics; ³Department of Radiology, University of British Columbia, Vancouver Canada, ⁴Division of Respiriology, Department of Medicine, The University of Western Ontario, London, Canada; Dr. Grace Parraga

RATIONALE: Bronchiectasis, the enlargement of airways due to inflammation, is typically evaluated using high resolution computed tomography (HRCT), analysis of sputum cultures, and pulmonary function tests. Although HRCT provides high resolution pulmonary anatomical features and measurements, it provides little or no functional information and exposes patients to ionizing radiation, thus limiting serial and longitudinal studies of the progression of bronchiectasis in these patients. An alternative imaging approach, involves Fourier-decomposition of conventional non-contrast proton magnetic resonance imaging (FDMRI). This method requires only conventional MR equipment with no exogenous contrast and only a few minutes to acquire. Also, this method may be optimized for use in patients with bronchiectasis to provide simultaneous structure-function information. Therefore, the objective of this proof-of-concept study was to optimize FDMRI in patients with bronchiectasis to visualize regional ventilation abnormalities and compare these with thoracic HRCT to determine structure-function relationships.

METHODS: Fifteen subjects were evaluated using hyperpolarized ³He MRI, spirometry, plethysmography, 6 minute walk test (6MWT), St. George's Respiratory Questionnaire (SGRQ), thoracic CT and FD MRI. For FDMRI, free-tidal breathing proton MR images were acquired over a period of two minutes at a rate of four frames per second using the FIESTA pulse sequence on a 3T scanner (GEHC 750MR platform). Non-rigid image registration was performed to compensate for respiratory motion. Pulmonary voxel intensities were aligned along a time axis and Fourier transforms were performed on the period voxel signal intensity sine wave to determine the contribution of periodic breathing/ventilation to this periodic signal intensity pattern. Semi-automated segmentation was used to generate FDMRI ventilation images that were compared with thoracic HRCT to identify regional relationships between peribronchial thickening, mucous plugs and FDMRI ventilation abnormalities.

RESULTS: Figure 1 shows the results for a single 45 yr female patient with a 20 year history of chronic bronchiectasis (FEV₁=45%pred, FVC=52%pred, RV=160%pred, TLC=97%pred) with the ventilation pattern acquired using FD MRI (in aqua) co-registered with thoracic HRCT (in greyscale) for a single coronal slice just posterior to the centre of the lung. The spatial relationship of ventilation abnormalities (regions with no aqua) and bronchiectic anatomical/morphological abnormalities and mucous plugging can be clearly identified for this subject.

CONCLUSIONS: In this pilot study in fifteen bronchiectic subjects, preliminary results show that FDMRI can be acquired to provide pulmonary functional images with regional ventilation abnormalities. Such functional abnormalities can be spatially related to airway and other anatomical abnormalities.

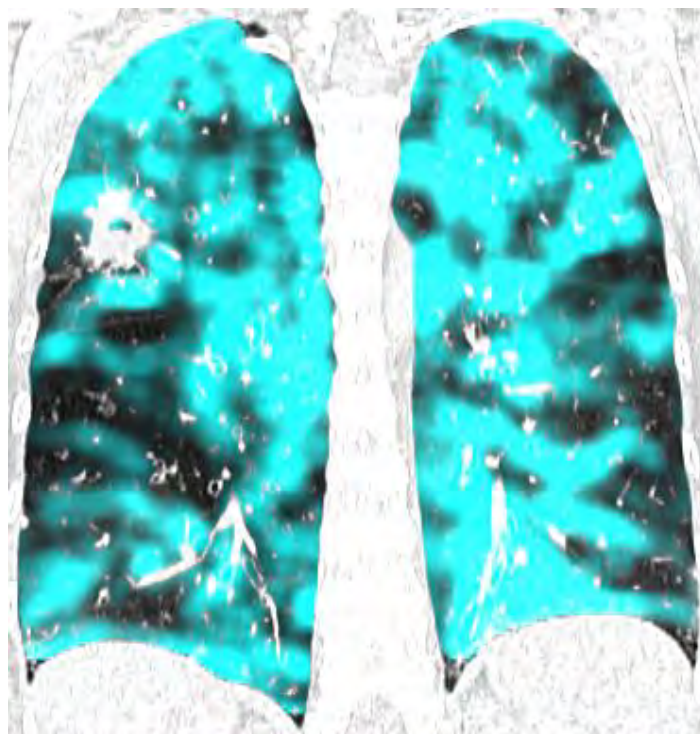


Figure 1: FDMRI in aqua co-registered with greyscale thoracic CT for 45 yr female subject with non-CF bronchiectasis.

Multi-modality Neuroimaging in a Porcine Model of Endothelin-1 Induced Cerebral Ischemia: Defining the Acute Infarct Core

¹Christopher d’Esterre, ²Richard Aviv, ³Enrico Fainardi, ⁴Ting Yim Lee

¹Hotchkiss Brain Institute, Foothills Medical Centre, Calgary, Alberta, Canada; ²Sunnybrook Health Sciences Centre, Toronto, Ontario, Canada; ³Neuroradiology Unit, Department of Neurosciences and Rehabilitation, Azienda Ospedaliero-Universitaria di Ferrara, Italy; ⁴Imaging Research Lab, Robarts Research Institute, London, Ontario, Canada;

Background: CT perfusion (CTP)-derived parameters and MR-diffusion weighted imaging (DWI) are currently used to delineate infarct volume; however, reversibility of such defects has been demonstrated for both modalities.

Methods: Twelve domestic pigs had a CTP scan prior to intracranial injection of endothelin-1 (ET-1; 0.01mL/kg) into the left striatum. Subsequent CTP scans at 30min, 1hr, 1.5hrs were done to monitor ischemic progression. A second dose of ET-1 (0.01mL/kg) was injected at 2hrs from the first injection. Twenty minutes after the second ET-1 injection, ¹⁸F-FDG was injected (300-380MBq). The animal was moved to a 1.5T MRI scanner where DWI was performed. The animal was then moved back to the CT scanner for a final CTP/PET acquisition within 10 minutes of the DWI. The brain was quickly removed and stained with tetrazolium-chloride (TTC). The infarct volume defined by low intensity TTC stain, low CBF (< 9.3ml·min⁻¹·100g⁻¹), low CBV (< 1.07ml·100g⁻¹), DWI hyper-intensity and low ¹⁸F-FDG uptake were determined. Linear regression was used to correlate the infarct volume measured by each imaging modality to that by the histological gold standard.

Results: R² values for CBF, CBV, DWI and FDG versus TTC-histology were 0.83, 0.69, 0.95 and 0.61, respectively. For the CBF and DWI parameters the slope of the fitted line was greater than 1, while the slope of the fitted line for the CBV and CBFxCBV parameters was less than 1. Mean normalized (relative to the histologically defined infarct) values were 1.38, 0.82, 0.99, and 0.67 for CBF, CBV, DWI and FDG, respectively.

Conclusion: The CTP-CBF and the imaging gold standard DWI both overestimated the TTC-infarct core in 66% and 58% of cases, while CTP-CBV, CBFxCBV and FDG-PET all underestimated the final infarct volume in 100% of animals. The CBF/CBV mismatch was observed within 4/12 DWI lesions, and 3/12 TTC defined infarcts (Figure 1). The CBF/CBV mismatch may not represent penumbra during the acute stroke setting.

	R ²	Slope	Normalized	Percent change
CTP-CBF	0.83	1.2	1.38±0.13	27%±6.8
CTP-CBV	0.69	0.69	0.82±0.12	-23%±19.9
DWI	0.95	1.3	0.99±0.08	1%±8.2
PET-FDG	0.61	0.6	0.67±0.19	-60%±58.8

Table. Coefficients of determination (R²) and slopes of the regression lines for predicted infarct core, as defined by the four imaging parameters, versus TTC-defined true infarct. Also shown are normalized values

(predicted infarct volume/true infarct volume) and the percent change between predicted and true infarct volumes.

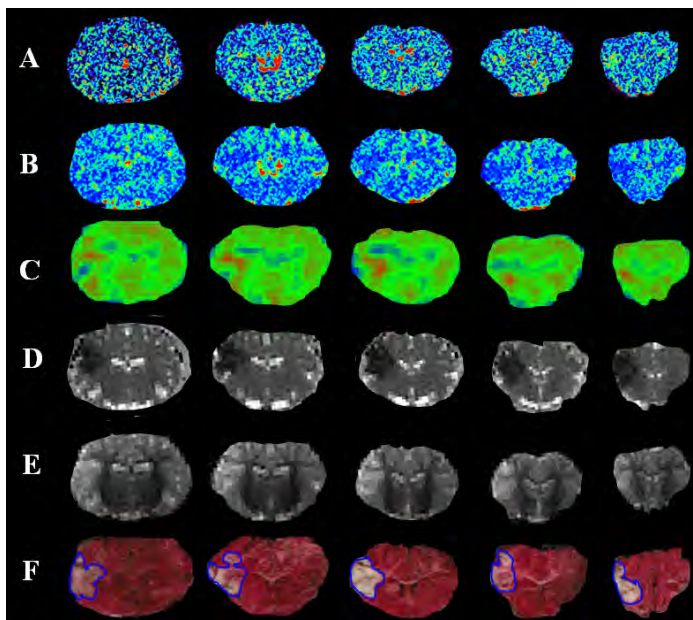


Figure. Coronal sections of a domestic pig brain one hour after injection of endothelin-1, causing focal ischemia. (A) CTP-CBV and (B) CBF functional maps, (C) ¹⁸F-FDG PET images, (D) MR-ADC and (E) DWI maps, and (F) TTC-stained excised brain. All imaging and histology were completed within 35 minutes. Within the infarcted tissue, outlined on TTC slices: 1) DWI-hyperintensities, and ADC-hypointensities are observed in all slices, 2) Uptake of FDG is increased and decreased in the periphery and core, respectively, 3) Normal or increased CBV and a decrease in CBF is observed. This CBF/CBV mismatch within infarcted tissue may be caused by the opening of arteriovenous shunts, representing acute non-nutritive hyperemia.

Longitudinal Hyperpolarized ³He Magnetic Resonance Imaging of Adult Cystic Fibrosis: Pilot Study results

Gregory Paulin^{1,2}, Sarah Svenningsen^{1,2}, Sindu Mohan^{1,2}, Brian N. Jobse¹, Miranda Kirby^{1,2}, James F. Lewis³ and Grace Parraga^{1,2}

¹Imaging Research Laboratories, Robarts Research Institute; ²Department of Medical Biophysics; ³Division of Respiriology, Department of Medicine, The University of Western Ontario, London, Canada; Dr. Grace Parraga

RATIONALE: Previous work has showed the potential utility of hyperpolarized ³He MRI for evaluating regional CF lung structure and function in both children and adults. In addition, the short-term variability of ³He gas distribution in CF adult patients has been previously shown to be relatively high over seven days. To our knowledge, longitudinal ³He MRI has not been evaluated in CF patients. To quantitatively evaluate longitudinal changes in adult CF using hyperpolarized ³He magnetic resonance imaging (MRI), we compared long-term (4-years) to short-term change (7-days) in pulmonary function measurements and ³He MRI ventilation defects.

METHODS: Five subjects with CF were evaluated who consented to a longitudinal visit after participating in a reproducibility study 4±1 years earlier and who were between the ages of 18 and 45 years, without claustrophobia or any other MRI contradictions and with a baseline FEV₁%_{pred} >60% on their first baseline visit. Spirometry, plethysmography, and imaging was performed in these subjects at 3 time points: 1) baseline, 2) 7±2 days and, 3) 4±1 years later. ³He ventilation defect percent (VDP) was quantified from the ³He MRI static ventilation images using a semi-automated segmentation algorithm. Subject-specific ³He MRI temporal variability maps were generated to qualitatively and quantitatively evaluate regional gas distribution at baseline and compare these to the short-term and the long-term follow-up measurements.

RESULTS: There was no significant change in pulmonary function test measurement or ³He MRI VDP at the 7-day or 4-year follow (Table 1). There was a strong and significant correlation (r=0.94, p=0.02) for the change in VDP at 7-days and at 4-years follow-up. In this small pilot group of subjects, 2/5 subjects had a large increase or worsening in VDP and as well significant declines in forced expiratory volume in 1 second (FEV₁) at their 4-year follow-up visit. Importantly, for these two subjects, there were numerous large ventilation defects and large baseline ³He MRI VDP that could be correlated with CT anatomical and morphological findings. In contrast, for 3/5 subjects there were no significant changes in VDP or FEV₁ from baseline.

CONCLUSIONS: Currently, there are few measurement tools that help predict those adult CF patients who will experience rapid disease progression and lung function declines. ³He MRI serial monitoring provides a better understanding of disease progression over time and ³He MRI VDP may be a sensitive disease biomarker with the potential to predict longitudinal lung function decline in CF.

Funding/Support: Natural Sciences and Engineering Research Council (NSERC) of Canada, Ontario Thoracic Society (Block Term Grant), Lawson Health Research Institute (Internal Research Fund), Ontario Research Fund Research Excellence Program.

Table 1. Baseline, 7-day, and 4-year Pulmonary Function and Hyperpolarized ³He MRI Measurements

Parameter	Time-point (n=5)			Significance of Difference (p-value) [‡]	
	Baseline	7-Day	4-Years	BL vs. 7-Day	BL vs. 4-Years
FEV ₁ (% _{pred})(±SD)	76 (17)	76 (16)	70 (21)	0.81	0.24
FVC (% _{pred}) (±SD)	87 (17)	87 (13)	85 (17)	0.92	0.45
FEV ₁ /FVC (%)(±SD)	74 (11)	73 (12)	68 (13)	0.42	0.01
TLC (% _{pred})(±SD)	108 (15)*	108 (21)*	108 (15)	0.87	0.18
RV (% _{pred})(±SD)	167 (46)*	158 (81)*	170 (83)	0.66	0.54
RV/TLC (% _{pred})(±SD)	147 (37)*	143 (45)*	152 (53)	0.85	0.79
IC (% _{pred})(±SD)	108 (28)*	106 (19)*	95 (21)	0.85	0.39
FRC (% _{pred})(±SD)	108 (34)*	113 (37)*	120 (35)	0.10	0.08
DL _{CO} (% _{pred})(±SD)	95 (6)*	103 (2)*	98 (13)	0.06	0.17
WL VDP (%)	16 (13)	17 (15)	21 (22)	0.56	0.29

SD, standard deviation; FEV₁, forced expiratory volume in 1 second; %_{pred}, percent predicted; BL, baseline; FVC, forced vital capacity; TLC, total lung capacity; RV, reserve volume; IC, inspiratory capacity; FRC, functional residual capacity; DL_{CO}, carbon monoxide diffusion capacity of the lung; VDP, ventilation defect percentage.

*n=4, [‡]Significance of difference between time-points was determined using paired students t-tests

Hyperpolarized ^3He MRI Ventilation Abnormalities of Cystic Fibrosis and Non-Cystic Fibrosis Bronchiectasis

Gregory Paulin^{1,2}, Sarah Svenningsen^{1,2}, James F. Lewis³, David McCormack³ and Grace Parraga^{1,2}

¹Imaging Research Laboratories, Robarts Research Institute; ²Department of Medical Biophysics; ³Division of Respiriology, Department of Medicine, The University of Western Ontario, London, Canada; Dr. Grace Parraga

RATIONALE: There are few therapies available for bronchiectasis -an airway disease characterized by localized, irreversible destruction of muscle and elastic tissue leading to dilation of the bronchial wall. Airway wall abnormalities typically result from chronic inflammation due to an inability to clear mucous secretions which is common in cystic fibrosis (CF) and in non-CF subjects. Until now, there has been no pulmonary functional imaging studies that directly compare CF and non-CF bronchiectasis. Hence, here our objective was to directly compare pulmonary function test measurements, CT and hyperpolarized ^3He MRI of a small group of CF and non-CF bronchiectasis patients to provide a better understanding of structure-function relationships. Our overarching aim is to validate MRI measurements of airway function as intermediate endpoints for bronchiectasis therapy studies and this pilot study was performed to provide an understanding of the relationship between ^3He MRI ventilation defects and well-established measurements of bronchiectasis.

METHODS: We enrolled non-CF and CF subjects with a diagnosis of bronchiectasis between the ages of 18 and 65 years of age and $\text{FEV}_1 \geq 25\%$. Within 10 minutes of completion of post-salbutamol pulmonary function tests, ^3He MRI was performed, and high resolution chest CT was acquired within 30 minutes of completion of MRI at the same lung volume (FRC+1L) to ensure similar parenchymal distension. ^3He MRI was analyzed for ventilation defect percent (VDP), a surrogate measurement of the normalized volume of the lung that is not ventilated. Thoracic CT volumes were also evaluated for the generation of quantitative airway measurements including airway wall area percent (WA%) and lumen area (LA), peribronchial thickening and mucous plugs.

RESULTS: In total, 15 subjects with bronchiectasis were evaluated including 11 non-CF bronchiectasis (mean age 68 ± 10 yrs) and 4 CF bronchiectasis (mean age 32 ± 14 yrs) subjects. As shown in Figure 1, $\text{FEV}_1\%_{\text{pred}}$ was strongly correlated with ^3He MRI VDP ($r = -.8$, $p < .005$ respectively). CT-derived airway wall area thickness and lumen area were not significantly related with any pulmonary function, plethysmography, or MRI measurements.

CONCLUSIONS: Pulmonary functional MRI with inhaled ^3He gas provides a way to visualize regional ventilation and ventilation defects in patients with bronchiectasis. A quantitative relationship was observed for FEV_1 and ^3He VDP and the spatial relationship between ventilation abnormalities with peribronchial thickening and mucous plugs is required to determine the direct structure-function relationships that are the foundation of potential treatment effects.

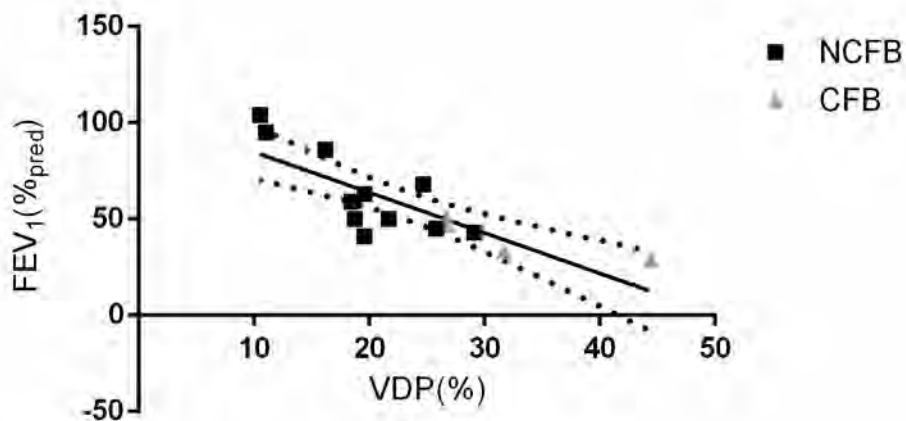


Figure 1: Linear regression for whole lung VDP with $\text{FEV}_1 (\%_{\text{pred}})$ for all subjects ($r^2 = .659$, $r = .812$, $p = .0002$). NCFB: non cystic fibrosis bronchiectasis; CFB: cystic fibrosis bronchiectasis

Pulmonary Computed Tomography and ³He Magnetic Resonance Imaging of GOLD Unclassified Ex-smokers: Does Imaging Matter?

Damien Pike^{1,2}, Miranda Kirby^{1,3}, Sarah Svenningsen^{1,2}, Don D Sin³, David G McCormack⁴, Harvey O Coxson³ and Grace Parraga^{1,2,5,6}

¹Imaging Research Laboratories, Robarts Research Institute, London, Canada; ²Department of Medical Biophysics, The University of Western Ontario, London, Canada; ³Department of Radiology and James Hogg Research Centre, University of British Columbia and Vancouver General Hospital, Vancouver, Canada; ⁴Division of Respiriology, Department of Medicine; ⁵Graduate Program in Biomedical Engineering; ⁶Department of Medical Imaging, The University of Western Ontario, London, CANADA

INTRODUCTION: Despite being the fourth leading cause of morbidity and mortality worldwide, chronic obstructive pulmonary disease (COPD) remains underdiagnosed and undertreated. Previous studies have shown that up to two thirds of patients who undergo spirometry have evidence of reduced pulmonary function but are not classified as having COPD under the Global Initiative for Chronic Obstructive Lung Disease (GOLD) staging criteria. Such patients, categorized as GOLD-Unclassified (GOLD-U), experience decreased forced expiratory volume in one second ($FEV_1\%_{pred} < 80\%$) with a preserved FEV_1 to forced vital capacity (FVC) ratio ($FEV_1/FVC \geq 0.70$). It is now established that spirometry may not completely characterize early or mild pulmonary abnormalities related to tobacco smoking and it remains uncertain whether the GOLD-U stage is predominated by airway- or emphysema phenotypes. We hypothesized that ³He magnetic resonance imaging (MRI) and computed tomography (CT) structure-function measurements in GOLD-U ex-smokers will help provide a better understanding of this important GOLD subgroup.

METHODS: We evaluated 73 ex-smokers (≥ 10 pack years) with $FEV_1/FVC \geq 0.70$ (70 ± 10 yr). All subjects underwent ³He MRI, CT and spirometry within 10 minutes of each other at the same lung volume (FRC+1L) to ensure similar parenchymal distension. ³He MRI was evaluated to generate the ventilation defect percent (VDP) – a surrogate of airways disease and apparent diffusion coefficients (ADC) – a surrogate of emphysema. CT volumes were analyzed for airway measurements of wall area percent (WA%) and lumen area (LA) of the subsegmental airways, as well as parenchyma measurements of relative area of the lung ≤ -950 HU (RA_{950}), and the 15 percentile of the CT density histogram (15HU).

RESULTS: GOLD-U subjects comprised 14% (10/73) of subjects evaluated. GOLD-U subjects had significantly larger WA% ($p=0.007$) and smaller LA ($p=0.002$) than subjects without GOLD stage U ($FEV_1\%_{pred} \geq 80\%$). There were no significant differences for RA_{950} , 15HU, LAC, VDP or ADC for GOLD-U subjects and those without COPD ($FEV_1\%_{pred} \geq 80\%$). In GOLD-U subjects ($n=10$), SGRQ symptom score was significantly correlated with LA ($r=-0.85$, $p=0.002$) and WA% ($r=-0.80$, $p=0.001$), and VDP was significantly correlated with $FRC\%_{pred}$ ($r=0.74$, $p=0.02$) and as shown in Figure 1, $RV\%_{pred}$ ($r=0.73$, $p=0.02$). These relationships were not observed in ex-smokers with $FEV_1 \geq 80\%$ ($n=63$).

CONCLUSIONS: In GOLD-U ex-smokers, small airway morphological abnormalities are related to respiratory symptoms and these remodeled airways may also be the cause of gas trapping and ³He ventilation defects.

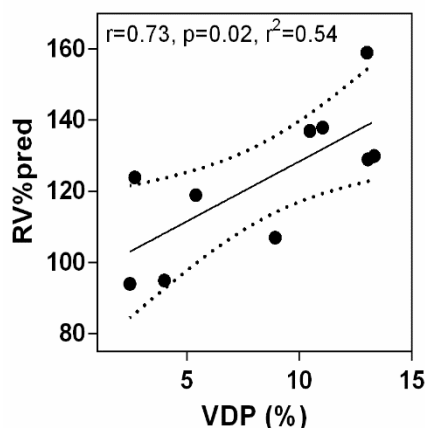


Figure 1: ³He MRI VDP was significantly positively correlated with residual volume ($r=0.73$, $p=0.02$) in GOLD-U subjects ($n=10$). This relationship was not significant in ex-smokers with $FEV_1 \geq 80\%$ ($n=63$).

Sex, Airways Disease and Emphysema in Ex-smokers with and without Airflow Limitation

Damien Pike^{1,2}, Miranda Kirby¹⁻³, Fumin Guo¹, Don D Sin³, Harvey O Coxson³, David G McCormack⁴ and Grace Parraga^{1,2}

¹Imaging Research Laboratories, Robarts Research Institute, London, Canada; ²Department of Medical Biophysics, The University of Western Ontario, London, Canada; ³Department of Radiology and James Hogg Research Centre, University of British Columbia and Vancouver General Hospital, Vancouver Canada; ⁴Division of Respirology, Department of Medicine, The University of Western Ontario, London, CANADA

MOTIVATION AND RATIONALE: In COPD patients, there is evidence that females are more vulnerable to the toxic effects of cigarette smoke than males. At the same time however, it has also been shown that females with COPD who are pack-year matched with males have lower all-cause and respiratory mortality than males and show less evidence of computed tomography (CT) findings of emphysema. These results suggest that the pathophysiology of COPD may manifest differently in males and females. Although thoracic CT imaging has been exploited to provide a better understanding of male-female differences in ex-smokers with and without COPD, we still don't understand the structure-function relationships of these sex differences. Therefore, here our objective was to evaluate ex-smokers from the Thoracic Imaging Network of Canada (TINCan) study with and without airflow limitation using ³He MRI, CT, pulmonary function tests (PFTs), the St Georges Respiratory Questionnaire (SGRQ) and the Six Minute Walk Test (6MWT) to quantify and better understand airway and emphysema phenotypes and their structure-function relationships in males and females with and without COPD.

METHODS: Ex-smokers (≥10 pack years) underwent ³He MRI, CT, PFTs, SGRQ and the 6MWT. ³He MRI and CT were acquired within 10 minutes and at the same lung volume (FRC+1L) to ensure similar parenchymal distension. ³He MRI was analyzed for ventilation defect percent (VDP) and apparent diffusion coefficients (ADC); CT volumes were analyzed to generate quantitative measurements including airway wall area percent (WA%) and lumen area (LA) as well as emphysema (relative lung area with attenuation values ≤ -950HU (RA₉₅₀)) measurements.

RESULTS: We evaluated male (n=103) and female (n=63) ex-smokers including 93 subjects with FEV₁/FVC<0.7, and 73 subjects with FEV₁/FVC ≥0.7. As shown in Table 1, females without COPD had significantly worse SGRQ scores, higher RV/TLC and lower DL_{CO} than males without COPD; females with COPD had lower BMI and higher RV/TLC than males. For males and females with or without COPD, there were no significant differences for ³He MRI microstructural (ADC) and airway functional (VDP) measurements or CT airway or emphysema measurements. Airway WA% was significantly but weakly correlated with VDP (r=0.40, p=0.03) in females without COPD and this relationship was not significant in males with or without COPD.

CONCLUSIONS: The expression of airways disease and emphysema in ex-smokers with and without COPD is heterogeneous with respect to sex.

Table 1: Comparison of males and females with and without COPD for demographic, pulmonary function test, CT and ³He MRI data

	Without COPD (n=73)		P	COPD (n=93)		P
	Male (n=41)	Female (n=32)		Male (n=62)	Female (n=31)	
Age yr (±SD)	70 (10)	69 (9)	0.83	72 (9)	69 (7)	0.08
BMI kg/m ² (±SD)	29 (3)	30 (5)	0.18	27 (4)	25 (5)	0.04
Pack yr (±SD)	28 (17)	26 (17)	0.48	47 (30)	50 (26)	0.93
6MWD (±SD)	407 (93)	395 (95)	0.59	375 (91)	359 (92)	0.44
SGRQ (±SD)	17 (18)	31 (23)	0.006	38 (20)	44 (17)	0.24
FEV ₁ % _{pred} (±SD)	103 (15)	94 (21)	0.06	64 (25)	57 (20)	0.22
FVC% _{pred} (±SD)	95 (14)	94 (15)	0.14	91 (20)	85 (17)	0.09
FEV ₁ /FVC (±SD)	80 (6)	81 (6)	0.62	49 (13)	51 (12)	0.61
RV% _{pred} (±SD)	108 (21)	110 (27)	0.81	157 (49)	159 (43)	0.91
RV/TLC (±SD)	38 (7)	45 (9)	<0.0001	48 (11)	55 (13)	0.02
TLC% _{pred} (±SD)	100 (12)	102 (15)	0.42	115 (18)	121 (19)	0.26
DL _{CO} % _{pred} (±SD)	84 (19)	69 (18)	0.0008	56 (21)	48 (17)	0.08
RA ₉₅₀ % (±SD)	1.2 (1.1)	1.1 (0.9)	0.67	11 (11)	11 (10)	0.94
WA% (±SD)	62 (3.0)	63 (2.9)	0.09	62 (7)	63 (3)	0.16
LA mm ² (±SD)	16 (4.1)	14 (4.0)	0.09	16 (5)	13 (6)	0.06
VDP % (±SD)	6.5 (3.6)	5.9 (3.3)	0.53	19 (10)	16 (8)	0.12
ADC cm ² /s (±SD)	0.27 (0.03)	0.28 (0.04)	0.43	0.42 (0.11)	0.42 (0.11)	0.89

BMI: Body mass index, 6MWD: Six-minute walk distance, SGRQ: St. George's Respiratory Questionnaire Total Score, FEV₁: Forced expiratory volume in one second, FVC: Forced vital capacity, TLC: Total lung capacity, RV: Residual volume, DL_{CO}: Diffusing capacity for carbon monoxide, WA%: Airway wall area percentage, LA: Airway lumen area, RA₉₅₀: Relative area of the lung with attenuation values below -950HU, ADC: Apparent diffusion coefficient, VDP: Ventilation defect percentage, SD: Standard deviation, %_{pred}: Percent of predicted value

Pulmonary Imaging of Chronic Obstructive Pulmonary Disease in Ex-smokers: Thoracic Imaging Network of Canada (TINCan) Cross-sectional Evaluation

Damien Pike^{1,2}, Miranda Kirby¹⁻³, Don D Sin³, David G McCormack⁴, Harvey O Coxson³ and Grace Parraga^{1,2,5,6}

¹Imaging Research Laboratories, Robarts Research Institute, London, Canada; ²Department of Medical Biophysics, The University of Western Ontario, London, Canada; ³Department of Radiology and James Hogg Research Centre, University of British Columbia and Vancouver General Hospital, Vancouver Canada; ⁴Division of Respiriology, Department of Medicine; ⁵Graduate Program in Biomedical Engineering; ⁶Department of Medical Imaging, The University of Western Ontario, London, CANADA

INTRODUCTION: Recent large-scale investigations such as the ECLIPSE and COPDGene studies have shown the unique regional pulmonary anatomical and morphological measurements derived from high resolution x-ray computed tomography (CT) of COPD. Complementary to such structural information, hyperpolarized ³He magnetic resonance imaging (MRI) has emerged as another non-invasive imaging tool with the advantage that it provides a way to quantify both pulmonary structure and function simultaneously and non-invasively. Whereas ECLIPSE and COPDGene did not include pulmonary functional imaging, the Thoracic Imaging Network of Canada (TINCan) prospectively planned to enroll up to 200 ex-smokers with and without COPD for physiological, CT and pulmonary functional and structural MRI measurements with three-year followup.

METHODS: Ex-smokers (≥ 10 pack years) underwent ³He MRI, CT, pulmonary function tests (PFTs), the St. George's Respiratory Questionnaire (SGRQ) and the six-minute walk test (6MWT). ³He MRI was acquired with subjects at inspiration (FRC+1L) to generate ventilation defect percent (VDP) and apparent diffusion coefficient (ADC) measurements. CT was performed within 10 minutes of ³He MRI with the subject at inspiration breath-hold at FRC+1L to ensure similar parenchymal distension. CT volumes were analyzed to generate airway (wall area percent (WA%) and lumen area (LA)) and emphysema measurements including the relative area of the CT density histogram with attenuation values ≤ -950 HU (RA₉₅₀), low attenuating clusters and 15th percentile of the density histogram.

RESULTS: We completed full evaluations for 197 ex-smokers including ³He MRI, CT, PFT, SGRQ and 6MWT data. As shown in Figure 1, a significant fraction (87/197=44%, 44 male) reported FEV₁/FVC ≥ 0.70 and were classified based on DL_{CO}%_{pred}, diagnosis of bronchiectasis and FEV₁ (GOLD-U=FEV₁<80%, FEV₁/FVC ≥ 0.70). The majority of subjects (110/197=56%, 72 male) reported FEV₁/FVC<0.70 and were staged according to Global Initiative for Chronic Obstructive Lung Disease (GOLD) criteria (1). Of subjects with airflow limitation, there were n=22 GOLD 1 subjects, n=50 GOLD 2 subjects, n=30 GOLD 3 subjects and n=8 GOLD 4 subjects. In ex-smokers without COPD, 6MWD was significantly correlated with ³He MRI measurements of airway function (VDP r=-0.30, p=0.02), and parenchyma microstructure (ADC, -0.49, p<0.0001) as well as CT RA₉₅₀ (r=-0.31, p=0.009) and these relationships for 6MWD were also observed in COPD subjects (VDP, r=-0.34, p=0.002; RA₉₅₀, r=-0.35, p=0.001; ADC, r=-0.25, p=0.02).

CONCLUSIONS: TINCan consists of 197 ex-smokers representing the largest prospective study of pulmonary structure-function relationships in ex-smokers with and without COPD.

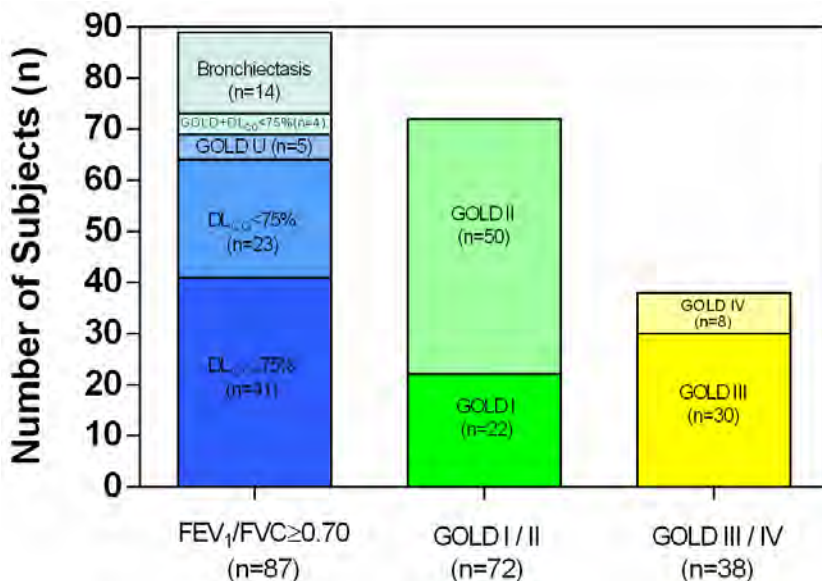


Figure 1: Subjects with FEV₁/FVC ≥ 0.70 were classified based on DL_{CO}%, clinical diagnosis of bronchiectasis and FEV₁ <80% (GOLD-U=FEV₁<80%, FEV₁/FVC ≥ 0.70). Subjects with FEV₁/FVC<0.70 were classified according to GOLD criteria. A total of 197 ex-smokers were evaluated including 87 subjects with FEV₁/FVC ≥ 0.70 , 22 GOLD 1, 50 GOLD 2, 30 GOLD 3 and 8 GOLD IV subjects.

IMAGE-CAD Pilot Study
Assessment of Patients with Suspected Coronary Artery Disease (CAD):
What is the best initial imaging strategy? Cardiac Computed Tomographic Angiography (CCTA) vs Stress Echocardiography (SE) vs Single-Photon Emission Computed Tomography (SPECT)

Victoria Sarban, MD,^a Jissy Thomas, NP,^a Eila Mirhadi, MSc,^a Patrick H. Gibson, BMBCh, MD,^a Sayra Khandekhar, MD, FRCPC,^a Anderson Chuck, PhD, MPH,^b Sean McMurtry, MD, PhD, FRCPC,^a Robert Welsh, MD, FRCPC,^a Ross Tsuyuki, BSc(Pharm), PharmD, MSc,^b Richard Coulden, MD, FRCP, FRCR^a Lucille Lallonde, MD, FRCPC,^a Jonathan Choy, MD, FRCPC,^a Harald Becher, MD, PhD, FRCPC,^a

^a **Mazankowski Alberta Heart Institute, University of Alberta Hospital, Edmonton, Alberta, Canada**

^b **EPICORE Centre, Edmonton, Alberta, Canada**

Background: Several imaging tests are available for assessment of patients with symptoms suggestive of CAD if an exercise stress test is not possible or non conclusive. There are major differences in costs and patient involvement between the tests. However, there is a limited evidence for what is gained by using a more invasive and costly test. We hypothesize that stress echocardiography is not inferior to SPECT and/or CCTA regarding patients outcome and downstream costs over one year.

Objective: To conduct a health economic analysis by comparing healthcare resource utilization and outcomes following randomization to one of the three different imaging strategies over one year in patients presenting with symptoms suggestive of CAD.

Methods: This is a prospective cohort randomized pilot trial of three imaging strategies in patients presenting with symptoms of CAD requiring initial diagnostic/prognostic work-up. The sample size in this pilot study is 80 patients for each imaging strategy. The imaging results are presented to the referring physician who decides on further diagnostics and treatment. The following data are collected: healthcare resource utilization (coronary angiography, coronary interventions, hospitalizations, medical costs, and radiation exposure), angina assessment and major adverse cardiac events. Telephone interviews are performed at 1, 6 and 12 months.

Preliminary results: 106 patients are recruited so far. The data is transferred to the EPICORE Centre database for analysis. Expected trial end is 2014.

Conclusion: With IMAGE-CAD pilot trial we have established an infrastructure which allows us to plan and perform a multicentre trial and we are looking for partners in other provinces.

**Ontario Consortium for Adaptive
Interventions in Radiation Oncology
OCAIRO**

Oral Presentation and Poster Abstracts

Characterization of a new gel dosimeter for radiation therapy using optical CT imaging

K.M. Alexander¹, A. Nasr², K.B. McAuley², L.J. Schreiner^{1,3}

(1) Department of Physics, Queen's University, Kingston, Ontario. (2) Department of Chemical Engineering, Queen's University, Kingston, Ontario. (3) Medical Physics Department, Cancer Centre of Southeastern Ontario, Kingston, Ontario.
Research supervisor: L.J. Schreiner

Gel dosimeters are well suited to the growing complexity of modern radiation delivery techniques and have many clinical applications, including commissioning of new treatment techniques and for characterizing small field irradiations. Recently, optical CT dosimeter read-out techniques have increased the potential for clinical gel dosimeter use, but past gel dosimeter systems present various problems when used with optical CT: polymer gels suffer from difficulties in quantifying optical CT number due to scatter, and Fricke gels lose spatial dose integrity because iron ions diffuse quite rapidly. In this work, we present steps in developing a leuco crystal violet (LCV) micelle gel dosimeter specifically intended for read-out by optical CT, which improves on existing leucodye gel dosimeters found in literature.

In our clinic, gel dosimeters are read out using a Vista Optical CT scanner (Modus Medical Devices Inc., London, Ontario). The Vista scanner is a cone beam optical scanner which can image cylindrical jars of dosimeter. A gel dosimeter jar is suspended in the water tank, attached to a stepping motor, and illuminated by an LED light panel (590 nm). On the opposing side of the tank, a CCD camera acquires individual image projections of the gel as the jar is rotated. These image projections are then reconstructed to produce a full, digital, and three-dimensional dose volume that can be compared to the expected/calculated dose. Our new gel formulation employs a different surfactant than used in the literature, and also includes a chemical sensitizer to improve the dose response. A Varian Trilogy 2100iX linear accelerator (Varian Medical Systems, Palo Alto, CA) was used to irradiate LCV micelle gel dosimeter jars with a VMAT prostate plan and another gel jar with a 12MeV electron beam (6x6cm², 1850 MU) to be used for calibration of the VMAT plan. The gels were imaged 30 minutes after irradiation, and after two weeks. Results examining light absorption of the LCV micelle gel solution in the Vista scanner, optimal temperature of the gel during irradiation, as well as its overall application as a tool for radiation therapy quality assurance will be reported in this work.

Background (pre-irradiation) scans of the new gel showed lower optical density values than that of Fricke gels, allowing for improved light transmission and a greater dynamic range of pixel values on-board the CCD camera. Experiments with this new gel found a dose sensitivity of $4.9 \times 10^{-3} \text{ Gy}^{-1} \text{ cm}^{-1}$. This dose sensitivity is a factor of 10 less than that of Fricke gels, but is sufficient for a wide range of clinical applications. Results also show that our new dosimeter is more stable than a Fricke gel dosimeter, which loses the spatial dose information in a matter of hours. Measurements with the new LCV micelle gels show that the dose distribution information is maintained over more than two weeks (see Fig. 1). Further characterization of this new gel dosimeter shows that the chemical response is dose rate independent, but that temperature effects need to be controlled during irradiation.

Our results show that this formulation of LCV micelle gel has great promise to remove some of the practical constraints of existing gel dosimeters. Further characterization is currently underway to improve this new dosimeter's clinical use.

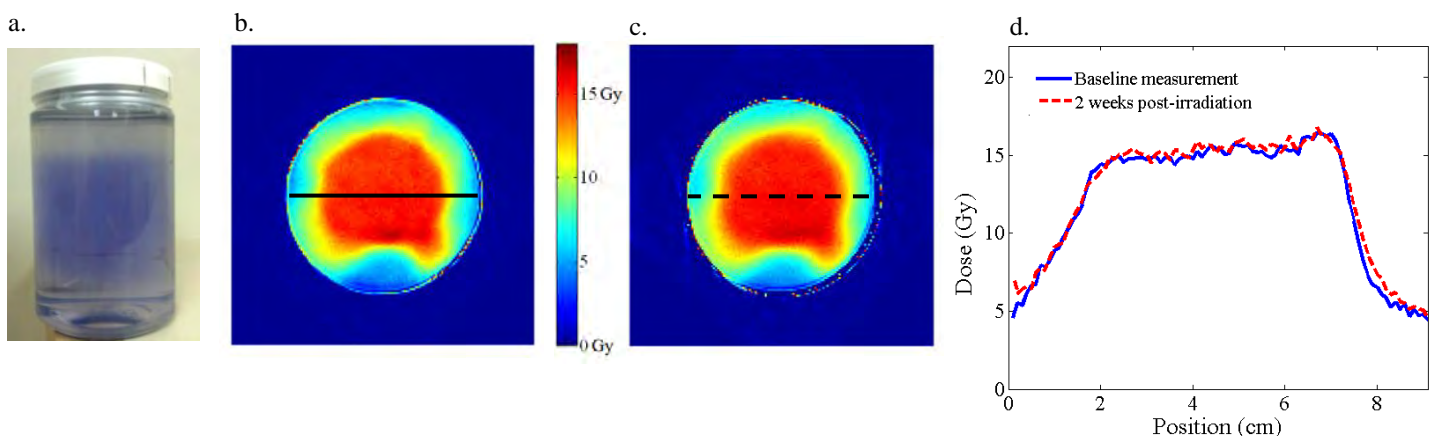


Figure 1.a) Photograph of a VMAT prostate plan LCV micelle gel dosimeter; b) Dose map of one slice of the gel dosimeter, imaged 30 mins after irradiation (baseline measurement); c) Dose map of one slice of the gel dosimeter, imaged 2 weeks after irradiation; d) Cross-plane profiles of the gel slices (as indicated in Fig.1b and 1c) showing gel dosimeter stability after two weeks.

Measurement of Attenuation and Phase Aberration From Pediatric Skulls During Transcranial MRI-guided High Intensity Focused Ultrasound

Matthew R. Ambacher¹, Thomas Looi¹, Charles Mougenot², Samuel Pichardo^{3,4}, Adam C. Waspe¹, and James M. Drake¹ ¹Centre for Image Guided Innovation and Therapeutic Intervention, The Hospital for Sick Children, ²Philips Healthcare Canada, ³Physical Sciences, Sunnybrook Research Institute, ⁴Electrical Engineering and Physics, Lakehead University

mrambach@uwaterloo.ca

This paper presents a method for measuring the attenuation and phase aberration due to the pediatric skull and proposes a phase correction strategy for transcranial high intensity focused ultrasound (HIFU) sonications. Due to the varied thickness of the skull, and differences in density and speed-of-sound between trabecular and cortical bone layers, an acoustic beam is defocused upon passing through a skull. As a consequence, the acoustic energy is spread to areas other than the target. Magnetic resonance imaging (MRI) is helpful for locating potential intracranial targets and for positioning the geometric focus of a HIFU transducer on the target. However, there is currently no way to predict and correct for phase aberrations introduced by the skull from a preoperative MRI scan. When considering the high doses of ionizing radiation from a cranial x-ray CT scan, especially dose concerns in young children, a method for predicting and correcting these phase aberrations on a case-by-case basis directly from MRI is desired.

Skull characterization is achieved by calculating the attenuation and phase delay introduced between the 256 elements of the phased-array HIFU transducer and the geometric focus. To do this, a hydrophone was positioned at the geometric focus of the transducer and a cadaveric skull was positioned in the sonication path. Each transducer element is activated individually and the amplitude and time-of-flight to reach the hydrophone is recorded. A reference channel is chosen and all signals are compared with this channel. Relative phase measurements between transducer elements are taken by calculating a cross-correlation between the reference channel and each channel. The lag between these two signals is measured in the time domain and, when multiplied by the speed of sound, provides a phase offset in units of distance. Attenuation measurements are taken for each element by calculating the change in the root mean square of the hydrophone signal after the cadaveric skull was positioned.

To correct for phase aberration, phase offsets are introduced to elements based on the time delay measured earlier. By introducing phase offsets, the acoustic wave can be electronically refocused on the target, after the wave traverses the skull. To refocus the wave, a signal delay between $-\pi$ and π is introduced to each element. This signal delay is proportional to the inverse of the time-of-flight delay measured earlier. An amplitude coefficient is introduced to elements based on the attenuation measurements earlier. This coefficient is used to adjust the acoustic power output of each element so that the desired temperature is reached at the intracranial target. In Figure 1 below, the phase aberrations introduced by a pediatric skull are shown (left) as well as the results of adjusting phase offsets to refocus (right). The scale shows relative phase difference between elements in units of distance and it is evident that the range is reduced by applying phase offsets.

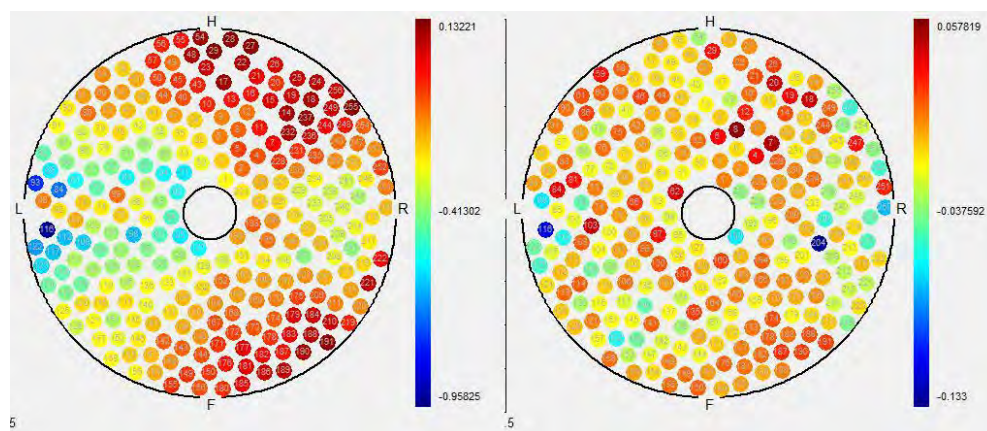


Figure 1: Differences in relative phase of elements between a pediatric skull with no phase correction (left) and a pediatric skull with phase correction (right).

Automated Planning of Breast Radiotherapy Using Cone Beam CT Imaging

Guy Amit¹, Thomas G. Purdie^{1,2,3}

⁽¹⁾ Radiation Medicine Program, Princess Margaret Cancer Centre, University Health Network, Toronto

⁽²⁾ Department of Radiation Oncology, University of Toronto

⁽³⁾ Techna Institute, University Health Network, Toronto

Introduction: Intensity-modulated radiotherapy (IMRT) is a standard approach for organ-preserving whole-breast irradiation. An automated technique for two-field tangential breast IMRT planning has been previously developed and is used routinely at the Princess Margaret Cancer Centre. This planning technique is based on automatic detection of radio-opaque markers in the CT simulation images, model-based segmentation of the organs at risk and an optimization process for determining the gantry and collimator angles [1]. Kilovoltage cone-beam CT (CBCT), which is becoming a widespread technology for image-guided treatment, is a desirable component in an adaptive radiotherapy framework. However, CBCT imaging does not produce accurate CT numbers and suffers from artifacts, which can affect both accurate dose calculation and automated segmentation algorithms based on CT numbers. In order to introduce CBCT for automated treatment planning, corrections must be applied [2]. The purpose of this work is to develop and evaluate methods for automated breast radiotherapy planning, based on analysis of CBCT images.

Methods: We aim to use machine learning techniques to learn the mapping between the CBCT grey levels and CT numbers from conventional CT imaging. This mapping is used to produce transformed CBCT images, to which the automated planning algorithms can be applied. For demonstrating the feasibility of the approach, a training dataset was constructed using pairs of CT and CBCT scans obtained from the Princess Margaret Cancer Centre. The scan resolution of the CBCT images was $1 \times 1 \times 1 \text{ mm}^3$ (Elekta Synergy). For each pair, the CT images were processed to detect the radio-opaque markers and to segment the lungs, heart and the body contour. The CBCT images were registered onto the CT images, using 3D intensity-based rigid registration. The histograms of each segmented region of interest (ROI) were calculated on the CT and CBCT images. The histograms of the CBCT images were equalized for each ROI, to resemble the CT's histograms. The automated planning algorithm was executed on the processed CBCT images and the resulting radiotherapy plans were compared to the ground-truth plans generated from the CT images.

Results and Discussion: The initial analysis included images from 8 patients. The histograms of the lungs, heart and the remaining body volume in the CBCT images showed larger inter-patient variance, compared to the corresponding CT images. In all patients, the automated plan generated from the CBCT images was acceptable according to the clinical protocol criteria, and was equivalent to the ground-truth CT-based plan. Comparison of the minimum and maximum target dose, ipsilateral lung dose and heart dose between CT-based and CBCT-based plans showed no statistically significant difference. Figure 1 shows an example of a processed CBCT image, along with the non-processed image and the corresponding CT.

In order to carry out automated planning on a new CBCT image set, without a corresponding CT scan, a similarity metric will be defined, based on anatomical and image features. Under this metric, the nearest CBCT image set will be retrieved from the training data, and its corresponding CT histograms will be used to transform the new CBCT image set. We intend to validate this approach on a large clinical dataset.

Conclusions: Automatic planning on CBCT images can potentially enable adaptive treatment without additional CT simulations. It is feasible to apply automated planning of breast radiotherapy to transformed CBCT images. It is expected that utilizing machine learning techniques will enable transforming CBCT images independently of information from the CT scan.

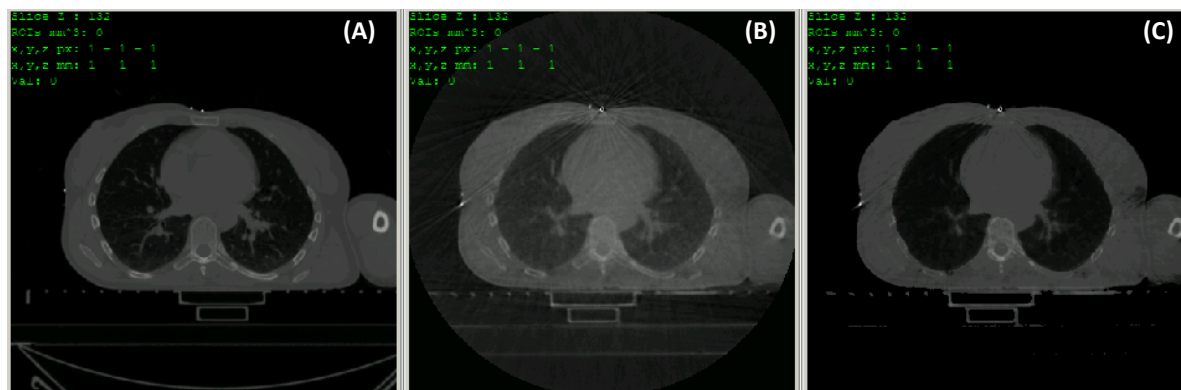


Figure 1: A CT image (A) and a registered CBCT image before processing (B) and after applying histogram equalization to the lungs, heart and remaining body contour (C). The transformed CBCT is used to automatically generate a breast IMRT plan.

References

- [1] Purdie TG et al., Automated Planning of Tangential Breast Intensity-Modulated Radiotherapy Using Heuristic Optimization. *Int. J. Radiation Oncology Biol. Phys.* 2011; 81(2): 575–583.
- [2] Fotina I et al., Feasibility of CBCT-based dose calculation: Comparative analysis of HU adjustment techniques. *Radiother. Oncol.* 2012; 104(2): 249–256.

Slicelet implementation for gel dosimetry analysis

Jennifer Andrea¹, Mattea Welch¹, Csaba Pinter¹, Kevin Alexander^{2,3}, John Schreiner^{2,3}, Gabor Fichtinger¹

¹ Laboratory for Percutaneous Surgery, School of Computing, Queen's University, Kingston, ON, Canada

² Medical Physics Department, Cancer Centre of Southeastern Ontario, Kingston, ON, Canada

³ Department of Physics, Queen's University, Kingston, ON, Canada

PURPOSE: The complexity of the open-source SlicerRT toolkit [1] provides a large degree of flexibility to the user, but can make some routine workflows inconvenient to perform. New features and interfaces are needed to streamline these processes into simple, user-friendly workflows. Gel dosimetry analysis is a tool used in commissioning new radiation techniques and to validate the accuracy of radiation treatment by enabling visual comparison of the planned dose to the delivered dose, where correspondence between the two dose distributions is achieved using embedded landmarks. Gel dosimetry is based on imaging chemical systems spatially fixed in gelatin, which exhibit a detectable change upon irradiation. This chemical change is related to the amount of radiation received and can be probed by several imaging techniques, allowing 3D dose information to be obtained. The purpose of this project was to design and implement a custom workflow and user interface, called a *slicelet*, based on the 3D Slicer platform and SlicerRT. This slicelet would enable simultaneous visualization and comparison of the computed treatment planning dose to the delivered gel dose, and would simplify a currently complex analysis process.

METHODS: 3D Slicer (www.slicer.org) is an open-source software platform for medical image visualization and analysis. SlicerRT (www.SlicerRT.org) is an open-source radiation therapy research toolkit developed for 3D Slicer [1]. SlicerRT provides specific measurement tools such as contour comparison, dose volume histograms and dose comparison. A slicelet is a simplified custom workflow and user interface that uses the features and functionalities of the 3D Slicer platform and 3D Slicer-based toolkits, including SlicerRT. We designed and implemented our slicelet in Python, utilizing many functions already existing in 3D Slicer and SlicerRT. Our slicelet currently consists of the following steps: data loading, registration using BRAINSFit general registration, registration using manually segmented fiducials, dose calibration, performing statistical tests, and extracting the statistics from the workflow. The optical CT data containing the measured dose is in a special format, called VFF. A file reader has been developed for this format that integrates into the data IO mechanism of 3D Slicer. The dose registration accuracy was evaluated using two different methods in order to show that the slicelet enabled visual comparison of the dose distributions. The first approach used visual confirmation that the registered and transformed fiducials corresponded correctly. The second method used target reconstruction error, computed after running 10 tests on sample IMRT planned dose data.

RESULTS AND DISCUSSION: The workflow has been implemented (Figure 1), and provides all of the required capabilities for image registration and transformation so that the planning distribution of the computed dose and that of the delivered dose can be compared. The image registration has been qualitatively validated using visual confirmation that the corresponding fiducials are correctly registered. This can be seen by observing that the fiducials from the two distributions, and their corresponding image volumes, are overlaid following registration and transformation. Image registration was also quantitatively validated by computing the target reconstruction error (TRE) of the registration. To do this we computed the registration of the delivered dose to the planned dose using five fiducial landmarks from each volume, and a sixth fiducial from each was randomly chosen each time to compute the TRE. The TRE was 1.7 ± 0.3 mm for 10 tests indicating that the registration was accurate, as this error is less than the typical treatment planning resolution of 2.5 mm, so the error will have no significant impact on the result of the gel dosimetry analysis. To reduce the current lengthy analysis time, this slicelet was designed to help streamline the gel dosimetry analysis process.

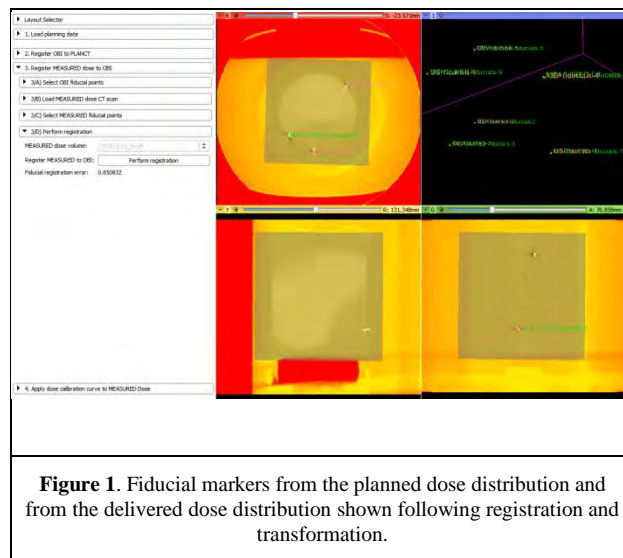
This slicelet provides a significant step in helping to bring gel dosimetry into common clinical use. Future developments will include improving the user interface and slicelet interactions to support more functions, such as contour comparison. We are also trying to select the most appropriate metrics to use in our slicelet, such as dose volume histograms and gamma evaluations. In conclusion, the initial steps of our slicelet have been implemented, and have been shown to produce the correct results. This has been demonstrated through visual confirmation that the delivered dose fiducials have been correctly registered and transformed, as well as by the low TRE that resulted after 10 tests. We believe that the simplicity of the slicelet will appeal to users who are inexperienced with 3D Slicer or SlicerRT, and will facilitate collaboration between the image guided therapy, radiation oncology, and medical physics communities.

ACKNOWLEDGEMENTS: This work was in part funded by Cancer Care Ontario through Applied Cancer Research Unit and Research Chair in Cancer Imaging grants.

Consortium member / research supervisor: Gabor Fichtinger

REFERENCES:

[1] C. Pinter, A. Lasso, A. Wang, D. Jaffray, and G. Fichtinger, "SlicerRT: Radiation therapy research toolkit for 3D Slicer", Med. Phys. 39(10), 6332/7 (2012).



A Mobile Handheld Augmented Reality Prototype for Imaged-Guided Head and Neck Surgery

M. A. Cachia^{1,2}, M. J. Daly^{1,4}, S. Haerle⁴, J. Qiu¹, W. Kucharczyk⁶, R. Weersink¹, D.A. Jaffray^{1,4}, J.C. Irish⁵, H. Chan^{1,3}

¹Techna Institute, University of Health Network; ²Department of Electrical and Computer Engineering, University of Waterloo;

³Ontario Cancer Institute, Princess Margaret Hospital; ⁴Institute of Medical Science, University of Toronto; ⁵Otolaryngology – Head & Neck Surgery, Princess Margaret Hospital; ⁶Toronto General Hospital, University Health Network

Introduction: Conventional image-guided procedures enable clinicians to navigate medical instruments in patient space. However, this procedure does not always allow the image space to be registered into real physical space. Difficulties arise from interpolating and registering the image to the patient’s physical space. The requirement for precise hand-eye coordination can potentially lead to complications in the procedure. To address these challenges and minimize the risk of potential complications, the Techna Institute’s Guided Therapeutics group has developed a handheld device, which is capable of augmenting an interventional site with medical images. The augmentation uses tri-planar views of volumetric data and pre-defined anatomical contours (e.g., lesions and critical structures), and superimposes the view to the real patient space. The medical image resulting from the augmentation can be manipulated with the tracked instruments.

Methods: A prototype handheld augmented reality device was designed to be compact and mobile, while allowing for medical imaging and planning data to be superimposed on the interventional site. The prototype hardware consists of an RGB laser light source pico projector (L1.V2, AAXA Technology Inc, Santa Ana) and an infrared real-time optical tracking system (Polaris Spectra, NDI, Waterloo, Ontario). In addition, the handheld device is affixed with an optical reference marker. This marker allows the augmented reality (AR) device to be dynamically tracked, providing different perspective views of the augmented subject. To fully realize the AR system, a calibration needs to be conducted in order to characterize the pico projector and compute the homogeneous transformation matrix of the reference marker relative to the projector. This calibration procedure enables the coordinate system of the image, pico projector and tracking system to be co-registered to the world space while maintaining augmentation accuracy during usage. The prototype had been integrated into the image-guided system and incorporated with the in-house software for 3D visualization and real-time navigation (“GTxEyes”).

Results: In order to determine the accuracy of the virtual image overlay onto a real object, an experiment with a 3D checkerboard was conducted. The parameters from the calibration procedure were imported into the navigation software. The virtual 3D image, taken with cone-beam CT, was projected directly on top of the checkerboard. Measurements of the centre divot of 25 real squares and virtual squares were taken with tracked pointer and the difference computed. These measurements were repeated at the distances 30cm and 50cm away from the physical object. The mean error for all trials was 4.97 ± 1.07 mm.

Conclusions: Given the diverse nature of information that can be projected, this prototype can be adapted to a variety of interventional procedures including sentinel lymph node biopsy, maxillary/mandible reconstruction and free-flap harvesting. The initial experimental results demonstrate the feasibility of the proposed augmentation method, however, there is room for improvement. Future work includes improving image overlay performance and tracking of the viewer’s pose and orientation to reduce parallax effects when viewing the image.



Figure 1: a) A mobile handheld augmented reality prototype with 3D head and neck phantom; b) Virtual image of a 3D checkerboard superimposed on the real object; c) Augmented reality information (e.g., coronal slice of cone-beam CT image) projected onto a skull phantom.

Development of In Vivo EPID Dosimetry for IMRT Quality Assurance

Peggy Le¹, Lean Bann¹, Matt Wronski¹, Angela Turner², Andrew Loblaw^{2,3,4}, Geordi Pang^{2,3,4} and Lee Chin^{2,3,4}

¹Department of Medical Physics, ²Odette Cancer Centre, Sunnybrook Health Sciences Centre, ³Department of Radiation Oncology, University of Toronto, ⁴

Intensity modulated radiation therapy (IMRT), is a complex technique that employs shaped radiation beams aimed from several angles of exposure to intersect at the tumour, providing a much larger absorbed dose in the tumour than in the surrounding, healthy tissue. Patient specific quality assurance (QA) is a vital component of the IMRT process. The goal is to assure that the dose calculation and delivery are of sufficient accuracy to produce the physician approved treatment plan (i.e. patient dose, DVH).

Quality assurance (QA) of complex IMRT plans (i.e. H&N, spine SBRT, prostate) are often performed via pre-treatment IMRT measurements on tissue equivalent solid water phantoms using 2-D diode arrays. While this approach provides an idea of the TPS modeling limitations it is not a patient specific evaluation of the plan and does not account for the: 1) geometric differences that could arise during treatment compared to the patient anatomy at the initial CT simulation (i.e. weight loss, gas pockets, tumour shrinkage) (this one may not have to be assessed *in vivo*) 3) intrafraction motion (breathing, bladder filling) and 4) machine variations at the exact time of treatment (i.e. output, MLC and jaw variations). These issues can only be assessed *in vivo* during the time of patient treatment.

Here we describe the development of an on-line electronic portal image device (EPID) that employs transmission images produced by radiation beams used to treat the patient. As such, geometric and machine variations can be evaluated *in vivo* with no added dose or disturbance to the patient treatment workflow. Experimental verification of our novel dose reconstruction algorithm was performed in phantoms and correlated with film and ion chamber measurements. The impact of the proposed technique on clinical workflow was evaluated by comparing treatment times with and without EPID dosimetry. Finally, we report on our first *in vivo* results during patient treatment (Figure 1).

Long term goals include comparing pre-treatment and *in vivo* patient measurements to establish appropriate baselines for initiating re-plan or evaluation. The presented EPID imaging technique allows for *in vivo* patient specific evaluation of IMRT plans and provides a potential solution to the limitations of pre-treatment IMRT QA.

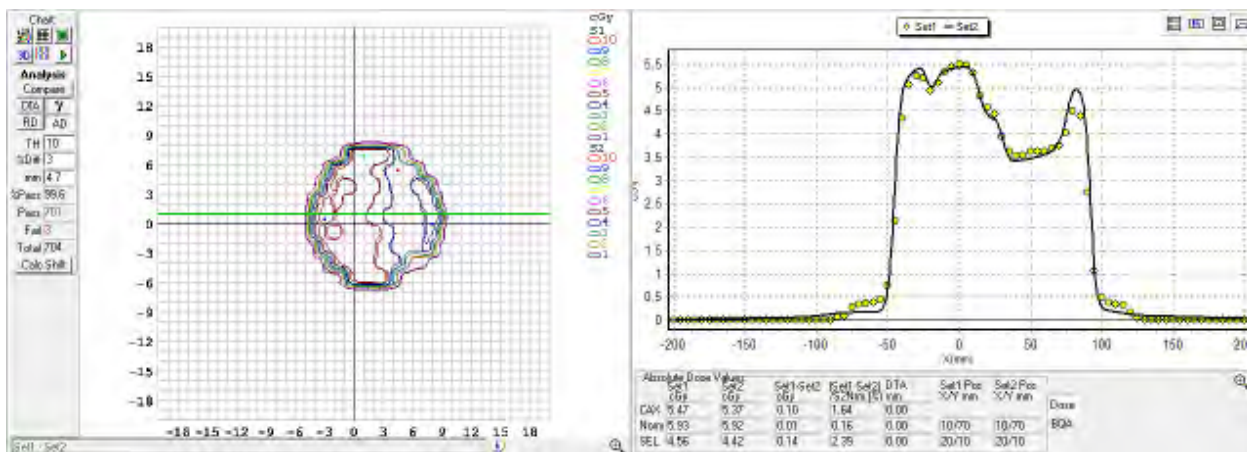


Figure 1: Gamma analysis (3%/3mm) of a 2D planar dose map acquired *in vivo* for a patient undergoing prostate IMRT. Gamma pass rates over all treatment beams range from 93.7 – 100%.

Integration of SlicerRT into the clinical adaptive radiation therapy workflow: deformable image registration algorithm optimization and validation

Jidney Cifuentes¹, Eric Vorauer¹, Peggy Le¹, Daniel Glick, M.D.^{1,3}, Jonathan Livergant, M.D.^{1,3}, Csaba Pinter, M.Sc.⁴, Andras Lasso, Ph.D.⁴, Gabor Fichtinger, Ph.D.⁴, Lee Chin, Ph.D.^{1,2}

¹Department of Medical Physics, ²Odette Cancer Centre, Sunnybrook Health Sciences Centre, ³Department of Radiation Oncology, University of Toronto, ⁴School of Computing, Queen's University, Lee Chin, Ph.D.^{1,2}

Adaptive radiation therapy (ART) integrates daily images into the radiotherapy process to evaluate and modify the plan in order to account for weight loss and geometric changes throughout treatment. SlicerRT (Pinter et al., 2012) is a powerful open-source software toolkit that includes the resources needed to evaluate various radiation therapy metrics (i.e. contour changes, dose volume histogram), that can potentially be incorporated as a module in a radiation therapy record and verify (RV) system to perform on-line adaptive RT. Such an application would integrate core components of: 1) pre-set input/output locations for DICOM-RT files 2) automatic implementation of optimized site-specific rigid and deformable registration routines and 3) dose accumulation and target/organ at risk violation reporting. Such a platform will likely allow clinicians to monitor and evaluate the necessity for adaptive re-planning.

In this work, we describe and validate an adaptive framework using SlicerRT to incorporate deformable image registration (DIR) routinely into the ART process. The DIR module, found in SlicerRT, uses non-rigid B-spline deformable image registration and gradient vector flow to generate deformation maps that can be utilized to 1) deform planning CT contours onto daily image guided radiation therapy (IGRT) images and 2) perform dose accumulation. In addition, the wide variety of adjustable DIR parameters in SlicerRT such as cost function routine, image subsampling rate, and maximum iterations allow for the development of class solutions optimized to the target site and imaging modality (i.e. KV-CBCT, MVCT) of interest.

Here, we describe our experience implementing rigid/deformable image registration routines for pancreatic and head and neck cancer cases. These deformed contours were evaluated against gold standard physician-drawn contours using dice similarity coefficient and Hausdorff distance metrics available in the SlicerRT's contour comparison module.

The overall accuracy and limitations of the SlicerRT DIR algorithm is part of an ongoing project that will perform site specific evaluation of the generated deformation maps with experimental phantom measurements. Overall, SlicerRT can be considered a flexible platform that allows the user to incorporate the necessary tools to aid clinical routines. In addition, our institution has tailored new modules, such as the overlap volume histogram (OVH) module, to describe the geometric relationship between targets and organs at risk, and eventually could be utilized for re-planning processes.

Acknowledgement: This work was in part funded by Cancer Care Ontario through Applied Cancer Research Unit and Research Chair in Cancer Imaging grants and the Ontario Research Fund – Research Excellence Ministry of Research and Innovation.

References

Pinter C, Lasso A, Wang A, Jaffray D, Fichtinger G. 2012 SlicerRT: Radiation therapy research toolkit for 3D Slicer. *Med Phys.* 39(10):6332-8

Quantitative Assessment of Vascular Changes in Late Oral Radiation Toxicity Patients

Bahar Davoudi^{1,5}, Kostadinka Bizheva², Victor X. D. Yang³, Robert Dinniwell^{4,5}, Wilfred Levin^{4,5}, Alex I. Vitkin^{1,4}

¹Department of Medical Biophysics, University of Toronto, Toronto, ON, Canada;

²Department of Physics and Astronomy, University of Waterloo, Waterloo, ON, Canada;

³Department of Electrical and Computer Engineering, Ryerson University, Toronto, ON, Canada;

⁴Ontario Cancer Institute/University Health Network, Toronto, ON, Canada;

⁵Department of Radiation Oncology, University of Toronto, Toronto, ON, Canada

Introduction

Late oral radiation toxicity occurs in about half of the head and neck cancer patients who undergo radiation therapy [1]. It has widely been discussed that vascular damage plays a major role in such late complications [2]. Therefore, understanding the mechanism of vascular damage in these patients can lead to more effective treatment prescription and even prevention in the future. Currently, diagnosis of late oral radiation complication is based on superficial examination and symptoms reported by the patients. Therefore, no objective tool exists for monitoring the subsurface oral layers and investigating radiation-induced microvascular changes.

To address this need, we have proposed to use optical coherence tomography (OCT) as a micron-scale resolution, subsurface imaging technique, to obtain oral microvascular images of late radiation toxicity patients *in vivo*. Moreover, we developed a quantification tool to measure specific vascular features in these patients and compare them to healthy volunteers [3].

Methods and materials

The OCT imager provides subsurface images of tissue depth profile (similar to histology) as well as microvasculature within 1-2 mm beneath the surface [3]. This system was used in a clinical study, approved by the Research Ethics Board of Princess Margaret Hospital (Toronto, Canada), to be performed on 15 patients and 5 age-matched healthy volunteers. A quantification platform was developed and used to calculate specific metrics from the acquired OCT images [3].

Results

After acquiring microvascular images from the patients and healthy volunteers, three major metrics were extracted from these images, using the developed quantification platform, and were then compared between the two cohorts. These three metrics were: average blood velocity, average vessel diameter, and average vessel tortuosity. In order to evaluate the significance of the differences observed between these metrics in the two cohorts, a Mann-Whitney ranking test was used.

The results demonstrated that the average blood velocity is significantly higher in the late oral radiation toxicity patients while the vessel diameter in these patients is significantly lower compared to the healthy volunteers. This test demonstrated no significant difference between the tortuosity in the two cohorts.

References:

[1] J. J. Sciubba and D. Goldenberg, *Lancet Oncol.* 7, 175-83, 2006

[2] R. F. Fajardo, M. Berthrong, and R. E. Anderson, "Radiation Pathology," 181-192, Oxford University Press, New York, 2001

[3] B. Davoudi *et al.*, *J. of Biomed. Opt.* 18 (7), 076008, 2013

Characterization of Refraction Artifacts in Optical Fan-Beam CT through Ray-Tracing

Kurtis Dekker¹, Jerry Battista^{1,2}, Kevin Jordan^{1,2}

¹Department of Medical Biophysics, Western University, ²London Regional Cancer Program

PURPOSE: Optical CT scanning of radiochromic gels is a method of performing 3-dimensional dosimetry, which is becoming more essential for commissioning of modern radiotherapy machines and techniques. Unlike X-rays, visible light undergoes reflection and refraction as it traverses across boundaries between media of different refractive indices (RI). In optical CT, this results in incorrect or missing projection data, which leads to artifacts in dose reconstructions. To minimize these effects, optical CT scans are acquired with the dosimeter placed within a liquid whose refractive index matches that of the gel. However, gels must be contained in a vessel or jar, in order to maintain shape and to prevent dissolution into the surrounding fluid. Generally it is impractical and/or impossible to achieve perfect RI matching between the gel, jar walls, and surrounding fluid. In this study, we model the effects of RI mismatch on the accuracy of optical CT reconstructions.

METHODS: A forward ray-tracing simulation program was coded in MATLAB (The MathWorks, Inc., Natick, Mass., USA) to simulate the propagation of primary rays through a cylindrical gel dosimeter placed in a fan-beam optical CT scanner. The program allows for variation of geometric and optical parameters in the system, and simulates Fresnel reflections and Snell refraction at each interface. The launch angle and intensity of simulated rays were used to generate projection data for uniform gels. Reconstructions were then performed using Filtered Backprojection (FBP) in MATLAB's *ifanbeam* function. Simulations and reconstructions were performed for a dosimeter with an outer radius of 7.5 cm, in a scanner with a source-to-axis distance of 50 cm and an axis-to-detector distance of 50 cm. The ratios of a) the reconstructed central attenuation coefficient (μ_{recon}) to the known value (μ_{known}), and b) the radius within which reconstructed images remained 'flat' to within 1% (R_{flat}) relative to the known inner radius of the jar (R), were calculated to assess the quality and scope of reconstruction. Figure 1 shows an example of a ray-tracing diagram. The thickness of the cylinder walls was varied between 0.05 and 0.75 cm, and the refractive indices of the walls and the surrounding fluid (n_{wall} and $n_{surround}$) were varied over +/- 15% of the gel's RI (n_{gel}), noting that the Fresnel and Snell equations depend on RI ratio at a boundary.

RESULTS AND DISCUSSION: Figure 2 shows the variation of μ_{recon}/μ_{known} as a function of refractive indices of both the jar walls and the surrounding fluid, for a specified wall thickness (0.2 cm). The *dependence* of this value on the jar's RI disappears when $n_{wall} > n_{gel}$. In this regime, the ratio of μ values becomes a quasi-linear function of $n_{surround}/n_{gel}$, with the slope and intercept monotonically increasing and decreasing, respectively, with increasing wall thickness. On average, for wall thicknesses ranging from 0.05 to 0.75 cm, an RI mismatch between gel and surrounding fluid will lead to a μ value error of approximately the same percentage at the dosimeter centre. The fraction of the dosimeter that is reconstructed uniformly, defined by the maximum radius for which μ is within 1% of the central value, was also analyzed (figure not shown). In the case of mismatched walls, the reconstructions remain flat for upwards of 90% of the true radius in the regime where both $n_{surround}$ and n_{wall} are equal to or greater than n_{gel} .

CONCLUSIONS AND FUTURE WORK: The results of these simulations suggest that the optimal scanning parameters for gel dosimetry using optical CT require matched surrounding fluids, and dosimeter vessels which are closely RI-matched and as thin-walled as possible. In a case where this cannot be achieved, the misplaced ray paths would need to be accounted for, before or during CT reconstruction. To that end, this simulation software will be extended in order to apply a "re-binning" algorithm to projection data, re-mapping the true paths through the dosimeter. Throughout the study, experimental measurements made using a prototype laser CT system will be used to validate the simulation model.

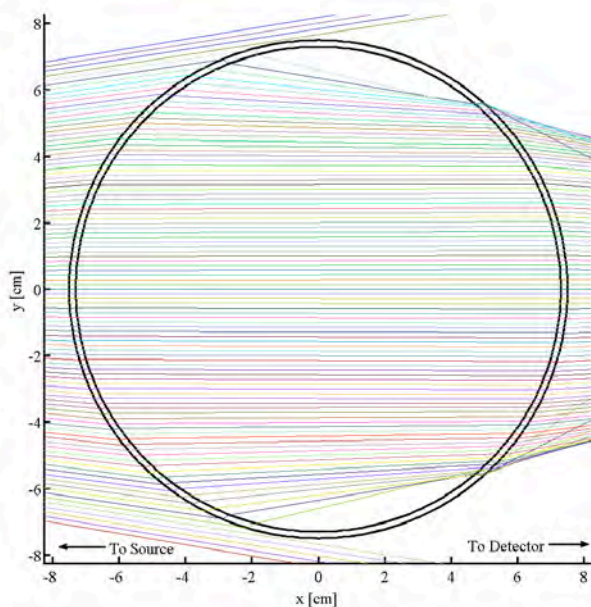


Figure 1: Example of Ray-Tracing diagram. Rays originate from source at $x = -50$ cm.

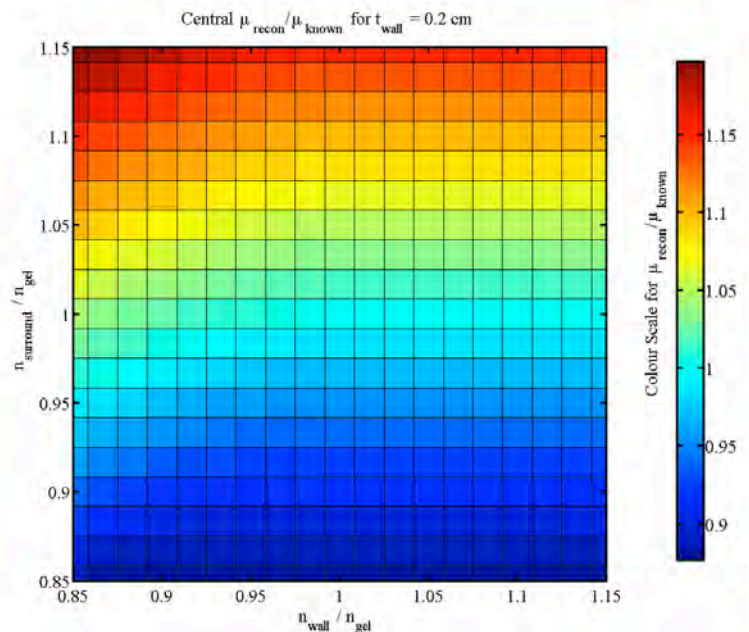


Figure 2: Variation of CT reconstructed central attenuation coefficient (μ_{recon}) as a function of wall and surrounding relative refractive indices.

Continuous dose delivery for choroidal melanoma using Gamma Knife Perfexion

Kimia Ghobadi¹, Dionne Aleman¹, Mostafa Heydarian², David Jaffray^{2,3}

¹Mechanical and Industrial Engineering, University of Toronto, Ontario

²Department of Radiation Oncology, University of Toronto, Ontario

³Radiation Medicine Program, Princess Margaret Hospital, Toronto, Ontario

Choroidal melanoma is the most common primary intraocular malignancy in adults, and can be treated noninvasively with linac-based stereotactic radiotherapy (SRT) with a prescription dose of 70 Gy, delivered over five fractions [1]. Linac-based SRT offers a high tumour control rate, but patient setup accuracy in linac-based plans is controlled with eye fixation and monitoring techniques. Gamma Knife® Perfexion™ (PFX) SRT techniques, wherein an ablative and highly conformal radiation dose is delivered to target structures, provides a more accurate patient setup system by using a relocatable head frame. However, the heterogeneous dose distribution of PFX may lead to high beam-on times in the obtained plans. We propose exploring inverse treatment planning approach for PFX using continuous dose delivery. Conventionally, PFX uses step-and-shoot dose delivery approach, where the couch is stationary whenever any dose is delivered. It has been previously shown that using continuous dose delivery, in which the couch continuously moves, can obtain inverse treatment plans with the same or better quality than forward plans, while reducing the beam-on time [2].

Continuous path treatment planning consists of two steps: (1) we first find an appropriate path inside the target, and (2) we then find the optimal beam durations for the selected path so that target structures are covered and healthy organs are properly spared.

(1) Path selection: A path, along which the dose is delivered, is selected inside the target volume based on a set of well-positioned basic isocentres (obtained with a hybrid grassfire and sphere-packing technique). A hamiltonian path is then found to connect all the basic isocentres without creating loops (to avoid hotspots). This hamiltonian path can be obtained using either distance-based greedy hamiltonian techniques, or by selecting intuitive spiral greedy hamiltonian paths. Figure 1 left shows a spiral path chosen in a choroidal melanoma in left eye of a patient case.

(2) Optimization of beams: The selected path is then fed into a linear optimization model to find the optimal beam durations for each isocentre on the path. In the optimization problem, different treatment and machine constraints are considered, including machine speed constraints, movement accuracy, preference for single or multiple paths, and smoothness of movement.

Continuous path treatment planning for PFX has been previously tested on brain cancer cases and has been shown to improve the beam-in time by an average of 28% compared to forward planning [2]. Our primary results for choroidal melanoma cases show that although plan quality suffers slightly compared to the forward plans, the obtained beam-on time are comparable. Figure 1 right shows the dose-volume histogram for a patient case with beam-on time of 60 minutes for $V_{100} = 98\%$.

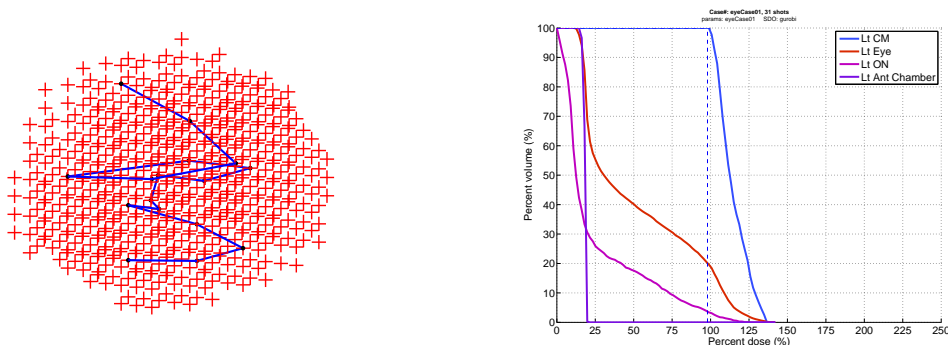


Figure 1: Left: A spiral path selected in a choroidal melanoma target (volume 0.2 cm^3). Right: Dose-volume histogram for a patient case with a beam-on time of 60 minutes.

[1] H. Krema, S. Somani, A. Sahgal, W. Xu., M. Heydarian, D. Payne, and N. Laperriere (2009), *Stereotactic radiotherapy for treatment of juxtapapillary choroidal melanoma: 3-year follow-up*. *British Journal of Ophthalmology*, 93(9), 1172-1176.

[2] K. Ghobadi, D. M. Aleman, D. A. Jaffray, and M. Ruschin (2013), *A Linear Model for Continuous Path Treatment Planning for Stereotactic Radiosurgery*, under review in the *INFORMS Journal on Computing*, August 2013.

Interfraction Variation in Dose and Position During the Treatment of Pancreatic Cancer Using Tomotherapy

Daniel Glick¹, Eric Vorauer², Jidney Cifuentes², Frances Tonolet², Csaba Pinter³, Gabor Fichtinger³, Andreas Lasso³, Lee Chin², Hans Chung¹

¹Department of Radiation Oncology, University of Toronto, ²Department of Medical Physics, Odette Cancer Centre, ³School of Computing, Queen's University

Purpose/Objectives: Intrafractional and interfractional variation exists during the treatment of pancreatic cancer due to respiratory motion, bowel gas, patient weight loss, tumor response and peritumoral edema. This study sought to investigate interfraction organ motion and its dosimetric consequences.

Methods: Initial planning KVCT images were compared to day 1 and day 30 MVCT images for 19 unresectable, locally advanced pancreatic cancer patients treated with radical radiotherapy (dose>45 Gy) using Tomotherapy. Organ motion was calculated by measuring centroid translation. Dice Similarity Coefficient (DSC) was performed to evaluate overlapping volumes on planning and daily scans. Dose distribution was calculated on electron density calibrated daily MVCT images and projected onto daily MVCT with daily physician drawn gross tumor volume (GTV), liver, kidney and spinal cord contours. This dose distribution was also deformed onto a reference planning KVCT image using SlicerRT to create a cumulative dose volume histogram that could be compared to the original treatment plan.

Results: Mean GTV and organ at risk translation were less than 1 cm with considerable variation between patients and fractions (Table 1). Mean DSC for GTV, liver, right kidney, left kidney and spinal cord were 0.60, 0.80, 0.73, 0.77 and 0.60, respectively. Compared to original plan, first treatment day mean GTV dose was 99.0%, minimum GTV was 96.7%, mean right kidney dose was 93.4%, mean left kidney dose was 95.0% and maximum spinal cord dose was 98.4%. Similarly, compared to original plan, last treatment day mean GTV dose was 100.4%, minimum GTV was 97.6%, mean right kidney dose was 96.4%, mean left kidney dose was 97.7% and maximum spinal cord dose was 101.3%. On day one, the volume of GTV receiving 95% of the prescribed dose (V95) was always above 95%; however, final day GTV V95 was more variable with three patients having GTV V95 less than 95%.

Table 1.

	Superior-Inferior		Anterior-Posterior		Lateral	
	Mean (mm)	SD	Mean (mm)	SD	Mean (mm)	SD
GTV	6.41	6.53	3.55	1.94	4.67	3.34
Right Kidney	5.30	4.95	4.00	3.65	3.03	2.40
Left Kidney	4.24	4.38	2.91	2.84	2.42	1.97
Liver	4.57	4.00	5.71	4.50	4.56	4.89
Spinal Cord	5.23	5.67	2.44	2.88	1.52	1.20

Conclusion: This study demonstrates that there is sub-centimeter variation in anatomy between planning CT scan and daily treatment scans which vary between patients and fractions. Typically, these variations have minimal impact on tumor and organ at risk dose; however, when significant changes in anatomy occur over the course of treatment, tumor coverage can be compromised. By better understanding organ motion and its impact on dose deposition, one can potentially customize or adapt PTV margins to improve OAR sparing and allow for dose escalation to tumor.

Acknowledgement: This work was in part funded by Cancer Care Ontario through Applied Cancer Research Unit and Research Chair in Cancer Imaging grants and the Ontario Research Fund – Research Excellence Ministry of Research and Innovation.

References

Pinter C, Lasso A, Wang A, Jaffray D, Fichtinger G. 2012 SlicerRT: Radiation therapy research toolkit for 3D Slicer. *Med Phys.* 39(10):6332-8

Dynamic contrast enhanced MRI parameter map sensitivity to imaging temporal resolution in the prostate

Tom Hrinivich¹, Trevor Thang¹, Charles McKenzie^{1,3,4}, Glenn Bauman^{2,5}, Aaron Fenster^{1,2,3,4*}, Eugene Wong^{2,3,5*}

¹Medical Biophysics, ²Oncology, ³Physics and Astronomy, Western University, London ON

⁴Robarts Research Institute, London ON

⁵London Regional Cancer Program, London ON

* Research Supervisors

Purpose: To determine the effects of dynamic contrast enhanced (DCE)-MRI temporal resolution on pharmacokinetic model-based and model-free parameter values in the prostate.

Background: Recent studies have shown that varying DCE-MRI temporal resolution or sampling time (T_s) can affect pharmacokinetic model-based parameter values in brain tumours. [1] Accurate lesion delineation is important in a variety of diagnostic and therapeutic applications such as targeted biopsy, focal ablative therapies, or focal boost with whole gland treatment. DCE-MRI has been proposed as a component in multi-parametric MRI tumour delineation schemes. Both model-based and model-free parameters have been used to characterize DCE-MRI of the prostate, demonstrating similar performance in the detection of peripheral zone tumours. [2] Parameters with relatively low sensitivity to T_s may provide increased lesion delineation performance and enable the use of DCE-MRI pulse sequences with higher spatial resolution at the cost of lower temporal resolution.

Materials and Methods: Two cohorts of patients scheduled to undergo radical prostatectomy (22 total) underwent DCE-MRI at 3T with two 3D fast spoiled gradient echo (FSPGR) pulse sequences at 7 s T_s (Cohort A) and 90 s T_s (Cohort B). Varying T_s was also simulated using the 7 s T_s data by averaging time points together. Mean mid-gland parameter map values were compared between simulated T_s values, and between pulse sequences. Figure 1 provides representative DCE-MRI parameter maps at varying acquired and simulated T_s .

Results: Mean K^{trans} values tended to decrease with simulated down sampling from $T_s = 7$ s, reaching relative decreases from 24 – 40 % across Cohort A at $T_s = 21$ s which was statistically significant based on a two-tailed unpaired t-test ($p < 0.05$). Mean K^{trans} and k_{ep} values were also found to be 40 % and 57 % lower at $T_s = 90$ s than $T_s = 7$ s respectively. Differences in late phase concentration gradient (C_{grad}) and wash-in-washout parameter (W_{io}) values between $T_s = 7$ s and $T_s = 90$ s were not statistically significant.

Conclusions: Late phase concentration gradient (C_{grad}) and the proposed wash-in-washout parameter (W_{io}) show promise as robust measurements over varying temporal resolution.

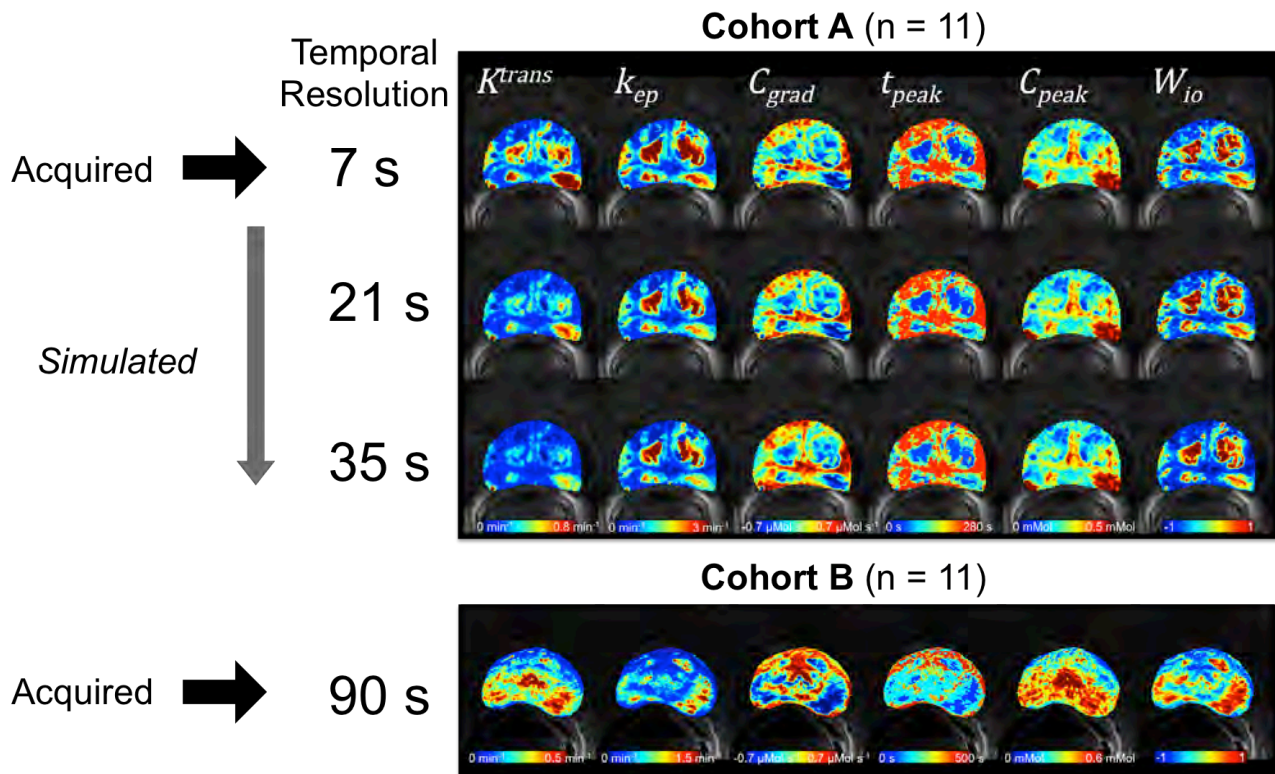


Figure 1 Axial cross sections of DCE-MRI parameter maps from two intermediate risk prostate cancer patients in Cohorts A and B acquired at 7 s and 90 s temporal resolution respectively. Image sets from Cohort A were also temporally down-sampled to simulate temporal resolutions from 7 s to 35 s. Mean mid-gland parameter values could then be compared across varying temporal resolutions.

[1] Larsson C et al. J of Magn Reson Im. 2013; 37(4)

[2] Rosenkrantz AB et al. Am J Roentgenol. 2013; 201(3)

Simulating Thermal Effects of High-Intensity Focused Ultrasound in Cortical Bone

Thomas James Hudson¹, Thomas Looi¹, Adam C. Waspe¹, Samuel Pichardo², James M. Drake¹

¹Center for Image Guided Innovation and Therapeutic Intervention, Hospital for Sick Children

²Department of Electrical Engineering, Lakehead University

To help improve therapeutic results for treatment of bone tumors, high intensity focused ultrasound (HIFU) is currently being investigated as a noninvasive alternative to surgery and radiotherapy. HIFU often uses magnetic resonance (MR) thermometry feedback to determine the temperature rise in the tissue during the treatment, however, the appropriate signal for thermometry is unavailable in bone tissue. As an alternative to temperature feedback, this project focuses on the design of a simulation tool aimed at predicting the temperature distribution from a HIFU therapy using acoustic tissue properties, ultrasonic treatment parameters, and an MRI scan of the bone as inputs. The software will have three main components. First, it will segment the bone and surrounding tissue from a set of 3D MRI images. Next, it will perform an acoustic field simulation of ultrasound propagation into the targeted tissue, calculating the distribution of acoustic energy. Lastly, it will input the deposited acoustic energy into a heat transfer model, determining the temperature distribution using tissue and perfusion parameters assigned based on the segmentation. The criteria for a successful model will be temperature prediction to within 1°C and computation time less than one minute.

The tool is currently capable of simulating a realistic acoustic field from focused ultrasound propagating into a 3D layered media. It uses a modified solution of the Rayleigh integral, which is capable of solving for the longitudinal and shear components of the reflected and transmitted waves at each medium interface, and then propagating these waves into their respective tissues to find the deposited energy. Figure 1 (A) shows preliminary acoustic simulation results. In this case, the focused ultrasound waves were targeted at the center of a virtual cylindrical bone phantom, as shown in Figure 1 (B). Note that the muscle and bone marrow were assumed here to be liquid. These results show the ultrasound wave refracted in the solid cortical bone, causing the focus to be shifted toward the ultrasound source.

As this simulation involves computing the same equations for each of the thousands of voxels in the 3D image, the algorithm has been implemented using the CUDA architecture for GPU parallel computing. By doing this, computation time has been reduced several orders of magnitude, from hours down to seconds. The demonstrated simulation took 32.8 seconds, propagating ultrasound into a 40x40x50 voxel volume.

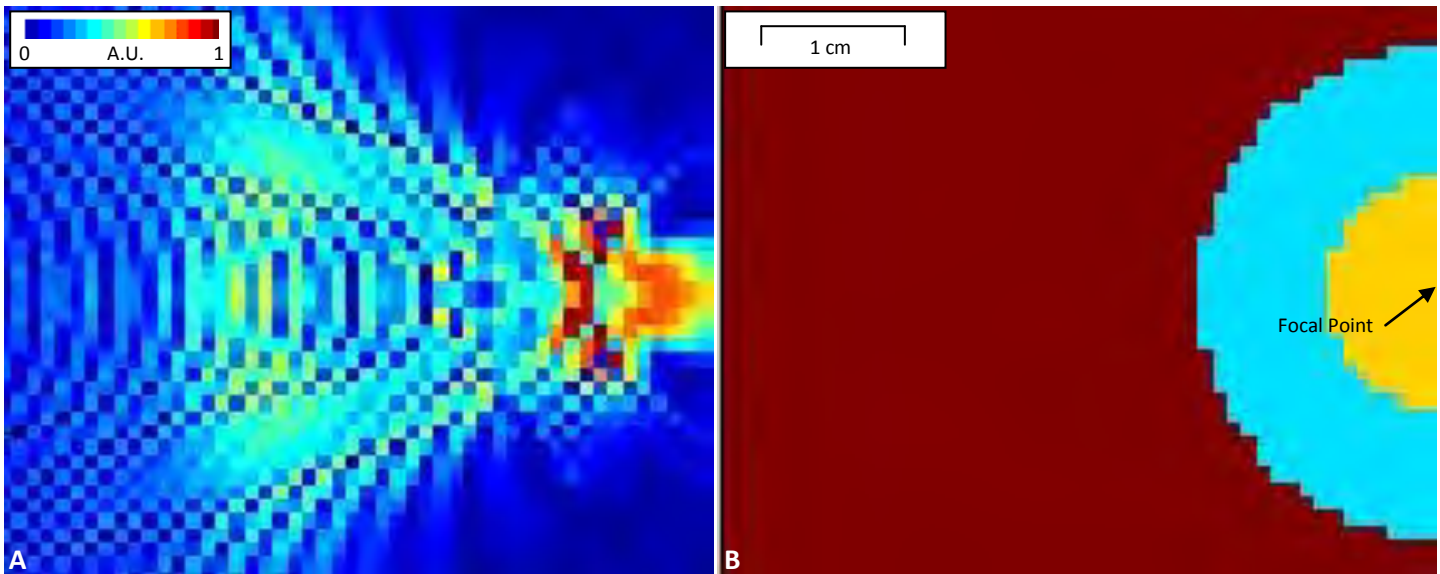


Figure 1 - (A) demonstrates the distribution High Intensity Focused Ultrasound energy attenuated in the layered media shown in (B), where red represents muscle, blue represents cortical bone (diameter 17mm) and yellow represents bone marrow (diameter 8mm) (Simulation time 32.8 seconds).

Custom Bolus Construction Using a 3D Printer

C. Jechel¹, G. Salomons^{1,2}, L.J. Schreiner^{1,2}

¹-Department of Physics, Queen's University, Kingston, Ontario

²-Medical Physics Department, Cancer Centre of Southeastern Ontario, Kingston, Ontario

Research Supervisor: L.J. Schreiner

The use of custom fitted bolus for photon and electron radiotherapy is a well-established method for ensuring accurate dose delivery to targets located beneath irregular surfaces. By filling in void spaces surrounding the irregular surface, bolus is used to present a flat surface normal to the incident beam, thus simplifying dose calculations and allowing greater dose to be delivered to target structures located at and near the surface of the patient's body. In some situations with complex patient contours, bolus is made through a labour-intensive process of moulding sheets of wax into the desired form. Until recently, the complicated geometry of these structures and unique nature of each piece made automation of bolus construction impractical. Newly developed three-dimensional printing technology has the potential to manufacture such complex geometries in a matter of hours. This technology is now widely available as the cost of printers and consumables continue to decrease and as open-source communities devoted to spreading knowledge and access to this technology flourish. The unique properties of 3D printing allow for construction of parts with geometries impossible to produce using traditional machining techniques. Thus, we believe that the one-of-a-kind nature of bolus construction is ideally situated to benefit from developments in 3D printing technology. To date, several significant steps have been made towards the goal of producing a clinically viable 3D printing alternative to traditional bolus construction.

Printed parts, composed of ABS plastic, were built on a Stratasys Dimension 1200es 3D printer, available through Queen's University. Using a technique known as fused-deposition modeling, an ABS filament is heated and extruded where it cools and hardens, adding to the existing part. Two simple 0.5 cm thick, 12 cm by 12 cm square slabs were manufactured for the purpose of examining the relevant radiological properties of the printed material. Ion chamber measurements were taken at varying depths along the central beam axis in a plastic water phantom irradiated by a 10 cm by 10 cm, 6MV photon field with the ABS slabs situated in the beam path. Imaging showed the printed ABS plastic to have a mean CT number of -70 ± 6 HU. Expected dose values beneath these slabs were calculated in Eclipse (Varian Medical Systems, Palo Alto, CA) using the measured CT number and agreed with the measured percent depth dose profile to within 1%. Meanwhile, a script to transfer bolus contour information found in the RT Structure set for a given treatment plan to a format appropriate for driving the 3D printer was developed in MATLAB (MathWorks, Natick, MA). After extracting the relevant bolus structure contours, a 3D binary array was used to define the bolus geometry and converted to a stereolithography (.stl) file. This approach has the benefit of allowing the user to specify the axial plane resolution of the output. Our preliminary effort highlighted the need to smooth the structure along the superior-inferior axis to reduce the effects of the finite slice thickness of the planning CT as seen in Figure 1 (b). Using the bolus contours in adjacent slices, intermediate contours were interpolated to reduce these discontinuities. Panes (b) and (c) of Figure 1 show the result of two iterations of this interpolated contour algorithm. This unique approach was necessary due to the asymmetry of the smoothing requirements between the 3 axes of the structure introduced by the slice thickness issue which rendered typical methods such as Laplacian smoothing ineffective.

Overall, this method shows promise and with revision of the smoothing algorithm is likely to yield a clinically viable alternative to traditional bolus construction which could be almost entirely automated given the desired bolus contours. Further work will involve using anatomical contours and other desired bolus parameters to automate the process of defining the bolus geometry. Another area for future work would examine the suitability of the range of available 3D printing materials and techniques.

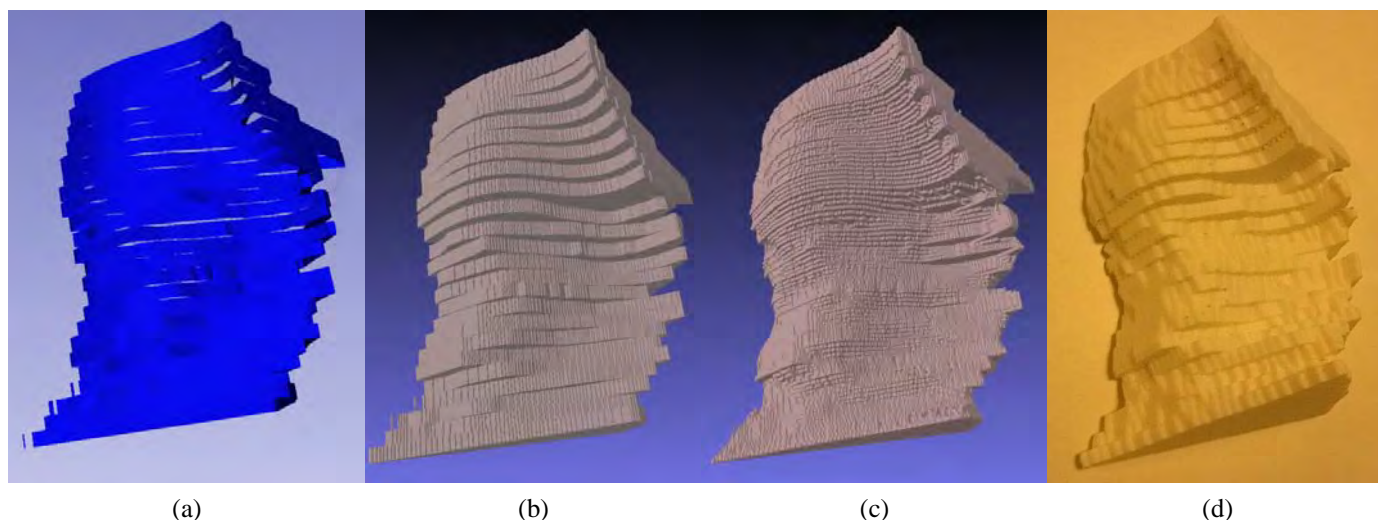


Figure 1: Stages of the RT structure to stereolithography conversion process: (a) contours exported from Eclipse viewed as a ribbon structure, (b) unsmoothed stereolithography file from contours, (c) stereolithography file resulting from two iterations of the interpolated contour smoothing algorithm, (d) photograph of unsmoothed printed structure produced from the contour to STL file conversion function in 3D Slicer (print time 2.3 hours).

The Accuracy and Reproducibility of Computer-Assisted Surgical Plane Resections in Orthopaedic Oncology

Aidin Kashigar¹, Amir Sternheim¹, Michael Daly^{2,3}, Jimmy Qiu³, Robert Weersink³, Harley Chan³, Anthony Griffin¹, Jonathan Irish⁴, Peter Ferguson¹, Jay Wunder¹

¹Division of Orthopaedic Surgery, Mount Sinai Hospital, ²Institute of Medical Science, University of Toronto, ³Radiation Medicine Program, Princess Margaret Hospital, ⁴Surgical Oncology, Princess Margaret Hospital

Ontario Consortium for Adaptive Interventions in Oncology

Objective: To assess the accuracy and reproducibility of pelvic bone cuts using a navigation system with a navigated osteotome and an oscillating saw.

Methods: Using a novel navigation system and 3D planning tool, we navigated pelvic bone cuts which were representative of typical cuts made in pelvic tumor resections. The system includes a prototype mobile C-Arm for intraoperative cone-beam CT, real-time optical tool tracking (NDI Polaris), and 3D visualization software. A 3D virtual view was utilized in addition to tri-planar navigation (axial/sagittal/coronal). A second post-procedure CT was acquired to assess results. In part one of the study, we navigated 24 sacral bone cuts in sawbones and validated our results in 16 similar cuts in cadavers. In part two, we developed three pelvic tumor sawbone models (a peri-acetabular tumor, a sacral tumor and an SI joint tumor) based on actual patient scenarios, and compared 3 navigated resections to 3 non-navigated resections for each tumor model. Part three assessed the accuracy of the system with multiple users. In part four of the study, experiments will be conducted on three custom sawbones models (proximal humerus, proximal tibia, distal femur) that included realistic tumor pathology in order to investigate for navigation accuracy when geometric resection of a tumor is performed with reconstruction through press-fit cuts of an allograft bone.

Results: There were 90 navigated cuts in sawbones which were compared to 54 non-navigated cuts. In the navigated sawbones cuts, the mean entry and exit cuts were 1.4 ± 1 mm and 1.9 ± 1.2 mm from the plan respectively. The entry and exit cuts in sawbones which were not navigated were 2.8 ± 4.9 mm and 3.5 ± 4.6 mm respectively. The navigated cuts were significantly more accurate ($p \leq 0.01$). In the cadaver study, entry and exit cuts were 1.5 ± 0.9 mm and 2.0 ± 1.5 mm from the planned cuts. The variation between three different users was less than 1 mm on both the entry and exit cuts. The mean image to tracker point-to-point registration error was 0.97 ± 0.3 mm in sawbones and 0.9 ± 0.3 mm in cadavers. The mean image-to-image registration error was 0.88 ± 0.24 mm in sawbones and 0.9 ± 0.3 mm in cadavers. Using a saw blade of actual width 1.25 mm, the mean cut width for the oscillating saw was 1.9 ± 0.7 mm. Part four of the study is currently being completed.

Conclusion: Using navigation for pelvic bone cuts is accurate and feasible. 3D views should be used for improved accuracy. Navigated cuts were significantly more accurate than non-navigated cuts. A margin of 5 mm between the target tumor volume and the planned cut plane would result in a negative margin resection in more than 95% of the cuts. Similar accuracy was achieved in cadavers.

A tool for intraoperative visualization of image registration results

Franklin King, Andras Lasso, Csaba Pinter, and Gabor Fichtinger

Laboratory for Percutaneous Surgery, School of Computing, Queen's University, Kingston, ON, Canada

Research supervisor: Gabor Fichtinger

PURPOSE: Image registration algorithms are essential ensuring the accuracy of image-guided medical interventions. The validation of such algorithms is frequently accomplished by the visual inspection of the resulting linear or deformable transformation due to the lack of ground truth information. The quick visualization of transformations produced by image registration algorithms during image-guided interventions would allow for a clinician to rapidly evaluate the accuracy of the result transformation. We present a tool that is capable of visualizing both linear and deformable transformations and is integrated in an open-source software application framework suitable for intraoperative use and general evaluation of registration algorithms.

METHODS: The transform visualizer tool was designed for intraoperative verification of transformations. Visualizations must allow for a quick evaluation of the results of a registration, the nature of the motion that occurred, and areas of maximum dislocation. The tool must also be capable of visualizing motion in all directions as opposed to only showing motion within a chosen image plane as is the case with methods such as image fusion based visualization. To this end, the transform visualizer tool provides several visualization modes with adjustable parameters. Glyph visualization modes are available that make use of oriented and scaled glyphs, such as arrows, to represent the transformation as a vector field. The glyphs are represented in either 3D or as a 2D vector field depending on the mode chosen. Similarly, the grid visualization modes create either a deformed 3D grid or a series of deformed 2D grids. Block visualization mode creates a deformed rectangular model. Finally, contour visualization mode creates isosurfaces and isolines at user-specified intervals that visualize the magnitude of deformation across a volume. The transform visualizer was implemented as an extension for the application 3D Slicer [1]. 3D Slicer is a comprehensive open-source application framework developed for medical image computing. Among 3D Slicer's features are state-of-the-art image registration algorithms, device tracking, support of numerous common data formats, and comprehensive data visualization. Integration of the transform visualizer tool into 3D Slicer also allows a user to overlay the visualization with models or images and access color assignments.

RESULTS: Implemented as an extension for 3D Slicer, the transform visualizer tool is capable of visualizing various kinds of transformations including translations, rotations, and non-linear deformations generated by image registration algorithms [2]. Figures 1 and 2 show visualizations generated from intra-operative patient data acquired during a biopsy procedure [3]. Figure 2 also demonstrates the use of the transform visualizer tool to visualize both a failed and successful registration and make apparent the contrast between both. Color assignments and warping are used to indicate regions of large dislocation. The nature of the motion in 3D is also made more apparent than it would otherwise be if visualized using a 2D visualization.

CONCLUSION: A tool for visualizing transforms was created and implemented in 3D Slicer allowing for easier validation of image registration algorithms. The tool satisfies requirements for intraoperative use. The tool is freely available as an extension for 3D Slicer listed under the name of Transform Visualizer [4].

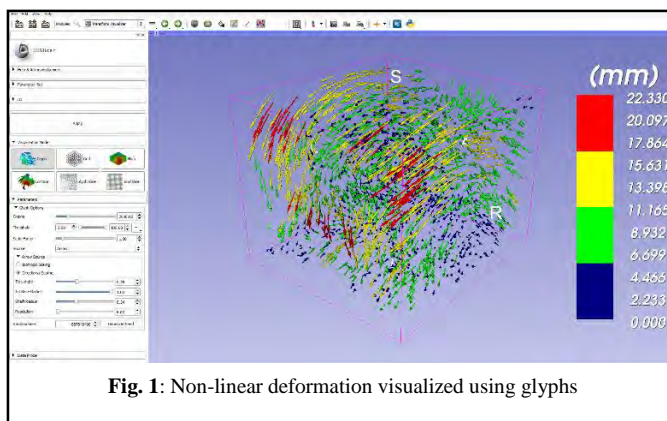


Fig. 1: Non-linear deformation visualized using glyphs

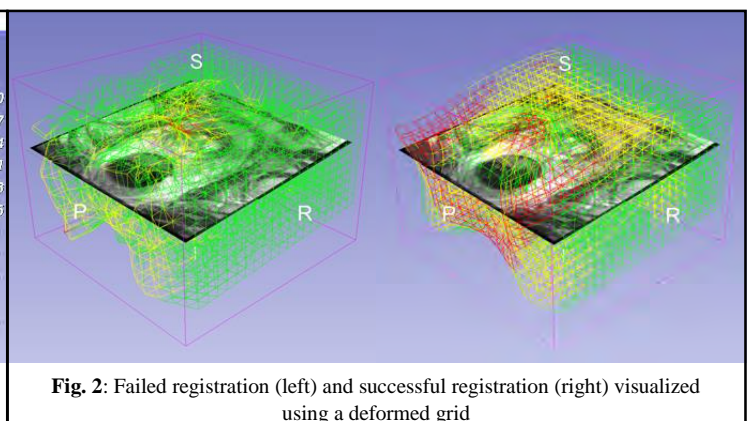


Fig. 2: Failed registration (left) and successful registration (right) visualized using a deformed grid

ACKNOWLEDGEMENT: This work was in part funded by Cancer Care Ontario through Applied Cancer Research Unit and Research Chair in Cancer Imaging grants.

[1] 3D Slicer, <http://www.slicer.org>

[2] King F., Lasso A., Pinter C., and Fichtinger G. "A tool for intraoperative visualization of registration results", *SPIE Medical Imaging 2014*, San Diego, California, USA, 02/2014.

[3] Fedorov A, Tuncali K, Fennessy FM, Tempany CM. *MR-guided Prostate Biopsy pre- and intra-procedural MRI Registration Evaluation Dataset*. NCICT 2012 March

[4] <http://www.slicer.org/slicerWiki/index.php/Documentation/Nightly/Extensions/TransformVisualizer>

Inverse planning for single needle radiofrequency ablation in liver cancer treatment using approximation

Shefali Kulkarni-Thaker[†], Dionne Aleman^{††}, Aaron Fenster^{†††}

[†] Mechanical and Industrial Engineering, University of Toronto

^{††} Research supervisor, Mechanical and Industrial Engineering, University of Toronto

^{†††} Robarts Research Institute, Western University

In radiofrequency ablation (RFA), an electrode is inserted into the tumor percutaneously, laproscopically or via an open surgery. A needle consists of two parts: a conducting part and an insulating shaft. The needle is placed so that the conducting part is in the tumor. High frequency alternating current, generated by an RF source, is passed through the tumor which is converted to heat due to tissue resistance. When the tumor is exposed to the heat for sufficiently long periods of time, it is killed via coagulation necrosis. In this work we develop mathematical models to design inverse treatment plans to completely obliterate the tumor cells while sparing healthy tissue. Our method is novel in that we design a two-stage algorithm for treatment planning: (1) identify needle position and orientation, referred to as needle orientation optimization (NOO) and (2) compute treatment time for optimal thermal dose delivery, referred to as thermal dose optimization (TDO). In NOO, we approximate the ablation shape to an ellipse or sphere to identify the needle's position and orientation. These variables are determined by solving minimum volume covering ellipse (MVCE) or sphere (MVCS) optimization models for the tumor. Once needle position and orientation is known, we compute the treatment time for optimal thermal dose delivery to the tumor. Thermal dose is computed using the Pennes' bioheat transfer equation (BHTE), a partial difference equation (PDE). Solving BHTE is a computationally intensive task and so we propose an exponential approximation based on voxel's distance from the conducting part of the needle and the treatment time. We test our approach on a 2D and 3D liver tumor. The results for MVCE and MVCS, obtained within negligible computational time, appear in Figure 1. For TDO, although the preliminary results (Figure 2) show promising treatment plans using approximation, the thermal equilibrium attained by the BHTE is not captured by the approximation. Further, since we use an explicit central finite difference scheme to solve the PDE, temperature of voxels at the same distance varies resulting in overestimation. Based on these promising results we will refine our approximation to better represent the thermal dose.

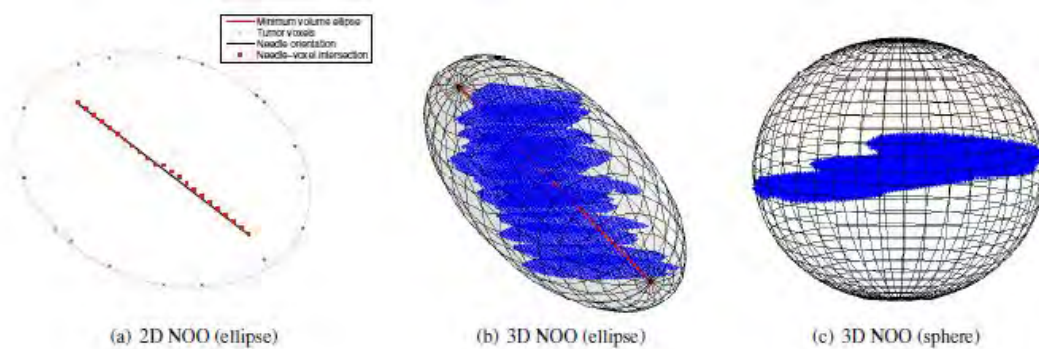


Figure 1: NOO results by solving MVCE and MVCS optimization models

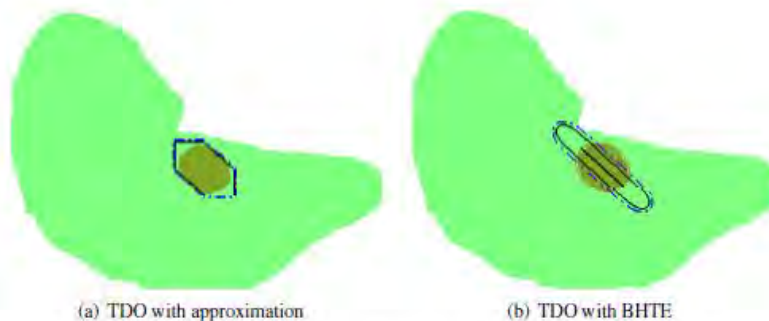


Figure 2: Preliminary TDO results using BHTE and approximation.

Digital Portal Imaging in Cobalt-60 Radiation Therapy

Matthew B. Marsh¹, Ingrid H. Lai², Andrew T. Kerr^{1,2}, L. John Schreiner^{1,2}

(1) Cancer Centre of Southeastern Ontario, Kingston, Ontario.

(2) Department of Physics, Engineering Physics & Astronomy, Queen's University, Kingston, Ontario.

Cobalt-60 (Co-60) treatment units were the most commonly used radiation therapy machines in cancer clinics prior to the introduction of linear accelerators (linacs). While they do not have many modern features of linacs, such as multi-leaf collimators, their advantages include lower cost, lower maintenance requirements and the ability to function in areas without a reliable power and water supply. Therefore, Co-60 units are still widely used around the world. Unfortunately, basic Co-60 units are not equipped with imaging capabilities and so are not able to deliver Image Guided Radiation Therapy (IGRT). A simple option for imaging is portal imaging using the treatment beam. However, Co-60 portal images with film suffer from low contrast and resolution due to the relatively high beam energy and large source size. Portal imaging may be improved with electronic portal imaging devices (EPIDs). We propose that many centres may benefit from the simple addition of EPID-based portal imaging capabilities combined with quick digital image processing. These panels would not provide full IGRT capabilities, but would enable patient setup validation to centres that have no guidance tools at present. In this study, we examine the image quality of raw and post-processed Co-60 portal images acquired using an EPID.

The experimental setup comprised of a Theratron T780C Co-60 unit, and a free-standing cart on which a PerkinElmer XRD1640 amorphous silicon EPID (or a Varian aSi500 EPID) was mounted across from a phantom. The phantom and the panel were positioned at SAD(cm)/SDD(cm) of 80/100, 80/120, 100/125 and 100/140. The frame integration time was 133ms for the XRD1640 (100ms for aSi500) and 4 frames were averaged for each image. Image processing was done with in-house software written in MATLAB. Images could be enhanced using techniques such as iterative deconvolution and contrast-limited adaptive histogram equalization (CLAHE), in addition to global contrast adjustments. For comparison, some images were also taken on a 6MV linac with a built-in aSi500 panel. Qualitatively, it was found that the post-processed Co-60 images were similar in quality to images obtained with the 6MV portal imager and were sufficient for identifying bony anatomy. Deconvolution sharpening increased the central peak of the point spread function by 30-40% and CLAHE improved local contrast, thus overcoming the two main disadvantages of the Co-60 source. Examples are shown in Fig. 1.

The results of this work indicate that Co-60 EPID based portal imaging would provide excellent tools for patient set-up validation with bony landmarks. This would be a significant improvement for Co-60 based radiation therapy in many centres worldwide.

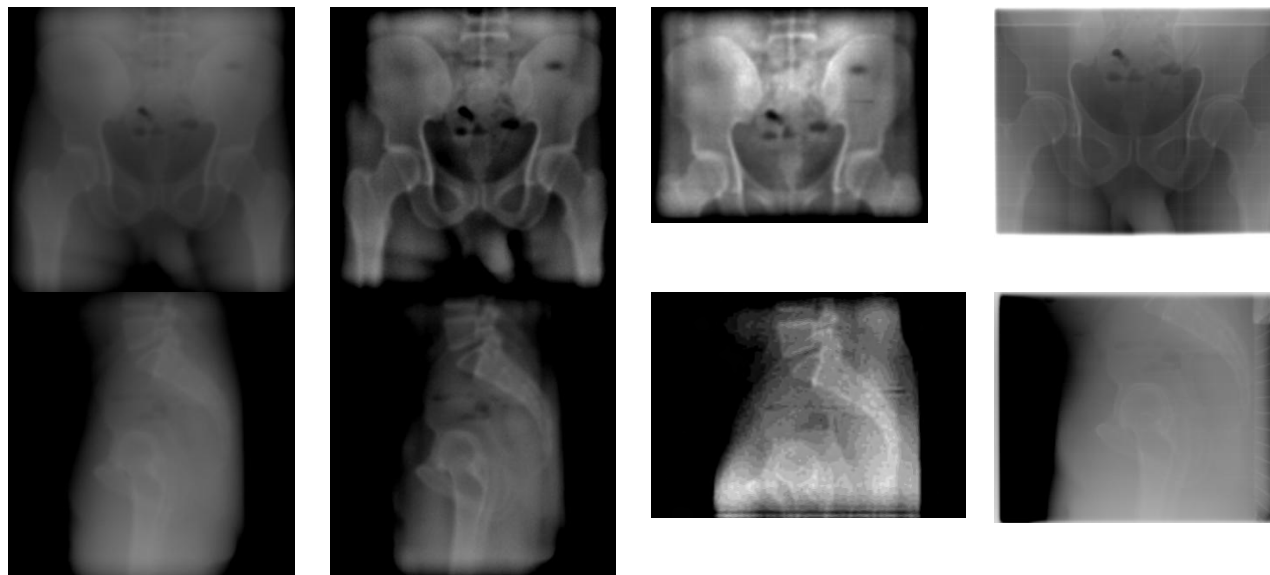


Figure 1: Pelvis, SAD 100 SDD 140 cm. Left to right: Co-60 portal with XRD1640 (contrast adjusted); same, post-processed; Co-60 portal with aSi500, post-processed; 6 MV portal with aSi500.

This work is funded through OCAIRO with industrial support from BEST/Theratronics (Kanata, ON).

Running Matlab® functions in 3D Slicer using Matlab Bridge

Andras Lasso¹, Kevin Alexander², Christopher Jechel², Kevin Wang³, John Schreiner⁴, Gabor Fichtinger¹

¹Laboratory for Percutaneous Surgery, School of Computing, Queen's University; ²Department of Physics, Queen's University; ³Radiation Medicine Program, Princess Margaret Cancer Centre, University Health Network; ⁴Cancer Centre of S.E. Ontario

Research supervisor: Gabor Fichtinger

Background: Matlab® is a very powerful and widely used software environment for development of computational algorithms. However, it is challenging to use Matlab® in medical image computing due to its limited capabilities in medical image data importing/exporting, pre/post-processing, and visualization. 3D Slicer (www.slicer.org) is a free, open source software package that has comprehensive medical image analysis and visualization capabilities and it can be further enhanced and customized by extensions developed in Python or C++ programming languages.

Purpose: Our goal is to implement a software bridge that allows running Matlab® functions directly from 3D Slicer, to: 1) provide rich medical image visualization and pre/post-processing capabilities during Matlab® algorithm development and optimization, and 2) make the developed Matlab® algorithms readily usable for clinicians in the 3D Slicer application. The implementation has to work on all operating systems where 3D Slicer is supported (Windows, Linux, MacOS) and should not require any manual configuration steps or installation of any software packages other than Matlab® and 3D Slicer.

Methods: A new 3D Slicer extension, MatlabBridge was developed, which can start Matlab® and send input data, run the algorithm, and receive processing results using the TCP/IP-based OpenIGTLink protocol (Fig. 1). Each user developed Matlab function has a corresponding MatlabBridge module in Slicer. The graphical user interface of the MatlabBridge module (input/output images, points, scalar value selectors, sliders, editboxes, checkboxes, etc.) are defined in the command-line module descriptor XML format, which is used by numerous medical image computing software applications. The MatlabBridge was used for making Matlab®-based computational algorithms for radiation therapy planning and evaluation accessible in 3D Slicer. Specifically, an implementation of a gamma comparison was evaluated for comparing planned vs. measured dose distributions. The gamma function, introduced by Low *et al.*, is a widely used dose distribution comparison tool which incorporates both dose difference and distance-to-agreement information into a single metric. Dose inputs for the algorithms were imported by the SlicerRT extension (www.slicerrt.org). Standard 3D Slicer volume reslicing and isodose surfaces were used for visualization and analysis of the results.

Results: The MatlabBridge module is available for the latest version of 3D Slicer, it can be installed and configured in a few minutes using the extension manager in 3D Slicer. The extension includes a helper tool (*MatlabModuleGenerator* module) for generating skeleton modules that the developer can customize and extend. The MatlabBridge also allows any other 3D Slicer modules (implemented in Python or C++) to run any Matlab® functions or commands (*MatlabCommander* module). User interface of a 3D gamma Matlab® function and the result of a dose comparison are shown in Fig. 2. No modifications of the original Matlab® functions were needed to run them in 3D Slicer.

Conclusion: Using the MatlabBridge extension, functions implemented in Matlab® can be run from 3D Slicer using a convenient graphical user interface. Practical usability has been demonstrated on computational methods for radiation therapy. Detailed documentation, examples are available at: <http://www.slicer.org/slicerWiki/index.php/Documentation/4.3/Extensions/MatlabBridge>

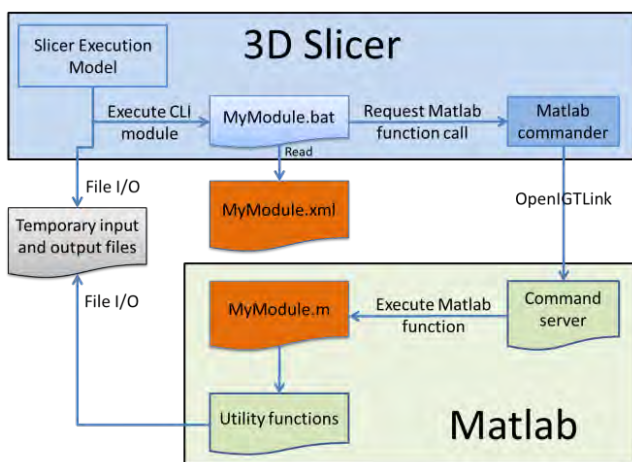


Fig. 1: Architecture overview of the MatlabBridge extension. 3D Slicer and Matlab® communicate through file input/output and OpenIGTLink commands.

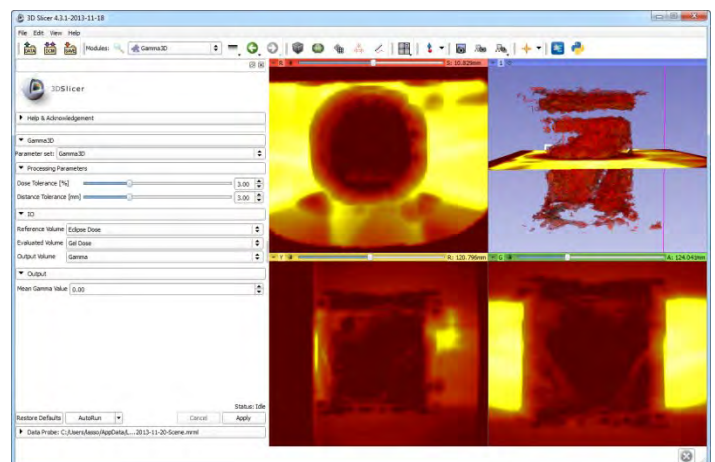


Fig. 2: Comparison result of dose volumes computed by the treatment planning system (Eclipse™) for a prostate IMRT treatment and a gel dosimeter measurement of the dose delivery read by optical CT.

Acknowledgement: This work was in part funded by Cancer Care Ontario through Applied Cancer Research Unit and Research Chair in Cancer Imaging grants and by the CIHR.

Improvements in SlicerRT, the radiation therapy research toolkit for 3D Slicer

Csaba Pinter¹, Andras Lasso¹, An Wang², Gregory C. Sharp³, David Jaffray^{2,4}, Gabor Fichtinger¹

¹Laboratory for Percutaneous Surgery, School of Computing, Queen's University, Kingston, ON, Canada

²Radiation Medicine Program, Princess Margaret Cancer Centre, University Health Network, Toronto, ON, Canada

³Department of Radiation Oncology, Massachusetts General Hospital, Boston, MA, USA

⁴Techna Institute for the Advancement of Technology for Health, University Health Network, Toronto, ON, Canada

Purpose: Recent years have seen growing interest in adaptive radiation therapy (RT), but the existing software tools are not ideal for research use, as they are either expensive and closed proprietary applications or free open-source packages with limited scope, extensibility, reliability, or user support. To address these limitations, we have developed SlicerRT, an open-source toolkit for RT research, providing fast computations and user-friendly interface for researchers. It is a medium for RT researchers to integrate their workflows in, assists clinical translation of experimental approaches, and enables comparative testing.

Methods: SlicerRT builds on the widely used medical image visualization and analysis platform, 3D Slicer (www.slicer.org). In addition to the tools that 3D Slicer offers for visualization, registration and segmentation, the toolkit provides functions specifically designed for RT research. Established development processes as well as testing and validation environment ensure software quality. Standardized software development mechanisms of 3D Slicer were applied for documentation, distribution, and user support. The design and architecture of the toolkit was outlined in [1]. SlicerRT has evolved to contain the most widely used features in the field (see www.slicerrt.org), which have been defined through consensus discussions with a large pool of RT researchers.

Results: Numerous modules have been developed for RT-specific features such as DICOM-RT data import and export, as well as dose analysis tools including dose volume histogram, dose accumulation, dose comparison, and isodose line and surface generation. The toolkit also includes contour analysis modules for handling various contour representations, contour morphology, and contour comparison. Advanced registration tools are provided by the included Plastimatch library [2]. The main new features developed in the last year are RT plan and RT image import and the subject hierarchy module, which arranges the loaded data to a structure familiar to clinicians, while providing advanced automation features through the underlying extendible mechanism. The toolkit is being used by several research groups to support and evaluate adaptive radiation therapy workflows. SlicerRT is available for download through the Extension Manager component of 3D Slicer 4.3 or later (see instructions on our website).

Future work: As SlicerRT has matured to contain most of the planned functions, our focus has shifted from feature development to usability and stability. The subject hierarchy module, and its coming features such as bulk deformation of studies embodies our efforts toward usability, while the integration of the subject hierarchy and the advanced contour handling mechanism into the 3D Slicer core points towards stability, also benefiting the whole 3D Slicer community. There is ongoing work to evaluate and potentially standardize the way the 2D contours are rasterized into 3D volumes, thus mitigating the great variability between the different solutions for this problem. Current funding ensures continuous development for several years, so SlicerRT is expected to develop further.

Acknowledgement: This work was in part funded by Cancer Care Ontario through Applied Cancer Research Unit and Research Chair in Cancer Imaging grants, and the Ontario Consortium for Adaptive Invention in Radiation Oncology (OCAIRO).

[1] C. Pinter, A. Lasso, A. Wang, D. Jaffray, and G. Fichtinger, "SlicerRT: Radiation therapy research toolkit for 3D Slicer", *Med. Phys.* 39(10), 6332/7 (2012)

[2] Sharp G.C., Li R., Wolfgang J., Chen G., Peroni M., Spadea M.F., Mori S., Zhang J., Shackelford J., Kandasamy N.: Plastimatch - An open source software suite for radiotherapy image processing. In Proceedings of the XVIth International Conference on the use of Computers in Radiotherapy (ICCR), Amsterdam, Netherlands.

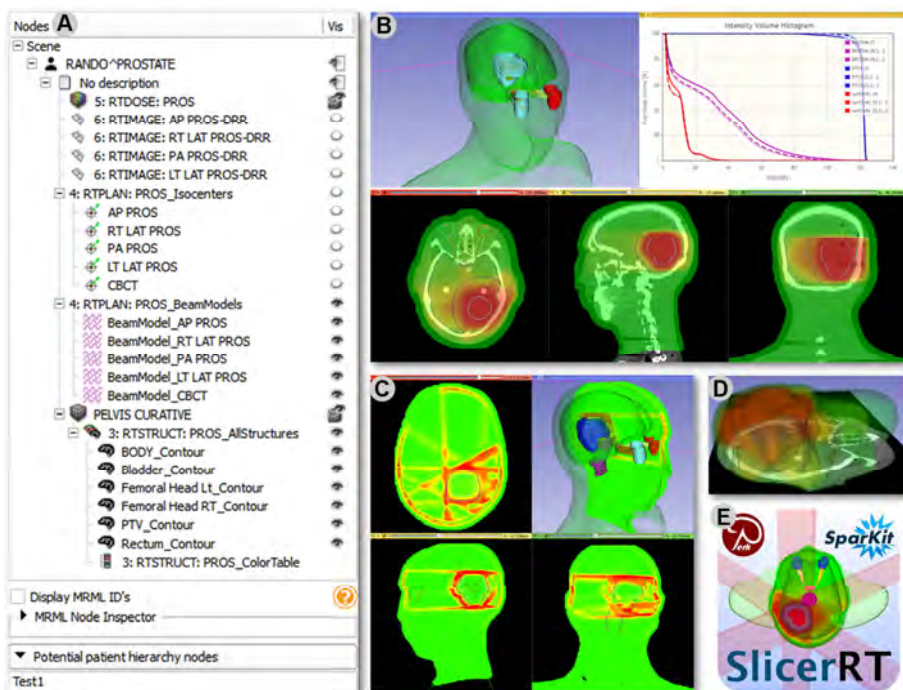


Fig. 1: Montage showing various SlicerRT user interfaces and outputs. A: Subject hierarchy module user interface; B: adaptive treatment evaluation by dose volume histogram comparison; C: gamma dose comparison; D: isodose surfaces; E: SlicerRT logo

Augmenting the parametric response map for guidance of locally adaptive radiotherapy in the presence of image registration error

Anthony Lausch¹, Jeff Chen^{2,3}, Eugene Wong^{1,4}

¹Department of Medical Biophysics, ²Department of Oncology; University of Western Ontario, London, Ontario, Canada

³Department of Radiation Oncology, London Regional Cancer Program, London, Ontario, Canada

⁴Research supervisor

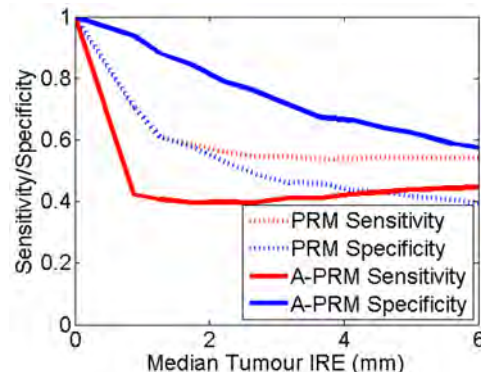
Introduction: Recently, there has been significant interest in developing personalized locally adaptive radiotherapy (RT) methods which use non-homogeneous dose distributions to take advantage of intra-tumoral variability in the response of tumours to radiation [Bentzen et al. Semin. Radiat. Oncol. 2011; 21(2):101-10]. To guide locally adaptive RT, robust imaging based biomarkers are needed which can predict the local influence of RT on the tumour during treatment. Galban et al [Nat. Med. 2009;15(5):572-576] proposed a promising biomarker based on voxel-wise analysis of repeated functional imaging. Their proposed parametric response map (PRM) classifies each tumour voxel as having undergone a significant increase, significant decrease, or insignificant change in function. This information was then found to correlate with treatment outcomes. However, voxel-based analyses such as the PRM may be particularly sensitive to image registration error (IRE). In a previous work [Lausch et al. Proc. 2013 ICCR], we demonstrated that IRE can cause functionally increasing and decreasing tumour voxels to be misclassified as one another which could lead to targeting errors if the PRM was used to guide adaptive RT. Here we present an augmented parametric response map (A-PRM) which may help to visualize and manage the influence of IRE on PRM analysis.

Materials and Methods: The original PRM is generated from a pair of spatially registered functional images by comparing the magnitude of each voxel-wise functional change (ΔF) within a region of interest (e.g. tumour) to a single threshold value, T . The functional images are acquired before (baseline) and during (follow-up) treatment. If $\Delta F \geq T$ or $\Delta F \leq -T$ for a voxel, then the voxel's functional change is classified as significantly increasing or decreasing respectively. If $|\Delta F| \geq T$ the change is not considered to be significant. T is determined by investigating the functional changes occurring in a region of similar healthy tissue that is outside of the tumour. $[-T, T]$ spans the 95% confidence interval (CI) for the residuals from a linear fit to a plot of follow-up scan voxel values versus baseline scan voxel values within this healthy region.

The proposed A-PRM uses multiple classification thresholds to classify the significance of the full range of functional changes within the ROI. Let $\{T_i\}$ for $i = 1 \dots 95$ represent the set of classification thresholds. Each threshold corresponds to a different CI in the residuals from the linear fit used to determine the classification threshold for the original PRM method (e.g. $[-T_{50}, T_{50}]$ is 50% CI). Each voxel-wise change could then be uniquely identified by the maximum threshold for which its magnitude exceeds. However, due to IRE it is uncertain which voxel in the follow-up scan should be compared to a given voxel in the baseline scan. Therefore there is a distribution of possible values for each voxel-wise comparison. To classify a voxel this distribution is first estimated. Let $D(\mathbf{x})$ represent the distribution of possible voxel-wise changes for a single voxel at position \mathbf{x} within the baseline scan. A summary estimate, $\bar{D}(\mathbf{x})$, is computed for $D(\mathbf{x})$. The standard deviation for $\bar{D}(\mathbf{x})$, denoted here by $\sigma_{IRE}(\mathbf{x})$, is also estimated. A voxel is uniquely classified by the maximum T_i for which $|\bar{D}(\mathbf{x})| - 3\sigma_{IRE}(\mathbf{x}) \geq T_i$. The A-PRM is an image of the ROI where each voxel value is given by $\pm i$. This indicates the maximum threshold (confidence interval) exceeded by the expected magnitude of the change, less its uncertainty, with the sign indicating whether the change was an increase or a decrease. If $|\bar{D}(\mathbf{x})| - 3\sigma_{IRE}(\mathbf{x}) < 0$ then the voxel is classified by $i = 0$.

The PRM and A-PRM methods were compared to one another through application to repeat functional imaging with simulated rigid IRE. Tumour blood volume (BV) maps generated from repeat CT-perfusion scans of 4 patients treated with RT for glioma were used. The baseline and follow-up maps were first non-rigidly registered to one another using a multi-resolution elastic registration algorithm. PRM and A-PRMs were generated from these maps and were defined as a reference result. Different amounts of rigid IRE were then simulated by perturbing each registered follow-up image volume by a thousand different rigid shift and rotation combinations. PRMs and A-PRMs were generated for each combination and the voxel classification sensitivity and specificity for the T_{95} threshold were computed by comparing to the reference result.

Results and Discussion: Classification sensitivity and specificity values for all magnitudes of IRE and all patients were binned according to median tumour voxel IRE and then averaged. Sensitivity and specificity as a function of median tumour voxel IRE is shown to the right. The A-PRM improved specificity at the cost of sensitivity. High specificity minimizes the chance that a voxel will be falsely classified as responding or progressing due to IRE. The reduced sensitivity means that fewer progressing or responding voxels will be detectable as IRE increases.



Conclusion: The high specificity of the A-PRM in the presence of IRE could facilitate a cautious approach towards guiding locally adaptive RT. Dose would only be modified away from convention in regions of the A-PRM classified by higher thresholds since these regions are both important with respect to treatment outcome and insensitive to the influence of IRE.

Deriving Planning Target Volume Margins for Intracranial Stereotactic Radiotherapy

Winnie Li^{1,2}, Tim Craig^{1,2}, Young-Bin Cho^{1,2}, Kevin Wang¹ & David Jaffray^{1,2*}

¹Radiation Medicine Program, Princess Margaret Cancer Centre, Toronto, ON, Canada

²Department of Radiation Oncology, University of Toronto, Toronto, ON, Canada

*Research Supervisor

Purpose/Objective(s): Awareness of inter- and intra-fraction uncertainties is increasingly important in the era of stereotactic radiotherapy (SRT); their incorporation into the margin of the planning target volume (PTV) is essential to ensure prescribed dose to the target. The purpose of this work is to develop a method to formulate PTV margins for gamma-knife intracranial SRT to manage uncertainties for the relocatable head frame (RHF).

Materials/Methods: A *Margin Calculator* tool was developed in SlicerRT™ for PTV margin derivation, and applied to gamma-knife intracranial stereotactic radiosurgery (SRS). Under ethics approval, 20 patient's targets (0 mm PTV margin originally) were re-planned in the treatment planning system with 3 PTV margins: isotropic 1 and 2 mm; and the clinical PTV margin used for the RHF, 1.5 mm anterior/posterior (AP) & left/right (LR), and 2 mm superior/inferior (SI). The dose distributions were imported into the *Margin Calculator* module for stochastic simulations using uncertainties measured on the RHF immobilization device. The RHF's localization (no image-guidance) and residual (image-guidance) systematic (Σ) and random (σ) errors were determined with cone-beam CT imaging from patients treated with LINAC-based SRT. In the AP, RL, SI directions, no image-guidance Σ and σ were [0.8, 0.8, 1.2]mm and [0.6, 0.6, 0.9]mm, respectively; image-guidance Σ and σ were [0.6, 0.2, 0.8]mm and [0.4, 0.3, 0.6]mm, respectively. For each patient, 4 fractionation schedules were assessed: 1, 3, 5 and 10. Dose population histograms were used to evaluate the differential effects of various factors on the required PTV margin. Cumulative dose population histograms were used to assess a goal of 95% population receiving a near-minimum dose (D_{98}) of 95%.

Results: Simulations were performed on 20 targets over 4 radiotherapy fractionation schedules using the RHF's Σ and σ uncertainties with and without image-guidance. Without image-guidance and a PTV margin of 2 mm, the D_{98} for 95% population was 78.4%, 89.7% and 92.7% for 1, 3 and 5 fractions, respectively. For a 10 fraction schedule, in the absence of image-guidance, the clinical margin ensures a near-minimum dose of 95.1% to 95% of the target. With image-guidance and the clinical PTV margin, the D_{98} for 95% population was 88.1%, 95.1% and 96.3% for 1, 3 and 5 fractions, respectively. For a 10 fraction schedule, a D_{98} of 96.4% for 95% of the population was achieved at a 1 mm PTV margin.

Conclusion: Using a specified objective of 95% population receiving a near-minimum dose of 95%, in the absence of image guidance, a PTV margin of > 2 mm is required for 1, 3, and 5 fraction intracranial SRT using the RHF while the clinical margin is sufficient for a 10 fraction schedule. With image guidance, the clinical margin is sufficient for 3 and 5 fraction treatment, while dose coverage for a 10 fraction schedule is assured with a 1 mm margin. The *Margin Calculator* tool is useful in deriving population specific PTV margins.

Elastic Registration of Prostate MR Images Based on Estimation of Deformation States

Bahram Marami^{a,b}, Suha Ghoul^a, Shahin Sirouspour^c, Jeremy Cepek^{a,b}, David W. Capson^d, Sean R. H. Davidson^e, John Trachtenberg^f, Aaron Fenster^{a,b,g}.

^aImaging Research Laboratories, Robarts Research Institute, London, Ontario; ^bBiomedical Engineering Graduate Program, The University of Western Ontario, London, Ontario; ^cDepartment of Electrical and Computer Engineering, McMaster University, Hamilton, Ontario; ^dDepartment of Electrical and Computer Engineering, University of Victoria, Victoria, British Columbia; ^eOntario Cancer Institute, University Health Network, Toronto, Ontario; ^fDepartment of Surgical Oncology, University Health Network, Toronto, Ontario; ^gDepartment of Medical Biophysics, The University of Western Ontario, London, Ontario, Canada;

Motivation: Clinically localized prostate cancer is being treated using magnetic resonance (MR) image-guided focal therapy techniques. Intra-treatment MR images have lower signal-to-noise ratio, spatial resolution and contrast than those of diagnostic images. In order to incorporate information from the diagnostic scans into the procedure, pre-treatment high-quality images have to be registered to intra-treatment images. Accurate registration of pre-treatment images with delineated tumor(s) to intra-treatment images can potentially improve the accuracy of the focal ablation therapy and reduce the duration of the intervention using updated pre-treatment therapy plans.

Method: A combined rigid and deformable registration technique is proposed to register pre-treatment 3T T₂ weighted MR images of the prostate, with identified target tumor(s), to intra-treatment 1.5T MR images. Four pairs of approximate corresponding points are manually identified in images, e.g., see Fig. 1. The rigid transformation aligning these points in two coordinates is used to initialize the optimization problem of intensity-based rigid registration between two images. An intensity-based similarity metric, which is the sum of absolute differences between modality independent neighborhood descriptors (MIND) in two images, is employed in both rigid and deformable registrations. The proposed deformable registration method is based on the concept of state estimation for dynamical systems. It employs a generic linear elastic finite element method (FEM)-based deformation model. The registration is achieved through a Kalman-like filtering process, which estimates deformation states of the prostate incorporating information from the deformation model and an observation error computed from the similarity metric between images.

Evaluation: The root mean square target registration error (TRE) of 84 manually identified fiducial points in 17 cases was found to be 2.23 ± 1.16 , 2.32 ± 1.12 , and 2.11 ± 1.21 mm for the whole gland (WG), central gland (CG), and peripheral zone (PZ) of the prostate, respectively after deformable registration. This is an improvement of over 1 mm from rigid registration. Dice similarity coefficients (DSC) in the WG, CG and PZ were 87.9 ± 2.8 , 85.5 ± 4.2 and 66.8 ± 5.1 mm, respectively. The maximum absolute surface distances (MAXD) were 5.72 ± 1.41 and 5.41 ± 1.34 mm in the WG and CG. Moreover, deformable registration resulted in the mean absolute surface distances (MAD) of 1.27 ± 0.27 and 1.26 ± 0.23 mm for the WG and CG volumes, respectively.

Discussion: Statistical analysis indicated that TREs in rigid and deformable registrations are significantly different. The whole registration process required less than 5 min for each case in MATLAB implementation.

Conclusion: The proposed technique improves the quality of registration especially in the peripheral zone where prostate tissue undergoes large deformation between imaging sessions. Using the proposed method, pre-treatment tumor outlines can be overlaid on intra-treatment images and pre-treatment therapy plans can be accurately updated, e.g., see Fig. 1.

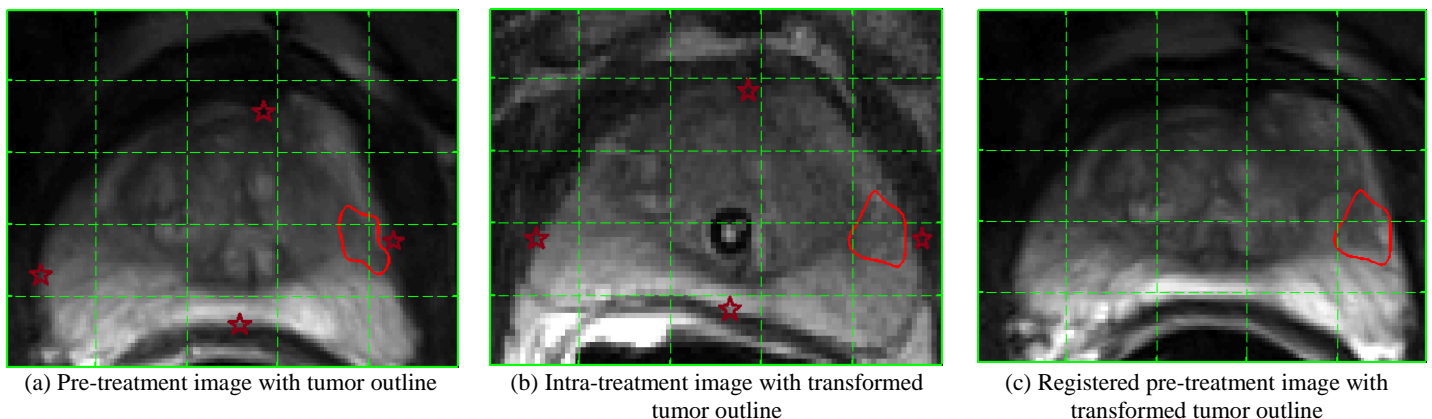


Fig. 1. Axial views of the prostate images with tumor outlines and approximate corresponding points.

Groupwise Conditional Random Forest Learning for Automated Region Of Interest Classification and Quality Assurance in Radiotherapy Planning

Chris McIntosh¹, Igor Svistoun¹, Thomas G. Purdie^{1,2,3}

- 1) Radiation Medicine Program, Princess Margaret Cancer Centre, University Health Network
- 2) Techna Institute, University Health Network
- 3) Department of Radiation Oncology, University of Toronto

Introduction: The delivery of radiation for treatment of cancer is a complicated process that requires the expertise of the multi-disciplinary radiation therapy (RT) team to ensure RT treatments are safe and effective. Sub-optimal treatment plans could seriously harm the patient. One aspect of treatment plan quality assurance (QA) involves reviewing delineated regions of interest (ROIs). If any of the ROIs are mislabeled or are of poor quality the safety of the treatment plan will be erroneously reviewed by RT team and an unsafe plan could be delivered.

Methods: We propose a technique to automatically label groups of ROIs from an RT plan for the joint purposes of providing QA and data mining. Given one or more ROIs and an associated image we seek to assign labels to each ROI and report a measurement of each ROI's quality. Our method automatically learns ROI relationships, e.g. a heart is typically smaller than a lung and is not typically observed in the same plan as a prostate. The algorithm uses the learned contextual information to ensure the ROIs are correctly labeled. Our approach extends state-of-the-art machine learning methods. We use random forests to learn joint distributions over the training features, and a set of learned potential group configurations to build a conditional random field (CRF) that ensures a consistent assignment of labels across the ROIs in a plan.

Results: We originally validated our method on 1574 plans consisting of 17,579 clinical ROIs across 77 different classes, using cross-validation with 60% of the data used for training and 40% for testing [1]. Our proposed method resulted in an overall classification accuracy of 91.58%, enabling it to detect 99.65% of ROI mislabeling errors, i.e. the true positive rate (TPR), while falsely reporting approximately 8 mislabeling errors per 100 ROIs, i.e. an 8.42% false positive rate (FPR) (Figure 1). Subtle contouring errors are more challenging to detect. 303 ROIs from 41 ROI classes were manually re-evaluated for contouring quality. Because human experts frequently disagree on exact ROI boundaries, no ROI is perfect. Our method provides a probabilistic estimate of contouring quality for each novel ROI in the plan. The user determines a threshold in order to flag ROIs that are of insufficient quality for planning. The TPR and FPR for contouring error detection depend on the selected threshold. The area-under-the-curve for our receiver operating characteristic (ROC) curve is 0.75, which means there is a 75% chance a low quality ROI will have a lower quality score than a higher quality ROI (Figure 2).

We have recently extended our results to 6,199 plans from 120 different treatment plan classes consisting of 59,400 clinical ROIs across 574 different classes, using cross-validation with 60%. Our preliminary results have demonstrated an overall classification accuracy of 79.04%, with 87.10% accuracy for organs at risk (OARs) and 66.10% accuracy for recognizing the 301 unique classes of targets. We are investigating new image and contextual features to improve target recognition accuracy for the new data.

Conclusions: By automating the multi-disciplinary QA process for RT planning using machine learning methods, we can improve treatment plan quality and patient safety by reducing errors and providing a framework for an evidence-based expert consensus approach to treatment. Our algorithm can also be used for data mining ROIs from a large number of plans.

References: [1] McIntosh, C., I. Svistoun, and T. Purdie. "Groupwise Conditional Random Forests for Automatic Shape Classification and Contour Quality Assessment in Radiotherapy Planning." IEEE transactions on medical imaging (2013)

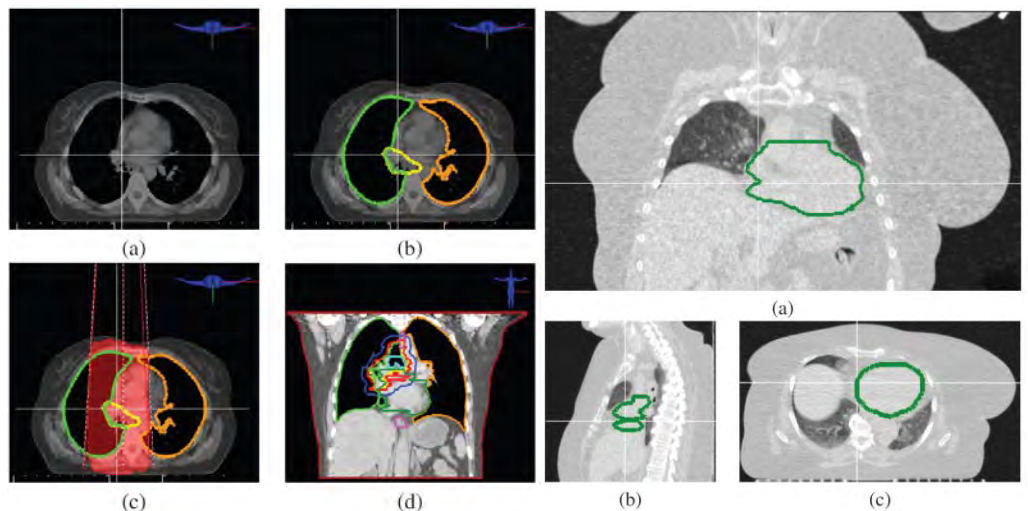


Figure 1: Example of incorrectly labeled left/right lung that was missed by the canonical QA process. ©2013 IEEE. Reprinted with permission from [1].

Figure 2: Example of automatically detected contouring error missed by canonical QA process. ©2013 IEEE. Reprinted with permission from [1].

18F-FAZA-PET Imaging in Colon, Rectal and Pancreatic Patient-derived Xenografts recapitulates the Hypoxic Microenvironment: Validation with Autoradiography and Immunofluorescence

Trevor D. McKee^{1,2}, Shawn Stapleton^{1,4}, Douglass C. Vines^{2,3}, Myles Smith¹, David E. Green², Neesha Dhanj¹, Cristiane Metran-Nascente¹, David Hedley^{1,4}, Catherine O'Brien^{1,5,6}, Bradly G. Wouters^{1,3,4,7}, David A. Jaffray^{1,2,3,4,8}

¹Ontario Cancer Institute, Princess Margaret Cancer Centre, University Health Network, Toronto, Canada

²Radiation Medicine Program, Princess Margaret Cancer Centre/ STTARR Innovation Centre

³Department of Radiation Oncology; ⁴Department of Medical Biophysics; ⁵ Division of General Surgery; ⁶Laboratory Medicine and Pathobiology, University of Toronto, Canada

⁷Ontario Institute for Cancer Research, Toronto, Canada

⁸Techna Institute for the Advancement of Health, University Health Network, Toronto, Canada

18F-Fluoroazomycin-Arabinoside (FAZA) is a 2-nitroimidazole that is useful for non-invasively monitoring of tumor hypoxia, through the use of either positron emission tomography (PET) imaging *in vivo*, or autoradiography of tissue sections *ex vivo*. As FAZA is entering clinical trials across a number of cancer types, it becomes increasingly important to define i) the reproducibility of this imaging procedure, and ii) the biological sensitivity of FAZA uptake within hypoxic tumors and tumor regions, in order to ensure accurate analysis and interpretation of FAZA-PET images.

To assess the reproducibility of the technique, we performed serial FAZA-PET, 24 hours apart, on 8 mice containing the subcutaneously implanted human cervical tumor model Me180. Quantification of the resulting images was performed by two independent operators, first by whole tumor average measures of FAZA uptake within the tumor, and subsequently by thresholding and voxel-based analysis to calculate the hypoxic fraction within each tumor, defined as the fractional area of tumor with uptake higher than the mean plus 3 standard deviations of muscle uptake. The hypoxic fraction varied from 57.2 ± 23.8 at Day 1 to 42.1 ± 24.7 on Day 2, with an average coefficient of variance of 41.7 and 58.7% respectively. The main source of variability was variation in FAZA uptake in muscle tissue between mice.

The biological sensitivity of FAZA towards monitoring tumors of differing hypoxic status was assessed by FAZA-PET imaging of subcutaneously implanted primary patient-derived pancreatic, colon, and rectal tumor xenografts that have known variations in hypoxia as assessed using EF5 uptake. Tumors that displayed high EF5 uptake also displayed enhanced uptake of FAZA, and increased hypoxic fractions, in comparison to low EF5 uptake lines. Finally, a novel technique was developed to combine autoradiography (following FAZA administration and PET imaging) directly with immunofluorescence histology on the same tissue sections. Assessment of these patient-derived tumors using this technique, with subsequent development of quantitative image analysis methods, allowed for direct comparison of FAZA distribution and EF5 uptake, providing a direct method for validation of the specificity of FAZA for hypoxia imaging. Together, these results demonstrate that FAZA-PET provides a reproducible method for assessment of hypoxia within tumors. Additionally, linking *in vivo* imaging using FAZA-PET with *ex vivo* autoradiography and immunofluorescence histology provides a powerful tool to improve the definition of tracer uptake, validation of quantitative image derived metrics of hypoxia, and the assessment of hypoxic status of tissues, pointing the way towards methods for improved image analysis and interpretation in the clinic.

Figures: 1) PET image of high and low EF5 pancreatic tumor uptake lines, 2) quantitation of hypoxic fraction within three patient-derived lines, 3) autoradiography image showing correspondence of EF5 and 18F-FAZA signal

Figure 1:

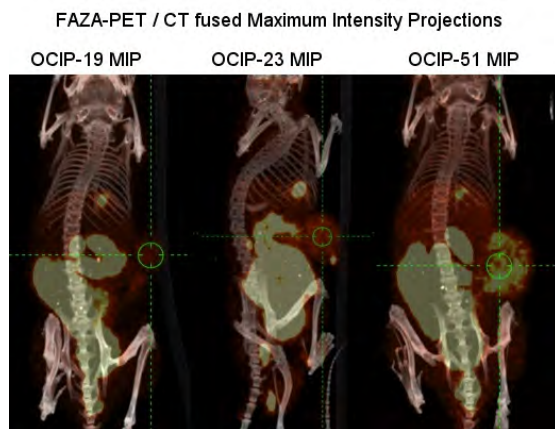


Figure 2:

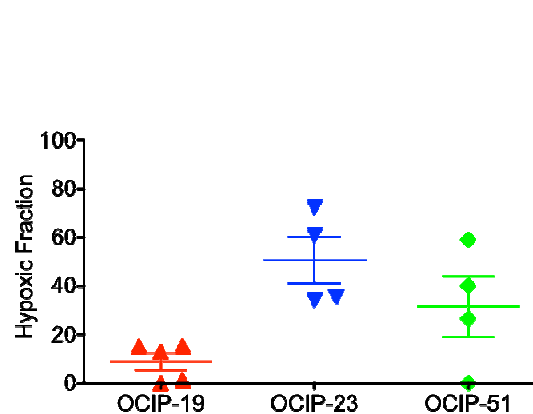
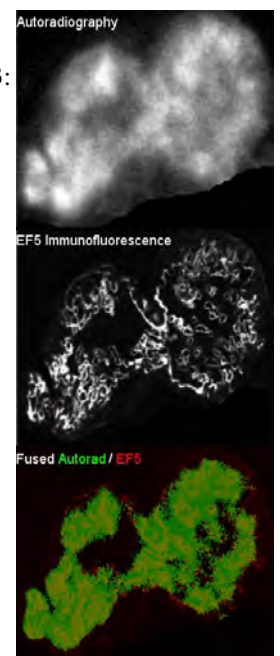


Figure 3:



Electromagnetic Catheter Digitization in Prostate High Dose-Rate (HDR) Brachytherapy Treatment Planning

Alexandru Nicolae^{2,3}, Shyam Bharat¹, Cynthia Kung¹, Niranjana Venugopal⁴, Ehsan Dehghan¹, Antonio Bonillas¹, Doug Stanton¹, Jochen Kruecker¹, Ananth Ravi^{2,3,‡}

¹ Philips Research North America, Briarcliff Manor, NY, USA

² Department of Medical Physics, Odette Cancer Centre, Sunnybrook Health Sciences Centre, Toronto, ON, CAN

³ Department of Radiation Oncology, the University of Toronto, Toronto, ON, CAN

⁴ Department of Medical Physics, Saskatchewan Cancer Centre, Saskatoon, SK, CAN

[‡]Research Supervisor

Purpose: In prostate HDR brachytherapy, Trans-Rectal Ultrasound (TRUS) image guidance may be used for transperineal insertion of up to 20 catheters directly into the prostate gland. The treatment planning system uses these catheter positions to optimize the dwell times and positions of the HDR source used to deliver the required prescription dose. Manual catheter identification using TRUS has many problems: high catheter echogenicity, shadowing artifacts, and poor US image quality [1]. Electromagnetic (EM) tracking technology has shown promise for improving catheter identification in prostate HDR brachytherapy and is reported here concurrent with manually-identified catheters using TRUS. Performance degradation, due to EM field distortions in the presence of magnetic objects, has occurred in the literature [2]; a characterization of the effects of various EM-signal distorters present in the clinical setting on the accuracy of the EM system was therefore also reported.

Materials and Methods: The EM tracking system (consisting of the field generator, compatible brachytherapy stepper, and guidewire), was setup in both a laboratory setting (no EM signal-distorters present), as well as a brachytherapy operating room (EM signal-distorters and operating equipment present) (**Figure. 1**). Catheter digitization was performed by retracting a 1.2 mm EM guidewire through 5-6 hollow plastic catheters inserted approximately the same depth into the prostate phantom.

Validation was obtained by comparing the EM catheter tracks with manually-delineated catheter positions on axial TRUS images for both lateral and anterior field generator (FG) orientations. Comparison between TRUS-delineated and EM-delineated catheter tracks was made by computing the in-plane error, calculated as the Euclidean distance between EM-tracked points and their corresponding positions on US axial slices. The effect of signal distorters present in the clinical environment was determined by introducing equipment used in brachytherapy procedures at incremental radial distances from the center of the field generator and computing the associated deviation from 3 reference sensors. The signal distorters evaluated in this study include the remote afterloader, TRUS, stainless steel supply cart, and treatment planning system.

Results: In-plane error in a laboratory setting was reported as an average of 4 trials per FG orientation. Average in-plane error was 0.70 ± 0.37 mm (max 1.83 mm) with a lateral FG orientation and 0.73 ± 0.35 mm (max 3.06 mm) with an anterior FG orientation. In-plane error for EM vs. TRUS-delineated catheter tracks in the brachytherapy operating room environment was 0.60 ± 0.28 mm (max 1.42 mm) with a lateral FG orientation and 0.68 ± 0.36 mm (max 1.50 mm) with an anterior FG orientation. The largest distortion in sensor signal was associated with the stainless steel brachytherapy supply cart with an absolute deviation of 0.41 mm from baseline readings, positioned at a distance of 45 cm from the FG.

Conclusions: The high level of agreement between EM-tracked and US-identified catheter positions illustrates the potential value of utilizing EM tracking for catheter mapping in prostate HDR brachytherapy. Further studies require clinical trials to determine the feasibility of using the EM system in a clinical workflow.

References: [1] Stromberg, J., et al. *Int J Radiat Oncol Biol Phys.* **1995**; 33:161-71
[2] Zhou J, et al. *Med Phys.* **2013**;40(2)



Figure. 1. Experimental apparatus in a brachytherapy suite environment. A prostate training phantom (CIRS Inc., Norfolk, VA, USA) was mounted on a plastic platform with a customized EM-compatible stepper and TRUS probe (BK Medical, Peabody, MA, USA). An Aurora EM field generator (NDI, Waterloo, ON, CAN) was positioned in an anterior orientation (shown), or lateral orientation.

This study was funded by a research grant from Philips Healthcare

Modified sampling technique for improving the GLOBE's modeling accuracy

Seungjong Oh¹, David Jaffray^{1,2,3,4}, and Young-Bin Cho^{1,2}

¹Radiation Medicine Program, Princess Margaret Cancer Center,

²Department of Radiation Oncology, University of Toronto,

³Institute of Biomaterials and Biomedical Engineering, University of Toronto,

⁴Department of Medical Biophysics, University of Toronto; Toronto

Research supervisor: Young-Bin Cho

Purpose: In previous study, we developed a technique of Geometric reLocation for analyzing anatomical OBjects' Evolution (GLOBE) in order to provide a numerical model of tumor evolution under radiation therapy. GLOBE consists of three main steps; step1) deforming a 3D surface object to a sphere by parametric active contour (PAC), step2) sampling a deformed PAC on 642 nodes and 1280 faces of a conventional 8-frequency icosahedron geodesic dome (IGD), and step3) unfolding 3D data to 2D plane for convenient visualization and analysis. The deformed PAC might be non-uniformly sampled in step2. If too many CTV nodes are located in a face (under-sampled), the GLOBE might inaccurately represent a tumor shape at the face. In this study, we improved the sampling technique by adaptively subdividing the sampling faces on extremely under-sampled region.

Material and Methods: A total of 152 clinical target volumes (CTVs) obtained from 28 cervical cancer patients were analyzed. The number of nodes from 152 CTVs was calculated on each face of the conventional IGD and the 10% of faces with most under-sampled region were identified. The sampling process was performed with the modified IGD in which the identified faces were subdivided into 4 small triangular faces. The performance of the modified IGD with increased sampling faces was evaluated with respects to 1) CTV nodal density, total number of sampled CTV nodes, on each face and 2) reconstruction error, difference between the reconstructed CTV using GLOBE nodes and the original CTV.

Result: The modified IGD consisted of 1026 nodes and 1664 faces. CTV nodal density on each IGD face ranged from 36 to 1081 with the conventional IGD and from 36 to 329 with the modified IGD. Averaged reconstruction error ranged from 0.4 to 2.6 mm with the conventional IGD and from 0.4 to 1.4 mm with the modified IGD. Figure 1 showed CTV nodal density and averaged reconstruction error on the conventional IGD and the modified IGD. Severely under-sampled regions and their large reconstruction errors were distinguishable with the conventional IGD. The modified IGD successfully reduced CTV nodal density and reconstruction error, accordingly.

Conclusions: Modified IGD improves the accuracy of GLOBE's tumor modeling specifically for patients with large reconstruction error. Although the improvement of reconstruction error is small on average, the modified IGD significantly reduces the maximum error from 15.7 mm to 4.7 mm in a certain CTV.

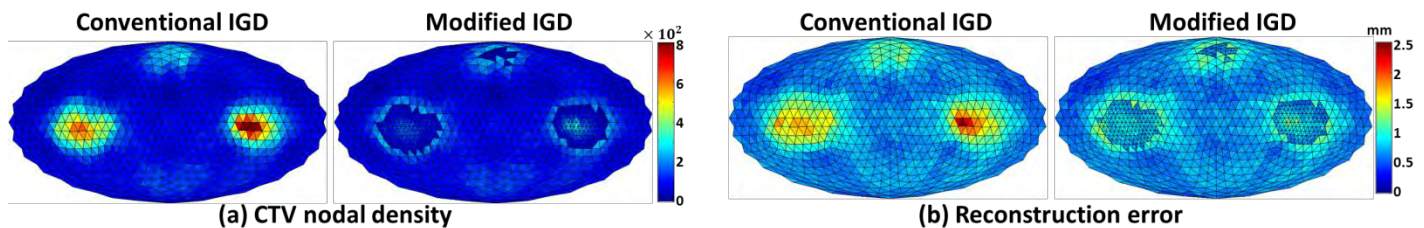


Figure 1. Performance comparison of the modified IGD with the conventional IGD. (a) CTV nodal density and (b) averaged reconstruction error on each IGD face were displayed on 2D plane by unfolding process of GLOBE. Extremely under-sampled region had large sampling error in initial uniform sampling. Resampling successfully reduces the CTV nodal density and the reconstruction error in resampled region.

Practical implementation of texture analysis techniques in large imaging databases using a GPU-based approach

Gregory M. Szilagy^{1,2}, Sandra E. Black^{1,2,3}, Jean-Paul Soucy⁴, Curtis B. Caldwell^{5,6}

¹*Institute of Medical Science, Faculty of Medicine, University of Toronto*, ²*L.C. Campbell Cognitive Neurology Research Unit, Sunnybrook Research Institute*, ³*Brain Sciences Research Program, Sunnybrook Research Institute*, ⁴*McConnell Brain Imaging Centre, Montreal Neurological Institute*, ⁵*Department of Medical Imaging, Sunnybrook Health Sciences Centre*, ⁶*Departments of Medical Imaging and Medical Biophysics, University of Toronto*

Introduction: We present a software tool for the Graphics Processing Unit (GPU)-accelerated generation of Neighbourhood Gray-Tone Difference Matrix [1] (NGTDM) and Gray-Level Co-occurrence Matrix [2] (GLCM)-based voxel-wise textural feature maps from 3D volumetric medical image data optimized for machine learning and interactive applications in large data sets.

Background: 3D medical imaging has led to ever-expanding sets of data. CPU-based image analysis techniques are often difficult to apply to large study groups simply because of the enormous volume of data. Recent advances in GPU-based processing offer the possibility of making detailed image analysis practical for even very large imaging databases. Two particular problems may be solved in this way: (1) the need for “real-time” image analysis of large 3D datasets (e.g., MRI or CT) for an individual patient study and (2) the desire to analyze large image databases, such as the Alzheimer's Disease Neuroimaging Initiative (ADNI) on a practical timescale (i.e., hours and days instead of weeks or months).

Methods: Our software makes use of Nvidia's CUDA parallel GPU computation application programming interface in conjunction with the NumPy scientific computing package. By manipulating the memory offsets used by NumPy to access consecutive array elements along multiple dimensions, we are able to process arbitrarily sized image volumes in overlapping tiled views without copying the underlying data. The overlapping tiles allow processing to be subdivided in accordance with the memory constraints of the GPU hardware while eliminating artifacts resulting from incomplete moving window data near tile boundaries.

The computationally intensive voxel-wise calculation of textural features is implemented in a series of CUDA kernel code templates. For GLCM features, our implementation is modeled on the methods described in [3], including the use of packed co-occurrence matrices to reduce the algorithms' demands on GPU memory. Through PyCUDA's support for metaprogramming [4], we further optimize kernel code with respect to user-configurable parameters, as well as architectural properties of the GPU hardware being used, prior to compiling at run-time.

Feature selection algorithms in machine learning applications and eventual interactive uses of the software in a clinical setting may each specify a variable combination of features of interest while making the calculation of others redundant. To efficiently calculate intermediate values and interdependent GPU textural features where only a subset of the available features may be required, we dynamically schedule host-to-GPU memory transfers and the execution of GPU kernels based on a dependency tree inferred through run-time introspection of the Python methods corresponding to each feature. After recursively pruning leaf nodes from the dependency tree until only the desired features remain, evaluating feature computation nodes in a topologically sorted order over the resulting directed acyclic graph ensures that their prerequisites are satisfied at each stage of execution. This method allows the computation of any subset of available features to be optimized with respect to memory transfers and execution order without having corresponding pre-determined sequences of operations permanently embedded into the program.

Results: We confirmed the accuracy of our GPU implementation in randomly placed sub-volumes of feature maps derived from baseline MRI and PET data from the ADNI study that were simultaneously processed through “naive” reference implementations of all NGTDM and GLCM-based feature calculations. Although not specifically optimized, an additional hybrid Python-C CPU implementation applied to full image volumes confirmed a relative GPU performance gain of up to two orders of magnitude, in line with improvements achieved by GPU implementations of similar algorithms.

Conclusion: We developed GPU-accelerated software capable of providing the higher computational speed and flexibility necessary to support the practical use of whole-volume voxel-wise NGTDM and GLCM textural feature maps in interactive and machine learning applications using large medical image data sets.

References:

- [1] Amadasum M, King R. Textural features corresponding to textural properties. *IEEE Transactions on System, Man and Cybernetics*, 1989: 19(5), 1264-1274.
- [2] Haralick R. Statistical and structural approaches to texture. *Proceedings of the IEEE*, 1979: 67(5), 786-804.
- [3] Gipp M., et al. Haralick's Texture Features Computed by GPUs for Biological Applications. *IAENG International Journal of Computer Science*, 2009: 36(1)
- [4] Klöckner A, et al. PyCUDA and PyOpenCL: A scripting-based approach to GPU run-time code generation. *Parallel Computing*, 2012, 38(3), 157-174.

In-phantom and Fluence-based Measurements for Quality Assurance of Volumetric-driven Adaptation of Arc Therapy

Bryan Schaly, Doug Hoover, Sylvia Mitchel, Dani Scott, Jeff Chen, **Eugene Wong**

Department of Radiation Oncology, London Regional Cancer Program, London, Ontario, Canada

Objective: To compare ArcCHECK (Sun Nuclear) in-phantom measurements and Portal Dosimetry (Varian) with an electronic portal imaging device (EPID) for quality assurance of adapted arc plans in the treatment of head and neck (H&N) cancer.

Method: We reviewed a cohort of H&N patients (Jan-Oct 2013) treated with VMAT (two 360° arcs) who had repeated CT simulation. Repeat CT scans were triggered by large volume changes as seen on daily cone-beam CT. For each patient, the original plan was evaluated on the new CT. New contours and an adapted plan were created if necessary. The ArcCHECK phantom was used to verify the dose distribution from the adapted plan. Here, we add pre-treatment Portal Dosimetry (integrated) fluence measurement per treatment arc to compare against ArcCHECK results. Detailed comparisons are presented here for one example patient who had been re-planned after 9 out of 20 fractions (Fig. 1).

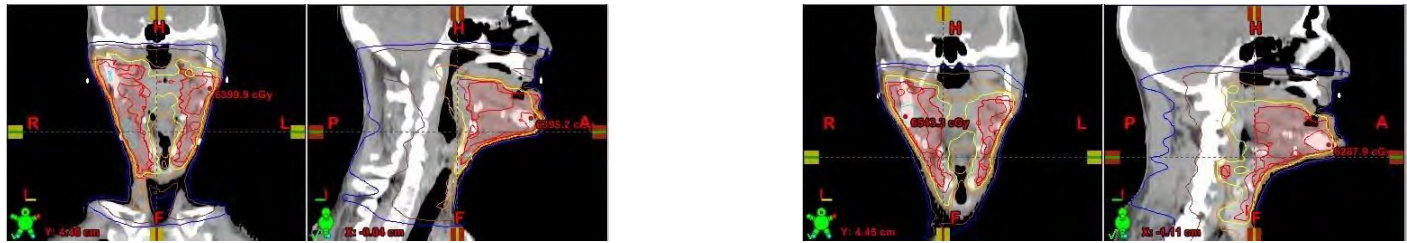


Figure 1: Original Plan (Two 360° arcs)

Adapted Plan (Two 360° arcs)

Results: Twenty one (13%) patients out of 167 H&N patients were re-CT scanned from Jan-Oct 2013. Of those, 50% continued to be treated with the same plan, while 15% had the same plan but adjusted monitor units, and 35% required new contours and a new plan.

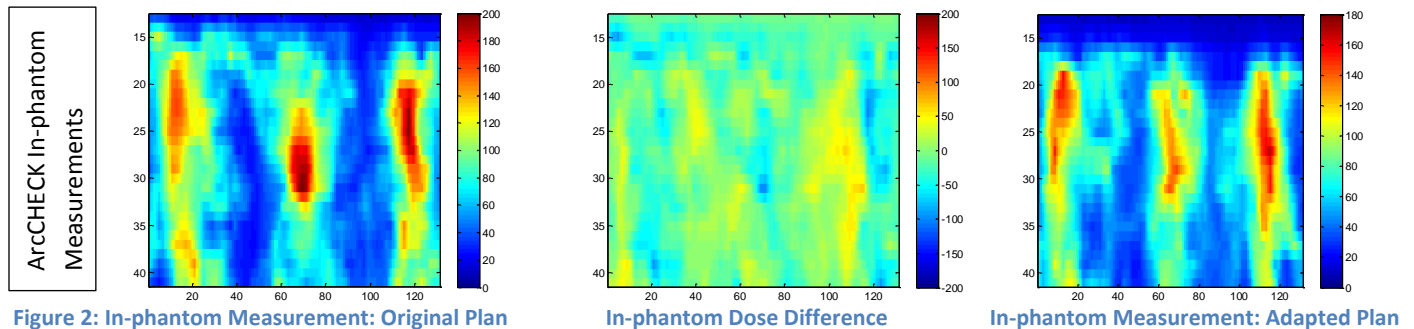


Figure 2: In-phantom Measurement: Original Plan

In-phantom Dose Difference

In-phantom Measurement: Adapted Plan

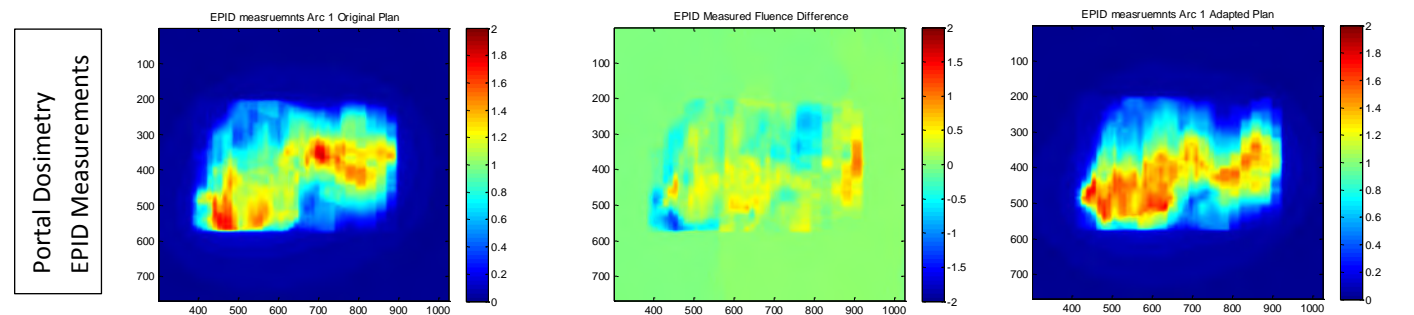


Figure 3: Original Arc 1 Integrated Fluence

Integrated Fluence Difference

Adapted Arc 1 Integrated Fluence

Discussions: In-phantom measurements (ArcCHECK in this instance, Fig. 2) allow us to check how un-intuitive fluences add up to the desired dose distribution as planned (by comparing to plan prediction). This includes collimator angle settings and the accumulation of doses. Pre-treatment Portal Dosimetry (integrated arc fluence map, Fig. 3) allows us to check that the intended fluence has been transferred to the unit as per treatment plan (by comparing to fluence prediction). For quality assurance of the adapted plan, the question we would like to address is whether portal dosimetry verification of the integrated fluence is sufficient.

Conclusions: Arc-based dose distributions are relatively insensitive to local volumetric changes because dose is accumulated from beams coming from many directions. Approximately half of the cases sent for repeat CT did not require any plan adjustments. Fifteen percent of the cases required a simple adjustment in monitor units, while the remainder required both new contours and plan adaptation/re-optimization. Integrated fluence-based measurements for these plans can detect the adapted plan changes and is therefore likely suitable for quality assurance of adapted arc treatments. Additional studies is needed to confirm that.

Variation in dose equivalent rate constant as a function of shielding thickness for radioisotopes used in nuclear medicine

1 Author(s) – **Trinette Wright, B.Eng.¹**; Maggie Kusano, B.Sc.¹; Curtis Caldwell, Ph.D.^{1,2}

Sunnybrook Research Institute, ²Departments of Medical Imaging and Medical Biophysics, University of Toronto

A primary goal of nuclear medicine facility design is to keep public and worker radiation doses As Low As Reasonably Achievable. To estimate dose and shielding requirements, one key factor required is the dose equivalent rate constant for soft tissue for the radioisotope in question. Dose equivalent rate constants are most commonly calculated using published air kerma or exposure rate constants and are dependent on the photon spectrum for the radioisotope in question. Low energy photons in a spectrum may have a large influence on the dose equivalent rate constant (DERC) calculated. These low energy photons are the most heavily attenuated when shielding is used. Thus, a dose equivalent rate constant calculated based on an “attenuated” spectrum could be quite different than one based on the emission spectrum, but it is currently standard practice to use the same DERC for a radioisotope source, regardless of the amount of shielding material used. In this study, we have applied Monte Carlo methods to determine the influence of shielding on the spectra of seven radioisotopes commonly used in Nuclear Medicine: Gallium-67, Iodine-123, Iodine-131, Technetium-99m, Indium-111, Xenon-133 and Thallium-201. The simulations contained a point source, lead or concrete shielding and a tally point. The spectra of each radioisotope were recorded at the tally point (Fig. 1).

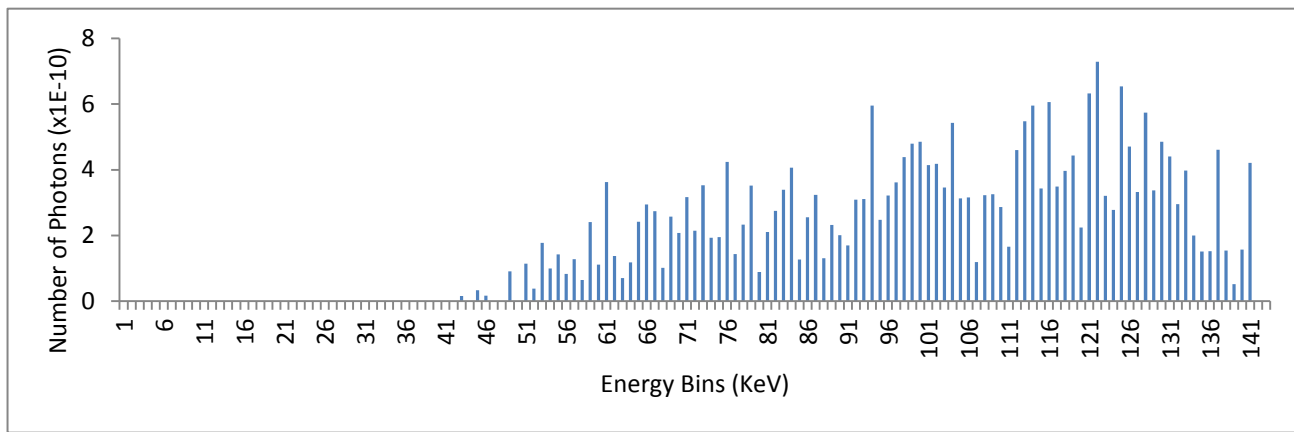


Fig. 1. The spectrum of Technetium-99m using 15.2 cm (6”) of concrete shielding calculated by Monte Carlo methods. The number of photons that cross that tally surface are normalized per source particle

Various thicknesses of shielding were used in the simulations. The thicknesses of the lead shielding were 0.08 cm (1/32”), 0.16 cm (1/16”), 0.32 cm (1/8”), 0.64 cm (1/4”) and 1.27 cm (1/2”) and the thicknesses of the concrete shielding were 7.6 cm (3”), 15.2 cm (6”), 30.5 cm (12”), 50.8 cm (20”), and 61 cm (24”). The dose equivalent rate constants for soft tissue can be given by:

$$st = \frac{1}{4\pi} \sum_i E_i Y_i \left(\frac{\mu_{en}}{\rho} \right)_i,$$

where Y_i and $(\mu_{en}/\rho)_i$ are the yield and mass energy-absorption coefficient of soft tissue (cm^2/g) for each of the radionuclide's photon energies $E_i > \delta$ keV. The spectra were used to calculate the DERC of each radioisotope at each shielding thickness (Fig. 2).

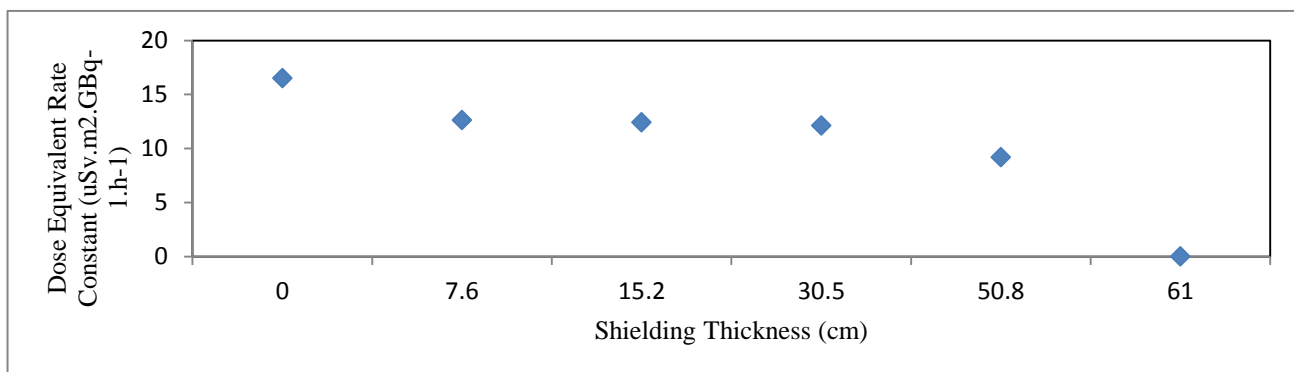


Fig. 2. Dose Equivalent Rate Constants for Technetium-99m at all concrete shielding thicknesses

Our results suggest that, for several radioisotopes, this effect can significantly influence the radiation dose calculated when shielding is used. The data provided by this study should assist in improving the accuracy of dose and shielding calculations for nuclear medicine facility design.

Software development for image guidance on the magnetic resonance-guided radiation therapy (MRgRT™) system

Wenyao Xia¹, Stephen Breen¹, Kevin Wang¹, Jeff Winter², David Jaffray¹

1. Radiation Medicine Program, Princess Margaret Hospital, University Health Network

2. IMRIS R&D

Background: The magnetic resonance-guided radiation therapy (MRgRT™) system utilizes a moveable MRI system to provide image-guidance in a linear accelerator (Linac) vault. By exploiting the superior soft tissue contrast available with MR-guidance, our goal is to provide more accurate patient positioning based on internal soft tissue. To implement cone beam CT (CBCT) and MR guidance effectively, we developed a novel software tool using the 3D Slicer platform.

Objectives: This software tool was built to handle reference CT (rCT) and MR (rMR) images from treatment simulation as well as guidance CBCT and MR (gMR) images from daily image guidance. Key design goals include: (i) support various data formats such as DICOM CT, DICOM MR, DICOM spatial registration objects; (ii) provide communication and data flow between different imaging, treatment and storage devices; (iii) perform accurate and robust image registration; (iv) provide a user-friendly graphical interface for users to manipulate data and assess registration quality; and, (v) output couch coordinate shift information to correct patient position for treatment.

Methods: We designed the software to import reference CT and MR images as well as guidance CBCT and MR images from the Mosaic Data Director (MDD), accurately register the guidance MR image to the reference MR, and export couch correction information to the Varian external interface to drive the couch to the correct position. In addition, we have implemented volume-of-interest (VOI) image registration capabilities, which allow the user to emphasize specific regions (e.g., tumour) of the internal soft tissue contrast in the registration process. To test the accuracy of MR guidance using our software tool, we imaged a CIRS triple modality abdominal phantom on a CT, MRI and Linac separately to simulate the complete image guidance workflow. For the CBCT and Guidance MR imaging sessions we performed fixed shifts of the phantom to simulate different patient positions.

Results: All image data from the simulated workflow were successfully loaded into our software tool. Registration of the reference MR to the guidance MR was successful with resulting mean squared errors (MSE) for the four phantom shifts of 0.23 mm, 0.40 mm, 0.11 mm, and 0.10 mm. Couch corrections were generated based on the registration information and exported.

Conclusions: In this study, we demonstrated the successful implementation of a comprehensive image-guidance tool for the MRgRT system in the 3D Slicer platform, which will be a powerful and flexible research tool to perform MRI guided radiation therapy. We plan to use this tool to study the MRgRT system's performance in guiding patient positioning based on soft tissue contrast and develop novel applications to enhance the clinical value of MR-guidance in radiation therapy.

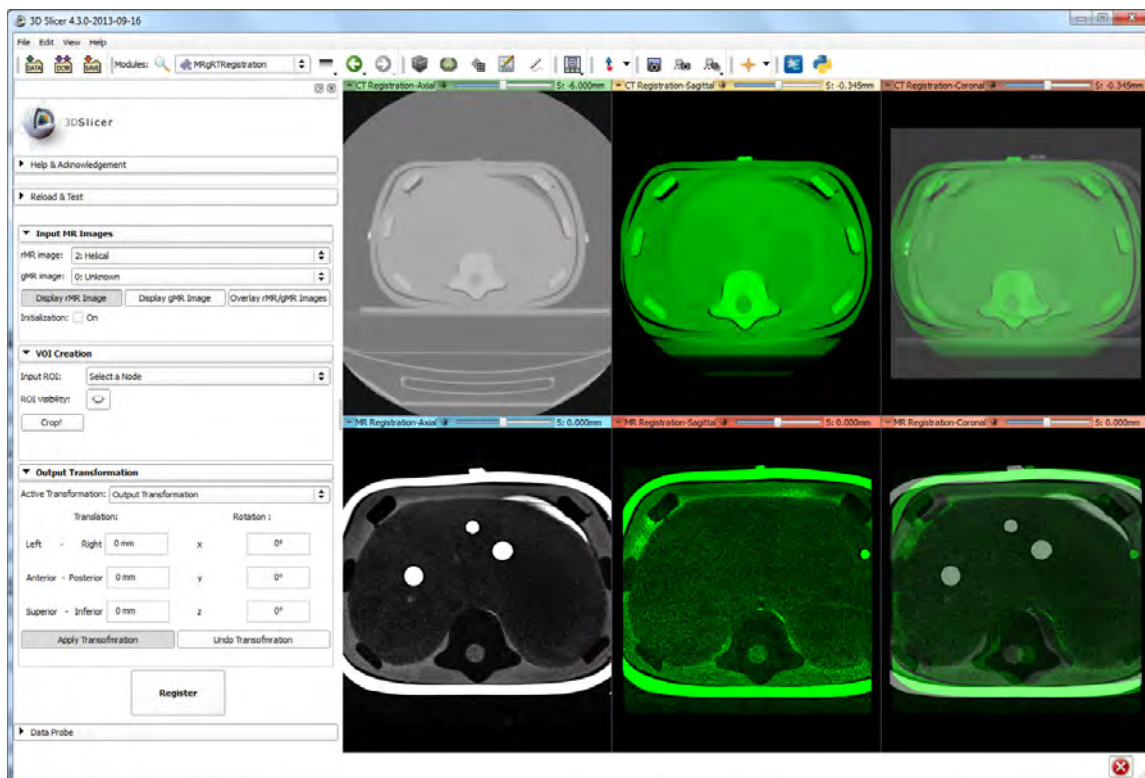


Figure 1. This is a demonstration of the guidance software. The panel on the left side provides various functionalities for user to perform MRI guidance. The viewer on the right side displays unaligned images imported from MDD, where the top row images are rCT, CBCT, rCT-CBCT overlay and the bottom row images are rMR, gMR, rMR-gMR overlay.

**Ontario Consortium in Imaging for
Cardiovascular Therapeutics
OCICT**

Oral Presentation and Poster Abstracts

Application of 3D echocardiography and gated micro-CT to assess cardiomyopathy in a Duchenne muscular dystrophy mouse model

Andrew Bondoc^{*†}, Sarah Detombe[‡], Joy Dunmore-Buyze[‡], Kelly Gudpell^{*§}, Linshan Liu^{*†}, Amanda Kaszuba^{*}, Rebecca McGirr^{*}, Jennifer Hadway^{*‡}, Maria Drangova^{*‡} and Lisa Hoffman^{*†§} (Supervisor)

^{*}Imaging Program, Lawson Health Research Institute, London, ON; [†]Department of Medical Biophysics, Western University, London, ON; [‡]Imaging Research Laboratories, Robarts Research Institute, London, ON; [§]Department of Anatomy & Cell Biology, Western University, London, ON, Canada

Duchenne muscular dystrophy (DMD) is a severe neuromuscular X-linked disorder occurring in approximately 1 in 3500 boys. It has classically been considered a skeletal and diaphragm muscle pathology that is characterized by progressive muscular degeneration; however, improvements in care have now extended the lifespan of patients such that clinically-relevant dilated cardiomyopathy is observed in >95% of patients. The most convenient and relevant pre-clinical model of DMD cardiomyopathy is the ‘double-knockout’ mouse model (mdx/utrn^{-/-}), which exhibits severe progressive skeletal muscle degeneration as well as cardiac pathology starting between 8-10 weeks of age. Unlike the skeletal muscle pathology, dilated cardiomyopathy in these mice has not been elaborately characterized. Changes in cardiac function have so far only been measured using two-dimensional ultrasound, which inherently requires assumptions to be made about the shape of the heart, and also results in substantial inter-user variability. Quantitative evaluation of cardiac ventricular sizes, ventricular function, and left ventricular mass, first in mdx:utrn^{-/-} dystrophic mice, is important for prognosis and management of the disease in patients; thus, cardiomyopathy in these mice needs to be assessed using a three-dimensional, non-invasive, quantitative method that circumvents the use of correction formulas.

To this end, this study sought to measure changes in cardiac function using three-dimensional, ECG-gated echocardiography (3DE). This study is the first to correlate cardiac volumes acquired using 3DE to those acquired using retrospectively-gated micro-CT (**Figure 1**). Both were further compared with the standard two-dimensional M-mode echocardiography method, and with histological analyses. We demonstrated that while each modality measures a decrease in cardiac function as disease progresses in mdx:utrn^{-/-} mice, 3DE measurements correlated well with those acquired with gold-standard micro-CT (**Figure 2B**), with little standard deviation between measurements (**Figure 3**). M-mode echocardiography measurements, in comparison, exhibit considerably greater variability and user-bias (**Figure 2A**).

Given the radiation dose associated with micro-CT and the geometrical assumptions made in M-mode echocardiography to calculate ventricular volume, we suggest that use of 3D echocardiography has important advantages that may allow for the measurement of early, subtle disease changes that occur prior to overt cardiomyopathy. This may help future studies characterizing the onset of cardiomyopathy in these mice, and may also help in studies that use the mice to explore novel DMD treatments, such as those involving stem cell therapies.

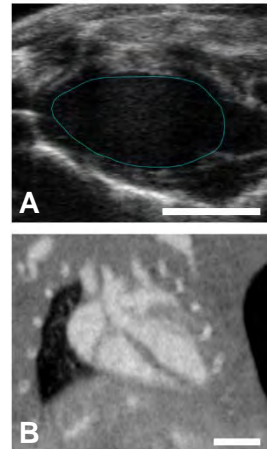


Figure 1. Representative image of 3DE (A) and micro-CT (B). Scale bars = 4mm

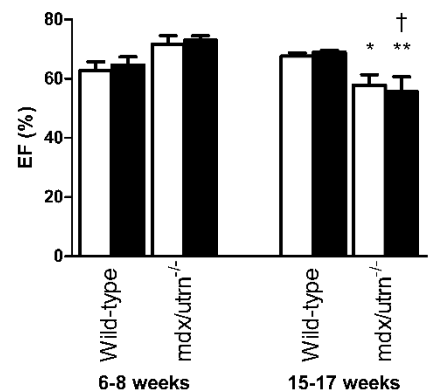


Figure 3. Evaluation of EF for wild-type and mdx/utrn^{-/-} mice using 3DE and CT. White bars represent values measured through 3DE, black bars represent values measured through CT (+ standard deviation). EF in mdx/utrn^{-/-} mice was significantly lower at 15-17 weeks of age than at 6-8 weeks (19.13% by 3DE, **p* < 0.05; 23.86% by CT, ***p* < 0.01), and as the CT data shows, was also significantly lower than in the age-matched control group (19.32%, †*p* < 0.05).

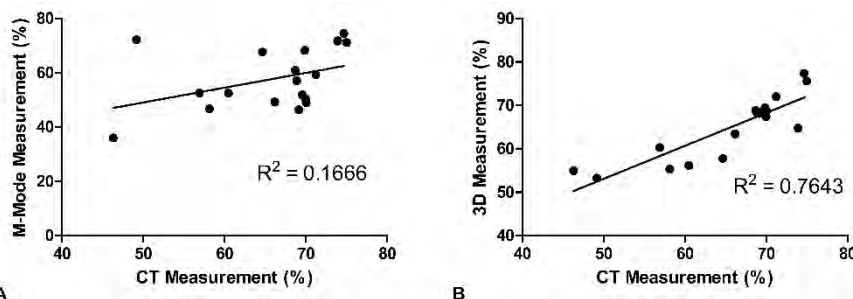


Figure 2. Linear regression correlation analysis of ejection fraction (EF) values measured via echocardiography vs. values measured by CT. (A) M-mode-measured EF showed low correlation with micro-CT ($R^2 < 0.70$), whereas (B) 3DE-measured EF correlated well with micro-CT ($R^2 \geq 0.70$)

Tracking a 6F catheter under MRI using a controllable susceptibility device: a new tracking mechanism

William Dominguez-Viqueira¹, Chris Dey², Hiran Karimi^{1,3}, and Charles H Cunningham^{1,3}

¹Physical Sciences, Sunnybrook Research Institute, Toronto, Ontario, Canada, ²Radiology, Sunnybrook Health Sciences Centre, Toronto, Ontario, Canada, ³Medical Biophysics, University of Toronto, Toronto, Ontario, Canada

Target Audience: Interventional radiologists and researchers.

Purpose: Due to the rich anatomic information available, MRI is an attractive tool for guiding catheters during interventional procedures. Susceptibility artifact-based tracking using paramagnetic markers¹ is a simple and economical approach, but has been used with limited enthusiasm partly because of the image degradation that results from such devices. More recently a novel susceptibility-based tracking device which can be mechanically turned ON and OFF was demonstrated *in vivo* with a 9F catheter tip and three layers of magnetic markers². For this work, a new 2 layer tracking element was designed and integrated into a 6F catheter with a lumen. The catheter was demonstrated *in vivo* using a novel approach to find the device in projection images.

Theory: Signal that is modulated in k-space is replicated (ghosted) in image space. Here we exploit this effect to create a ghost of the catheter tip that is outside the anatomy, at precisely FOV/2 (in the phase-encode direction) from the true device location. This is done by turning the susceptibility effect ON and OFF every other TR (here we use a long TR and manual toggling for proof-of-concept). The utility of this is that the position of the device tip can then be quickly located in full projection images. The requirements are that the toggling of the ON/OFF states are synchronized with the TR and that the FOV is large enough that the ghost is outside of the anatomy.

Materials and Methods: The new tracking device design consisted of two concentric cylinders of titanium and graphite giving an outer diameter of 2mm and length of 3mm (Fig.1). The layer thicknesses were designed by numerical optimization to create a minimum susceptibility artifact in MRI when the cylinders are aligned (OFF position); and a large artifact when the cylinders are miss-aligned (ON position)². The catheter was constructed by attaching the titanium cylinder to biocompatible Pebax-Polyimide tubing with heat-shrink. Polyimide tubing was glued and heat-shrunk to the graphite cylinder to push and pull this piece in and out relative to the titanium part (Fig.1.a). A guidewire of up to 0.022 inch diameter can be inserted through the inner lumen. Larger guidewires can be used and contrast agents can be administered by removing the inner graphite-polyimide tube during a procedure

A Yorkshire pig (36 kg) was anaesthetized and intubated under a protocol approved by the institutional animal care and use committee. A 6F sheath was placed in the femoral artery and the catheter was advanced to the carotid bifurcation using a guidewire under x-ray fluoroscopy. Once at the bifurcation, an angiogram was performed to advance the catheter into the carotid artery. The animal was repositioned in a 1.5T MR scanner (Signa, GE Healthcare, Waukesha, WI), with a 5 inch diameter receive-only surface coil. The novel tracking mechanism was demonstrated by acquiring gradient echo full-volume projection images and manually switching the device between ON and OFF configurations every TR, with TR=2s, TE=1.2ms, FOV=48cm, matrix=256/128. After locating the device, real-time tracking and visualization was performed by imaging every 0.64 sec around the device using a fast GRE pulse sequence². High resolution fast gradient-recalled echo images were also taken with the tracking device in ON and OFF positions to quantify the susceptibility artifacts in both positions (TR/TE=300/2.3, FOV=20cm, matrix=256/128, slicethickness=3mm).

Results and Discussion: Figure 1 b shows the picture of the 6F catheter built. The inner lumen of this design permitted the use of conventional guidewires and contrast under fluoroscopy to guide the catheter through the bifurcation in to the carotid. The maneuverability of this new design was significantly better comparing to the earlier 9F design with guidewire in monorail².

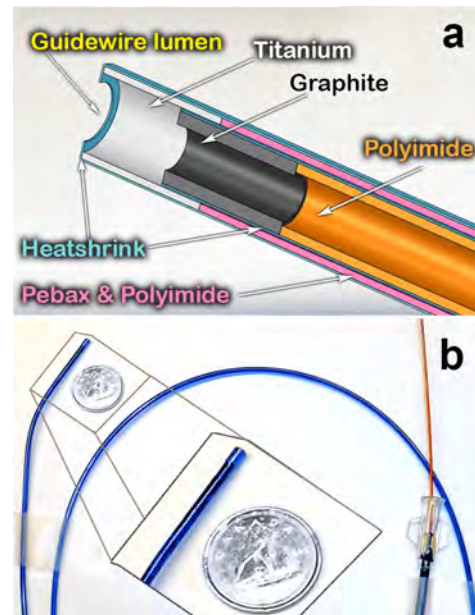


Figure 1. Catheter assembly with the susceptibility device. a: 3D model of the assembly. b: actual catheter picture.

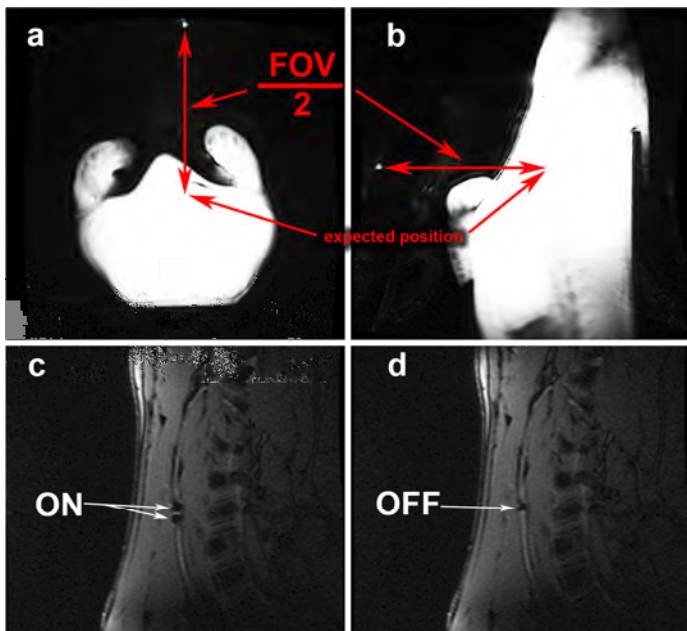


Figure 2: Images of the catheter *in vivo* acquired at 1.5T. a and b: Axial and Sagittal Gradient Echo projection images of the neck area of a pig with the device alternating between ON and OFF position every TR, finding the device tip displaced FOV/2 of the phase encode direction. c and d: Fast GRE images of the area where the device was located in ON and OFF position respectively.

comparing to the earlier 9F design with guidewire in monorail². *In vivo* images acquired to find and track the catheter tip are shown in

Fig. 2. By switching the device between ON and OFF positions every TR, the dephasing area around the device appears bright in the phase-encode direction displaced by half of the FOV (Fig. 2 a and b). This method can be more efficient comparing to the off resonance excitation used before² if an automatic actuator was used to switch the device between ON and OFF positions allowing much shorter TR. High resolution FGRE images of the neck area of a pig with the catheter in ON and OFF positions are shown in Fig.2 c and d respectively. Image distortions are smaller than those produced by the earlier 9F version of this device², but enough to facilitate tracking.

Conclusions

A new passive tracking catheter with a susceptibility effect that can be enabled and disabled by sliding one of the components was designed, fabricated and demonstrated *in vivo*. A novel tracking method was demonstrated in which the graphite layer was periodically moved every TR, creating a ghost of the catheter tip at precisely FOV/2 from the true location. The tracking tip demonstrated here can also be implemented on different tools or devices for interventional MR procedures. In future work, an automated actuator will be designed and constructed to permit toggling of the device during rapid, short-TR projection images, enabling quick snap-to-slice functionality.

Acknowledgements: Funding from the Ontario Centres of Excellence.

References:

- 1- Bakker CJ, et al. MR-guided endovascular interventions: susceptibility-based catheter and near-real-time imaging technique. *Radiology* 1997; 202:273–276.
- 2-Dominguez-Viqueira W, et al. A controllable susceptibility marker for passive device tracking. *MRM*, DOI: 10.1002/mrm.24899, 2013.

Rapid Selective Brain Cooling Using a Nasopharyngeal Method

Mohammad Fazel Bakhsheshi MSc^{1,2,3}, Errol E. Stewart, PhD^{1,3}, Laura Morrison, BSc, RVT¹, Ting-Yim Lee, PhD, FCCPM^{1,2,3}

¹Imaging Program, Lawson Health Research Institute, London, Ontario, Canada, ²Department of Medical Biophysics, University of Western Ontario, London, Ontario, Canada, ³Imaging Research Laboratories, Robarts Research Institute, London, Ontario, Canada.

BACKGROUND & PURPOSE: Clinical investigators have reported that mild hypothermia (HT_{33°C}) can be neuroprotective to reduce brain injury and decrease death and disability in patients with cardiopulmonary arrest (CPA) and in children after head injuries or neonatal encephalopathy, especially if applied prior to or during reperfusion [1, 2]. However, cooling the whole body below 34°C can cause complications including arrhythmias, infection, myocardial ischemia and coagulopathy [3]. In the present study, we evaluate the feasibility and efficiency of nasopharyngeal selective brain cooling by continuously blowing humidified cold air into the nasal cavities on normal new-born piglets with developed thermal regulation and juvenile pig.

METHODS and MATERIALS: Animals were anesthetized with 1-2% isoflurane. A tracheotomy was performed and the animal was ventilated with a volume-controlled mechanical ventilator to deliver Oxygen (O₂) and medical air mixture. Animals were randomized into the different groups: I. control group in which whole body of piglet was covered with blankets, (n=3); II. nasopharyngeal cooling group in which hypothermia was induced by directing humidified and cooled medical air (≈8°C) at the flow rate of 14-15 Liter.min⁻¹ into the nasal cavities via catheters while core body temperature was maintained within 35.5-36.5°C using heating blanket and hot water gloves by iteratively turning heating blanket "on" and "off" at; II-a. new-born piglets with an average age 1-2 days old and an average weight of ≈1-2kg, (n=3) and; II-b. juvenile pigs with an average age of 3 weeks old and an average weight of ≈16kg, (n=2). Rectal temperature was recorded from a rectal probe inserted to 3-4 cm from the anal margin. Deep brain temperature was also measured continuously with a thermocouple probe. A hole was made in the skull with a Dremel tool. The needle thermocouple probe was inserted laterally through the skull into the brain to a depth of 2 cm vertical from the brain surface and 1.5 cm posterior to the bregma to make sure to achieve whole brain cooling (about 7-8 cm from catheter).

RESULTS: Figure 1 displays the maximum absolute cooling rates achieved at each group as monitored in the brain and core rectal compartment. Results of comparing both groups in the nasopharyngeal cooling approach using cold and high air-flow rate reveals that it was possible to increase the brain-rectal temperature gradient in the heavier pigs compared to new-born piglets, i.e. 16 kg versus 2-3 kg. Figure 2(a,b) demonstrate the mean brain and rectal temperature profile as a function of time in both groups.

CONCLUSIONS: We have demonstrated that nasopharyngeal cooling by spraying humidified and cooled air into nasal cavities is an effective, safe and simple method to selectively reduce and maintain the brain-body temperature gradient in the heavier pig compare to new-born ones. This method can be easily implemented in hospitals and even on ambulances to cool down the brain to ameliorate brain damage from hypoxia-ischemia, traumatic brain injury in children and adult, cardiac arrest in resuscitated patients and stroke.

BIBLIOGRAPHY:

1. Busch, H.J., et al., Resuscitation, 2010. **81**(8): p. 943-9.
2. Lampe, J.W. and L.B. Becker, 2011. **62**: p. 79-93.
3. Culic, S., Arch Med Res, 2005. **36**(5): p. 532-8.

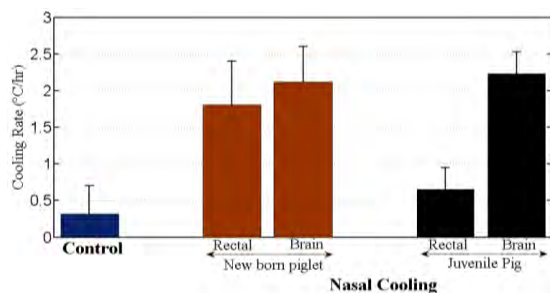


Figure 1. Maximum cooling rate for brain as a function of different conditions in Nasal cooling.

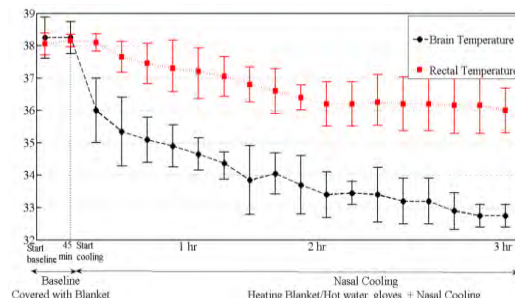
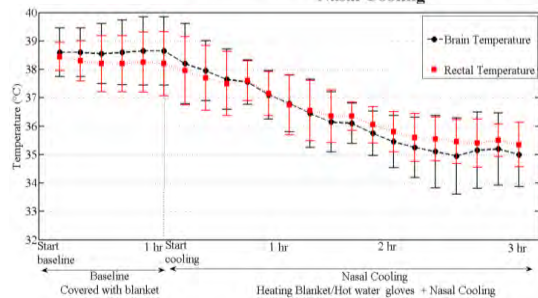


Figure 2. Changes in the brain-rectal temperature over time for intra-nasal cooling method with setting the air flow rate to 14-15 L.min⁻¹ for (a) piglets with average weight of ≈2-3kg; and (b) juvenile pig with average weight of ≈16kg.

MagA Reporter Gene Expression for MRI

Donna E. Goldhawk^{1,2,3}, Anindita Sengupta^{1,2,3}, Casey Lee^{1,2,3}, Karina Quiaoit^{1,2,3}, Linshan Liu^{1,2,3}, Neil Gelman^{1,2}, Lisa Hoffman^{1,2,3}, R. Terry Thompson^{1,2} and Frank S. Prato^{1,2}

¹Imaging, Lawson Health Research Institute, London, ON; ²Medical Biophysics, Western University, London, ON; ³Collaborative Graduate Program in Molecular Imaging, Western University, London, ON

We are developing reporter gene expression for magnetic resonance imaging (MRI) using strategies from magnetotactic bacteria. These organisms synthesize iron biominerals in membrane enclosed compartments called magnetosomes. Under the control of numerous genes, the magnetosome serves as a model upon which to develop gene-based iron contrast for MRI (Goldhawk et al, 2012). We have used the putative iron transporter *MagA* as a prototype for magnetotactic bacterial gene expression in mammalian cells. Our studies show that *MagA* expression in N2A and MDA-MB-435 cells results in MR contrast enhancement both *in vitro* (Goldhawk et al, 2009) and *in vivo* (Rohani et al, 2014). Iron-supplemented, *MagA*-expressing cells significantly increase transverse relaxation rates ($R2^*$, $R2$ and $R2'$) and cellular iron content (Sengupta et al, 2014). To improve the sensitivity and specificity of detection, we are examining the fundamental nuclear magnetic resonance (NMR) signal of *MagA*-expressing cells and the relationship between $R2$ and interecho time (2τ , Lee et al, ImNO abstract, 2014). Iron-supplemented, *MagA*-expressing cells show greater decreases in $R2$ with decreasing 2τ than unsupplemented and control cells. This dependence of $R2$ on 2τ may provide insights into the design of MRI acquisition strategies for detecting gene-based iron-labelled cells in small animals. The sequences we develop will be used in conjunction with *MagA* reporter gene expression for the *in vivo* detection of a developmentally important cardiac transcription factor, *Nkx2.5*, in established models of cell transplantation (MDA-MB-435, Quiaoit et al, ImNO abstract, 2014) and cardiac differentiation (P19 cells, Liu et al, ImNO abstract, 2014). *MagA* reporter gene expression for molecular MRI is a promising and versatile pre/clinical tool, with broad applicability to multiple areas of medicine, including diagnosis of disease, guiding therapy and long-term monitoring of cellular and molecular activity.

References: Goldhawk et al (2012) WIREs Nanomed Nanobiotechnol **4**, 378-388.
Goldhawk et al (2009) Mol Imaging **8**, 129-139.
Rohani et al (2014) Mol Imaging Biol **16**, 63-73.
Sengupta et al (2014) Frontiers in Microbiol **5**, article 29.

High Renal Retention of the novel [¹⁸F]FPyKYNE-Losartan in Pigs: Translational Work Towards Imaging AT₁ Receptors

Maryam Hachem^{ab}, Julie A. Ting^a, Tayebah Hadizad^a, Robert A deKemp^a and Jean N DaSilva^{ab}

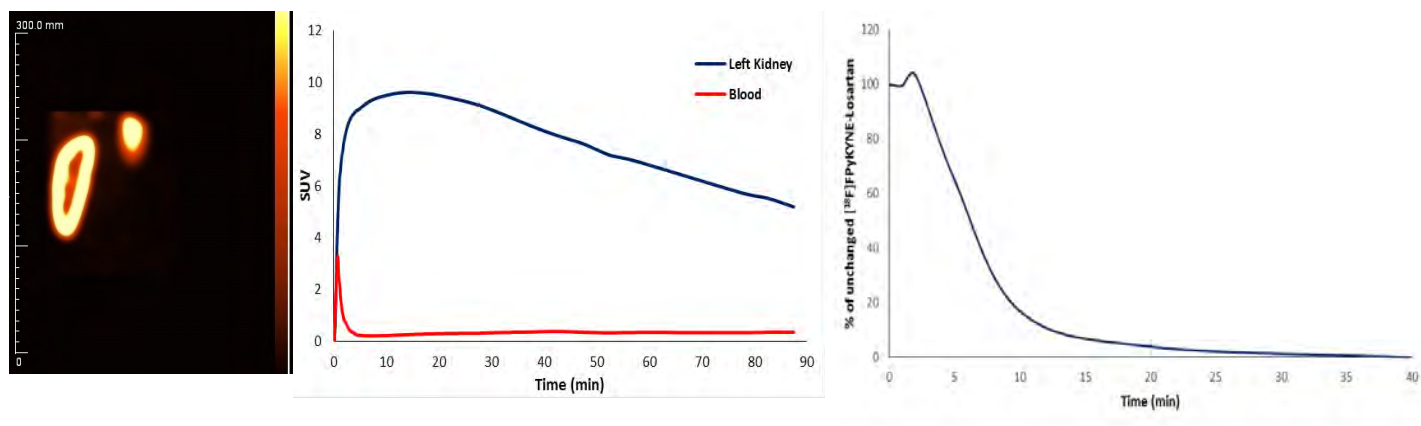
^aUniversity of Ottawa Heart Institute, Cardiac PET Center

^bUniversity of Ottawa, Department of Cellular and Molecular Medicine

Introduction: Hyperactivity of local renin-angiotensin-system (RAS) in cardiac and renal diseases results in altered angiotensin II type I receptor (AT₁R) expression. Unlike previous C-11 AT₁R PET tracers (20 min half-life), the longer half-life of F-18 (110 min) has the following advantages: shorter positron range and thus higher image resolution, multiple scans per formulation and distribution to other facilities. [¹⁸F]FPyKYNE-Losartan exhibited a dose-response attenuation in rat kidneys following Candesartan injection, demonstrating AT₁ binding specificity in vivo. The aim of this work was to evaluate [¹⁸F]FPyKYNE-Losartan in pig kidney for translational work towards imaging renal AT₁Rs in humans.

Methods: Pigs (n=3) were injected with [¹⁸F]FPyKYNE-Losartan (5MBq/Kg) into pig ear vein and scanned for 90 min in the GE Discovery PET/CT (64 Slice) D690 human PET scanner, then retested the next week. Image analysis was carried out with Siemens Inveon Acquisition Workplace software and standardized uptake values (SUVs) were generated. Metabolism studies were performed via HPLC column-switch. Trunk blood samples were collected at -5, 1, 2, 5, 10 and 20 min, centrifuged, mixed with 1 g urea, filtered, and injected onto HPLC. HPLC data was corrected for noise, radioactive decay, and unretained peak of parent tracer (control). To account for the amount of tracer in plasma relative to whole blood, blood samples were removed, centrifuged, then blood and plasma samples were counted for radioactivity.

Results: High kidney-to-blood contrast images (ratio of ~3) with highest uptake (SUV 12.6±2.6) were obtained at 12.5 min- frame 20, and time-activity curves exhibited slow clearance. Similar results were obtained in retest studies. Metabolism analysis displayed presence of unchanged tracer until 20 min post injection and only one hydrophilic metabolite. A constant ratio of 1.4 was obtained for plasma-to-blood over time, which facilitates arterial input function corrections.



Figures: Left: Representative coronal image of pig kidney (5-10 min frame) [¹⁸F]FPyKYNE-Losartan uptake. **Middle:** Corresponding TAC. **Right:** Unchanged [¹⁸F]FPyKYNE-Losartan is mostly cleared at 20 min from plasma.

Conclusion: The absence of ¹⁸F labeled hydrophobic metabolite in plasma will facilitate renal AT₁R uptake quantification of [¹⁸F]FPyKYNE-Losartan. High activity retention and image contrast in pig kidney provides a good potential for translational work of [¹⁸F]FPyKYNE-Losartan in humans to monitor AT₁R expression and guide therapy.

Patient-Specific Left Atrial Wall-Thickness Measurement and Visualization for Radiofrequency Ablation

Jiro Inoue,^a Allan C. Skanes,^b James A. White,^{ab} Martin Rajchl,^a Maria Drangova^{ac}

^aRobarts Research Institute, University of Western Ontario, London, ON, Canada

^bDepartment of Medicine, University of Western Ontario, London, ON, Canada

^cResearch supervisor

INTRODUCTION: For radiofrequency (RF) catheter ablation of the left atrium, safe and effective dosing of RF energy requires transmural left atrium ablation without injury to extra-cardiac structures. The thickness of the left atrial wall may be a key parameter in determining the appropriate amount of energy to deliver. While left atrial wall thickness is known to exhibit inter- and intra-patient variation, this is not taken into account in the current clinical workflow. Our goal is to develop a tool for presenting patient-specific left atrial thickness information to the clinician in order to assist in the determination of the proper RF energy dose.

METHODS: Segmentation of the left atrial myocardium is challenging due to the thinness of the tissue, the presence of other muscular tissue nearby, and low contrast between muscle and nearby non-muscle tissue. Thus, we use an interactive segmentation method with manual correction to segment the left atrial blood pool and myocardium from contrast-enhanced cardiac CT images. We then create a mesh from the segmented blood pool and determine the myocardial thickness, on a per-vertex basis, orthogonal to the mesh surface. The thickness measurement is visualized by assigning colors to the vertices of the blood pool mesh. We applied our method to 5 contrast-enhanced cardiac CT images.

RESULTS: Our visualization displays a high-resolution map of the left atrial wall thicknesses across the left atrium in a patient-specific manner. Figure 1 shows an example of our visualization. In this view of the left atrium, the blue/green regions in the posterior region between the two sets of pulmonary veins has a thickness of about 1.5 to 2 mm, whereas the thickness drops to under 1.0 mm towards the inferior region. These values are consistent with published literature on CT-based left atrial wall. As expected, variation was found to exist between patients, and between regions within each patient.

CONCLUSION: Previous work has shown considerable inter- and intra-patient variability in left atrial wall thickness, but for use in assisting in the dosing for RF ablation, this information must be measured accurately and presented to the clinician in a usable form. In order to achieve a truer 3D thickness measurement, we have presented a method for measuring thickness orthogonally to the blood pool. By presenting this measurement as a high-resolution colour-coded 3D map of the atrial wall, we enable the clinician to visually determine the thickness of the left atrial wall precisely at each ablation target point.

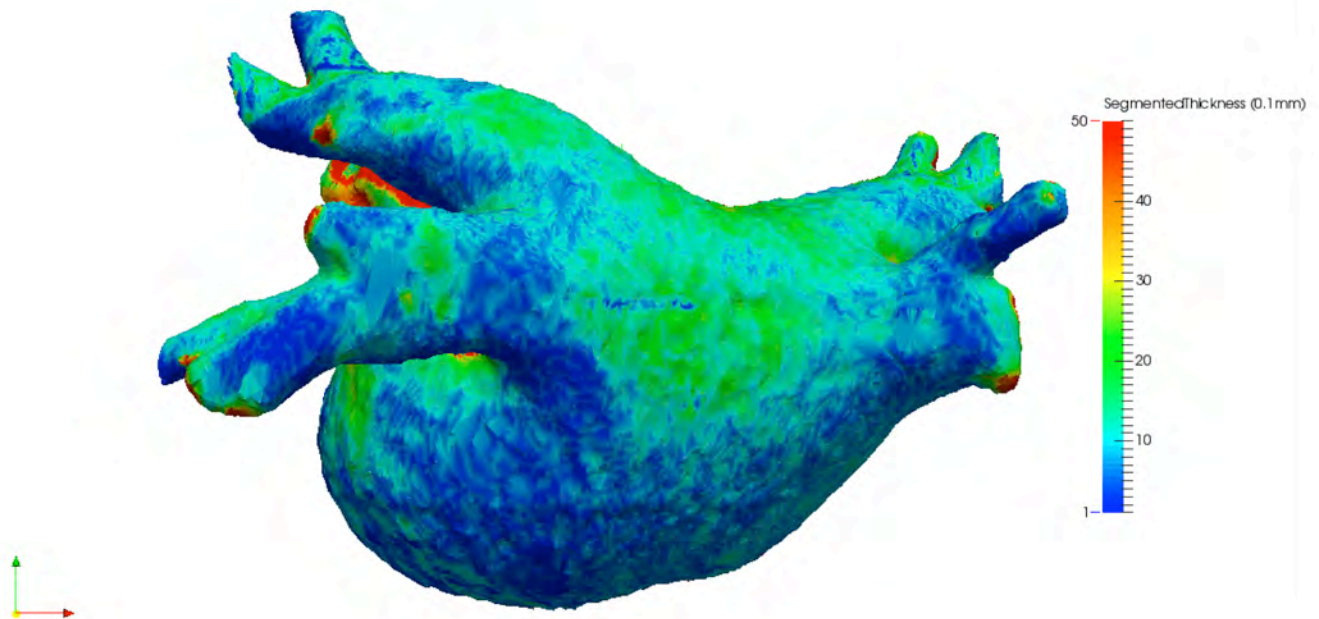


Figure 1: Example of left atrium mesh augmented with thickness map.

Towards Practical Spherical Navigator Echo Registration for 3D Motion Detection

P. Johnson,¹ J. Liu,¹ and M. Drangova^{1*}

¹Imaging Laboratories, Robarts Research Institute, Schulich School of Medicine, Western University, London, Ontario, Canada

*Research Supervisor

Introduction: The spherical navigator echo (SNAV) technique can be used to measure 3D rigid body motion in MRI (1-4). Motion in all 6 degrees of freedom is measured by registering SNAVs acquired throughout image acquisition with a baseline SNAV. The original registration algorithms were iterative and time consuming, which limited the method to retrospective applications (3). The technique also showed low accuracy in measuring rotations across the threads of the SNAV trajectory (1-2). A prerotated baseline SNAV (PreRot-SNAV) technique proposed by our group demonstrated improved speed and accuracy of registration, making real-time prospective motion correction with SNAVs feasible (4). A template is generated by prerotating a set of 512 SNAVs, acquired at a reference position, by known angles that evenly cover a predefined range. This template then serves as a lookup table for physically moved (trial) SNAVs. The motion information can be determined from a trial SNAV by finding the best matched templates from the baseline SNAV data set. The total prerotated baseline acquisition takes 25.6 s. (512 x 50 ms), with an acquisition time this long, subject motion is a potential problem. A method with which we can replace many of the acquired templates with simulated templates, reducing the actual acquisition time of the prerotated baseline is proposed.

Methods: The SNAV data used for this experiment were obtained from a previous experiment that assessed the performance of the PreROT -SNAV technique in measuring continuous head motion (4). In this study, 512 baseline templates were acquired followed by 512 trial SNAVs acquired while a volunteer smoothly performed axial head motion. The angles θ_x , θ_y , and θ_z describe rotations about the right-left (X), anterior-posterior (Y), and superior-inferior (Z) axes, respectively. A non-rotated SNAV ($\theta_x = \theta_y = \theta_z = 0$) was isolated from the baseline data set and used to generate 64 simulated templates with θ_z ranging between -20° and 20° . These simulated templates mimic object rotation about the Z axis. The simulation was performed using MATLAB (MathWorks, Natick, MA). To simulate a rotation by an angle θ_z , the SNAV co-ordinate system was rotated by $-\theta_z$ and the SNAV magnitude profile was interpolated at the transformed data point locations. These templates were then used to replace 64 of those 512 previously obtained; creating a hybrid set of baseline templates of acquired and simulated prerotated SNAVs. In order to assess the performance of the hybrid set of templates, continuous head rotation was measured by registering the set of trial SNAVs to the hybrid baseline.

Results and Discussion: The hybrid baseline includes 64 simulated templates as well as 448 acquired templates. This baseline set was tested in its ability to detect the continuous head motion and yields similar results to the original 512 baseline data set as shown in figure 1; the mean difference between the measurements was less than 0.2° in all 3 directions.

The prerotated baseline registration technique makes SNAVs promising for real-time tracking and prospective motion correction. A reduced baseline acquisition time is desirable as this lessens the likelihood that subject motion will occur during the acquisition. The accuracy of the PreRot-SNAV technique is determined mainly by the number of baseline templates (4). This creates a trade-off between baseline acquisition time and motion measurement accuracy. By simulating rotated templates from acquired templates we can reduce the baseline acquisition time while still avoiding an accuracy penalty. The interpolation process used for simulating rotation is similar to the original SNAV registration which has been shown to perform better in measuring along thread rotations than across thread (1,2). Therefore prerotating templates about the X and Y axes by a range of θ_x and θ_y (across thread rotations) and simulating rotations about Z (along thread rotations) will likely yield the best results.

Conclusions: In this work the number of acquired baseline templates was reduced by 12% by including simulated templates to the acquired ones. The encouraging results suggest that it may be possible to reduce the number of acquired templates down to about 100 by using an even distribution of θ_x and θ_y prerotations. This would reduce the baseline acquisition time from 25.6 to 5 seconds.

Acknowledgements: This work was supported through funding from NSERC and the Ontario Research Fund.

References: (1) Welch, et al., MRM 47:32-41, 2002. (2) Petrie, et al., MRM 53:1080-1087, 2005. (3) Welch, et al., MRM 52:1448-52, 2004. (4) Liu et al., MRM 65:506-14, 2010.

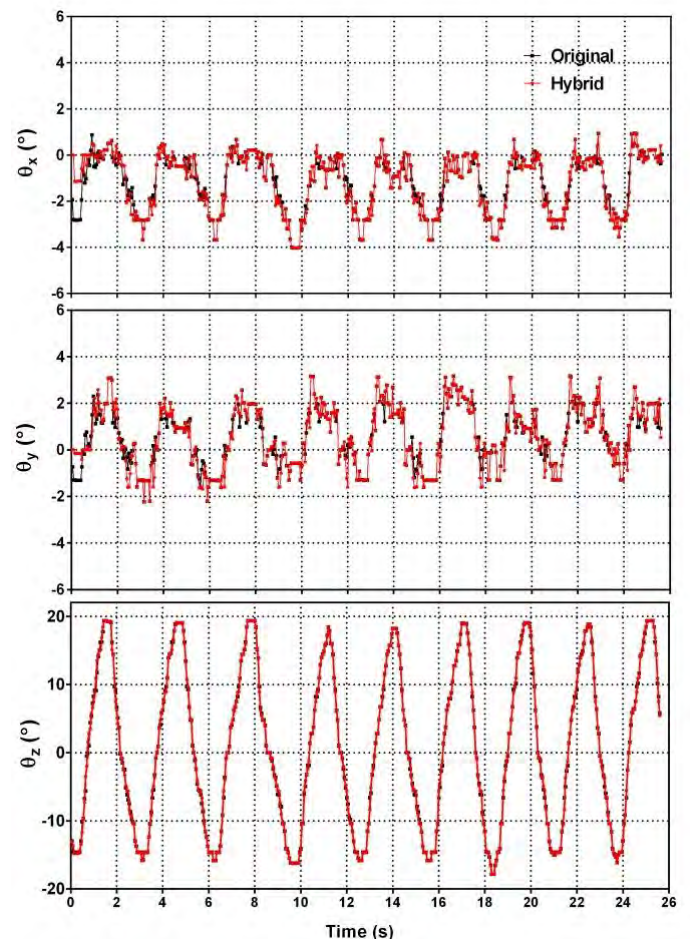


Figure 1. Rotation measurement results determined using the hybrid baseline (red) and the original baseline data (black).

Influence of Change in Interecho time (2τ) on Transverse Relaxation Rate (R2) in MagA-expressing Cells

Casey Y. Lee^{1,2,3}, R. Terry Thompson^{1,2}, Frank S. Prato^{1,2}, Donna E. Goldhawk^{1,2,3}, and Neil Gelman^{1,2}
Medical Biophysics, Western University, ²Imaging Program, Lawson Health Research Institute, ³Molecular Imaging, Western University, London, ON (Research Supervisors: Drs. Neil Gelman and Donna Goldhawk)

Introduction:

Gene-based iron-labeling is an emerging method of providing magnetic resonance imaging (MRI) contrast for long-term cell tracking and monitoring of cellular activities¹. The influence of the iron labeling on the MRI signal is often quantified by measuring transverse relaxation rate (R2) using a single interecho time (2τ). Although these R2 values are influenced by iron, they also depend on other cellular and tissue characteristics and, hence, lack iron-related specificity. In iron-containing tissues, measured values of R2 decrease with decreasing 2τ ². A mathematical model based on water diffusion through microscopic magnetic field inhomogeneities (typically from iron) has been developed² to describe this phenomenon. Investigating the dependence of R2 on 2τ in gene-based iron-labeled cells will provide insights into the microscopic distribution of iron in these cells and lead to more iron-specific strategies for detection with MRI. In this study, we investigate this relationship in iron-rich mammalian cells expressing a putative iron transport reporter gene known as *MagA*³.

Methods:

Untransfected (P) and stably transfected, MagA-expressing mammalian cancer cells (MDA-MB-435) were cultured in the presence and absence of 250 μM ferric nitrate ($\pm \text{Fe}$). Nuclear magnetic resonance (NMR) studies were performed on compact pellets of cells with a 9.4T NMR spectrometer (Agilent Inova 400). R2 was measured using the Carr-Purcell-Meiboom-Gill sequence (180° pulse $\sim 25 \mu\text{s}$) and $2\tau = 0.2 - 16 \text{ ms}$. The dependence of R2 on 2τ for iron-supplemented, MagA-expressing cells was analyzed using a theoretical model² that provides a value of $r_c/2D$, where r_c is the spatial correlation length associated with microscopic magnetic field variations and D is the water diffusion coefficient. The value of D was determined from measurement of the apparent diffusion coefficient (with a Siemens 3T, mMR system) in compact pellets of MagA-expressing cells ($n=4$). To establish that any changes in R2 observed for cell samples were not due to artifacts from the increasing number of refocusing pulses, R2 was also measured as a function of 2τ for 100 μM $\text{MnCl}_2(\text{aq})$.

Results and Discussion:

Iron-supplemented, MagA-expressing cells showed greater decreases in R2 with decreasing 2τ than unsupplemented and P cells [Fig. 1]. The mathematical model² applied to the R2 measurements of iron-supplemented, MagA-expressing cells ($n=2$), along with our measured mean value of D ($0.55 \pm 0.08 \mu\text{m}^2/\text{ms}$), provided r_c values of 0.43 and 0.23 μm ($n=2$). Previously², r_c was found to be 2.3 – 3.1 μm in brain tissues and 0.9 μm in liver, assuming D = 1.0 $\mu\text{m}^2/\text{ms}$. These data suggest that in iron-labeled, MagA-expressing cells the iron particles may be in closer proximity than those found in iron-containing tissues.

The R2 dependence on 2τ could potentially provide insights into designing MRI acquisition strategies for detecting gene-based iron-labeled cells in small animals. To achieve short 2τ values in MRI, a train of refocusing pulses may be used for magnetization preparation prior to single slice image acquisition⁴ or prior to one segment of a 3D acquisition.

Conclusion:

NMR studies of samples containing iron-supplemented, MagA-expressing cells have revealed that the dependence of R2 on 2τ has a similar form to that found in iron-containing tissues. However, an analysis using a mathematical model suggests smaller spatial correlation lengths in these cells compared to tissues.

References:

- ¹Goldhawk, *et al.*, WIREs Nanomed Nanobiotechnol 2013; doi: 10.1002/wnan.1165. ²Jensen and Chandra, Magn Reson Med 2000; 44:144-156. ³Rohani, *et al.*, Mol Imaging Biol 2013; doi:10.1007/s11307-013-0661-8.
- ⁴Ye, *et al.*, Magn Reson Med 1996; 36:153-8.

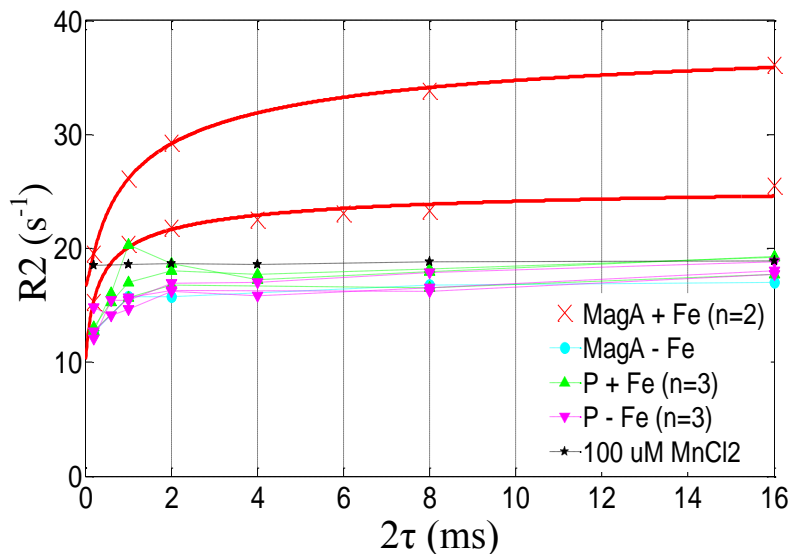


Fig 1. R2 dependence on 2τ . Measured R2 values are represented by symbols. Solid red lines represent a theoretical model² applied to the data collected from iron-supplemented, MagA-expressing cells.

Ultrasound based mitral valve annulus tracking for off-pump beating heart mitral valve repair

Feng P. Li^{a,b}, Martin Rajchl^{a,b}, John Moore^b, Terry M. Peters^{a,b}

^aBiomedical Engineering Graduate Program, Western University, London, Ontario

^bImaging Research Laboratories, Robarts Research Institute, Western University, London, Ontario

Introduction:

Mitral valve prolapse is one of the most common causes of non-ischemic mitral regurgitation, with a prevalence in an average population of 2-3% without age or sex preponderance. A widely used technique to correct leaflet prolapse is to implant an artificial chorda tendinea, which can be performed on a closed beating heart without using a cardiopulmonary bypass. The NeoChord DS-1000 [NeoChord, Minnetonka, MN] is such a device capable of performing off-pump transapical mitral valve repair. The current imaging modality used for guiding this procedure is transesophageal echocardiography (TEE). However, it is difficult to determine whether the visualization of the tool represents the tip or an arbitrary part of the shaft that intersects with a 2D plane, to maintain both the tool tip and the target simultaneously in a 2D plane, and to maintain sufficient spatio-temporal resolution and field of view in 3D. Our previous work has shown that the efficiency and safety of this procedure can be significantly improved by employing augmented virtuality techniques to provide a 3D context in terms of virtual presentation of tool, surgical targets, and surrounding anatomy for the TEE images. However, one of the limitations of this work is that the virtual model of the mitral valve annulus (MVA) is not automatically updated during the procedure. Since the annulus may move by even centimeters due to organ shift through manipulation, and it is time-consuming to manually re-define the position of annulus using TEE, it is necessary to develop a method that automatically tracks the annulus and updates its virtual representation. This paper describes an image based approach that tracks the MVA automatically for the guidance of off-pump mitral valve repair.

Methods:

Our tracking approach consists of two components (Figure 1b): i) image based phasing, which identifies the cardiac phase of each image based on image similarity and determines the optimal phase for tracking update and ii) registration-based updating provides the updated positions of tracked points based on image registration results.

At the beginning of the tracking procedure, the echocardiographer identifies points along the mitral annulus (two points for 2D images, four points for bi-plane images) at a selected cardiac phase (e.g. mid-diastole). For each of the initial points, a square-shaped image patch centered at the point is extracted from the full TEE image. (Figure 1a) These initial patches will be compared to the successive image patches for both phasing and tracking purposes. Our approach then continuously receives TEE images from the ultrasound scanner, and stores them in a queue. For each TEE image in the queue, patches are extracted at the same locations as those initially selected. Then we compute the sum of absolute differences (SAD) of grayscale values between the initial patches and every patch from the queue. A low-pass filter is applied, and when a new minimum SAD is detected, we assume that the corresponding TEE image has a cardiac phase similar to the initial image. This approach allows us to rapidly perform image-based phasing.

We then perform an image based registration between the initial patches and the image detected by phasing, where we again employ the SAD metric. We use a brute force approach which searches for every possible location in the translation space to ensure a global optimum. We parallelize that brute force search in a GPU-based implementation, in which all the SADs with different translation parameters are computed simultaneously and subsequently compared hierarchically to determine the minimal SAD. For each MVA point, we perform this registration step providing us with the new locations of the MVA points.

Results:

We retrospectively analyzed this approach on 5 sets of 2D TEE images with 6676 images in total and 2 sets of bi-plane images with 706 images in total. These images were recorded during porcine validation studies of our augmented virtuality image guidance platform. We compute the distance between those tracked points with manually defined MVA points. The average absolute distance error was 2.55 mm with a standard deviation of 1.99mm. With an Nvidia GeForce 480 graphic card and CUDA 4.0 programming interface [Nvidia Corp, Santa Clara, CA, USA], we were able to perform up to 10 registrations per second using the brute force search approach, which is sufficiently fast for our application that aims to update the MVA once every cardiac cycle.

Conclusion:

The proposed approach showed good potential in improving the guidance for off-pump transapical mitral valve repair.

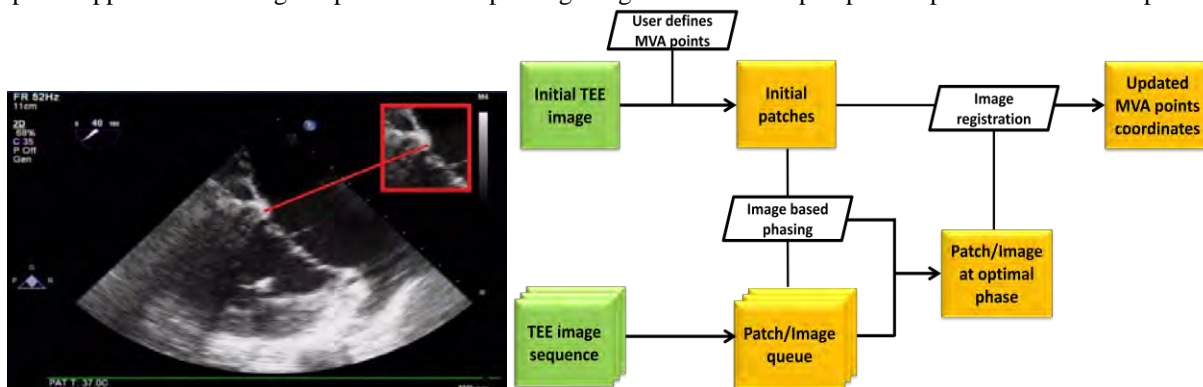


Figure 1: a) Extracting a square-shaped image patch from a TEE image. The center of the patch defines a selected MVA point. b) Workflow of image-based phasing and registration-based MVA tracking

Targeting P19-derived Cardiomyocytes for Treatment of Duchenne Muscular Dystrophy-Related Cardiomyopathy using PET/MRI

Linshan Liu^{1,2,4}, Rebecca McGirr¹, Andrew Bondoc^{1,2,4}, Terry Thompson^{1,2}, Frank Prato^{1,2}, Donna Goldhawk^{1,2,4}, and Lisa Hoffman^{1,2,3,4}

¹Imaging program, The Lawson Health Research Institute; ²Medical Biophysics, Western University; ³Anatomy & Cell biology, Western University; ⁴Collaborative Graduate Program in Molecular Imaging, Western University, London, Ontario

Introduction: Duchenne Muscular Dystrophy (DMD) is a severe, X-linked form of muscular dystrophy characterized by progressive degeneration of both skeletal and cardiac muscle. Recent advances in cardiovascular research suggest that transplantation of cardiomyocytes into patients' hearts may be able to repair damaged heart muscle and prevent heart failure (Blake et al. *Physiol Rev* 2002). However, a limitation to the use of cell replacement therapy is the lack of reliable, non-invasive technology to monitor implanted cells over time. We have generated P19-derived cardiomyocyte cell lines, engineered to stably co-express MagA and sr39tk (mutant herpes simplex virus type 1 thymidine kinase), for magnetic resonance imaging (MRI, Rohani et al. *Mol Imaging Bio* 2013) and positron emission tomography (PET, Pritha Ray et al. *Cancer Res* 2004), respectively. The stem cell features of P19 cells (Marcel et al. *Cardiovasc Res* 2003), together with contrast gene expression, will provide a novel and non-invasive means of MRI/PET imaging of cardiogenic differentiation.

Methods: P19 cells were transfected with MagA, alone and in combination with a trifusion reporter gene that contains sr39tk under the control of a cardiac-specific promoter (α -myosin heavy chain). MagA was genetically engineered to express the hemagglutinin (HA) epitope to enable protein detection by immunoblotting and immunocytochemistry (ICC). These cells are chemically differentiated into cardiomyocytes by supplementing culture medium with 0.8% dimethyl sulfoxide for 18 days, MagA-derived contrast was measured in cells using a spherical gelatin phantom. Transverse relaxation rates were acquired on a 3T Biograph mMR.

Results: Generation of the tagged MagA-HA construct has been completed and stable overexpression confirmed by Western blot and ICC using a mouse anti-HA monoclonal antibody. Co-transfection of this cell line with the sr39tk construct has been completed and evidence of cardiomyocyte differentiation in co-transfected cells has been confirmed. Preliminary data shows that MagA-derived contrast can be detected by MRI using a gelatin phantom to measure transverse relaxation rates in undifferentiated cells (Figure 1, Table 1). As observed in other cell lines, the contrast signal depends on the presence of extracellular iron.

Conclusion: We have generated P19 cell lines expressing MagA alone and in combination with the PET reporter gene sr39tk. We have also demonstrated the feasibility of assessing MagA-derived MR contrast in undifferentiated cells. Optimization of these tools, will provide a means of non-invasively assessing cardiac regeneration in a mouse model of DMD using PET/MRI.

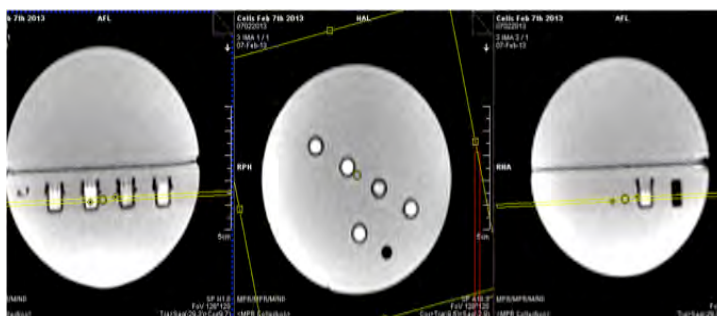


Figure 1. MRI of P19 cells in a spherical gelatin phantom. Cells are mounted as compact pellets in individual wells within the gelatin hemisphere. Imaging was conducted using single echo spin echo and multi-echo gradient echo sequences for R2 and R2* measurements, respectively, according to Sengupta et al 2013 (manuscript submitted). A yellow line indicates the 1.5 mm slice used to estimate transverse relaxation rates. A plastic peg is the black object

Relaxation Rates (S ⁻¹)			
Samples	R2	R2*	R2'
P19	9.36	11.15	1.79
P19+Fe	12.33	13.51	1.18
MagA	12.24	12.64	0.4
MagA+Fe	13.78	15.48	1.7

Table 1. Transverse relaxation rates in undifferentiated, wild-type cells (P19) and transgenic P19 cells overexpressing MagA-HA (MagA). Cells were cultured in medium with (+Fe) or without 250 μ M ferric nitrate. For all samples, n=1.

Using magnitude and phase data to automate 4D phase-contrast un-aliasing

Junmin Liu¹ and Maria Drangova^{1,2,*}

¹Imaging Research Laboratories, Robarts Research Institute, ²Department of Medical Biophysics
Schulich School of Medicine & Dentistry, Western University, London, Ontario, Canada

(* denotes supervisor)

PURPOSE: Blood flow information can be derived from phase images acquired with 2D and 3D phase-contrast (PC) MRI. Time-resolved 3D PC-MRI, also termed 4D flow MRI [1], has gained increased interest due to its capability to evaluate 3D hemodynamics in entire vascular structures. Because phase-aliasing occurs when the velocity encoding value (VENC) is lower than the blood peak-velocity, high VENC values are typically selected in clinical practice. While selecting high VENC values is a convenient solution, it is often not optimal because it results in reduced sensitivity to slow flow and may increase scan time if a repeat scan is needed. Alternatively, spatial and temporal phase unwrapping techniques [2-4] can be used to recover true phase from wrapped (aliased) phase images. This abstract addresses a common problem with spatial and temporal unwrapping techniques, which often fail to successfully un-alias 4D phase images because the images are both spatially and temporally under-sampled, i.e., the true phase difference between spatially neighboring pixels or temporal neighboring frames of a single pixel are larger than π . Here we present a newly developed un-aliasing method for 4D flow MRI.

METHODS: The proposed method first performs 3D spatial phase unwrapping [5] of the volume on a frame-by-frame basis. To solve the problem of flow-direction swap caused by spatial under-sampling, the method applies temporal unwrapping from diastole to systole on a pixel-by-pixel basis. First, a reference frame is identified in a pixel's velocity profile as the first frame where a phase jump $> \pi$ is observed. A "cut off" frame is then defined based on the magnitude profile; specifically, the frame with the minimum magnitude value is considered as the "cut-off" frame.

Time-resolved 3D phase contrast data were acquired on a 3T MR scanner using a 3D PC-MRI sequence (TR/TE = 5.8/1.7 ms, flip angle = 15, 1.2 mm slice thickness, 256x192 in-plane resolution, 83.33 KHz readout bandwidth, matrix size 256x256x128, 50 cm/s VENC; 70 ms temporal resolution; 20 cardiac phases were reconstructed over the cardiac cycle).

RESULTS and DISCUSSION: Representative magnitude and phase images are shown in Fig 1, with phase aliasing clearly observed in the measured phase image (Fig. 1b). A white line is plotted across the superior vena cava and aorta, which represent a challenging area for phase un-aliasing because flow occurs in two directions in neighbouring pixels, making differentiation simply based on spatial phase unwrapping impossible. The change in phase (of the voxels along the white line) over the cycle is shown in Fig 2., with the long and short arrows in Fig. 2b indicating spatial and temporal under-sampling regions, respectively. 3D spatial phase unwrapping alone (Fig. 2c) cannot determine the flow direction in the aorta correctly. This is expected when spatial under-sampling exists. However, the reference-frame can be easily identified from Fig. 2c. Using the magnitude profiles (Fig. 2a) the cut-off frame is easily determined. Use of the magnitude rather than the phase profile to determine the cut-off frame is more robust because a non-trivial threshold value of phase difference between frames is required if the phase profiles alone are used. Fig. 2d demonstrates that the proposed method correctly recovers the velocity direction in a case with both spatial and temporal under-sampling.

Figure 3 shows an un-aliased phase images generated using the proposed method. Figure 3a corresponds to Fig 1b and Fig. 3b shows a sagittal slice of the aorta. The results in Fig. 3 demonstrate that most phase-aliased pixels are recovered. Some remaining aliasing is observed near the aortic valve and aortic wall suggesting that further post-processing, such as spatial-smoothing, may be required.

CONCLUSION: Using the temporal variations of the magnitude profile to tackle temporal under-sampling allows aliasing-free 4D flow images to be generated even when the phase contrast data are acquired with a single low VENC (~ 50 cm/s) and low temporal resolution.

ACKNOWLEDGEMENTS: We would like to thank Drs. Marcus T. Alley and Shreyas Vasanaawala from Department of Radiology at Stanford University for providing the raw 4D flow data. Funding was provided by the Ontario Research Fund.

REFERENCES: [1] Markl et al., 4D Flow MRI, JMRI 36: 1015-36, 2012. [2] Xiang et al, Temporal phase unwrapping for CINE velocity imaging, JMRI 5:529-34, 1995. [3] Yang, et al., Dynamic range extension of cine velocity measurements using motion-registration spatialtemporal phase unwrapping, JMRI 6:495-502, 1996. [4] Salfity et al., Extending the dynamic range of phase contrast magnetic resonance velocity imaging using advanced higher-dimensional phase unwrapping algorithms, Interface 3:415-27, 2006. [5] Liu and Drangova, Intervention-based multidimensional phase unwrapping using recursive orthogonal referring, MRM 68: 1303-1316, 2012.

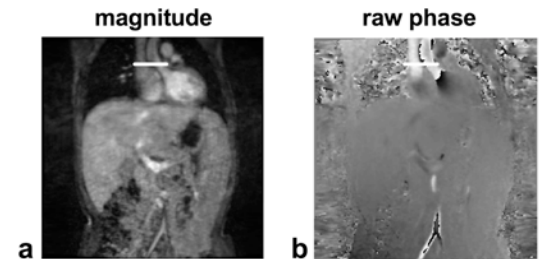


Fig. 1 Representative coronal slice, velocity-encoding is along the SI direction. The white line identifies a region of phase aliasing.

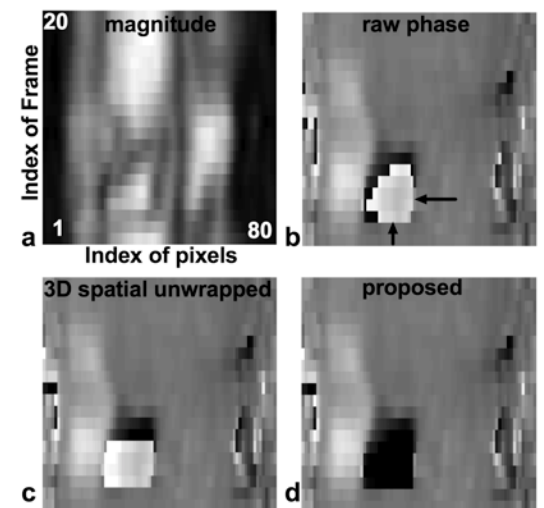


Fig. 2 The temporal profiles of the pixels along the white line defined in Fig. 1.

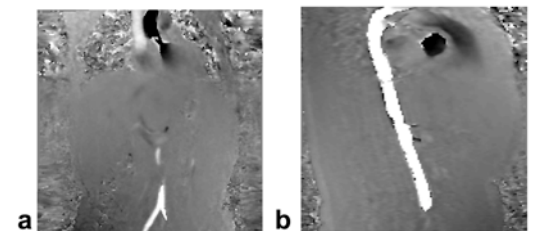


Fig. 3 Examples of un-aliased phase images. (The display range is capped at $\pm \pi$.)

Automatic myocardium segmentation of LGE MRI by deformable models with prior shape data

YingLi Lu,¹ Kim A. Connelly,^{2,3} Yuesong Yang,¹ Graham A. Wright,^{1,4} and Perry E. Radau¹

¹Imaging Research, Sunnybrook Health Sciences Centre, Toronto, ON, Canada; ²Keenan Research Centre in the Li Ka Shing Knowledge Institute, St. Michael's Hospital and University of Toronto, Toronto, ON, Canada; ³Cardiology, Sunnybrook Health Sciences Centre, Toronto, ON, Canada; ⁴Medical Biophysics, University of Toronto, ON, Canada;

Introduction: Previously a myocardial tissue classification algorithm has been developed to locate and quantify infarct in a given myocardial region-of-interest specified on late gadolinium enhancement (LGE) MR images[1]. To complete the automation requires an endocardial and epicardial contour detection algorithm to replace the current practice of manual contouring that is time-consuming and subject to intra- and inter-observer variability. Challenges include: 1) the intensity inhomogeneity of both the healthy and infarct myocardium; 2) the existence of an infarct on a given slice is not known a priori; 3) a sub-endocardial infarct region's boundary can be easily mistaken for the endocardial contour due to the proximity and strength of the edge (gradient); and 4) incorporating prior anatomical information (e.g. cine steady-state free precession (SSFP) MRI) while allowing for possible motion between separate studies.

Methods: The proposed deformable contour algorithm addresses these challenges by minimizing an energy function that: 1) incorporates intensity overlap into the deformable model by applying Bhattacharyya coefficient[2]; 2) eliminates the image gradient term of the energy function; and 3) incorporates hard constraints based upon prior information about contour shape and myocardium thickness from the pre-delineated contours of the corresponding cine SSFP image (see Eq.1). Fifteen patients with known CAD and chronic MI had cardiac LGE MR scans. Our method uses pre-delineated endo- and epicardial contours from the corresponding cine MRI as a priori knowledge. We registered the corresponding cine MR image to the LGE image using mutual information image registration with affine transformation, then applied the resulting transform to the pre-delineated endo- and epicardial cine MRI contours, to initialize the LGE MRI segmentation. The contours were refined by minimizing the deformable contour energy function locally with greedy optimization[3].

Results: The average perpendicular distance between manually drawn and automatically detected contours was 1.77 ± 1.92 mm and 1.63 ± 1.93 mm for endocardial and epicardial contours, respectively. The average Dice coefficient was 0.91 ± 0.12 for endocardium and 0.94 ± 0.09 for epicardium and 0.75 ± 0.22 for the myocardium. Representative results in Fig.1. By visual examination 21% contours (41/198 contours) required manual corrections. This is a substantial improvement compared with previous rate of about 50% when propagating cine contours without the deformable contour algorithm.

Discussion and Conclusions: Our method provides a high degree of automation and accuracy. The results for the proposed automated segmentation technique indicate that it will streamline accurate quantification of myocardial infarct on LGE MR infarct images in clinical practice.

$$\min_C \left\{ E(C, I) = \lambda_1 \int |C'(s)| ds + \lambda_2 \int |C''(s)| ds + \frac{\lambda_3}{R_B} \int_B |I(x, y) - \bar{B}| dx dy + \frac{\lambda_4}{|\bar{M} - \bar{B}|} + \lambda_5 \times Ba(P(B) / P(M)) \right\}$$

Eq. 1. Energy function of the deformable model. $C(s)=(x(s),y(s))$ is the parameterized contour (endo- and epicardial), $P(B)$ is the histogram of blood pool and $P(M)$ as the histogram of myocardium. $Ba(f/g)$ is the Bhattacharyya coefficient measuring the amount of overlap between two statistical samples f and g . Shape is the Fourier descriptors of the discretized contour. Each contour is constrained by the corresponding cine contour shape, and by myocardial thickness.

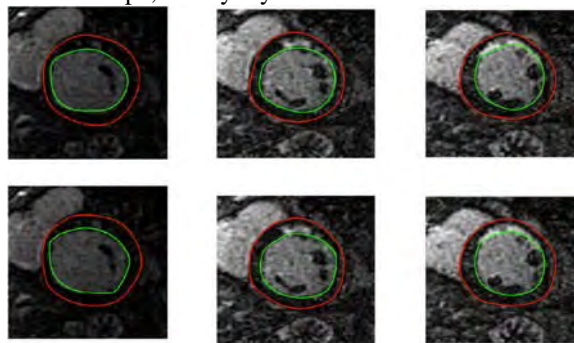


Fig. 1. Representative automatic segmentation results (top row) compared to expert results (bottom row).

References

1. Lu YL, et al. Automated quantification of myocardial infarction using graph cuts on contrast delayed enhanced magnetic resonance images. *Quantitative Imaging in Surgery and Medicine* 2012;2:81-6.
2. Williams DJ, et al. A fast algorithm for active contours and curvature estimation. *CVGIP: Image Understanding* 1992;55:14-26.
3. Comaniciu D, et al. Real-time tracking of non-rigid objects using mean shift. *IEEE conference on Computer Vision and Pattern Recognition* 2000;2:142-9.

Funding:

MaRS Innovation 2011 Medical Sciences Competitive Proof of Principle (MSCPoP) for Medical Devices and Ontario Research Fund, (Imaging for Cardiovascular Therapeutics)

Multifrequency intravascular ultrasound for imaging of coronary plaque

Chelsea Munding¹, Emmanuel Cherin², David Goertz^{1,2}, Brian Courtney², Stuart Foster^{1,2}

1. Department of Medical Biophysics, University of Toronto, 2. Sunnybrook Research Institute, Toronto

It is generally acknowledged that most acute coronary syndromes arise from the rupture of a vulnerable atherosclerotic plaque in the coronary arteries. Though the histological characteristics of ex vivo plaques have been well studied, the ability to image these features in vivo remains limited due to the lack of an appropriate imaging technique. These features include a large lipid core, a thin fibrous cap (<65 μm) and outward remodeling of the vessel wall. The lack of an ideal diagnostic imaging method limits our understanding the disease progression and the efficacy of possible treatments. At the present time, intravascular ultrasound (IVUS) is one of the most widely used techniques for directly visualizing coronary plaque in vivo. IVUS can easily distinguish large-scale morphological plaque features. It allows the plaque size, lumen dimensions and extent of remodeling to be measured. Unfortunately, with an axial resolution of 100 - 200 μm , conventional IVUS is unable to resolve finer details, such as the cap thickness. While an increased ultrasound frequency would improve the axial resolution, it would also result in an unacceptable loss of imaging depth.

To allow imaging of both large-scale plaque morphology and superficial details, and overcome the tradeoff in depth penetration versus resolution, we developed a dual-frequency IVUS device. One frequency was chosen to be similar to existing IVUS devices (35 MHz), and the other was chosen to provide sufficient resolution to visualize the fibrous cap (70 MHz). An important design consideration was to incorporate dual-frequency functionality into the limited footprint available for IVUS devices. To achieve our goal of multifrequency imaging within this limited space we designed a novel bi-directional IVUS transducer stack. This design incorporated two independent transducer elements sharing a common backing layer. Complementary, coplanar cross-sectional images can be obtained by mechanically rotating the transducer stack.

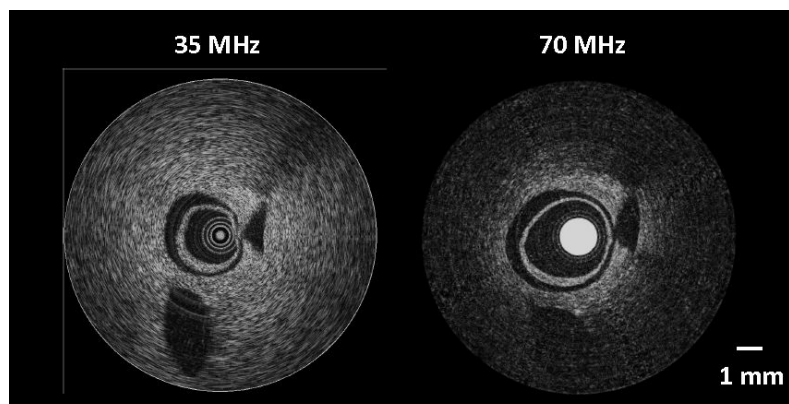
Each element of the prototype was independently optimized for the desired centre frequencies. Each transducer element incorporated an active piezoelectric layer of PZT-5H ceramic and a matching layer of silver-loaded conductive epoxy. The width of each element was fixed at 550 μm to ensure fit in a 4 French imaging catheter. Using PiezoCAD transducer modelling software, the element lengths and PZT and matching layer thicknesses were modified iteratively to achieve optimal insertion loss and pulse length at the centre frequencies. The prototype was built in-house by fabricating each transducer element independently with a thin backing layer. Each transducer included a 180 μm coaxial cable to provide the electrical connections. Finally, a 35 MHz and 70 MHz transducer were aligned back-to-back and adhered using silver-loaded epoxy.

To ensure the utility of this device, it was important that its performance be at least comparable to that of existing devices. For this reason, the prototype was fully characterized alongside a commercial control: the 30 MHz Ultracross 2.9 (Boston Scientific). The characterization process included measurements of the insertion loss, beam characteristics and pulse length using a hydrophone and pulse-echo experimental setup. From these experiments, it was found that the 35 MHz prototype had similar performance to the commercial transducer (8 dB greater insertion loss), with a slightly shorter -6dB pulse length (40 vs. 58 nsec). As expected, the 70 MHz element had a much shorter pulse length of 22 nsec, corresponding to an axial resolution of 39 μm in water.

Next, we tested the ability of our prototype to produce complimentary co-planer images. For this experiment, a multilayer vessel phantom was created with hypoechoic inclusions and a central lumen of 3 mm. The transducer stack was fixed over a rotating stage, with the axis of each element parallel to the stage. The phantom was placed on this stage and the transducer was introduced into the lumen. Using single-cycle sinusoidal pulses cross-sectional images of the phantom were acquired. 40 acquisitions were averaged for each 35 MHz A-line, and 100 acquisitions were used for each 70 MHz A-line. 360 A-lines were acquired per cross-section.

As predicted, the 35 MHz element produced images extending deep into the phantom (> 6 mm). These images showed a general view of the features present in the phantom, including the different layers and hypoechoic inclusions with good sensitivity. However, due to lower resolution, it was not always clear from the images precisely where the borders of each structure were. The 70 MHz element had much lower sensitivity, and the signal was more heavily attenuated by the phantom. However, it was evident from the images that this transducer produced much higher resolution images, with clear delineation of the superficial layers. Similar results were seen when repeating the experiment with an ex vivo atherosclerotic right coronary artery.

The acquired images confirmed that this prototype was able to obtain complimentary, co-planer images of both large-scale morphology and superficial details using a single device. Further development of this prototype will require experiments showing that images can be acquired through blood and through an IVUS imaging sheath. Further ex vivo experiments and comparison with histology will allow us to demonstrate that accurate imaging of the fibrous cap is feasible in a more clinically relevant setting.



High resolution cardiac T1* maps of chronic fibrosis correlate with collagen content

^{1,2}Mihaela Pop, ^{1,2}Nilesh R Ghugre, ¹Venkat Ramanan, ³Susan Newbigging, ^{1,2}Graham A Wright
¹Sunnybrook Research Institute, ²Dept. Medical Biophysics, Univ. of Toronto, ³CMHD Pathology Core Toronto

Introduction: The gold standard MR imaging method to identify myocardial viability in ischemic hearts with prior infarct (a major contributor to sudden cardiac death), is late gadolinium-enhancement (LGE) [1]. A current challenge for the clinicians is the correct identification of the arrhythmia substrate, which has a *gray zone* (GZ) appearance in MR images due to the mixture of viable myocytes and collagen strands interfacing normal myocardium and infarct core (IC). Our group has developed superior MRI methods which probe the intrinsic MR properties of infarcted myocardium based on a multi-contrast late enhancement (MCLE) sequence with a balanced steady state SSFP readout [2], from which pixel-by-pixel parametric T1* maps can be calculated and used in robust tissue classification algorithms [3]. However, a quantitative histological validation of the extent and severity of fibrosis (GZ vs. IC) determined from such MCLE-based T1* maps has yet to be performed. The current pre-clinical MR imaging study addresses this issue.

Methods: High resolution MCLE images (0.6x0.6x1.2mm) were obtained *ex vivo* in five swine hearts with chronic infarct (5-6 weeks). A bolus of Gd-DTPA was injected i.v. prior to sacrifice. Each explanted heart was placed in a plexiglass box filled with Fluorinert, then was imaged in a head coil with a 1.5T GE Signa Excite system. Other MR parameters included: TR = 4.26 ms, flip angle = 45° and variable inversion times. The resulting pixel-wise SS and T1* maps were used as input to a fuzzy-clustering algorithm [3] which classified the tissue into 3 categories: healthy, GZ and IC. The hearts were then formalin-fixed for 3-4 days. Ten slices were cut to match the short-axis view of MR images and prepared for histology using collagen-sensitive stains such as Masson Trichrome (MT) and Picosirius Red (PR). Based on collagen content, we defined 3 grades of fibrosis: F0 for healthy tissue (< 20% fibrosis, *no or mild*), F1 for GZ (20-70% fibrosis, *moderate*) and F2 for IC (≥ 70% fibrosis, *severe*), as per [4]. The chronic lesions were manually delineated as F1 or F2, based on scoring the fibrosis severity within a sliding box of 0.6x0.6mm (to match the MR imaging in-plane resolution). All digital PR images were analyzed with the Aperio ImageScope software (Vista, CA). The GZ and IC areas were calculated relative to the total area of left ventricle (LV) in all classification maps and histology images. For the MR-histopathology comparison, the calculation of correlation coefficients and associated linear fits were performed in Excel.

Results and Discussion: Figure 1 shows an example comparing the resulting tissue classification map (1b) calculated from the SS and T1* parametric images (1a), and a histopathology image (1c). The healthy and IC pixels in (1b) were color-coded to match those in the corresponding histopathology MT stain (i.e. healthy in purple and IC in cyan-green). The GZ pixels were color-coded yellow and corresponded to a heterogeneous area comprised of healthy myocytes intermingled with collagen fibers, as observed in the magnified histology image. Very good correspondence was observed between the extent of F1 and F2 fibrotic areas identified by the collagen-specific stains and the GZ and IC tissue areas in the classification map at the same topographic location. The quantitative analysis demonstrated very good correlations between the histologically-determined areas of heterogeneous and dense fibrosis and the corresponding GZ ($R^2=0.96$, exemplified in Fig 2, *top*) and infarct core, IC ($R^2=0.97$) as categorized from MRI data using the fuzzy-logic clustering algorithm. No bias in measurement was determined using the Bland-Altman analysis (Fig. 2, *bottom*).

Conclusion: Our quantitative MRI-histopathology study is the first to demonstrate, using histopathology based on collagen content, that areas of heterogeneous and dense fibrosis in hearts with chronic infarction can be accurately identified from parametric SS and T1* maps. Future work will focus on translating these findings by optimizing *in vivo* MCLE imaging of GZ, the substrate of potentially lethal arrhythmias.

References: [1] Bello D *et al* J Am Coll Cardiol 2005, 45: 1104-1108; [2] Detsky J *et al* Magn Res Med 2007, 58: 365-372; [3] Detsky J *et al* IEEE Trans Med Imag 2008, 10: 1606-1614; [4] Pop M *et al* Phys Med Biol 2013, 58: 5009-5028.

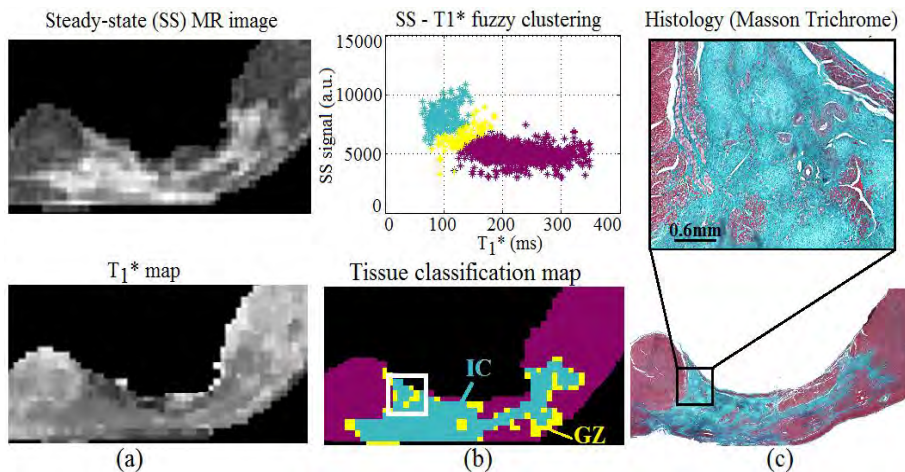


Figure 1 Qualitative comparison between the extent of GZ (heterogeneous fibrosis) and IC (dense fibrosis) identified in the MCLE images and histology MT image (see text for details).

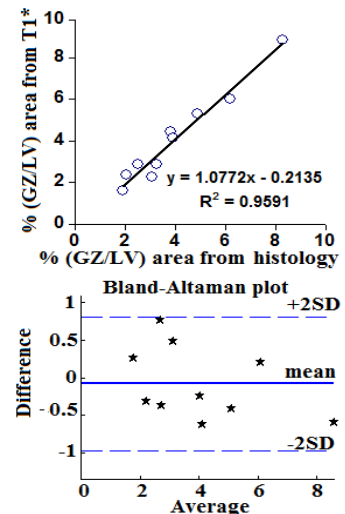


Figure 2 Correlation between % (GZ/LV) area from T1* and histology: linear fit (*top*); no bias (*bottom*).

A modified iterative Triple Energy Window (TEW) approach to cross talk correction in dual isotope In-111/Tc-99m small animal SPECT

Paul Prior and Glenn Wells

Department of Physics, Carleton University; Div. Cardiology, University of Ottawa Heart Institute (UOHI)

Background: Single Photon Emission Computed Tomography (SPECT) imaging is a functional modality that incorporates the use of biological molecules labeled with radioactive tracers that can be used to examine disease processes in small animals. SPECT's unique ability to distinguish signals from multiple probes via energy discrimination offers the potential for quantitative dual-isotope imaging, doubling the information obtained per scan. At the University of Ottawa's Heart Institute (UOHI), Tc-99m (140 keV emissions) tetrofosmin is commonly used to monitor myocardial uptake under stress/rest conditions and to find areas of ischaemia and infarct.¹ Additionally, In-111 (two photons, 171 keV and 245 keV, per decay) labeled liposomes can be used to trace the blood pool². Images may be simultaneously acquired upon injection in rats, but quantitative accuracy of the Tc-99m images is degraded in regions where In-111 is present due to cross talk. Cross talk results from the Compton scatter of In-111 photons and detection of these scattered photons at energies corresponding to Tc-99m.

The Triple Energy Window (TEW) scatter correction method estimates scatter in the Tc-99m window using a weighted mean of counts recorded in narrow energy windows above and below the primary Tc-99m window. For In-111 and Tc-99m, any scatter window placed between the 171 keV In111 peak and 140 keV Tc99m peak will contain unscattered photons due to the 10% energy resolution of the camera. This leads to an overestimation of the scatter. A modified TEW was developed that — applied in projection space—subtracts the estimated primary contribution from the scatter windows as a fraction of counts recorded in the Tc-99m primary window before making the scatter estimation. Previous work in our lab³ showed that the modified version of the TEW cross talk correction accurately estimates the In-111 scatter counts contaminating the Tc-99m signal in phantom experiments where there are comparable concentrations of both isotopes present. It failed to fully subtract the In-111 scatter counts from the Tc-99m images in regions where Tc99m concentrations were low. In these regions, the modified TEW estimates a primary Tc99m contribution to the scatter windows where there is none and results in an underestimation of scatter.

Objective: To use an iterative TEW method to improve upon the modified TEW method in regions where there is no Tc-99m present.

Methods: The iterative TEW method is applied to the projections and uses the following algorithm:

- 1) The Tc99m-primary photon contamination of the TEW scatter windows is estimated from the measured signal in the Tc99m photopeak window.
 - 2) The contamination is subtracted from the scatter windows and the corrected counts in the scatter windows are used to estimate the scatter in the Tc99m-photopeak window.
 - 3) The measured signal in the Tc99m photopeak window is corrected for the estimated scatter.
- Steps 1-3 are repeated until the difference between subsequent scatter estimations is low.

The iterative TEW method was evaluated in a phantom consisting of three 10mL syringes in a pyramid configuration filled with 2mL of diluted In-111 and Tc-99m in the following amounts: Syringe (1): All Tc-99m. Syringe (2): All In-111. Syringe (3): A mixture of In-111 and Tc-99m. The phantom was scanned using a 4-head Bioscan nanoSPECT/CT system. First, a CT scan was acquired for use in creating an attenuation map, used for attenuation correction of SPECT images. For SPECT acquisition, each of the 4 NaI(Tl) detector heads used nine 2.5mm diameter pinholes for collimation, resulting in multiplexed projection images. 360° of projections were obtained with a 90° gantry rotation at 7.5° intervals. The corrections were applied in projection space, where it has been determined that the best scatter estimate can be obtained. The corrected projections are reconstructed with attenuation correction using an OSEM iterative technique incorporating the system point spread function.⁴ The accuracy of the correction was measured as the percent of In111 scatter remaining in a region-of-interest drawn around the In111-only syringe, applied to the Tc99m image.

Results and discussion: Results in phantom experiments indicate that the iterative method provides a more complete removal of cross-talk in syringes containing only In-111. In this most extreme case of cross talk where only the higher energy isotope is present, the amount of residual scatter is decreased by an additional 40% over the modified TEW, but still leaves up to 14% of the initial cross talk counts. With a cross-talk fraction of 12%, a remaining 1-2% of Indium photons are being falsely detected as Tc-99m. For the syringe with a mixture of isotopes, the estimated scatter was similar.

In vivo work is in progress wherein rats are imaged with both Tc99m-tetrofosmin (cardiac perfusion) and In-111-labelled liposome (blood-pool imaging). It is expected that the iterative approach will result in more accurate Tc-99m activity estimation and provide higher contrast between the myocardia and ventricles.

Conclusion: Phantom results show that the iterative TEW approach subtracts 86% of In-111 scatter in the Tc-99m image in regions where no Tc-99m is present compared to the modified TEW method which only subtracted 60% of cross-talk. More analysis is needed in order to explore its effectiveness in in vivo studies.

[1] Giorgetti et al (2007). Feasibility and Diagnostic Accuracy of a Gated SPECT Early-Imaging Protocol: A Multicenter Study of the Myoview Imaging Optimization Group. *J Nucl Med* **October 2007** vol. 48 no. 10 **1670-1675**

[2] Boermann OC et al (1995). Sterically stabilized liposomes labeled with indium-111 to image focal infection. *J Nuc Med* **1995** vol. 36 no. 9 **1639-1644**

[3] Timmins, R. (2012). Dual isotope cross-talk correction in Tc-99m/In-111 small-animal SPECT. Unpublished master's dissertation, Carleton University, Ottawa

[4] Strydorst, J, (2012). Quantitative Multiplexed Multi-Pinhole Small-Animal SPECT. Unpublished doctoral dissertation, Carleton University, Ottawa

Determination of the characteristics of thermal ablation lesions in rabbit muscle by MRI and histology

Xiuling Qi, Benu Sethi, Mihaela Pop, Jennifer Barry, Sudip Ghate, Eugene Crystal, Graham Wright
Sunnybrook Research Institute, Sunnybrook Health Sciences Centre, Toronto, Canada

Introduction Radio-frequency thermal ablation is an important therapeutic option for eradication of arrhythmias. Previous studies have shown that contrast enhanced MR imaging can visualize the extent of an ablation lesion [1]. However, to improve the effectiveness of EP procedures, it is valuable to understand the MR signature of the border zone (BZ) between the thermally damaged and surrounding myocardium. This study was designed to evaluate the characteristics of ablation lesions at the BZ in skeletal muscle using high-resolution (resolution=156 μ m) *ex-vivo* MR imaging and histology.

Methods Seven New Zealand white rabbits were included in this study. Using clinical ablation catheters, as part of a broader investigation described in [2], seven RF lesions were created in the Latissimus dorsi muscles by RF power at 35 Watts for 35-40 sec. Rabbits were divided into two groups: Acute (3 rabbits euthanized at 3 hours) and Chronic (4 rabbits euthanized at 6 weeks). Seven selected tissue slab samples from the RF lesion area (one per animal) were obtained and preserved in formalin for 7 days. MRI was performed on a 3.0 T GE Excite Scanner (GE Healthcare, Milwaukee, Wisconsin) using a custom-made small receive-only surface coil for signal reception. Fast spin echo (FSE) 2D T1W and T2W images (BW=15.63 kHz, Matrix=256x256, FOV=4cm, Slice thickness=0.6mm) were obtained. Following the MRI study, the corresponding samples were prepared for histological study. Masson's trichrome (MT) staining was performed on 4- μ m thick formalin-fixed paraffin-embedded sections. An outline of the whole ablation lesion from an axial section of each sample was demarcated to determine the total ablated area (dark grey stained rim in histology and the bright edge in T2W MRI). The dark red stained region in histology and the corresponding uniform dark area in MRI at the center of each lesion were measured as the necrotic tissue core. Then the BZ (the total lesion area minus the necrosis area) was calculated and expressed as percent area relative to the total area of the whole lesion. The correlation between the MRI and histology was assessed with the Pearson's correlation coefficient. The analysis was conducted with Amira software (Visage Imaging Inc., Andover, MA). Statistical significance was set as $P < 0.05$.

Results and Discussions Our results indicated that the area of lesion measured from MRI correlated well with the histological findings ($R=0.95$, $P < 0.05$). The BZ area was significantly larger in the acute lesion ($45.55\% \pm 13.84$ of total lesion area) compared to the chronic lesions ($9.72\% \pm 6.27$; $p < 0.05$). Interestingly, the red in the acute lesions and grey in chronic areas of the BZ (as depicted by the MT stain), contain viable and inflammatory cells, and related well to the uneven dark and bright features in corresponding topographical zones in the MR images (Fig.1). This study suggested that non-contrast MRI can adequately identify the RF thermal lesion structure in fixed tissue *ex-vivo*. This may provide valuable information for assessing anatomic correlates to ablation success including the transmural extent and gaps between lesions. Future work will focus on translating such MR characterization studies to myocardial tissue, with a final aim being to evaluate clinical therapy with RF ablation.

Figure1. Acute lesion demonstrated by Histology and MRI

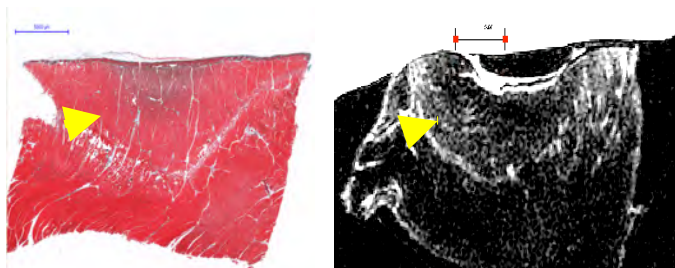
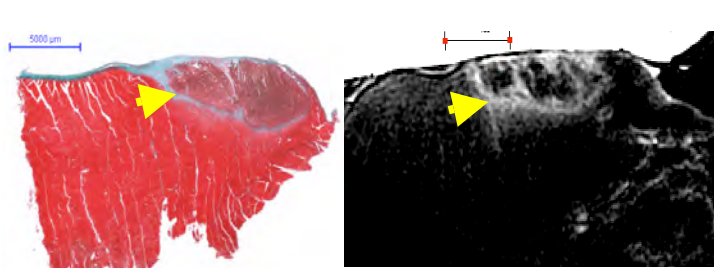


Figure2. Chronic lesion demonstrated by Histology and MRI



BZ (yellow arrows) in acute lesions was much thicker than that in chronic lesions. All bars = 5 mm

References

1. Nordbeck P, Hiller KH, Fidler F, et al. *Circ Cardiovasc Imaging*. 2011;4(3):282-294.
2. Shmatukha A, Sethi B, Shurrab M, et al. *Phys. Med. Biol.* 2013(58):3321-3337.

MagA Reporter Gene Expression for Magnetic Resonance Imaging

Karina Quiaoit^{1,2,3}, Anindita Sengupta^{1,2,3}, Terry Thompson^{1,2}, Frank Prato^{1,2}, Neil Gelman (co-supervisor)^{1,2} and Donna Goldhawk (co-supervisor)^{1,2,3}

¹Department of Medical Biophysics, Western University; ²Imaging Program, Lawson Health Research Institute; ³MolecularImaging Program, Western University, London, Ontario

Introduction. The development of methods to monitor cellular activity with magnetic resonance imaging (MRI) will provide powerful tools for studying disease progression and monitoring therapy. A gene-based contrast agent for reporter gene expression will allow long-term cell tracking, and notably, the monitoring of cellular activity. We are developing *MagA*, a putative iron transporter, as a reporter gene for MRI. *MagA* is a magnetotactic bacterial protein that contributes to iron accumulation when expressed in mammalian cells (Zurkiya et al., 2008; Goldhawk et al., 2009). In culture, an extracellular iron supplement promotes both iron uptake and magnetic sensitivity in *MagA*-expressing cells. In a model of tumour growth from transplanted cells, *MagA* expression increases tissue contrast, with respect to fractional void volume and contrast to noise ratio, earlier than untransfected cells (Rohani et al., 2013). Whereas previous studies have relied on constitutive expression of *MagA*, we are now developing a *MagA* reporter gene expression system to monitor the activity of *Nkx2.5*, a cardiac-related transcription factor. Based on the work of Dentice et al. (2004), we propose that the minimal promoter from the sodium iodide symporter gene, *P_{NIS-min}*, will permit *Nkx2.5* activity to be detected by *MagA* expression using MRI. This genetic construct may provide an early imaging marker of cardiomyocyte differentiation.

Methods. Our cloning strategy is depicted in Figure 1. Small protein tags (HA and Myc) flank the *MagA* sequence to enable detection of expressed protein using commercial antibodies. Cells expressing the reporter gene construct are cultured in the presence and absence of 250 μ M ferric nitrate. For MR mapping, compact pellets of cells are mounted in a spherical gelatin phantom and transverse relaxation rate measurements are obtained from single echo spin-echo and multi-echo gradient echo sequences for R2 and R2* respectively (Sengupta et al., 2013, submitted). Cellular iron content is measured using inductively-coupled plasma mass spectrometry (ICP-MS, Western Analytical Service). Statistical analysis consists of the Kruskal-Wallis, non-parametric test.

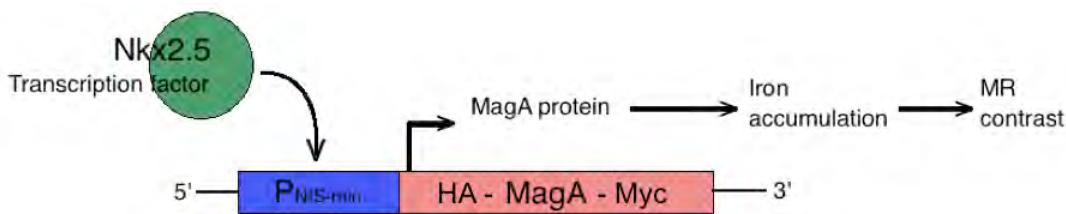


Figure 1. *MagA* reporter gene expression. *Nkx2.5* activation of *P_{NIS-min}* will result in MR contrast due to *MagA* expression and iron supplementation.

Results. MRI has been conducted on untransfected cells (Parental) and those constitutively overexpressing *MagA*, cultured with and without iron supplementation. These cells serve as a baseline comparison for cells with *Nkx2.5* stimulated *MagA* reporter gene expression. Iron supplemented cells constitutively overexpressing *MagA* had significantly greater R2*, R2 and R2' than their non-iron supplemented counterpart or the parental control based on non-parametric bivariate statistical analysis (Table 1).

Mean Relaxation Rate (s ⁻¹)	Parental (n=4)			MagA (n=8)		
	Fe (-) (SD)	Fe (+) (SD)	p	Fe (-) (SD)	Fe (+) (SD)	p
R2*	13.70 (3.07)	15.68 (5.83)	0.66	13.91 (3.69)	26.46 (8.69)	< 0.005
R2	9.69 (0.76)	11.58 (2.30)	0.15	11.17 (2.95)	17.37 (4.80)	< 0.01
R2'	4.01 (2.41)	4.10 (3.94)	0.56	2.74 (1.03)	9.09 (4.12)	0.001

Table 1. Transverse relaxation rates of parental and constitutively *MagA*-expressing cells cultured in the presence (+Fe) and absence (-Fe) of iron supplementation.

Conclusions. Constitutive overexpression of *MagA* in MDA-MB-435 cells significantly increased transverse relaxation rates and cellular iron. Generation of a *MagA* reporter gene construct and a statistically valid method for measuring relaxation rates allows for longitudinal detection of cellular activity using MRI. These tools will be applied in detecting *Nkx2.5* activity in transfected cells.

Localization of x-ray attenuating objects from a single cone-beam x-ray projection

Normand Robert, **Benu Sethi**, George Polack, John Rowlands, Eugene Crystal
Schulich Heart Program, Sunnybrook Health Sciences Centre, Sunnybrook Research Institute

Introduction: Single-plane fluoroscopic systems provide two-dimensional (2D) projections of interventional devices but lack positional “depth” information. During electrophysiology (EP) interventions, mapping systems provide three-dimensional (3D) position estimates of catheters, but the coordinates obtained are not in context of the anatomical features seen in the x-ray images. Since mapping systems are limited by the high per-use costs associated with specialized catheters, there is a need for x-ray image-based 3D guidance of minimally invasive devices for a wide variety of fluoroscopy-guided procedures.

Methods/Technique: We have developed a method to provide 3D localization of x-ray attenuating objects using single view 2D fluoroscopic images. We exploit small changes in magnification of the x-ray image of said objects as they move closer or farther from the x-ray source to achieve localization. The resulting object coordinates are x-ray system centric and thus tied to the position of the x-ray source and the imaging detector as shown in Figure 1. Synthetic x-ray cone beam projections of a 3D model of a catheter are computed for various positions (x, y, z) and orientations (3 angles) of said model until a synthetic projection that matches the x-ray image of the catheter is found. X-ray models of EP catheters can be obtained from high-resolution μ CT data. Validation of the method was performed with a catheter moving in a water tank with the aid of a computer-controlled three-axis motorized stage. An independent method was developed to determine the true position of the catheter in x-ray centric coordinates allowing not only reproducibility but also accuracy to be determined. Catheter localization was also applied to raw unprocessed images obtained during clinical EP procedures.

Results: The reproducibility for the catheter coordinates (x, y, z) in a water tank is (0.2 mm, 0.2 mm, 4 mm) and a 4% correctable systematic error in positional coordinates was found. Reproducibility in the z -direction is least because it depends on subtle changes in magnification. The reproducibility in the (x, y) directions is superior to conventional navigation systems. We show that localization is practical in clinical images exhibiting signals due to anatomical structures superimposed on the catheter. We show that localization can be done at fluoroscopic x-ray exposure rates and also provide a comparison to data obtained using a commercial navigation system.

Discussion: Initially, localization was performed on previously acquired clinical images because our method was too slow to analyze images in real time. The method has been adapted such that these intensive computations are done using a combination of Central Processing Units (CPUs) and Graphics Processing Units (GPUs). As a result, computations can in many circumstances be performed quickly enough to provide results as the images are acquired at 7.5frames/s. The challenge, which we have undertaken, is to make effective use of multiple graphics cards, further parallelizing the algorithms, thus allowing dependable real-time localization for all images.

Conclusion: Our results have shown that x-ray based localization is possible for EP catheters and additional clinical evaluation is required to better quantify the impact of image quality on position measurements. Our approach can be applied to other objects having components that provide increased x-ray attenuation and therefore sufficient object contrast relative to image noise.

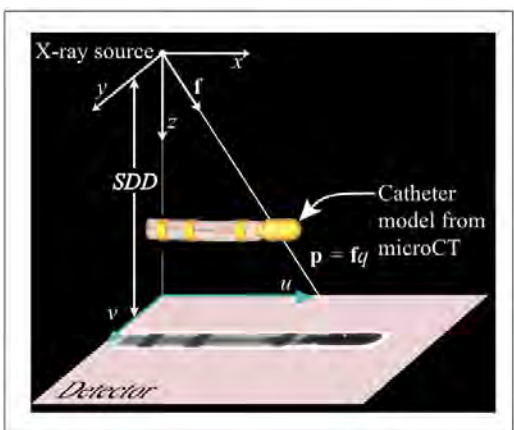


Figure 1: Diagram showing a 3D catheter model obtained from μ CT and the associated computed x-ray projection used to achieve 3D localization of said catheter in an x-ray image.



Figure 2: The Graphical User Interface for 3D device navigation is divided into 4 different columns/segments showing: a) thumbnails of the most recently acquired x-ray sequences, b) a small view of the catheter and x-ray detector whose perspective can be adjusted (top) and a view of the synthetic projection of the catheter superimposed on the x-ray image (bottom), c) a larger view of the catheter of interest, highlighted in green, for which 3D localization is being performed (perspective can be varied), d) the control panel to enable localization, select image source.

Simultaneous assessment of myocardial ischemia and edema and viability with a single bolus of contrast injection and CT acquisition

Author(s) – Aaron So, Gerald Wisenberg, Patrick Teefy, Frank Prato, James White, Ting-Yim Lee
Lawson Health Research Institute, Robarts Research Institute, London Health Sciences Centre
London, Ontario, Canada

Introduction

We developed a functional CT technique to allow rapid and simultaneous assessment of myocardial ischemia, edema and viability with a single dynamic CT acquisition and bolus injection of contrast agent. This technique can be used to evaluate different myocardial tissue states after ischemic injury.

Background

Our lab previously pioneered a dual energy CT Perfusion technique for accurate and quantitative measurement of myocardial perfusion (MP, in ml/min/g) by removing the beam hardening effect arising from the CT contrast agent in the heart chambers during the perfusion study. In this method, a small bolus of contrast agent is injected intravenously before the heart is scanned at consecutive diastoles with breath-hold for 30 s. Exchange of contrast between blood and interstitium measured by gated dynamic contrast-enhanced cardiac images is modeled with the Johnson-Wilson (JW) model to derive absolute MP. CT contrast agent is extracellular but can enter into injured cardiomyocytes due to the breakdown of cell membrane. As such, measurement of extravascular contrast distribution volume (ECDV, in ml/g) provides surrogate assessment of myocardial viability. Similarly, edema in ischemic myocardium expands the interstitial space where contrast can distribute hence ECDV can also be a marker of myocardial edema. To facilitate the measurement of ECDV with dual energy CT Perfusion, we modified the perfusion imaging protocol to include a 'delayed' phase of scanning and the JW model by adding a compartment to account for the exchange of contrast between interstitium and cellular cytosol in ischemic myocardium.

Experiments

We tested this novel functional CT technique in a pig model of reperfused acute myocardial infarction (MI) created by an interventional procedure, in which inflation of a balloon catheter was introduced into the distal LAD under fluoroscopic guidance. MI was confirmed by the ST segment elevation in the ECG monitored during the procedure. At one hour post inflation, the balloon was deflated. At 3 and 10 days post, 4 cm of the heart below the LAD occlusion/reperfusion site was scanned under breath-hold with a ECG-gated two-phase dynamic acquisition protocol using a dual-energy scanner (GE Healthcare HD750 VCT) at 140/80 kV and 224 mAs: first-phase: 26 axial scans every diastole; second-phase: 6 axial scans at diastole every 15 s. MP and ECDV parametric maps were derived from the acquired image data using prototype CT Perfusion software (GE Healthcare). The pig also had T2 and delayed enhancement (DE) T1 MRI scans to determine edema and viability respectively in-vivo using a Siemens Biograph mMR scanner. At 10 days post, the heart was excised and stained with TTC solution to determine viability ex-vivo.

Results

In **Fig 1**, the apical wall exhibited 2 times higher ECDV (A, 0.54 vs. 0.21 ml/g) but similar MP (B, 0.86 vs. 0.93 ml/min/g) compared to the remote lateral wall at day 3 post. The T2 (C) and DE T1 (D) MR images showed massive edema and no delayed enhancement in the apical wall, confirming this region was successfully reperfused with persistent edema. In **Fig 2**, ECDV (A) on a different slice of the apical myocardium was higher than remote (0.79 vs. 0.32 ml/g) while MP (B) in the same apical wall was much lower than remote (0.31 vs. 0.76 ml/min/g) at 10 days post. TTC staining (C) confirmed the apical wall was infarcted (unstained).

Conclusion

Functional CT measurements compared well with the respective gold standards in different degrees of ischemic injury in myocardium. Successful reperfusion in ischemic myocardium (Fig 1) was evidenced by the normalized MP while persistent edema was reflected by the higher than normal ECDV. In infarcted myocardium (Fig 2), microvascular obstruction resulted in MP > 2 times lower than normal, while cellular accumulation of contrast led to ECDV > 2 times higher than normal. The proposed functional CT technique can be useful for assessing different myocardial conditions after acute ischemic injury (heart attack) and hence guiding treatments and predicting clinical outcomes.

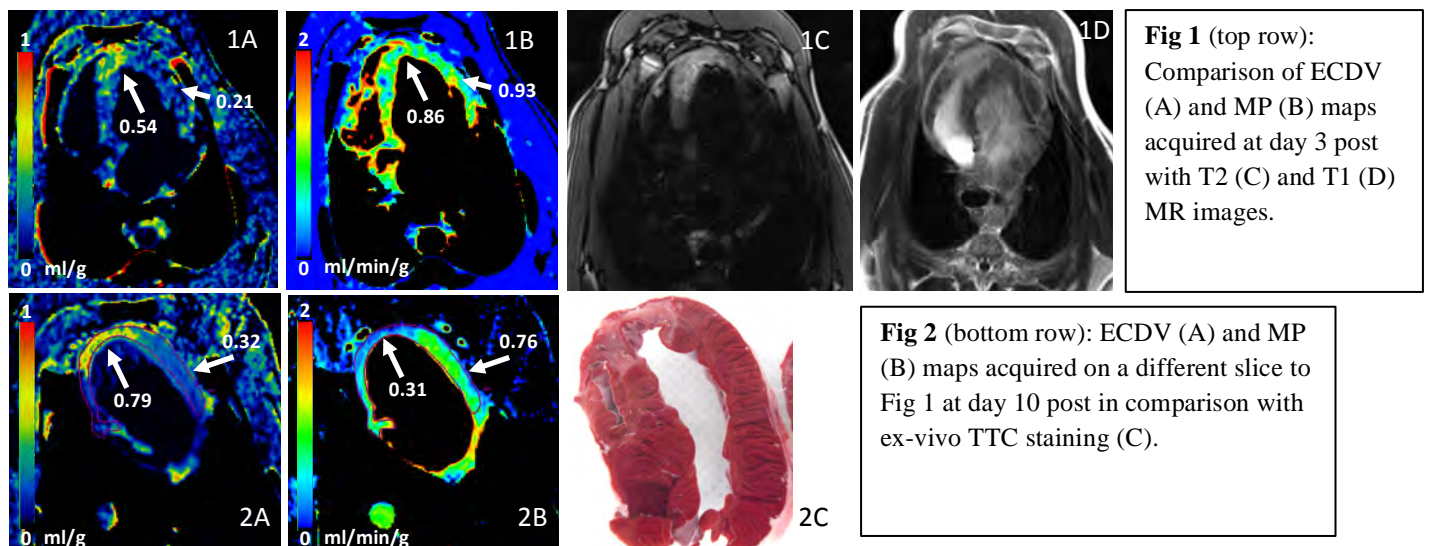


Fig 1 (top row): Comparison of ECDV (A) and MP (B) maps acquired at day 3 post with T2 (C) and T1 (D) MR images.

Fig 2 (bottom row): ECDV (A) and MP (B) maps acquired on a different slice to Fig 1 at day 10 post in comparison with ex-vivo TTC staining (C).

Fully MRI-Compatible Dynamic Motion Stage

Mohammad Ali Tavallaei¹ and Maria Drangova^{1,2}

¹Robarts Research Institute, Biomedical Engineering Graduate Program, Western University, Canada, ²Department of Medical Biophysics, Schulich School of Medicine & Dentistry, Western University, Canada
Supervisor: Professor Maria Drangova

INTRODUCTION

Controlled dynamic motion of phantoms in MRI may be used in applications including but not limited to: verification of 4D MRI, MRI guided therapy, MRI motion correction and tracking techniques, cross modality comparison, gated imaging and MRI elastography. To address this need we have developed an MRI compatible linear motion stage that can deliver highly accurate and reproducible dynamic motion profiles inside the bore during imaging. While other attempts have been made to develop MRI compatible motion stages (1-3) to the best of our knowledge the proposed system is the first that is completely MRI compatible and can be placed within the scanner bore at arbitrary orientations. The stage is designed to either carry conventional phantoms or be used to deform flexible phantoms.

METHODS

A travelling wave rotary ultrasonic motor (USR60-NM, Fukoku-Shinsei) is used to drive a linear motion stage made of nonmagnetic material. Following the methods described in (4) an embedded system was developed that enables dynamic control of the motor's position. In laboratory settings the accuracy of the system in reaching fixed reference positions was evaluated using an optical microscope (STM6, Olympus). For this test the motion stage was loaded with 1.5 kg. Reference positions of ± 1 , ± 5 , ± 10 , and ± 20 mm were prescribed and each prescription was repeated 10 times for both positive and negative directions. To evaluate the execution of dynamic motion the motion stage was loaded with 1.5 kg and an optical tracking tool was attached to the moving carriage. Dynamic reference motion profiles were prescribed. The profiles were sinusoidal waves with frequencies of 0.5, 0.33 and 0.25 Hz. For each frequency, amplitudes of 1, 5, 7.5 and 10 mm were selected. During the execution of these motions the position of the tracking tool was tracked using an optical tracker (Vicra, NDI) and logged at a rate of 50 frames per second for a period of 5 minutes. The embedded system simultaneously logged the motor's encoder position to a computer at a sampling time of approximately 10 ms. To evaluate the performance of the stage during imaging, the stage was positioned close to the isocenter inside the bore of a 3 T scanner (MR750, GE). During GRE imaging (TR/TE = 500/10 ms, flip angle 60° , slice thickness 5 mm, 256x160 matrix, body coil) the motion stage was set to execute a typical sinusoidal motion with amplitude of 5 mm and period of 3 seconds. Similar to the laboratory setting, the encoder data were recorded throughout the scan. To demonstrate the system's performance during gated imaging, a FIESTA cine sequence (TR/TE=8/4 ms, flip angle 20° , slice thickness 5mm, 192x160 matrix, HD T/R Knee array coil) was obtained of a tangerine, which was moved by the stage with a prescribed sinusoidal motion with amplitude of 10 mm and frequency of 0.33 Hz. A TTL pulse provided by the embedded system once per cycle provided triggers for the gated scan.

RESULTS AND DISCUSSION

The mean absolute error of the system in reaching fixed positions measured with the measuring microscope was 0.14 ± 0.06 mm. This accuracy was obtained when direction of travel was alternating and therefore includes backlash that can be compensated for. For dynamic motion the worst-case RMSE measured with the optical tracking tool was 0.3 mm and the worst-case normalized RMSE was 6%. The 95% confidence interval and the mean of a typical motion profile over a five-minute session are illustrated in Fig 1. The logged encoder data of several motion profiles with the stage inside the scanner during GRE imaging and FIESTA imaging were compared with that of the stage in the laboratory setting and showed to be identical. Several frames (5 frames apart) from the gated FIESTA cine acquisition of the moving tangerine are shown in Fig. 3 and demonstrate the feasibility of using the stage for a range of applications.

REFERENCES

1. M. Drangova et al., *J Magn Reson Imaging* 6, 513 (May-Jun, 1996). 2. M. Gunther et al., *Magnetic Resonance in Medicine* 52, 27 (Jul, 2004). 3. M. E. Huber et al., *J Cardiovasc Magn Reson* 2, 181 (2000). 4. M. A. Tavallaei et al., *IEEE Trans Biomed Eng* 60, 899 (Apr, 2013).

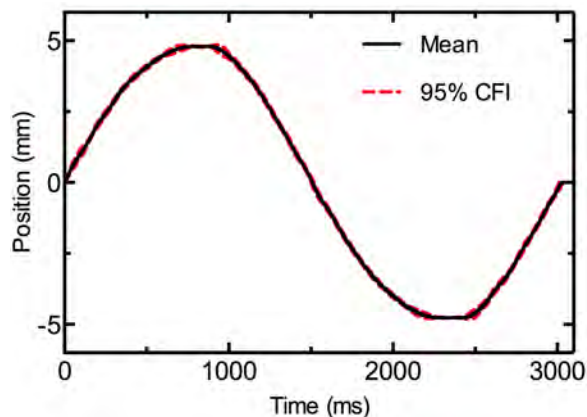


Fig. 1. Position vs time for a representative sinusoidal motion profile (3 second period, 5 mm amplitude). The 95% confidence interval was calculated from 100 measured waveforms (5 minutes).

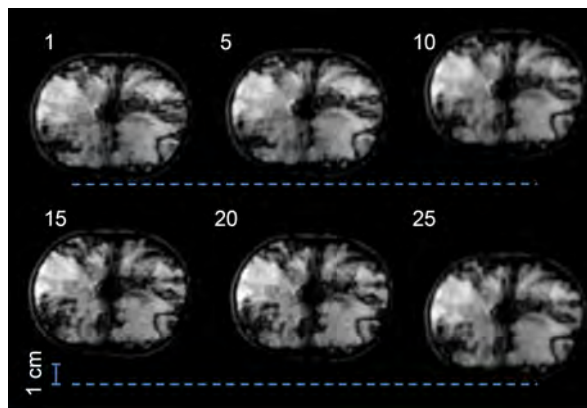


Fig. 2. Selected frames from a gated FIESTA Cine sequence of a tangerine undergoing sinusoidal motion with amplitude of 10 mm at 0.33 Hz.

OICR Imaging Translation Program

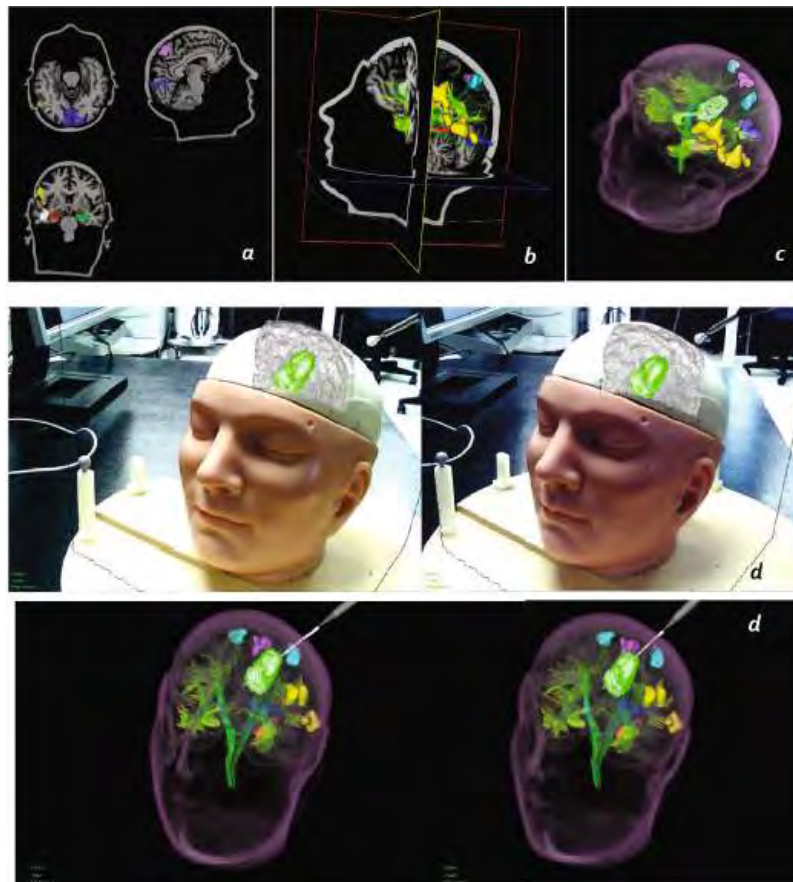
OICR ITP

Oral Presentation and Poster Abstracts

Role of Augmented Reality in Training the Planning of Brain Tumor Resection

Kamyar Abhari, John S.H. Baxter, Elvis S. Chen, Ali R. Khan, Chris Wedlake, Terry Peters, Roy Eagleson, and Sandrine de Ribaupierre
Robarts Research Institute
Western University, London, ON, Canada

The environment in which a surgeon is trained profoundly effects their preferred method for visualizing patient images. While classical 2D viewing might be preferred by some older experts, the new generation of residents and novices has been raised navigating in 3D through video games, and are accustomed to seeing 3D reconstructions of the human anatomy. In this study, we evaluate the performance of different groups of users in 4 different visualization modalities (2D planes, orthogonal planes, 3D reconstruction and augmented reality). We hypothesize that this system will facilitate the spatio-visual abilities of individuals in terms of assessing patient-specific data, an essential requirement of many neurosurgical applications such as tumour resection. We also hypothesize that the difference between AR and the other modalities will be greater in the novice group. Our preliminary results indicate that AR is better or as good as other modalities in terms of performance.



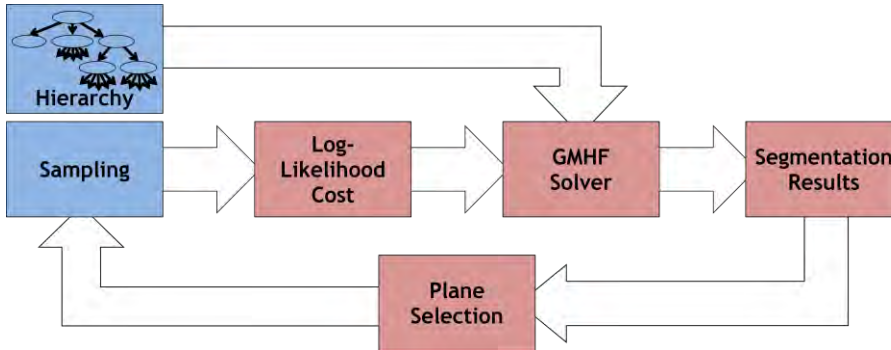
Different Visualization Modalities: a) 2D, b) XP, c) 3D, and d) AR

Open-Source Interface for Interactive Segmentation with Generalized Hierarchical Max-Flow Segmentation

J.S.H. Baxter^(1,2), E.C.S. Chen⁽²⁾, & T.M. Peters^(1,2),

(1) Biomedical Engineering Graduate Program, (2) Robarts Research Institute, Western University, London, ON

Interactive segmentation occupies a necessary middle ground between manual segmentation, which is tedious and subject to human error and insufficiencies, and automatic segmentation which often lacks generality and the ability to handle pathological cases. In interactive segmentation, a user provides a rough, incomplete segmentation of a small subset of slices in the image. An automatic segmentation algorithm is then used to complete the segmentation for those slices and extrapolate to the entire image, possibly simultaneously.



Pipeline for SEGUE: Blue regions are provided by the user and red automatically provided by the computer

One issue with many current segmentation interfaces is the ability to handle multiple interacting labels. SEGUE addresses these limitations through the use of generalized hierarchical max-flow with a user-defined hierarchy. This allows for the user to readily incorporate some anatomical knowledge in an easier and more intuitive manner. The hierarchy widget is combined with one that allows for users to specify, name, and control the colour of different labels, seamlessly incorporating it into the interface. Log-likelihood cost terms [1] are defined for each label based on the intensity distribution of the

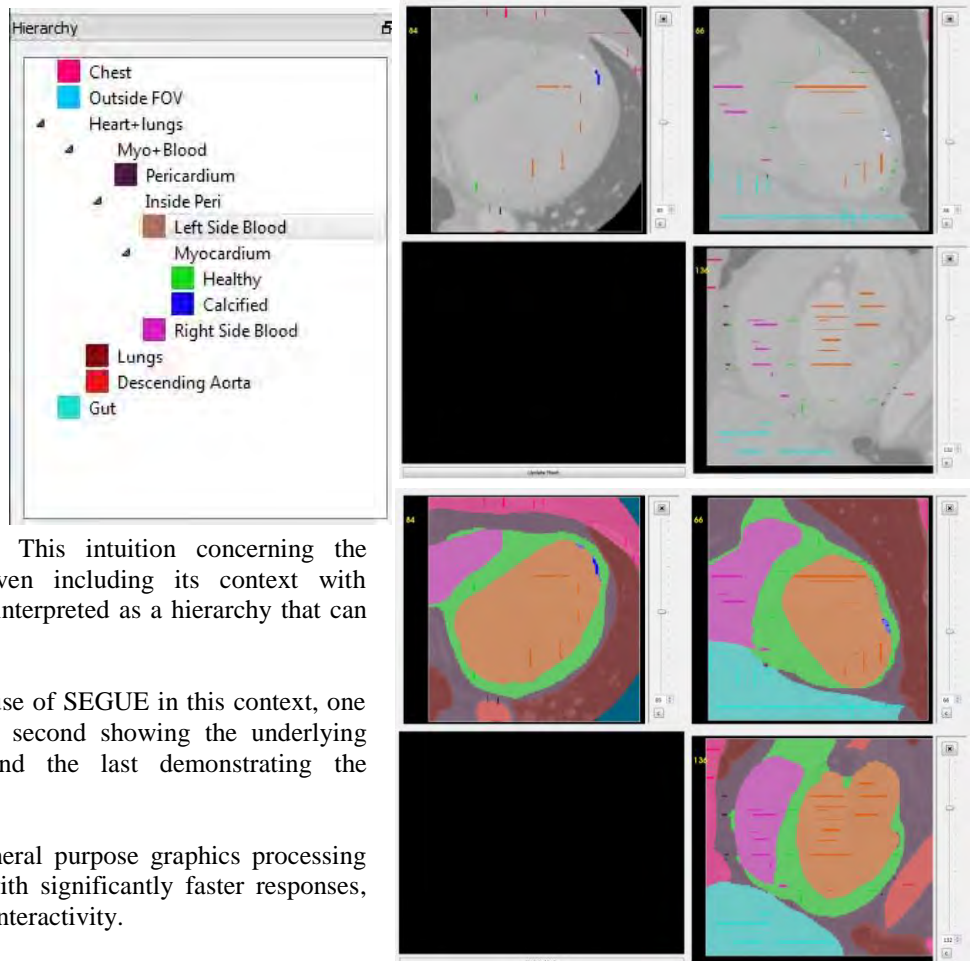
sampled voxels, and are used in conjunction with the hierarchy to find an optimal segmentation under those costs and constraints.

To improve interactive segmentation, more nuanced feedback from the computer to the human is required, specifically feedback as to where the algorithms are uncertain and require more user interaction. [2] SEGUE implements a plane selection algorithm in which the computer can suggest planes to the user where user effort would have the highest impact.

An example application of SEGUE is the segmentation of cardiac anatomy from contrast enhanced CT. This anatomy has an inherent hierarchical structure, with regions of myocardium surrounding blood pools, all aggregating together to define the whole heart. This intuition concerning the hierarchical structure of the heart (even including its context with surrounding organs) can be very readily interpreted as a hierarchy that can aid segmentation.

The images to the right demonstrate the use of SEGUE in this context, one showing the user-defined hierarchy, the second showing the underlying image with user-provided samples, and the last demonstrating the extrapolated segmentation.

This interface was accelerated using general purpose graphics processing unit programming to provide the user with significantly faster responses, necessary for maintaining a high level of interactivity.



[1] van der Lijn et al, "Hippocampus segmentation in MR Images using atlas registration, voxel classification, and graph cuts"
 [2] Top et al, "Active Learning for Interactive 3D Image Segmentation"

Computational imaging techniques for histological quantification of cortical architecture in epilepsy

Charlotte Blinston^(1,4), Robert Hammond⁽²⁾, Terry Peters^(1,4), Ali R. Khan^(3,4)

1. Biomedical Engineering Graduate Program 2. Department of Pathology, Division of Neuropathology
3. Department of Medical Biophysics 4. Robarts Research Institute, Western University, London, ON, Canada.

Introduction: Approximately one third of epilepsy patients suffer from refractory temporal lobe epilepsy (TLE), which is commonly treated with resection of the epileptogenic tissue [1]. However, localization of the epileptogenic zone can be difficult and could be improved with advances in MR imaging. Development of such techniques could be validated with neuropathology of the excised cortical tissue, which is the objective of our ongoing study. Focal cortical dysplasias (FCD) are neuropathological cortical malformations [2] that are often unseen on conventional MRI scans, and are also subtle and difficult to quantify histologically. Thus we are employing histology image analysis techniques to better characterize these abnormalities at the neuronal and laminar level, allowing for correlative MRI-histology studies and improved lesion detection.

Methods: TLE patients recommended for anterior temporal lobectomy were recruited and scanned pre-operatively in 3T and 7T MRI [3]. The excised tissue was scanned overnight in 9.4T MRI, then histology slides were cut with a slice thickness of 4 μ m, immunohistochemically stained with NeuN antibody and digitized at a resolution of 0.5 μ m. An automated neuron segmentation algorithm was developed in MATLAB, utilizing a colour deconvolution method combined with a watershed transform to segment individual neurons for analysis. We validated the accuracy of the automated neuron segmentation algorithm by comparison with manual counting (Fig 1). Neuron-specific histopathologic features in 100 μ m x 100 μ m fields were computed and included neuron count, size, clustering, orientation and eccentricity. These were compared against field fractions, a commonly used measure representing the fraction of positively stained pixels in each field, to highlight the added value of multivariate features in cortical architecture analysis.

Results & Conclusion: Our automated neuron counts (over 14 fields) were in strong agreement (Pearson correlation) with manual counts ($R=0.98$), close to inter-rater ($R=0.99$) and intra-rater agreement ($R=0.99$). An example NeuN slide is shown along with the field fraction image and neuron-specific feature maps depicted the mean neuron size and neuron count (Fig 2). We see greater contrast in cortical layers with the neuron-specific feature maps, especially apparent in layer IV. This improvement in contrast was quantified by comparing contrast-to-noise ratios between layer III and layer IV using the count ($CNR=1.0$) and size ($CNR=0.66$) feature maps, and using the field fraction ($CNR=0.41$). These results suggest that detection and quantification of regions of mildly dysplastic cortex can be improved using the proposed method. In addition, these maps may be implemented in a digital pathology workflow to assist in computer-aided diagnostics. Future work includes the correlation of neuropathology with MRI to better understand imaging correlates of FCD lesions, which can lead to tailored surgical resection of lesions and thus better surgical outcomes.

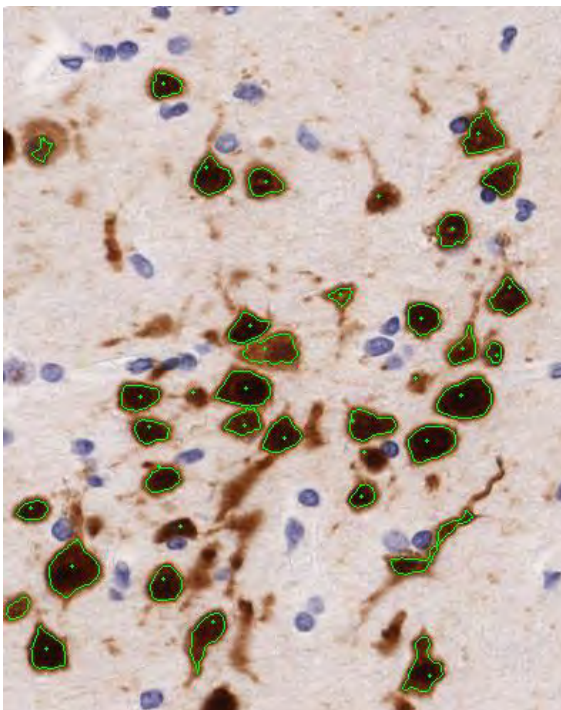


Fig. 1. Example of automated neuron segmentation (green outlines), demonstrating high agreement with manual counts (green dots).

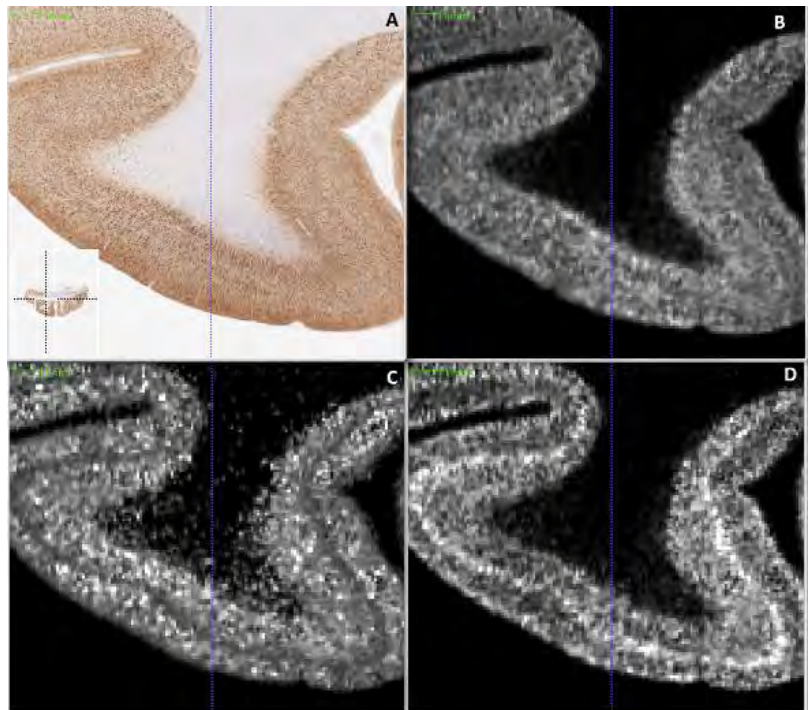


Fig. 2. A. NeuN Histology slide, magnified to area of interest. B Field fraction estimate. C. Neuron size D. Neuron count. Feature maps of neuropathological features demonstrate higher contrast to noise ratio than field fraction estimates, demonstrating their used in analysis of cortical architecture.

References: [1] Engel J. *Neurology* (1998) vol. 51(5) pp. 1243-4 [2] Blümcke I. et al. *Epilepsia* (2011) vol. 52(1) pp. 158-74 [3] Goubran M. et al. *Neuroimage* (2013) vol.83 pp. 770-81

MRI-Guided Prostate Focal Laser Ablation Therapy using a Mechatronic Needle Guidance System: Initial Experience and Future Directions

Jeremy Cepek^{a,b}, Uri Lindner^c, Sangeet Ghai^d, Sean RH Davidson^e, John Trachtenberg^c, Aaron Fenster^{a,b,f}

^aRobarts Research Institute, London, ON, Canada; ^bBiomedical Engineering, The University of Western Ontario, London, Canada; ^cDepartment of Surgical Oncology, Division of Urology, University Health Network, Toronto, Canada; ^dDepartment of Medical Imaging, University Health Network, Toronto, Canada; ^eOntario Cancer Institute, University Health Network, Toronto, Canada; ^fResearch Supervisor

Purpose: The concept of focal therapy for prostate cancer is currently being evaluated in the urologic community, with the goal of reducing treatment-related side effects associated with common prostate cancer treatments.¹ Among several emerging techniques, MRI-guided focal laser ablation (FLA) therapy is particularly attractive, as it offers intraoperative cancer localization, needle guidance, real-time thermometry, and immediate post-treatment imaging of the ablated region.² Despite these attractive features, performing a needle-based procedure within an MRI environment presents many challenges due to the high magnetic field strength, presence of fast-switching magnetic field gradients and RF fields, and a limited amount of workspace for the physician. In addition, the small scanner bore size prevents positioning of the patient in a full lithotomy position, thereby limiting transperineal access to the prostate. These challenges are important to overcome, since the placement of needles for FLA therapy must be done with high accuracy in order to ensure complete ablation of the target volume and avoid damage to surrounding sensitive structures. Standard methods of guiding needles to the prostate, such as with the use of a grid template, present a hindrance to the workflow within the MRI environment because the patient must be removed from the MRI scanner for needle insertion, and re-inserted for imaging of needles.² This process is time consuming and causes additional patient motion that may reduce the accuracy of needle placement. In an attempt to overcome these challenges and take full advantage of the utility of intra-operative MRI, we developed an MRI-compatible mechatronic needle guidance system for accurate delivery of needles to the prostate for FLA therapy.

Methods: A custom MRI-compatible mechatronic needle guidance device was designed, built, and integrated with custom 3D visualization software. The resulting system gives the operator the ability to specify desired angulated needle trajectories using a 3D imaging interface, precisely align the device's needle guides to this trajectory, and manually insert needles into the prostate under MRI guidance. The device was evaluated for compatibility within the MRI environment, needle guidance accuracy, and safety before being used to guide 29 needles in eight cases of MRI-guided prostate FLA therapy. Following the treatment of eight patients, error in needle placement was quantified. Monte Carlo stochastic simulations of needle placement error were then performed to determine the relationships between target size and shape, the level of uncertainty in needle placement error (*i.e.* the standard deviation, when modeled as a 2D Gaussian), and the probability of achieving complete focal target ablation. The goal of the simulations was to determine the maximum target size that can be confidently ablated with the current system, and to quantify the clinical benefit that could be gained by increasing needle guidance accuracy.

Results: Clinical Evaluation - The median error in guiding needles to their target was 3.4 mm, and device alignment and needle insertions were performed with the patient and device remaining inside of the MRI scanner bore. This feature contributed to a significant decrease in the time required to guide each needle to its target, as compared to a fixed grid template approach (median 8 vs. 18 minutes, $p < 0.0001$, Mann-Whitney U test). The device's ability to target arbitrary points in the prostate through angulated trajectories was found to be extremely valuable, and ensured that each tumor was reachable.

Patient Selection Guidelines - The standard deviation of needle placement error in the vertical and horizontal directions was 2.5 mm and 3.1 mm, respectively. For a given level of needle placement uncertainty, our model predicts the maximum length of tumors that can be completely ablated with at least 90% certainty. Table 1 shows how the maximum treatable length of tumor varies with the size of ablation volume created, and the tumor aspect ratio (length/width, as seen from the "needle's eye view"). Data in this table are valid for the case where 4 laser fibers are used for each tumor (this number of laser fibers is compatible with the current MRI-guided FLA delivery workflow and time constraints). Currently, the achievable diameter of each individual ablation region is ~15 mm, limiting the treatable target length to 10 – 14 mm, depending on its aspect ratio.

Conclusions: The MRI-guided FLA therapy procedure was improved with the use of a mechatronic needle guidance system. However, the maximum size of target that can be confidently ablated using the current technique is ~14 mm, which limits its applicability to about 1/3 of the patients who were otherwise deemed potentially good candidates for focal therapy. Improved methods of reducing needle deflection are being developed to enable larger targets to be confidently ablated with MRI-guided FLA therapy.

Table 1: Maximum target length treatable. Treatability is defined as having a predicted probability of achieving complete target ablation of > 90%.

Ablation Diameter (mm)	Tumor Aspect Ratio (length/width)			
	1	1.5	2	2.5
10	< 5	< 5	6	6
15	10	11	13	14
20	16	18	21	23

¹G. Bozzini, P. Colin, P. Nevoux, A. Villers, S. Mordon and N. Betrouni, "Focal therapy of prostate cancer: energies and procedures," Urol. Oncol.-Semin. Ori. **31**, 155-167 (2012).

²O. Raz, M. A. Haider, S. R. H. Davidson, U. Lindner, E. Hlasny, R. Weersink, M. R. Gertner, W. Kucharczyk, S. A. McCluskey and J. Trachtenberg, "Real-time magnetic resonance imaging-guided focal laser therapy in patients with low-risk prostate cancer," Eur. Urol. **58**, 173-177 (2010).

2D-3D registration for motion compensation during biopsy using learned prostate motion data

T. De Silva^{1,3}, D. W. Cool^{1,3}, J. Yuan¹, C. Romagnoli³, A. Fenster^{1,2,3,4}, A.D. Ward^{2,4}

1 Robarts Research Institute; 2 The Department of Medical Biophysics; 3 The Department of Medical Imaging; 4 Biomedical Engineering Graduate Program; The University of Western Ontario

Purpose: Three-dimensional (3D) transrectal ultrasound (TRUS)-guided systems have been developed to improve targeting accuracy during prostate biopsy. However, prostate motion due to transrectal ultrasound (TRUS) probe pressure and patient movement causes target misalignments during 3D TRUS-guided biopsy. Several solutions have been proposed to perform intensity-based registration to compensate for prostate motion by registering the live 2D TRUS images acquired during the biopsy procedure to a pre-acquired 3D TRUS image. The clinical workflow requires both speed and accuracy during registration. In order to improve the convergence robustness of the registration optimizer to accurate solutions, we developed an algorithm that utilizes learned prostate motion characteristics.

Methods: We acquired 3D TRUS images from 29 patients at each sextant probe position, in addition to the baseline 3D TRUS image acquired initially during the procedure. We performed a principal component analysis of observed prostate motion at each sextant position to identify principal motion directions. 2D TRUS images extracted at sextant probe positions were registered to the baseline 3D TRUS image utilizing the learned motion directions to initialize Powell's direction set method during optimization with the normalized cross-correlation (NCC) as the image similarity metric. Registration accuracy was measured by calculating the target registration error (TRE) using manually-identified fiducial landmarks (micro-calcifications) within the prostate. A graphics processing unit (GPU)-based parallel implementation was used to improve registration speed.

Results: Our learning-based approach improved target registration error to 2.53 ± 1.25 mm after registration. This was an improvement over 4.95 ± 2.37 mm before registration. Compared with an initialization determined without learned motion characteristics, the reduction (9.2% to 2.3%) in failed registrations (TRE > 5 mm) of this approach (Fig. 1) mitigates challenges to clinical translation. With the GPU implementation, the registrations were performed with a mean execution time of 3.2 s. Fig. 2 shows the improvements qualitatively after registration.

Conclusion: Compensating for patient motion and accurately mapping pre-identified targets to real-time 2D TRUS images is an important step towards improving the cancer detection rate during biopsy. The reported accuracy, speed and robustness of the method are supportive of successful clinical integration.

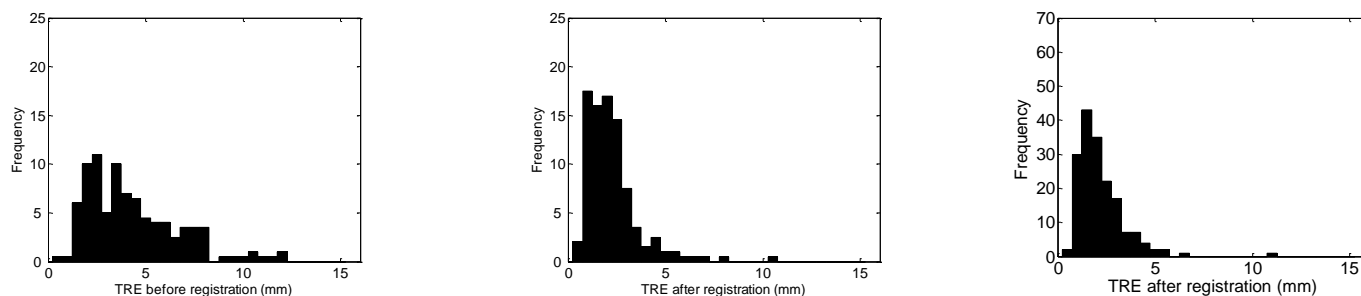


Fig. 1: Left: TRE distribution before registration. **Middle:** TRE distribution after registration with the standard method. **Right:** TRE distribution after registration with the updated method.

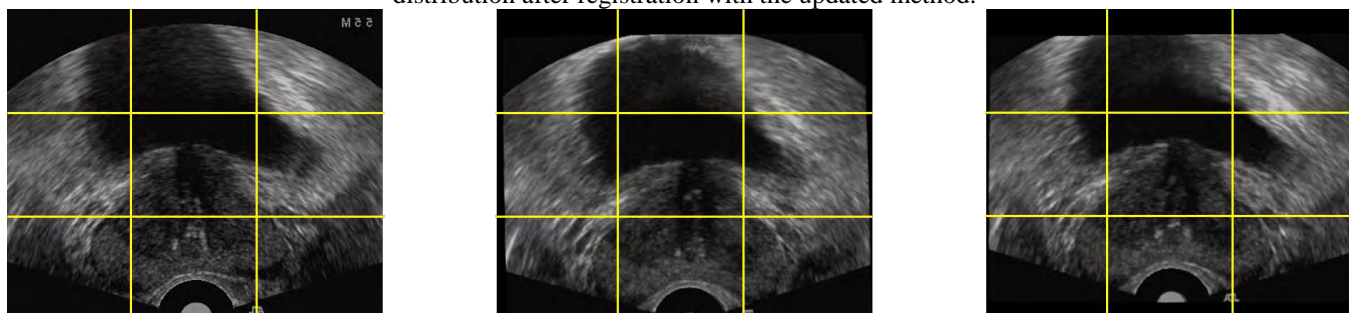


Fig. 2: Left: Live 2D TRUS. **Middle:** Corresponding image before registration. **Right:** Corresponding image after registration.

Development of a Multi-Center Clinical Trial Data Archiving and Analysis Platform

B. Driscoll¹, C. Coolens^{1,2,3}, I. Yeung^{1,2}, T. Lui^{1,3}, N. Gonzalez¹, G. Disney¹, I. Svistoun¹ & D. Jaffray^{1,2,3}

(1) Radiation Medicine Program, Princess Margaret Cancer Center, Toronto, Canada

(2) Dept Radiation Oncology, University of Toronto, Toronto, (3) Techna Institute, University Health Network, Toronto, Canada

Purpose: To provide clinicians & researchers participating in multi-center clinical trials with a central repository for their imaging data as well as a set of tools for providing end-to-end testing and image analysis standards of practice (SOP).

Methods: There are 4 main components to the Clinical Trial data archiving and analysis system: the Clinical Trials Patient Database, the Clinical Trials PACS, the data analysis engine(s) and the high-speed networks that connect them (Figure 1).

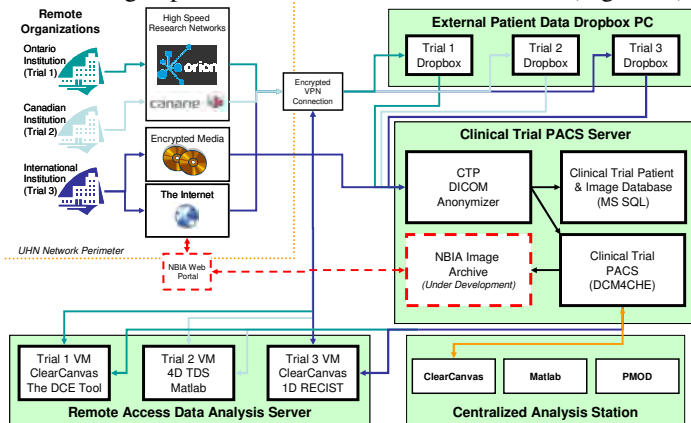


Figure 1: System overview of the Clinical Trial data archiving and analysis system.

Trial Registration Administration

When a clinical trial is registered with the QIPCM (Quantitative Imaging for Personalized Cancer Medicine) initiative, trial specific user credentials are generated. This provides the user(s) with the means to remotely access the Clinical Trial Data Archive and analysis system via encrypted VPN connection. During registration the partitions on the Clinical Trial PACS and data analysis machine for that trial are also setup.

Data Transfer & Anonymization

Registered QIPCM users can connect to the UHN network in order to transfer their data via the ORION fibre-optic research network (or CANARIE for the rest of Canada), or send the data by encrypted hard disk or DVD. The DICOM data for the trial are placed into a trial specific drop-box folder where initial image QA is performed by the QIPCM system administrator to ensure the dataset being added to the system is complete.

The highly customizable CTP anonymizer, a known and validated program developed by RSNA, is then utilized to anonymize the DICOM data according to the trial specific anonymization protocol and forward it the Clinical Trial PACS.

Data Storage, Organization & Back-up

The Clinical Trial PACS Server has been commissioned as a clinical trial data repository running the DICOM archive and image manager software DCM4Chee (DCM4chee.org). The images and study derivatives stored within the PACS are visible only to the appropriate users by AE Title access control. Incremental data backup is performed nightly and full backup is performed monthly on the full contents of the clinical trial PACS. Monthly backups are maintained for 1 year.

Trial Data Repository Data Sharing

In order to facilitate the archiving and exchange of DICOM data with other research organizations around the world, a copy of the National Cancer Institute (NCI) National Biomedical Image

Archive (NBIA) has been installed on the server in parallel with our existing setup. This database is currently in its testing phase.

Data Analysis Computers

A separate high powered data analysis server is also accessible to the remote users through this system. Within this data analysis engine, multiple virtual machines exist (1 per clinical trial). Each virtual machine currently runs a Clear Canvas Workstation as well as the pertinent functional imaging analysis tools which were developed for the Clear Canvas platform; one for kinetic modeling (The DCE-Tool®, www.theDCETool.com) and one for RECIST (Response Evaluation Criteria in Solid Tumors). This system has also been designed to support the QIPCM goal of providing procedures for tests and trials by providing tools such as the DCE-QA Tool, for use in the QA of DCE-CT scanners¹, and the PET/CT region of interest image co-registration for the QA of PET/CT scans. Other customized tools can also be installed on the clinical trial virtual machine including 4D functional image analysis tools such as 4D TDS², Matlab or PMOD.

The analysis framework also provides the ability to export the study derivatives back to the Clinical Trial PACS.

Results: A framework has been set up and currently serves 12 clinical trials spanning 5 hospitals with more trials to be added over the upcoming months. The image store currently holds over 865,000 individual tomographic slices (> 4900 3D volumes) from over 124 functional imaging studies. After initial rapid image transfer, (> 2 MB/s over ORION), all data analysis is done server-side, making it robust and rapid. This has provided the ability to perform computationally expensive operations such as voxel-wise kinetic modeling on very large data archives (+20 GB/50k images/patient) remotely with minimal end-user hardware. This centralized data analysis and storage model also greatly simplifies the addition of new trials and remote sites as very minimal set up is required for the end user.

The database is constantly growing and the infrastructure needed to support the trials has recently been upgraded from proof of concept to a new more powerful server with robust back-up and storage space enough to hold over 16 million images.

Conclusions: The Multi-Centre Clinical Trial Data Analysis and Archival system is fully operational on its newly installed hardware with robust backup and increased data transfer speeds. It has been used successfully to send and analyze data from remote hospitals as well as to support a number of internal high volume functional imaging trials. More recently the system has been applied to support the multi-site TH-302 FAZA Melanoma Trial and is slated for use in analysis of other multi-centre trials in the coming months.

By having a centralized analysis point using standardized tools, variations in results can be minimized while allowing multiple observer studies to use the same image files under the same conditions which will increase the reliability of the results.

Over the next two years the system will also move towards web based viewer platform which is currently in development.

References:

- [1] Driscoll BD, Keller H, Jaffray DA, Coolens C, "Development of a dynamic quality assurance testing protocol for multi-site clinical trial DCE-CT accreditation." Med. Phys. 40(8), (2013)
- [2] Coolens C, Wee W, Driscoll B, Jaffray D. "Novel Methodology for Visualization and Analysis of Functional Vasculature for 4D DCE-CT" Int J Radiat Oncol Biol Phys, 78(3), S22 (2010)

An Automated System To Assess Axillary Lymph Node Malignancy From Sonographic Images

Aneta Chmielewski, Paul Dufort, Ryan Ramos, and Anabel Scaranelo

Joint Department of Medical Imaging, University of Health Network, Toronto, Canada

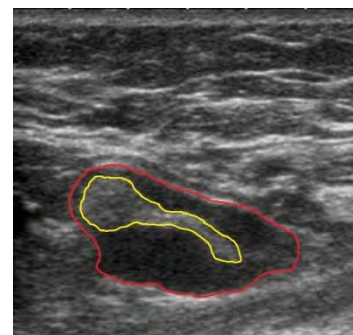
OBJECTIVE: To develop and test an automated computer algorithm for assessing the malignancy of axillary lymph nodes from sonographic images.

BACKGROUND: Ultrasonography is frequently used as part of diagnosis and guidance during lymph node biopsy. Axillary lymph node dissection (ALND) and sentinel lymph node biopsy (SLNB) are widely used surgical staging procedures. ALND alone has not been shown to improve survival of breast cancer patients and is associated with more complications than SLNB. SLNB has false negative rates ranging from 5.6 to 29.6 %¹ for lymph node metastasis staging and has been associated with a significant risk of lymphoedema (14%), a progressive pathologic condition associated with disfigurement and permanent limitations in arm mobility. Establishing an accurate, non-invasive method of lymph node metastasis staging would increase the accuracy of diagnosis with ultrasound alone, decreasing the number of unnecessary surgical staging procedures, and lowering healthcare costs. It is therefore of significant interest to explore the feasibility of developing a CAD system for this purpose.

Work toward this goal has made steady progress over the past decade and a half, but state-of-the-art methods² still require manual interventions such as clicking on the node centre to focus the analysis. In addition to accelerating workflows, fully automated methods can be used for processing entire databases of images unattended, to gather statistics and mine sonographic acquisitions for useful clinical data. Contemporary methods² also use human-understandable image features like cortical thickening, absence of fatty hila, round morphology, the presence of increased blood flow, and the long/short axis ratio to perform their analyses, but have not yet taken full advantage of more data-driven approaches recently made feasible with advances in machine learning.

METHODS: The larger project of achieving a fully automated method for lymph node metastasis staging has been separated into two parts: (i) development of an automated method for segmenting the lymph node and hilum; and (ii) training a classifier to take as input the image intensities and segmentations, and generating a prediction of lymph node malignancy. In order to ensure the basic feasibility of accurately identifying metastases from sonographic images before committing further resources, it is the second phase of this project that was completed first and is reported here.

REB approval was obtained for this pilot study and informed consent was waived. A database of 123 consecutive women undergoing surgical treatment of breast cancer was reviewed. Nodes were considered positive or negative by fine needle aspiration and surgical procedures, using axillary lymph node dissection (ALND) or sentinel lymph node biopsy (SLNB) as gold standards. Cases where a surgical procedure showed isolated tumor cells (ITC) were excluded. One hundred and ten ultrasound lymph node images (81 benign and 29 malignant lymph nodes) were evaluated and each lymph node was manually segmented delineating both the whole lymph node (red in the figure) and the lymph node hilum (yellow).



Our goal was to develop a machine learning approach to classification that could take as input the sizes, shapes, and intensities of the nodes and hila, and produce a probability estimate of malignancy. To this end, signed distance transforms were computed from the segmented boundaries of both structures, negative outside and positive inside. All distances were then normalized such that the maximum distance inside each node was one, to confer a degree of size-invariance on this feature data. The distribution of such normalized distances remains invariant to isotropic scaling, while still showing significant variation with the node's topological shape.

Feature triplets (intensity, distance from lymph node boundary, distance from hilum boundary) were collected for each pixel inside a region including the node plus pixels at a distance of 2.56 cm or less from the lymph node contour. The collection of triplets was then used to populate a 3D histogram, whose bin counts served as the predictor inputs to a support vector machine (SVM) learning algorithm. The responses used for training were the node labels of malignant or benign. Classification of the 110 lymph nodes was tested under a 10-fold cross-validation regime to estimate generalization performance and to produce receiver operating characteristic (ROC) curves.

RESULTS AND DISCUSSION: Experiments revealed the optimal histogram bin sizes to be 60/0.80/0.80 and 60/0.20/0.20 for intensity, distance from lymph node boundary, and distance from hilum boundary, outside and inside the lymph node, respectively. Using a Cauchy kernel in conjunction with the SVM produced the best results. This combination resulted in an ROC area under the curve (AUC) of 0.96, yielding for example a sensitivity/ specificity of 0.9/0.9 along the ROC diagonal, or 0.986/0.5 in the more realistic case where false negatives are vastly more problematic than false positives. Thus, the classifier could be used to identify metastases with a 1.4% miss rate, while eliminating the need for 50% of patients to undergo needless invasive procedures. This provides a strong justification for pursuing the first phase of the work, to automate the node and hilum segmentation process.

CONCLUSIONS: Our results demonstrate the feasibility of lymph node metastasis staging with computerized analysis of sonographically imaged lymph nodes.

1. Xing, Y., et al., *Meta-analysis of sentinel lymph node biopsy after preoperative chemotherapy in patients with breast cancer*. Br J Surg, 2006. **93**(5): p. 539-46.
2. Drukker K., et al., *Quantitative ultrasound image analysis of axillary lymph node status in breast cancer patients*. Int J CARS, 2013. **8**(6): p 895-903.

Tumor Perfusion Measured by Dynamic PET Imaging of First-Pass FAZA Uptake: Preliminary Results from Pancreatic Cancer Patients

Ivan Yeung¹, Alborz Gorjizadeh^{1,2}, Cristiane Metran-Nascente³, Doug Vines¹, Neesha Dhani³, David Green¹, Ur Metser⁴, Michael Milosevic¹, David Hedley³, David Jaffray^{1,2}

¹Radiation Medicine Program, Princess Margaret Hospital, ²Department of Medical Biophysics, University of Toronto and ³Department of Medical Oncology and ⁴Joint Department of Medical Imaging, Princess Margaret Hospital, Toronto, ON, Canada

Hypoxia is an important character in tumour microenvironment and it is believed to negatively impact the efficacy of radiation therapy and chemotherapy. The dysfunctional microvasculature arisen from tumour angiogenesis plays a key role in cancer therapies because perfusion is the delivery vehicle of oxygen and chemotherapeutic agents to the tumour. Therefore, measurement of both hypoxia and tumour perfusion provides an opportunity to quantify the tumour microenvironment and hence to customize therapy for individual patients. ¹⁸F-fluoroazomycin arabinoside (FAZA) is a second generation hypoxia tracer which has successfully been studied in various disease sites. Dynamic acquisition of FAZA uptake during the first pass of tracer may be able to provide measurement in tumour perfusion. This work reports our preliminary experience with tumour perfusion measurements for pancreatic cancer using PET-FAZA and first-pass tracer uptake.

FAZA PET/CT imaging was conducted for 21 patients with pancreatic cancer on a GE Discovery CT/PET Ste 16 scanner. FAZA was injected at a dosage of 5 MBq per kg body weight, followed by a dynamic scan (list mode) for 60 min. The patient rested for an hour followed by a static scan at 2 hr. Binning of the list mode scan started at 10 s interval in the first 90 s and gradually increased to 5 min toward the end of the first hour. We applied the dynamic data within the first minute to the first pass approximation to obtain tumour perfusion. The tumour was identified and contoured on the CT scans by a radiologist. The tumour contours were transferred to the dynamic PET images to give the temporal FAZA uptake in each tumour voxel. The descending aorta was also contoured on a CT slice and the arterial input function (AIF) was determined on the PET images after applying partial volume correction. Relative blood flow was computed using the first-pass approximation proposed by Mullani et al (1):

$$F = \frac{Q(t)}{E \int_0^t AIF(u) du}$$

Where F is tumour perfusion, Q(t) is the FAZA uptake in each voxel in tumour and E is the extraction fraction of FAZA. As E is between 0 and 1 but is known for FAZA, F is strictly speaking a relative measurement of tumour perfusion if we assume E=1. Applying this methodology, relative perfusion at the tumour was estimated from the initial uptake of FAZA at three consecutive times near peak arterial blood concentration. Results of median tumour perfusion (i.e. over the whole tumor) for individual patients ranged from 0.212-1.02 mL/g-min with an average value of 0.472 ± 0.175 mL/g-min amongst 21 patients. The range of tumour perfusion values is consistent with published data of studies of pancreatic cancer using DCE CT and ¹⁵O-PET (Table 1). When plotted against the max SUV values normalized to muscle SUV, a rather weak correlation was found ($r = -0.1799$) between tumour perfusion and max SUV as shown in Fig 1.

To our knowledge, this work is the first attempt to measure tumour perfusion with the first-pass uptake of FAZA. The preliminary result suggests that the method may help provide an estimate of perfusion in pancreatic tumours giving valuable insight and information for personalized cancer treatment.

Pancreas Measurement	No. patients	Modality	Value
Regional blood flow index (Kubo et al 1991) ²	11	¹⁵ O PET	0.249 ± 0.076 (max 1)
Blood flow (Miles et al 1995) ³	8 (healthy)	DCE CT	1.52 ± 0.14 (mL/g-min)
Blood flow (Abe et al 2005) ⁴	8	DCE CT	0.347 ± 0.121 (mL/g-min)
Blood flow (Xu et al 2009) ⁵	36	DCE CT	0.687 ± 0.448 (mL/g-min)
Blood flow (Komar et al 2009) ⁶	11	¹⁵ O PET	0.457 ± 0.185 (mL/g-min)

Table 1: Summary of pancreas perfusion studies using DCE-CT and ¹⁵O labeled water.

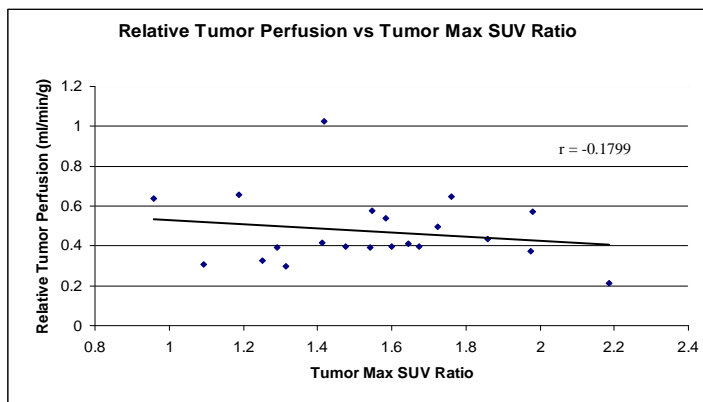


Figure 1: Comparison between relative tumor perfusion and tumor max SUV ratio for 21 patients ($r = -0.1799$)

- Mullani NA, Gould KL. First-pass measurements of regional blood flow with external detectors. *J Nucl Med.* 1983;24:577-581
- Kubo S, Yamamoto K, Magata Y et al. Assessment of pancreatic blood flow with positron emission tomography and oxygen-15-water. *Ann Nucl Med* 1991; 5: 133-138.
- Miles KA, Hayball MP, Dixon AK. Measurement of human pancreatic perfusion using dynamic computed tomography with perfusion imaging. *Br J Radiol* 1995; 68:471-475
- Abe H, Murakami T, Kubota M et al. Quantitative tissue blood flow evaluation of pancreatic tumor: comparison between xenon CT technique and perfusion CT technique based on deconvolution analysis. *Radiat Med* 2005; 23: 364-370.
- Xu J, Liang ZH, Hao SJ, Zhu L, Ashish M, Jin C, Fu DL, Ni QX. Pancreatic adenocarcinoma: dynamic 64-slice helical CT with perfusion imaging. *Abdom Imaging* 2009; 34: 759- 766.
- Komar G, Kauhaneen S, Liukko K, et al. Decreased blood flow with increased metabolic activity: a novel sign of pancreatic tumor aggressiveness. *Clin Cancer Res* 2009; 15:5511-5517.

Correlation of quantitative MRI and histology of surgical specimens in drug-resistant focal epilepsy

Maged Goubran¹, Robert R. Hammond², Sandrine de Ribaupierre³, Terry M. Peters¹, and Ali R. Khan¹

¹Imaging Laboratories, Robarts Research Institute, London, Ontario, Canada,

²Department of Pathology, Western university, London, Ontario, Canada,

³Department of Clinical Neurological Sciences, Western university, London, Ontario, Canada

Introduction

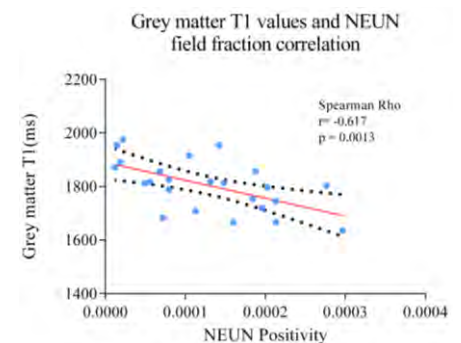
In the past decade there has been an emerging trend in research towards correlation of pre-operative brain imaging with histology in order to validate both novel and existing imaging techniques. These research protocols provide access to complementary and high resolution anatomical information that can validate, optimize, and inform pre-operative imaging techniques. A clinical example where histological validation can significantly impact patient care is drug resistant temporal lobe epilepsy (TLE). Current clinical MRI protocols used for pre-operative assessment of focal epilepsy lack sensitivity, with greater than 30% of patients diagnosed as MR negative [1]. The histology evaluation of the surgical tissue, nevertheless, often reveals gliosis or malformations of cortical development undetected pre-operatively. Such data have motivated the need for MRI-histology correlation, to validate improved pre-operative imaging for localizing epileptogenic foci, and to understand the pathological correlates of MRI signal. To this end, our objective here is to correlate quantitative MRI and histology metrics of surgical specimens from drug-resistant TLE patients.

Methods

10 temporal lobe epilepsy patients who were candidates for epilepsy surgery were recruited for this study. All patients underwent pre-operative imaging (relaxation mapping and diffusion-tensor imaging) on a 3T Discovery MR750 scanner (General Electric, Milwaukee, WI, USA). For T1 & T2 mapping the DESPOT approach [2] was used with a 1 mm isotropic resolution. Diffusion tensor imaging (DTI) was performed using DTI sequence with 41 diffusion directions, a resolution of 2.5 mm isotropic and a b-value of 1000. Following surgery the excised neocortical specimens were scanned *ex-vivo* on a 9.4T small bore magnet (Varian, Palo Alto, CA, USA), then processed for histological assessment and digitization in our collaborating pathology department. Field maps of NeuN (representing neuronal density) and GFAP (representing gliosis) immunohistochemistry stains from digitized histology of surgically resected tissue were automatically computed using the positive pixel algorithm (Aperio Technologies, Vista, CA, USA). Regions of interest (ROIs) were subsequently delineated on 100 μ m downsampled histology slices in histology space: grey matter (GM) regions defined on the cortical crown of the middle temporal gyrus and white matter (WM) regions within the deep white matter of the same gyrus. Using our previously reported histology to MRI registration protocol [3], the histology ROIs were warped to match corresponding regions on *in-vivo* quantitative maps (T1, T2, FA, MD). A final step of manual ROI correction was employed, if needed, to account for registration errors and partial volume effects. Spearman's rank correlation was employed to test for correlation between the quantitative MRI metrics: T1, T2, FA & MD, and field fractions of NeuN & GFAP in both brain tissues (GM & WM).

Results & Discussion

A negative correlation between NeuN field fraction and the T1 value in gray matter was found using both tests ($r = -0.617$, $p = 0.001$). T1 relaxation is related to water content, macromolecule concentration and water binding. Neuronal loss in the grey matter will likely result in the loss of macromolecules, which in turn decreases the amount of bound water and subsequently increases T1 [4]. A negative correlation was found between T1 and FA in white matter ($r = -0.806$, $p = 1e-05$), as well as a positive correlation between WM T1 and MD ($r = 0.643$, $p = 0.002$) and a negative correlation between WM FA and MD ($r = -0.527$, $p = 0.014$). Existing studies have also shown reduced FA and increased MD in the ipsilateral white matter in TLE [5]; our results reveal that T1 is also affected in these regions. These changes may be due to degeneration of axons, reduced packing, or demyelination [6] which may facilitate isotropic diffusion and accumulation of free water.



Conclusion

Our registration and correlation pipeline allows for quantitative assessment of the pathological correlates of MRI by employing information from both modalities, and the potential prediction of pathology from *in-vivo* MRI. This study is the first to relate *in-vivo* T1 values to the proportion of neurons in the grey matter for focal epilepsy. These preliminary findings suggest that T1 in gray matter may act as a predictor of neuronal density and thus *in-vivo* T1 mapping may provide a non-invasive tool for estimating pyramidal cell loss in neurological disorders such as epilepsy and multiple sclerosis, as well as neurodegenerative diseases as Alzheimer's disease.

References

[1] Sylaja et al. *Epilepsia* (2004) vol. 45 (7) pp. 803-808. [2] Deoni. *JMRI* (2007) vol. 26 pp. 1106-1111. [3] Goubran et al. *Neuroimage* (2013) vol. 83 pp. 770-781. [4] Schmierer et al. *Brain* (2010) vol. 133 pp. 858-867 [5] Focke et al. *Neuroimage* (2008) vol. 40 pp. 728-737. [6] Gross. *Epilepsia* (2011) vol. 52(Suppl4) pp. 32-34.

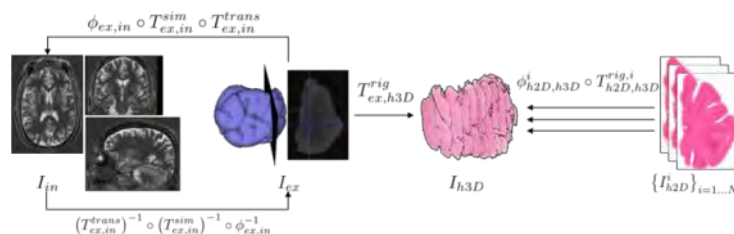


Figure 2. Overview of our histology to *in-vivo* MRI registration protocol.

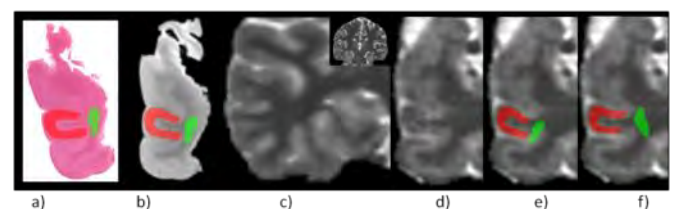


Figure 3. a) Histology ROI, b) ROI on *ex-vivo* scan, c) Unregistered *in-vivo* T1 map, d) Registered T1 map, e) Mapped ROI to match MRI slice, f) Corrected ROI

Relations of mechanical properties to CT Numbers in Human Lung

Elham Karami^{1,2}, Ting-Yim Lee^{1,2,3} (Supervisor) Abbas Samani^{1,2,4,5} (Supervisor)

¹Department of Medical Biophysics, Western University, London, Ontario; ²Imaging Research Laboratories, Robarts Research Institute, London, Ontario; ³Imaging Program, Lawson Health Research Institute, London, Ontario; ⁴Department of Electrical Engineering, Western University, London, Ontario; ⁵Graduate Program in Biomedical Engineering, Western University, London, Ontario, Canada

Lung Cancer is the leading cause of cancer death in both men and women. Among various treatment methods currently being used in the clinic, External Beam Radiation Therapy (EBRT) is used widely not only as the primary treatment method, but also in combination with chemotherapy and surgery. However, this method may lack desirable dosimetric accuracy because of respiration induced tumor motion. Recently, biomechanical modeling of the respiratory system has become a popular approach for tumor motion prediction and compensation. This approach requires reasonably accurate data pertaining to thoracic pressure variation, diaphragm position and biomechanical properties of the lung tissue in order to predict the lung tissue deformation and tumor motion.

The focus of this study is the biomechanical properties of lung tissues, and in particular tissue stiffness. The lung is known to be heterogeneous, indicating that its tissue mechanical properties are also heterogeneous. In addition, these properties are slightly different from patient to patient while pathology and aging are known to lead to significant tissue elasticity changes [1]. As such, using patient specific heterogeneous lung tissue mechanical properties is very important for achieving desirable tumor tracking accuracy which is necessary for EBRT dosimetric accuracy.

The motivation behind this study is to test a hypothesis of correlation between lung tissue stiffness and its local appearance in CT images characterized by the CT number. One rationale for this hypothesis with normal lung tissue is the variability of the microstructure within the lung where by moving down the bronchi, the concentration of alveoli increases while the vessels and bronchi become thinner. The rationale with pathological lung tissues follows the fact that pathology changes tissue structure and composition. In this study, 14 tissue samples were obtained from different regions of a porcine's lung. The stiffness of these samples, which is characterized by the tissue Young's modulus, was measured using indentation test. The samples were scanned afterwards to obtain high resolution CT images. The Young's modulus of each sample was obtained using an inverse finite element algorithm. The lung parenchyma was segmented in the CT images to exclude the vessels and bronchi. Figure 1 illustrates the Young's modulus versus the mean values of CT number for all the samples. Preliminary results indicate that the mean CT number and stiffness of lung tissue samples are correlated with $R^2 = 0.464$. While the results are encouraging, further research is necessary to consolidate the conclusion.

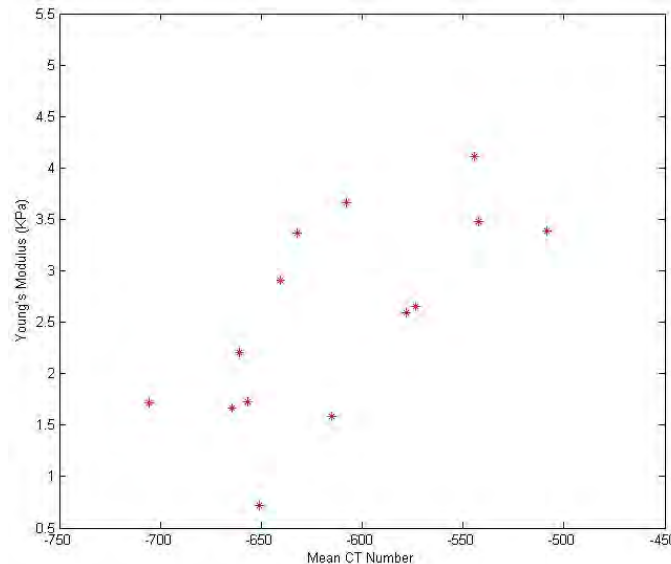


Figure 1: Young's modulus vs. mean CT number for a porcine lung tissue

References

- [1] Turner JM, Mead J, Wohl ME. Elasticity of human lungs in relation to age. *J Appl Physiol.* 1968 Dec;25(6):664–671

In Vivo Validation of a 3D Ultrasound System for Imaging the Lateral Ventricles of Neonates

Kishimoto, J¹, Fenster, A¹, Chen, N³, Lee, D³, de Ribaupierre, S^{1,4}

¹Department of Medical Biophysics, University of Western Ontario, London, Ontario, Canada

²Robarts Imaging, University, Western Ontario, London, Ontario, Canada

³Department of Medicine, University of Western Ontario, London, Ontario, Canada

⁴Department of Neonatology, University of Western Ontario, London Health Sciences Centre, London, Ontario, Canada

⁵Department of Clinical Neurological Sciences, University of Western Ontario, London Health Sciences Centre, London, Ontario, Canada

Research Supervisor: Sandrine de Ribaupierre

Dilated lateral ventricles in neonates can be due to many different causes, such as brain loss, or congenital malformation; however, the main cause is hydrocephalus, which is the accumulation of fluid within the ventricular system. Hydrocephalus can raise intracranial pressure resulting in secondary brain damage, and up to 25% of patients with severely enlarged ventricles have delayed development, neurological deficits or epilepsy later in life¹. Ventricle enlargement in preterm neonates is clinically monitored with head circumference and using 2D US through the fontanel. The sensitivity of 2D US to dilation is poor because it cannot provide accurate measurements of irregular volumes, so most clinical evaluations are of a qualitative nature.

We developed a 3DUS system to image the cerebral ventricles of neonates within the confines of incubators and can be easily translated to more open environments. Previously, we have validated this system using ventricle-like agar phantoms.² Ventricle volumes can be segmented from these images giving a quantitative volumetric measurement of ventricle enlargement without moving the patient into an imaging facility.

We report on two *in vivo* validation studies: 1) comparing 3D US ventricle volumes before and after clinically necessary interventions (ventricle tap) removing CSF from the ventricles of incubator bound neonates, and 2) comparing 3D US ventricle volumes to those from MRI in term equivalent preterm infants. Post-intervention ventricle volumes were less than pre-intervention measurements for all patients and all interventions. We found high correlations ($R = 0.97$) between the difference in ventricle volume and the reported removed CSF with the slope not significantly different than 1 ($p < 0.05$) (Figure 1). Comparisons between ventricle volumes from 3D US and MR images taken 4 (± 3.8) days of each other failed to show significant difference ($p=0.44$) between 3D US and MRI through paired t-test (Figure

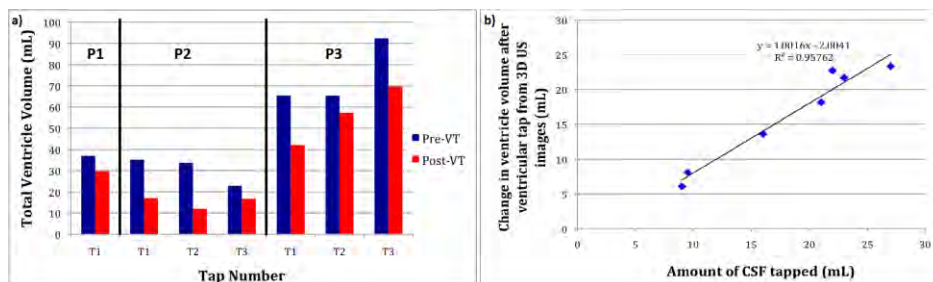


Figure 1a) Three different IVH patients who required taps for clinical reasons imaged pre (blue) and post (red) ventricular tap and the ventricle volumes (mL) segmented from each 3DUS image. **b)** Least squared fit of the change in ventricle volume measured before and after tap against reported amount of CSF removed.

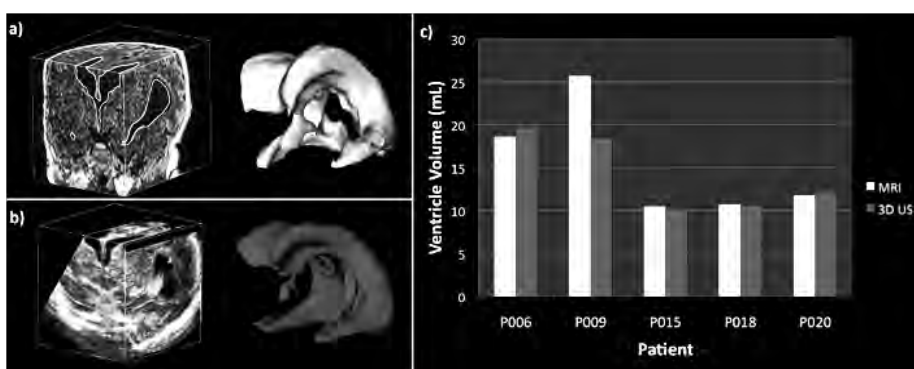


Figure 2 – Segmented ventricles from patient P015 in MRI **a)** and 3DUS **b)**. Ventricle volumes measured for all 5 IVH patients at term equivalent age from MRI (white) and 3DUS (grey) are shown in **c)**.

Figure 2 – MRI and 3D US Measurement

[1] Miranda, P., "Intraventricular hemorrhage and posthemorrhagic hydrocephalus in the preterm infant," *Minerva Pediatr*, 62(1), 79-89 (2010).

[2] Kishimoto, J., de Ribaupierre, S., Lee, D. S. *et al.*, "3D ultrasound system to investigate intraventricular hemorrhage in preterm neonates," *Phys Med Biol*, 58(21), 7513-26 (2013).

Early prediction of lung cancer recurrence after stereotactic radiotherapy using second-order texture statistics

Sarah A. Mattonen¹, David A. Palma^{1,2}, Cornelis J. A. Haasbeek³, Suresh Senan³ and Aaron D. Ward¹

¹ Department of Medical Biophysics, Western University, London, Ontario, Canada

² Division of Radiation Oncology, London Regional Cancer Program, London, Ontario, Canada

³ Department of Radiation Oncology, VU University Medical Center, Amsterdam, Netherlands

Research supervisors: Aaron D. Ward & David A. Palma

Purpose: Benign radiation-induced lung injury (RILI) is a common finding following stereotactic ablative radiotherapy (SABR) for lung cancer, and is often difficult to differentiate from a recurring tumour due to the ablative doses and highly conformal treatment with SABR. Current approaches to treatment response assessment have shown limited ability to predict recurrence within 6 months of treatment. The purpose of our study was to evaluate the accuracy of second-order texture statistics for prediction of eventual recurrence based on computed tomography (CT) images acquired within 6 months of treatment.

Methods: We studied 22 SABR patients with a total of 24 lesions (11 recurrence, 13 RILI). Consolidative (from which longest axial diameter measures were taken) and ground-glass opacity (GGO) regions were manually delineated on post-SABR CT images (Fig. 1). For each region, we calculated the 3D volume, mean and standard deviation of density (the latter measuring global texture), and seven second-order gray-level co-occurrence matrix texture features: energy, entropy, correlation, inertia, difference moment, cluster shade, and cluster prominence. Recurrence vs. RILI classification was performed using a linear Bayes normal classifier and cross validation (CV). Automatic consolidation expansion (“peri-consolidative GGO”) was also investigated to act as a GGO surrogate.

Results: 46 diagnostic CT scans scheduled for approximately 3 and 6 months post-treatment were binned based on their recorded scan dates into 2–5 month and 5–8 month follow-up time ranges. The top features for prediction of recurrence were all texture features within the GGO and included energy, entropy, correlation, inertia, and first-order texture (standard deviation of density). These features predicted recurrence with 2-fold cross validation (CV) accuracies of 70–77% at 2–5 months post-SABR, with energy, entropy (Fig. 2), and first-order texture having leave-one-out (LOO) CV accuracies greater than 80%. Our results also suggest that automatic expansion of the consolidation region produced reproducible results when compared to manually delineated GGO, as seen in Fig. 3.

Conclusions: Second-order texture features within the GGO have the potential to predict recurrence in individual patients within 6 months of SABR, with LOOCV accuracies greater than 80%. Automatic expansion of the consolidative region shows excellent reproducibility, eliminating the need for manual GGO delineation. If validated on a larger data set, this could lead to a clinically useful computer-aided diagnosis system which could allow for early salvage therapy for patients with recurrence.

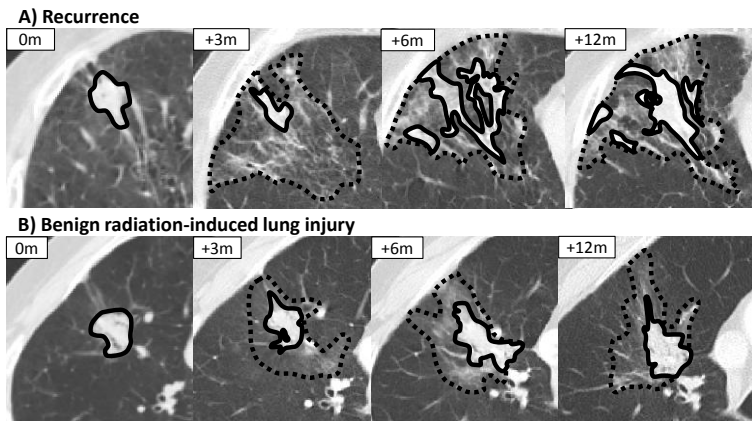


Figure 1: Delineations of consolidative (solid lines) and ground-glass opacity (dashed lines) regions throughout follow-up for a patient with recurrence (A) and radiation-induced lung injury (B).

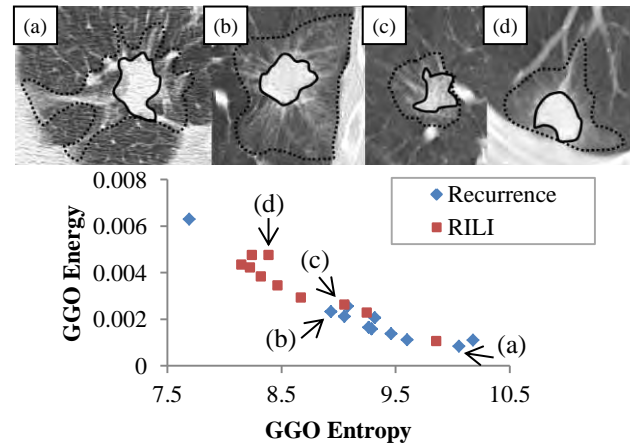


Figure 2: All lesions plotted by their energy and entropy values in the GGO at 2–5 months post treatment. Representative appearances of the GGO are shown for 2 recurrence and 2 RILI lesions.

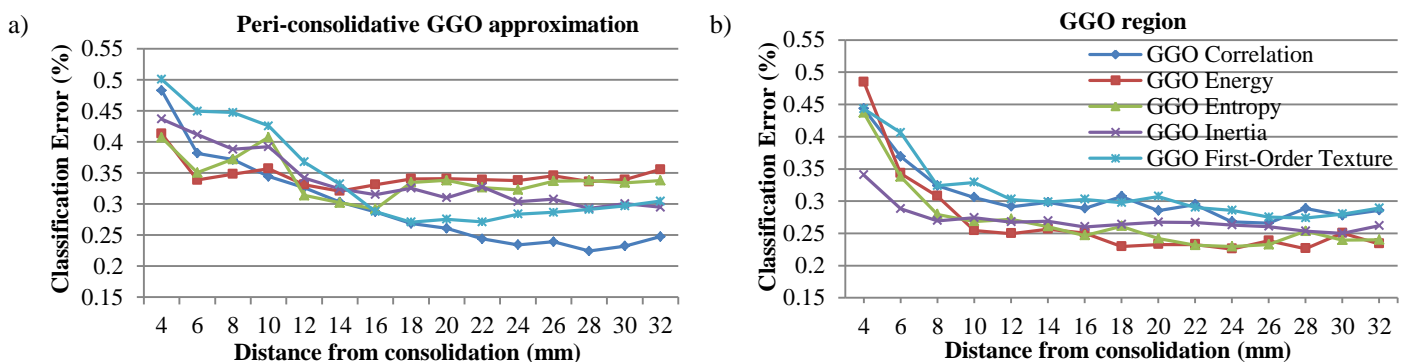


Figure 3: Classification error on 2-fold cross validation for our top five features at 2–5 months post-SABR where (a) corresponds to peri-consolidative regions (extents of which are indicated on the horizontal axis) and (b) is the manual GGO within the same extents. In an ideal scenario, a) would have identical errors to b).

Motion Magnification for Vessel Sparing and Avoidance in Endoscopic Surgery

A. Jonathan McLeod and Terry M. Peters

Robarts Research Institute, Western University, London Ontario

Vessel sparing and avoidance is a major challenge in many endoscopic and laparoscopic procedures. The limited angles of view and lack of haptic feedback in these procedures can make identifying and avoiding vessels difficult. When arterial vessels are close enough to the surface their pulsatile motion provides a valuable cue to the surgeon which aids in their identification. However, in many cases this motion is too subtle to be noticed and even in the best conditions can require great effort to detect. A recent technique proposed by Wu et al, Eulerian Video Magnification, creates a synthetic video with enhanced motion by spatially and temporally filtering the video stream [1]. Based on this approach, a method is presented here to enhance motion of important vessels during surgery that uses adaptive filtering to identify the heart rate and amplify motion due to the pulsation. This method is applied to videos acquired from robotic prostatectomy and endoscopic third ventriculostomy procedures.

Laparoscopic and robot assisted radical prostatectomy are minimally invasive alternatives to open surgery where the cancerous prostate is removed under laparoscopic guidance. Nerve sparing procedures are especially challenging as the neurovascular bundles, which must be spared, are difficult to identify. Pulsation of the neurovascular bundles can provide an important cue to the surgeon but is very subtle and requires a bloodless field and a laparoscope with appropriate magnification to detect [2]. Motion magnification can reveal pulsation that appears nearly imperceptible in the original video. The proposed method was applied to a laparoscopic video acquired during a robot assisted prostatectomy (Figure 1).

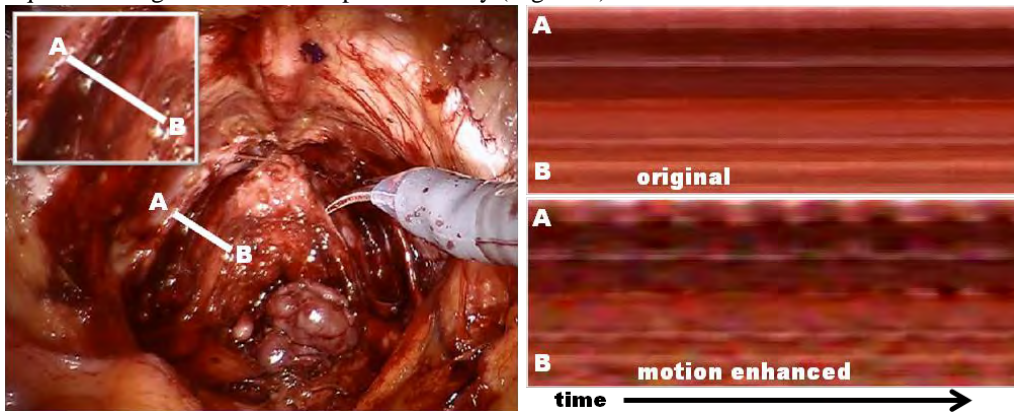


Figure 1: A frame from the original video is shown on the left with the line AB running through the region where the neurovascular bundles are located. The pixels along this line are shown with respect to time on the right. While nearly invisible in the original video, pulsation in this region becomes evident after motion magnification.

Another surgery that can benefit from motion magnification is endoscopic third ventriculostomy (ETV) which is used to treat obstructive hydrocephalus. This procedure bypasses the obstruction, including congenital aqueductal stenosis or obstruction by a tumor/cyst, by fenestrating the floor of the third ventricle allowing cerebral spinal fluid to flow directly into the basilar cistern. A major challenge during this procedure is to avoid damaging the basilar artery which lies under the floor of the third ventricle. In some cases, the basilar artery is clearly visible but in others it is not. Motion magnification can help in identifying the basilar artery by enhancing its pulsation. When applied to a video acquired during ETV, the motion of the basilar artery is greatly enhanced (figure 2).

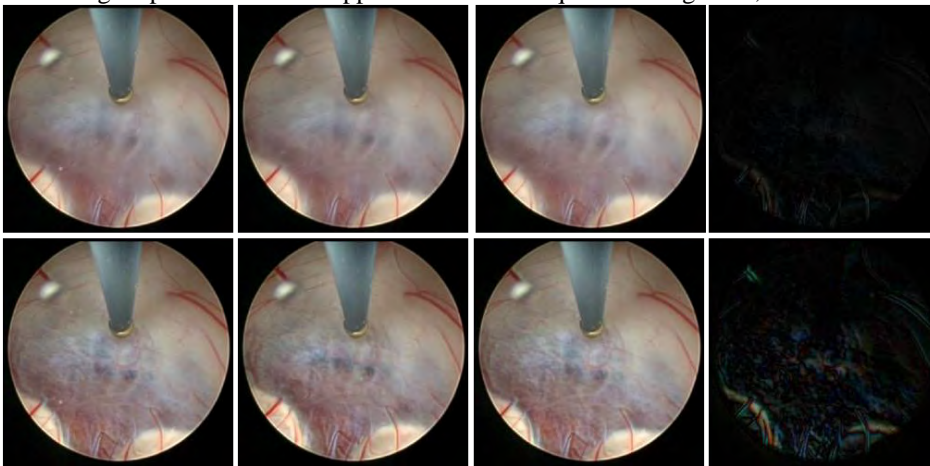


Figure 2: A series of 3 frames covering a cardiac cycle acquired during ETV are shown both before (top) and after (bottom) motion magnification. The pulsation is much more visible in the motion magnified video especially during systole (second frames) where a slight exaggeration of the highlights and shadows helps enhance the perception of motion. On the far right are difference images between systole and diastole with the basilar artery much more visible in the difference image of the motion magnified video which is indicative of the greatly enhanced pulsation.

[1] H.-Y. Wu, M. Rubinstein, E. Shih, J. Guttag, F. Durand, and W. Freeman, "Eulerian video magnification for revealing subtle changes in the world," *ACM Trans. Graph.*, vol. 31, no. 4, pp. 65:1–65:8, Jul. 2012.

[2] A. Tewari, J. O. Peabody, M. Fischer, R. Sarle, G. Vallancien, V. Delmas, M. Hassan, A. Bansal, A. K. Hemal, B. Guillonnet, and M. Menon, "An Operative and Anatomic Study to Help in Nerve Sparing during Laparoscopic and Robotic Radical Prostatectomy," *European Urology*, vol. 43, no. 5, pp. 444–454, May 2003

Preliminary Clinical Study of a True Elastography Method for Prostate Cancer Assessment

Seyed Reza Mousavi¹, Ali Sadeghi-Naini², Gregory J. Czarnota², and Abbas Samani^{1,3}

¹Department of Electrical and Computer Engineering, Western University, London, ON

²Odette Cancer Research Program, Sunnybrook Research Institute, Sunnybrook Health Sciences Centre, Toronto, ON

³Department of Medical Biophysics, Western University, London, ON

Research Supervisor: Dr. Abbas Samani

Prostate cancer detection at early stages is crucial for desirable treatment outcome. Various types of cancers including prostate cancer are known to be associated with biological changes that lead to tissue stiffening. Hence, among available imaging modalities, ultrasound (US) elastography is being developed as an effective clinical tool for prostate cancer diagnosis. Current clinical US elastography systems utilize strain imaging where tissue strain images are generated to approximate the tissue elastic modulus distribution. While strain images can be generated in real-time fashion, they lack the accuracy necessary for having desirable sensitivity and specificity. Furthermore, strain images are qualitative; hence they are not suitable for tumor classification which is necessary for accurate distinction of aggressive prostate cancers from more indolent forms. To improve strain imaging, full inversion based elastography techniques were proposed. Among these techniques, a constrained elastography technique was developed which showed promising results as long as the tumor geometry can be obtained accurately from the imaging modality used in conjunction with the elastography system. This requirement is not easy to fulfill, especially with US imaging. To address this issue, we present an unconstrained full inversion prostate elastography method in conjunction with US imaging where knowledge of tissue geometry is not necessary. The proposed technique is a quasi-static elastography technique which uses ultrasound imaging to acquire tissue displacements resulting from transrectal ultrasound mechanical stimulation. The displacements are used as data for the tissue elasticity reconstruction. This reconstruction is formulated using an inverse problem framework where elastic tissue deformation equations are fully inverted using an iterative scheme. Each iteration in this scheme involves stress calculation followed by elastic modulus updating. The iterative process is continued until convergence is achieved.

In this work, *in silico* and tissue mimicking phantom studies were conducted to validate the proposed technique. These studies were followed by a clinical pilot study involving prostate cancer patients with whole-mount histopathology analysis on prostatectomy specimens to confirm a cancer location. The phantom studies demonstrated robustness and reasonably high accuracy of the proposed method. Obtained Young's modulus ratios indicated reconstruction errors of less than 12%. Also, comparison of reconstructed elastic modulus images of the clinical cases to whole-mount histopathology slides indicated reasonably accurate consistency observed between cancerous lesions identified by histopathology and high stiffness areas of the elastography images. Results show highly favorable ability of the proposed method to detect and classify prostate cancer compared to B-mode and strain imaging. The proposed elastography system does not require any additional hardware attachment for mechanical stimulation or data acquisition while the elasticity reconstruction algorithm can be easily implemented, leading to a low cost system that can be potentially utilized as an effective clinical tool for prostate cancer diagnosis.

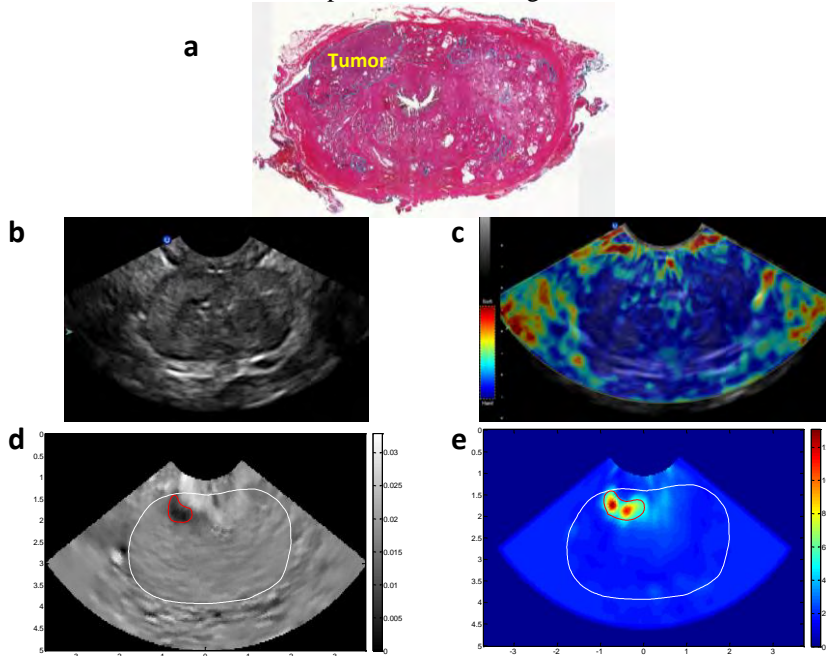


Figure 1. Macroscopic image of the whole-mount histopathology section of a prostatectomy specimen (a), demonstrating the cancerous areas contoured by a pathologist. The scale bar is ~1 cm. B-mode ultrasound image (b), clinical strain image (c), calculated strain image (d) and reconstructed YM image corresponding to patient 1. Prostate cancer is visible as a hypo-intensity area in the reconstructed strain image and as two nodules in the reconstructed YM image (contoured in white). (the depth of the fan in all images is 4 cm)

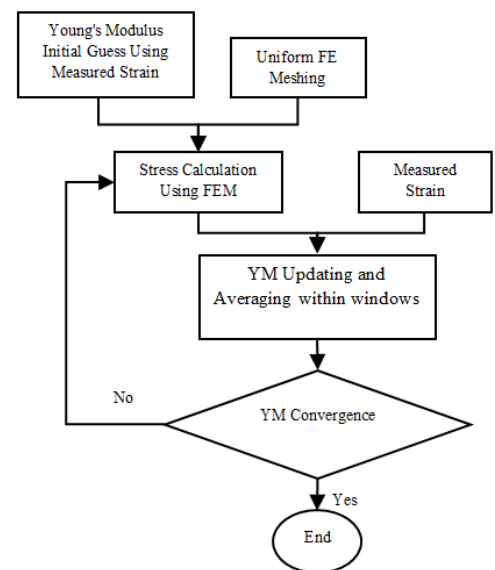


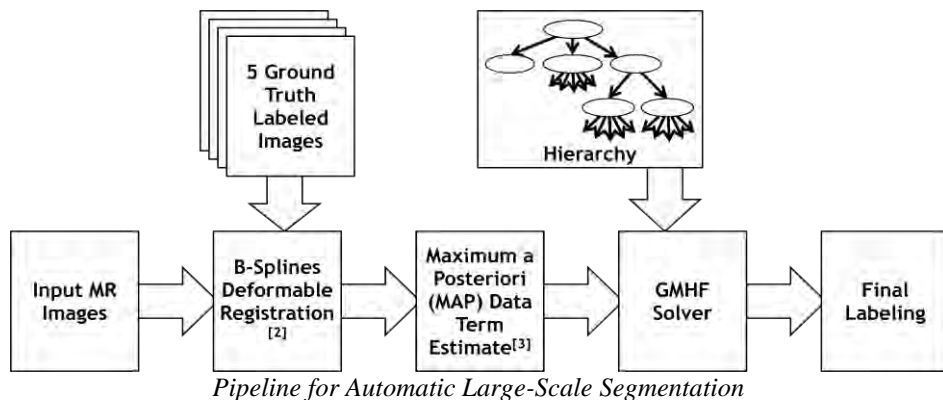
Figure 2. Flow chart illustrating the unconstrained iterative procedure for YM reconstruction.

Large-Scale Image Segmentation under Hierarchical Constraints

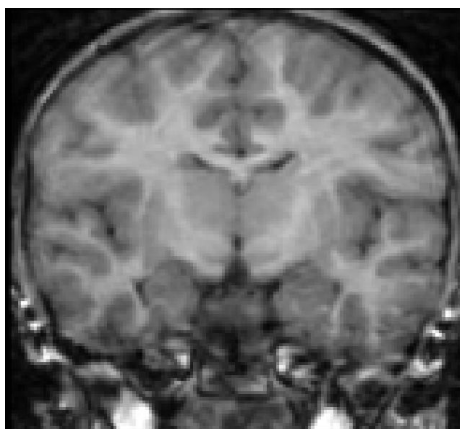
M. Rajchl^(1,2), J.S.H. Baxter^(1,2), T.M. Peters^(1,2), & J. Yuan⁽²⁾

(1) Biomedical Engineering Graduate Program, (2) Robarts Research Institute, Western University, London, ON;

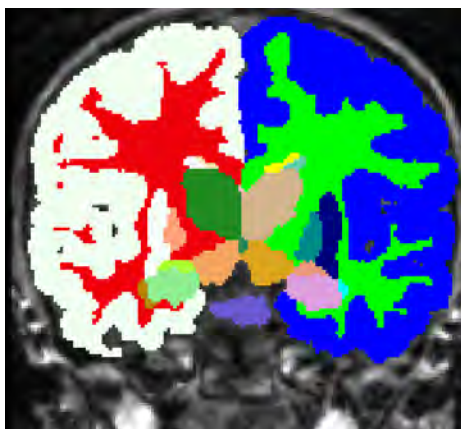
Multi-region segmentation problems involve the partitioning of images into a large number of regions simultaneously, and pose an interesting problem for medical imaging. In particular, a large portion of knowledge about some anatomical features can be expressed in relative terms, that is, relative to other anatomical features in the image. To account for anatomical knowledge concerning the grouping and hierarchical structure of the anatomy, one can use hierarchical grouping constraints. [1] Generalized hierarchical max-flow segmentation, which allows for large-scale segmentation problems under hierarchical constraints, handles these constraints simultaneously and with global optimality.



The large-scale segmentation problem such as whole brain or whole heart partitioning can be automated using a robust, multi-atlas approach. In this approach, multiple labeled images are used as a collection of atlases. Once a new image is registered to these atlases, [2] a maximum *a posteriori* cost term can be assigned to each voxel based on its intensity and consistency in which the atlases agree on its label. [3] These terms are then used as input to a generalized hierarchical max-flow solver.



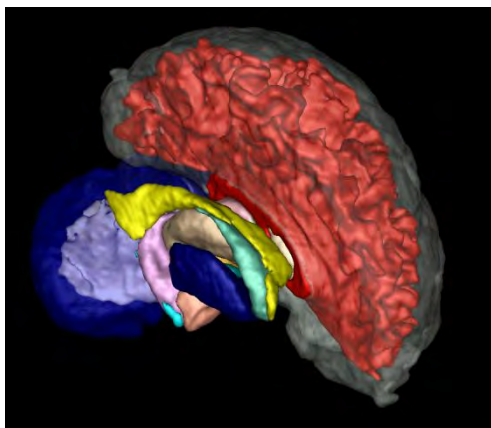
T1w MRI (IBSR)



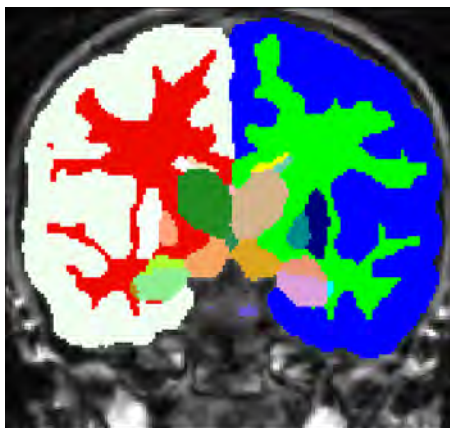
Potts Model Segmentation

This framework was evaluated against the commonly used Potts model using the same maximum *a posteriori* cost terms. The images used were from the IBSR database including 36 distinct labels. Both performed better than the un-regularized segmentation. Qualitatively, GHMF segmentations retained more fine details without under-segmentation where the Potts model experienced difficulty.

In future, this framework will be extended to the segmentation of gadolinium enhanced cardiac MRI, and to the segmentation of co-registered cranial MRI from the MICCAI 2013 challenge database.



Isosurface Rendering



GHMF Segmentation

[1] Rajchl et al, "Interactive Hierarchical Max-Flow Segmentation of Scar Tissue from Late-Enhancement Cardiac MR Images"

[2] Modat et al, "Fast free-form deformation using graphics processing units"

[3] van der Lijn et al, "Hippocampus segmentation in MR Images using atlas registration, voxel classification, and graph cuts"

A Hybrid Biomechanical Intensity Based Deformable Image Registration For Lung 4DCT

Navid Samavati¹, Mike Velec², Kristy K. Brock^{1,2,3}

1) Institute of Biomaterials and Biomedical Engineering (IBBME), University of Toronto, ON

2) Department of Radiation Oncology, University of Toronto, ON

3) Department of Radiation Oncology, University of Michigan, Ann Arbor, MI

Purpose. Deformable Image Registration (DIR) has become a necessary tool in various image guided interventions. Previous studies have indicated that Morfeus, a biomechanical model based deformable registration algorithm is an accurate and reliable technique for a variety of anatomical sites [1]. However, in some cases, Morfeus may lead to clinically significant local regions of residual error identified by Target Registration Error (TRE). These local uncertainties may result due to lack of accurate material property measurement and complexity of the actual boundary conditions. These limitations could be addressed by taking into account the image contrast or features. In this work, a hybrid DIR method is presented to ensure consistent, high-level accuracy across the entire anatomy by combining an intensity-based algorithm with Morfeus.

Methods. Morfeus, was used to register inhale to exhale images of the lungs obtained using 4DCT scans of 26 patients. For each patient, a 3D volumetric multi-organ model was generated by semi-automatic segmentation of the lungs, body and the tumor(s). The interface of the lungs and the chest cavity was modeled using frictionless contact surface allowing the sliding of the lungs in the pleural cavity. Lungs, tumors, and body were assigned Young's moduli of 7.8KPa, 78KPa, and 1.5KP, respectively and Poisson's ratio of 0.4 with the assumption of linear elasticity. The deformed inhale image was determined based on the Displacement Vector Field (DVF) by warping the inhale image using linear interpolation of elemental displacements on the image grid. This image was then registered to the exhale image by Drop (Munich, Germany) [2], a registration algorithm based on BSpline deformation modeling and Markov Random Field (MRF) energy linear programming. Drop registration refined the deformations provided by Morfeus in the regions where further alignment is required due to large intensity differences quantified using the Sum of Absolute Differences (SAD) similarity metric. The majority of Drop parameters were set empirically while an explicit adjustment process was applied for the number of pyramid levels, grid spacing, and regularization coefficient. To assess the quality of registration, Target Registration Error (TRE) was calculated by the distance of common anatomical (bifurcation) points on the images before and after registration. For each patient a minimum of 30 points/lung were used with the average of 83 points per patient.

Results. The performance of the hybrid method was compared against Morfeus and Drop-alone. The hybrid method reduces the average mean±SD (90th percentile) TRE to 1.5±1.4 (3.0) mm compared to 3.1±2.0 (5.8) using Morfeus, and 2.7±2.9 (6.9) using Drop-alone. A 1-tail student t-test reveals that hybrid method on average TRE performs better than Morfeus and Drop-alone with p-values of 1.3E-11 and 4.2E-7, respectively. In addition, the average 90th% TRE of all patients using hybrid was significantly lower than that of both Morfeus and Drop-alone with p-values of 4.9E-8 and 1.5E-5, respectively. The 90th% TRE values of all three methods for each patients is shown in Figure 1.

Conclusion. In this work, an accurate hybrid biomechanical model based DIR was developed by a refinement step using Drop. Biomechanical modeling component of this hybrid method could approximately model the physical deformation of the lungs based on surface matching as the boundary condition and allowing a contact surface between the lungs and the chest cavity. A fine refinement step allowed significant reduction in the residual errors while preserving the desired properties of the biomechanical model.

References

[1] Brock, K. K., Sharpe, M. B., Dawson, L. A., Kim, S. M., & Jaffray, D. A. (2005). Accuracy of finite element model-based multi-organ deformable image registration. *Medical physics*, 32, 1647.

[2] Glocker, B., Komodakis, N., Tziritas, G., Navab, N., & Paragios, N. (2008). Dense image registration through MRFs and efficient linear programming. *Medical image analysis*, 12(6), 731-741.

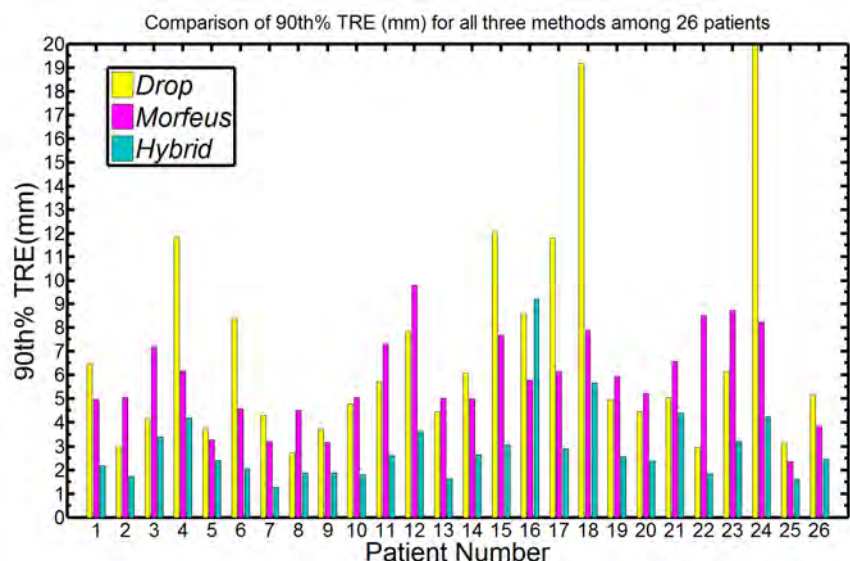


Figure 1. 90th percentile TRE (in mm) for all 26 patients

Inter-operator variability of 3D prostate MRI segmentation using manual and semi-automatic methods

Maysam Shahedi^{1,2,3}, Derek W. Cool^{2,5}, Cesare Romagnoli^{2,5}, Glenn Bauman^{1,4,6}, Matthew Bastian-Jordan⁵, Eli Gibson^{2,3}, George Rodrigues^{1,6}, Belal Ahmad^{1,6}, Michael Lock^{1,6}, Aaron Fenster^{2,3,4,5}, Aaron D. Ward^{1,3,4,6}

¹London Regional Cancer Program, London, ON; ²Robarts Research Institute, ³Graduate Program in Biomedical Engineering, ⁴Department of Medical Biophysics, ⁵Department of Medical Imaging, ⁶Department of Oncology, The University of Western Ontario

Purpose: 3D prostate image segmentation is useful for prostate cancer diagnosis and therapy guidance, but is time-consuming to perform manually and subject to inter-observer variability [1]. We have developed a semi-automatic segmentation method for T2-weighted endorectal magnetic resonance (MR) images and measured its accuracy, inter-operator variability, and user interaction time.

Materials and methods: MR images of 42 patients were acquired at 1.5T or 3T field strengths. Our segmentation technique utilizes inter-subject prostate shape and local boundary appearance similarity that is learned via the calculation of a point distribution model (PDM) and a set of local mean intensity patches on the prostate border during training. The user selects the base and apex slices as well as the prostatic centre on apex, base and a mid-gland and defines the anteroposterior symmetry axis at the mid-gland. These inputs are used to orient a set of 36 equally spaced rays on each axial slice, one corresponding to each of the learned mean intensity patches, along which we translated each corresponding mean intensity patch to find the point with the highest normalized cross-correlation. These boundary points were then regularized using the PDM. We evaluated our method against one manual segmentation reference using leave-one-out cross validation with complementary boundary-based (mean absolute distance, MAD), regional overlap (Dice similarity coefficient [DSC], recall, and precision) and volume difference (ΔV) metrics. We applied these metrics to the whole gland as well as to the most superior third (base region), the middle third (mid-gland) and the most inferior third (apex region) of the gland. To measure the inter-operator variability for the semi-automated tool, 9 operators used this algorithm to segment a subset of 10 3D images. Three manual segmentation references were available for these 10 images. We measured differences in time and accuracy as well as inter-operator variability for manual and our semi-automatic method on this subset comparing the results to Simultaneous Truth and Performance Level Estimation (STAPLE) [2] reference.

Results: On our 42 subjects with a single operator, we measured a mean \pm std MAD of 2.0 ± 0.5 mm, DSC of $82\pm 4\%$, recall of $77\pm 9\%$, precision of $88\pm 6\%$, and ΔV of -4.6 ± 7.2 cc for the whole gland. For the prostatic apex, mid-gland, and base, respectively, we measured MADs of 2.0 ± 0.7 mm, 1.6 ± 0.5 mm and 2.6 ± 0.8 mm, DSCs of $79\pm 6\%$, $90\pm 3\%$ and $73\pm 10\%$, recalls of $82\pm 14\%$, $90\pm 7\%$ and $61\pm 14\%$, precisions of $80\pm 13\%$, $91\pm 6\%$ and $93\pm 6\%$, and ΔV s of 0.1 ± 3.3 cc, -0.1 ± 2.0 cc and -4.5 ± 3.7 cc. Figure 1 shows some qualitative results of the algorithm.

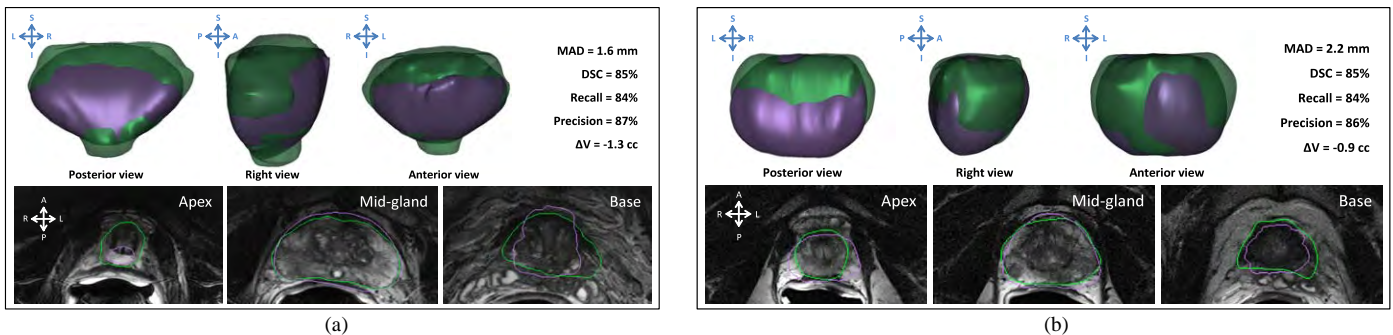


Figure 1: Qualitative results for two subjects (a, b) in 3D and for three sample slices at apex, mid-gland and base, with the evaluation metric measurements for whole gland.

The mean accuracies for 9 operators on 10 subjects did not differ by more than 0.9 mm for MAD, 12% for DSC, 18% for recall, 14% for precision, and 4.8 cc for ΔV . Table 1 shows the measured inter-operator variability based on 95% prediction interval for manual and semi-automatic segmentation, respectively.

Table 1: Inter-operator variability for manual/semi-automatic segmentation based on 95% prediction interval range in different anatomical regions based on different metrics

Region of interest	MAD (mm)	DSC (%)	Recall (%)	Precision (%)	ΔV (cc)
Whole gland	$\pm 1.6/\pm 0.6$	$\pm 22/\pm 8$	$\pm 12/\pm 14$	$\pm 37/\pm 6$	$\pm 21.2/\pm 5.8$
Mid-gland(1/3)	$\pm 1.4/\pm 0.6$	$\pm 10/\pm 4$	$\pm 4/\pm 6$	$\pm 20/\pm 5$	$\pm 4.1/\pm 1.3$
Apex (1/3)	$\pm 2.0/\pm 0.8$	$\pm 29/\pm 9$	$\pm 16/\pm 16$	$\pm 45/\pm 15$	$\pm 6.5/\pm 2.4$
Base (1/3)	$\pm 2.4/\pm 1.1$	$\pm 27/\pm 13$	$\pm 22/\pm 23$	$\pm 43/\pm 12$	$\pm 9.4/\pm 4.8$

The algorithm required an average of 28 seconds of user interaction time, and total computation time for segmentation was less than 2 minutes for each subject using a non-optimized Matlab research platform.

We tested the impact of the trainer, operator and reference segmentation on our algorithm using a three-way ANOVA test, and observed that in all regions of interest, the reference has a significant impact on a minimum of three metrics. This test also showed that with the exception of the base, no significant impact of the operator on any of the metrics was detected.

Conclusions: Learned shape and local intensity information can usefully guide a prostate segmentation algorithm to accurate solutions with minimal user input and inter-operator variability compared to manual segmentation inter-operator variability. For accuracy measurement of a segmentation algorithm using only one manual segmentation as a reference standard, it is important to consider the measured segmentation errors in the context of inter-operator variability; the use of multiple reference segmentations is advisable.

References:

- [1] W Smith *et al*, Int J Rad Onc Biol Phys 67(4), 123–47 (2007) [2] S Warfield *et al*, IEEE Trans Med Imaging 23, 903-921 (2004)

Ultra-short Echo Time (UTE) MRI and CT of Bronchiectasis and Emphysema: Tissue Density Measurements and Relationship to Pulmonary Function Tests

Weijing Ma¹, Khadija Sheikh^{1,2}, Damien Pike^{1,2}, Sarah Svenningsen^{1,2}, Harvey O Coxson³, David G McCormack⁴, and Grace Parraga^{1,2}

¹Imaging Research Laboratories, Robarts Research Institute, London, CANADA; ²Department of Medical Biophysics, The University of Western Ontario, London, CANADA; ³Department of Radiology, University of British Columbia, Vancouver, CANADA;

⁴Division of Respiriology, Department of Medicine, The University of Western Ontario, London, CANADA

RATIONALE: While CT is the main pulmonary imaging tool for clinical and research evaluations, serial studies of chronic obstructive lung disease including emphysema and bronchiectasis are sometimes limited because of concerns related to ionizing radiation from repeated CT examinations. In addition, although magnetic resonance imaging (MRI) methods have been developed using noble gas and other contrast mechanisms, these have not yet been translated to clinical use because of their cost and complexity. To address these limitations, we are developing ultra-short echo time MRI (UTE MRI) that can be made available on all conventional MR scanners to quantitatively evaluate tissue density, inflammation and mucous plugging in obstructive lung diseases such as bronchiectasis and COPD. We hypothesize that UTE signal intensity measurements directly reflect tissue density measurements related to parenchymal abnormalities including emphysema, mucous plugging and airway abnormalities.

METHODS: Twenty-eight subjects including 12 subjects with a diagnosis of bronchiectasis (70±9yr, four males) and 16 subjects with COPD (66±9yr, nine males) provided written informed consent to pulmonary function tests (PFTs), UTE and hyperpolarized ³He MRI and CT. ³He MRI ADC and CT emphysema measurements (RA₉₅₀: relative area of the density histogram ≤ -950; HU₁₅: 15th percentile of the frequency distribution histogram in HU) were generated for comparison with mean signal intensity measurements from the MRI signal intensity histogram. Linear regression and nonparametric Spearman correlations were used to evaluate the relationship between UTE and ³He MRI, CT and PFTs.

RESULTS: Figure 1 shows the centre coronal slice of normalized UTE SI maps, CT images with relative area (RA) emphysema mask for 15th percentile of the HU (HU₁₅), and -950 HU (RA₉₅₀) and ³He apparent diffusion coefficient (ADC) maps for two representative subjects. There were significant differences for subjects with bronchiectasis and COPD for FEV₁/FVC (p<.0001), FRC% (p=.001), RV% (p=.002), RA₉₅₀ (p=.01) and ³He ADC (p=.007). In subjects with bronchiectasis, UTE MRI signal intensity significantly correlated with CT measurements including HU₁₅ (r=.91, p<.0003) and RA₉₅₀ (r=-.85, p<.0003) as well as FEV₁/FVC (r=.67, p=.04), RV% (r=-.83, p=.008) and TLC% (r=-.76, p=.02). In COPD patients with emphysema, UTE MRI signal intensity significantly correlated with HU₁₅ (r=.73, p=.008) and RA₉₅₀ (r=-.72, p=.006) as well as DL_{CO} (r=.60, p=.048), FEV₁/FVC (r=.71, p=.02), FRC% (r=-.62, p=.04), RV% (r=-.50, p=.048), and ³He ADC (r=-.55, p=.03).

CONCLUSIONS: Bronchiectasis and emphysema are chronic regional pulmonary diseases that require new robust, regional and non-invasive measurement tools for serial and longitudinal studies. Conventional MRI methods for pulmonary tissue imaging can be enhanced using UTE methods to directly reflect regional abnormalities related to pulmonary function and CT measurements of disease.

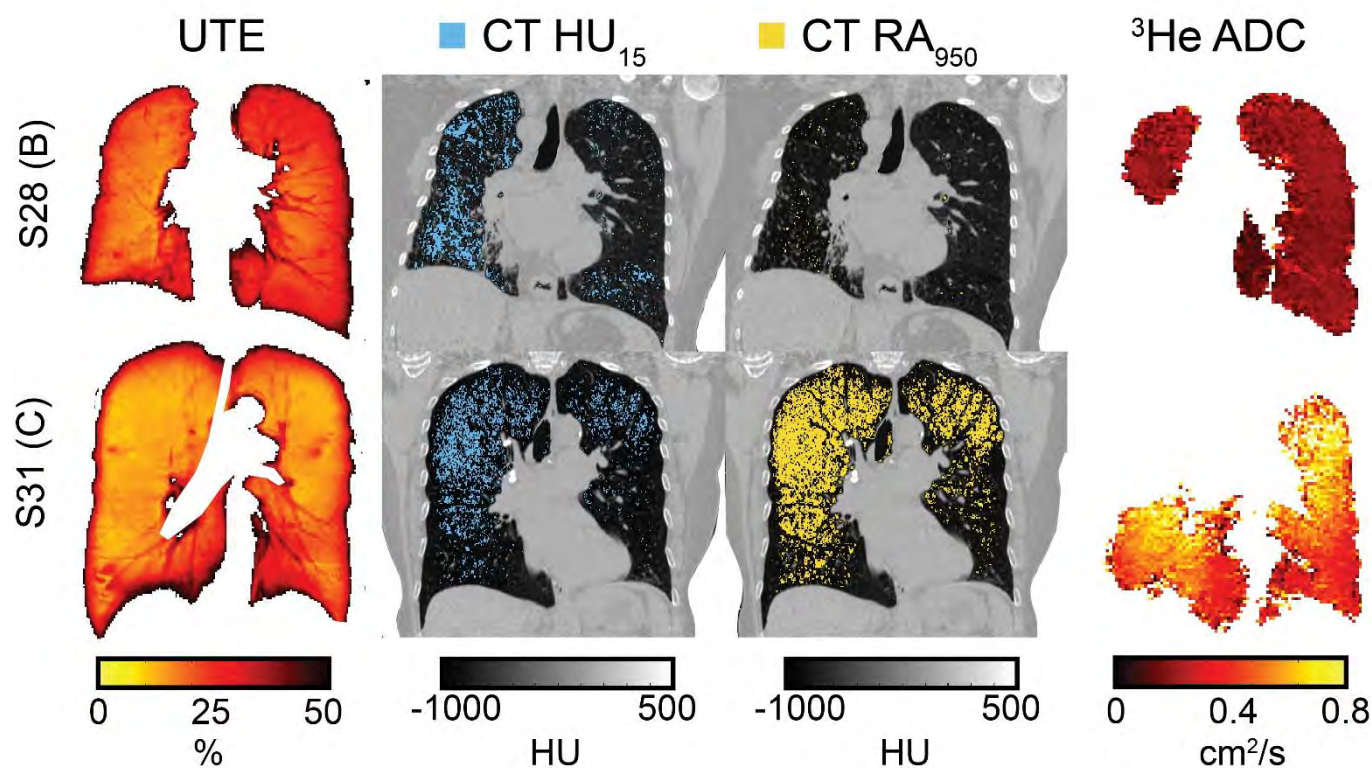


Figure 1. Centre coronal slice MRI and CT for two representative subjects.

Normalized UTE SI maps, CT images with relative area (RA) emphysema mask for 15th percentile of the HU (HU₁₅), and -950 HU (RA₉₅₀) and ³He apparent diffusion coefficient (ADC) maps. S28 is 58 yr female with a diagnosis of bronchiectasis with FEV₁=43%_{pred}, FEV₁/FVC=77%, DL_{CO}=113%_{pred}. S31 is a 75 yr female with a diagnosis of COPD with FEV₁=46%_{pred}, FEV₁/FVC=39%, DL_{CO}=29%_{pred}.

Two Dimensional Radial Pulmonary Ultra-short time ^1H MRI: Reproducibility in COPD and Bronchiectasis

K Sheikh^{1,2}, W Ma^{1,2}, F Guo^{1,3}, S Svenningsen^{1,2}, TM Peters¹⁻³, HO Coxson⁴, DG McCormack⁵ and G Parraga¹⁻³

¹Imaging Research Laboratories, Robarts Research Institute; ²Department of Medical Biophysics; ³Graduate Program in Biomedical Engineering, The University of Western Ontario, London CANADA ⁴Department of Radiology University of British Columbia Vancouver CANADA, ⁵Division of Respiriology, Department of Medicine; The University of Western Ontario, London, CANADA.

Purpose: The lung is challenging to image using conventional MR pulse sequences due to the combined effects of low proton density, magnetic susceptibility, and to a lesser extent because of the effects of cardiac and respiratory motion.¹ Ultra-short echo-time (UTE) ^1H MRI has been proposed as a potential solution because it combines fast RF excitation pulses and efficient k -space sampling trajectories to minimize MR signal decay. Previous studies have shown that ^1H UTE signal intensity (SI) is sensitive to lung density changes that accompany fibrosis² and emphysema.³ However, before ^1H SI can be used in longitudinal clinical studies of respiratory disease, it is critical to understand inherent variability that can be attributed to image acquisition methods, including those related to the scanner (field strength, coils used) and subject compliance. Therefore, the objective of this study was to evaluate the three-week reproducibility of ^1H UTE MRI SI in subjects with a clinical diagnosis of bronchiectasis and subjects with mainly chronic bronchitis/chronic obstructive pulmonary disease (COPD) and compare this directly with the reproducibility of ^3He MRI measurements of apparent diffusion coefficients (ADC) (a surrogate measure of lung microstructure) in the same subjects with images acquired within a few minutes of UTE MRI. We hypothesized that ^1H UTE SI would be highly reproducible in subjects with mainly emphysema-dominant COPD (similar to hyperpolarized ^3He MRI reproducibility), but not in subjects with bronchiectasis or chronic bronchitis-dominant COPD. We also hypothesized that ^1H SI and ^3He ADC reproducibility would not be statistically significantly different.

Methods:

Subjects with a diagnosis of bronchiectasis or COPD provided written informed consent to the study protocol approved by the local research ethics board and Health Canada. All subjects underwent spirometry, plethysmography, and ^1H UTE and ^3He MRI in a single study visit at baseline and at a three-week follow-up. Imaging was performed on a whole body 3.0 Tesla Discovery 750MR (General Electric Health Care, Milwaukee, WI) with broadband imaging capability as previously described.⁴ UTE ^1H MRI was obtained using a 32-channel torso coil (GEHC) and a half RF excitation, 2D radial acquisition UTE sequence (a research prototype sequence provided by GEHC). UTE MRI was used to acquire a single centre slice in the coronal plane with the following parameters: 13s acquisition time, TE/TR/flip angle=0.05ms/13.0ms/10°, field-of-view (FOV)=40×40cm, matrix=256×439, NEX=4, and 15mm slice thickness. Hyperpolarized ^3He MRI diffusion weighted images were acquired on the same scanner as previously described.⁴ ^3He ADC values were generated as previously described.⁴ The lung parenchyma was manually segmented from the heart, mediastinum, central pulmonary vessels, diaphragm, and chest wall. The mean SI of the segmented lung was normalized to the mean SI of the liver (which served as a reference organ in the same image to account for potential inter-scan variability). The normalized contrast-to-noise ratio (C_R) and the apparent signal-to-noise ratio (S_R) were calculated using methods described by Johnson et al.⁵

A repeated measures analysis of variance (ANOVA) was used to determine the differences between repeated scans for ^1H SI and ADC using IBM SPSS Statistics 21.0 (SPSS Inc., Chicago, IL, USA). Linear regression and Pearson correlation coefficients (r) were used to determine the variability as well as the relationships between ^1H SI and S_R using GraphPad Prism version 4.00 (GraphPad Software Inc, San Diego, CA, USA). The coefficient of variation (COV) was also calculated to determine the variability between repeated scans. A two-way mixed model intra-class correlation coefficient (ICC) analysis was used to determine the degree of agreement between different scans. Results were considered statistically significant when the probability of making a Type I error was less than 5% ($p < 0.05$).

Results: There was no significant difference between baseline and 3-week ^1H MRI SI for both bronchiectasis ($\Delta^1\text{H SI} = -1 \pm 2$, $p = 0.5$) and COPD ($\Delta^1\text{H SI} = 0 \pm 2$, $p = 0.9$) subjects. COV values for ^1H SI for bronchiectasis and COPD subjects were 6% and 4%, respectively. There were significant linear regressions for 3-week rescan for ^1H SI (bronchiectasis: $r = 0.97$, $p = 0.007$; COPD: $r = 0.86$, $p = 0.03$) and ^3He ADC (bronchiectasis: $r = 0.99$, $p = 0.002$; COPD $r = 0.97$, $p = 0.03$). There was no significant difference in ^1H SI Pearson correlation coefficients between COPD and bronchiectasis ($p = 0.4$). In addition, there was no significant difference between ^1H SI and ^3He ADC Pearson correlation coefficients ($p = 0.2$) for all subjects. Finally, there was no significant correlation between ^1H SI and S_R ($r = 0.22$, $p = 0.5$).

Discussion and Conclusions: To our knowledge, this is the first evaluation of ^1H UTE MRI SI reproducibility in bronchiectasis and COPD subjects. We reported high ^1H SI reproducibility for 3-week rescan for both bronchiectasis and COPD subjects which was consistent with high Pearson correlation coefficients, relatively low COV and high ICC. To further understand the relationship of reproducibility with image quality, we investigated whether differences in S_R would influence ^1H SI, but did not find a significant relationship between them. We also reported no significant difference between Pearson correlation coefficients between ^1H SI and ^3He ADC.

References: 1. Bergin CJ. *et al. Radiology.* (1992); 2. Ohno *et al. Eur J Rad.* (2013); 3. Zurek *et al. MRM.* (2012); 4. Kirby M *et al. Acad Rad.* (2012); 5. Johnson KM. *et al. MRM.* (2012)

Pulmonary Functional Imaging of Bronchiectasis: A First Look at Ventilation Abnormalities and their Relationship with Pulmonary Function and Symptoms

Sarah Svenningsen^{1,2}, Gregory Paulin^{1,2}, Damien Pike^{1,2}, Sindu Mohan³, David G McCormack³ and Grace Parraga^{1,2}

¹Imaging Research Laboratories, Robarts Research Institute; ²Department of Medical Biophysics; ³Division of Respiriology, Department of Medicine, The University of Western Ontario, London, Canada.

Supervisor: Dr. Grace Parraga

RATIONALE: Bronchiectasis is a chronic pulmonary disease characterized by damaged airways which causes abnormal dilation of the bronchi leading to poor clearance and pooling of mucous in affected areas. Although bronchiectasis can be highly localized, it is typically evaluated using spirometry, providing a global measure of lung function. Hyperpolarized gas magnetic resonance imaging (MRI) provides an *in-vivo* assessment of regional gas distribution in the lung and has the advantage of showing exactly where regional functional abnormalities occur. Previous studies in asthma, chronic obstructive pulmonary disease and cystic fibrosis (CF) have revealed heterogeneously distributed lung function abnormalities that are associated with pulmonary function and symptoms, however, ³He gas distribution has not been evaluated in non-CF bronchiectasis. Therefore, our objective was to evaluate ³He MRI ventilation distribution for the first time in subjects with a clinical diagnosis of bronchiectasis. We hypothesized that MRI pulmonary function abnormalities would be strongly related to pulmonary function and symptom scores.

METHODS: Subjects with a diagnosis of bronchiectasis (45-85 years) were evaluated using spirometry, plethysmography, six-minute walk test (6MWT), hyperpolarized ³He MRI, high-resolution computed tomography (HRCT), Patient Evaluation Questionnaire (PEQ),¹ and the St. George's Respiratory Questionnaire (SGRQ). Distribution of ³He gas was evaluated using semi-automated segmentation of ³He voxel intensities to generate the ³He MRI ventilation defect percent (VDP).² Linear regression and Pearson Correlations were used to evaluate the relationship between ³He MRI VDP and measurements of pulmonary function and symptoms.

RESULTS: Fourteen subjects with both CT-evidence and a clinical diagnosis of bronchiectasis were evaluated (68±10 years, 4M/10F, FEV₁=67±21%_{pred}, FVC=72±21%_{pred}, 6MWD=419±85m). The mean SGRQ scores were as follows: Symptom score: 68±17; Activity Score: 48±20; Impacts Score: 36±17; Total Score: 45±15; the mean PEQ derived patients' global assessment was 11±3. All subjects had visually obvious ³He MRI ventilation abnormalities with a mean whole lung VDP of 17±8% (range: 2%-29%). Figure 1 shows the spatial relationship between heterogeneous ³He MRI ventilation defects and CT structural abnormalities for a representative subject with extensive cylindrical bronchiectasis mainly in the lower lobes. For all subjects, ³He VDP was associated with FEV₁%_{pred} (r=-0.78, r²=0.61, p=0.0009), SVC%_{pred} (r=-0.62, r²=0.38, p=0.02), RV/TLC%_{pred} (r=0.73, r²=0.54, p=0.003), sRaw (r=0.61, r²=0.40, p=0.02) and the mean PEQ derived patients' global assessment (r=0.78, r²=0.60, p=0.02).

CONCLUSIONS: For the first time, subjects with both CT-evidence and a clinical diagnosis of bronchiectasis were evaluated using hyperpolarized ³He MRI revealing heterogeneously distributed ventilation abnormalities that were related to worse pulmonary function and symptoms.

1. Thomas L. Petty. The National Mucolytic Study: Results of a Randomized, Double Blind, Placebo-Controlled Study of Iodinated Glycerol in Chronic Obstructive Bronchitis. 1990. Chest 97(1):75-83.
2. Kirby M, Heydarian M, Svenningsen S et al. Hyperpolarized ³He magnetic resonance functional imaging semiautomated segmentation. 2011. Acad Radiol 19(2):141-52

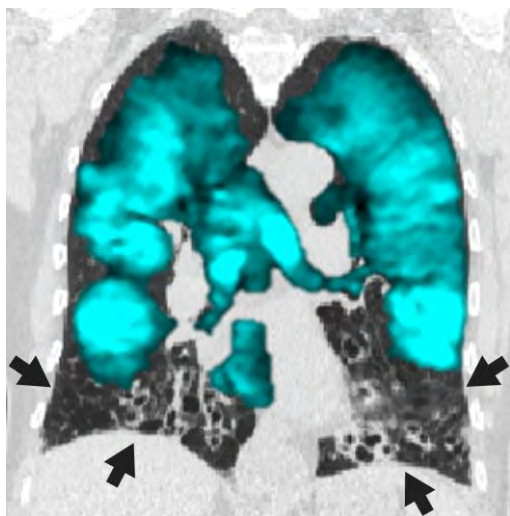


Figure 1. Hyperpolarized ³He magnetic resonance imaging (MRI) static ventilation image of a 75 year old male (FEV₁=50%_{pred}, VDP=24%) with bronchiectasis. The ³He gas distribution (in blue) is co-registered to the corresponding CT slice of the thorax to display structural abnormalities (in grey scale).

Ventilation defects (indicated by black arrows) are spatially related to extensive cylindrical bronchiectasis in the lower lobes.

Mapping of Surgical Resection Areas to Post-Surgery CT Images Using Endoscopic Contouring: Validation in a Cadaver Model

Robert A. Weersink^{1,2}, Nidal Muhanna³, Jimmy Qiu¹, Mike Daly¹, Harley Chan¹, John Cho⁴, Brian O'Sullivan⁴, Jon Irish³, David A. Jaffray^{1,2,4}

1. Techna Institute, University Health Network, Toronto, 2. Depart. Radiation Physics, Princess Margaret Cancer Centre, 3. Dept. Surgical Oncology, University Health Network, 4. Dept. Radiation Medicine, Princess Margaret Cancer Centre.

Successful adjuvant radiation therapy following surgery requires knowledge of areas of highest risk for local recurrence, typically along the area of surgical excision. In the current treatment approach, pre-operative CT imaging fused with post-operative CT is used to identify the original tumor location, a region identified as the High Risk Treatment Volume (HTV). Pathology information is only generally noted, without full consideration of biopsy location and details of the pathology results. Given the extensive anatomical changes following surgery, it is obvious this method does not represent a true physical registration between the surgical intervention and the radiation treatment plan. Because of these inaccuracies, generous isotropic margins are added to the contouring of the HTV and possible nodal extension. The inaccuracies in the planning process increase the possibility of treatment failure, while the large margins intended to reduce this possibility only add to the patient toxicity.

We have developed a unified multimodal approach for the treatment of high risk head & neck patients receiving both surgery and radiation therapies. The technology quantitatively relates surgical and pathology information with the radiation treatment process with the goal of creating a single coordinated treatment framework for the patient that unites surgery, pathology and radiation therapy. The technology requires intraoperative volumetric imaging integrated with navigation and tracking of surgical tools to the intra-operative imaging including registration of endoscopic imaging and pathology sampling. This arrangement enables the clinician to contour superficial lesions visible in endoscopy but not visible on the volumetric imaging and transfer these contours into the 3D radiation treatment planning space. This technology enables the registration of any information visible in the 2D image into the 3D volumetric image space. For registration of the surgical procedure to the radiation treatment plan, quantitative endoscopic tracking and video overlay enables retrospective contouring of the surgical excision. The surgical excision contour is projected onto the intraoperative and post-operative images. The contours are fused with the radiation treatment plan by registration of the intra- and post-operative imaging to the radiation planning CT.

To validate the accuracy of this workflow, we used 3 cadaveric head samples, each receiving 3 surgical resection procedures: removal of a portion of the larynx, tongue and floor of mouth. Cone-beam CT images were acquired of the specimens immediately post-resection and following reconstructive surgery. Endoscopic imaging, registered to the CT images was used to image the surgical field and multiple image frames of the surgical excision were captured. The resected area was contoured on each image and then registered with the CBCT. The true surgical excision area was defined by applying a mixture of CT contrast agent and tissue epoxy to the resected area. The pre-reconstruction endoscopic contours were compared to contours segmented in both pre and post-resection CBCT images using the contrast-epoxy mixture as a marker.

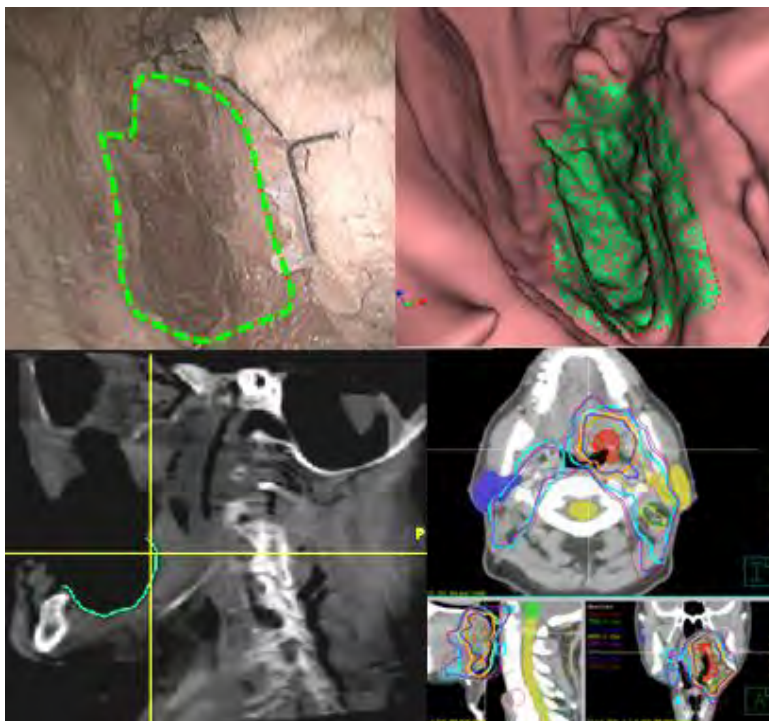


Figure 1: Endoscopic contouring of surgical excision of the floor of mouth on a cadaveric sample.

Two average minimum distance metrics were used to assess the overlap of the contours: the mean distance to agreement, and the surface distance at the 90th percentile distance (Dist-90). In the pre-reconstruction imaging, the mean distance between the endoscopic and contrast-based contours ranged between 0.9 – 2.3 mm while Dist-90 values ranged between 1.6 – 5mm depending on the surgical site. In the rigid sites (larynx and floor of mouth) the distances were small, while it was larger for the tongue. Comparing the contours to the post-reconstruction images, the mean distance ranged between 2.3 – 3.3mm and Dist-90 ranged between 4- 6.5 mm.

For rigid tissues (larynx, floor of mouth) there was generally excellent overlap between the endoscopic contours and the post-reconstruction contrast-based contours. The typical margin used in current radiation treatment plan for contours defining the surgical excision sites is 10 mm, substantially larger than the values observed here. Clinical validation of this approach has been initiated.

OICR Smarter Imaging Program

OICR SIP

Oral Presentation and Poster Abstracts

Short-term assessment of blood-tumor-barrier permeability following focused ultrasound and microbubble treatment - Can we improve drug delivery?

^{1,2,4}H. Ahmed, ³R. Chopra, ³K. Hynynen, ^{1,2,4}TY Lee

¹Department of Medical Biophysics, The University of Western Ontario,

²Imaging Research Laboratories, Robarts Research Institute,

³Sunnybrook Health Research Institute,

⁴Lawson Health Research Institute.

Purpose: To quantitatively evaluate short-term blood-tumor-barrier response following focused ultrasound (FUS) and microbubble (MB) treatment using dynamic contrast-enhanced computed tomography (DCE-CT) in a primary rat and metastatic rabbit brain tumor model.

Materials and Methods: A stereotactic frame was used to surgically implant 1×10^6 C6 glioma cells in the right cerebral hemisphere (3mm to the right, and 1 mm inferior to the bregma) of six rats which were broken into the following groups: 1) acute monitoring out to 4 hours post treatment (n=3), and 2) recovery at 60 min post following by scans at 24 and 72 h post (n=3). For the rabbit group, 0.5 ml of VX2 carcinoma suspension was similarly implanted (n=4). At 10-15 days post treatment, when the tumor diameter was greater than 5mm, the tumor was trans-cranially sonicated with a 10ms burst length and a 1 Hz repetition frequency for 120s, at an acoustic power of 0.5W using a 0.563-MHz FUS system. The contralateral hemisphere was sonicated as a control. Definity microbubbles at a dose of 2 μ l/kg were administered simultaneously with each sonication. The sonications were guided by baseline axial CT images and the corresponding blood-tumor-barrier (BTB) permeability surface area product (PS) maps calculated by CT Perfusion software. CT Acquisition parameters of 80 kVp, 200 mA, 1.25 mm thickness were used for a two phase DCE-CT protocol (1st phase: continuous 0.5s rotation for 30s, 2nd phase: 0.5s rotation at 14.5s delay for 150s). A 2.5 ml/kg bolus of Isovue-300 (~800 Da) was used as tracer to calculate BTB permeability.

Results: Instead of an immediate transient 3-4 times increase in PS that is seen over normal brain tissue, the BTB PS gradually decreases in the hours following FUS and MB treatment. The BTB PS at 150 minutes post sonication (2.7 +/- 1.3 ml/min/100g) was significantly lower ($p < 0.05$) than at baseline (5.7 +/- 1.7 ml/min/100g). In the rat recovery group, the BTB PS at 24 h post sonication (3.0 +/- 0.9 ml/min/100g) was significantly lower ($p < 0.05$) than at baseline (5.6 +/- 1.6 ml/min/100g). In the rabbit group, the BTB PS at 60 min post (2.6 +/- 1.5 ml/min/100g) was also significantly lower ($p < 0.05$) than at baseline (1.2 +/- 0.8 ml/min/100g).

Conclusions: A decrease in BTB PS following FUS and MB treatment was a surprising result, and is something we are currently exploring. It has been reported that BTB response is influenced by acoustic and microbubble parameters, as well as tumor treatment size. It has been suggested that strategies that can lower the vasogenic fluid accumulation brain tumors by decreasing BTB PS should lower the abnormally elevated interstitial fluid pressure and improve drug penetration of macromolecules that depend on convective fluid transport (i.e. agents that are unable to passively diffuse across BTB). We are also currently repeating these experiments with a larger iodine contrast agent EXIA (~60 kDa) to investigate the difference between diffusive and convective transport across the BTB.

Polarized light imaging for localizing the bladder morphological complications in outlet obstruction disease

Sanaz Alali, Karen J. Aitken, Adam Gribble, Annette Schröder, Darius J. Bagli, I. Alex Vitkin

Abnormal growth of prostate is common among aging men [1]. Enlargement of prostate leads to bladder outlet obstruction (BOO) which creates excessive pressure in the bladder and may result in *irreversible* structural damage to the bladder wall, with further muscle dysfunction [1]. The location of these morphological changes cannot be identified with current imaging methods, thus in many cases the bladder has to be removed [1].

Among different animals, rats have been widely used as BOO models since they exhibit similar tissue complication and urodynamics to humans [1]. In this study, we use polarized light imaging to locate the obstruction-induced morphological changes in *ex vivo* distended rat bladders. Polarized light imaging can noninvasively quantify microstructural organization and tissue anisotropy in terms of optical birefringence [2].

We have conducted two studies: 2 week obstruction (12 rats) and 6 weeks obstruction (12 rats). Each group was divided into two, obstructed and control (which have undergone surgery without obstruction). All bladders were harvested and distended up to maximum distension pressure of a normal bladder. The Mueller matrix of different regions of each bladder wall was measured in backscattering geometry using polarized light. The Mueller matrices were mathematically analyzed via polar decomposition, and resultant retardance values were derived [2]. As our results show in Fig.1, the local retardance (birefringence) of the ventral urethral regions increases significantly due to obstruction. The increase of retardance in the ventral urethral region scales with the bladder mass increase due to the obstruction. The potential of this new polarimetric imaging technique in urology is discussed.

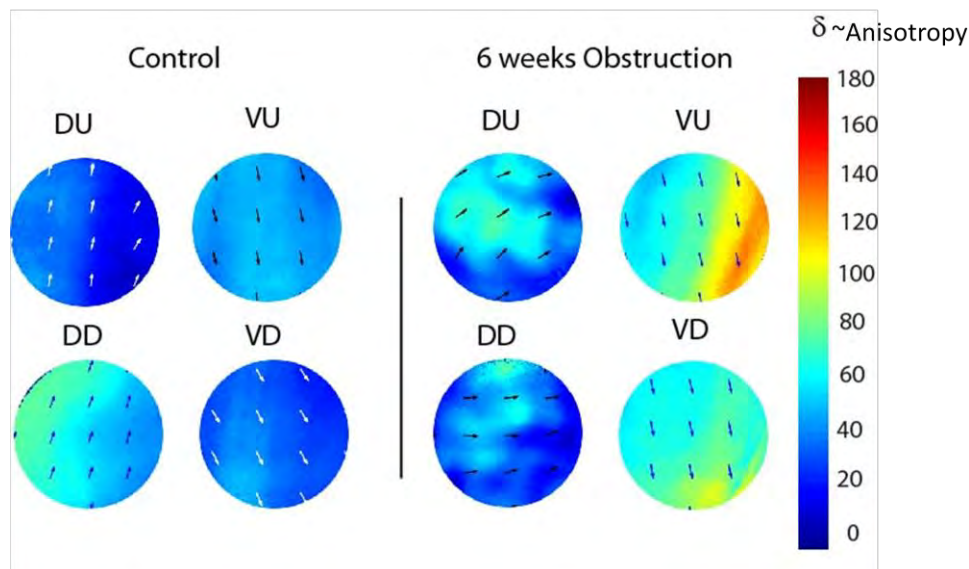


Fig.1- Representative retardance images of control rat bladder and obstructed rat bladder, DU is the Dorsal Urethral, VU is the Ventral Urethral, DD is the Dorsal Dome and VD is the ventral Dome region, respectively.

[1] K. Aitken et al, Nat. Rev. Urol. (2009) 6: 596-621.

[2] S. Alali et al, J. Biomed. Opt. (2012) 17:086010.

Correlation between Hyperpolarized ^3He MR-Derived Measurements of Lung Function and Body Mass Index

Sana Alharbi^{1,2}, Marcus J. Couch^{1,2}, Tao Li², Matthew S. Fox², Birubi Biman^{3,4}, and Mitchell Albert^{1,2}.

(1) Lakehead University, Thunder Bay, Ontario. (2) Thunder Bay Regional Research Institute, Thunder Bay, Ontario (3) Thunder Bay Regional Health Sciences Centre, Thunder Bay, Ontario. (4) Northern Ontario School of Medicine, Thunder Bay, Ontario.

Introduction: Obesity is a significant healthcare burden, and more than 70% of the North American population is overweight (1). Obesity has been correlated with respiratory problems, including alveolar hypoventilation and atelectasis. Many obese people are referred for pulmonary function testing (PFT), and obesity has been associated with reduced expiratory reserve volume (ERV) and total lung capacity (TLC). Several studies have shown a correlation between body mass index (BMI) and decreased lung volume for patients with a BMI of 30 or greater employing pulmonary function test (PFT) measurements alone (2). Hyperpolarized (HP) ^3He MRI has emerged as a safe and non-invasive method for obtaining high-resolution information on pulmonary lung function without the use of any ionizing radiation or injected contrast agents (3). HP ^3He MR image-derived measurements of ventilation volume (VV) and ventilation defect percent (VDP) are expected to have a stronger correlation with BMI than previous studies that used PFT measurements only.

Methods: This study was conducted under a protocol approved by the local ethics review board and by the appropriate governmental agencies. All volunteers provided written informed consent prior to their participation in the study. In this study, HP ^3He MRI was used to image the lungs of eight healthy volunteers (3 males, 5 females) with no smoking history and no history of lung disease. The mean age of all the volunteers was 32 ± 11 . The BMI ranges were defined as follows: normal individuals had a BMI of 18.5 to 24.9, overweight individuals had a BMI of 25 to 29.9, and obese individuals had a BMI greater than 30. Imaging was performed using a Philips 3T Achieva scanner and a flexible wrap-around radiofrequency (RF) coil tuned to the ^3He resonant frequency (Clinical MR Solutions). BMI was recorded for all volunteers. Prior to ^3He imaging, subjects inhaled a 1 L Tedlar bag of air to acquire conventional proton (^1H) MR images for localization. ^3He MR images were acquired following inhalation of a 1 L Tedlar bag containing 330 mL of hyperpolarized ^3He balanced to 1 L with N_2 . 2D multi-slice images were obtained in the coronal plane with the following settings: TR = 56ms, TE = 1.53ms, FOV = $450 \times 450 \text{mm}^2$, 14 slices, thickness = 15mm, and flip angle = 7° . A semi-automated segmentation algorithm written in MATLAB was used to calculate VV and VDP (4). The statistical significance of BMI and lung volume correlations was determined using the statistical programming environment R.

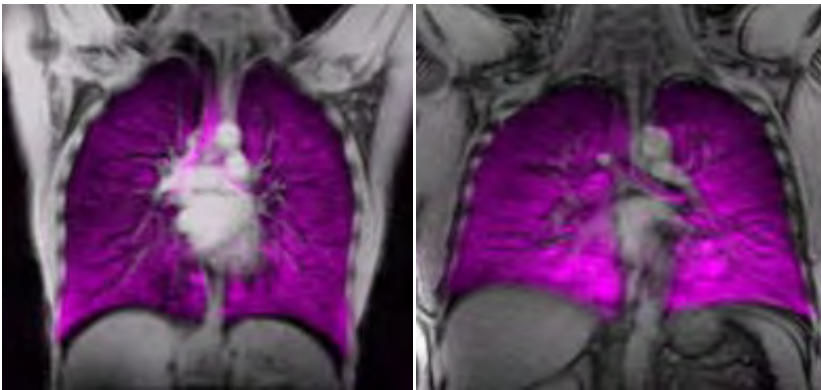


Figure 1: HP ^3He coronal MR images overlaid in purple on conventional ^1H MR lung images from a representative normal weight volunteer (left), and obese volunteer (right).

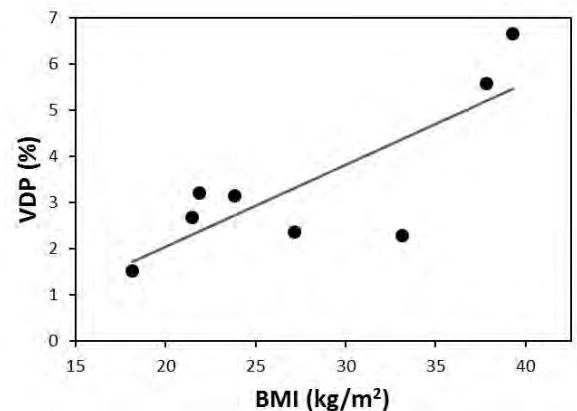


Figure 2: Correlation of BMI and VDP. ($R^2 = 0.64$, $P = 0.02$).

Results and Discussion: Figure 1 shows representative center slice ^3He MR images in the coronal plane overlaid in purple on conventional ^1H MR lung images from a normal weight volunteer (left), and obese volunteer (right). Figure 2 shows a plot of VDP versus BMI, and there was a statistically significant correlation (Correlation-test, $n = 8$, $R^2 = 0.64$, $p = 0.02$). These results agree with expectations from the literature. In order to compare the strength of the MR-derived correlation to the literature, the coefficient of determination, $R^2 = 0.16$, was obtained from the plot of TLC versus BMI in Jones et al. (2). Therefore, it appears that VDP is more strongly correlated with BMI than PFT measurements ($R^2 = 0.64$, compared to $R^2 = 0.16$). In the future, it will be of great interest to further our understanding of the effects of obesity on pulmonary function by scanning volunteers while also having them perform exercise tasks.

Conclusion: Overall, eight healthy volunteers were imaged in this study using HP ^3He MRI. Image-derived measurements of VDP had a statistically significant correlation to BMI, and this correlation was stronger than in previously reported PFT measurements.

References: [1] Walpole AC, et al., (2012) BMC Public Health 12:439. [2] Jones R, (2006) Chest, 130:827-833. [3] Leawoods J, et al., (2001) Concepts Magn Reson, 13:277-293. [4] Kirby M, et al., (2012) Acad Radiol, 19:141-152.

Simulating the Effect of Venous Dispersion on Graphical Analysis of PET Studies

Adam Blais^{1,2,3}, Ting-Yim Lee^{1,2,3}

Research Supervisor: Ting-Yim Lee

¹Robarts Research Institute, London, ON

²Lawson Health Research Institute, London, ON

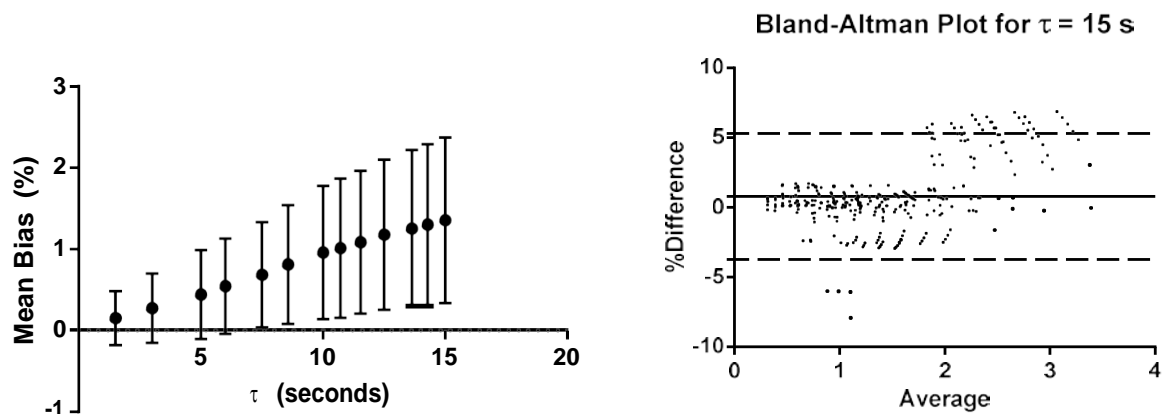
³Department of Medical Biophysics, Western University, London, ON

Introduction: Measurement of radioligand distribution volume with the Logan Plot is of potential interest for the analysis of ¹⁸F-Fluorocholine imaging of prostate cancer. This technique requires an arterial time activity curve (TAC). The gold standard for measuring arterial activity concentrations is arterial blood sampling. Arterial cannulation carries with it a risk of arterial occlusion, ischemic damage, excessive bleeding, and is painful for the patient. Conversely, venous cannulation is safer, easier, and more common in clinical practice. This work simulated the effects of venous dispersion on the Logan Plot in order to determine the feasibility of using venous TAC's for graphical analysis with the Logan Plot.

Methods: A representative arterial TAC was selected from an ¹⁸F-Fluorocholine PET patient study. Simulated tissue TAC's were generated based on a three compartment kinetic model using the representative arterial TAC, for 343 unique sets of kinetic parameters. Venous TAC's were simulated by convolving the arterial TAC with gamma variate functions, which represent different transit time spectra between the arterial and venous sampling sites. Multiple arterio-venous transit times (τ) were investigated.

Gaussian noise based on counting statistics, the length of the PET acquisition frame, and radioactive decay was added to the tissue and input TAC's. Logan analysis was performed using the arterial TAC's and again using the venous TAC's for the wide range of kinetic parameters simulated. The mean percentage bias and standard deviation over all parameter sets were calculated for each arterio-venous transit time. Bland-Altman analysis was performed to assess the agreement between distribution volumes calculated with the arterial and venous TAC's.

Results: Bland-Altman analysis showed that there was good agreement between distribution volume values calculated with the simulated arterial and venous TAC's for both noiseless and noisy cases. The agreement between the arterial and venous values was only slightly dependent on the dispersion of the venous TAC's relative to the representative arterial TAC. The longest arterial to venous transit time tested was 15 seconds and the mean bias for this case was 1.35 ± 1.02 % for the noiseless case.



(Left) Mean bias \pm SD between distribution volumes calculated via the arterial and venous Logan Plots in the noiseless case over 343 kinetic parameter sets. The bias was slightly dependent on the arterio-venous transit time (τ). (Right) Bland-Altman analysis indicated good agreement between methods for $\tau = 15$ seconds.

Conclusion: Results suggest that venous sampling is a feasible alternative to arterial sampling for measurement of radioligand distribution volume with the Logan Plot. This would reduce the risks to the patient that are typically associated with arterial cannulation and result in improved patient comfort.

⁶⁴Cu-NOTA-Panitumumab F(ab')₂ Fragments for PET/CT Imaging of Pancreatic Cancer

Amanda Boyle¹, Raymond Reilly^{1,2}

Department of Pharmaceutical Sciences¹, Leslie Dan Faculty of Pharmacy², University of Toronto, Ontario, Canada

Background: Pancreatic cancer is the 4th leading cause of cancer related death with the highest mortality rate of all cancer related deaths. Panitumumab (Pmab) has potential as an imaging and therapeutic agent as a fully human monoclonal antibody which targets human epidermal growth factor receptor (EGFR), which is known to be over-expressed in many pancreatic cancers. We employ NOTA to chelate ⁶⁴Cu for its very stable ⁶⁴Cu-binding properties. This study examines various Pmab antibody forms then employs F(ab')₂ fragments for PET/CT imaging and biodistribution studies in EGFR+ xenograft mouse models. Our goal is to develop a radioimmunoconjugate that can be used as a PET theranostic agent for individualized treatment of pancreatic cancer in patients.

Methods: Pmab Fab fragments (PmabFab), Pmab F(ab')₂ fragments (PmabF(ab')₂), and intact Pmab IgG (PmabIgG) were NOTA-derivitized with p-SCN-Bn-NOTA, then ⁶⁴Cu-labeled for *in vitro* and *in vivo* assessment. RICs were injected intravenously by tail vein injection in BalbC mice and biodistribution was performed at 18 hours post injection to assess normal tissue uptake. The immunoreactivity of RICs was assessed *in vitro* by binding assays with EGFR-overexpressing cell lines: PANC-1 (4 × 10⁵ EGFR/cell), a pancreatic cancer cell line, and MDA-MB-468 (1 × 10⁶ EGFR/cell), a breast cancer cell line. Two mouse models were developed: NodScid mice were inoculated with 1 × 10⁷ PANC-1 cells, and CD1 Nude mice were inoculated with 1 × 10⁷ cells, both subcutaneously on the right flank. ⁶⁴Cu-labeled PmabF(ab')₂ was injected intravenously into these mouse models then PET/CT imaging and biodistribution studies were performed at 24 and 48 hours post injection.

Results: Notable differences in normal organ uptake were seen in the renal uptake and circulating blood content of radioimmunoconjugates. Renal uptake of ⁶⁴Cu-PmabFab was significantly higher at 90.8% ID/g than that of ⁶⁴Cu-PmabF(ab')₂ and PmabIgG, observed at 6.7 and 11.2% ID/g, respectively. Circulating blood content of ⁶⁴Cu-PmabFab was markedly lower at 0.6% ID/g than ⁶⁴Cu-PmabF(ab')₂ or ⁶⁴Cu-PmabIgG, with 23.8 and 18.2% ID/g, respectively. While considering the results listed above, ⁶⁴Cu-PmabF(ab')₂ was selected for PET/CT imaging (Figure 1) and biodistribution studies. The tumour:blood ratio in MDA-MB-468 xenografted mice was observed at 1:1 at 24 hours, but improved at 48 hours with 5:1, and tumour accumulation of 8.6% ID/g. The tumour:blood ratio in PANC-1 xenografted mice was also observed at 1:1 at 24 hours, and improved to 2.4:1 at 48 h, with 6.2% ID/g tumour uptake.

Conclusions: The optimal form of panitumumab for PET/CT imaging is as F(ab')₂ fragments with lower renal accumulation than the Fab fragments and higher blood circulation than the intact IgG. Excellent imaging of PANC-1 and MDA-MB-468 xenografted mice can be achieved with ⁶⁴Cu-PmabF(ab')₂ at 48 hours post injection (Figure 1).

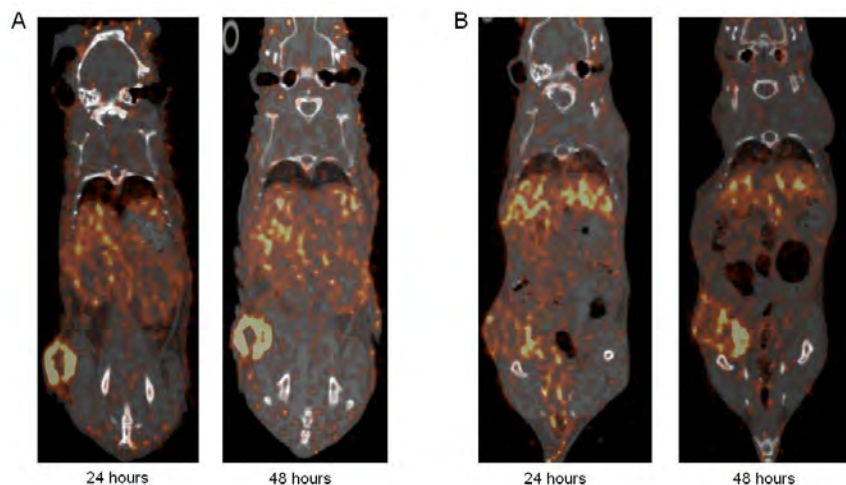


Figure 1. PET/CT imaging of ⁶⁴Cu-PmabF(ab')₂ in A) MDA-MB-468 xenograft and B) PANC-1 xenograft mouse models at 24 and 48 hours post injection.

Experimental validation and comparison of image quality for proposed energy dependent and reference conventional vascular x-ray imaging methods

Christiane S Burton and Ian A Cunningham

Imaging Research Laboratories, Robarts Research Institute, 100 Perth Drive, London Ontario, N6A 5K8, Canada
Department of Medical Biophysics, The University of Western Ontario, London, Ontario N6A5C1, Canada

Introduction:

Cardiovascular disease accounts for 30% of all deaths in Canada and x-ray angiography is used in ~80% of all CVD cases.^{1,2} Digital subtraction angiography (DSA) is an x-ray imaging technique used to selectively enhance arteries and suppress other anatomic structures by subtracting a mask image (pre contrast-injection) from a contrasted image (post contrast-injection). These may be separated by many seconds and hence, respiratory and cardiac motions may cause image artifacts that have largely prevented its use for imaging coronary arteries. Coronary angiography (CA) does not use subtraction methods and instead uses only contrasted images with high iodine concentrations and patient exposures to enhance coronary arteries. An alternative may be to exploit the energy dependence of the iodine attenuation coefficient by acquiring two images at different x-ray energies in rapid succession (milliseconds apart) to create an iodine-specific image. This energy subtraction angiography (ESA) idea has been proposed in the past but was unsuccessful for technical reasons we believe we can now solve. For example, we demonstrated by theory³ that ESA has the potential to produce subtraction-like images with comparable image quality in terms of signal and noise to conventional DSA for the same patient entrance exposure. We are currently in the process of developing a prototype ESA system for concept validation. The purpose of this study is to show experimentally that signal, noise and patient exposure for optimal ESA conditions is comparable to that of optimal DSA, and that ESA has the ability to remove non-uniform overlying soft-tissue and bone structure.

Methods:

- a) Iodine signal and noise was measured experimentally by constructing a vascular phantom consisting of an iodinated step-wedge submerged in 20 cm of water. In a horizontal beam set-up, ESA and DSA images of the phantom were acquired using a bench-top fast kV-switching x-ray system⁴ with a cesium iodide flat-panel detector. For ESA low and high applied tube voltages of 60 kV and 130 kV, respectively, and for DSA the applied tube voltage was 76 kV. Entrance exposure was measured using an ion chamber (Unfors Xi Platinum Plus). Iodine SNR per root entrance exposure was calculated for each iodine concentration for both ESA and DSA.
- b) Removal of non-uniform soft-tissue was measured experimentally by constructing a PMMA step-wedge and adding the steps to the x-ray path. Using the same setup and same imaging parameters as experiment 1, DSA and ESA images were acquired and the signal change due to the PMMA steps determined.
- c) We set up an anthropomorphic RS 310 lung/chest phantom and tissue equivalent iodine filled tubing. In a horizontal beam set-up ESA and DSA images of the phantom were acquired. For ESA low and high applied tube voltages of 60 kV and 130 kV, respectively, and for DSA the applied tube voltage was 76 kV. The final images of ESA and DSA were visually compared.

Results:

- a) For the imaging parameters considered, experimental iodine SNR for ESA is within 30% that of DSA for the same patient entrance exposure and this shows excellent agreement with theoretical calculations.
- b) ESA shows complete removal of non-uniform soft-tissue and the iodine SNR per root exposure for ESA is within 30% to that of DSA as was the case for uniform background.
- c) ESA shows removal of soft-tissue and partial subtraction of bone.

Significance of results: ESA can produce vascular images with background suppression, similar to DSA, without the need for a mask image. For the same patient entrance exposure, iodine signal-to-noise ratio is comparable between ESA and DSA indicating that the total patient exposure does not need to be increased. ESA shows removal of non-uniform background which indicates that it can be used in applications where there is a varying soft-tissue background.

Future work: Demonstrate real-time ESA by implementing both a fast kV-switching generator and fast high quality sensor leading to a demonstration system. We will also compare real-time ESA SNR per root exposure with coronary angiography, and show other ways of optimizing parameters for ESA and compare to DSA.

Reference:

1. "Statistics Canada, CANSIM Table 102-0529: Deaths, by cause, Chapter IX: Diseases of the circulatory system (I00 to I99), age group and sex, Canada, 2000 to 2006," 2010.
2. D. G. Manuel, M. Leung, K. Nguyen, P. Tanuseputro, H. Johansen, and Canadian Cardiovascular Outcomes Research Team, "Burden of cardiovascular disease in Canada." *Can J Cardiol*, vol. 19, no. 9, pp. 997-1004, 2003.
3. Tanguay, J; Kyung Kim, H; Cunningham, IA. 2011. A theoretical comparison of x-ray angiographic image quality using energy-dependent and conventional subtraction methods.
4. EMD

¹⁹F MRI of Human Lungs: Comparison of UTE and Gradient Echo Imaging

Marcus J. Couch^{1,2}, Iain K. Ball², Tao Li², Matthew S. Fox², Alexei V. Ouriadov², Birubi Biman^{3,4}, and Mitchell S. Albert^{1,2}. (1) Lakehead University, Thunder Bay, Ontario. (2) Thunder Bay Regional Research Institute, Thunder Bay, Ontario. (3) Thunder Bay Regional Health Sciences Centre, Thunder Bay, Ontario. (4) Northern Ontario School of Medicine, Thunder Bay, Ontario.

Introduction: Fluorine-19 (¹⁹F) magnetic resonance imaging (MRI) of the lungs using inhaled inert fluorinated gases can potentially provide high quality images of the lungs that are similar in quality to hyperpolarized (HP) noble gas MRI. Inert fluorinated gases have the advantages of being nontoxic, abundant, inexpensive compared to HP gases, and they do not need to be hyperpolarized. Averaging within a single breath-hold is also possible due to short longitudinal relaxation times. Inert fluorinated gas MRI of the lungs has been previously demonstrated in animals (1), and more recently in healthy volunteers (2) and subjects with lung diseases (3). Since the image quality reported thus far has been lower than what can currently be achieved using HP noble gas MRI, the purpose of this study was to investigate and optimize image acquisition strategies for ¹⁹F 3D MR imaging of inert fluorinated gases. In this study, ultra-short echo time (UTE) and gradient echo images of inert fluorinated gases were obtained in both a resolution phantom and in the lungs of healthy volunteers, and the image quality was compared.

Methods: All imaging was performed using a 3.0T Philips Achieva scanner and a flexible wrap-around quadrature transmit/receive coil (Clinical MR Solutions). A hollow resolution phantom was filled with 100% sulphur hexafluoride (SF₆) and placed inside the coil. The phantom had five circular obstructions with various diameters of 19, 10, 6.5, 5 and 3 mm. UTE, gradient echo, and radial images were acquired with the following settings: TR = 20 ms, matrix = 128x128, 7 slices, in-plane FOV = 200x200 mm², in-plane resolution = 1.56 mm, 15 mm thickness, flip angle = 90°, and BW = 140 or 200 Hz/pixel. Both gradient echo and radial imaging used the same partial echo factor of 62.5%. The number of averages was set to yield similar scan durations for each acquisition: UTE images used 12 averages, gradient echo images used 49 averages, and radial images used 24 averages. Five healthy volunteers (4 female, 1 male) were enrolled in this study with no previous history of lung disease. 2D multi-slice gradient echo ¹H images were acquired prior to ¹⁹F imaging. Static breath-hold ¹⁹F UTE and gradient echo images were acquired during a 15 second breath-hold following continuous breathing of a mixture of 79% perfluoropropane (PFP) and 21% O₂. ¹⁹F 3D UTE imaging used the following settings: TR/TE = 20/0.2 ms, matrix = 64x64, 12 slices, in-plane FOV = 450x450 mm², 15 mm thickness, flip angle = 70°, 75% radial sampling density, and BW = 140 or 200 Hz/pixel. ¹⁹F 3D gradient echo images were acquired with the following settings: TR/TE = 27/1.12 ms, matrix = 64x64, 12 slices, in-plane FOV = 450x450 mm², 15 mm thickness, flip angle = 70°, 2 averages and BW = 200 Hz/pixel.

Results and Discussion: Figure 1 shows one slice from a ¹⁹F 3D gradient echo, ¹⁹F 3D UTE, and ¹⁹F 3D radial image acquired at bandwidths of 140 and 200 Hz/pixel in the resolution phantom. SF₆ was chosen for phantom imaging, since its T₂^{*} was measured to be 1.2 ms, which is close to the T₂^{*} of 2.2 ms for PFP in human lungs (2). As expected, UTE had the highest SNR, compared to gradient echo and radial imaging. Radial imaging was performed to provide a point of reference that had the same k-space sampling as UTE, and also had a TE similar to gradient echo imaging. The UTE image SNR also benefits from a lower bandwidth, at the expense of increased image blurring due to the short T₂^{*} and long acquisition window. Figure 2 shows a comparison of four central slices from the ¹H localizer, ¹⁹F 3D UTE, and ¹⁹F 3D gradient echo lung images acquired in

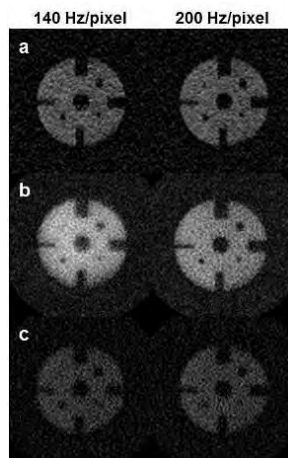


Figure 1: SF₆ resolution phantom images obtained using (a) gradient echo, (b) UTE and (c) radial acquisitions.

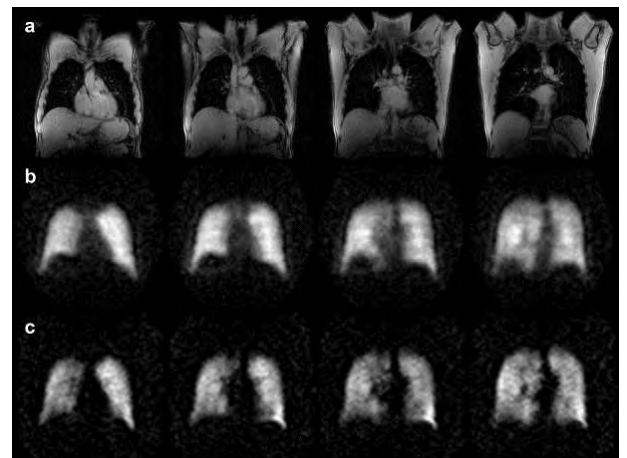


Figure 2: Comparison of four central slices from (a) ¹H localizer, (b) ¹⁹F 3D UTE and (c) ¹⁹F 3D gradient echo lung images from one subject breathing the PFP/O₂ mixture.

subject #3 during the same imaging session. Each 3D image was acquired during a separate 15 second breath-hold of the PFP/O₂ mixture, and imaging parameters were adjusted to keep the scan duration to within that breath-hold. Similar to the phantom measurements, the SNR for UTE lung images was significantly higher than gradient echo lung images ($p = 0.04$, by a two-tailed, paired t-test). For all five subjects, the mean whole-lung SNR was 27 ± 12 for UTE, and 16 ± 6 for gradient echo images. The difference in TE alone should theoretically lead to a 52% larger SNR in UTE images (assuming a T₂^{*} of 2.2 ms for PFP in the lungs). UTE images also suffer from substantial blurring due to the short T₂^{*} of PFP in combination with a long acquisition window at a bandwidth of 140 Hz/pixel.

Conclusion: Overall, UTE lung images had a high SNR, but also had poor edge definition and low resolution. On the other hand, gradient echo images had a lower SNR than UTE, but showed more edge detail and higher resolution. This preliminary study demonstrates the potential of ¹⁹F MRI for visualizing the distribution of ventilation in human lungs, and this may be a viable clinical imaging modality that can provide useful information for the diagnosis of chronic respiratory diseases.

References: [1] Kuethe DO et al, (1998) *Magn Reson Med*, 39:85–88. [2] Couch MJ et al, (2013) *Radiology*, doi:10.1148/radiol.13130609. [3] Halaweish AF et al, (2013) *Chest*, 144(4):1300-1310.

CT-Perfusion Measurements as a Predictor of RFA/TACE Outcomes and Evaluation of Early Response

^{1,3,4}Mark Dekaban, ⁴Feng Su, ^{2,3}Nirmal Kakani, ^{2,3}Amol Mujoomdar, ^{1,2,3,4}Aaron Fenster, ^{1,2,3,4,5}Ting-Yim Lee

Research Supervisor: Ting-Yim Lee

¹Department of Medical Biophysics; ²Department of Medical Imaging; ³The University of Western Ontario; ⁴Imaging Research Lab, Robarts Research Institute; ⁵Imaging Division, Lawson Health Research Institute; LONDON ONTARIO, CANADA

Purpose: Hepatocellular carcinoma (HCC) is the third most common cause of cancer-related death and the fifth most common cancer worldwide. Treatments include resection and transplant, which can be curative but are available to few, and systemic chemotherapy that suffers from low response rates (<30%). Local tumour management using radiofrequency ablation (RFA) or transarterial chemoembolization (TACE) is often the only option for patients with non-resectable HCC. Arteriography, conventional CT, and MRI are used to assess arterial blood supply to the tumor and plan the treatment. CT Perfusion Imaging (CTP) can offer more complete and quantitative information about tumour perfusion. The purpose of this study is to evaluate the ability of CTP to predict tumor response to RFA/TACE as well as evaluate the usefulness of CTP imaging for early response assessment.

Methods: Two CTP scans were performed on patients one week prior to RFA/TACE intervention to establish baseline measurements and determine the reproducibility of perfusion parameters. Follow up CTP scans were performed at 2 and 4-6 weeks after intervention. Parametric maps including total hepatic blood flow (BF), arterial hepatic blood flow (aBF), hepatic arterial fraction (HAF) and, hepatic blood volume (BV) were calculated.

Results: Four pairs of baseline scans were acquired. Coefficients of variation for the CT-Perfusion biomarkers were all within the range of 10-23% in both normal liver and tumor. Follow-up scan for two patients, one treated with RFA, one with TACE were completed. Both patients showed zero BF in most of the tumour one week after ablative treatment. The remaining regions of blood flow in the ablated zones were predominately arterial blood flow, suggestive of incomplete tumor ablation. 4 weeks after ablative treatment the regions of remaining BF in the ablated zones continued to grow suggestive of recurrence.

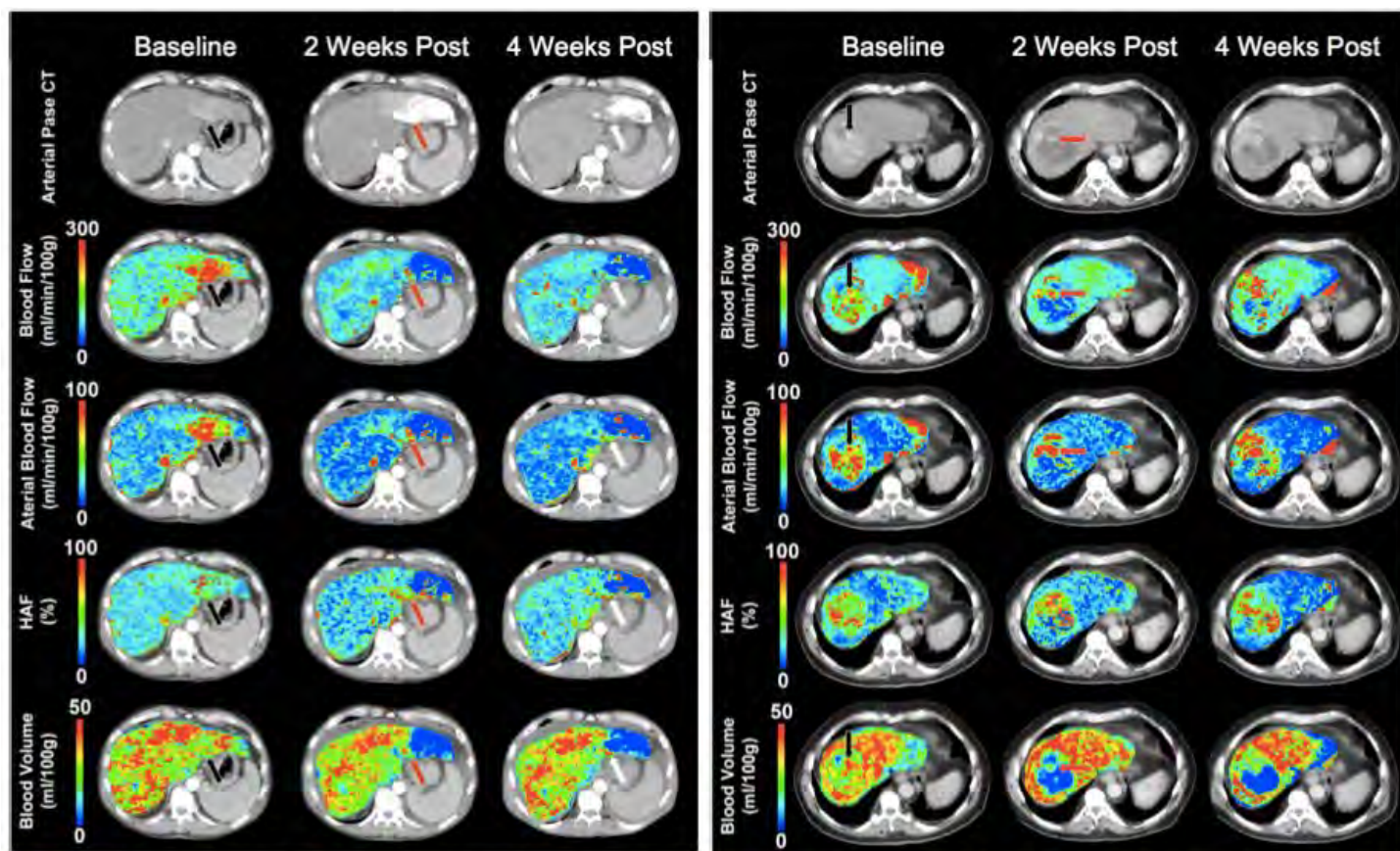


Figure 1 Perfusion parameters (BF, aBF, HAF, BV) calculated from a DCE-CT exam using CT-Perfusion software. The baseline scan (left column) shows a large arterial enhancing tumour mass (black arrows). 2 week post TACE (middle column) shows high concentration of lipiodol through out the tumour, suggestive of successful treatment. CT-P analysis however, reveals blood flow remaining in a portion of the tumour (red arrows). 4 weeks post (right column) shows that the lipiodol had been cleared from the region of the tumour with remaining blood flow (white arrows).

Figure 2 Perfusion parameters (BF, aBF, HAF, BV) calculated from a DCE-CT exam using CT-Perfusion software. At baseline a large vessel (black arrows) supplies the tumour with arterial blood. A combination of high blood flow and blood volume in this region of the tumour allows it to dissipate larger amounts of heat and resist RFA ablation as seen at 2 week post (red arrows).

Cancer Immunotherapy: Dendritic Cell Tracking using Fluorine-19 with a 9.4T MRI

J. Gaudet^{1,2}, C. Fink^{3,4}, E. Ribot^{1,2}, R. Foley⁵, G. Dekaban^{3,4}, P. Foster^{1,2}

¹Imaging Research Laboratories, Robarts Research Institute ²Department of Medical Biophysics, University of Western Ontario
³BioTherapeutics Research Laboratory, Robarts Research Institute ⁴Department of Microbiology and Immunology, University of Western Ontario ⁵Department of Pathology and Molecular Medicine, McMaster University

Background: Cancer immunotherapy has the potential to revolutionize modern medicine and clinical trials are already underway. Treatment involves recruiting the patient's immune system to attack the cancer. This is accomplished by loading dendritic cells (DC) with tumor specific antigens *ex vivo*. Well over a 1000 cancer patients have already been treated with DC vaccines; these trials have shown that DC-based immunotherapy is technically feasible and non-toxic. Nevertheless, translation from preclinical studies to humans has been difficult and largely disappointing. One key reason for this failure is the lack of tools to study the fate of cells non-invasively and longitudinally. Many questions still remain about what happens to DC after they are administered. In order to elicit an immune response, DC must migrate to draining lymph nodes where they encounter T and B cells. The degree of immune activation is related to the number of DC that arrives at the lymph node. To move forward with clinical trials we require novel imaging tools for qualitative and quantitative monitoring of DC to determine their anatomical location, cell numbers, and functional lifespan. Fluorine-19 (¹⁹F) MRI can address this limitation because of the potential for unambiguous detection and accurate quantification, since mammalian tissues have negligible ¹⁹F.

Methods: Our technique involves pre-labeling cells with a ¹⁹F-based imaging probe, Cell Sense, to allow them to be tracked by MRI. Monocyte derived-DC (moDC) were prepared using elutriation samples enriched for peripheral blood mononuclear cells from human prostate cancer patients. Following maturation, Cell Sense labeled DC were injected into the footpad of nude (n=4) and C57Bl/6 (n=10) mice to track their migration to lymph nodes. Proton (¹H) and ¹⁹F images were acquired at 9.4T with a dual-tuned ¹H/¹⁹F mouse body coil using a 3D-balanced steady state free precession (bSSFP) sequence. Image resolution was 1x1x1mm³ for ¹⁹F and 200x200x200μm³ for ¹H. Total scan time was under 90 minutes. Mice were anaesthetized with isoflurane and imaged 48 hours following footpad injection. Quantification of the ¹⁹F-labeled cells was performed by measuring the signal in the region of interest and in a reference of known concentration using Voxel Tracker software. NMR was performed using 2x10⁶ ¹⁹F-labeled DC in order to determine the intracellular loading.

Results/Discussion: We tested the accuracy of ¹⁹F-MRI quantification using a phantom made of 5 different cell pellets (Fig1). Precision was found to be very good, with a linear correlation value of R²= 0.87. Labeling of the DC with the ¹⁹F-agent Cell Sense did not affect the viability or phenotype of the cells as shown by flow cytometry. *In vivo*, ¹⁹F signal can be seen within the popliteal lymph node of nude mice following a footpad injection of 2x10⁶ DC (Fig2). Quantification of the migrated ¹⁹F-labeled DC agrees with percentages previously reported in the literature by other techniques. DC migration was tracked from the footpad along the lymphatic pathway to three draining lymph nodes in C57Bl/6 mice: the popliteal, the inguinal, and the iliac. Once again, quantification of the signal reveals approximately 5% of the DC migrate to the draining lymph nodes. Future work will focus on translating the ¹⁹F-tracking technique to clinical strength (3T) MRI systems for use in clinical trials of prostate cancer immunotherapy.

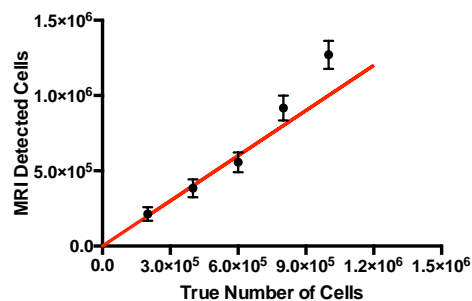


Figure 1: Verification of Quantification Accuracy using Cell Sense labeled cells. Cell pellets were collected ranging from 2x10⁵ to 1x10⁶ cells. ¹⁹F-MRI and ¹⁹F-NMR was performed on the pellets alongside a reference tube of known ¹⁹F concentration. Voxeltracker™ software was used for quantification. The red line represents the ideal result of a 1:1 correlation.

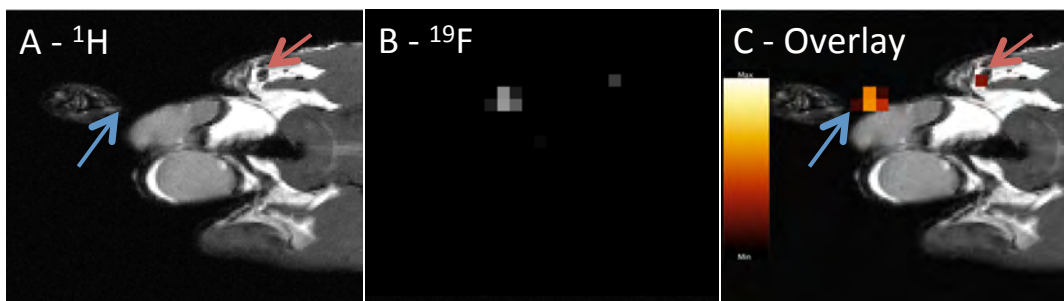


Figure 2: MRI of a mouse following injection of 2 million ¹⁹F- Cell Sense labeled human DC via footpad. Two MRI images were collected in the coronal orientation, first a ¹H image (A), then a ¹⁹F image (B). The injection point is indicated by a blue arrow. A red arrow points to the popliteal lymph node. (C) An overlay of the ¹⁹F signal due to DC onto the ¹H image provides anatomical context. Fluorine signal can be seen localized to the lymph node after migrating from the injection point. Quantification of the signal in the node indicates 110k ± 40k human DC. Approximately 5% of injected DC are expected to migrate to the LN.

Model Based Reconstruction for Simultaneous [1-¹³C]Pyruvate and Lactate Imaging

Benjamin J. Geraghty^{1,2}, Justin Y. C. Lau^{1,2}, Albert P. Chen³, and Charles H. Cunningham^{1,2}

¹Dept. of Medical Biophysics, University of Toronto, Toronto, Ontario, Canada, ²Physical Sciences, Sunnybrook Research Institute, Toronto, Ontario, Canada, ³GE Healthcare, Toronto, Ontario, Canada

PURPOSE: Hyperpolarized ¹³C imaging offers the potential to dynamically probe metabolism *in vivo*. The most prevalent imaging methods include fast chemical shift imaging (CSI), frequency selective spectral-spatial (Sp-Sp) excitation [1] and IDEAL [2]. Recently, a joint spectral-spatial (k-t) technique was demonstrated on a small animal scanner, effectively combining CSI and IDEAL within a single shot [3]. Joint spectral and spatial encoding is achieved by oversampling the FOV during a spiral acquisition and performing a model based, least squares reconstruction. Large oversampling rates are required to improve the conditioning of the reconstruction problem; however, due to limited gradient performance, the oversampling rate necessary to resolve multiple metabolites within a single shot cannot be achieved on conventional clinical scanners. We propose to combine k-t oversampling with Sp-Sp excitation to reduce gradient demands and resolve images of [1-¹³C]pyruvate and [1-¹³C]lactate within a single shot.

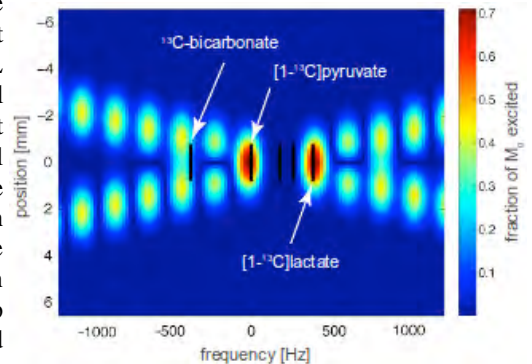


Figure 1 – Dual-band Spectral-Spatial excitation profile

METHODS: A numerical phantom was developed in Matlab to correspond directly with the standard GE ¹³C phantom. Its chambers contain formate, lactate, bicarbonate and alanine. Formate is used in place of pyruvate in the GE phantom. A spiral trajectory (16384pts, 125KHz BW, 65ms readout) was computed for an FOV of 10cm, corresponding to an oversampling factor of 2X. Analytical spiral k-space data was derived for each chamber, modulated to the respective chemical shifts and summed to generate the synthetic signal. The effect of Sp-Sp excitation on reconstruction was evaluated by generating data which excluded the bicarbonate and alanine signals. The signal equation can be cast as a linear system of equations $b = Ax$, where x is the vectorized concatenation of spatial profiles, and can be solved by least squares minimization. A dual-band, Sp-Sp pulse (figure 1) was designed to selectively excite formate/pyruvate and lactate while minimizing sideband interaction with ¹³C-bicarbonate. Thermally polarized ¹³C data were acquired with a dual-tuned ¹H/¹³C quadrature rat coil using the same 10cm FOV spiral k-space trajectory as in the synthetic data. For the *in vivo* acquisition, 2.5mL of 80mM [1-¹³C]pyruvate, prepolarized using the SpinLab DNP polarizer (GE Healthcare), was injected into a healthy rat (GE MR750, FOV=15cm, TR/TE=5000/25ms, FA=10deg, BW=125KHz, 15 time points, 1 slice, 2cm thick). A fast spin echo axial anatomical image was acquired following the ¹³C acquisition (FOV=15cm, TR/TE 3500/102ms).

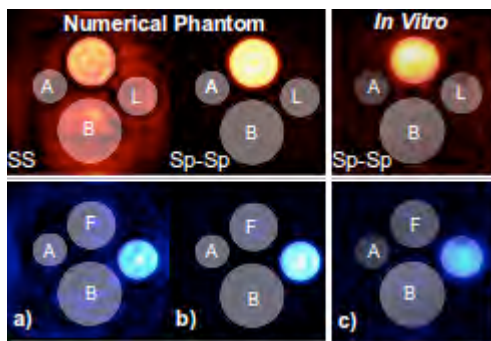


Figure 2 - A= Alanine, B = Bicarbonate, F = Formate, L = Lactate a) formate (red) and lactate (blue) images depicting signal contamination due to inadequate oversampling b) improved image reconstructions when alanine and bicarbonate are not excited c) Experimental GE ¹³C phantom data, TR/TE 5000/25ms, 150 averages

RESULTS & DISCUSSION: The simulated results indicate that an oversampling rate of 2X is insufficient for resolving four metabolites. Figure 2a reveals considerable contamination from bicarbonate and alanine within the formate (red) and lactate (blue) images. By excluding bicarbonate and alanine, formate and lactate are well resolved (figure 2b). The thermally polarized *in vitro* phantom images (figure 2c) acquired with the tailored Sp-Sp pulse are in good agreement with the simulation results. Time points 2 through 6 of the reconstructed pyruvate and lactate images are presented in figure 3. The simultaneous excitation and acquisition of pyruvate and lactate reduces the number of TRs that would otherwise be necessary in a purely Sp-Sp acquisition. For a fixed spiral readout duration, image resolution is effectively

traded off for improved temporal resolution.

CONCLUSION: We have demonstrated a unified spectral-spatial excitation and encoding scheme which allows the simultaneous acquisition of pyruvate and lactate images on a clinical scanner. Further research into the optimal use of the spatial / temporal resolution trade off is underway.

REFERENCES:

- [1] Lau, Angus Z. et al. MRM 65.5 (2010): 1323-1331
- [2] Wiesinger, Florian et al. MRM 68.1 (2012): 8-16
- [3] Gordon, Jeremy W. et al, DOI:10.1002/mrm24796 (2013)

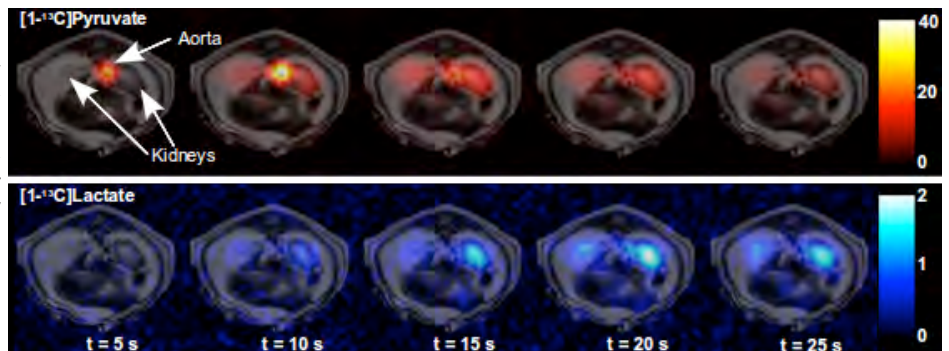


Figure 3 – Dynamic simultaneous acquisition of [1-¹³C]Pyruvate and [1-¹³C]Lactate. Images were cropped to a nominal FOV of 7.5cm. The peak SNR was estimated to be 100 for pyruvate and 20 for lactate

Toward prostate cancer contouring guidelines for focal therapy on MRI: assessment of target volume dominant lesion coverage via accurate histology fusion

Eli Gibson^{12†}, Mena Gaed^{134‡}, José A. Gómez³, Madeleine Moussa³, Cesare Romagnoli⁴, Zahra Kassam⁴⁹, Matthew Bastian-Jordan¹⁰, Derek Cool¹⁴, Stephen Pautler⁵⁶⁸, Joseph L. Chin⁵⁶, Cathie Crukley¹⁸, Glenn S. Bauman⁶, Aaron Fenster¹²⁶⁷⁸, Aaron D. Ward²⁶⁷⁸

¹Robarts Research Institute, ²Graduate Program in Biomedical Engineering, ³Departments of ³Pathology, ⁴Medical Imaging, ⁵Surgery, ⁶Oncology and ⁷Medical Biophysics, The University of Western Ontario; ⁸Lawson Health Research Institute; ⁹St. Joseph's Hospital; London, Canada. ¹⁰Qld Health, Brisbane, Australia

[†]Supervisors: Aaron Fenster, Aaron D. Ward; [‡]Supervisors: Aaron Fenster, Madeleine Moussa

Introduction: Multi-parametric magnetic resonance imaging (MPMRI) can be used to detect and stage prostate cancer (PCa); however, its suitability for accurate delineation of gross tumour volumes (GTVs) for disease monitoring or therapeutic planning is unknown. We measured (1) the histological coverage of GTVs with respect to Gleason score 7 (GS7) peripheral zone (PZ) tumours contoured on radical prostatectomy (RP) histology via highly accurate registration to endorectal MPMRI and (2) the necessary GTV expansion to achieve full coverage.

Methods: On each MPMRI sequence [T2-weighted (T2W), dynamic contrast enhanced (DCE) and apparent diffusion coefficient (ADC)] for 6 RP patients, 4 radiology observers delineated GTVs assessed as equivocally, likely or highly likely PCa (prostate imaging reporting and data system [PI-RADS] scores of 3 – 5). All 7 identified histological PZ GS7 foci (volumes of 0.1 – 0.8 cm³) were deformably registered to MPMRI (mean target registration error 2 mm). We measured the *residual* areas of histological PCa missed by each MPMRI GTV, with GTV expansions from 0 – 10 mm.

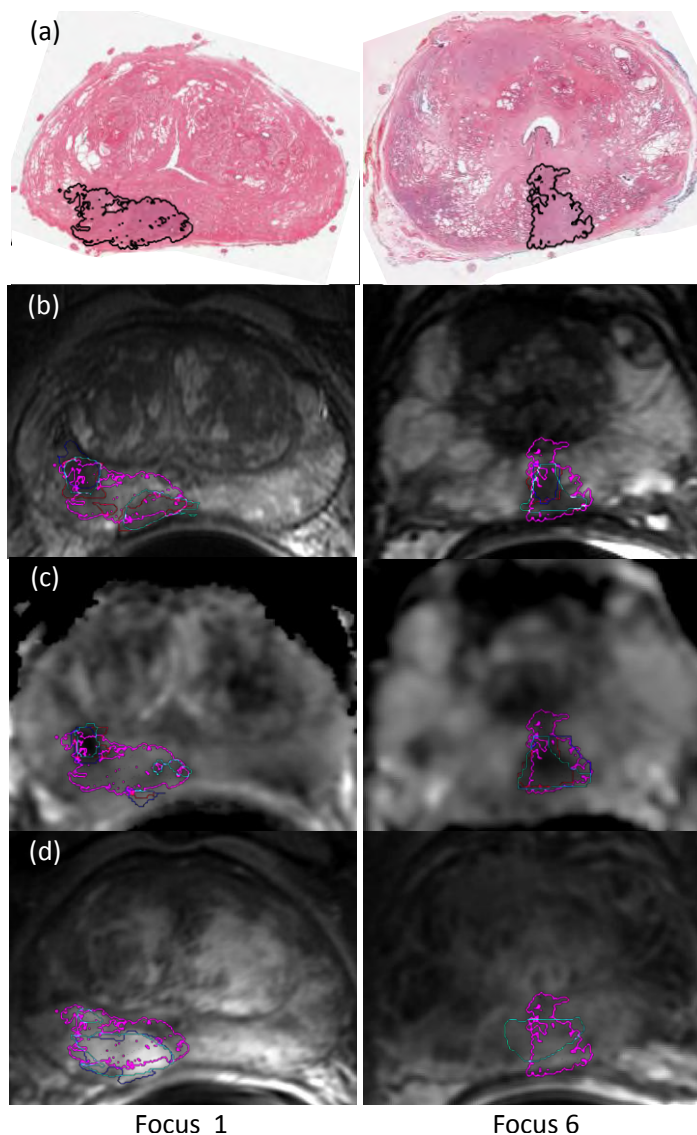


Fig. 1: Co-registered (a) histology, (b) T2W, (c) ADC and (d) DCE images for foci 1 & 6 (Fig. 2). Histologic foci are in black (a) and magenta (b – d). GTVs are in red/cyan/green/blue.

Results: Of the potential 7 foci × 3 sequences × 4 observers = 84 GTVs overlapping with histological foci, 49 were true positives and 35 false negatives, with 1 focus (with the lowest proportion of Gleason 4) missed by all observers. Fig. 1 illustrates registered images with histological foci and GTVs. Fig. 2 shows residual tumour percentages aggregated for margin expansions of 0 – 10 mm, and for each GTV with 0 and 8 mm expansions.

Conclusion: Despite variability in delineations of gross tumour volumes on multi-parametric magnetic resonance imaging, this study generates the hypothesis that delineations on T2W and ADC sequences, expanded by 8 mm margins, provide 98% coverage of histologically identified Gleason score 7 peripheral zone prostate cancer. Given known uncertainties in therapy delivery, such coverage may be acceptable for targeting lesion-focused therapies with curative-intent for suitable patients.

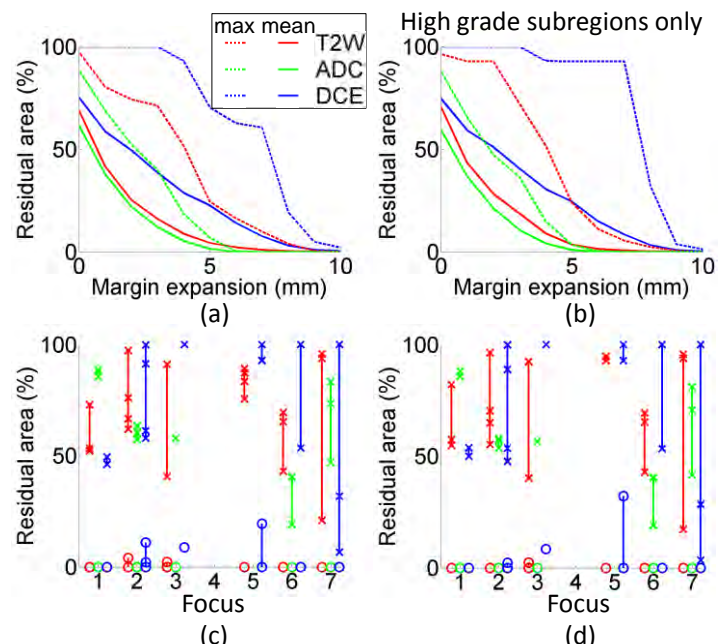


Fig. 2: (a – b) Aggregated percentage residual areas over all foci and observers. (c – d) Percentage residual areas for 0 mm (×) and 8 mm (○) margin expansions (1 ×/○ per observer for each expansion).

Technical Factors affecting Apparent Diffusion Coefficient in Women with Locally Advanced Cervical Cancer

Dr. Adam Gladwish, Dr. Kathy Han*, Dr. Warren Foltz*

Department of Radiation Oncology, Princess Margaret Cancer Centre, University Health Network

*Research Supervisors

Background: Diffusion-weighted MRI (DWI-MRI) imaging and the apparent diffusion coefficient (ADC) are becoming increasingly prevalent as a biomarker for cancer detection, progress and outcome. However, ADC values can depend on multiple technical factors, particularly b-value selection but also vendor and field strength differences (1,2). Accounting for these factors is important in the setting of clinical comparison across studies and institutions. Prior studies have characterized the relevance of these factors for the brain and abdomen, yet not within the female pelvis. We investigate whether ADC values measured from women with locally advanced cervical cancer on different MRI systems and with different b-value parameter sets can be pooled to improve evaluation of baseline ADC as a prognostic biomarker. This study reports on the linearity of the logarithmically-transformed tumor DWI signal with b-value, and overall ADC variability. We also identify and report on potential internal reference structures.

Materials and Methods: Sixty-four women with locally advanced cervical cancer (FIGO stage Ib - IVa) who were treated with definitive chemoradiation at Princess Margaret Cancer Centre between 2008 - 2011 were retrospectively selected from an anthological database. All women had pre-treatment DWI-MRI imaging on a 1.5T or 3.0T Siemens MRI scanner with varying b-values to a maximum of 1000 s/mm². Rectangular, 1 cm², regions-of-interest (ROI) were drawn on a single corresponding slice for each b-value, including the tumor, skeletal muscle (gluteus maximus) and bladder (urine). ADC values were calculated via linear regression to the logarithmically-transformed DWI signal and b-value sets, and the coefficient of determination recorded. Mean ADC, standard deviation, and covariance were calculated for each ROI. Two by two contingency tables were generated to assess efficacy of tumor ADC for prediction of histology (squamous cell carcinoma vs. adenocarcinoma), based on a reported threshold ADC of 1.1 mm²/s (3). Contingency tables were recalculated using tumor normalized to internal references.

Results: Mean age of the cohort was 54 years (range 25 - 85). Histologies included squamous cell carcinoma (44 cases), adenocarcinoma (17) and adenosquamous carcinoma (3). Thirty-three women underwent imaging at 1.5T; 23 with b-values of 0, 50, 400, and 1000 s/mm², and 10 with b-values of 0, 100, and 800 s/mm². Of the 31 women scanned at 3T, the b-values were 0, 50, 400, 800 s/mm² for 23, and 0, 100, and 800 s/mm² for 8. Linear regression to the logarithmically transformed DWI signal and b-value pairs was a valid model for data fitting across all ROIs, field strengths, and b-value combinations, with mean R² of 91%, 84% and 99% for tumor, muscle and urine respectively. Coefficients of variance were 31% for tumor, reducing to 10% for urine. In general, there was a trend for higher ADC with increasing field strength and lower number of fitted b-values. Urine provided superior linearity and reproducibility to gluteal muscle (>85% of subjects with ADC within 15% of the mean of 2.9 x 10⁻³ mm²/s), suggesting its potential as an internal reference for data pooling. Without normalization, tumor ADC stratified between histology classes with a sensitivity and specificity of 44% and 70%, respectively. Normalizing tumor ADC to urine ADC improved sensitivity and specificity to 67% and 84%, respectively.

Conclusion: Pooling of ADC datasets from cervical cancer patients is not prohibited by model fitting to b-values to 1000 s/mm², yet significant data variability was noted between data sets acquired at 1.5 and 3 T and with different total number of fitted b-values. ADC variability associated with MRI system considerations was reduced by normalization to urine ADC, based on improved predictive value for ADC between cervical cancer subclasses.

- 1) Makoto, S., et. al. *Variability in Absolute Apparent Diffusion Coefficient Values Across Different Platforms May Be Substantial: A Multivendor, Multi-institutional Comparison Study*. Radiology., 249 (2), 2008.
- 2) Dale, B., et. al. *Field Strength and Diffusion Encoding Technique Affect the Apparent Diffusion Coefficient Measurements in Diffusion-Weighted Imaging of the Abdomen*. Invest. Radiol., 45 (2), 2010.
- 3) Kuang, F., et. al. *The value of apparent diffusion coefficient in the assessment of cervical cancer*. Eur Radiol., 23: 1050-1058, 2013.

Development and application of pulmonary structure-function registration methods: Towards pulmonary image-guidance methods for improved airway targeted therapies and outcomes

Fumin Guo^{1,3}, Damien Pike^{1,2}, Sarah Svenningsen^{1,2}, Harvey O Coxson⁵, John J. Drozd¹, Jing Yuan¹, Aaron Fenster¹⁻⁴ and Grace Parraga¹⁻⁴

¹Imaging Research Laboratories, Robarts Research Institute,

²Department of Medical Biophysics,

³Graduate Program in Biomedical Engineering,

⁴Department of Medical Imaging,

The University of Western Ontario, London, CANADA;

⁵Department of Radiology, Vancouver General Hospital and James Hogg Research Centre,
University of British Columbia, Vancouver, CANADA

ABSTRACT

Hyperpolarized ³He magnetic resonance imaging (MRI) has emerged as a non-invasive imaging method to visualize and measure pulmonary function. Complementary to ³He MRI, x-ray computed tomography (CT) provides high-resolution structural and morphological information and has been more widely used to provide regional information of lung morphology. Therefore, our objective is to develop pulmonary imaging registration methods to provide robust, rapid and user-friendly image-guided structure-function maps for targeted pulmonary therapies. Twelve subjects with chronic obstructive pulmonary disease (COPD) were enrolled in this study. Proton (¹H) and ³He MRI were acquired using a coached breath-hold technique and CT was performed within ten minutes of MRI using the same breath-hold volume and maneuver. We proposed to register CT and ¹H MR images using shape-matching method and compared the results with that using landmark-based affine registration, which was performed using corresponding landmarks in both CT and ¹H MR images. For comparison, we proposed a shape-based non-rigid registration by first identifying the shapes of the lung cavities manually, and then matching the two shapes using affine and thin-plate spline transformation. In addition, we proposed to split the lung into two halves and register the left and right (LR) lungs separately and compared the results with that by registering the whole lung (WL) using both methods. Registration accuracy for WL and LR was evaluated using the fiducial localization error (FLE) and target registration error (TRE). For landmark-based method, we reported TREs of 7.81 ± 4.60 mm for WL registration versus 8.41 ± 5.34 mm for LR registration. Similarly, for shape-based method, TREs were 6.92 ± 4.43 versus 7.99 ± 4.64 mm. Our FLE was 1.84 mm and did not dominate the TREs. We obtained that it was significantly different in WL and LR registration using shape method ($p=0.01$) and LR registration using shape and landmark-based methods ($p=0.04$).

KEYWORDS: Hyperpolarized ³HeMRI, ¹H MRI, CT, landmark-based registration, shape-based registration, affine, thin-plate spline

Design, Synthesis and Application of a Novel Cell Permeable and Trappable MRI T₁ Contrast Agent

Inga E. Haedicke,^{a,b} Kelvin Y. Zhu,^{a,b} Joris T. Nofiele,^{d,e} Hai-Ling M. Cheng,^{d,e,f,g} Xiao-an Zhang^{*a,b,c}

^aDepartment of Chemistry, University of Toronto, Toronto, Canada, ^bDepartment of Physical and Environmental Sciences, ^cDepartment of Biological Sciences University of Toronto Scarborough, Toronto, Canada, ^dThe Hospital for Sick Children., Toronto, Ontario, Canada, ^eDepartment of Medical Biophysics, University of Toronto, Toronto, Canada, ^fLeslie Dan Faculty of Pharmacy, University of Toronto, Toronto, Canada, ^gInstitute of Biomaterials and Biomedical Engineering, University of Toronto, Canada

Cellular MRI is becoming an important tool for monitoring the progress of cell-based therapies, including adoptive immunotherapy and stem-cell therapy.¹ MRI has been valuable for *in vivo* cell tracking because it offers high spatial resolution with detailed anatomical images of opaque subjects with excellent soft tissue contrast and no ionizing radiation. This strategy has been demonstrated in both research and clinical settings with SPIO labeled cells. One limitation for T_2 contrast agents, such as SPIOs, is lack of specificity due to the negative contrast mechanism. Conventional T_1 agents are primarily Gd-chelates with little application for cell labeling since most Gd-chelates are limited by lack of cell permeability, low relaxivities at fields above 0.2 Tesla and serious concerns about intracellular release of free Gd^{III} ion as this has been associated with nephrogenic systemic fibrosis (NSF) in patients with decreased renal function. MnCl₂ has been used for cell labeling and similar to Gd-chelates these agents suffer from relatively low relaxivities, in particular at high magnetic fields. While Mn, an endogenous micronutrient, is more biocompatible than Gd, a highly stable chelate would further eliminate possible toxicity of high-dose Mn, especially for longitudinal tracking of labelled cells *in vivo*. To overcome these limitations we have designed a novel cell permeable and trappable Gd-free T_1 contrast agent utilizing a manganese (III) porphyrin platform. MnPs form highly stable metal chelates and have been shown to exhibit an 'anomalously high relaxivity' at high field.² The molecular design started from 5, 10, 15, 20-tetra(carboxyporphyrinato)manganese(III), (MnTCP), developed by us as an extracellular, small and hydrophilic, contrast agent with rapid renal clearance and efficient relaxivity at high fields (r_1 of 7.9 mM⁻¹ s⁻¹ at 3 T).^{3,4} Acetoxymethyl ester groups were used to mask the polar carboxylates resulting in high cell permeability. Upon hydrolysis by intracellular esterase, the hydrophobic ester groups are cleaved trapping the negatively charged MnTCP inside the cell for longitudinal tracking *in vivo*.

A synthetic method was developed to prepare this novel agent MnTriAMP from MnTCP in 2 steps. Preliminary cell labelling with human breast cancer cell line MDA-MB-231 was done with an incubation time of 2 hours at 83 uM, and resulted in significant uptake of MnTriAMP compared to the cell impermeable control MnTCP. As both compounds are deeply coloured this was evident by eye after formation of the cell pellets, as seen in the photograph, figure 1a. MRI of the cell pellets on a 3 Tesla scanner using a T_1 weighted spin-echo pulse sequence showed significant contrast enhancement of MnTriAMP labelled cells over MnTCP and control cells, figure

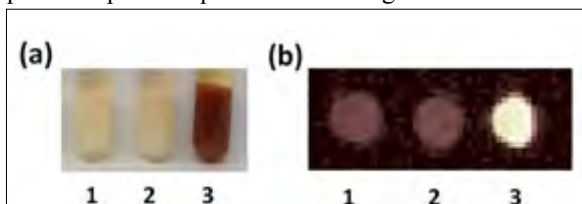


Fig. 1 (a) Photograph of cell pellets prior to MRI: from left untreated cells (1), cells treated with MnTCP (2) and MnTriAMP (3); (b) the corresponding MR image of same cells at 3 T and 25 °C. TR = 100 ms, TE = 14.163 ms, 3 mm slice thickness, 0.5 × 0.5 mm in-plane resolution.

1b. Calculation of the T_1 and T_2 relaxation times from the signal intensities gave a much shorter T_1 of 215 ± 12.1 ms for MnTriAMP treated cells and a minimal decrease for control sample with MnTCP, T_1 = 1072 ± 28.0 ms, compared to 1107 ± 26.6 ms for the untreated cells. This confirmed that MnTriAMP was indeed cell permeable because of the introduction of hydrophobic acetoxymethyl ester groups. Cell viability test showed > 96 % viable directly after cell labelling indicating good biocompatibility for both MnTriAMP and MnTCP. In conclusion, we have successfully designed and synthesized a novel cell permeable and trappable T_1 contrast agent, MnTriAMP. Cell labeling demonstrated efficient uptake of MnTriAMP into MDA-MB-231 cells with significant positive contrast enhancement at 3 T with little influence on cell viability, making MnTriAMP a promising new contrast agent for cellular MRI applications.

[1] N. P. Restifo et al, *Nat. Rev. Immun.* **2012**, 12,(4), 269. [2] Koenig et al., *Magn. Reson. Med.* **1987**, 4, 252. [3] Cheng et al, *J. Magn. Reson. Imaging*, **2013**, 0, 00. [4] Zhang et al, Gd-free MRI Contrast Agents. [United States Patent 13/765,458](#), filed February 12, 2013, Patent Pending.

Accurate tracking of interventional devices using spectrally-selective excitation and a controllable susceptibility device

Hirad Karimi^{1,2}, William Dominguez-Viqueira², Zahra Faraji-Dana^{1,2}, Simon J Graham^{1,2}, Charles H Cunningham^{1,2}

¹Dept. of Medical Biophysics, University of Toronto, Toronto, Ontario, Canada, ²Physical Sciences, Sunnybrook Research Institute, Toronto, Ontario, Canada

Introduction: Tracking of interventional devices under MRI guidance remains an active area of research. Magnetic resonance imaging offers superior soft tissue contrast compared to other modalities such as x-ray fluoroscopy. Passive tracking with susceptibility effects offers easy-to-make and cost efficient ways to track interventional devices. We have recently proposed a controllable tracking device in which the susceptibility effect of the device can be switched ON and OFF [1]. In this abstract we investigate a rapid and accurate tracking scheme using the proposed device. Once the device is at the intended position, the susceptibility effect can be turned OFF in order to acquire high quality MR images without the susceptibility effect present.

Theory and Methods: The new tracking device that consists of three concentric layers of Titanium (Ti) and Graphite (G) [1]. Once the three layers are aligned (OFF), the device will create minimal magnetic field perturbations, which minimizes the susceptibility artifact in MR images. However, if the graphite layer is retracted (ON), the device will perturb magnetic field quite substantially, producing a controlled artifact in the images. The tracking device that was used in this study is 9F in outer diameter and 15 mm in length. Spectrally-selective RF excitation and refocusing pulses with 200 Hz (FWHM) passbands were used to excite and refocus isofrequency contours as shown in Fig.1 [2]. The spatial location and extent of the isofrequency contours are dependent on the carrier frequency (ω_c) and the frequency profile of the combined excitation/refocusing pulses. The RF pulses were then used to rapidly acquire 1-dimensional projections of the object along each of the physical axes. Off-resonance projections with high signal-to-noise ratio (SNR) for different angles of the tracking device with respect to main field, were used to build a look-up table. Once a set of new projections has been acquired (GE MR750 3T, TR/TE = 100/15ms, FA=90°, BW=64kHz, 512 samples, FOV=50cm), cross-correlations between these new projections and the look-up table projections can be calculated. The maximum cross-correlation and the spatial shift associated with that cross-correlation were then used to calculate the position of the excited isofrequency contours for each physical axis (total time= 0.22s) as shown in Fig.2. The ground-truth positions of the tracking device at each TR were recorded using a set of MR-compatible stereo cameras to compare with our position calculations. The accuracy and precision of the cameras are 0.04 ± 0.01 mm in “Z” axis [3]. The first and last position measurements were used to translate the coordinates from the cameras to that of the scanner.

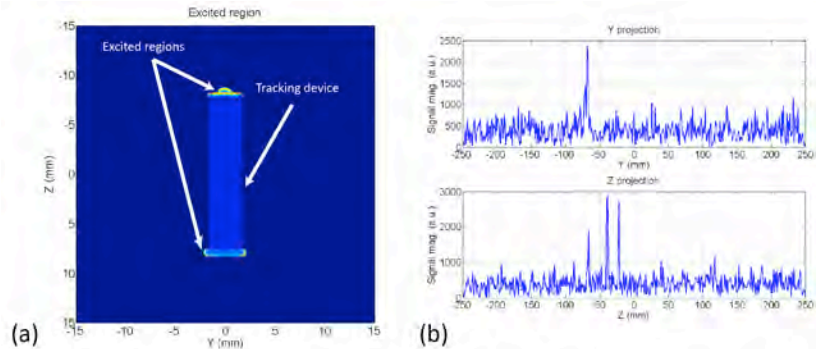


Fig.1: (a) Excited isofrequency contours which are between 920 Hz and 1120 Hz from Larmor Frequency (b) Projection along Y and Z axes

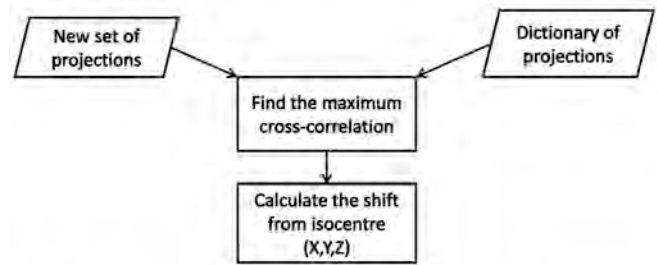


Fig.2: Flowchart for calculating the position of the tracking device using a dictionary of high SNR projections for different angles of the device with respect to main field

Results and Discussion: Fig.3 shows good agreement between the calculated position using the tracking device and measured positions using stereo cameras. The average error in “Y” and “Z” axes is 0.65 and 0.36 mm respectively. With projections acquired each TR, the temporal resolution of this technique (~3 frames/s) allows rapid tracking of interventional tools. It should be noted that if the tracking device is stationary, due to 90° flip angle, the projected signal is heavily saturated on successive TRs and no position measurement can be made (although no update is necessary for a stationary device). However, if the device is moved, new spin isochromats will be excited/refocused and the new position of the device can be measured with adequate SNR. The average SNR for the projections acquired in our phantom study with a 5-inch surface coil was 6, which was sufficient for position measurement. We expect that if the same coil were used, the SNR and position accuracy in *in vivo* measurements would be comparable to those measured in this study.

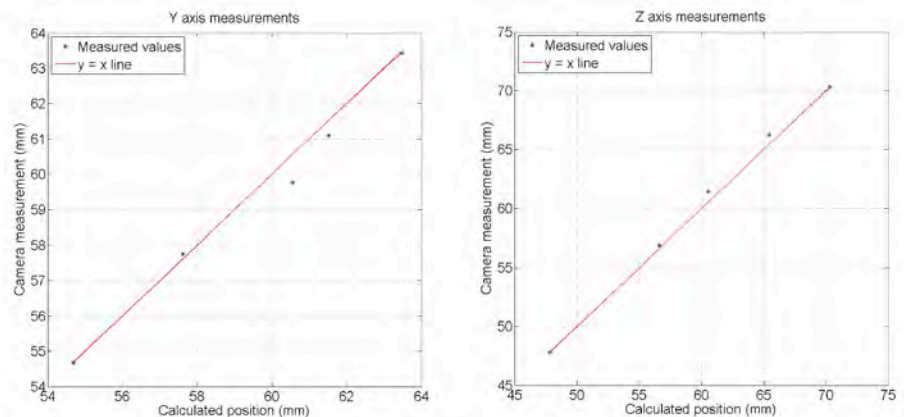


Fig.3: Calculated positions vs measurements of the stereo camera for Y and Z

References: [1] Dominguez-Viqueira W, et al. *MRM*, DOI: 10.1002/mrm.24899, 2013 [2] Cunningham C.H. et al, *MRM*, 53, 5:999-1005, 2005 [3] Rotenberg et al, *MRM*, *Magn Reson Med*, 69, 3:734-48

Subjective application-based measurement of reconstruction quality for under-sampled MRI

Mohammad Kayvanrad^{1,2}, Amy Lin³, Terry Peters^{1,2,3}

¹ Robarts Research Institute, Western University, Canada ² Biomedical Engineering program, Western University, Canada ³ Department of medical imaging, Western University, Canada

Purpose: Parallel imaging (PI) ¹ and compressed sensing (CS) ² are two major approaches to accelerating MRI acquisitions by acquiring under-sampled k-space data. Although quantitative quality measures, such as the normalized root mean square error (NRMSE), are commonly used to assess the reconstruction quality of these techniques, these measures do not necessarily correlate with the practical image quality as perceived by radiologists and other expert end users. Therefore, unless accompanied by subjective assessments, any quantitative measure of reconstruction quality will be of limited clinical impact. We present the results of our study on the subjective quality measurement of CS and combined CS and PI (where multiple-channel data are available) reconstructions.

Methods: Two common clinical applications of MRI in neuroradiology were studied:

(1) **Detection of white matter lesions:** This task involved detection of small non-specific white matter lesions on FLAIR images. Realistic artificial lesions were incorporated into whole-brain T2-FLAIR images of a healthy volunteer, in random locations in the cerebral white matter where these lesions are commonly seen clinically, with a probability of 50%. Lesion detection performance was studied for CS and low-resolution (used as a control baseline) reconstructions at under-sampling factors of 1 (i.e., no under-sampling), 2, 3, 4, and 5. The experiments involved identification of the lesion or declaring there to be none while the participants also indicated their level of confidence. (2) **Magnetic resonance angiography (MRA):** Whole brain 3D time of flight (TOF) MR angiogram of a healthy volunteer was acquired at 3T using a 32-channel head coil. Raw k-space data were retrospectively under-sampled with under-sampling factors 2, 3, 4, and 5, for PI (GRAPPA), combined CS and PI, and low-resolution (lowres) reconstructions, which were then reconstructed by the corresponding reconstruction technique. The reconstructions were scored by three senior radiology residents based on subjective diagnostic quality, with a 5-point scoring system. Human data used in this work were acquired using a protocol approved by the institutional office of research ethics.

Results: Figure 1 shows the pooled results of the lesion detection task for the lowres and CS reconstructions. Corresponding ROC curves were computed based on the confidence levels indicated by the participants, following the methodology of Metz ³. The area under the ROC curves (AUC) and the average NRMSE with respect to the fully-sampled reference images are shown in Table 1. MRA scoring results are shown in Table 2 and Figure 2 shows sample projection reconstructions at x5 under-sampling.

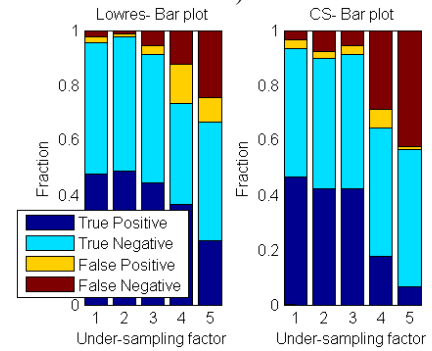


Figure 1- Lesion detection performance (pooled) for CS and lowres.

UF	AUC		NRMSE	
	lowres	CS	lowres	CS
1	0.99	0.96	0	0
2	1.0	0.97	0.013	0.0081
3	0.96	0.97	0.024	0.012
4	0.81	0.77	0.033	0.023
5	0.78	0.67	0.042	0.038

Table 1- Area under ROC curves (AUC) and the average NRMSE for different under-sampling factors (UF) in the lesion detection task (pooled results).

UF	Recon.	Avg. score	NRMSE
2	GRAPPA	5	0.0082
	lowres	4	0.029
	CS+PI	4.7	0.014
3	GRAPPA	1.7	0.11
	lowres	3	0.037
	CS+PI	4	0.025
4	GRAPPA	1	0.14
	lowres	2	0.045
	CS+PI	3.3	0.027
5	GRAPPA	1	0.15
	lowres	2	0.051
	CS+PI	3	0.030

Table 2- Average subjective scores given by three participants for the MRA scoring task and the NRMSE of the corresponding reconstructions with respect to fully-sampled reference.

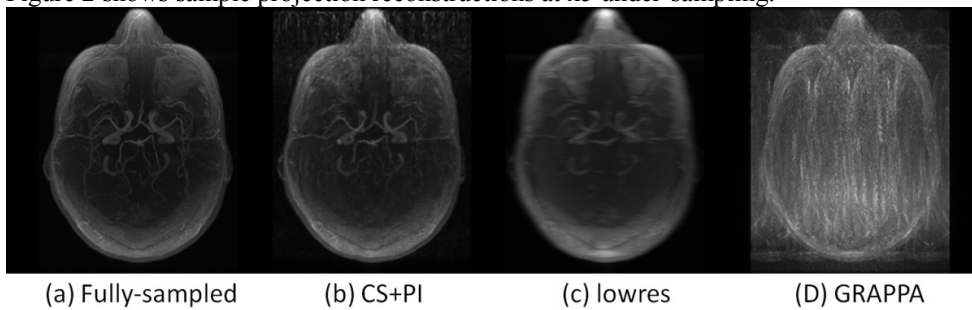


Figure 2- Axial MRA projection reconstruction: (a) fully-sampled (b,c,d) 5x under-sampled.

Discussion: While CS reconstruction of the FLAIR images results in significantly lower NRMSE values than the corresponding lowres reconstruction, the results show no improvement in lesion detection performance with CS over lowres. In fact, lowres results in higher detection accuracy in terms of the true positive and false negative fractions and AUC. However, for MRAs, while the subjective diagnostic quality score drops for the GRAPPA and lowres reconstructions very rapidly with increasing under-sampling factor, the combined CS+PI reconstruction maintains a reasonably high score up to an under-sampling factor of 3, suggesting that diagnostic quality (i.e., a subjective score of 4 or higher) images are achievable with under-sampling factors as high as 3 by combined CS and PI.

Conclusion: The results primarily suggest that the advantages of CS depend on the application. For example, while they indicate that higher under-sampling factors, while maintaining the diagnostic quality, are achievable with combined CS+PI for MRAs, no improvement over a simple lowres acquisition is achieved by CS in the lesion detection task. While for some applications, especially those requiring high resolution, CS may be of advantage, for some others, e.g., certain lesion detection tasks, one might simply reduce the acquisition time by appropriately reducing the resolution.

Reference: 1. Larkman, D. J. & Nunes, R. G. Parallel magnetic resonance imaging. *Phys. Med. Biol.* **52**, R15–55 (2007). 2. Lustig, M., Donoho, D. & Pauly, J. M. Sparse MRI: The application of compressed sensing for rapid MR imaging. *Magn. Reson. Med.* **58**, 1182–1195 (2007). 3. Metz, C. E. *Applications of Roc Analysis in Diagnostic Image Evaluation*. (Chicago Univ., IL (USA); Franklin McLean Memorial Research Inst., Chicago, IL (USA), 1979).

PLGA Encapsulated Enzyme for Kinetics Modelling of Hyperpolarized Pyruvate Metabolism

Justin Y.C. Lau^{1,2}, Jeanie Z. Fei³, Albert P. Chen⁴, Minseok Seo², and Charles H. Cunningham^{1,2}

¹Medical Biophysics, University of Toronto, Toronto, Ontario, Canada, ²Physical Sciences, Sunnybrook Research Institute, Toronto, Ontario, Canada, ³Health Sciences, McMaster University, Hamilton, Ontario, Canada, ⁴GE Healthcare, Toronto, Ontario, Canada

Introduction:

Overtreatment of asymptomatic prostate cancer is a current clinical problem. Additional tests that can better distinguish latent tumours from aggressive disease would benefit both patients and physicians. One common observation among aggressive prostate cancers is an altered metabolism that may include an upregulation of the enzyme lactate dehydrogenase (LDH). Dynamic nuclear polarization¹ is a signal enhancement technique that facilitates *in vivo* ¹³C magnetic resonance (MR) monitoring of metabolic activity.² Quantification of *in vivo* measurements, however, is challenging because the model must account for many variables including vascular transport, LDH activity, and a gradual loss of signal enhancement. Simpler *in vitro* systems, such as cells in a bioreactor³ and alginate-encapsulated LDH⁴, have been designed to validate *in vivo* metabolic models. This study explores the feasibility of *in vitro* LDH activity monitoring by encapsulation in poly(lactic-co-glycolic) acid (PLGA) beads, which can eventually be incorporated into a flow system. Validation of *in vivo* metabolic models is important because quantitative analyses of MR measurements to extract parameters characterizing LDH enzyme kinetics may offer additional information about the aggressiveness of asymptomatic prostate tumours

Methods:

Beads are synthesized using a double emulsion process. An aqueous solution of LDH (1.13 mg, 709 U/mg) and bovine serum albumin (5 mg) were added to a 5% solution of 50:50 PLGA in chloroform. This mixture was added to an aqueous solution of 7.5% dextrose and 1% polyvinyl alcohol (PVA). The double emulsion was stirred for 2 hours in an aqueous solution of 7.5% dextrose and 0.3% PVA to evaporate the chloroform. Beads recovered by centrifugation were washed five times before lyophilization.

A mixture of 30 μ L [^{1-¹³C}] pyruvic acid, 1 mM ProHance (Gadoteridol), and 15 mM OX63 was polarized using the GE SpinLab. A 2 mL solution of beads containing 0.113 mg of LDH was mixed with 1 mL of 80 mM disodium NADH. A pulse-acquire sequence was started upon adding 2 mL 80 mM pre-polarized pyruvate. Data were acquired with a ¹H/¹³C volume coil on a GE MR750 3 T scanner.

Results:

A polydisperse mixture of LDH-encapsulated PLGA beads with an average diameter was 20 μ m was synthesized. A representative micrograph in solution is shown in figure 1. Figure 2 summarizes the reaction kinetic profile showing the ¹³C MR signal of [^{1-¹³C}] pyruvate (substrate) and [^{1-¹³C}] lactate (product).

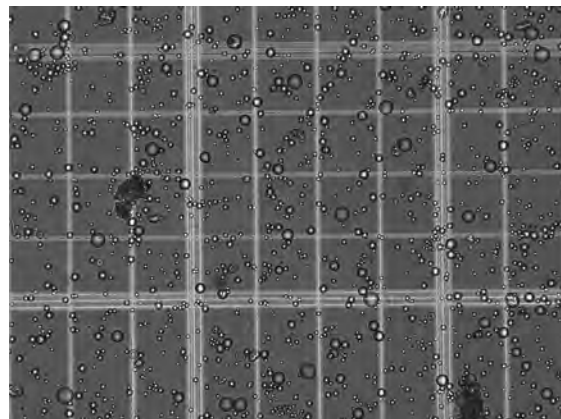


Figure 1: PLGA beads with encapsulated LDH. Each grid subunit has dimensions of 50 μ m.

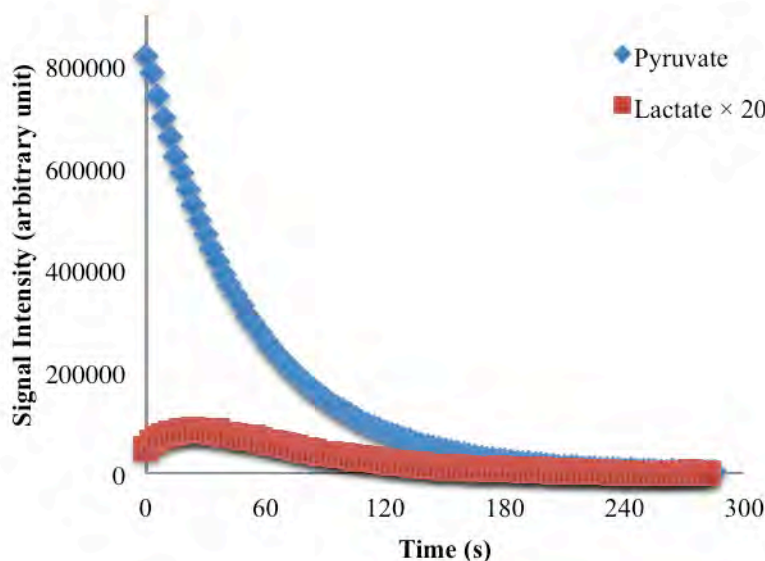


Figure 2: LDH kinetic profile monitored using ¹³C MR spectroscopy.

Discussion:

The measured peak lactate to peak pyruvate ratio is 0.00526, which is approximately 10-fold lower than typical ratios observed in the rat kidneys. By varying the synthesis and MR protocols, it may be possible to generate a wide range of reaction conditions to model the metabolism of different grades of prostate cancer. Further work is underway to assess the reproducibility and controllability of this *in vitro* system.

Conclusion: We have demonstrated the feasibility of ¹³C MR monitoring of enzyme activity in LDH-encapsulated PLGA beads.

Acknowledgements: Funding support from the Ontario Institute for Cancer Research and the Natural Sciences and Engineering Research Council of Canada.

References: [1] JH Ardenkjær *et al. Proc. Natl. Acad. Sci. USA* 100: 10158 (2003). [2] SJ Nelson *et al. Appl. Magn. Reson.* 34: 533-544 (2008). [3] KR Keshari *et al. Mag. Reson. Med.* 63: 322-329 (2010). [4] DK Hill *et al. Proc Intl. Soc. Mag. Reson. Med.* 20: 4471 (2012).

Evaluation of Physiological Noise Removal Techniques on the Resting-State fMRI Signal

Lily Lau^{1,2}, Jean Chen^{1,3}

¹Rotman Research Institute, Baycrest Centre for Geriatric Care, University of Toronto, ²Division of Engineering Science, University of Toronto ³Department of Medical Biophysics, University of Toronto

The removal of physiological noise, primarily cardiac and respiratory, is essential for studying brain function using resting-state functional MRI (fMRI). In this project, we evaluate five different physiological denoising methods for resting-state fMRI, using data acquired at high temporal resolution to ensure proper characterization of cardiac and respiratory signal components. The methods are the following: (1) RETROICOR, which requires external physiological recordings for noise removal, (2) CompCor, which estimates noise from select white-matter and cerebrospinal fluid regions, (3) PHYCAA+, which uses data-driven canonical autocorrelation analysis, (4) global mean phase signal regression, and (5) voxel-wise phase signal regression. RETROICOR and CompCor methods are commonly used in resting-state fMRI studies. The potential of more novel methods such as PHYCAA+ is unknown. Alternatively, the fMRI phase signal may also be used to estimate physiological artifacts. In this work, we compare the effectiveness of these methods for removing physiological noise in both gray and white matter of the resting-state blood-oxygen level-dependent (BOLD) fMRI signal. We found RETROICOR to be the most effective in removing cardiac and respiratory noise, but when physiological recordings are not available, CompCor was the second best choice for removing physiological noise.

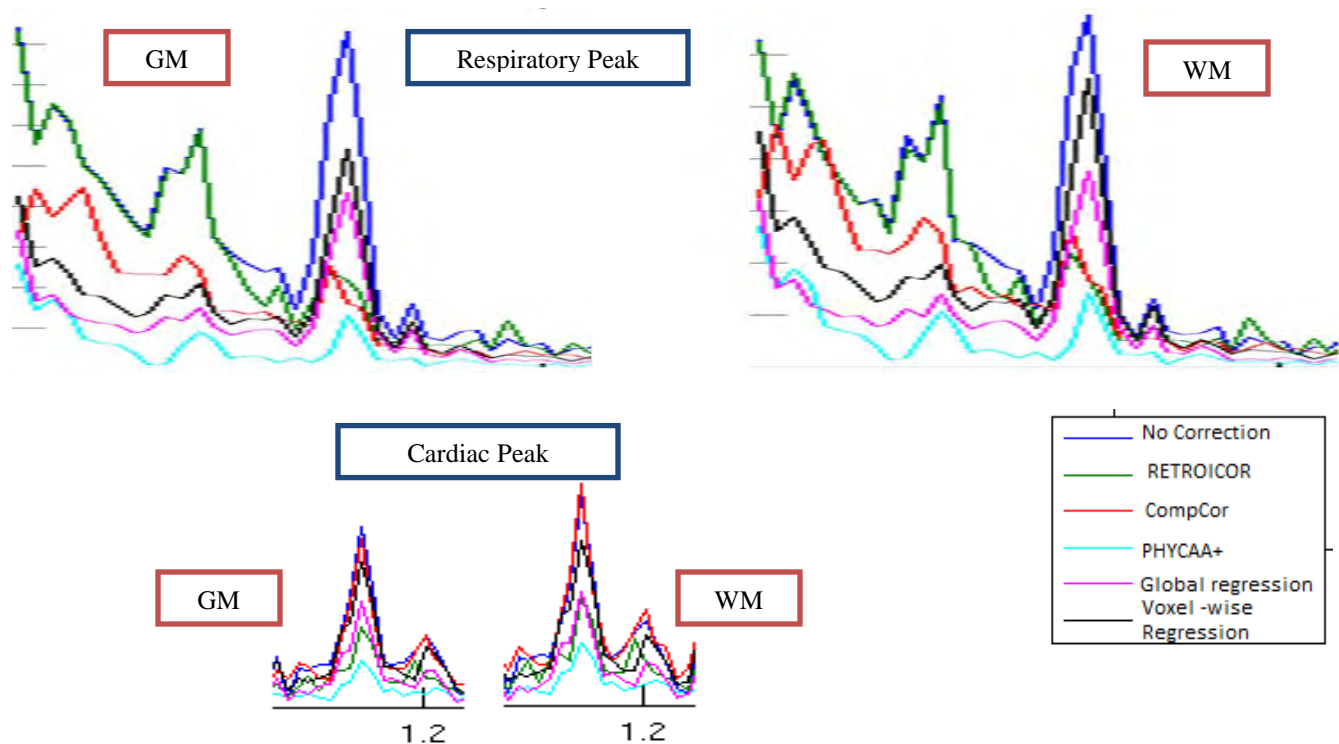


Figure 1. Respiratory and cardiac frequencies were identified from the physiological recordings. Power spectra were averaged over gray matter (GM) and white matter (WM) voxels at respiratory and cardiac frequencies resolved with peaks around 0.15 and 1.1 Hz, respectively. Fractional power was calculated for respiratory and cardiac spectral components as a measure of residual noise.

Non-invasive measurement of cellular membrane pH gradient in brain tumors using hyperpolarized ^{13}C -bicarbonate MSRI and CEST imaging.

Heeseung Lim¹, Nevin McVicar¹, Francisco M. Martínez-Santesteban¹, Robert Bartha^{1,2}, Timothy J. Scholl^{1,2}

¹ Medical Biophysics, Schulich School of Medicine and Dentistry, Western University, Canada. ² Robarts Research Institute, Western University, Canada

Introduction: Tumors are well adapted to an acidic microenvironment arising from poor vascularization and upregulated glycolysis. Excess lactate and H^+ ions from tumor cells are transported into the extracellular space. This creates a pH gradient across the cellular membrane producing an intracellular pH (pH_i) that is basic and an acidic extracellular pH (pH_e). Hyperpolarized ^{13}C bicarbonate chemical shift imaging (CSI) can be used to measure pH_e (1). Conversely, pH_i can be measured by chemical exchange saturation transfer (CEST)(2) of magnetization from endogenous amine and amide protons to bulk water. The purpose of this study is to measure the intracellular/extracellular pH gradient in tumor using hyperpolarized ^{13}C bicarbonate MRSI and CEST MRI.

Methods: A Wistar rat brain was surgically implanted with one million C6 glioma cells. Ten days after implantation, T_2 -weighted proton images of the rat brain were acquired using a 3.0T GE Discovery MR750 to localize the extent of the tumor. pH_e was measured by injecting 100-mM hyperpolarized ^{13}C cesium bicarbonate solution in the rat tail vein. ^{13}C spectra of the rat brain were acquired using 2D FID-CSI (TR = 80ms, matrix 8x8, FOV = 60x60mm, slice thickness = 5.5mm and BW = 5000Hz) to measure the regional distributions of ^{13}C -bicarbonate and $^{13}\text{CO}_2$. Extracellular pH maps of the healthy brain and tumor were calculated from the regional ^{13}C data using the Henderson-Hasselbalch equation.(1) On the same day, the same rat was imaged on a 9.4T Agilent (Palo Alto, CA) small animal MRI scanner. T_2 weighted proton images were acquired to localize the tumor, followed by single slice CEST MRI(3,4). CEST spectra were acquired using a standard fast spin echo (FSE) pulse sequence (TR/TE = 7000/7 ms, ETL=32, ETE=7 ms, matrix=64x64, FOV=40x40 mm², 2 prescans, slice thickness=4 mm, 4 s and 1.5 uT pre-image saturation pulse) An intracellular pH map was calculated from the CEST data using a previously described amine and amide concentration-independent detection (AACID) technique.(4)

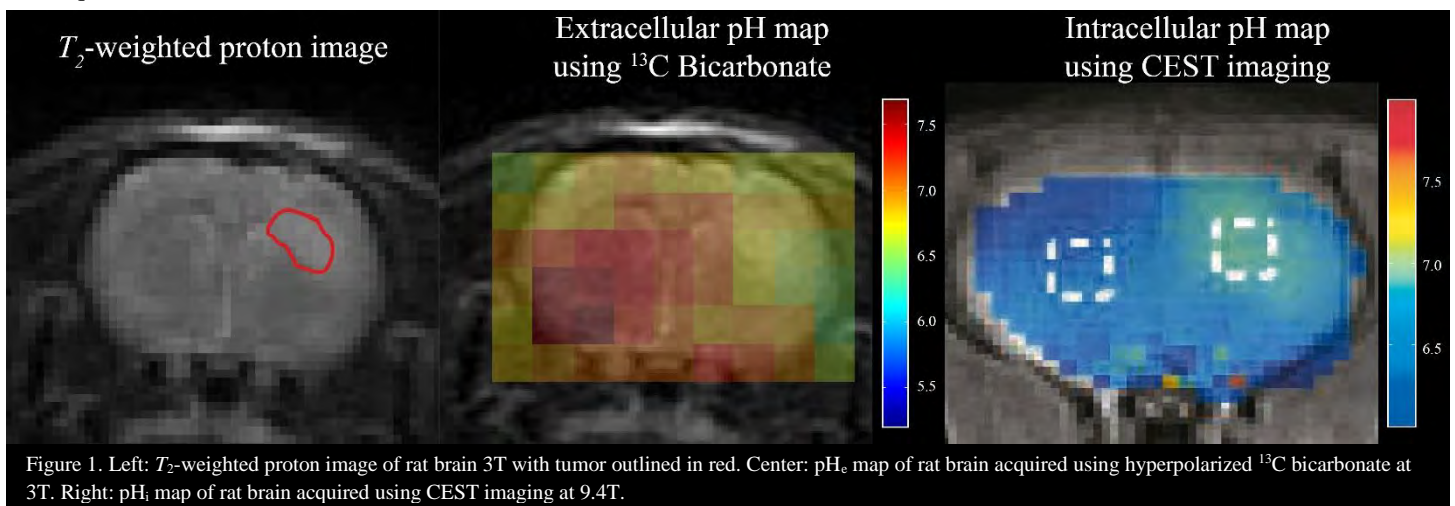


Figure 1. Left: T_2 -weighted proton image of rat brain 3T with tumor outlined in red. Center: pH_e map of rat brain acquired using hyperpolarized ^{13}C bicarbonate at 3T. Right: pH_i map of rat brain acquired using CEST imaging at 9.4T.

Results: Intercellular (pH_i) and extracellular pH (pH_e) maps of the rat brain are shown in Figures 1 respectively. In contralateral tissue, the average pH_e was 7.09 ± 0.06 and the average pH_i was 6.75 ± 0.12 ($\Delta\text{pH} = (\text{pH}_i - \text{pH}_e) = -0.34 \pm 0.13$). In the tumor, the average pH_e was 6.91 ± 0.11 and the average pH_i was 7.05 ± 0.09 ($\Delta\text{pH} = 0.14 \pm 0.14$). Errors represent one standard deviation of the mean.

Discussion: Endogenous buffers such as bicarbonate (extracellular) and phosphate (intracellular) normally maintain tight control of the acid-base balance in mammalian tissue. The maintenance of an alkaline tumor pH_i increases the activity of several metabolic enzymes that drive cellular proliferation.(5) Acidic pH_e in tumors occurs due to increased lactic acid production in tumor cells and the subsequent active transport of H^+ out of the cell. Clearly, results showed that tumor with positive gradient and vice versa on contralateral brain tissue. These results are consistent with previous measurement of pH_e in C6 gliomas using pH-sensitive T_1 relaxivity, which found a heterogeneous pH distribution with a mean value of 6.87(6). Also ^{31}P -MRSI studies of glioma report pH_i values ranging between 7.12 and 7.24 compared with 6.99 to 7.05 in normal human brain.

Conclusion: We have *non-invasively* measured pH_i and pH_e in a rat glioma and contralateral brain tissue. A large trans-membrane pH gradient ($\Delta\text{pH} \approx 0.14 \pm 0.14$) was observed in the glioma. Since most therapeutic agents are weak acids or bases, *a priori* knowledge of the trans-membrane pH gradient might be an indicator to guide choice of therapeutic agent.(7,8)

References:

1. Gallagher FA et al. Nature 2008;453(7197):940-943.
2. Ward KM et al. Magnet Reson Med 2000;44(5):799-802.
3. McVicar N et al. Magn Reson Med 2012.
4. McVicar N et al. Proceedings of International Society for Magnetic Resonance in Medicine 21st annual meeting (2013), Salt Lake City, Utah, USA 2013.
5. McLean LA et al. Am J Physiol-Cell Ph 2000;278(4):C676-C688.
6. Garcia-Martin ML et al. Magn Reson Med 2006;55(2):309-315.
7. Gerweck LE et al. Brit J Cancer 1999;79(5-6):838-842.
8. Raghunand Net al. Br J Cancer 1999;80(7):1005-1011.

Molecular imaging of tumor metabolism: a longitudinal study of tumor response to therapies using hyperpolarized [1-¹³C]pyruvate

Heeseung Lim¹, Kundan Thind¹, Timothy Pok Chi Yeung^{1,2}, Francisco M. Martínez-Santesteban¹, Eugene Wong^{2,3}, Paula J. Foster^{1,4} and Timothy J. Scholl^{1,4}

¹ Department of Medical Biophysics, Western University, Canada. ² London Regional Cancer Program, London Health Sciences Centre, Canada. ³ Department of Physics and Astronomy, Western University, Canada. ⁴ Robarts Research Institute, Western University, Canada.

Introduction: Glioma is the most common and aggressive brain cancer with poor long-term patient outcomes. It is essential to detect and monitor brain tumor as early as possible so that patient can receive the appropriate personalized therapy. Tumor cells modify their own metabolism in response to their microenvironment to encourage proliferation (1). We have used hyperpolarized [1-¹³C]pyruvate imaging, to image and quantify longitudinal metabolic changes of brain cancer in response to therapies. This study measures the intracellular ratio of lactate to pyruvate (Lac/Pyr) to detect longitudinal metabolic changes in response to cancer therapy in an animal model of glioma.

Methods: The brains of 18 Wistar rats were implanted with C6 Glioma cells. Ten days after surgery, rats were divided into four groups; no therapy, radiotherapy, chemotherapy, combined radio- and chemotherapy. All animals were imaged with ¹H MRI and hyperpolarized ¹³C MRSI on days 7, 12, 15, 18, 21, 24 (experimental end point) after the surgery. For hyperpolarized ¹³C MRSI, [1-¹³C]pyruvic acid was hyperbolized by a Hypersense DNP (2) (Oxford instruments) and injected through a tail vein catheter. 2D ¹³C spectra of the rat brains were acquired using FID-CSI. All images and spectroscopy were acquired using a custom-built switch-tuned ¹³C-¹H RF coil to achieve high SNR and facilitate image registration (3).

Results: For all animals receiving therapy their tumors showed significant (p<0.05) early response measured as a decrease of the lactate to pyruvate ratio (lac/pyr). Some animals in the radiotherapy group showed a subsequent increase in lac/pyr at later days. The chemotherapy group didn't survive as long as the radiotherapy or combined group despite that the lac/pyr was significantly (p<0.05) suppressed. The combined therapy group showed the best survivability and a low lac/pyr was maintained post therapy.

Discussion: Hyperpolarized [1-¹³C]pyruvate imaging has the capability of detecting changes in the tumor metabolism related to glycolysis and lactic acid formation. As shown in Figure 1, tumors showed significant metabolic changes as early as two days after therapy. Commensurate changes in tumour volume were not readily noticeable with proton imaging or were significantly later than observed changes in tumor metabolism (Figure 2). ¹³C MRSI indicated the likelihood of tumor recurrence for the radiotherapy-only cohort based on an increase in lac/pyr later in the longitudinal study, which was not detectable by measurements of tumor volume using from ¹H MRI. (This will be confirmed with future histopathology.)

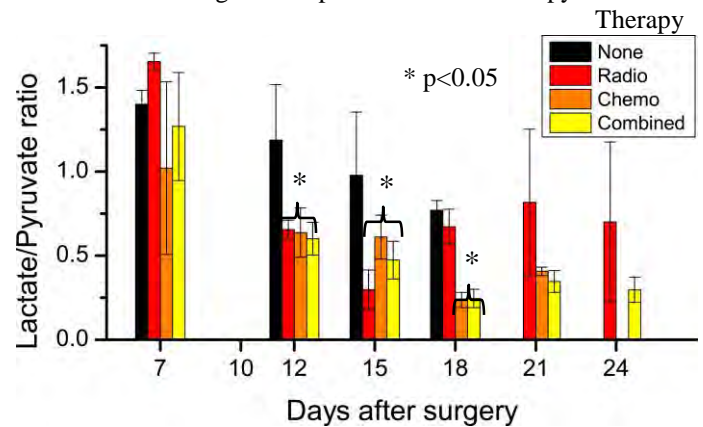


Figure 1. Longitudinal measurements of lactate to pyruvate ratio of tumors undergoing therapy. Animals receiving only chemotherapy or no therapy did not survive to day 24.

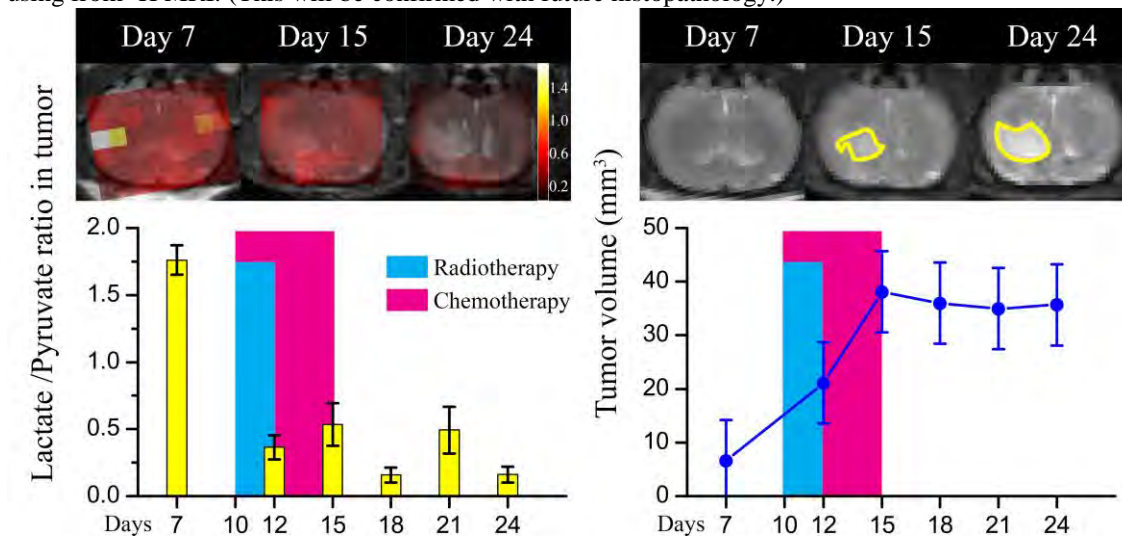


Figure 2. Longitudinal therapeutic response of a representative combined therapy animal. Left: ¹³C lactate/pyruvate ratio map & graph. Right: T₂ weighted image and tumor volume graph.

Conclusion: This work demonstrated that the use of hyperpolarized [1-¹³C] pyruvate to probe real time tumor metabolism can provide *longitudinal non-invasive biomarkers* for therapeutic response to therapy. Also, it has provided strong evidence of detection of early metabolic changes as a result of tumor response to radiotherapy and chemotherapy. In the future, we would compare with clinical applications such as DSC, DWI and histology to direct towards for clinical practice.

References:

1.Hanahan D, et al. Cell 2011;144(5):646-674. 2.Chattergoon N, et al. Contrast media & molecular imaging 2013;8(1):57-62. 3.Lim H, et al.J Magn Reson Imaging.

The Dependence of Stiffness on Fluid Pressure, Stress and Strain in Phantoms and *Ex Vivo* Kidneys using Ultrasound Shear Wave Elastography

Stuart Locke¹, Ross Williams², John Hudson¹, Peter Burns^{1,2}

¹Department of Medical Biophysics, University of Toronto, Toronto, ON, Canada

²Sunnybrook Research Institute, Toronto, ON, Canada

Background: As cancers grow, they promote the development of new blood vessels, a process known as angiogenesis. These new blood vessels are leaky and permeable compared to those of healthy tissue, allowing high pressure plasma to leak out into the interstitial space. This raises the interstitial fluid pressure, which is one factor that may contribute to tumour stiffness, a known property of tumours. Anti-angiogenic therapies, which suppress the tumour vasculature, reduce the tumour's interstitial pressure by ~10 mmHg, which could in turn reduce the tumour's stiffness.

If the effect of a change in fluid pressure can be reliably seen and differentiated from other effects with elastographic methods, then it could be possible to use changes in tissue stiffness as a noninvasive method of determining interstitial fluid pressure. This in turn might be used as a surrogate early-response marker of tumour response to anti-angiogenic therapy. We investigate here how the stiffness of a tumour will change with interstitial pressure, using supersonic shear imaging of gelatin phantoms and *ex vivo* porcine kidneys under different models of pressurization.

Materials and methods: In supersonic shear imaging (SSI), a focused beam of ultrasound is used to create a shear wave *in situ*, which travels through the tissue. The shear wave is imaged as it travels using plane wave ultrasound at frame rates of approximately several thousand hertz, allowing its speed to be inferred. Because shear waves travel faster in stiffer tissue, the stiffness of the tissue (specifically its shear modulus) can be determined.

To investigate the effect of hydrostatic pressure on a viscoelastic medium, blocks of gelatin were placed in a chamber, and the surrounding water was pressurized. To investigate the effects of anisotropic forces and distortion, a gelatin phantom was placed on a hard surface and underwent uniaxial vertical stresses. It was either constrained laterally or allowed to expand laterally, and the results were compared for different orientations relative to the compressive force. In *ex vivo* porcine kidneys, the renal artery was cannulated and pressurized. In each case, the change in stiffness as a function of pressure or stress was characterized from the ultrasound data using MATLAB.

Results: In both the gelatin under hydrostatic pressure, and the constrained uniaxially-compressed phantom, the change in shear modulus with applied pressure was found to be negligible, with a magnitude of less than 0.001 kPa/mmHg. In the unconstrained compressed gelatin phantom, the change in shear modulus with pressure depended on the orientation of the transducer relative to the compressive force; ranging from +0.12 kPa/mmHg to -0.08 kPa/mmHg. In the *ex vivo* pig kidneys, the mean change in shear modulus with pressure was 0.73 ± 0.13 (SD) kPa/mmHg.

Discussion and Conclusion: A gelatin phantom placed in a fluid of varying pressure will see no change in its stiffness as a function of pressure even under very large pressures. A gelatin phantom that is placed on a hard surface and compressed vertically will see a change in stiffness if allowed to deform under the force; by contrast, if deformation is prevented, then no stiffness change is seen under the same force. This demonstrates that deformation is critical to a change in shear modulus, and that applied pressure alone cannot change stiffness. In the unconstrained gelatin phantoms, the changes in stiffness with pressure are large enough to be seen over the biologically relevant range of stresses. In the *ex vivo* kidneys, a more accurate analogue of living tissue, the change in stiffness with pressure is substantial, changing by a factor of two over the biologically relevant range of pressure and should be detectable by shear wave elastography. A comparably large change in *in vivo* tumours is therefore plausible. Future work will include experiments on the relationship between elastographic stiffness and interstitial fluid pressure in a rabbit VX2 tumour model.

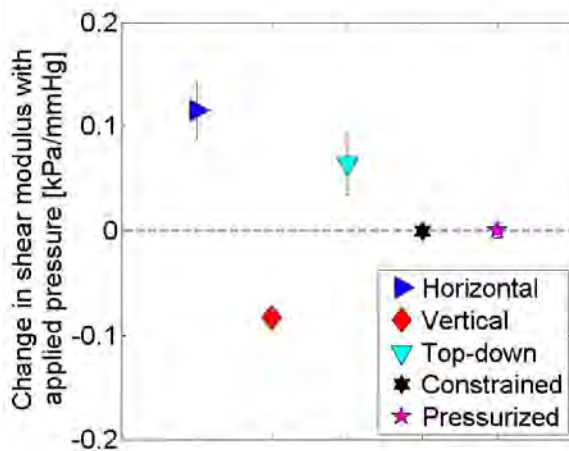


Figure 1: Change in shear modulus with applied pressure in gelatin phantoms under different conditions. 'Horizontal', 'vertical' and 'top-down' are shear wave orientations for the unconstrained phantom.

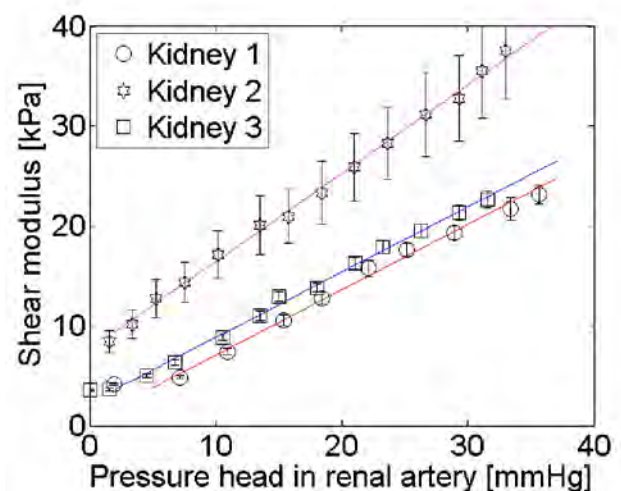


Figure 2: Change in shear modulus with pressure in three *ex vivo* porcine kidneys.

Automated Volumetric Fat Quantification of Adipose Tissue in Mice

Colin M McCurdy¹, Bryan T Addeman¹, Curtis N Wiens², Lanette J Friesen-Waldner^{1,3}, Trevor P Wade^{1,3}, Jacqueline K Harris¹, Abraam S Soliman⁴, Kevin J Sinclair¹, and Charles A McKenzie^{1,4}

¹Medical Biophysics, The University of Western Ontario, ²Radiology, The University of Wisconsin, Madison, Wisconsin, ³Robarts Research Institute, The University of Western Ontario, ⁴Biomedical Engineering, The University of Western Ontario, London, Ontario

Target Audience: Researchers interested in adipose quantification in rodents.

Introduction: Intra-Abdominal Adipose Tissue (IAAT) is an indicator of disease onset, specifically long-term development of type-2 diabetes and cardiovascular disease¹. Recently, a method for automated quantification of adipose distribution in human water-fat separated magnetic resonance (MR) images was validated². Research using animals allows studies with shorter time scales, invasive procedures, and reduces the difficulty of longitudinal research. We propose an adaptation of the human method to quantify Total Adipose Tissue (TAT), Subcutaneous Adipose Tissue (SAT), and IAAT in mouse MR images.

Methods: *In vivo* data were obtained from 5 mice (3 obese mice, 2 lean mice) that were anesthetized with isoflurane under a protocol approved by the institution's Animal Use Subcommittee. Coronal images were collected using an investigational version of IDEAL (# echoes = 6, Echo Spacing = 1.05 ms, 0.7 mm slice thickness, FOV = 11 cm x 6.6 cm x 3 cm, Scan Time = 15 min, matrix = 148x148x58, NEX = 10) using a single channel proton coil in a GE 3.0 T MR750 (GE Healthcare, Waukesha, WI). Images were reformatted to the transverse plane and a subset of 10 slices located between the diaphragm and pelvis were analyzed for fat distribution. Our automated method uses fat fraction values to identify adipose and lean muscle tissue. Then, using the water image, a 3D surface is fit over the external muscles in polar coordinates to segment SAT from internal adipose tissue. Then IAAT is determined to be the remaining adipose tissue inside the SAT. The human method was adapted by changing the fat fraction thresholds ranges for lean muscle and adipose tissue to account for prevalent partial volumes of water-fat boundaries in mice. This threshold is manually adjusted based on the apparent fat fraction of the muscle tissue layer. The volumes of TAT, IAAT and SAT were calculated from the segmented images and were compared to manual segmentations³ (Figure 1).

Results: Manual segmentation required 480 s/slice while automated segmentation required only 4 s/slice. Average TAT volume per slice for the mice was 125.7 mm³. Manual and automated segmentation results showed good agreement with no substantial bias (Figure 2). The mean absolute difference

between the manual and automated segmentation was (5.2 ± 3.6) mm³ for IAAT and (6.7 ± 4.7) mm³ for SAT.

Discussion: The automated technique was over 100x faster than manual segmentation, while requiring minimal interaction. The difference between automatically and manually segmented adipose compartment volumes is small relative to the total volume (7%). In-plane resolutions for these images were 0.7 mm, which is much larger than most segmentation techniques have displayed, demonstrating the ability of this method to accurately segment relatively low resolution images. The short time for segmentation and manageable imaging time makes use of this technique desirable for analysis of fat in large data sets. Future research will measure the reproducibility of this algorithm.

Conclusions: We have validated a method for rapid, automated fat segmentation that produces reliable and accurate quantification of adipose distributions in mice.

References: [1] Sam S *et al.*, Relation of Abdominal Fat Depots to Systemic Markers of Inflammation in Type 2 Diabetes, *Diabetes Care*. 2009 May; 32(5): 932–937 [2] Addeman B *et al.*, Validation of Volumetric and Single Slice MRI Adipose Analysis using a novel Fully Automated Segmentation method, *JMRI*, 2013 (In Press) [3] Alabousi A *et al.*, Evaluation of adipose tissue volume quantification with IDEAL fat-water separation, *J Magn Reson Imaging*;34(2):474-479.

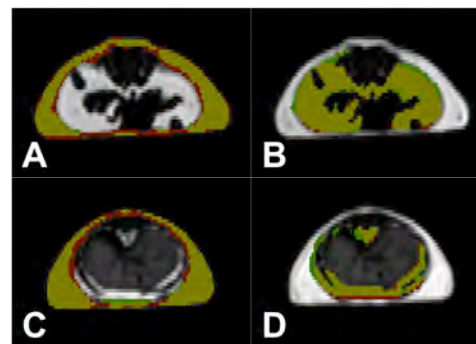


Figure 1. Example segmentations of SAT (A,C) and IAAT (B,D) from two slices in a mouse. A and B are a slice with high internal fat, while C and D are a slice with low internal fat including the liver. Red pixels were selected by the manual segmentation, green pixels were selected by the automated segmentation, and yellow pixels were selected by both methods.

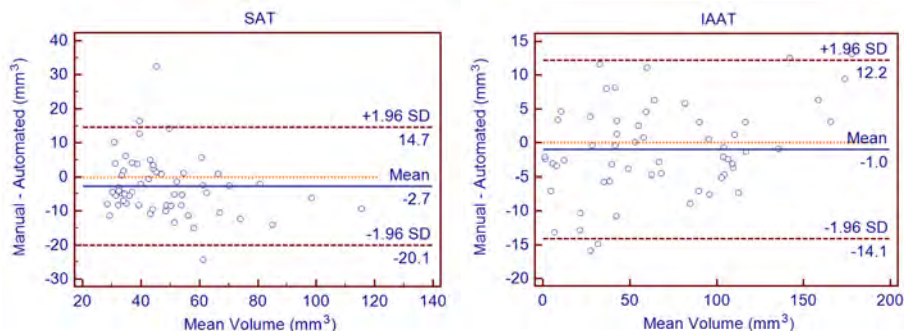


Figure 2. Bland-Altman plots of Subcutaneous Adipose Tissue (SAT) and Intra-Abdominal Adipose Tissue (IAAT). The solid line shows the mean measurement difference between manual and automated segmentations, while the long lines show the 95% confidence interval.

Intracellular pH Mapping Using AACID-CEST MRI: Imaging brain tumor-selective acidification by lonidamine

N McVicar,^{1,2} AX Li,¹ S Meakin³, R Bartha^{1,2}

Centre for Functional and Metabolic Mapping, Robarts Research Institute¹
 Departments of Medical Biophysics², Biochemistry³, The University of Western Ontario
 Research Supervisor: Dr. Robert Bartha

Synopsis

Lonidamine is an anticancer drug that selectively decreases intracellular pH in tumor cells. A ratiometric CEST approach called amine/amide concentration independent detection (AACID) was recently developed to measure absolute intracellular pH *in vivo* using MRI. In this study, we produce pH maps before and ~1 hour after injection of lonidamine and then immediately post mortem in a brain tumor mouse model. Results show that lonidamine exclusively decreases tumor intracellular pH by ~0.2 pH units and AACID is capable of mapping local changes in brain tumor pH *in vivo*.

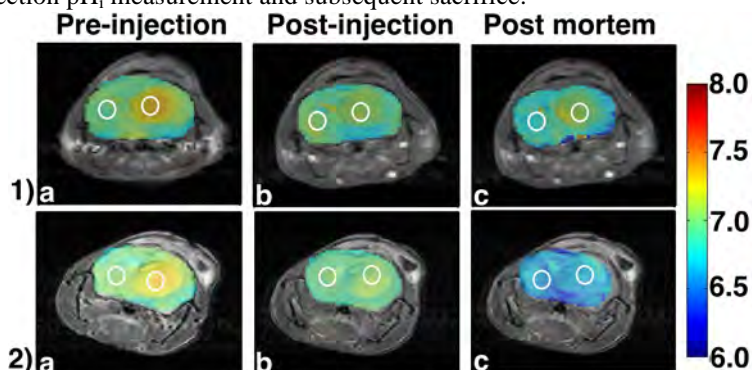
Purpose: Zhou et. al measured *in vivo* pH_i using exchanging amide protons (resonating at 3.50 ppm) associated with endogenous intracellular proteins following cerebral ischemia.¹ Recently, several groups have measured CEST contrast from both amine and amide protons *in vivo*.²⁻⁴ Amine/amide concentration independent detection (AACID) is a ratiometric CEST technique used to generate absolute intracellular pH measurements *in vivo*.⁴ The anticancer drug lonidamine induces tumor-selective acidification of the intracellular space.⁵ The purpose of the current study was to map and quantify the change in pH_i following injection of lonidamine in a mouse model of glioblastoma multiform.

Methods: The **AACID ratio** is defined by the ratio of amine (resonating at 2.75 ppm) and amide CEST effects (Equation [1]), where $M_Z(\omega)$ is the MRI signal intensity measured following a saturation pulse of frequency ω .

$$\text{AACID} = \frac{M_Z(3.50\text{ppm}) \times (M_Z(6.0\text{ppm}) - M_Z(2.75\text{ppm}))}{M_Z(2.75\text{ppm}) \times (M_Z(6.0\text{ppm}) - M_Z(3.50\text{ppm}))} \quad (\text{Eqn. 1})$$

Glioblastoma multiforme brain tumors were induced in two NU/NU mice by injection of 1×10^5 U87MG glioma cells. pH_i maps were produced using the AACID ratio from CEST spectra acquired before and after injection of lonidamine, and post mortem. Following pre-injection pH_i map acquisition, lonidamine was injection intraperitoneally (IP; dose = 100mg/kg, dissolved in dimethyl sulfoxide or DMSO) and the animal was returned to the magnet for post-injection pH_i measurement and subsequent sacrifice.

MRI Experiments: All MRI data were acquired using a 9.4 T horizontal bore Agilent (Palo Alto, CA) MRI scanner. Standard T₂-weighted images (TR = 3000 ms, effective TE = 40 ms) were acquired to localize the tumor. CEST spectra were acquired using a 4 sec, 1.5 μ T continuous wave radiofrequency (RF) saturation pulse and a standard fast spin echo (FSE) pulse sequence (TR/TE = 7000/7 ms, ETE=10 ms, matrix= 64x64, FOV=19.2x19.2 mm², slice thickness=2 mm). AACID ratiometric values derived from CEST data were previously calibrated with pH_i measured by ³¹P-MRS as the gold-standard.⁶



Results: Pre- and post-injection and post mortem contralateral and brain tumor pH_i values (mean \pm std. dev.) are provided in **Table 1** for two animals. **Figures 1** and **2** demonstrates pre- and post-injection and post mortem pH_i maps derived using AACID values for two animals. pH_i maps calculated in brain tumor mice before (**Figs. 1a, 2a**) and after (**Figs. 1b, 2b**) injection of lonidamine show tumor-selective acidification (tumor Δ pH_i ~ 0.2 pH units). In contrast, post mortem pH_i maps (**Figs 1,2c**) show global brain acidification.

Table 1

	Mouse #1		Mouse #2	
	Contralateral	Tumor	Contralateral	Tumor
Pre-Injection pH_i	7.11 \pm 0.03	7.32 \pm 0.03	7.06 \pm 0.02	7.25 \pm 0.01
Post-injection pH_i	7.15 \pm 0.07	7.15 \pm 0.07	7.01 \pm 0.02	7.05 \pm 0.04
Post mortem pH_i	6.67 \pm 0.04	7.02 \pm 0.05	6.89 \pm 0.04	6.87 \pm 0.02

Discussion: Intracellular pH is an important physiological parameter that may predict tumor treatment response. The use of lonidamine to acidify tumors could be used to enhance the efficacy of existing chemotherapeutic agents.⁵ Mapping and monitoring tumor acidification could be used to optimize treatment paradigms.

Conclusion: The novel ratiometric CEST approach called AACID is capable of producing accurate pH_i maps and measured acidification by lonidamine in glioblastoma multiform brain tumors. Lonidamine decreased intracellular pH by ~0.2 pH units exclusively within the tumor ~1-2 hours after injection.

References: 1. Zhou et al. *Nature*. (2003) **9**:1085-1090 2. Jin et al. *NeuroImage*. (2012) **2**:1218-1227. 3. Desmond et al. *OctoberCEST Workshop*. MA, USA (2012). 4. McVicar et. al. *ISMRM Annual Meeting*, UT, USA (2013). 5. Nath et al. *NMR in Biomed*. (2013) **26**:98-105. 7. Webb et al. *Nature*. (2011) **11**: 671-677. 6. Moon et al. *Journ. of Biol. Chem*. (1973) **248**:7276-7278.

Pharmacokinetic Modeling of Prostate Tumor Using Independent Component Analysis

Hatef Mehrabian^{1,2}, Masoom A. Haider³, and Anne L. Martel^{1,2}

¹Medical Biophysics, University of Toronto, Toronto, Ontario, Canada, ²Physical Sciences, Sunnybrook Research Institute, Toronto, Ontario, Canada, ³Medical Imaging, Sunnybrook Health Sciences Centre, Toronto, Ontario, Canada

Introduction: A major component of Multi-parametric MRI is used in cancer detection and diagnosis is Pharmacokinetic (PK) modeling of Dynamic contrast enhanced (DCE)-MRI of the tumor tissue¹. PK modeling provides information about tumor perfusion and vascular permeability². Application of such information that is related to prognostic factors is increasing in anti-angiogenic therapies³. However, the quantitative PK parameters vary significantly between studies and needs to be improved.

PK analysis requires measurement of contrast agent concentration in the vasculature as an input. This vascular input function (VIF) is inseparable from the signal in the interstitial space (EES) in the tumor. Thus, it is approximated with an arterial input function (AIF) measured outside of the tissue of interest. Variations and error in calculation of this AIF is one of the major sources of discrepancy between PK parameters reported by different studies. Calculating the vascular enhancement locally (local VIF) at the tissue of interest has the potential to improve PK analysis and helps to better understand contrast agent kinetics in the tissue. Such a VIF could also be used in cases that there is no artery in the FOV to measure AIF or in animal studies where it is difficult to find such an artery.

The PK parameters reflect the tissue characteristics and for a specific tissue type, its values should be independent of the AIF or VIF used in the analysis. Moreover, the method that results in a smaller variation in the calculated parameters for this tissue has a better performance. We have developed an independent component analysis (ICA)-based⁴ algorithm for VIF calculation which uses complex-valued MR signal and applies an ICA algorithm with adaptive cost function. This study validates the performance of the proposed local VIF calculation algorithm in prostate cancer and compares its results to PK parameters estimated using an AIF.

Methods: Adaptive Complex Independent Component Analysis (AC-ICA): Assuming DCE-MRI sequence Z , is a linear mixture of source signals S , ($Z = AS$), ICA identifies the S and A , assuming the sources are independent. AC-ICA assumes intravascular and extravascular MR signals are spatially independent. It also assumes the distribution of the MRI signal can be approximated as a linear combination of 3 to 5 generalized Gaussian distributions given by: $p_y(y) = \frac{\beta}{2\alpha\Gamma(1/\beta)} \exp\left(-\frac{|y|^\beta}{\alpha^\beta}\right)$ where $\Gamma(\cdot)$ is Gamma function.

ACICA calculates model parameters (α, β) of the intravascular space through an expectation maximization framework at each iteration of ICA. The ICA non-linearity is then derived from this distribution and intravascular signal is separated⁴.

Pharmacokinetic modeling: Two compartmental extended Tofts model⁵ is used in this study. Assuming c_t , c_e and c_p are the contrast agent concentrations in tissue, EES and plasma, the model equations are: $v_e \frac{dc_e}{dt} = K^{trans}(c_p(t) - c_e(t))$, & $c_t = v_e c_e + v_p c_p$, where v_e and v_p are the EES and plasma fractions and K^{trans} is the volume transfer constant.

Analysis: DCE-MRI of 20 prostate cancer patients with biopsy proven tumors are used (3D SPGR $B_0=3T$, TR/TE=3.9/1.8 ms, FA=8°, FOV 20x20cm, Matrix 112x112x20, slice thickness 3.5mm). For every patient AC-ICA was applied to the prostate tissue and VIF was calculated. This intravascular enhancement curve was then normalized with respect to its area under the curve (AUC) and was used as the input to the PK model. For comparison the femoral artery was identified and its contrast enhancement was used as the AIF in PK analysis of the prostate tissue. Normal peripheral zone (PZ) tissue of the prostate was identified using the T_2 -w MRI and the K^{trans} value was calculated for this tissue using both AIF and VIF (both with and without normalization with AUC).

Table 1 K^{trans} value obtained using the VIF and AIF (with and without normalization) for normal PZ and tumor tissues for 20 prostate cancer patients.

Method		VIF [min^{-1}]	AIF [min^{-1}]
Normalized	Normal PZ	0.21±0.05	0.26±0.11
	Tumor	0.9±0.51	1.12±0.54
Not Normalized	Normal PZ	1.09±0.53	0.29±0.34
	Tumor	5.05±4.74	1.01±1.23

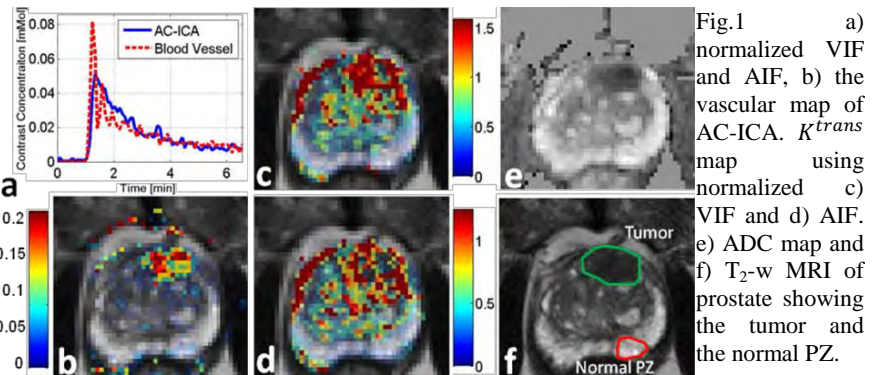


Fig.1 a) normalized VIF and AIF, b) the vascular map of AC-ICA. K^{trans} map using normalized c) VIF and d) AIF. e) ADC map and f) T_2 -w MRI of prostate showing the tumor and the normal PZ.

Results: The VIF (normalized) calculated for a sample slice and its AIF are shown in Fig.1a. Fig.1b shows the vascular map (overlaid on the T_2 -w image) that is calculated using AC-ICA. This map was used as the v_p parameter in VIF-based PK analyses. Fig.1c,d show the K^{trans} map for VIF-based and AIF-based PK analyses. The T_2 -w image of the prostate showing normal PZ tissue and tumor ROIs and ADC map are shown in Fig.1e,f. Table 1 reports the K^{trans} value for normal PZ tissue and tumor tissue, averaged over 20 patients, for VIF-based and AIF-based PK analyses (with and without normalization).

Conclusions: K^{trans} maps show both AIF-based and VIF-based methods result in high K^{trans} values in the tumor region (they have similar performances in detecting tumor). Table1 shows both methods result in similar values for normal PZ tissue. The normalized VIF results in smaller variation in K^{trans} of normal PZ tissue showing that it performs better compared to AIF-based (with and without normalization) and VIF-based analysis without normalization and results in better separation of normal PZ and tumor tissues.

References: [1] Hoeks C, et al., Radiol.261(1), 2011. [2] Hylton N, et al., J. Clin. Oncol. 24(20), 2006. [3] Kanematsu et al., Am. J. Roentgenol. 184, 2005. [4] Mehrabian H, et al., IEEE Trans. Med. Imaging 32 (4), 2013. [5] Tofts P, et al., JMRI, 10(3), 1999.

Spinal Cord Injury Induced using Focused Ultrasound

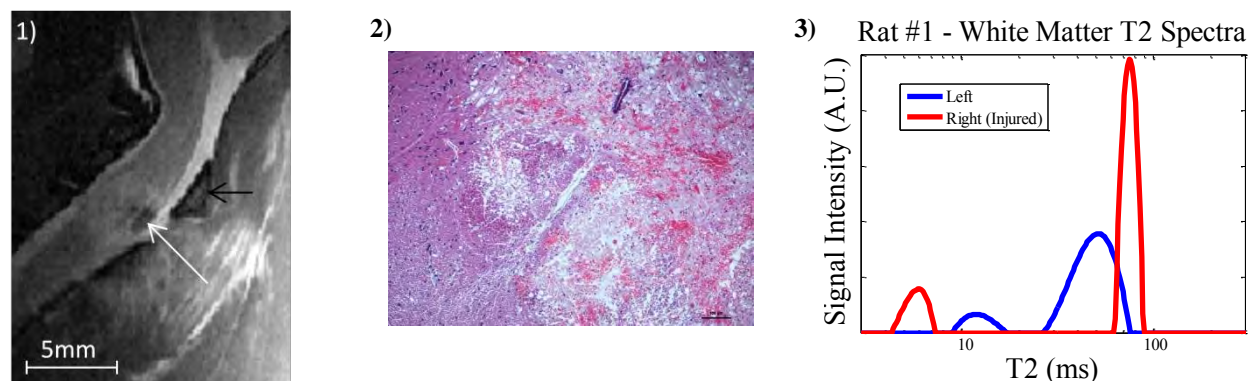
Author(s) – Wendy Oakden¹, Meaghan A. O'Reilly², Margarete K. Akens³, Isabelle Aubert^{4,5}, Cari Whyne^{6,7}, Kullervo Hynynen^{1,2}, Jacek Kwicien⁸, Greg J. Stanisz^{1,2}

Medical Biophysics¹, Laboratory Medicine and Pathology⁵, Department of Surgery⁷, University of Toronto; Imaging Research², Brain Sciences Research Program⁴, Orthopaedic Biomechanics Laboratory⁶, Sunnybrook Research Institute; TECHNA Institute³, University Health Network; Pathology and Molecular Medicine, McMaster University

Purpose: Current preclinical models of spinal cord injury (SCI) are extremely invasive and result in large amounts of unintended collateral damage to surrounding tissue. Focused Ultrasound (FUS) in combination with microbubbles has been used to transiently open the blood brain barrier in order to enhance drug delivery¹, and to create lesions in the brain². The goal of this study was to assess the ability of FUS and microbubbles to create a highly localized injury of the spinal cord. This novel, non-invasive model of spinal cord injury was characterized *in vivo* using quantitative T2 (qT2) MRI and diffusion.

Methods: Spinal cord injuries were induced in nineteen male Wistar rats at the C2 level of the spinal cord using FUS in combination with microbubbles. The animals were anesthetized using ketamine/xylazine and secured to a platform which could be moved between the FUS treatment system and a 7T Bruker Biospin MR scanner. The location for induction of injury was prescribed using structural MR images. The right side of the spinal cord was treated with FUS (1.114 MHz, 10 ms bursts at a pulse repetition frequency of 0.5 Hz for 5 minutes, 6 sonication spots at 1mm spacing, RF driving powers of 1.6 W) following an injection of 0.2 ml/kg of Definity microbubbles. Quantitative MR imaging was performed 24 hours (19 animals), 1 week (9 animals) and 2 weeks (6 animals) following FUS treatment. Anatomical images were acquired at a resolution of 0.15x0.15x1.0mm³ using a fast spin echo sequence. QT2 measurements were made using a single slice sequence with composite refocusing pulses, TE 5ms, TR 3s, 0.2x0.2x1.0mm³ resolution and 2 averages, lasting 20 minutes. Diffusion tensor images were acquired with an EPI sequence, 18 directions and b-value of 800s/m². Analysis of qT2 data was done using a non-negative least squares algorithm. Histologic sections were stained with H&E and Luxol fast blue.

Results: This was a mild injury with minimal post-injury care. Four animals developed partial paw paralysis and all recovered fully within 2 weeks. Both hemorrhage and extensive vacuolization were seen on histology. Very short components were seen on qT2 in areas corresponding with hemorrhage, and an increase in intra/extracellular T2 was observed in areas corresponding with vacuolization in both gray and white matter. Fractional anisotropy was decrease in injured white matter.



Figures: 1) Sagittal FSE of FUS treated spinal cord, C1 (black arrow), site of injury (white arrow). 2) H&E stained spinal cord showing hemorrhage and vacuolization 3) T2 spectra of white matter in both injured and uninjured white matter.

Discussion: It is possible to induce physical disability using a combination of FUS and microbubbles. The pathology resembles that seen in other models of SCI, matching pathology seen during the secondary phase of injury which follows the initial insult in human SCI and is the target of new therapies. QT2 results demonstrate an increase in intra/extracellular water T2 indicative of inflammation³, which corresponds to areas of inflammation seen on histopathology as well as a short component corresponding to hemorrhage. Diffusion results show a slight decrease in FA in the injured side relative to the uninjured side and an overall decrease in FA compared with the healthy rat.

Conclusion: This is a promising model of spinal cord injury as it causes minimal extraneous damage, and is highly localized. QT2 and diffusion MR provide *in vivo* insight into the nature and extent of the injury.

References: 1. O'Reilly M, Hynynen K. Ultrasound enhanced drug delivery to the brain and central nervous system. *Int.J.Hyperthermia*. 2012; 28(4):386-396.

2. McDannold NJ, Vykhodtseva NI, Hynynen K. Microbubble contrast agent with focused ultrasound to create brain lesions at low power levels. *Radiology*. 2006; 241(1):95-106.

3. Stanisz GJ, Webb S, Munro CA, et al. MR properties of excised neural tissue following experimentally induced inflammation. *MRM*. 2004; 51(3):473-479.

Ratiometric Magnetic Resonance pH Sensing Method based on Slow Proton Exchange Mechanism

Loïse H. Perruchoud,^{1,2} Michael D. Jones¹, Andre Sutrisno^{1,2}, Deborah B. Zamble¹, Andre J. Simpson^{1,2} and Xiao-an Zhang^{*1,2,3}

¹Department of Chemistry, University of Toronto, Toronto, ON M5S 3H6, Canada

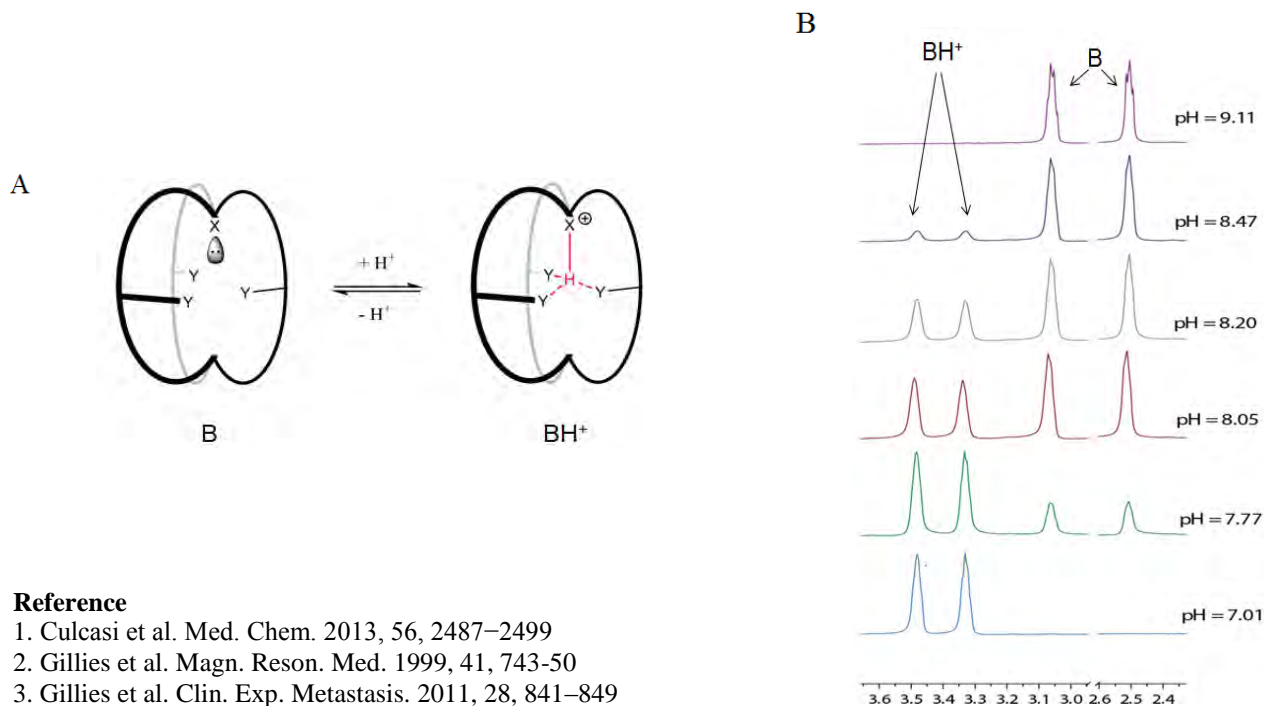
²Department of Environmental and Physical Sciences, University of Toronto Scarborough, Scarborough, ON M1C 1A4, Canada

³Department of Biological Sciences, University of Toronto Scarborough, Toronto, ON M1C 1A4, Canada

Acid-base homeostasis needs to be tightly regulated *in vivo* for proper physiological functions. pH imbalance has been linked to different pathological states, such as inflammation, cystic fibrosis and cancer. Development of methods for *in vivo* pH monitoring in real time are therefore important for understanding the role of pH balance in health as well as in diseased states. For this purpose, magnetic resonance (MR) based methods are advantageous since they are able to detect pH non-invasively deep within tissues. The conventional MR pH-sensors are compounds in which the protonated and deprotonated species are in fast exchange, due to the rapid proton exchange rate and display pH-dependent chemical shift changes. Even though chemical shift-based sensors, such as inorganic phosphate² or IEPA^{3,4} have been used successfully, they have limited accuracy, since various factors, such as temperature, ionic strength or local magnetic field inhomogeneities can affect the NMR chemical shift in a pH independent manner. Recently, a new method of MR pH detection was established based on the pH-dependent ratio of bicarbonate (HCO_3^-) and carbon dioxide (CO_2), which are in slow exchange under physiological conditions. Hyperpolarization can be applied to increase the sensitivity of this technique¹. However, since bicarbonate is involved in different metabolic pathways and the $[\text{HCO}_3^-]/[\text{CO}_2]$ ratio is also dependent on the activity and concentration of the enzyme carbonic anhydrase, improving accuracy is desirable.

Our aim was to overcome the aforementioned limitation of chemical shift based pH probes by slowing down proton exchange rate in a small molecule, which eliminates errors from pH-independent factors and allows ratiometric pH measurements while avoiding issues with enzyme dependent artifacts. Slow proton exchange can be obtained by trapping protons using intramolecular hydrogen bonds inside a cage-shaped molecule with a hydrophobic core (Fig A), similar to protons found in the interior of proteins which cannot exchange rapidly with the external aqueous environment. A small molecule pH sensor, SPE1, was thus designed, synthesized and characterized. Using SPE1, which exhibits significantly slow proton exchange rate (slower than the NMR time scale), pH could accurately be determined by the ratio of the deprotonated (B) and protonated (BH^+) states of the pH sensor (Fig B). We also demonstrated that real time pH monitoring of living cells (*E. coli*) was possible by using simple 1D NMR settings.

In conclusion, a new ratiometric strategy of pH detection for MR spectroscopy was introduced. This approach based on ratio between the protonated and deprotonated forms of the pH sensor is more accurate and selective than the existing fast exchanging MR methods and has been applied to monitor pH in living biological systems.



Reference

1. Culcasi et al. *Med. Chem.* 2013, 56, 2487–2499
2. Gillies et al. *Magn. Reson. Med.* 1999, 41, 743-50
3. Gillies et al. *Clin. Exp. Metastasis.* 2011, 28, 841–849
4. Gallagher, F. A. et al. *Nature.* 2008, 453, 940-973

Sodium MRI of *In Vivo* Human Prostate Cancer

Justin Charles Peterson¹, Adam Farag², Trevor Szekeres², Eli Gibson^{2,3}, Aaron Ward^{2,3}, Joseph Chin⁴, Stephen Pautler⁵, Glenn Bauman⁴, Cesare Romagnoli⁴, Robert Bartha^{1,2}, and Timothy J. Scholl^{1,2}

¹Medical Biophysics, Western University, London, Ontario, Canada, ²Robarts Research Institute, Western University, London, Ontario, Canada, ³Biomedical Engineering, Western University, London, Ontario, Canada, ⁴London Health Sciences Centre, Ontario, Canada, ⁵St. Joseph's Health Care, Ontario, Canada

Target Audience: Scientist developing MRI methods for prostate cancer detection and sodium imaging

PURPOSE:

Prostate cancer (PCa) is the most common malignancy in men. While the age-standardized relative survival ratio is 95%, men who are diagnosed experience a greatly diminished quality of life. Aggressive prostate tumors must be identified, differentiated from indolent tumors, and treated to ensure survival of the patient. Currently, clinicians use a combination of multi-parametric MR including T_2 -weighted, diffusion-weighted, and dynamic contrast enhanced imaging to improve PCa detection [2]. While these techniques provide superb resolution, the specificity is often insufficient to identify malignant lesions, particularly in the peripheral zone of the prostate. D. Hausmann *et al.* [2] was the first to demonstrate *in vivo* endogenous sodium imaging of the prostate, expanding on this work, a preliminary study from our lab showed a reduction in sodium concentration in mouse prostate tumors at 9.4 Tesla. The overall goal of this study is to determine whether prostate tissue sodium concentration (TSC) is related to tumor malignancy. The purpose of this report is to demonstrate the feasibility of *in vivo* ^{23}Na MRI in patients with PCa.

METHODS:

MRI: All ^{23}Na images were acquired using a custom built endorectal (ER) receive radio frequency (RF) coil and dedicated asymmetric transmit birdcage RF coil, both resonating at the ^{23}Na Larmor frequency on a 3T GE Discovery-MR750 scanner. Three vials (one-milliliter volume) that span the entire length of the receive loop are incorporated into the endorectal coil as reference standards. These vials contain different concentrations of NaCl: 150, 90, and 30 mM (**Figure 1**). Image processing was performed in Matlab (MathWorks, Natick, MA, USA).

Patients: Four male patients were recruited as part of a multi-modality, image-guided prostate cancer study. Each patient was studied with both ^{23}Na MRI and standard multi-parametric ^1H imaging protocols.

Phantom: *In vivo* images required signal normalization due to the sensitivity profile of the surface ER coil. Phantom images were used to normalize for sensitivity using a method developed by Axel *et al.* [1]. The probe was placed in a cylindrical ^{23}Na phantom of known concentration (150 mM) and imaged with parameters identical to those of the *in vivo* experiments. The resulting images were exported to DICOM and rigidly registered to ^1H *in vivo* images using OsiriX (5.8, © Pixmeo Sarl).

RESULTS:

Figure 1, shows typical MR images of an axial slice through a prostate with biopsy-proven cancer before (a-c) and after (d-f) intensity normalization. The distribution of endogenous sodium concentration (left) is overlaid (center) on a T_2 -weighted ^1H image (right). The sodium ER coil provided sufficient sensitivity and coverage over a large volume of the prostate. Internal vials containing sodium were used to calibrate sodium concentrations and for image registration. Image heterogeneity in the sodium signal is visible.

DISCUSSION:

The ER probe sensitivity is highly spatially dependent. Sensitivity normalization for the receive profile is necessary to correct the image at distances greater than the loop radius. Normalized images were more uniform over the peripheral and central zones of the prostate. Sodium intense regions are visible within the prostate (**Figure 1**: b, e); future comparison of sodium concentration with histopathology will determine whether tissue sodium concentration is correlated with tumor grade.

CONCLUSION:

This proposed method produces *in vivo* ^{23}Na images (normalized for detector sensitivity) covering the peripheral and central zones of a human prostate. These preliminary results will prove useful in determining the relationship between TSC and malignant PCa.

ACKNOWLEDGEMENTS: Ontario Institute for Cancer Research, Smarter Imaging Program

REFERENCES:

- [1] Axel L. et al., "Intensity correction in surface-coil MR imaging", *Amer J Roentgenol.*, (1987), 148, 418-420
- [2] Hausmann D. *et al.*, "Apparent Diffusion Coefficient and Sodium Concentration Measurements in Human Prostate Tissue via Hydrogen-1 and Sodium-23 Magnetic Resonance Imaging in a Clinical Setting at 3 T", *Radiology*, (2012), 47(12)

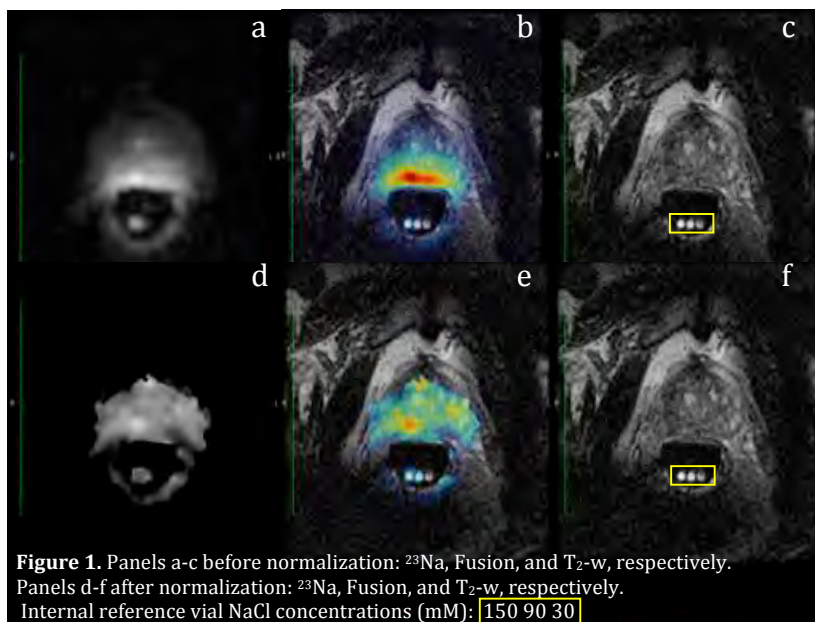


Figure 1. Panels a-c before normalization: ^{23}Na , Fusion, and T_2 -w, respectively. Panels d-f after normalization: ^{23}Na , Fusion, and T_2 -w, respectively. Internal reference vial NaCl concentrations (mM): 150 90 30

Fast Globally Optimal Segmentation of 3D Prostate MRI with Axial Symmetry Prior

Wu Qiu¹, Jing Yuan¹, Eranga Ukwatta^{1,2}, Yue sun^{1,2}, Martin Rajchl^{1,2}, Aaron Fenster^{1,2,3}

¹Imaging Research Laboratories, Robarts Research Institute

²Biomedical Engineering Graduate Program, Western University, London Canada

³Depts of Medical Biophysics and Medical Imaging, Western University, London Canada

➤ Motivation

- Prostate cancer (PCa) is one of the most frequently diagnosed cancers in North American men with over 200,000 new cases diagnosed each year.
- Superimposing 3D TRUS image used to guide the biopsy onto pre-segmented regions of interest in MRI is highly desired in a fused 3D TRUS/MRI guided biopsy system.
- An efficient and accurate prostate segmentation of the 3D prostate MR image is required for such a 3D MRI to TRUS registration procedure.

➤ Methods

We propose a novel global optimization-based approach to segmentation of 3D T2 weighted magnetic resonance (MR) images, enforcing inherent axial symmetry of prostate shapes to simultaneously adjust a series of 2D slice-wise segmentations in a 'global' 3D sense. We show that the proposed challenging combinatorial optimization problem can be solved globally and exactly by means of convex relaxation. With this regard, we introduce a novel coupled continuous max-flow model, which is dual to the studied convex relaxed optimization formulation and leads to an efficient multiplier augmented algorithm based on the modern convex optimization theory. Moreover, the new continuous max-flow based algorithm was implemented on GPUs to achieve a substantial improvement in computation.

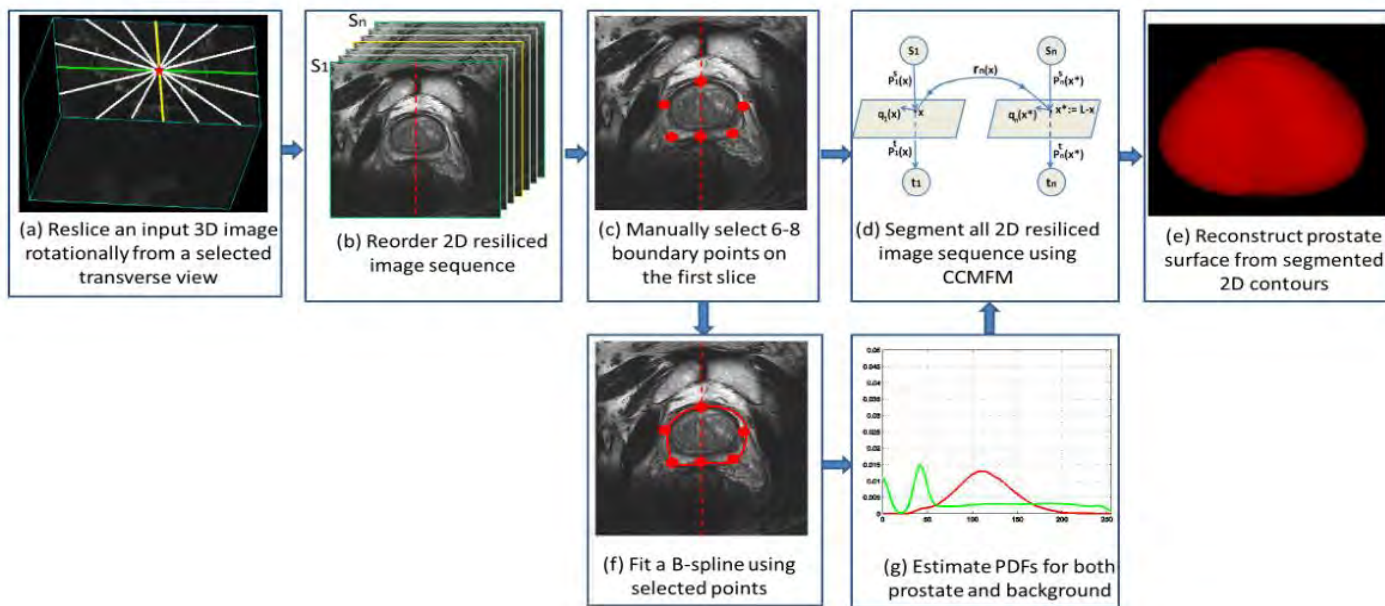


Figure 1: The block diagram of the segmentation pipeline.

➤ Experiments & Results

• Accuracy:

the segmentation results by the proposed method for three sets of 46 images: the proposed approach obtained a DSC of $85.2 \pm 4.5\%$ for 26 images from the public dataset, $90.7 \pm 1.0\%$ for 10 bodycoil images, and $89.4 \pm 1.4\%$ for 10 endocoil images, acquired in our institute; the MAD and MAXD also suggests small distance errors.

• Computational time:

GPU implemented code yielded a mean segmentation time of 0.65 ± 0.15 sec in addition to 4 ± 1 sec for initialization, leading to less than 5 sec for segmenting a single 3D MR prostate image.

• Variability:

The intra-operator variability experiments yielded a DSC of $88.0 \pm 1.5\%$ and a CV of 1.7% for 5 segmentations from the same operator. ANOVA analysis with a single factor showed that there is no statistically significant difference between the three segmentations ($p = 0.61, F = 0.52$). In the intra-observer variability experiments, the proposed method yielded a DSC of $89.5 \pm 2.1\%$, $88.6 \pm 1.2\%$ and $90.3 \pm 2.2\%$, and a CV of 2.3%, 1.4% and 2.4% for the three observers respectively. ANOVA analysis with a single factor failed to demonstrate a statistically significant difference between these three segmentations ($p = 0.85, F = 0.90$).

Formation of submicrometer, monodisperse PFC droplets for ultrasound imaging

Minseok Seo¹ and Naomi Matsuura^{1,2} (E-mail: mseo@sri.utoronto.ca)

¹Physical Sciences, Sunnybrook Research Institute

²Department of Medical Biophysics, University of Toronto

Introduction. Liquid perfluorocarbon (PFC) droplets can be vaporized to form highly echogenic microbubbles *in situ* following ultrasound (US) exposure for imaging or therapy. Small, high-quality PFC droplets of sizes ranging from ~ 100 to ~ 400 nm are required for accumulation in diseased tissues with characteristic leaky vasculature prior to their conversion to bubbles. However, the production of PFC droplets with appropriate small size and high monodispersity remains a challenge. Synthesis methods such as microfluidics (MFs) are ideal for producing larger, micron-scale monodisperse bubbles and droplets with excellent size control, but cannot easily produce agents in the submicrometer size regime. Here, we investigate if a combination of condensation and solvent dissolution from monodisperse, solvent-integrated precursor microbubbles (MBs) can overcome the minimum droplet size limit of standard MF systems to directly form significantly smaller, submicrometer and monodisperse, PFC droplets.

Methods. Micron-scale (~ 4 μm), solvent-incorporated PFC (perfluoropentane, C_5F_{12} , and perfluorohexane, C_6F_{14}) precursor MBs were synthesized using MF systems, with volume ratios of PFC in the DEE/PFC mixture from ~ 50 to 1%, at temperatures higher than the boiling points of the PFC and the solvent (diethyl ether, DEE). Optical microscopy was used to monitor the formation of the precursor MBs, their subsequent condensation into droplets, and the dissolution of DEE. Final droplet sizes were measured using a Coulter Counter and dynamic light scattering, and ultrasound (US) was used to validate the droplet conversion to MBs.

Results. Monodisperse, solvent-incorporated MBs from 120 to 4 μm were produced using MFs. Using MB condensation alone, the final droplet diameter was reduced by ~ 5.8 times compared to the generated MB, and using solvent dissolution alone, the final droplet diameter was reduced by up to ~ 4.6 times (at 1.4% PFC in the DEE/PFC mixture) compared to the generated MB. The combination of condensation and solvent dissolution resulted in final monodisperse droplets with sizes ~ 27 times smaller than the minimum droplet size that could be generated at the orifice of the MF system.

Conclusions. For the first time, it was demonstrated that the condensation and dissolution of MF-generated, solvent-incorporated precursor PFC MBs can directly form nanoscale and monodisperse PFC droplets, overcoming the minimum droplet size limit of standard MF systems by ~ 27 times.

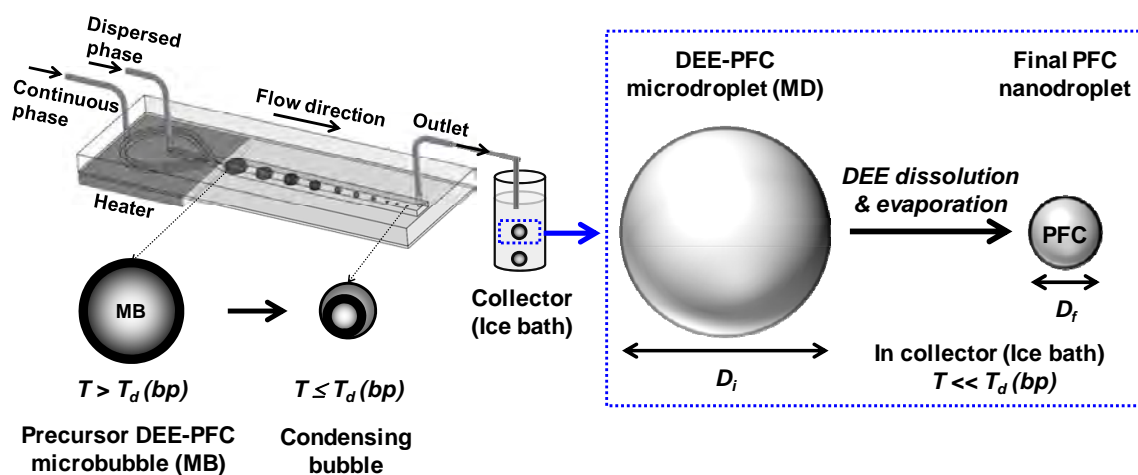


Figure 1. Formation of submicrometer, monodisperse, PFC droplets from condensation of and DEE dissolution from monodisperse, DDE-PFC microbubbles generated using MFs.

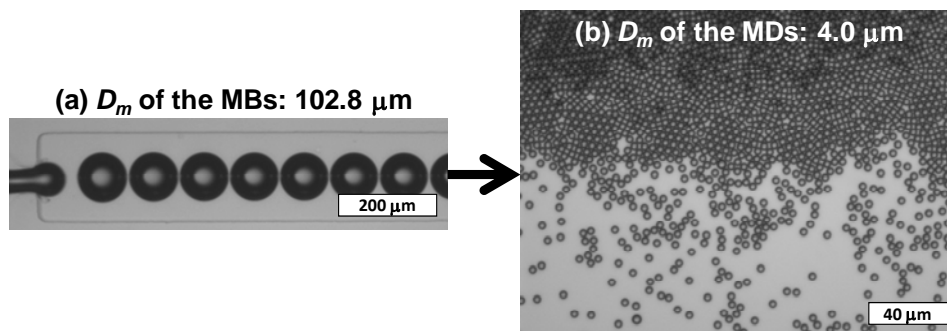


Figure 2. Optical microscope images of: (a) generated DEE-PFC MBs at the orifice of the MF device; and (b) corresponding final monodisperse PFC droplets after condensation and DEE dissolution.

In-Vivo Near-Infrared Imaging of a Cathepsin-D Targeted Contrast Agent for Early Detection of Alzheimer's disease

Jonatan A. Snir^{1,2}, Mojmir Suchy^{2,3}, Keith St. Lawrence^{1,4}, Robert H.E. Hudson³, Stephen H. Pasternak^{5,6} and Robert Bartha^{1,2}

¹Department of Medical Biophysics, University of Western Ontario, London, Ontario, Canada,

²Centre for Functional and Metabolic Mapping, Robarts Research Institute, University of Western Ontario, London, Ontario, Canada,

³Department of Chemistry, University of Western Ontario, London, Ontario, Canada,

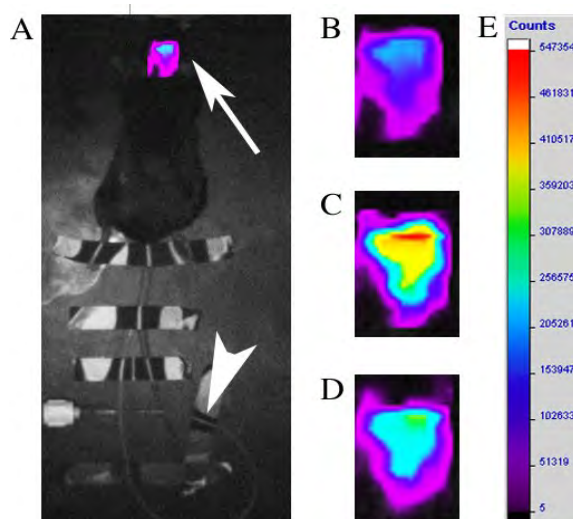
⁴Medical Imaging Lawson Health Reserach Institute,

⁵J. Allyn Taylor Centre for Cell Biology, Molecular Brain Research Group, Robarts Research Institute, University of Western Ontario, London, Ontario, Canada,

⁶Departments of Clinical Neurological Sciences, Schulich School of Medicine, The University of Western Ontario, London, Ontario, Canada

Research supervisors: Drs. Robert Bartha and Stephen Pasternak.

Background: Cathepsin D (CatD) is a lysosomal protease that is elevated in Alzheimer's disease (AD) and is a potential biological marker. We have previously developed a contrast agent to detect CatD in-vivo, consisting of a magnetic resonance imaging/fluorescent moiety linked to a cell penetrating peptide (CPP) by means of a CatD cleavage site. The purpose of this study was to characterize the *in vivo* performance of a Near Infra-Red (NIR) labeled version of this CA. **Methods:** Six adult C57Bl/6 wild-type (WT) mice and six adult 5XFAD transgenic AD mice were studied using a GE eXplore Optix pre-clinical whole animal imaging system at five months of age. Three contrast agents were studied: 1) the full Cat-D targeting agent including the fluorescent moiety, CatD cleavage site, and CPP, 2) a cleaved, non-penetrating, agent including the fluorescent moiety but only a portion of the CatD targeting site sequence, and 3) a non-targeting agent that includes the CPP but lacks the entire CatD cleavage site sequence. Following administration of 5 nmol CA, the optical signal washout curve was fitted to a one phase exponential decay curve using either the entire data, or data only within the first hour after peak enhancement. Extra sum of squares F test was used to test for significant differences ($P < 0.05$ considered significant). **Results:** In all WT and 5XFAD mice, the washout of the CA that included a CPP domain was significantly different than the washout of the cleaved and non-targeting CA. Furthermore, the washout of the Cat-D targeting CA was significantly different in 5XFAD compared to the age matched WT controls ($p < 0.05$). **Conclusions:** This study demonstrates prolonged retention within brain tissue of a contrast agent targeting CatD in 5XFAD AD mice compared to WT control suggesting future implementation for AD detection.



A. Mouse is observed placed on the imaging table, with a catheter (arrowhead) and head placed comfortably within anaesthesia apparatus (arrow). **B.** Zoomed image showing the background fluorescence observed with a laser power of $80\mu\text{W}$ before injection of contrast agent. **C.** Zoomed image showing the measured fluorescence observed immediately after delivery of the contrast agent I.V. with a laser power of $40\mu\text{W}$. **D.** Zoomed image showing the measured fluorescence observed 3 hours after delivery of the contrast agent I.V. **E.** The colour bar (look-up-table) for the photons count as measured by the detector.

Three-Dimensional Non-Rigid MR-TRUS Registration Using Duality-Based Optimization Method

Yue Sun^{1,2}, Jing Yuan², Cesare Romagnoli³, Aaron Fenster¹⁻³

¹Biomedical Engineering Graduate Program

²Imaging Research Laboratories, Robarts Research Institute

³Department of Medical Imaging

Western University, London, Ontario, Canada

Purpose: Two dimensional transrectal ultrasound (TRUS) guided prostate biopsy is the standard approach for definitive diagnosis of prostate cancer and guiding biopsy needles to suspicious regions in the prostate. However, due to the lack of image contrast of prostate tumours needed to clearly visualize early-stage prostate cancer, prostate biopsy often results in false negatives, requiring repeat biopsies. Magnetic Resonance (MR) has been considered to be the most promising imaging modality for noninvasive identification of prostate cancer, since it can provide a high sensitivity and specificity for the detection of early stage prostate cancer. Our main objective is to develop and validate a registration method of 3D MR-TRUS images, allowing generation of volumetric 3D maps of targets identified in 3D MR images to be biopsied using 3D TRUS images. In this study, we propose an efficient non-rigid MR to TRUS deformable registration method in order to improve the accuracy of targeting suspicious regions during a 3D TRUS guided prostate biopsy.

Methods: We initialized six approximately corresponding anatomical landmarks on 3D images to generate a rigid transform from MR to TRUS as an initial alignment. Following manual initialization, each pair of images were registered using a multi-modal deformable registration method, which employed the multi-channel modality independent neighborhood descriptor (MIND) as the local similarity feature across the two modalities of MR and TRUS (See Figure 1). A novel and efficient duality-based convex optimization-based algorithmic scheme was introduced to extract the deformations and align the two MIND descriptors.

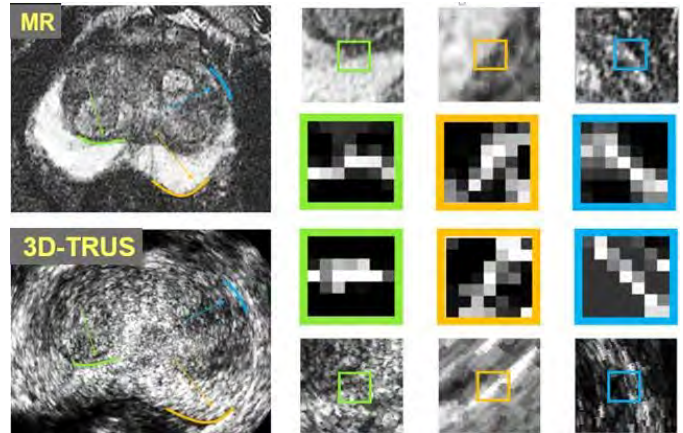


Figure 1: Proposed concept for the use of MIND for multi-modal registration. MIND is calculated for each voxel in the MR and 3D-TRUS images.

The registration accuracy was evaluated using 20 patient images by calculating the target registration error (TRE) using manually identified corresponding intrinsic fiducials in the whole gland and peripheral zone. Additional performance metrics, Dice similarity coefficient (DSC), mean absolute surface distance (MAD) and maximum absolute surface distance (MAXD), were also calculated by comparing the MR and TRUS manually segmented prostate surfaces in the registered images.

Results: Experimental results show that the proposed method yielded an overall median TRE of 1.76 mm. The results obtained in terms of DSC show an average of $80.8\% \pm 7.8\%$ for the apex of the prostate, $92.0\% \pm 3.4\%$ for the mid-gland, $81.7\% \pm 6.4\%$ for the base and $85.7\% \pm 4.7\%$ for the whole gland. The surface distance calculations show an overall average of 1.84 ± 0.52 mm for MAD and 6.90 ± 2.07 mm for MAXD.

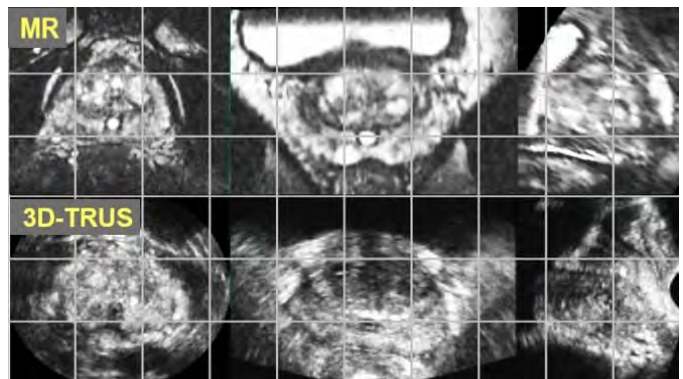


Figure 2: Examples of axial (left column), coronal (middle column) and sagittal (right column) views through registered MR (top row) and 3D-TRUS (bottom row) images.

Conclusion: To reduce false negative rate for prostate biopsy, we proposed an efficient duality-based convex optimization-based approach to extract the non-rigid MR-TRUS deformation field by registering the given two MIND descriptors (See Figure 2), which does not require segmentation of the prostate boundaries. Our results demonstrate that the proposed method yields clinically sufficient accuracy (less than the clinical acceptable target TRE of 2.5 mm).

Combined perfusion and Doppler imaging using plane-wave nonlinear detection and microbubbles

Charles Tremblay-Darveau *, Ross Williams †, Laurent Milot * †, Matthew Bruce ‡ and Peter N. Burns* †

*University of Toronto, Toronto, Canada †Sunnybrook Health Sciences Centre, Toronto, Canada ‡Supersonic Imagine, Aix-en-Provence, France

Colour and power Doppler imaging have established their preeminence in clinical diagnosis through their ability to show flow in major arteries and veins. However, blood flow at the capillary level cannot be detected clinically using Doppler imaging because of the strong Doppler-shifted echoes from tissue motion. Ultrasound imaging using microbubble contrast agents, on the other hand, enables low velocity perfusion to be detected and separated from the tissue echo using nonlinear methods such as pulse inversion, but is unable to depict large vascular structures within perfused tissue. While there is a clear advantage in having an imaging method that would be capable of displaying perfusion and vascular imaging simultaneously, it has been challenging to date to combine these methods due to practical limitations in acquisition time. Microbubble contrast agents are selectively imaged using non-linear imaging techniques which enable segmentation of the blood from the tissue at the cost of additional pulses. Since real time images (~10 images/s) are critical for clinical diagnosis, compromises such as low ensemble length power Doppler are often employed, sacrificing the ability to differentiate fast and slow moving bubbles in the image. With the recent progresses in GPU parallel processing, ultrasound images can now be created using a single plane-wave. The frame rate achieved through plane-wave imaging is considerably higher (13000 images/s) than the conventional line-by-line imaging (60 images/s). The present work sets to demonstrate that contrast-enhanced Doppler microbubble imaging should now be possible using plane-wave imaging.

It was found that, for low acoustic pressure, long Doppler ensembles can be acquired without considerably affecting the coherence of the echoes from microbubbles. In theory, long Doppler ensembles should reduce the effect of spectral broadening on the tissue signal, resulting in an improved flow sensitivity. Experiments showed that increasing the ensemble length indeed resulted in an improved slow sensitivity for both conventional (no microbubble) and contrast-enhanced Doppler, but that microbubble remained essential in detecting very slow flow when other factors such as tissue acceleration were considered. Plane wave contrast-enhanced power Doppler was then performed on an *in-vivo* rabbit kidney as a proof of principle. This, combined with the high velocity resolution achieved, allowed us to identify fast moving blood vessels from the background perfusion in a contrast-enhanced image (Figure 1a,b and c). An alternative application of plane-wave Doppler imaging was found to selectively image the perfusion-only (capillary) by removing the fast flow from the non-linear signal. This novel imaging mode required both the non-linearity of the microbubbles to reduce clutter amplitude and long sampling times for high frequency resolution. An example of a perfusion-only power Doppler image is shown in Figure 1d.

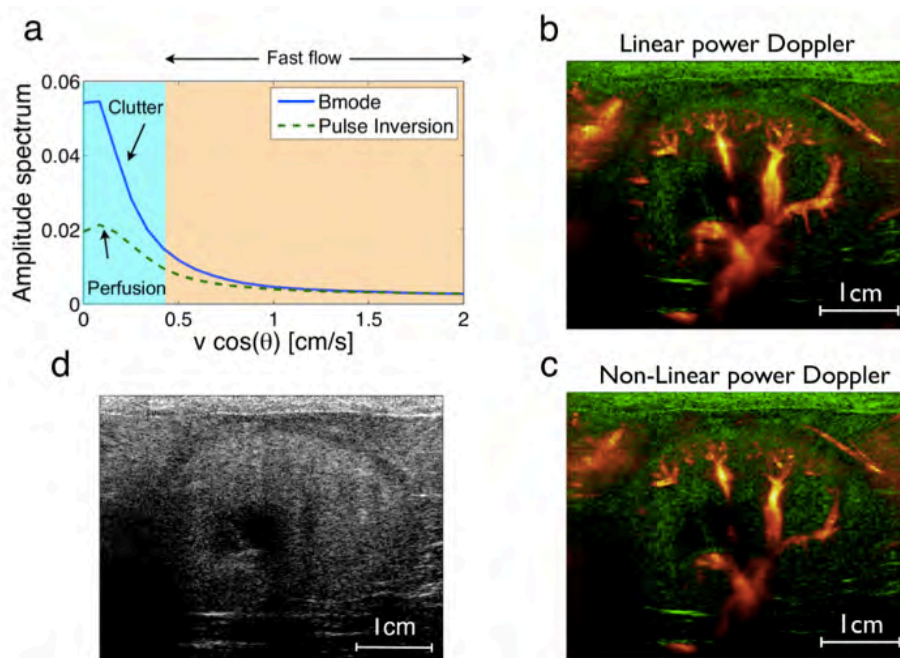


Fig. 1. Segmenting fast from slow flow using non-linear contrast-enhanced Doppler (PRF = 5 kHz). a) The Doppler spectrum (linear and non-linear) is integrated over the full image. The bandwidth of the clutter, evaluated using the linear Doppler spectrum, can be used to optimize the wall-filter for fast flow detection. b-c) Contrast enhanced B-mode (green colormap) overlaid with power Doppler (temperature colormap) mapping the fast flows. The fast flow is evaluated using the linear signal in (b) and the non-linear signal in (c). d) The perfusion-only power Doppler is produced by integrating the non-linear Doppler over the clutter region only, effectively removing the signal from the fast flow component.

Improving contrast-to-noise ratio of dynamic contrast-enhanced computed tomography (DCE-CT) images

Timothy Pok Chi Yeung, BSc^{a,d}, Mark Dekaban, BEng, BSc^{b,d}, Nathan De Haan^a, Laura Morrison, BSc^b, Lisa Hoffman^{b,d,e}, Yves Bureau^{b,d,f}, Xiaogang Chen^c, Slav Yartsev^{a,d,g}, Glenn Bauman^{a,d,g}, Ting-Yim Lee^{b-d,f,g}

^aLondon Regional Cancer Program, London Health Sciences Centre; ^bImaging Imaging, Lawson Health Research Institute; ^cRobarts Research Institute, Departments of ^dMedical Biophysics, ^eAnatomy and Cell Biology, ^fMedical Imaging, and ^gOncology

Research Supervisor: Drs. Glenn Bauman, Slav Yartsev, and Ting-Yim Lee

Purpose: To evaluate the improvements in image contrast-to-noise ratio (CNR) and measurements of blood flow (BF), blood volume (BV), and permeability-surface area product (PS) after principal component analysis (PCA) filtering of dynamic contrast-enhanced computed tomography (DCE-CT) images of a digital phantom. To evaluate the improvement in DCE-CT image quality with poor CNR in a rat glioma model.

Materials and Methods: A digital phantom with DCE-CT images reflecting known values of BF, BV, and PS was created, and was filtered using PCA. Intraclass correlation coefficients (ICC) and Bland-Altman plots were used to assess reliability of measurements and reduction in measurement errors, respectively. Wistar rats ($n = 8$) implanted with C6 glioma cells were scanned using DCE-CT, and the raw DCE-CT images were filtered using PCA. Differences in CNR, BF, BV, and PS before and after PCA filtering were assessed using repeated measures analysis of variance.

Results: Bland-Altman plot showed improved agreement, with mean errors decreased to 1.4 ml/min/100g (95% confidence interval, CI = -27.6 – 30.4), -0.1 ml/100g (-1.1 – 0.8), and 0.2 ml/min/100g (-3.5 – 3.9) for BF, BV, and PS, respectively. Map noise in BF, BV, and PS were decreased to 11.6 ml/min/100g (95% CI = -7.9 – 31.2), 0.5 ml/100g (0.1 – 1.0), and 1.4 ml/min/100g (-0.4 – 3.1), respectively. Figure 1 shows the measurements of BF, BV, and PS, without and with PCA filtering. For *in vivo* experiments, CNR significantly improved with PCA filtering in the normal brain ($P < 0.05$) and tumor ($P < 0.05$). Tumor and brain BF was significantly different from each other after PCA filtering with 4 principal components ($P < 0.05$) (Figure 2).

Conclusion: PCA filtering of CT perfusion images improved CNR *in vivo* and *in silico*; and reduced measurement errors of BF, BV, and PS *in silico*.

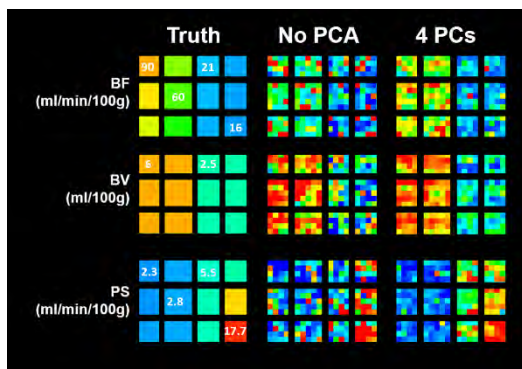


Figure 1. Maps of BF, BV, and PS of the digital phantom without noise (i.e. truth), with noise, and after PCA filtering with 4 PCs. Some values of BF, BV, and PS are labeled.

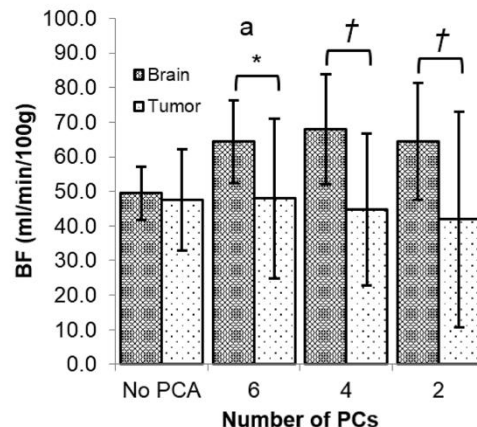


Figure 2. Brain and tumor blood flow (BF) before and after filtering different number of PCs. Asterisk (*) indicates a marginal significance of $P = 0.06$. Dagger (†) indicates $0.01 \leq P < 0.03$.

Quantitative monitoring of radiation induced skin toxicities in nude mice using optical biomarkers measured from diffuse optical reflectance spectroscopy

Darren Yohan^{1,5}, Anthony Kim^{3,5}, Elina Korpela², Stanley Liu^{2,4}, Carolyn Niu², Brian C Wilson², Lee CL Chin^{1,3,4*}

¹Department of Physics, Ryerson University

²Department of Medical Biophysics, University of Toronto and Ontario Cancer Institute / Campbell Family Institute for Cancer Research

³Department of Medical Physics, Odette Cancer Centre, Sunnybrook Health Sciences Centre

⁴Department of Radiation Oncology, University of Toronto, Toronto, ON

⁵These authors contributed equally to this work

*Lee.Chin@sunnybrook.ca

Abstract

Monitoring the onset of erythema following external beam radiation therapy has the potential to offer a means of managing skin toxicities via biological targeted agents – prior to full progression. However, current skin toxicity scoring systems are subjective and provide at best a qualitative evaluation. Here, we investigate the potential of diffuse optical spectroscopy (DOS) to provide quantitative metrics for scoring skin toxicity. A DOS fiberoptic reflectance probe was used to collect white light spectra at two probing depths using two short fixed source-collector pairs with optical probing depths sensitive to the skin surface. The acquired spectra were fit to a diffusion theory model of light transport in tissue to extract optical biomarkers (hemoglobin concentration, oxygen saturation, scattering power and slope) from superficial skin layers of nude mice, which were subjected to erythema inducing doses of ionizing radiation. A statistically significant increase in oxygenated hemoglobin ($p < 0.0016$) was found in the skin post-irradiation – confirming previous reports. More interesting, we observed for the first time that the spectral scattering parameters, A ($p=0.026$) and k ($p=0.011$), were an indicator of erythema at day 6 and could potentially serve as an early detection optical biomarker of skin toxicity. Our data suggests that reflectance DOS may be employed to provide quantitative assessment of skin toxicities following curative doses of external beam radiation.

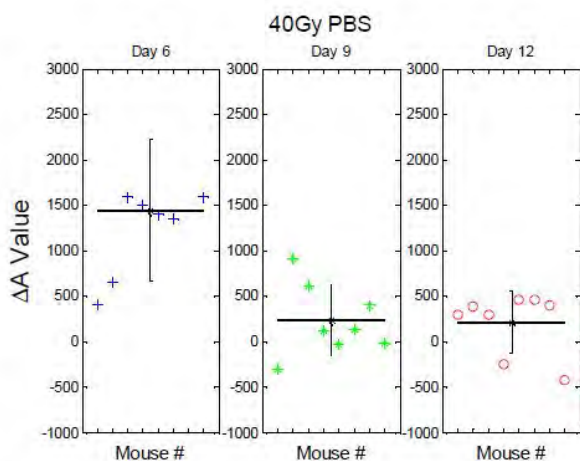


Figure 1: The statistically significant change in the A value on day 6 following 40 Gy irradiation is shown.

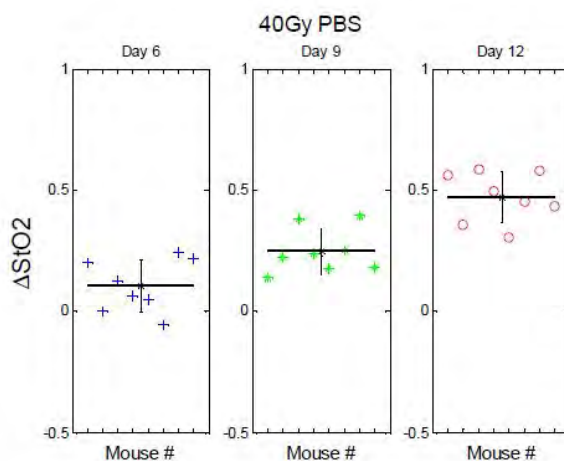


Figure 2: The steady increase in oxygenated hemoglobin on days 6, 9 and 12 following 40 Gy irradiation.

Development of ^{18}F -Labeled Peptides for Imaging EGFL7 in Prostate Cancer

Lihai Yu^a, Choi-Fong Cho^b, John D. Lewis^b, Leonard G. Luyt^{a,c}

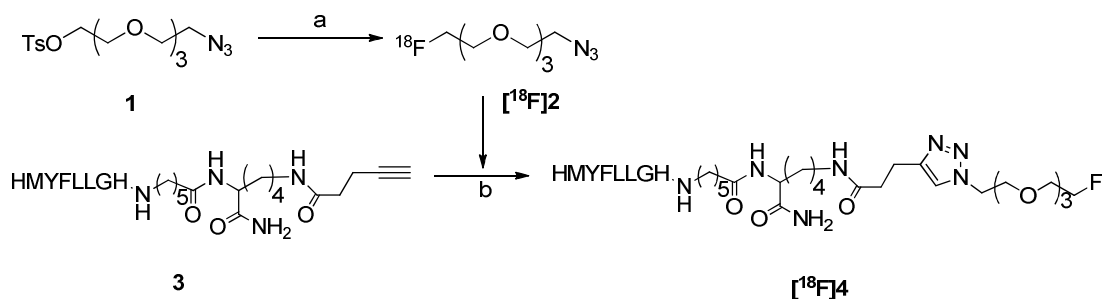
^aLondon Regional Cancer Program, 790 Commissioners Road East, London, Ontario N6A 4L6; ^bDepartment of Oncology, University of Alberta, Edmonton, Alberta T6G 2E1; ^cDepartments of Oncology, Chemistry, Medical Imaging, The University of Western Ontario, 1151 Richmond Street, London, Ontario N6A 5B7.

Introduction: Angiogenesis performs a critical role in malignant tumor growth. Epidermal growth factor-like 7 (EGFL7), a 30 kDa secreted protein, is highly expressed in angiogenic vessels and promotes solid tumor growth and metastasis via stimulating tumor-associated angiogenesis. Therefore, EGFL7 is proposed as a reliable and specific biomarker for cancer diagnosis and for evaluation of anti-angiogenic therapy. PET imaging is an effective non-invasive molecular imaging procedure and herein we describe the development of a ^{18}F -labeled PET radiotracer targeting EGFL7.

Method: An octapeptide (8 amino acids) library was screened for binding to EGFL7 by one-bead one-compound (OBOC) methodology. The binding affinity of peptides to EGFL7 was measured through surface plasmon resonance (SPR). Both fluorescein-LCE72 peptide and CPMV-LCE72 nanoparticles exhibit high binding affinity for EGFL7. Based on the chemical structure of LCE72, the corresponding fluorine-substituted LCE72 was prepared and labelled with F-18 for PET imaging of EGFL7.

Discussion: Four peptides, including LCE72, were discovered from the octapeptide library, with LCE72 having the highest affinity to EGFL7 ($K_d = 13.2$ nM) by SPR. The uptake of fluorescein-LCE72 in EGFL7-overexpressing HT1080 cells was more than 2 times higher than in regular HT1080 cells. Fluorescent microscopy shows CPMV-LCE72, but not control CPMV-PEG nanoparticle, bound substantially to the tumor and neovasculature both in an avian embryo model and in the xenograft mouse model, since EGFL7 is expressed in endothelial and tumor cells. This demonstrates that LCE72 has high binding affinity to EGFL7 in vitro and in vivo. In order to keep its affinity to EGFL7, LCE72 was modified with an alkyne group (**3**) via Ahx-lys at the C terminus. Peptide **3** was conjugated with [^{18}F]**2** by click chemistry to get [^{18}F]**4** with a radiochemical yield of 20-30% and radiochemical purity >95% (Scheme).

Conclusion: We have successfully discovered a peptide, LCE72, with high binding affinity to EGFL7 in vitro and in vivo. The corresponding F-18 radiotracer was synthesized and radiolabelled using click chemistry resulting in [^{18}F]**4**. PET imaging and biodistribution studies in a tumor mouse model will be performed in the near future.



Condition: a) $\text{K}_{2.2.2}$, K_2CO_3 , 90°C , 10 min; b) CuSO_4 , Sodium ascorbate, 90°C , 10 min

scheme

Ontario Preclinical Imaging Consortium OPIC

Oral Presentation and Poster Abstracts

Molecular Beacons for Fluorescence-Guided Resection of Oral Carcinoma

Laura Burgess^{1,2}, Tracy Liu^{1,2}, Juan Chen², Alex Vitkin^{1,2}, Gang Zheng^{1,2}

¹Department of Medical Biophysics, University of Toronto, ²Ontario Cancer Institute, University Health Network, Dr. Gang Zheng

While there have been improvements in therapeutic management of oral cancer, there has been no improvement in prognosis over the past 50 years. Much of the failure can be attributed to poor delineation of lesions. This has led to thirty percent of patients who have surgery (the current standard of therapy, along with radiotherapy) having recurrent oral cancer. There are trials underway to help better identify lesions and their boundaries to assist surgeons, specifically the Canadian Optically Guided Approach for Oral Lesions Surgical Trial (COOLS study). In the COOLS study, fluorescence visualization is used to differentiate normal tissue from dysplastic and malignant disease to allow for negative margins during surgery. They use autofluorescence, but this method is plagued with high rates of false positives. Expanding upon this idea, we have created near infrared optical probes with theranostic capabilities for detection and treatment of diseased oral tissue.

Molecular beacons consist of a fluorophore conjugated to a fluorescence quencher via a short disease-specific linker. When the fluorophore is replaced with a photosensitizer (both photoactive and fluorescent), creating a photodynamic molecular beacon (PMB), the beacon is capable of both diagnostics, by its fluorescence, and therapy, by its photoactivity. The photodynamic therapy works by simultaneous administration of a photosensitizing agent (PS) and activating light, in the presence of oxygen to generate cytotoxic singlet oxygen. The PMB remains quenched until cleaved by the appropriate biomarker. For these studies, two biomarker targets were used. Fibroblast activation protein (FAP) is highly expressed in cancer-associated fibroblasts in human epithelial cancers. It is also overexpressed in human dysplastic oral tissue and oral carcinoma *in situ*. Matrix metalloproteinase (MMP) is an enzyme that degrades the extracellular matrix and basement membrane, the main mechanism of oral cancer invasion. Once cleaved, both the FAP-specific and MMP-specific PMB became fluorescent, identifying diseased regions and, thus, guiding subsequent resection and/or treatment by laser.

A spontaneously forming hamster oral cancer model was used to study detection and delineation capabilities as well as treatment efficacy on both dysplasia and ESC. Hamsters were treated with 7, 12-Dimethylbenz(a)anthracene (DMBA), as hamsters develop oral carcinoma very similarly to humans and the model shows each distinct stage in the development (i.e. dysplastic and early stage lesions can be obtained). Once the malignant lesions had formed, they were incubated topically for only 15 minutes with either the FAP-specific or MMP-specific PMB. Malignant regions were clearly and specifically visualized in this short time period, with fluorescence imaging. This allowed for fluorescence-guided resection to immediately follow, selectively destroying lesions while sparing healthy tissue. Fluorescence imaging with highly specific PMBs targeting malignant lesions allow for same-day treatment by surgical resection and eventually can be expanded for treatment with PDT. This offers a new theranostic approach to oral carcinoma, overcoming the hurdles that have plagued conventional treatment of this disease, providing a highly selective and effective therapy.

Intravascular Imaging using a Frequency Domain Photoacoustic Method

Robin F. Castelino^{1,2}, Hyunggyun Lee¹ and F. Stuart Foster^{1,2}

¹Imaging Research, Sunnybrook Research Institute, Toronto, Canada

²Medical Biophysics, University of Toronto, Toronto, Canada

Photoacoustic (PA) imaging is a hybrid imaging modality based on the photoacoustic effect – the generation of acoustic waves by the absorption of electromagnetic radiation. By illuminating biological tissue using light, the delivered energy will be absorbed and converted into heat which leads to a transient thermo-elastic expansion creating ultrasonic emissions. PA imaging is most commonly performed using pulsed lasers. More recently, it has also been shown that continuous wave (CW) lasers can be used to generate PA signals, and this technique has been denoted as frequency domain photoacoustic (FDPA) imaging. Although, the efficiency of generating FDPA signals is lower when compared to the pulsed technique, it is possible to attain good SNR using signal processing methods such as cross-correlation.

Intravascular ultrasound (IVUS) imaging is an established technology for diagnostic and guidance protocols in interventional procedures. Although routinely used, it is reported to have low sensitivity in the detection of thrombus and lipid-rich lesions due to the limited acoustic contrast of soft tissues. Intravascular photoacoustic (IVPA) imaging has potential to characterize lipid-rich structures based instead on the optical absorption contrast of these tissues and has been previously reported using the pulsed PA technique. We demonstrate IVPA imaging using a CW laser diode and the FDPA method.

A challenge in FDPA imaging, especially in intravascular applications, is to amplitude modulate light at high frequencies sensitive to the bandwidth (BW) of the detector. In this study, we also develop a novel multi-frequency intravascular imaging prototype capable of simultaneous IVUS and FD-IVPA imaging. The probe consists of two back-to-back transducers viewing outward at 180 degrees with independent signal electrodes, sharing a common backing layer. The IVUS transducer has an active area of 0.5mm by 0.5mm and centered at 40MHz (35% BW). The active area of the FD-IVPA transducer is 1mm by 1mm, centred at 22MHz (60% BW) and co-aligned with a 600µm fiber delivering 1.5W over an amplitude modulated linear chirp from 16-25MHz. An agar vessel phantom with thin absorbing graphite rods was used showing an 18dB increase in PA signal of the targets when compared to the surrounding.

High Relaxivity Gd-free MRI Blood Pool Contrast Agent

Weiran Cheng^{1,2}, Tameshwar Ganesh^{3,4}, Francisco Martinez^{5,6}, Jolie Lam¹, Hyung Yoon¹,

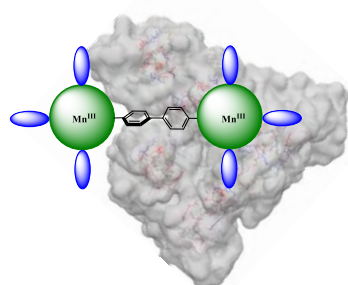
Robert B. Macgregor Jr.³, Timothy J. Scholl^{5,6}, Hai-Ling Margaret Cheng^{3,4,7,8}, and Xiao-an Zhang^{1,2}

¹Department of Physical and Environmental Sciences, University of Toronto Scarborough ²Department of Chemistry, University of Toronto, ³Leslie Dan Faculty of Pharmacy, University of Toronto, ⁴Physiology & Experimental Medicine and Diagnostic Imaging, Hospital for Sick Children, ⁵Imaging Research Laboratories, Robarts Research Institute, ⁶Department of Medical Biophysics, The University of Western Ontario ⁷Department of Medical Biophysics, ⁸The Institute of Biomaterials and Biomedical Engineering, University of Toronto, ON, Canada

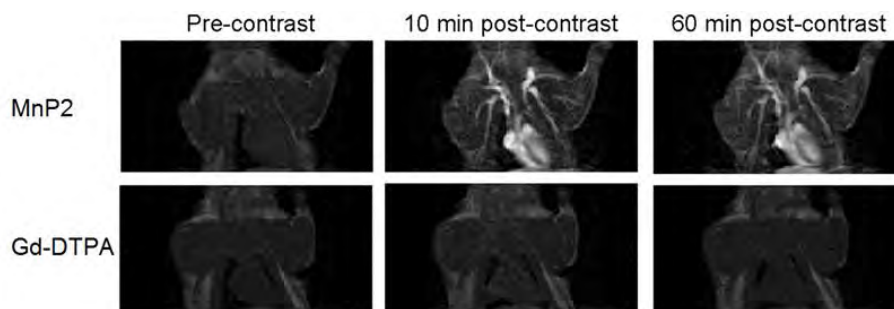
Magnetic resonance angiography (MRA) has become an increasingly important tool to evaluate the structural integrity and function of blood vessels, therefore is widely applied for diagnosis of various vasculature-related diseases in different organs. Limitations of applying conventional small Gd-based extracellular fluids (ECFs) contrast agents (CAs) include non-specific extravasation, resulting in low relaxivity and short time window for imaging. Therefore, blood-pool MRI contrast agents (CAs) are designed to bind to large molecules such as proteins to extend the circulation time in the blood stream. The first clinically approved blood pool agent is MS-325, a Gd-based MRI CA that binds reversibly to serum albumins, exhibiting long blood half-lives and high relaxivity. MS-325 is also cleared mainly by the kidney via glomerular filtration.¹ Despite the above mentioned merits, the risk of Gd release is still present and toxic free Gd(III) is implicated in Nephrogenic Systemic Fibrosis (NSF), a side effect correlated with the use of Gd-based CAs.² The prolonged vascular retention required for MRA and the fast clearance of Gd-based CAs required to minimize Gd accumulation remain a dilemma for the design of any Gd-based blood pool agent.

These challenges motivate us to synthesize a new class of blood pool agents using metal species which are more biocompatible and ideally with high relaxivity. Water soluble Mn(III) porphyrin (MnP) was chosen as the scaffold of design. Mn(III) is very stable in porphyrin chelates at physiological pH,³ and is an endogenous micronutrient, relatively much more tolerable than free Gd(III). In order to achieve high relaxivity, a dimeric MnP2, was recently synthesized as a non-Gd based T1 blood pool agent. The biphenyl group connecting two MnP is a common functional group known to form strong interaction with HSA. The binding of MnP2 to human serum albumin (HSA) was evaluated by UV-visible absorption, circular dichroism (CD), and fluorescence spectroscopies. In vitro efficiency of the MnP2 with or without HSA was evaluated by determining the field-dependent relaxivity of MnP2-HSA complex and free MnP2 respectively. Implications of HSA-binding in the pharmacokinetics of MnP2 was evaluated in rats.

Tight binding of $<2\mu\text{M}$ was obtained for MnP2 with HSA using CD spectroscopy. Similar binding constant was obtained from the change in fluorescence of the apo form of MnP2, (TPPS₃)₂, upon HSA binding. Long retention and significant contrast enhancement in the vascular compartment and heart was observed after administration in rats under a 3 T high-field clinical MRI scanner. In conclusion, our results suggest that MnP2 is a new class of Gd-free blood pool agent, compatible for high field applications.



Cartoon of Blood Pool Agent:
MnP2-HSA



Strong enhancement of the heart and vasculature was demonstrated by MnP2 in rats under a 3 T scanner. Same dosage of 0.05 mmol/kg per metal ion was used for MnP2 and Gd-DTPA

1. Caravan, P.; Cloutier, N. J.; Greenfield, M. T.; McDermid, S. A.; Dunham, S. U.; Bulte, J. W. M.; Amedio, J. C.; Looby, R. J.; Supkowski, R. M.; Horrocks, W. D.; McMurry, T. J.; Lauffer, R. B. *J. Am. Chem. Soc.* **2002**, *124*, 3152
2. Cowper, S. E.; Robin, H. S.; Steinberg, S. M.; Su, L. D.; Gupta, S.; LeBoit, P. E. *The Lancet* **2000**, *356*, 1000
3. Lyon, R. C.; Faustino, P. J.; Cohen, J. S.; Katz, A.; Mornex, F.; Colcher, D.; Baglin, C.; Koenig, S. H.; Hambright, P. *Magn. Reson. Med.* **1987**, *4*, 24

Endoglin-Targeted Ultrasound Contrast Imaging in the Mouse Embryo Model

Denbeigh, J.M.¹(H.BSc.), Nixon, B.A.¹(B.A.Sc.), Lee, J.J.Y.³(H.BSc.), Jerkic, M.²(Ph.D., MD.), Marsden, P.A.³(MD.), Letarte, M.²(Ph.D.), Puri, M.C.^{1,4}(Ph.D.), Foster, F.S.¹(Ph.D.)

- ¹ University of Toronto, Department of Medical Biophysics, Sunnybrook Research Institute, Toronto, Ontario M4N 3M5, Canada.
² University of Toronto, Department of Immunology, The Hospital for Sick Children, Toronto, Ontario M5G 1X8, Canada.
³ University of Toronto, Department of Laboratory Medicine and Pathobiology, Li Ka Shing Knowledge Institute, St. Michael's Hospital, Toronto, Ontario M5B 1W8, Canada.
⁴ Lunenfeld-Tanenbaum Research Institute, Mount Sinai Hospital, Toronto, Ontario M5G 1X5, Canada

Background: The growing demand for a personalized approach to treatment of disease has accentuated the importance of molecular imaging. As the characterization and measurement of key biomolecules in vivo, molecular imaging has the potential to dramatically impact all facets of patient care, from early disease detection to diagnosis, staging, treatment monitoring and follow-up. In ultrasound, functional and molecular imaging is possible through the use of microbubbles (MB), a contrast agent that can be transformed into targeting agents that bind to vascular biomarkers of interest. This strategy has been employed by a number of groups to demonstrate the ability of targeted ultrasound contrast imaging to monitor molecular expression in a variety of tumour models¹⁻³ and it is suggested that a positive correlation between specific biomarker expression levels and the detected acoustic signal of the bubbles exists.

We believe that targeted ultrasound contrast agents provide quantification of surface receptors in endothelial cell populations. The purpose of this study was to evaluate whether targeted contrast enhanced ultrasound imaging may provide a noninvasive measure of endoglin - an endothelial biomarker involved in the processes of development and vascular regulation as well as disease, being linked to haemorrhagic telangiectasia type 1 and tumour angiogenesis⁴.

Methods & Results: Our hypothesis was tested using a parallel plate perfusion chamber in which endoglin-targeted and control bubbles (rat isotype IgG₂ control and untargeted) were perfused across embryonic mouse endothelial cells (endoglin wildtype [Eng^{+/+}], knockdown [Eng^{+/-}] and knockout [Eng^{-/-}]) and adhesion was quantified as number of MB/cell. We also measured the binding of endoglin-targeted microbubbles in late-gestation stage isolated, living, transgenic endoglin embryos (Eng^{+/+}, Eng^{+/-}). Nonlinear contrast-specific ultrasound imaging, performed at 21MHz with a Vevo-2100 scanner, was used to collect contrast mean power ratios for all bubble types. Statistically significant differences in microbubble binding were found across genotype for both in vitro (Kruskal Wallis Anova: at the $p < 0.05$ level, the populations were significantly different [see Figure 1c.]) and in vivo studies (Linear Mixed Model Analysis: both genotype and microbubble type are significant [$p < 0.001$] factors [see Figure 1d.]). These initial results suggest that molecular ultrasound is capable of reliably differentiating between molecular genotypes and relating receptor densities to quantifiable molecular ultrasound levels.

Conclusion: If we can effectively characterize and quantify the molecular expression of biomarkers with microbubbles, microultrasound has the potential to become a reliable molecular imaging tool. This could easily influence the current trend towards personalized patient care. Our challenge, therefore, is to improve our understanding of targeted microbubble behaviour in the context of endothelial cell, developmental and cancer biology.

1. Lyshchik, A. *et al.*, J US Med, 2007 2. Deshpande, N. *et al.*, Radiology, 2011 3. Unnikrishnan, S. *et al.*, AJR, 2012 4. ten Dijke, P. *et al.*, Angiogenesis, 2008

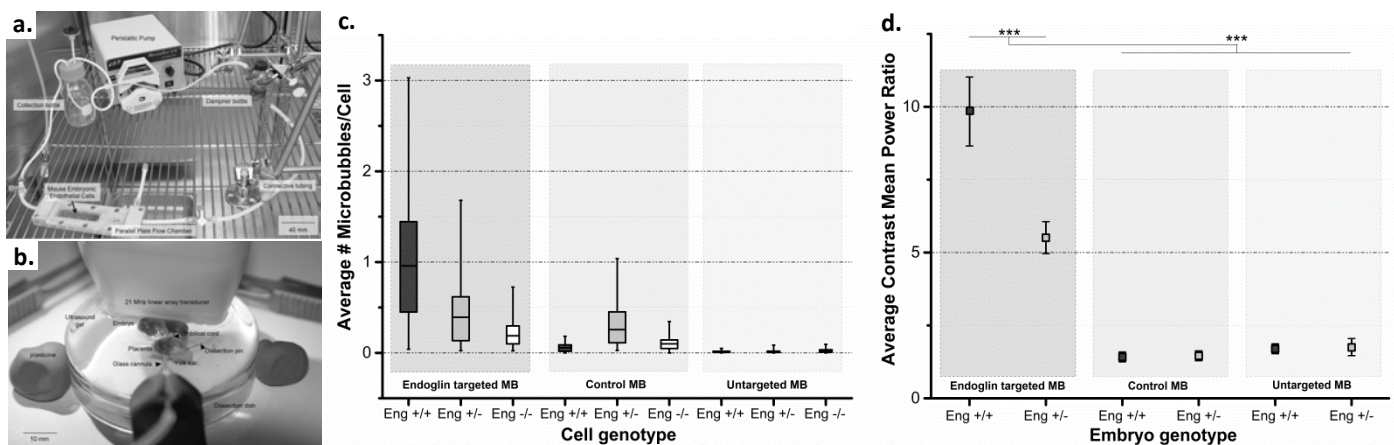


Figure 1: a. Experimental set up of a parallel plate flow chamber for testing targeted MB binding in vitro b. Experimental set up for the injection and imaging of MB in isolated living mouse embryos c. Distribution of number of MB per cell plotted according to cell genotype and MB group. Results are presented as box and whisker plots (min; first quartile; median; third quartile; max) d. Distribution of average contrast mean power ratios plotted according to embryonic genotype and MB group. Results are presented as averages + 95% confidence intervals of the mean, where *** is $p < 0.001$

Three-dimensional imaging of the mouse heart and vasculature using micro-CT and whole-body perfusion of iodine or phosphotungstic acid

Joy Dunmore-Buyze,¹ Elsbeth Tate,¹ Fu-li Xiang,² Sarah A. Detombe,¹ Zengxuan Nong,¹ J. Geoffrey Pickering,^{1,3,4} and Maria Drangova^{1,3}

¹Robarts Research Institute, The University of Western Ontario, London ON, Canada

²Department of Physiology and Pharmacology, The University of Western Ontario, London ON, Canada

³Department of Medical Biophysics, The University of Western Ontario, London ON, Canada

⁴Departments of Medicine and Biochemistry, The University of Western Ontario, London ON, Canada

Background: Recently, the use of heavy-metal-containing histological staining compounds have been explored to provide tissue enhancement in micro-CT images. To date, most approaches to integrate tissue staining with micro-CT have entailed excising the target tissue and soaking it for various amounts of time in staining solution, preventing the ability to assess structural relationships among organs and tissues. In addition, because stain delivery to tissues is determined by passive diffusion, larger specimens may be subjected to uneven or incomplete stain penetration, creating inconsistent enhancement. An alternative approach that has the potential to circumvent these limitations would be perfusing stain via the vasculature of an intact mouse. This study describes a perfusion approach using iodine or phosphotungstic acid (PTA) stains, delivered to an intact mouse, to capitalize on the microvasculature as a delivery conduit for parenchymal staining and direct contact for staining artery walls.

Methods: Twelve C57BL/6 mice, were arterially hand-perfused with either 25% Lugol's (iodine) solution or 5% PTA solution: once the vasculature was flushed with saline, approximately 10 mL of the staining agent was perfused and the solution was left in the vessels for 5 minutes before a second "dose" of stain was delivered. This procedure was repeated over a period of 15 minutes for the Lugol's and 30 minutes for the PTA solution before a final saline flush to clear the stain. All animals were scanned intact using a GE eXplore Vision 120 micro-CT scanner and reconstructed with 26 μ m isotropic voxels. The animals were fixed and the heart and surrounding vessels were excised, embedded, and scanned using the GE Locus SP scanner; isolated heart images were reconstructed with 13 μ m isotropic voxels. Myocardial enhancement and artery diameters were measured from the isolated heart images.

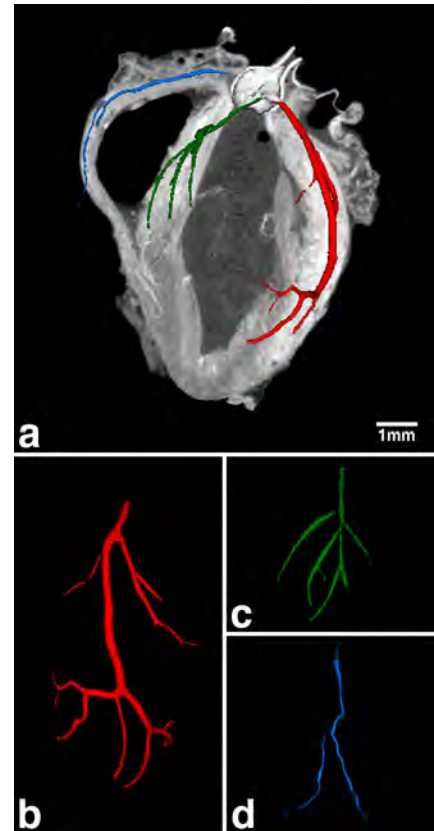


Figure 2: (a) An example of the 3D isosurfaces generated from a PTA-stained mouse overlaid on a coronal slice from the originating 3D image. Red: left coronary artery; blue: right coronary artery; green: septal artery. (b) The left coronary; (c) Septal branch; (d) The right coronary artery.

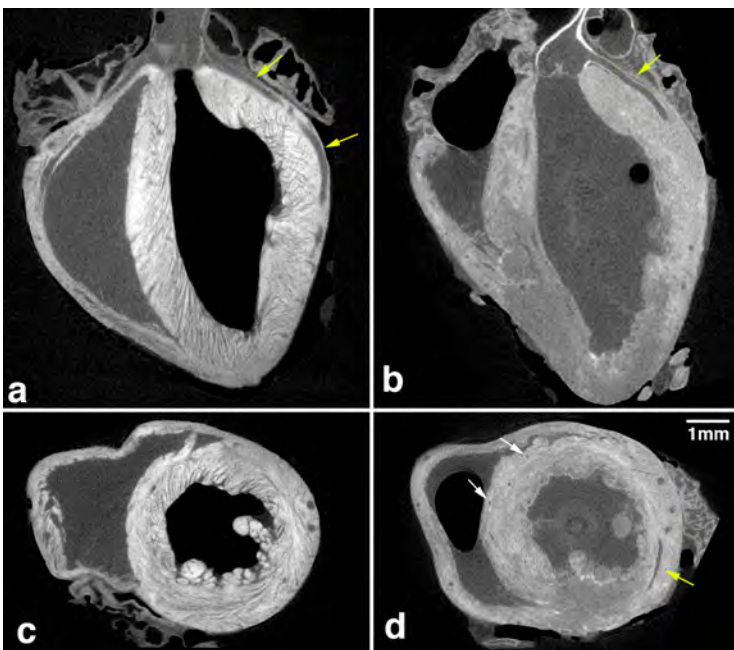


Figure 1: Coronal (a, b) and axial (c, d) slices from 3D micro-CT images of the mouse heart excised from a Lugol's solution- (a, c) or PTA- (b, d) infused mouse. Note the distinct myocardial muscle fibers visible in the Lugol's-stained heart. The yellow arrows indicate the left coronary artery. The white arrows indicate small coronary vessels in the myocardial wall.

Results: Both stains successfully enhanced the myocardium and vessel walls. Interestingly, Lugol's solution provided a significantly higher enhancement of the myocardium than PTA (2502 ± 437 HU vs. 656 ± 178 HU; $p < 0.0001$), delineating myofiber architecture and orientation (Fig. 1). There was no significant difference in vessel wall enhancement (Lugol's: 1036 ± 635 HU, PTA: 738 ± 124 HU; $p = 0.29$) but coronary arteries were more effectively segmented from the PTA-stained hearts, enabling segmented imaging of 5th order coronary artery branches (Fig. 2).

Conclusion: The combination of whole mouse perfusion delivery and use of heavy metal-containing stains affords high resolution imaging of the mouse heart and vasculature by micro CT. The differential imaging patterns of Lugol's- and PTA-stained tissues reveals new opportunities for micro-analyses of cardiac and vascular tissues.

^{129}Xe Imaging of the Lung using Spiral IDEAL

Ozkan Doganay^{1,2}, Trevor Wade¹, Elaine Hegarty¹, Krzysztof Wawrzyn^{1,2}, Rolf Schulte⁴, Charles McKenzie^{1,2,5}, Giles Santyr^{1,2,4}

¹Imaging Research Laboratories, Robarts Research Institute, ²Department of Medical Biophysics, ³Department of Medical Imaging, Western University, London, ON, Canada, N6A 5C1, ⁴GE Global Research, Munich, Germany, ⁵Biomedical Engineering, Western University, London, Canada

Introduction: MR imaging of hyperpolarized (Hp) ^{129}Xe promises to provide unique functional information for diagnosis of lung disease, including ventilation, perfusion and gas exchange. Although most of the inhaled Hp ^{129}Xe stays in gas phase, approximately 2% of HP ^{129}Xe gas dissolves in the pulmonary tissue and red blood cell (RBC) compartments and these can be spectrally resolved using Dixon-based methods, taking advantage of the unique chemical shifts of ^{129}Xe dissolved in the tissue (197 ppm) and RBC (217 ppm) compartments respectively. In particular, the IDEAL (Iterative Decomposition of water and fat with Echo Asymmetry and Least-square estimation) approach has been shown to be an efficient technique to image gas, tissue and RBC phases simultaneously [1, 2]. It is also anticipated that Hp ^{129}Xe imaging will benefit from single-shot reads-outs (eg. Spiral), that cover k-space following a single excitation pulse, thereby making most efficient use of the non-renewable Hp magnetization compared to cartesian read-out approaches [3]. In this study, we implemented a spiral IDEAL approach for imaging dissolved Hp ^{129}Xe in phantoms and rat lungs and compared to conventional cartesian IDEAL on the basis of SNR efficiency and spatial resolution.

Methods: 2D axial phantom and *in vivo* lungs of Hp ^{129}Xe images were acquired using a 3 T MRI system (MR750 GEHC, GE, Wisconsin, USA) and a custom built transmit-only/receive-only birdcage coil, consisting of a bird-cage coil for homogeneous B_1 transmit and a saddle-shaped single-turn receive-only surface coil conforming to the rat thorax. A phantom consisting of a 125-ml plastic bottle filled with 65-ml water and 60-ml Hp ^{129}Xe (natural abundance, polarization of ~5%) was used to compare SNR efficiency and spatial resolution of the spiral and cartesian IDEAL acquisitions as shown in Figure 1. Imaging of healthy Sprague Dawley rats was performed using a MRI-compatible mechanical ventilator for delivery of Hp ^{129}Xe to the lung following an animal care protocol approved by the Animal Care and Veterinary Service of Western University. The pulse sequence parameters were as follows: (i) Spiral IDEAL: number of averages = 8, FOV = 10 cm, pixel size = 6 mm, scan time = 3 s, three echo-time shifts with a constant spacing of $\Delta TE = 48 \mu\text{s}$, flip angle = 15° , pixel size (nominal resolution) = 3mm (ii) Cartesian IDEAL: matrix size = 40×40 , number of averages = 5, FOV = 10 cm, pixel size = 2.5 mm, scan time = 9 s, number of RF pulses = 600, flip angle = 7° . A pre-installed spiral gradient waveform optimized for ^{13}C IDEAL was used in this study with a read-out duration of 45 ms. The radiofrequency (RF) excitation rectangular pulses had a pulse width of 144 μs and were centered at the resonance frequency of the dissolved phase in order to optimize the flip angle of the dissolved phase resonances and minimize the flip angle of the gas phase resonance.

Results and Discussion: Figure 2 shows representative axial images obtained from the bottle phantom containing Hp ^{129}Xe in the dissolved phase of water on bottom (a) and the gas phase on top (b) using spiral IDEAL. Due to short T_2^* (~5ms) decay, the nominal resolution of dissolved phase and gas phase images drops to 12ms causing blurry artifact on the image. Despite some additional blurring due to the effect of T_2^* (~5ms) decay during the longer spiral read-out (~40 ms) compared to cartesian (~5 ms), the spiral IDEAL approach provides an SNR improvement factor of approximately two compared to the cartesian IDEAL approach, mainly due to the fewer number of RF excitation pulses, allowing the use of larger flip angles with spiral IDEAL. The spiral IDEAL images show some additional blurring from T_2^* decay during the relatively long read-out time required for the spiral k-space trajectory (45 ms).

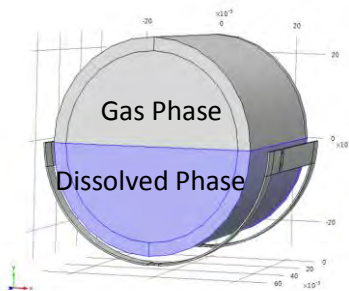


Figure 1: Receive coil/Phantom geometry. The hyperpolarized ^{129}Xe phantom consisted of a bottle containing water (bottom) and gas (top).

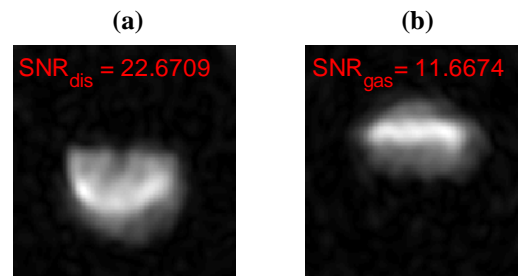


Figure 2: Axial 2D spiral IDEAL images of phantom. Dissolved phase of water and gas are shown separately in (a) and (b) respectively.

This study shows that IDEAL-spiral approach is feasible for Hp ^{129}Xe imaging of the rodent lung, providing an increase in SNR efficiency of a factor of approximately of two. In future, we expect to improve spatial resolution of spiral IDEAL by shortening the read-out gradient waveform and implementing interleaved spirals to help mitigate T_2^* blurring, particularly in the dissolved ^{129}Xe phase *in vivo*. Improvements in polarization are expected to enable resolution of RBC compartment for studies of lung injury (eg. radiation-induced lung injury).

References: [1] A. V. Ouriadov et al., Abstract in Proceedings of the 19th Annual Meeting of ISMRM, Montreal, Canada, 2011. (Abstract 6040); [2] K. Qing et al., J Magn Reson Imaging. 2013 May 16. doi: 10.1002/jmri.24181; [3] F. Wiesinger et al., Magn. Reson. Med. 2012 Jul; 68(1):8-16

PK11195-Cryptophane-A as a Contrast Agent in ^{129}Xe Hyper-CEST Studies for Enhanced Hyper-CEST Efficiency

Krista M. Dowhos^{1,2}, Matthew S. Fox², Iain K. Ball², Tao Li^{1,2}, Gowtham Gajawada^{1,2}, Jordan Wentzell¹, Brenton DeBoef³, and Mitchell S. Albert^{1,2}

1. Lakehead University, Thunder Bay, Ontario, Canada, 2. Thunder Bay Regional Research Institute, Thunder Bay, Ontario, Canada, 3. Rhode Island University, Rhode Island, United States

INTRODUCTION: Hyperpolarized (HP) ^{129}Xe gas as an MRI probe has become a highly attractive field of study for MR researchers, as it provides a 100,000-fold signal enhancement compared to thermally polarized ^{129}Xe , is extremely sensitive to its molecular environment and has a large chemical shift range of over 200 ppm. ^{129}Xe is also soluble in a wide variety of biological media, allowing for *in vivo* molecular imaging. Cryptophane-A molecules can encapsulate ^{129}Xe , causing a shift in the ^{129}Xe NMR spectrum of approximately +65 ppm with respect to the gas phase¹. Functionalized cryptophane-A molecules can potentially dissolve into the blood stream and are carried to biological targets of interest where they then encapsulate dissolved ^{129}Xe . Here, the encapsulated ^{129}Xe is in exchange with the dissolved phase ^{129}Xe so that Chemical Exchange Saturation Transfer (CEST) can be used to achieve further signal enhancement. As a result, a 10^8 -fold signal enhancement is possible with the combination of HP ^{129}Xe and CEST, a technique termed Hyper-CEST, which can be used to detect nanomolar concentrations of biomarkers². In this study, a more efficient pulse sequence was used to demonstrate Hyper-CEST, which provided higher Hyper-CEST efficiency and a much greater signal enhancement than has previously been achieved. The cryptophanes used for Hyper-CEST in this study have been functionalized with PK11195; and when bound to ^{129}Xe , cause a shift in the ^{129}Xe NMR spectrum of approximately +78 ppm. PK11195 targets peripheral benzodiazapine receptors (PBRs) present in glial cells at inflammation sites in the body. Thus, our method of Hyper-CEST has the potential to detect these inflammation sites, which can be caused by diseases such as COPD or arthritis.

METHODS: 2.5 mL of 30 mM PK11195 functionalized cryptophane-A in DMSO was shaken with 2.5 mL of HP ^{129}Xe in a plastic 5 mL LuerLok syringe prior to ^{129}Xe NMR spectroscopy. HP xenon, isotopically enriched to 83.5% ^{129}Xe , was prepared with a Xemed xenon polarizer, yielding up to 10% polarization. Spectroscopy of the sample was performed on a 3T whole-body Philips Achieva MRI using a T/R quadrature birdcage coil tuned to 35.33 MHz. Spectra were acquired after presaturation pulses were applied at +78 ppm with respect to the gas phase (on the cryptophane-encapsulated ^{129}Xe resonance). The presaturation pulses were 3-lobe sinc pulses of 6 ms duration, applied with 3 ms inter-pulse spacing, followed by a crusher gradient. Four sets of pulses were used consisting of 3, 5, 7 and 10 pulses. Hyper-CEST imaging was also performed using a gradient echo pulse sequence preceded by a train of 10 of the previously described presaturation pulses. Data were processed using Matlab and MNova NMR processing software.

RESULTS AND DISCUSSION: Figure 1 shows the MR spectrum of a 5.0 mL sample of HP ^{129}Xe gas dissolved in a cryptophane-A solution (red). Two separate resonances can be seen at +78 and +242.2 ppm with respect to the gas phase (not shown), which can be attributed to ^{129}Xe encapsulated by cryptophane-A and ^{129}Xe dissolved in DMSO, respectively. Overlaid on this spectrum is a separate MR spectrum (blue) of the same sample acquired after applying 10 presaturation pulses at +78 ppm. By using pulsed saturation to demonstrate Hyper-CEST as opposed to continuous wave saturation, we were able to limit the specific absorption rate (SAR). The SNRs of the dissolved and encapsulated ^{129}Xe peaks were calculated to be 94.3 and 40.3, respectively, for the spectrum acquired without presaturation. The dissolved ^{129}Xe peak SNR was decreased by 87% to 12.3 after applying 10 presaturation pulses at +78 ppm. This signal decrease, which can be attributed to Hyper-CEST, is to our knowledge the largest decrease yet reported. To verify that this signal decrease was actually due to Hyper-CEST, we applied presaturation pulses at +406.4 ppm, on the opposite side of the dissolved phase signal, and observed no decrease in the dissolved phase signal. Figure 2 is a plot of percent decrease in SNR of the dissolved ^{129}Xe peak after Hyper-CEST vs. the number of presaturation pulses, suggesting that the Hyper-CEST effect increases linearly with increasing number of presaturation pulses. Figure 3a is a ^{129}Xe dissolved phase image after presaturation pulses at +164.2 ppm (control image). Figure 3b is the ^{129}Xe dissolved phase image after applying presaturation pulses at -164.2 ppm, showing depletion in dissolved phase ^{129}Xe signal due to Hyper-CEST. Figure 3c is a subtraction image (a-b), which spatially locates the PK11195-cryptophane-A molecules in solution. By providing signal enhancement of several orders of magnitude compared to conventional MRI, Hyper-CEST has potential to serve as a promising molecular imaging technique. Since the cryptophane molecules are functionalized with PK11195, which targets PBRs, this technique can potentially detect inflammation sites in the body, such as in the case of COPD and arthritis.

CONCLUSION: Hyper-CEST holds promise for molecular imaging using MRI. This work demonstrated achievement of enhanced Hyper-CEST efficiency with signal depletion approaching 90%, as well as demonstrating imaging using Hyper-CEST to achieve high contrast for future use in molecular imaging.

REFERENCES: 1. Leif Schröder et al. (2006) *Science* 314:446-449. 2. Todd Stevens et al. (2012) *Magn Reson Med*. 69(5): 1245-52.

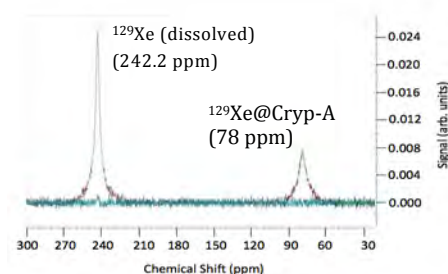


Figure 1: ^{129}Xe Hyper-CEST NMR spectrum of PK11195 functionalized cryptophane-A with presaturation pulses on (blue) and off (red).

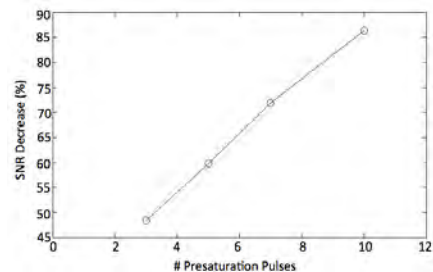


Figure 2: Plot of percent SNR decrease vs. number of presaturation pulses applied at the cryptophane-A resonance.

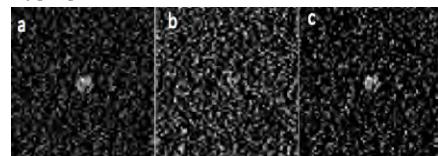


Figure 3: ^{129}Xe dissolved phase images after presaturation pulses at +164.2 ppm (control) (a); and -164.2 ppm (Hyper-CEST) (b); and a subtraction image (a-b) (c).

Magnetic Resonance Imaging of Dissolved Phase ^{129}Xe Using an X-Centric Pulse Sequence

Matthew S. Fox¹, Alexei V. Ouriadov¹, Tao Li^{1,2}, Iain K. Ball¹, and Mitchell S. Albert^{1,2}

¹Thunder Bay Regional Research Institute, Thunder Bay, Ontario, Canada, ²Lakehead University, Thunder Bay, Ontario, Canada

Introduction: Recent advancements in hyperpolarized (HP) noble gas magnetic resonance imaging (MRI), specifically those contributing towards improved production of HP ^{129}Xe [1,2] have renewed interest in the isotope for use as a medical imaging probe using MRI and as a possible alternative for ^3He lung MRI [3,4]. In Ontario alone, there are three permanently sited high production commercial ^{129}Xe polarizers dedicated for research and clinical trials, as well as a few home-built systems. Unlike ^{129}Xe 's counterpart ^3He , ^{129}Xe is readily available, is in high abundance (~26% natural abundance), is highly soluble in a variety of solvents and biological materials, and exhibits a large range of chemical shifts within these distinct chemical environments. Of particular interest is dissolved phase ^{129}Xe residing in and exchanging with tissue and blood. Exploiting these signals for diagnostic imaging purposes can be difficult (e.g., only about 2% of inhaled xenon dissolves into tissue and blood and T_2^* s can be prohibitively short (~2ms)). More efficient methods for sampling these short lived signals are needed in order to investigate various lung pathologies (e.g., impaired gas exchange) and even more exotic, imaging of the brain [5]. The X-centric pulse sequence was first applied to mouse lung imaging, reducing the high signal decay due to diffusion during imaging gradients and the short T_2^* within the lungs [6]. We present the utility of the x-centric pulse sequence applied to imaging dissolved phase xenon within a water-filled resolution phantom and compare results to conventional partial k-space sampling gradient echo imaging.

Methods: Imaging was performed using a Philips 3T Achieva clinical scanner. A dual-tuned RF coil was used (Clinical MR Solutions) sensitive to ^{129}Xe and ^1H frequencies at 3T (35.3 MHz and 127.6 MHz respectively). HP ^{129}Xe was produced to levels of up to 4% using a home-built xenon polarizer. To compare imaging sequences, a water-filled resolution phantom was filled with freshly thawed HP ^{129}Xe . The phantom was shaken for 5 seconds, placed inside the coil and a coronal full projection image was acquired. Two imaging sequences were compared: X-centric gradient echo imaging and conventional gradient echo imaging. For each comparison pair, acquisitions were acquired using the same batch of gas. Sequence parameters include: FOV 250mm x 250mm, slice thickness of 300mm, BW 310 Hz/pix, and a TR of 50 ms. Differences included, TEs of 0.81 ms/1.08 ms, matrix sizes of 128 x 80 vs. 128 x 128 and partial echo factors of 0.505 and 0.625 for X-centric and conventional gradient echo respectively. X-centric images were reconstructed using a custom-written algorithm using IDL-6.4. Image quality was assessed by comparing the resolvability of geometric features of various sizes within the resolution phantom as well as SNR.

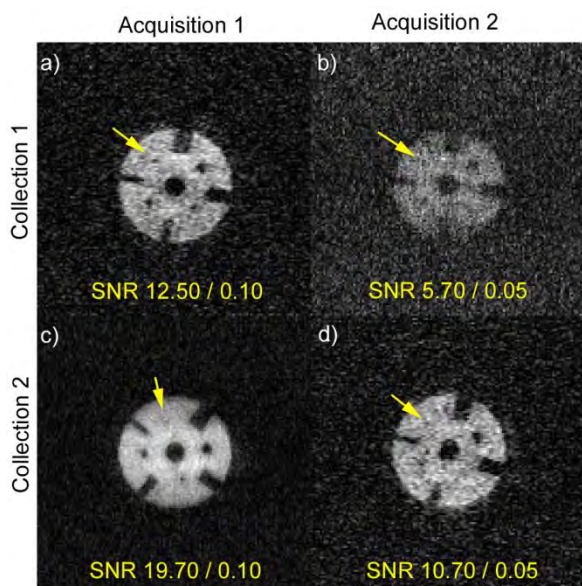


Figure 1: X-centric (a,d) and gradient echo (b,c) images obtained in pairs for independent collections of HP ^{129}Xe . Raw SNR values together with SNR values normalized by gas quantity appear at the bottom of each panel. Arrows indicate the 2mm diameter feature of the resolution phantom.

Results: Figure 1 depicts dissolved phase HP ^{129}Xe obtained from within a water-filled resolution phantom using the X-centric (Fig. 1a and 1d) and conventional gradient echo (Fig. 1b and 1c) pulses sequences. The pair of acquisitions was repeated in reverse order using a second collection. The raw and normalized SNR values are displayed in the bottom of each panel where normalization accounts for different quantities of gas in each batch. There is a consistent factor of two drop in SNR for acquisition 2 in each collection.

Discussion: In this study, it is demonstrated that x-centric can be used to image dissolved phase ^{129}Xe efficiently (within a breath-hold duration) and with reasonable SNR. After reconstruction, the smallest geometric features of the resolution phantom in the X-centric images are discernable (yellow arrows) where they appear unresolved in gradient echo images. Even for the case of Figure 1c) where the conventional method has the highest SNR overall, the resolution of the smallest geometric feature in the phantom is lost. Though the T_2^* of our phantom was long compared to those in tissues and blood the potential for using x-centric for imaging xenon in tissue and blood is high and the benefits of a fully sampled k-space are demonstrated here. Future directions include phantom studies producing shorter relaxation times ($T_2^* < 2$ ms) and demonstration of dissolved phase ^{129}Xe within tissue and blood in rat and human lungs and brain.

References: [1] Driehuys et al., 1996 Appl Phys Lett, 69:1668-1670, [2] Hersman et al, 2008 Acad Radiol 15(6):683-692, [3] Fox et al., 2013 Magn Reson Med epub DOI 10.1002/mrm.24746, [4] Mugler et al., 2013 J Magn Reson Imaging 37(2):313-331, [5] Driehuys et al., 2011 Proc ISMRM P879, [6] Ouriadov et al., 2008 Proc ISMRM P3789

Polarized Light Investigations of Biological Tissues, with Applications to Breast Cancer

Adam Gribble¹, David Layden², I. Alex Vitkin^{1,3,4}

¹ Department of Medical Biophysics, University of Toronto, Toronto, ON, Canada

² Department of Physics and Astronomy, University of Waterloo, Waterloo, ON, Canada

³ Ontario Cancer Institute/University Health Network, Toronto, ON, Canada

⁴ Department of Radiation Oncology, University of Toronto, Toronto, ON, Canada

Background: In addition to using harmful ionizing radiation, mammography is hindered by dense connective tissues, such as collagen, which are relatively opaque to x-rays. Furthermore, increased collagen deposition is associated with an increased risk of developing breast cancer. Therefore, it is important to develop new diagnostic techniques, free of ionizing radiation and uncomplicated by dense breast tissue.

Recent work done by collaborators at the Laboratory for Optical and Computational Instrumentation (LOCI) at the University of Wisconsin has shown that connective tissues, specifically collagen, undergo organizational changes early in breast cancer development, through to metastasis¹. These different collagen signatures can potentially be used as diagnostic indicators for the presence and staging of breast cancer.

A promising method to probe the structural arrangement of biological tissues non-invasively, with particular sensitivity to collagen, is using polarized light. Optical polarization properties of a sample are contained in its Mueller matrix, a complete mathematical description of its interaction with polarized light. To derive this 4x4 'transfer function' matrix it is necessary to measure how a sample interacts with different light polarizations, using measurements under at least 16 different orientations of static optical polarization components. However, the mechanical rotation of optical components is slow and leads to large random and systematic errors. Furthermore, the turbid nature of biological tissue causes light to undergo multiple scattering events, leading to increased depolarization. Thus, it is imperative to detect and isolate the weak, information-carrying, remaining polarized fraction with a high level of accuracy and high SNR amidst a large depolarized noise background.

A well-suited approach for tissue polarimetry is the dual photoelastic modulator (dual PEM) polarimetry system. PEMs dynamically modulate the polarization of light passing through them. Combining polarization modulation with synchronous signal detection allows for accurate measurement of weak polarization signals with improved SNR, much faster than with static measurements and without moving parts.

Previous work in the Vitkin lab has shown that the accuracy of tissue properties measured with the dual-PEM polarimetry system is theoretically optimal when probing the tissue with a specific set of incident light polarization states. This optimum set corresponds to polarization states forming the vertices of a cube on the Poincaré sphere².

Hypothesis: Polarization properties of breast tissue can be most accurately measured using the optimized polarimetry methodology developed in the Vitkin Lab. Furthermore, I posit that polarized light can be used to examine structural organization of collagen in breast tissue, enabling non-invasive breast cancer detection, staging and treatment monitoring.

Methods: The Mueller matrix of a liquid biological phantom was repeatedly measured with different sets of input polarization vectors (including the theoretically optimal set). The error associated with each set was calculated as the mean RMS Mueller matrix error.

Results: Experimental studies on a liquid biological phantom revealed that the set of theoretically predicted optimum input polarization states do indeed allow for the most robust Mueller matrix determination with a dual PEM polarimetry system³.

Future Work: This optimized polarimetry system will be used for tissue polarimetry studies aimed at cancer detection and treatment monitoring in excised pathologic breast tissues (initially mouse model). Findings will be compared to complimentary non-linear microscopy studies of LOCI researchers to gain a more complete biophysical picture of the complex breast milieu, pathology development and treatment response. The ultimate goal is a tissue polarimetry platform for fast, non-invasive, non-harmful and relatively inexpensive cancer characterization and assessment, with eventual *in-vivo* applications.

1. P. P. Provenzano, K. W. Eliceiri, & P. J. Keely (2009) Multiphoton microscopy and fluorescence lifetime imaging microscopy to monitor metastasis and the tumor microenvironment. *Clin. Exp. Metastasis* 26: 357-70.
2. D. Layden, M. F. G. Wood, & I. A. Vitkin (2012) Optimum selection of input polarization states in determining the sample Mueller matrix: a dual photoelastic polarimeter approach. *Opt. Express* 20: 20466-81.
3. A. Gribble, D. Layden, & I. A. Vitkin (2013) Experimental validation of the optimum input polarization states for Mueller matrix determination with a dual photoelastic modulator polarimeter. *Opt. Lett.* (Submission number: 196725) (Accepted Nov. 6, 2013).

Optimization of High-Frequency Ultrasound-to-Robot Registration to Meet Workflow Requirements of Preclinical Interventions

Adem Hadj Boussaad^{1,2}, Christopher Waring⁶, Jeffrey S. Bax⁶,
Aaron Fenster^{1,2,3,4,6}, and James C. Lacefield^{1,2,3,5}

¹Imaging Research Laboratories, Robarts Research Institute, ²Biomedical Engineering Graduate Program, and Departments of ³Medical Biophysics, ⁴Medical Imaging, and ⁵Electrical & Computer Engineering, Western University, and ⁶Centre for Imaging Technology Commercialization, London, Canada

A mechatronic device has been developed to perform needle injections to within 500 μm for preclinical interventions.

Our first technique for registering a VisualSonics® ultrasound scanner to our robotic device employed printed circuit boards containing a prescribed pattern of nine 317.5- μm diameter conductive pads serving as fiducial markers (6 pads) and targets (3 pads) arranged in a non-coplanar pattern (Fig. 1). A three-dimensional stage, controlled by three high-precision ($\sim 2.5 \mu\text{m}$) actuators with encoders, was used to advance the needle to each fiducial pad. Electrical contact between the needle's tip and each pad was used to determine the pad positions in robot coordinates. Within the registration phantom were 9 small (400 μm diameter) tungsten carbide/cobalt spheres mounted on plastic dowels near each pad. The spatial relationship between each pad and its paired bead was determined beforehand by analyzing a micro-CT scan (with 49.6 μm isotropic voxels) of the phantom. A single 40 MHz 3-D ultrasound scan was sufficient to localize all beads. A point-based rigid-body transformation was performed between the ultrasound and micro-CT volumes using the beads as fiducials. A second transformation, between the micro-CT volume and the robot's coordinate system, was performed using the pads as fiducials thereby registering the robot's needle tip location in ultrasound coordinates in two steps. A mean target registration error (TRE) of $135 \pm 46 \mu\text{m}$ was estimated over five registration trials.

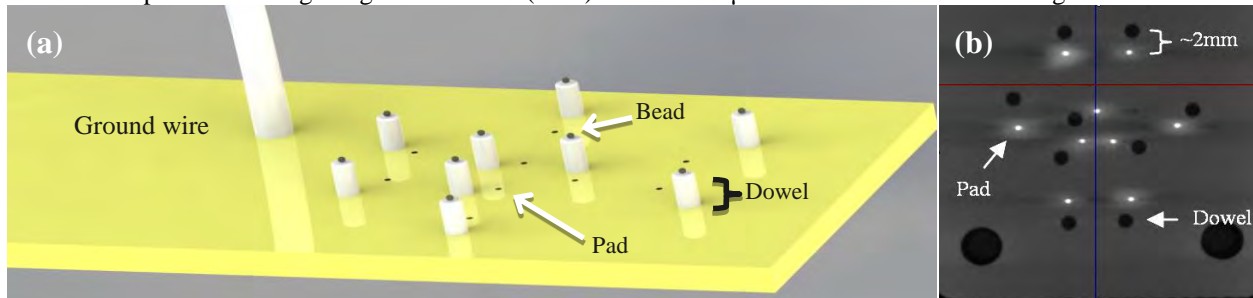


Fig. 1: (a) Solidworks® rendering and **(b)** micro-CT cross-sectional view of registration phantom.

Although sufficiently accurate for the small scale of our intended application, this registration technique is not suitable when taking into account several considerations of preclinical workflow. During a targeted injection, a mouse is typically anesthetised using isoflurane; this requires constant monitoring of dosage, body temperature, and heart rate to maintain sufficient anesthesia without overdosing. While our first method allows for good image-to-robot registration, it can take up to one hour to complete – close to the maximum knock-out time specified by many animal protocols. Unless done pre-operatively, without an accidental break in registration during a procedure, this registration method is not feasible, and a technique yielding similar accuracy is required.

A direct ultrasound-to-robotic-workspace registration technique has been developed. This involves moving the needle to a number of predefined robot positions (fiducials) and visually localizing the lumen centroid of the needle tip in ultrasound. Some criticisms of direct needle localization in ultrasound versus in CT, as in our first registration technique, include: 1) CT has a higher resolution than ultrasound when radiation dose is not a consideration. 2) Ultrasound images are anisotropic while CT's are isotropic. 3) In ultrasound imaging of needles, there are reverberation artifacts, which cause a blurring effect, and signal dampening under the needle. 4) Signal reflections may occur if the needle is tilted away from parallel to the transducer face. The accuracy of localizing a needle parallel to the transverse plane in micro-ultrasound was compared to that of micro-CT. It was found that, across 10 pairs of images in each modality, the localization error resulting from needle lumen centroiding in ultrasound was $\sim 50 \mu\text{m}$ on average. This fiducial localization error (FLE) is acceptable when compared to the $\sim 65 \mu\text{m}$ FLE of ultrasound bead localization in our previous two-step registration technique. Given that this proposed one-step technique to register a micro-ultrasound scanner to our robotic device yields comparable error metric results, eliminates the expenses associated with constructing and scanning a registration phantom, and simplifies the registration procedure by removing tedious and time-consuming steps; this change in registration method is an acceptable choice to reasonably meet the requirements of preclinical workflow.

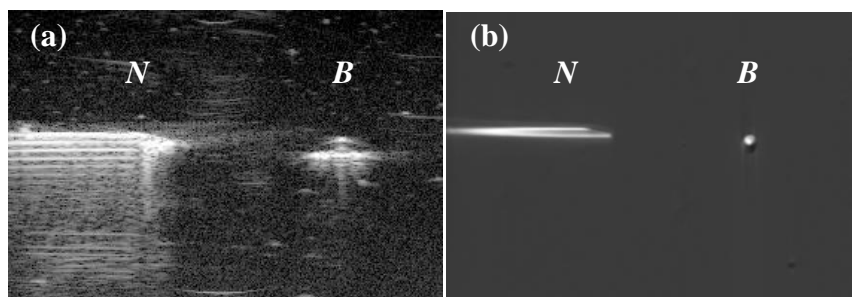


Fig. 2: Cross-sectional view of 27 gauge needle, *N*, and 400 μm tungsten bead, *B*, scanned in (a) high frequency ultrasound and (b) micro-CT.

Automated Registration of 3D Optical and MRI Whole Mouse Image Volumes

Jacqueline K. Harris¹, Eli Gibson^{2,3}, Amanda M Hamilton³, Colin McCurdy¹, Lanette J Friesen-Waldner^{1,3}, Aaron D Ward^{2,3}, Charles A McKenzie^{1,2}

1. Medical Biophysics, 2. Biomedical Engineering, 3. Robarts Research Institute, University of Western Ontario, London, Ontario

Purpose: Novel MR imaging techniques can be evaluated using accurate co-registration with histology. Whole-animal histological sections allow for simultaneous analysis of multiple tissues distributed throughout the animal, and also aid in registration by providing contextual information and structural support to tissues, such as adipose tissue, which if isolated from the body would be difficult to register. Currently, techniques exist to register whole mouse histological sections with 3D MR image volumes, where both MRI and histological sections are registered to an intermediate optical image volume¹. Of the two transformations required for these techniques, the 3D co-registration of MRI and optical image volumes is more challenging to perform than the 2D registration of histological sections with their corresponding optical image. This challenge results from changes in contrast, slice orientation, and resolution between optical and MRI volumes. In this work, we demonstrate a fully automated non-rigid registration technique to accurately register 3D whole mouse optical images with MRI, as a first step towards automated registration of histological sections.

Methods: *Animals:* One 129/SvJ and two C57BL/6 mice were imaged under a protocol approved by the Institution's Animal Use Subcommittee. *MRI:* In a 3T MRI (Discovery MR750, GE Healthcare, Waukesha, USA), 3D quantitative IDEAL (an investigational version), T1w, and T2w acquisitions were performed with approximately 0.7mm isotropic resolution. Mice were euthanized prior to imaging and subsequently developed *rigor mortis* over the duration of scanning, minimizing otherwise substantial tissue deformation between imaging modalities. *Optical:* Following MRI, mice were immediately embedded in an optimal cutting temperature medium and flash frozen in liquid nitrogen. Sectioning was performed by a CryoVizTM cryo-imaging system (BioInvision, Cleveland Ohio, USA). High-resolution optical images were acquired with an in plane resolution of 17 μ m and with a 200 μ m slice spacing. *Registration:* High-resolution optical images were down-sampled for registration to an approximate in-plane resolution of approximately 0.2mm and slice spacing of 0.8mm and compiled into a 3D volume. MRI and optical image volumes were initialized so animals had the same orientation in physical space. Each optical image volume was co-registered to all available MRI contrasts (water-only IDEAL, T1w, T2w). All remaining steps were fully automated and performed using software developed in C++/ITK². Optical volumes were converted to grey scale using a luminance filter and geometric centers of the two image volumes were aligned (Figure 1A). A rigid registration followed by two B-spline registrations of increasing grid sizes (3x2x5 and 7x5x10 nodes) were used to register MRI to optical image volumes (Figure 1B). Both rigid and non-rigid components of the automated registration minimize Mattes Mutual Information image similarity metric³. *Evaluation:* Target registration error (TRE) was calculated as the post-registration 3D Euclidean distance between anatomically homologous landmark pairs (12-17 per image volume, 82 total) selected in optical and MRI volumes using 3D Slicer⁴. A fiducial localization error (FLE) was quantified by choosing the same landmark in three different sessions, calculating the sample variance for each landmark, and taking the square root of the average sample variance for all landmarks in the same image volume⁵.

Results: The mean post-registration TRE was determined to be 1.2 \pm 0.1mm (mean \pm standard deviation) for all MR-optical image pairs. After initialization, TRE was calculated to be 5.9 \pm 1.1mm, which was reduced to 1.9 \pm 0.4mm following the rigid component of the algorithm. The average FLE of landmarks used in TRE calculations was 0.4 \pm 0.1mm for both optical and MR image volumes. There was not any substantial difference in TRE or FLE when registering optical volumes to any of the available MRI contrasts.

Discussion: Figure 1C demonstrates agreement between anatomical structures in post-registration optical and MRI volumes. Euthanizing animals prior to imaging reduced motion artifacts in MRI images and also allowed *rigor mortis* to set in before preparation for cryo-sectioning. Rigidity of the animals between imaging modalities reduced tissue deformation between imaging sessions, and likely accounts for the low TRE following the rigid portion of the registration.

Conclusion: Here we demonstrate a fully automated 3D registration algorithm for MRI and optical image volumes of whole mice achieving a TRE of 1.2 \pm 0.1mm with an FLE of 0.4 \pm 0.1mm.

References: [1] Gibson, E., et al., ISMRM, 2013.3729. [2] Yoo, T.S., et al., Stud Health Technol Inform, 2002. 85: p. 586-92, [3] Mattes, D., et al., Medical Imaging: 2001: Image Processing, Pts 1-3, 2001. 2(27): p. 1609-1620., [4] 3D Slicer, <http://slicer.org>, 2010, [5] Fitzpatrick, J.M., J.B. West, and C.R. Maurer, Jr., IEEE Trans Med Imaging, 1998. 17(5): p. 694-702.

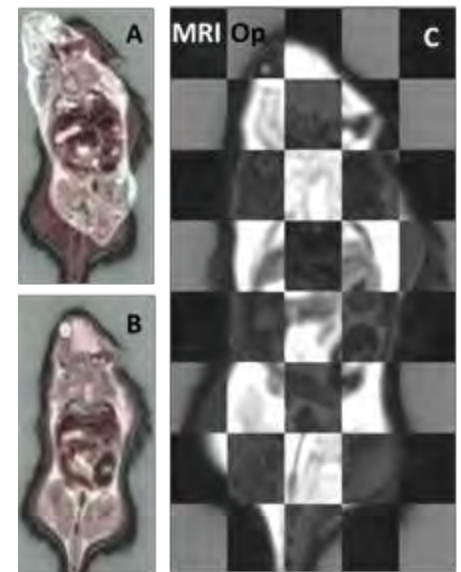


Figure 1: A single-slice view of T2w MRI and optical image volume overlay before (A) and after (B) registration. The optical image volume remains stationary and MRI is transformed to align volumes. (C) Checkerboard of optical (Op) and transformed MRI volumes shows agreement of anatomy in post-registration volumes. All images are of the same coronal slice in the optical image volume.

Quantifying whole-body vibrations in live mouse based on motion blur

Zhengyi Hu¹, David Holdsworth^{1,2,3}

¹ Imaging Research Laboratory, Robarts Research Institute, London, Ontario

² Department of Surgery, Western University, London, Ontario, Canada

³ Department of Medical Biophysics, Western University, London, Ontario, Canada

Osteoporosis is a disease in which the bone undergoes excesses demineralization. As result, it is significantly weakened structurally such that even a minor physical trauma such a fall could cause bone fracture. This disease cost Canadian economy \$2.3 billion, or 1.3% of Canada's healthcare expenditures in 2010. Worst of all, it affects mostly the senior population. As baby boomers age, this number will only continue to rise.

Current acceptable treatment of osteoporosis involves drug administration. However study have shown that it can actually cause localized bone fracture due to excess induced bone remodeling, a process in which the bone resorb itself so that it can form new bony material. Recent research into potential non-pharmaceutical treatment and prevention for osteoporosis has been focused on bone stimulation from external mechanical force. One such way of delivering such stimulation is the whole-body vibration (WBV).

As the name suggests, the WBV is a carefully controlled mechanical vibration that is introduced to the entire body of a person or animal through the feet. In a way, it is like experiencing a miniaturized earthquake. WBV methodology works on the principle of Wolff's Law, which states that bones of healthy people or animals are constantly adapting to their local mechanical environment. This law manifests itself in our everyday lives. For example, astronauts in space lose bone density over time because of lack of mechanical stimulation in space due to micro-gravity. On the contrary, athletes have higher bone density than an average person courtesy of their daily physical training, which stimulate bone growth. Hence, Wolff's Law could be exploited to promote bone growth in a person who is suffering from osteoporosis, or be used as a prevention tool. In fact, studies have shown the positive effects of WBV both in human and animals.

While the effects of WBV have been well observed and documented, the amount of vibration that gets transmitted at the skeletal level is not well studied. This is especially true in small animal studies. While in human studies, accelerometers can be directly attached to the bone and thus provide insights into how much vibration is transmitted to the bone. This method cannot be applied to small animal such as a mouse, as the weight of currently available accelerometer will introduce significant weight bearing to the animal which will affect vibration propagation. Therefore, there's a need in novel imaging technique to quantify transmissibility of whole body vibration in small animal.

Here we present an imaging technique that is capable of measuring the transmissibility at the skeletal level in a live, non-induced mouse during a WBV experiment using x-ray. The key to this technique is the 280 μ m tungsten beads that are implanted in the trabecular bone of the femur and under the periosteum of the tibia. This technique relies on the blurring of the bead, which is caused by the vibration. The blurring can be quantified as a function of vibration amplitude by measuring the changes in its intensity profile. Our initial *in-vivo* results show that our technique is capable of attaining accuracy of as high as 2 micron. And we are able to differentiate transmissibility at different part of the limb.

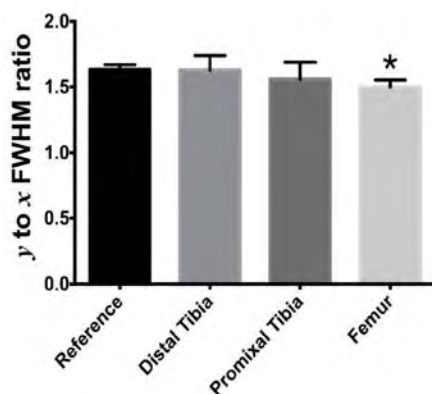


Figure 1. The measured bead blurring at different limb regions of a mouse with the implanted beads. Asterisk denotes statistical difference $p \leq 0.05$ in comparison to the reference bead.

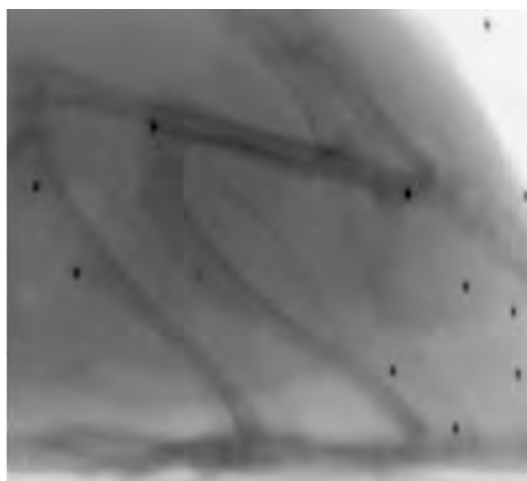


Figure 2. The x-ray image of a mouse with the implanted beads (three far left) and reference beads (far right) during a whole-body vibration. Notice the elongation of the bead, i.e., blurring, due to the vibration, which is used to quantify transmissibility.

Real-time imaging of live cells during dynamic fluid shear: design and fabrication of a novel platform

Lorusso, D.^{1,2,3}, Nikolov, H.³, Sims, S.M.², Dixon, S.J.², Holdsworth, D.W.^{3,4,5}

1. Western's Bone & Joint Initiative; Schulich School of Medicine & Dentistry, The University of Western Ontario, London, ON, Canada.
2. Department of Physiology & Pharmacology; Schulich School of Medicine and Dentistry, The University of Western Ontario, 1151 Richmond Street, London, ON, Canada. N6A 3K7
3. Imaging Research Laboratories, Robarts Research Institute; Schulich School of Medicine and Dentistry, The University of Western Ontario, 100 Perth Drive, London, ON, Canada. N6A 5K8
4. Department of Medical Biophysics; Schulich School of Medicine and Dentistry, The University of Western Ontario, 1151 Richmond Street, London, ON, Canada. N6A 3K7
5. Department of Surgery; Schulich School of Medicine and Dentistry, The University of Western Ontario, 1151 Richmond Street, London, ON, Canada. N6A 3K7

Introduction: Mechanotransduction is the process by which cells sense – and respond to – the local mechanical environment. This ability to react to external loads and forces is a critical component of mammalian physiology and is essential for normal functioning of our bones, lungs, and blood vessels; yet, the underlying mechanisms are still poorly understood. A form of mechanical stimulation that is commonly implicated in mechanotransduction is shear stress due to fluid flow. Our goal is to observe the immediate responses of cells to pulsatile fluid shear. Here, we describe the development of a microfluidic chamber for live cell cultures, which is compatible with real-time optical microscopy.

Methods: A microfluidic chamber was designed and fabricated from polydimethylsiloxane (PDMS) using multilayer soft lithography. Thin PDMS membranes were applied to a cell-culture dish with a thin glass-bottom window. Chambers were then cast and sealed to this base membrane, creating a microfluidic chamber with channels 300- μm wide by 100- μm tall. A 13.5% saline solution containing 6- μm diameter polystyrene beads was pumped through the chambers. Imaging of the channels under flow was performed using an inverted microscope and high-speed digital camera (300 – 1200 frames per second). Flow parameters were calculated by micro-particle imaging velocimetry, using the polystyrene beads as markers. Chambers were disinfected with 70% ethanol for 1 hour and sterilized by treatment with UV overnight. Following sterilization, chambers were pretreated with medium containing 50% fetal bovine serum to enhance cell attachment. MC3T3-E1 osteoblast-like cells were then seeded into the chamber and imaged. In addition, cells were treated with fluorescent calcium dye fura-2 and exposed to shear stress during photometry.

Results: Several prototype microfluidic flow chambers have been successfully fabricated in a reproducible manner. Steady flow rates up to 30 $\mu\text{L}/\text{min}$ have been introduced into the chambers, generating shear stresses of up to 3 Pa. In addition, MC3T3-E1 cells adhered and survived within the microfluidic chamber for at least 24 hours. Calcium photometry shows an increase in intracellular Calcium levels in response to fluid shear stimulus.

Conclusions: We have developed, fabricated and tested a microfluidic system capable of delivering physiologically relevant fluid shear stresses, under steady flow conditions. Such stresses can be applied to a chamber capable of hosting live cells, which can be imaged while subjecting cells to controlled flow-induced shear stress. Further development of the platform will enable application of high-frequency oscillatory stimuli. Additionally, future studies will involve microscopic imaging of live-cell reactions to pulsatile fluid shear.

These studies are supported by the Canadian Institutes of Health Research.

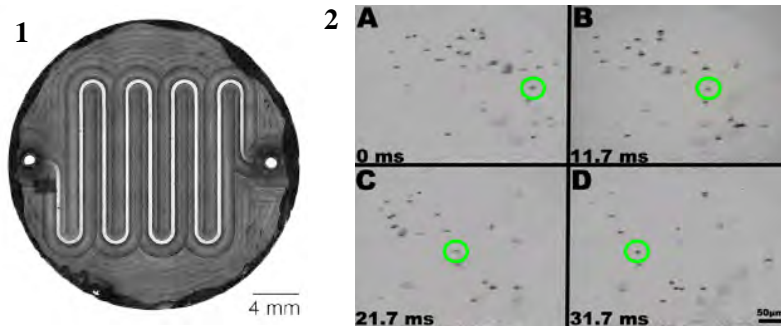


Figure 1. A micrograph of the PDMS constructed microfluidic chamber before it is sealed to the cell culture dish

Figure 2. Frames (A) 1, (B) 7, (C) 13, and (D) 19 of a 600 FPS video, showing particle flow over time within the channel

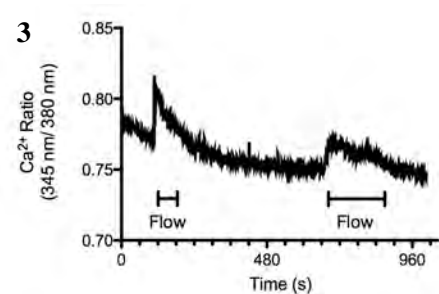


Figure 3. Representative preliminary calcium response plotted as the ratio of the fluorescence intensities at 345 nm / 380 nm. Flow was introduced at 30 $\mu\text{L}/\text{min}$ where indicated for the bars below the trace.

Magnetic Resonance Imaging of 5-Fluorouracil: A Preliminary Study for Monitoring Drug Resistance

Jordan A. Lovis^{1,2}, Matthew S. Fox², Iain K. Ball², Tao Li², Marcus J. Couch^{1,2}, and Mitchell S. Albert^{1,2}

¹Lakehead University, Thunder Bay, Ontario, Canada, ²Thunder Bay Regional Research Institute, Thunder Bay, Ontario, Canada

Purpose: After several decades of use, 5-Fluorouracil (5-FU) remains one of the most heavily used cytotoxic drugs used for the treatment of cancer. Research into 5-FU's mechanisms of action has led to an increase in anticancer activity. Despite these advances, drug resistance remains a significant limitation to clinical use.¹ 5-FU is converted intracellularly into fluorinated metabolites, such as fluorinated nucleotides (Fnuc.) and fluoro-B-alanine (FβAL). Fnuc. actively inhibit RNA synthesis and key enzyme function activity, monitoring this metabolite is essential when assessing drug efficiency.¹ MRI utilizes the unique chemical shifts of each metabolite to create metabolite distribution maps, which promise to yield important information on drug uptake and resistance. This means that monitoring 5-FU with the use of fluorine-19 (¹⁹F) chemical shift imaging may lead to decreases in clinical response times, facilitating personalized cancer treatment. Variations in bulk and local perfusion affect the amount of measurable signal from 5-FU and its metabolites. Previous work demonstrating imaging of 5-FU *in-vivo* utilized high field MRI's to attain metabolite distribution maps.³ In this study, a clinical 3T whole-body scanner was used to obtain distribution images of 5-FU and its metabolites in a live rat.

Methods: All animal experiments were conducted in accordance with the Canadian Council on Animal Care (CCAC). MR experiments were performed using a Philips 3T Achieva whole body scanner with a custom quadrature birdcage coil. Rats (487g ± 26.7 g) were initially anaesthetized by isoflurane induction, followed by a 50 mg/kg injection of ketamine. Anaesthesia was maintained with a constant infusion of ketamine/propofol. Coronal ¹H gradient-echo multi-slice images were acquired. A dose of 200 mg/kg of 5-FU (2 mL bolus) was injected into the tail vein over a 5-minute period. CSI maps were then acquired at continuous intervals up to 113 minutes after injection at which point the session was concluded and the animals were euthanized. All CSI maps were then overlaid onto their corresponding ¹H image to give an accurate biodistribution of 5-FU and its metabolites.

Results and Discussion: Figure 1a displays a ¹⁹F spectrum from a distribution map acquired at 113 minutes after the injection of 5-FU (our reference signal). Two other resonances were detected (-18.9 ppm and 5.2 ppm) which are believed to be that of FβAL and Fnuc. It is to be noted that signals found at 82.89 ppm and 88.8 ppm are due to the isoflurane used during initial anaesthetization. Figure 1b shows the time courses of 5-FU, FβAL, and Fnuc. distribution images overlaid onto a corresponding ¹H image. 5-FU signals were seen mainly in the areas of the liver and bladder, and decreased gradually (with the exception of the bladder). FβAL signals were obtained mainly within the liver, kidney, and bladder regions where signal was found to increase gradually. Fnuc. signals were obtained primarily in the bladder and liver regions. These findings agree with previously published work in a 7T animal MRI.³ The present study successfully demonstrates that sufficient chemical shift dispersion is attainable using a clinical whole-body scanner to acquire distribution maps of 5-FU and its metabolites.

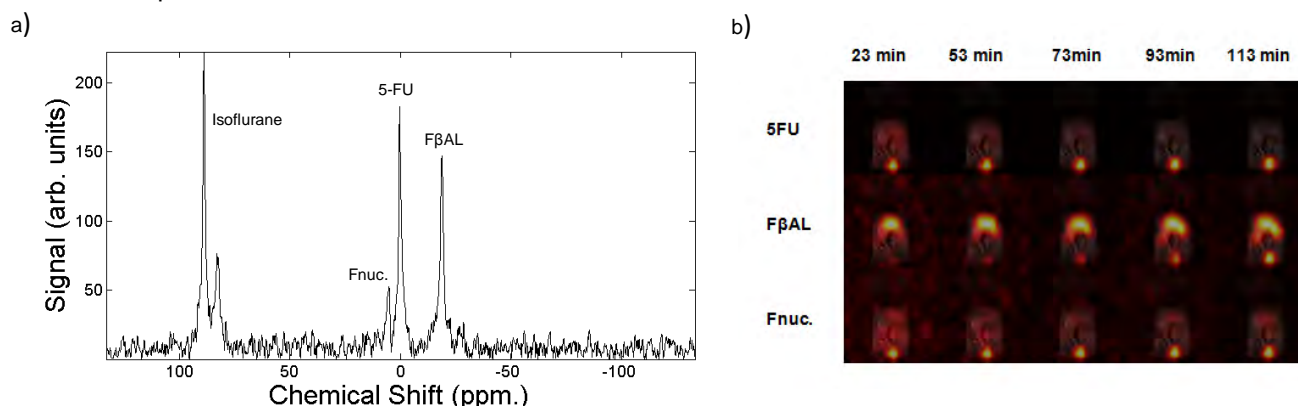


Figure 1: Panel a) depicts a typical ¹⁹F spectrum showing 5-FU and its metabolites. b) displays the CSI maps of 5-FU, FβAL and Fnuc. at 23, 53, 73, 93, and 113 minutes after injection of 5-FU.

Conclusion: Distribution maps of 5-FU, FβAL, and Fnuc. were acquired at continuous intervals until 113 minutes after the injection of 5-FU. Thus, successfully demonstrating the ability of ¹⁹F CSI to monitor metabolisim of 5-FU. To our knowledge, this is the first report of CSI mapping of 5-FU in a rat using a clinical 3T system. This proof-of-principle study demonstrates sufficient chemical shift dispersion laying the groundwork for future preclinical animal trials, and subsequent clinical imaging trials of patients administered with 5-FU as part of their cancer therapy. The results of such studies promise to facilitate improvements in personalized therapy for cancer.

References:

¹ Longley *et al.* (2003) *Nat Rev Cancer* 3(5):330-8 ² D. McIntyre *et al.*, (2011) *Cancer Chemother Pharmacol* 68:29–36. ³ Otake *et al.*, (2010) *Proc. ISMRM*. p 1009.

Hemiplegic cerebral palsy patients treated with constraint-induced movement therapy: Resting state functional magnetic resonance and diffusion imaging predictors and neuroplastic reorganization

Kathryn Y. Manning^{1,2}, Darcy Fehlings³, Ravi Menon^{1,2}

¹Department of Medical Biophysics, University of Western Ontario, London, Ontario, Canada

²Centre for Functional and Metabolic Mapping, Robarts Research Institute, University of Western Ontario, London, Ontario, Canada

³Academic Health Science Centre, University of Toronto, Toronto, Canada

Research Supervisor: Dr. Ravi Menon

Introduction: Hemiplegic cerebral palsy (CP) is characterized by unilateral upper extremity impairment as a result of subcortical injury due to stroke or trauma prenatally or in early life. Due to the early onset of the disease, patients experience learned non-use where the hemiplegic arm is further inhibited from healthy development as most tasks are done with the unaffected arm. Constraint-induced movement therapy (CIMT) directly combats learned non-use by restraining the unaffected limb, forcing the patient to repetitively use the hemiplegic limb¹. There is currently little understanding of the neurological basis behind this therapy and functional MRI (fMRI) experiments have focused on variable task-based studies². Resting state fMRI and diffusion tensor imaging (DTI) are useful tools to explore *global* network reorganization, neuronal integrity, and neuroplasticity.

Objectives: The objective of this study was to evaluate hemiplegic CP patients using various standard clinical assessments and MRI to (a) determine baseline fMRI resting state and diffusion quantitative measures that accurately predict a positive response to CIMT, and to (b) better understand the relationship between CIMT-induced functional changes and neuroplasticity. To the best of our knowledge, this is the first work aimed to identify resting state and diffusion neuroimaging predictors and correlated changes following CIMT in hemiplegic CP patients.

Methods: Twelve hemiplegic CP patients (7 treated, 5 control) from two different facilities were evaluated at baseline and 1-month after CIMT. The patients were clinically assessed using the Quality of Upper Extremity Skills Test (QUEST), a Jebsen-Taylor Test of Hand Function (JTTHF) task (occupational therapists identified lifting a large, but light object as being the most sensitive task), and the Canadian Occupational Performance Measure (COPM). All MRI data was acquired on the 3T MR scanner (Tim Trio; Siemens, Erlangen, Germany) using a 32-channel human head coil. Two different anatomical images were taken for registration purposes and in order to best delineate the lesions; an axial T2-weighted turbo spin echo sequence (TE/TR = 95/7770 ms, flip angle (FA) = 120°, matrix size = 320x225, FOV = 256x200 mm, No. slices = 35, slice thickness = 3mm) and an axial T2-weighted turbo inversion recovery fluid attenuated inversion recovery (TIRM-FLAIR) sequence (TE/TR = 120/8000 ms, FA = 130°, matrix size = 256x232, FOV = 220x200 mm, No. slices = 35, slice thickness = 4mm). Two 5 minute resting state fMRI gradient echo echo-planar imaging (GE-EPI) sequences (TE/TR = 30/2350 ms, FA = 90°, matrix size = 80x80, FOV = 240x240 mm, No. slices = 40, slice thickness = 3mm) were performed while the patient was simply asked to remain still and not fall asleep. And finally, a spin echo (SE) DTI sequence (TE/TR = 85/6800 ms, matrix size = 100x100, FOV = 200x200 mm, No. slices = 56, slice thickness = 2mm, b1 = 0, b2 = 1000 s/mm², gradient directions = 30) was used for creating diffusion-weighted images. Image preprocessing and analysis was done using FSL FMRIB software. Independent component analysis (ICA) was applied to cleaned, concatenated data to identify the sensorimotor resting state network (RSN). Dual regression algorithms were used to back-reconstruct the sensorimotor RSN connectivity layout at each time point and from this various laterality indices (LI) were calculated. The eddy current corrected DTI data was used to find the fractional anisotropy (FA) and mean diffusivity (MD) at the posterior limb of the internal capsule (PLIC), midbrain and the pons along both the right and left corticospinal tracts (CST).

Results: There was a significant correlation between the LI calculated from the number of above-threshold voxels in the sensorimotor RSN and the change in COPM score from baseline to 1-month ($r=-0.814$, $p=0.026$), as well as a trend with the change in time to complete the JTTHF task ($r=0.722$, $p=0.067$). (Figure 1) There was also a significant correlation between the time to complete the JTTHF task and the MD of the PLIC in the ipsilesional hemisphere ($r=-0.832$, $p=0.020$). The LI based on the number of above-threshold voxels and QUEST scores had correlated changes between baseline and 1-month post-CIMT ($r=0.748$, $p=0.053$). Figure 2 shows a representative subject and sensorimotor RSN reorganization after CIMT with increased activation in ipsilesional motor areas.

Conclusions: Both of the predictor relationships indicate that patients with more unilateral sensorimotor RSN and a further compromised ipsilesional CST improved the most as measured using both COPM and JTTHF assessments. This result could be influenced by a ceiling effect because of our high-performing baseline subjects. A further range of subjects is needed to confirm predictors based on disease severity and baseline MRI measures. The correlated changes between sensorimotor RSN reorganization and QUEST clinical measures provide further evidence of neuroplasticity.

References: 1. Mark et al. *Eura Med.* 2006; 42(3): 269-284. 2. Cope et al. *Dev. Neurorehab.* 2010; 13(1): 19-30.

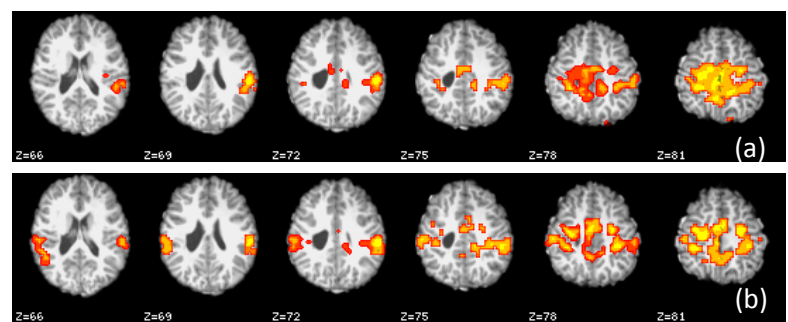
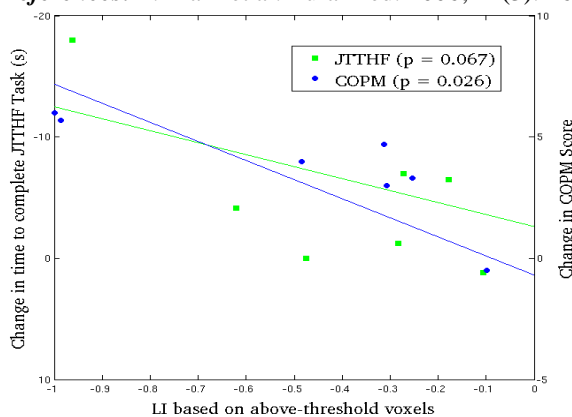


Figure 1 (left): Resting state neuroimaging predictor of clinical success following CIMT. Figure 2 (above): ICA-derived sensorimotor RSN (a) before and (b) after CIMT

MRI characterizes the effects of whole brain radiotherapy in a model of breast cancer brain metastases

Donna H Murrell^{1,2}, Niloufar Zarghami¹, Yuhua Chen², Ann Chambers^{1,3}, Eugene Wong¹, Paula J Foster^{1,2}

¹Department of Medical Biophysics, Western University, London ON ²Imaging Research Laboratories, Robarts Research Institute, London ON ³London Regional Cancer Program, London ON

INTRODUCTION: Metastasis to the brain occurs in up to 30% of metastatic breast cancer patients¹ and in about half of those who over express the human epidermal growth factor receptor 2 (HER2)². The median survival time for these patients is 4-6 months and only 20% of patients can expect to live to one year.³ This lack of effective therapy for patients diagnosed with brain metastases is largely due to inability for injected contrast agents and systemic therapies to cross the intact blood-brain barrier (BBB). This obstacle prevents early diagnosis and complicates treatment strategies thus rendering the brain a sanctuary site for metastatic growth. Whole brain radiation therapy (WBRT) is the standard of care for patients diagnosed with multiple brain metastases and research has shown radiation may increase BBB permeability^{4,5}. This experiment monitors the spatial and temporal development of HER2+ brain metastases from breast cancer and investigates tumour response to WBRT. We explore these phenomena in a murine model using a unique micro-irradiation system and novel MRI techniques developed in our lab.

STUDY DESIGN: 9 female nude mice received 100,000 231-BR-HER2 cells by intracardiac injection. 4 mice received WBRT of 20Gy in 2 fractions on day 24/25 post cell injection using a modified micro-CT system. All mice were imaged at 3T on day 23, 32, and 36 to visualize spatial and temporal metastatic development and tumour response to radiotherapy. Metastasis number, volume, and distribution were quantified by balanced steady state free precession (bSSFP) images and tumour permeability was assessed by T1-weighted spin echo (T1w SE) images post IV administration of gadolinium (Gad). Mice were sacrificed at endpoint and brains were excised for immunohistochemistry including hematoxylin and eosin, Ki67, and CD31.

RESULTS: We monitored 177 tumours in this experiment; each individual volume is shown in Figure 1. Blue symbols represent metastases in untreated mice and black symbols represent metastases in WBRT treated mice. Over time, the number of metastases increased in both all mice. In the untreated group, metastasis volume increases with time in almost every case; however, in the mice treated with WBRT, tumour growth was often halted and many tumours decreased in volume between days 32 and 36. There is a trend for decreased tumour volume after WBRT compared to control that almost reaches significance by the latest time point - day 36 ($p=0.06$). Metastases that were permeable to Gad are shown as circles and those non-permeable to Gad as triangles. The number of permeable metastases was not different for WBRT versus untreated mice at any time point. Of particular interest, however, was the observation that at the late imaging time point the volume of the permeable metastases is significantly smaller in WBRT treated mice compared to untreated mice ($p<0.05$). Figure 2 shows the MRI appearance of brain metastases and the corresponding histology. Metastases appear with high signal intensity in the bSSFP images due to their high fluid content and longer T2 compared to the brain parenchyma. The tumors shown in A and C are also visible in the post Gad images indicating that the BBB is compromised. The tumour shown in B is non-permeable. In histology, untreated metastases appear as dense cell clusters surrounded by edema. In comparison, metastases that have been treated with WBRT appear “empty” and lack these cancer cell clusters. There is excellent correlation between MRI and the whole brain sections.

SIGNIFICANCE: Longitudinal MRI studies are key to better understanding the progression of brain metastases; contrary to traditional microscopy – which can only assess *ex vivo* at endpoint – these experiments allow us to monitor the whole brain over time and characterize the evolution of brain metastatic growth and permeability as well as responses to therapy *in vivo*. We hope this research will contribute to advances in new treatment strategies and improve the clinical management of breast cancer patients with HER2+ brain metastases.

REFERENCES:

1. Canadian Cancer Statistics 2010
2. Sperduto PW *et al* (2012) Int J Radiat Oncol Biol Phys
3. Ohno S *et al* (2004) Breast Cancer
4. Fauquette W *et al*. Brain Research 2012
5. Li Y-Q *et al*. Cancer Research 2003

* $p < 0.05$

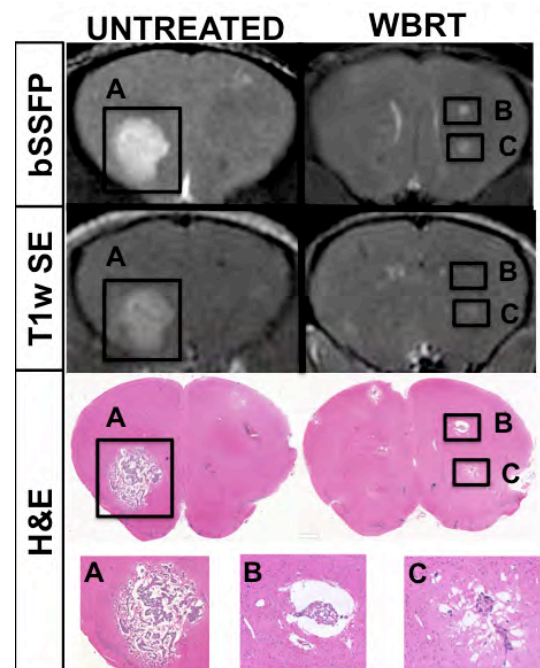
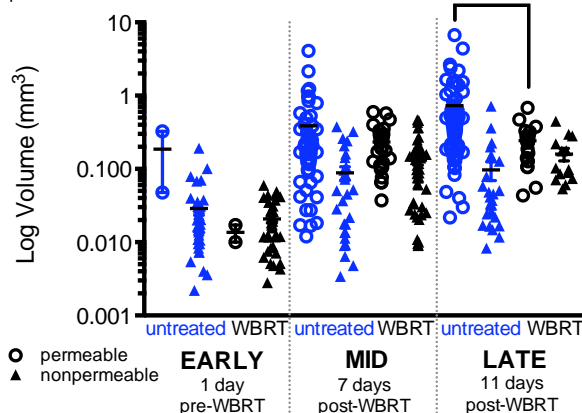


Figure 1 (left): The growth and distribution of metastasis volumes over time. **Figure 2 (right):** bSSFP and T1w SE MR images and correlative histology for untreated and WBRT-treated tumours. Tumours A and C are permeable to Gad; Tumour B is not.

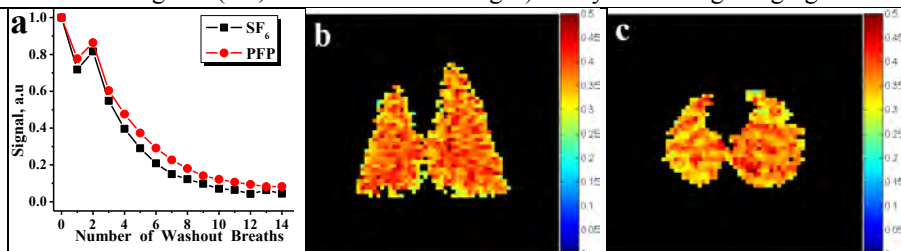
In Vivo Regional Ventilation Mapping by Using Fluorinated Gas MRI

Alexei V. Ouriadov¹, Matthew S. Fox¹, Marcus J. Couch^{1,2}, Tao Li¹, Iain K. Ball¹, and Mitchell S. Albert^{1,2}.

(1) Thunder Bay Regional Research Institute, Thunder Bay, Ontario. (2) Lakehead University, Thunder Bay, Ontario.

Introduction: Hyperpolarized gas lung MRI requires expensive isotopes and polarizers, which has prevented this imaging modality from becoming widespread due to its expense and requirement of specially trained personnel. Inert fluorinated gas lung MRI is a new and promising alternative to hyperpolarized gas lung MRI; it is less expensive and it does not require expensive isotopes and polarizers to perform. Imaging with these gases (e.g. sulfur hexafluoride (SF₆) and perfluoropropane (PFP, C₃F₈)) can be conducted using any clinical scanner that is equipped with a multi-nuclear amplifier and receiver [1-2]. Fluorine-19 has a large gyromagnetic ratio (~95% of ¹H), the gases typically used have many fluorine-19 atoms per molecule and have very short longitudinal relaxation times, which helps to overcome their inherently low thermal polarization compared to hyperpolarized gases. In addition, inert fluorinated gases can be mixed with oxygen without significantly sacrificing image quality, so that patient safety can be increased during a breath hold scan. Due to the thermally polarized nature of inert fluorinated gases, it is relatively easy to use these gases for dynamic lung imaging and for obtaining lung ventilation maps, lung heterogeneity maps, and gas trapping maps. To our knowledge, only one study investigating dynamic ventilation of SF₆ in the rat lung has been published [3]. In this pilot study we employed SF₆ and PFP mixed with O₂ for obtaining regional ventilation maps of normal rat lungs by using a washout approach with a two-breath X-Centric method (greatly improving image quality for nuclei with short signal lifetime values, particularly SF₆/PFP) [4] on a clinical scanner as a transitional step for converting to more sustainable gases (i.e., HP ³He/¹²⁹Xe to ¹⁹F gas) for dynamic lung imaging studies.

Fig. 1. (a) Dependence of bulk FID signal as a function of oxygen washout breaths obtained for SF₆ (black solid squares) and PFP (red solid circles) for the same rat. **(b)** 2D whole lung projection fractional ventilation map obtained for SF₆ in coronal plane. **(c)** 2D whole lung projection fractional ventilation map obtained for PFP in axial plane. (b) and (c) were obtained for the same rat.



Methods: All SF₆ and PFP ventilation measurements were performed using a 3.0T Philips Achieva scanner with maximum gradient strengths of 4 G/cm and a home-built rat-sized quadrature transmit/receive coil tuned to the ¹⁹F resonance frequency of 120.15 MHz. Experiments were performed on healthy Sprague Dawley rats (428 ± 28 g) following an animal care protocol approved by the local animal care committee. 2D rat lung SF₆ and PFP images were obtained in the axial and coronal planes using two separate acquisitions of the X-Centric pulse sequence (i.e., one breath per one readout gradient polarity) and normal k-space Cartesian sampling with a partial echo factor of 0.505 (TE=0.54 ms, TR=4 ms for SF₆, and TR=20 ms for PFP, 6 x 6 cm, 64 x 64 pixels, FA=70°, BW=400 Hz/pixel for SF₆, and BW=300 Hz/pixel for PFP, 60 averages for SF₆ and 20 averages for PFP). A home-built, MR compatible pneumatic ventilator was employed in all rat measurements, based on the work of Nouls [5]. Data acquisition was synchronized to breath-hold durations using the ventilator. The following washout protocol was used in our ventilation mapping study: rat lungs were saturated with an SF₆/O₂ or PFP/O₂ 80/20 gas mixture during 3 min of normal free breathing at a breathing rate of 60 breaths/min. After 3 min, the fluorinated gas/O₂ mixture was suspended followed by a 10 s breath-hold to obtain a baseline image. One washout breath of pure O₂ was then provided, followed by a 10 s breath-hold to collect the second image. This breathing scheme was repeated 14 successive times in order to completely eliminate fluorinated gas from the rat lungs to fully sample the washout curve. Because only half of k-space (50.5% of the readout window) was collected in each of the 14 washout-breaths, the entire washout protocol was repeated using the opposite readout gradient polarity in order to create a fully sampled k-space data set for reconstruction. Off-line reconstruction was used to create rat lung images using a custom-made IDL 6.4 routine. The fluorinated gas washout data were fitted (custom-made Matlab 2012 routine) with the following equation [6-7]:

$$S(n) = \text{const} \cdot (1-r)^n$$

Where S is the available signal at breath number n, and r is the fractional ventilation, which is defined as the ratio of new gas entering a voxel at each breath, divided by the total amount of gas in each voxel:

$$r = \frac{V_{\text{new}}}{V_{\text{total}}} = \frac{V_{\text{new}}}{V_{\text{old}} + V_{\text{new}}}$$

Results and Discussion: Fig. 1a shows the typical dependence of the bulk FID signal as a function of O₂ washout breaths. The data indicate that one could completely replace either fluorinated gas with O₂ after approximately 10 washout breaths. Interestingly, the signal level after the second washout breath is slightly elevated for unknown reasons, but it does not complicate the washout protocol for studying dynamic ventilation *in vivo*. Figs. 1b and 1c show typical whole lung ventilation maps obtained for SF₆ (overall rats <r> = 0.35±0.037) and PFP (overall rats <r> = 0.31±0.42) with a normal rat. The overall SF₆ <r> value is 11% larger than overall PFP <r> value. Previous work [8] reported <r>=0.37 for ³He and <r>=0.36 for ¹²⁹Xe for the case of normal rats. Mean r values obtained in our study are close to those published, especially for the SF₆/O₂ mixture, assuming that ventilator settings for normal rats were similar. These results suggest that fluorinated gases can be used for *in vivo* dynamic lung studies, and are a less expensive and more deployable alternative to hyperpolarized noble gases. Further improvement in the imaging methods and MR hardware should permit us to obtain 3D ventilation maps of the lungs and extend our techniques to clinical studies. Our next goal is to use the X-Centric method and washout protocols for a comparison study between cohorts of normal and elastase induced rats (to model emphysema) using fluorinated gas MRI.

References: [1] Couch MJ et al, (2013) *Radiology*, e-pub. [2] Halaweish AF et al, (2013) *Chest*, 144(4):1300-1310. [3] Adolphi NL et al, (2008) *MRM*, 59:739-746. [4] Santyr GE et al, (2009) *J Appl. Phys.*, 105:1-13. [5] Nouls J et al, (2011) *Concepts in MR Part B*, 39B(2):78-88. [6] Emami K et al, (2010) *MRM*, 63(1):137-150. [7] Santyr GE et al, (2011) *NMR in Biomed.*, 24:1073-1080. [8] Couch MJ et al, (2012) *MRM*, 68:1623-1631.

Development of a Novel Functional Orthopaedic Implant for Use in a Rodent Model of Partial Hip Replacement

Adam D.M. Paish,^{1,3} H.N. Nikolov,¹ I.D. Welch,² D.W. Holdsworth^{1,3}

¹Imaging Research Laboratories, Robarts Research Institute

²Veterinary Services and Care

³Department of Medical Biophysics
Western University, London ON, Canada

Osseointegration, the structural amalgamation of living bone with a load-bearing orthopaedic prosthesis, ensures that uncemented implants (not secured with bone cement), remain fixed in bone and stable over time. Maintaining this stability in a load-bearing prosthesis is important for implant longevity. If loosening occurs at the metal-bone interface, patients experience pain and discomfort, often requiring that a revision surgery be performed to replace the component. This poses added risk to the patient, and incurs an additional cost to the healthcare system. Consequently, the development special coatings and implant surface geometries that aim to improve osseointegration is an active area of study. The ability to utilize a small animal model, such as the rat, would be ideal compared to traditional large-animal model testing in orthopaedic research and development. This is because a small animal model would lend to increased cost-effectiveness, reduced variability, higher statistical throughput, more repeatable experiments and better access to pre-clinical imaging compared to traditional large animal models in the initial stages of research. Historically, functional implants do not exist in sizes required for testing in rats due to the difficulty of manufacturing such small components via traditional methods. However, recent advances in additive manufacturing, 3D selective laser melting (SLM), have made it possible to create precise, functional components small enough to be implanted and tested in a rat. Thus, we propose to design and fabricate custom, functional metal-alloy orthopaedic implants for use in a rodent model of partial hip replacement.

Two proof of concept investigations were undertaken to demonstrate the ability of the 3D SLM metal printer (*3D Systems DM 125*) to accurately produce an implant scaled down to a size appropriate for a rat (Figure 1). First, a human femoral prosthesis (*Smith&Nephew Synergy*) was scanned using micro-CT (*eXplore speCZT*, GE). Image data was next transferred to computer-aided design (CAD) software (*Solidworks* and *Geomagic*) and then printed in 316L stainless steel. Second, micro-CT image data was obtained from two cadaveric rat femora; one intact, and one with the neck and head surgically resected. These data were again transferred to the same design software. Each 3D femur volume was then registered to the other using anatomical landmarks. Next centerlines running parallel through these features were found and used to form an implant geometry matching rat femoral anatomy. A CAD model was then generated using the acquired centerline template. This design was also then printed in 316L stainless steel.

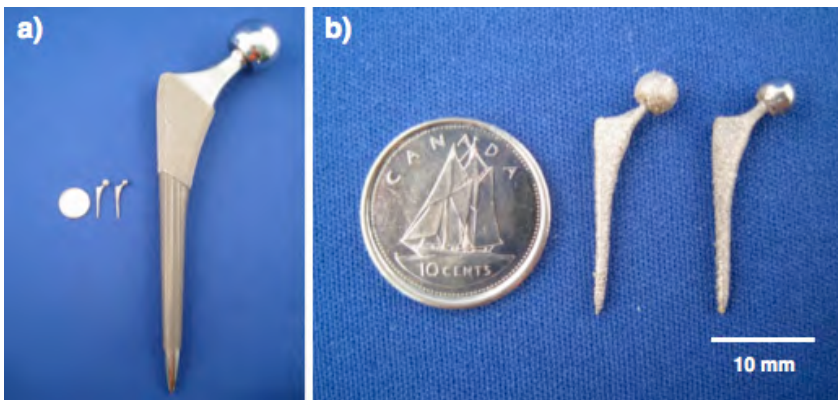


Figure 1: Results of fabrication of a preliminary component design, using the DM-125 SLM system. The preliminary design was fabricated in 316L stainless steel, as shown in a) in comparison to the original (10x larger) human implant. The close-up view in b) shows the implant at two stages of manufacture: directly after fabrication (left) and after polishing of the 4mm diameter metal ball (right).

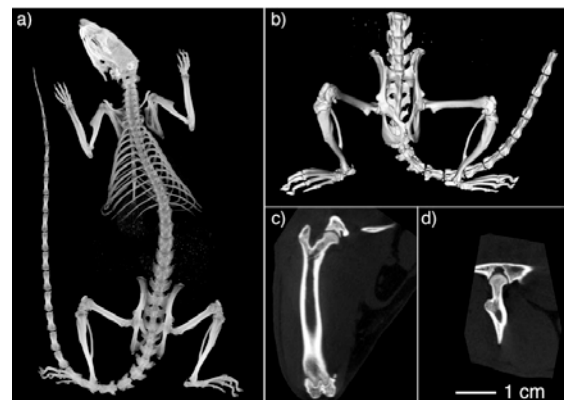


Figure 2: Representative maximum-intensity projection data for this rat is shown in (a) and 3D rendering in (b). The 3D data can be re-oriented to provide arbitrary oblique views through the anatomy (c, d), allowing exact measurements of bone dimensions.

The SLM 3D metal printer was successful in producing identical copies of both the scaled-down human and custom-rat implant prototypes. Surgical installation of components into cadaveric rat femora was then attempted. Based on these attempts, it was determined that an implant maintaining the overall geometry of a human implant, modified to fit rat femoral anatomy would be ideal since neither prototype provided an ideal fit, thus it was determined that the development of a hybrid implant design would be optimal. To accomplish this, previously acquired micro-CT image data (GE *eXplore Locus Ultra*) of 77 (n=52 male, n=25 female) Sprague-Dawley rats (250-600g), scanned at 90kVp and reconstructed at 150 microns, are being analyzed to ascertain how key features of rat proximal femoral anatomy vary across animals of different gender and size (Figure 2). These data will allow us to modify existing human implant geometries so that we produce an implant that can be successfully installed into a rat, while still maintaining applicability to large animal and human studies of osseointegration. These data will also enable us to determine a range of implant sizes that will be required to accommodate animals of different size and weight.

Optimization of a staring transducer array for photoacoustic imaging

Avery Raess, Philip Wong, Ivan Kosik, Dr. Jeffrey Carson

Imaging Program, Lawson Health Research Institute; Department of Medical Biophysics, Schulich School of Medicine and Dentistry, The University of Western Ontario; Supervised by Dr. Jeffrey Carson

Photoacoustic imaging is a modality which quantifies the optical properties of a sample. This technique can distinguish between oxygenated and deoxygenated blood non-invasively, which can identify areas where cancer is present due to high tumour metabolism. However, the technique is still in its infancy and may require further optimization before it can be used effectively in the clinic.

Photoacoustic imaging utilizes laser light to induce thermoelastic expansion. The pressure waves created from the expansion are then detected with ultrasound transducers. Transducers may scan around the imaging target or may be in a fixed array surrounding the object, known as a staring array. Staring arrays offer advantages in acquisition time and image quality and are frequently hemispherical or spherical with all transducers directed at the centre of the array (Ephrat et al., *Opt. Express* 16, 2008; Wang et al., *Opt. Express* 3, 2012). This configuration was designed intuitively and we hypothesize that it causes oversampling in the centre of the array while undersampling nearby areas.

A model of the image space of a staring transducer array was developed to determine if oversampling occurs. A custom-made 2.6 MHz ultrasound transducer was characterized and used to model a hemispherical 128 channel staring array. Several configurations of transducers were modeled by directing transducers towards points located within the imaging volume. Both the number and spacing of the points were varied. The crosstalk matrix was calculated, giving the sensitivity and aliasing of each voxel with the aim being to maximize sensitivity and minimize aliasing while increasing coverage of the imaging volume. By varying the directionality of the transducers away from the centre of the array, the sensitive area of the array made more uniform but the overall sensitivity decreased. The mean absolute error and structural similarity index were computed to compare the imaging potential of different configurations.

Quantification of total adipose tissue in fetal guinea pigs subjected to suboptimal in utero conditions using water-fat MRI

Kevin J Sinclair¹, Lanette J Friesen-Waldner¹, Colin M McCurdy¹, Curtis N Wiens², Trevor P Wade^{1,3}, Barbra de Vrijer⁴, Timothy RH Regnault^{4,5}, and Charles A McKenzie^{1,3}

¹Department of Medical Biophysics, University of Western Ontario, ²Department of Radiology, University of Wisconsin, Madison, Wisconsin ³Robarts Research Institute, University of Western Ontario, ⁴Department of Obstetrics and Gynaecology, University of Western Ontario, ⁵Department of Physiology and Pharmacology, University of Western Ontario, London, Ontario

Target Audience: Researchers interested in the use of MRI to detect metabolic disease, particularly with respect to its fetal origins.

Purpose: The metabolic syndrome (MetS) encompasses a number of morbidities, including insulin resistance and abdominal obesity, that when presented together increase the risk of developing cardiovascular disease and diabetes.¹ Currently in North America, approximately 25% of the population is afflicted with MetS, a number that is rising.¹ Although MetS is a disease that typically presents itself in adulthood, it has been shown that the propensity to become afflicted with MetS can be established during fetal development.² There is an increased incidence of MetS in adulthood for people born within one of two groups: large infants who were over-nourished as fetuses, as well as very small infants that developed within an intrauterine growth restricted (IUGR) environment.² It is hypothesized that the altered nutrition of the fetus present in these two cases leads to abnormal fat distributions in the developing fetus. Thus, the goal of this study is to use water-fat separated MRI to image fetal adipose tissue and to identify abnormalities in adipose tissue deposition in these two cases.

Methods: For the current study, pregnant guinea pigs were used due to their similarity to humans in regard to adipose tissue development during fetal growth.³ Three groups of pregnant guinea pigs were anaesthetized and scanned ~60 days into an ~68 day gestation. These groups included: a high fat diet group where the mother's food consisted of 46% fat by weight; a surgically induced IUGR group on a chow diet; and a control group. IUGR was induced either by vessel ablation or placing an occluder over uterine blood vessels, restricting nutrient and oxygen flow to the fetus. Imaging was performed at 3T (MR750, GE, Waukesha, WI) using a 32 channel receive coil under a protocol approved by the institution's Animal Use Subcommittee. T₁- and T₂-weighted images were acquired with TR/TE/flip angle = 5.1ms/2.4ms/15° and 2000ms/120ms/90°, respectively, with voxel dimensions = 0.875x0.875x0.9mm³ for both acquisitions. IDEAL water-fat images were also collected for each guinea pig with TR/ Δ TE/flip angle = 9.4ms/0.974ms/4° and voxel dimensions = 0.933x0.933x0.9 mm³. The T₁- and T₂-weighted images were used to locate each fetus and to segment their volumes. IDEAL fat-only images were used to manually segment fetal adipose tissue volumes, and hepatic and intrascapular fat pad fat fractions were determined using proton density fat fraction (PDFF) maps.

Results: Compared to the control group, there was a noticeable difference in hepatic fat fractions of pups born to mothers on a high fat diet (28% vs. 22%), but this difference was not statistically significant (ANOVA, p=0.1). There was however a significant increase in the intrascapular fat fraction of the high fat diet group compared to the control group (84% vs. 77%, ANOVA p=0.01). The proportion of fetal volume comprised of adipose tissue was increased in the high fat diet group (22%), whereas this proportion was decreased in the IUGR (12%) pups compared to the control pups (19%).

Discussion: The elevated liver fat fraction values in the pups born to mothers on a high fat diet points to early evidence of non-alcoholic fatty liver disease (NAFLD). The increased fetal adiposity of the high fat diet group is also suggestive of NAFLD, but further work must be done to separate the visceral from the subcutaneous adipose tissue in the fetuses. The presence of NAFLD at such an early stage could have a detrimental effect on adult metabolic capabilities. Furthermore, the elevated intrascapular fat fraction in this group signifies a decreased amount of brown adipose tissue, which is characterized by decreased fat fraction due to increased vasculature and mitochondria compared to white adipose tissue.⁴

Conclusions: It is demonstrated here that adipose tissue can be identified and quantified in the fetus. In addition, there is a detectable difference in adipose tissue in pups born to mothers on a high fat diet as well as IUGR pups when compared to controls.

References: 1) Grundy SM. *Arterioscler Thromb Vasc Biol* 2008; 28: 629-636. 2) Brenseke BM, et al. *J Pregnancy* 2013; 2013: 368461, doi:10.1155/2013/368461. 3) Castañeda-Gutiérrez E, et al. *Am J Clin Nutr* 2011; 94(6 Suppl): 1838S-1845S. 4) Hu HH, et al. *Magn Reson Med* 2010; 31(5): 1195-1202.

Acknowledgements: We acknowledge support from GE Healthcare, NSERC, the Ontario Research Fund and the Canada Research Chairs Program.

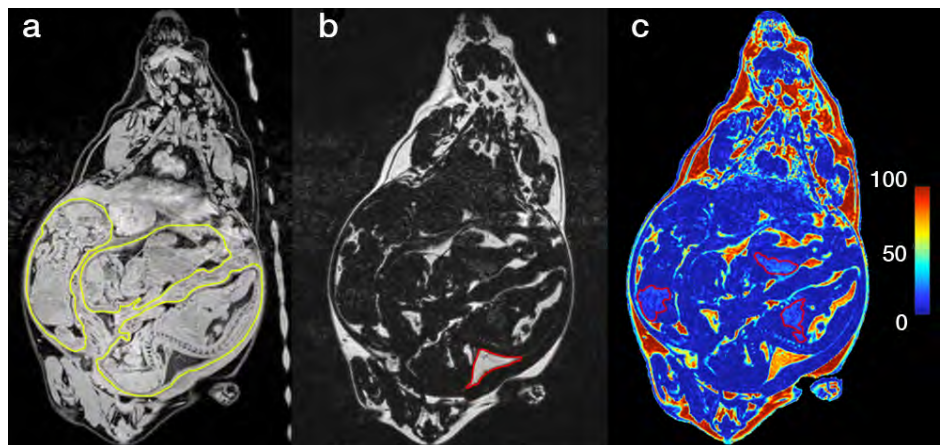


Figure 1: Coronal IDEAL water-fat separated images of a pregnant guinea pig. a) Coronal water only image with fetuses contoured in yellow, b) Fat only image with an intrascapular fat pad contoured in red, and c) Fat fraction map with fat fraction denoted by colour bar and fetal livers contoured in red.

Chemical-Shift Imaging with an Interleaved Bipolar Acquisition

Abraam S. Soliman^{1,2}, Curtis Wiens⁴, Trevor Wade^{2,3}, Ann Shimakawa⁵, Terry M. Peters^{1,2,3}, and Charles A. McKenzie^{1,2,3}

¹Biomedical Engineering, ²Imaging Research Laboratories, Robarts Research Institute, ³Medical Biophysics, Western University, London, ON

⁴Radiology, University of Wisconsin-Madison, Madison, WI

⁵Global MR Applied Science Laboratory, GE Healthcare, Menlo Park, CA

Introduction: Chemical-shift based water/fat separation has gained increasing use in clinical practice. It can be achieved with multiple gradient echo acquisitions using either unipolar [1] or bipolar readout gradients [2]. Typically, fat quantification is performed using at least 6 unipolar echoes separated with fly-back readout gradients [3]. Multiple shots are required to achieve optimal echo-spacing within the recommended range that provides the best SNR performance [4]. This increases the scan time. On the other hand, in a bipolar acquisition data is acquired with positive and negative readout polarities, potentially resulting in 1) shorter echo-spacing, 2) shorter scan time, and 3) higher SNR efficiency [2]. However, phase errors are produced between positively and negatively acquired data; if uncorrected, severe artefacts are produced in water and fat components. We propose a new bipolar acquisition scheme that overcomes this problem without requiring direct correction of the phase errors.

Theory and Methods: Bipolar multi-echo sequences acquire odd and even echoes with positive and negative polarities respectively (all k-space lines +,-,+,-,+,-) [2, 5]. In this work, the readout gradients also alternate their polarities every other k-space line (odd lines +,-,+,-,+,- vs. even lines -,+,-,+,-,+). By grouping k-space lines with same polarity, parallel imaging reconstruction can be used to obtain two full k-spaces with opposite readout polarities. By complex averaging, the inconsistent phase errors between odd and even echoes are removed [6] and water/fat separation techniques employed with conventional unipolar sequences can be performed. This approach does not attempt to directly correct the phase errors like previous phase correction techniques [2, 5]. Instead, the complex averaging adds a fixed phase term to all the echoes [6], removing the inconsistency between even and odd phase errors.

Phantoms and in-vivo experiments were performed on a 3T MR (Discovery MR 750, GE Healthcare, Waukesha, WI) using a knee T/R 8-coil array. A 3D IDEAL-SPGR sequence was modified to acquire data in an interleaved bipolar readout scheme. To achieve similar echo-spacing for a 6-echo acquisition, 2 shots of three echoes were used in the unipolar experiments. In phantom experiments, TR/TE1/ Δ TE = 5.74/0.88/0.69 and 5.65/0.84/0.704 ms for unipolar and interleaved bipolar respectively. BW=142.86 kHz, acquisition matrix=128x128x28, FOV=35 cm for both sequences. For in-vivo experiments, TR/TE1/ Δ TE = 8.09/1.11/0.87 ms and 6.74/1.02/0.86 ms for unipolar and interleaved bipolar, respectively. BW=142.86 kHz, acquisition matrix=128x128x28, FOV=25 cm for both sequences. Conjugate-gradient SENSE [7] was used for parallel imaging reconstruction. T₂-corrected water/fat separation was performed using Max-IDEAL [8]. SNR efficiency ($\text{SNR}/\sqrt{\text{acquisition time}}$) was calculated using the method described in [9].

Results: The aim is to compare the proposed method with the well-established unipolar technique as a reference. Table 1 shows fat fractions from selected ROIs in Fig. 1. Fat fraction maps from a healthy volunteer are shown in Fig. 2 (a-b), with the corresponding SNR efficiency maps of water images shown in Fig. 2 (c-d). The proposed method demonstrated accurate fat fraction and higher SNR efficiency compared to the unipolar sequence. Overall scan times were 58s for unipolar and 31s for interleaved bipolar.

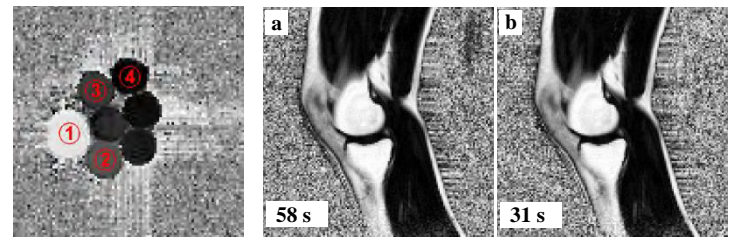
Discussion: Although additional reference lines were acquired to map the coil sensitivities, the overall acquisition time is still less than a unipolar sequence with similar echo-spacing, particularly at higher bandwidth. This approach is not vulnerable to residual phase errors that might occur in previous phase correction methods employed in bipolar reconstruction [2, 5]. Moreover, the number of acquired reference lines does not affect the accuracy of the correction as in Yu *et al.* [5]. This method is limited to coil-arrays as the reconstruction pipeline implicitly decimates the data by a factor of 2 and uses parallel MRI to reconstruct two fully sampled data sets. However, this limitation is not significant given the widespread usage of coil-arrays in clinical practice.

Conclusion: Fat quantification using a new bipolar sequence was demonstrated. The interleaved acquisition scheme allows accurate fat measurement in shorter scan time, with higher SNR efficiency, compared to unipolar acquisitions.

References:

- [1] Reeder *et al.*, MRM 2004; 51:35
- [2] Lu *et al.*, MRM 2008; 60:198
- [3] Yu *et al.*, MRM 2008; 60:1122
- [4] Chebrolu *et al.*, JMRI 2010; 32:493
- [5] Yu *et al.*, JMRI 2010; 31:1264
- [6] van der Zwaag *et al.*, JMRI 2010; 30:1171
- [7] Pruessmann *et al.*, MRM 2001; 46:638
- [8] Soliman *et al.*, MRM 2013 (in press)
- [9] Wiens *et al.*, MRM 2011; 66:1192

Fig.1: Selected ROIs on a fat fraction map from a phantom experiment with its corresponding fat fractions shown in Table 1.



	Unipolar	Interleaved Bipolar
ROI #1	95.93 ± 0.7	95.36 ± 0.7
ROI #2	22.21 ± 1.1	20.78 ± 1.3
ROI #3	10.81 ± 1.1	10.59 ± 1.0
ROI #4	1.53 ± 0.7	1.50 ± 0.7

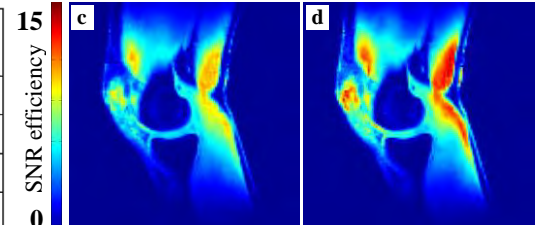


Fig.2: Fat fraction and SNR efficiency maps of water images from unipolar (a, c) and interleaved bipolar (b, d) sequences, respectively.

Cadaveric In-Situ Testing of Optical Coherence Tomography System Based Skull Base Surgery Guidance

Cuiru Sun¹, Osaama H. Khan², Peter Siegler¹, Ronnie Wong¹, Jamil Jivraj¹, Kenneth Lee¹, Barry Vuong¹, Beau A. Standish¹, Victor Yang^{1,2,3}

¹Dept. Electrical and Computer Engineering, Ryerson University, Toronto

²Division of Neurosurgery, Sunnybrook Health Sciences Centre, Toronto

³Dept. Neurosurgery, Faculty of Medicine, University of Toronto

Supervisor: Dr. Victor Yang

Optical Coherence Tomography (OCT) is a high resolution imaging modality with initial clinical success in ophthalmology, and has extensive potential for producing significant clinical impact in the field of neurological diseases. A novel neurosurgical OCT hand-held forward viewing probe in the familiar form factor of Bayonet shape has been developed. The probe design suits the transphenoidal approach through the nose to guide operations in narrow approaches with limited abilities for direct visualization. It provides high-resolution images of both tissue structure and blood flow velocity and profile. The hand-held OCT imaging probe has been successfully tested on porcine femoral artery structure and flow imaging *in vivo* as shown in Figure 1. In this study, we test the feasibility of integrating this intraoperative imaging probe with navigation technology for guidance and monitoring of skull base surgery. Cadaver heads were used to simulate relevant surgical approaches for treatment of sellar, parasellar and skull base pathology. We hypothesize that the intraoperative OCT imaging probe can be used during initial surgical trials to provide high-resolution structural and microvascular real-time imaging. These include: a) identification of adenoma vs normal pituitary gland tissue based on microstructural/morphology differences; (b) more complete resection of macroadenomas; (c) more efficient exploration of microadenomas; (d) decreased risk of endocrine dysfunction; and (e) decreased risk of cerebrospinal fluid (CSF) leak by improving sub-surface visualization.

In order to use OCT probes to guide surgical procedures, the OCT probe is integrated with modern Optical tracking system currently available in our cadaveric surgical labs. The surgeon-probe-OCT interface was calibrated and tested. A high-resolution 3D CT scan was performed on the cadaver head to provide baseline data for navigation. The cadaver heads were mounted on existing 3- or 4-point fixation systems. A schematic diagram showing the OCT probe with tracking markers attached and reached to the pituitary gland through nose is shown in Figure 2. The location of the OCT probe was recorded via HDTV, during OCT imaging. 2D OCT images are shown in real time together with the optical tracking images to the surgeon, which was important to deal with tissue shifts and deformations that occur during surgery. Real-time 2D and 3D OCT images from the cadaveric pituitary gland were saved and compared to the ex-vivo/ex-situ OCT imaging results. The intraoperative video and multimodality imaging data set, consisting of real time OCT images, OCT probe location registered to neurosurgical navigation were assessed.

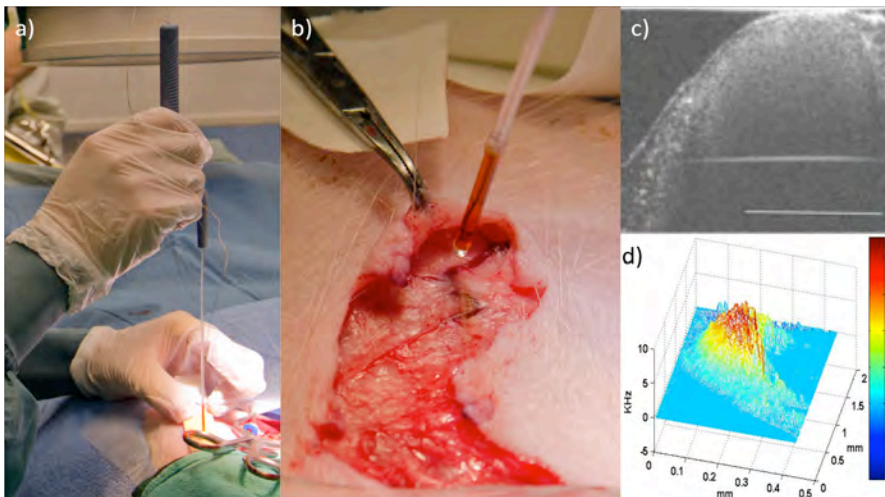


Figure 1 Imaging a porcine femoral artery using the probe. a) probe held by a surgeon; b) probe tip and the blood vessel; c) OCT structural image; d) blood flow profile

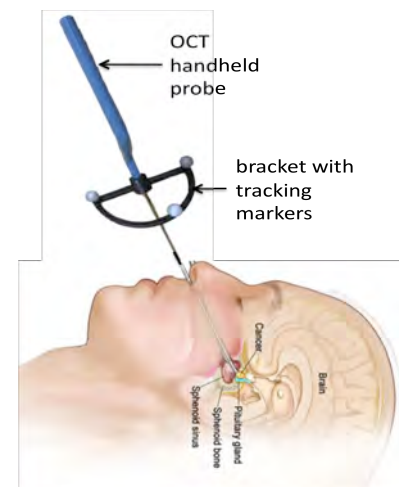


Figure 2 Schematic of the OCT probe used for transsphenoidal procedure

Integration of intraoperative OCT imaging with navigation technology provides the surgeon with updated image information, improve image interpretation and precision and accuracy of the therapeutic procedure. Preliminary results demonstrate that the clinical neurosurgical navigation system could provide the hand held OCT probe gross anatomical localization. Therefore surgeon may accurately navigate the tools into the patient with high precision based on image information. The near-histological imaging resolution of intraoperative OCT can improve the identification of adenoma vs normal pituitary gland tissue based on microstructural/morphology differences feature identification. The OCT imaging data, combined with the neurosurgical navigation tracking has shown to be important for obtaining improved tumor resection. The trials of the probe on cadaver head will facilitate the translation of the "bench top" system to provide clinically relevant improvements in surgical guidance and patient care.

Potential for photoacoustic imaging of the neonatal brain

Pantea Tavakolian^{a,b}, Ivan Kosik^{a,b}, Astrid Chamson-Reig^a, Keith St. Lawrence^{a,b},
and Jeffrey J.L. Carson^{a,b,*}

^aImaging Program, Lawson Health Research Institute, London, ON, Canada; ^bDepartment of Medical Biophysics, Schulich School of Medicine and Dentistry, University of Western Ontario, London, ON, Canada

*Correspondence: jcarson@lawsonimaging.ca

ABSTRACT

Photoacoustic imaging (PAI) has been proposed as a non-invasive technique for imaging neonatal brain injury. Since PAI combines many of the merits of both optical and ultrasound imaging, images with high contrast, high resolution, and a greater penetration depth can be obtained when compared to more traditional optical methods. However, due to the strong attenuation and reflection of photoacoustic pressure waves at the skull bone, PAI of the brain is much more challenging than traditional methods (e.g. near infrared spectroscopy) for optical interrogation of the neonatal brain. To evaluate the potential limits the skull places on 3D PAI of the neonatal brain, we constructed a neonatal skull phantom (1.4-mm thick) with a mixture of epoxy and titanium dioxide powder that provided acoustic insertion loss (1-5MHz) similar to human infant skull bone. The phantom was molded into a realistic infant skull shape by means of a CNC-machined mold that was based upon a 3D CAD model. To evaluate the effect of the skull bone on PAI, a photoacoustic point source was raster scanned within the phantom brain cavity to capture the imaging operator of the 3D PAI system (128 ultrasound transducers in a hemispherical arrangement) with and without the intervening skull phantom. The resultant imaging operators were compared to determine the effect of the skull layer on the PA signals in terms of amplitude loss and time delay.

Keywords: 3D photoacoustic imaging (PAI), skull mimicking phantom, ultrasound attenuation, periventricular leukomalacia

Novel contrast agent for dual-energy micro-CT to characterize bone vasculature

Justin J. Tse^{1,2,3}, Joy Dunmore-Buyze^{2,3}, Maria Drangova^{1,2,3}, and David W. Holdsworth^{1,2,3}

¹Department of Medical Biophysics, Western University, London, ON

²Imaging Research Laboratories, Robarts Research Institute, London, ON

³Schulich School of Medicine and Dentistry, Western University, London, ON
Supervisor: David W. Holdsworth

Introduction: Osteoarthritis (OA) is a growing concern among many aging individuals. With the huge complexity surrounding the cause of OA, many questions regarding the initiation and progression of this joint disease still remain. One interesting hypothesis suggests that bone vascular deficiencies may result in decreased nutrient and oxygen flow to the bone, in conjunction with decreased waste removal from the same bone. Combined, these effects may lead to the cartilage and bone loss associated with OA. Thus, studying the vascular changes, such as their quantification, changes in density, patency, and micro-architecture, that occur near and inside bone will be beneficial in understanding their effect on bone and will provide more information into the initiation and progression of OA. Changes in bones can be well characterized using micro-computed tomography (micro-CT); however, vascular visualization possess two challenges: very small size (5-10 μm), and poor inherent X-ray contrast.

Objective: We propose a combination of dual-energy high-resolution micro-computed tomography (DECT) with a novel perfusion contrast agent for the visualization of the vascular network associated bone to overcome the challenges, when using micro-CT, of vasculatures' small size and poor inherent X-ray contrast.

Materials and Methods: Lanthanide nanoparticles will act as the base of the contrast agent as they possess an absorption K-edge (50-60 keV) which falls within the energy range of high-resolution micro-CT scanners (30-90 kVp). Additionally, nanoparticles will ensure filling of the smallest vessels (5-10 μm). Validity of the contrast agent was tested through whole-body perfusions of post-mortem C57BL/6 mice. The mice are initially scanned on a GE pre-clinical Vision120 (GE Healthcare, London, ON, Canada) at 100 μm Regions of interest are scanned at 20 μm on our GE Locus (GE Healthcare, London, ON, Canada).

Results: The lanthanide based contrast agent perfused and cured homogeneously throughout the entire mouse, providing a contrast enhanced visualization of the mouse's vascular networks (Fig. 1). A single energy (90 kVp) micro-CT scans showed a CT value >3500 HU (Hounsfield units) for the lanthanide based contrast agent, in contrast, bone has a CT value of ~ 2750 HU. DECT on the hindlimb region results in separate images of perfused vasculature and bone (Fig. 2). Additionally, vessels such as nutrient arteries, that lay within the tibia and femur surrounded by bone, become visible with the aid of the lanthanide based contrast agent; in addition to small vessels, such as the dorsal metatarsal veins and digital arteries.

Conclusion: The successful demonstration of the combination of a novel perfusion contrast agent in conjunction with DECT imaging resulted in individual images of bone and vasculature. Used with a well-characterized surgically induced OA rat hindlimb model, this combination technique will allow us to study vessel micro-architecture, patency or blockage, and density quantification. This information will provide more insight into the initiation and progression of OA.



Fig. 1. Maximum intensity projection through a mouse perfused with the lanthanide based contrast agent

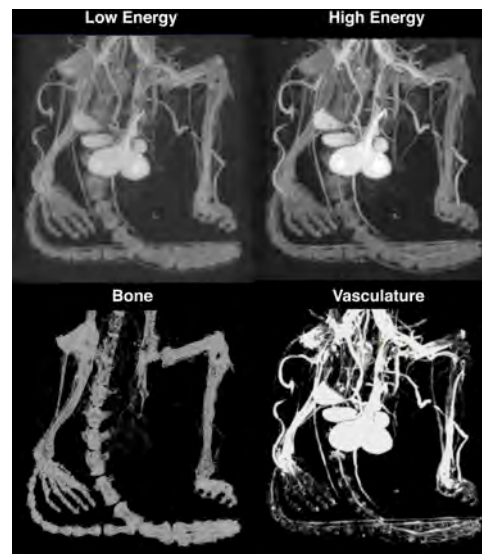


Fig. 2. DECT results demonstrating the ability of a lanthanide based contrast agent in aiding and producing specific images of perfused vasculature (Vasculature) and nearby bone (Bone)

***In vivo* Micro-CT Estimation of Visceral and Subcutaneous Adipose Tissues in Mouse Whole-Body Composition**

Joseph U. Umoh¹, Amy Burke², Chris Norley¹, Steven Pollmann¹, Joy Dunmore¹, Maria Drangova^{1,3}, Murray Huff², and David W. Holdsworth^{1,3}
¹*Preclinical Imaging Research Centre (PIRC), Robarts Research Institute,*
²*Department of Medicine and Biochemistry, and* ³*Departments of Medical Biophysics and Surgery, Western University, London, ON, Canada*

Introduction: Deposits of excess visceral adipose tissue (VAT) and subcutaneous adipose tissue (SAT) are linked to different risks of obesity or diabetes. It is, therefore, important to separate, differentiate, and quantify them. Whole-body composition (WBC) analysis, using micro-computed tomography (micro-CT), usually separates the body tissue into three major components: total adipose tissue (AT), lean tissue (LT) and skeletal tissue (ST) based on gray-scale (CT number) thresholds. It has been shown that the density of the VAT is indistinguishable from that of SAT; hence a thresholding method cannot be used to separate VAT and SAT. We present an *in vivo* micro-CT technique, which extends the traditional whole body composition, to determine the volumes and masses of the VAT, SAT, LT, and ST, in a mouse model.

Methods: Twelve mice, weighing 25 to 54 g were anesthetized and imaged *in vivo* using a *GE Locus Ultra* micro-CT scanner (with scan protocol and reconstruction parameters of 80 kV, 55 mA, 1000 views, 16 sec., and 154 μ m isotropic voxels). WBC analysis was done by determining the threshold values separating the three tissue types and this yielded total, whole-body values for AT, LT and ST. Then, the visceral tissue was segmented such that the included voxels were used for the VAT analysis, while excluded voxels were used for SAT analysis. Based on the segmentation of visceral and subcutaneous regions, and using the threshold values, software was used to rapidly compute the volumes of the VAT, SAT, LT and ST. Masses for each of these quantities were then calculated using previously-reported density values for each tissue type. The total, computed mass of the mouse was then compared with the gravimetrically-measured mass. Using repeated scans of six mice, precision error of the micro-CT methodology was calculated to determine the reproducibility of the method.

Results: The threshold CT numbers separating AT, LT, and ST were -380, -30, and 190 HU. Mouse whole-body composition analysis (example Fig. 1) had the following mass ratio: VAT 15%, SAT 31%, LT 44%, and ST 10%. The analyzed and measured mass of the 12 mice agreed to less than 1%. Precision error of the VAT mass was 0.76% while that of the SAT mass was 0.49%.

Conclusions: This extension to a whole-body composition technique combines the separation of the total adipose tissue into VAT and SAT in addition to the analysis of total, whole-body AT, LT and ST. This technique is highly precise and accurate and can be applied in small-animal models, such as rats and mice, for preclinical investigations of the pathogenesis and treatment of diseases.



Fig. 1: Micro-CT image of a whole-body mouse showing VAT (red), SAT (blue), lean (green), and skeletal (white) tissues. Measured mass was 54.0 g while computed mass was 53.4 g.

A Pseudo Non-Cartesian Pulse Sequence for Hyperpolarized Xenon-129 Gas MRI of the Lungs at Low Magnetic Field Strength

Krzysztof Wawrzyn^{1,2}, Alexei Ouriadov³, Elaine Hegarty¹, Susannah Hickling⁴, and Giles Santyr^{1,2}

¹Imaging Research Laboratories, Robarts Research Institute, London, Ontario, Canada, ²Department of Medical Biophysics, Western University, London, Ontario, Canada, ³Thunder Bay Regional Research Institute, Thunder Bay, Ontario, Canada, ⁴Department of Medical Physics, McGill University, Montreal, Quebec, Canada

BACKGROUND: The combination of hyperpolarized xenon gas (¹²⁹Xe) with magnetic resonance imaging (MRI) is an emerging technique that permits direct visualization of lung structure and function. Furthermore, the magnetization available from hyperpolarization is independent of magnetic field strength, providing images at field strengths substantially lower (< 0.1T) than used for clinical MRI [1]. The most commonly used imaging sequence for ¹²⁹Xe MRI is the fast gradient-recalled-echo (FGRE) sequence [2]. However, the Cartesian k-space acquisition scheme of FGRE possesses undesirable attributes for ¹²⁹Xe. Since only a single line of k-space is sampled per excitation, it requires a large number of radio frequency (RF) excitations per image, which reduces the non-renewable hyperpolarized signal. In this work, an ultra-short echo time (TE) imaging sequence based on a pseudo non-Cartesian k-space trajectory, known as *sectoral* [3], is implemented at low magnetic field strength (0.07 T) for efficient use of the non-equilibrium hyperpolarized magnetization. *Sectoral* is expected to be advantageous because it uses fewer RF pulses to fill k-space and has reduced T₂*- and diffusion-weighted data sampling at the center of k-space, leading to improved efficiency over FGRE approaches. In this work, the *sectoral* approach is compared to FGRE and a multi-breath *sectoral* approach, on the basis of SNR efficiency.

METHODS: MRI was performed using a custom-built saddle RF coil tuned to the resonant frequency of ¹²⁹Xe (0.883 MHz) with a custom-built resistive magnet MRI system at 75 mT [4]. Naturally-abundant ¹²⁹Xe gas was hyperpolarized using an in-house continuous flow spin exchange optical pumping system. A flow-through syringe phantom (diameter=1.5 cm, length=10 cm) was used to assess the feasibility of the 2-D single-breath *sectoral* (16 RF pulses, TE=3 ms, TR=219 ms, matrix size=64×64, bandwidth=4.85 Hz, scan time=6 s), and multi-breath *sectoral* (one breath per sector) sequences and compared with conventional 2-D FGRE (TE=2.6 ms, TR=23.8 ms, matrix size=64x64, and 64 RF pulses, bandwidth=48.85 Hz, scan time=4 s). An individual sector is a sub-trajectory that begins at the center of k-space and ends on the periphery. The single-breath *sectoral* and FGRE imaging pulse sequences incorporated a variable flip angle approach [5] while the multi-breath *sectoral* sequence incorporated a constant 90° flip angle for each acquired sector. The 2-D SNR efficiency ($\eta = SNR / (resolution^2 \times \sqrt{scan\ time \times bandwidth})$) was determined from the obtained *sectoral* and FGRE images. All imaging was performed with naturally-abundant ¹²⁹Xe gas (~ 3-5 % polarization). *Sectoral in vivo* lung imaging of a Sprague-Dawley rat (517 g) was performed using an MR-compatible mechanical ventilator (PIP=16 cm H₂O, TV=2.6 mL) following 4 wash-out breaths of ¹²⁹Xe. All procedures followed animal use protocols approved by Western University's Animal Use Subcommittees.

RESULTS AND DISCUSSION: Figure 1 shows representative 2-D FGRE [Fig. 1(a)], single-breath *sectoral* [Fig. 1(b)], and multi-breath *sectoral* [Fig. 1(c)] images of the flow-through syringe phantom using ¹²⁹Xe. Comparisons of *sectoral* to FGRE images of the syringe phantom filled with ¹²⁹Xe indicate favorable SNR and efficiency improvements (Table 1). Figure 2 shows a representative 2-D *sectoral* whole-lung coronal projection image from a rat ventilated with hyperpolarized ¹²⁹Xe gas, with SNR and efficiency of 212 and 33 (mm²·s^{1/2})⁻¹, respectively. These results indicate that *sectoral* is feasible and utilizes the available ¹²⁹Xe signal more efficiently than FGRE, maintaining comparable spatial resolution. Furthermore, multi-breath *sectoral* compared favorably to single-breath *sectoral* and may improve SNR at the cost of higher ¹²⁹Xe consumption. Maps of apparent diffusion coefficient (ADC), alveolar partial pressure of oxygen and T₂* are also feasible with the *sectoral* approach. Future work will involve *in vivo* imaging to acquire ADC and T₁- and T₂*- weighted ¹²⁹Xe images of rodent models of emphysema.

Table 1: SNR and SNR efficiency for FGRE, single- and multi-breath *sectoral* images.

Sequence	SNR	SNR efficiency (mm ²) ⁻¹
FGRE	22	2.24
Single-breath Sectoral	70	18.30
Multi-breath Sectoral	171	44.71

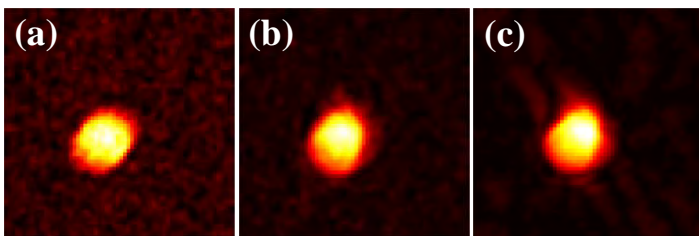


Figure 1: Flow-through syringe phantom using (a) FGRE (b) single-breath *sectoral* and (c) multi-breath *sectoral*.

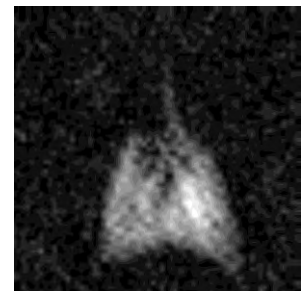


Figure 2: *Sectoral* 2-D coronal projection image a rat lung with ¹²⁹Xe.

REFERENCES: [1] Dominguez et al., CMR, 2008 [2] Moller et al., MRM, 2002 [3] Khrapitchev et al., JMR, 2005 [4] Dominguez et al., CMR 2010 [5] Zhao L et al. JMR, 1996.

ACKNOWLEDGEMENTS: The authors thank Adam Farag for his technical assistance. This work was supported by CIHR, NSERC and the Ontario Preclinical Imaging Consortium (OPIC).

Dynamic contrast-enhanced 3D photoacoustic imaging

Philip Wong^{a, b}, Ivan Kosik^{a, b}, and Jeffrey J.L. Carson^{a, b, *}

^a Imaging Program, Lawson Health Research Institute, London, ON, Canada

^b Medical Biophysics, Schulich School of Medicine and Dentistry, University of Western Ontario, London, ON, Canada

(Corresponding author: Jeffrey J.L. Carson, jcarson@lawsonimaging.ca)

Photoacoustic imaging (PAI) is a hybrid imaging modality that integrates the strengths from both optical imaging and acoustic imaging while simultaneously overcoming many of their respective weaknesses. In previous work, we reported on a real-time 3D PAI system comprised of a 32-element hemispherical array of transducers. Using the system, we demonstrated the ability to capture photoacoustic data, reconstruct a 3D photoacoustic image, and display select slices of the 3D image every 1.4 s, where each 3D image resulted from a single laser pulse. The present study aimed to exploit the rapid imaging speed of an upgraded 3D PAI system by evaluating its ability to perform dynamic contrast-enhanced imaging. The contrast dynamics can provide rich datasets that contain insight into perfusion, pharmacokinetics and physiology. We captured a series of 3D PA images of a flow phantom before and during injection of piglet and rabbit blood. Principal component analysis was utilized to classify the data according to its spatiotemporal information. The results suggested that this technique can be used to separate a sequence of 3D PA images into a series of images representative of main features according to spatiotemporal flow dynamics.

Contrast-enhanced CT reveals the early hemodynamic changes of focal cerebral ischemia and amyloid protein toxicity in a rat model

Jun Kevin Yang¹, Zareen Amtul², Christopher D. d'Esterre¹, David F. Cechetto², Ting Yim Lee^{1,3}

¹Imaging Laboratories, Robarts Research Institute, Department of Medical Biophysics, University of Western Ontario;

²Department of Anatomy and Cell Biology, University of Western Ontario; ³Imaging Program, Lawson Health Research Institute, London, ON, Canada.

Background & Purpose: Clinical evidence indicates that cerebral ischemia (CI) and a pathological factor of Alzheimer's disease, the β -amyloid ($A\beta$) protein, can increase the rate of cognitive impairment in the ageing population. Using the CT Perfusion (CTP) functional imaging, we sought to investigate the interaction between CI and the $A\beta$ protein on cerebral hemodynamics.

Methods: $A\beta_{25-35}$ peptides were bilaterally injected into cerebroventricles, while CI was induced by the unilateral injection of a vasoconstrictor, endothelin-1, into the right striatum (N=6) of male Wistar rats. The combined ($A\beta$ +CI) group (N=7) received both injections. Controls (N=3) had unilateral injection of saline into the right striatum. Iodinated contrast was given intravenously, while serial CT images were acquired over 2 minutes. Each imaging acquisition was performed at a gantry speed of 0.4s/rotation and sixteen image slices were collected at 1.25mm thick per slice. Cerebral blood flow (CBF) and blood volume (CBV) parametric maps were co-registered to a rat brain atlas and region of interests were drawn on the parametric maps to determine striatal CBF and CBV. Neuroinflammation and vascular alteration were investigated with histopathology.

Results: CTP maps revealed that ipsilateral striatum of $A\beta$ +CI and CI groups showed significantly lower CBF and CBV than the $A\beta$ and control groups at the acute phase. CBF and CBV increased significantly (i.e. hyperperfusion and hyperemia, respectively) at day 7 in the CI and $A\beta$ +CI groups, but not in the $A\beta$ and control group. At day 28, only $A\beta$ +CI group had elevated CBF and CBV compared to the baseline. Histopathology showed that average density of dilated microvessels in the ipsilateral striatum in CI and $A\beta$ +CI groups was significantly higher than controls at day 7. Microglial cells became more abundant and activated from day 7 to day 28 in CI and $A\beta$ +CI groups, indicating neuroinflammation was involved.

Conclusion: We demonstrate that CTP can quantitatively measure the hemodynamic disturbance on CBF and CBV functional maps in a rat model of cerebral ischemia interacting with pro-inflammatory $A\beta$ protein. Moreover, histological results of vascular pathology and inflammation support these hemodynamic findings.

Abstract and Biography Index

Last Name	First Name	Presentation Type	Page Number
Abhari	Kamyar	Poster	114
Ahmed	Hassaan	Poster	136
Alali	Sanaz	Poster	137
Alexander	Kevin	Poster	60
Alharbi	Sana	Poster	138
Ambacher	Matthew	Poster	61
Amit	Guy	Poster	62
Anand	Manjunath	Oral and Poster	18
Anderson	Ryan	Poster	19
Andrea	Jennifer	Poster	63
Baxter	John	Poster	115
Bertrand	Marie-Jeanne	Oral and Poster	48
Black	Sandra	Poster	49
Blais	Adam	Poster	139
Blinston	Charlotte	Poster	116
Boesen	Mari	Oral	50
Bondoc	Andrew	Oral and Poster	92
Boyle	Amanda	Poster	140
Bronskill	Michael	Commercialization Panel Member	9
Burgess	Laura	Poster	172
Burton	Christiane	Poster	141
Capaldi	Dante	Poster	51
Castelino	Robin	Poster	173
Cepek	Jeremy	Oral	117
Chambers	David	Poster	20
Chan	Harley	Poster	64
Cheng	Weiran	Oral and Poster	174
Chin	Lee	Poster	65
Cifuentes	Jidney	Poster	66
Cocker	Myra	Oral and Poster	12
Couch	Marcus	Poster	142
Daly	Michael	Oral and Poster	21
Davoudi	Bahar	Poster	67
De Silva	Tharindu	Poster	118
Dekaban	Mark	Poster	143
Dekker	Kurtis	Poster	68
Demidov	Valentin	Poster	22
Denbeigh	Janet	Poster	175
d'Esterre	Christopher	Oral	52
Detombe	Sarah	Oral	176
Doganay	Ozkan	Poster	177

Last Name	First Name	Presentation Type	Page Number
Dominguez-Viqueira	William	Oral	93
Dowhos	Krista	Oral and Poster	178
Driscoll	Brandon	Poster	119
Dufort	Paul	Poster	120
Eilaghi	Armin	Oral	13
Elfarnawany	Mai	Poster	23
Fazel Bakhsheshi	Mohammad	Poster	94
Fenster	Aaron	Commercialization Panel Member	9
Fox	Matthew	Poster	179
Gaudet	Jeff	Oral and Poster	144
Geraghty	Benjamin	Oral	145
Ghobadi	Kimia	Poster	69
Gibson	Eli	Oral and Poster	146
Gladwish	Adam	Poster	147
Glick	Daniel	Poster	70
Goldhawk	Donna	Oral	95
Gorjizadeh	Alborz	Poster	121
Goubran	Maged	Oral and Poster	122
Gribble	Adam	Poster	180
Guo	Fumin	Poster	148
Hachem	Maryam	Poster	96
Hadj Boussaad	Adem	Poster	181
Haedicke	Inga	Poster	149
Hamilton	Amanda	Poster	24
Harris	Jacqueline	Poster	182
Hegarty	Elaine	Poster	25
Holden	Matthew	Poster	26
Holdsworth	David	Oral	27
Hrinivich	Thomas	Oral and Poster	71
Hu	Zhengyi	Poster	183
Hudson	Thomas	Poster	72
Huisman	Henkjan	Keynote Speaker	7
Imani	Farhad	Poster	28
Inoue	Jiro	Poster	97
Jalilian	Farhang	Oral and Poster	14
Jayarathne	Uditha	Oral and Poster	29
Jechel	Christopher	Poster	73
Johnson	Patricia	Poster	98
Karami	Elham	Poster	123
Karimi	Hirad	Poster	150
Kashigar	Aidin	Oral and Poster	74
Kayvanrad	Mohammad	Poster	151
King	Franklin	Poster	75
Kishimoto	Jessica	Oral and Poster	124

Last Name	First Name	Presentation Type	Page Number
Kowalczyk	Izabela	Poster	30
Kulkarni-Thaker	Shefali	Oral and Poster	76
Lai	Ingrid	Poster	77
Lasso	Andras	Poster	78
Lasso	Andras	Oral	79
Lau	Lily	Poster	153
Lau	Justin	Poster	152
Lausch	Anthony	Oral and Poster	80
Lee	Casey	Poster	99
Leipsic	Jonathon	Keynote Speaker	7
Li	Winnie	Poster	81
Li	Feng	Poster	100
Lim	Heeseung	Poster	154
Lim	Heeseung	Poster	155
Liu	Linshan	Poster	101
Liu	Junmin	Poster	102
Locke	Stuart	Poster	156
Lorusso	Daniel	Oral and Poster	184
Lovis	Jordan	Oral and Poster	185
Lowerison	Matthew	Poster	31
Lu	Qian	Oral and Poster	15
Lu	YingLi	Poster	103
Mackie	Rock	Commercialization Keynote Speaker	9
Mallick	Amirul	Poster	32
Manning	Kathryn	Poster	186
Marami	Bahram	Oral and Poster	82
Martin	Peter	Oral and Poster	33
Mattonen	Sarah	Oral and Poster	125
McCurdy	Colin	Poster	157
McIntosh	Chris	Oral	83
McKee	Trevor	Oral and Poster	84
McLeod	Jonathan	Poster	126
McVicar	Nevin	Poster	158
Mehrabian	Hatef	Poster	159
Mousavi	Seyed Reza	Oral and Poster	127
Munding	Chelsea	Oral and Poster	104
Murrell	Donna	Oral and Poster	187
Nicolae	Alexandru	Poster	85
Oakden	Wendy	Poster	160
Oh	Seungjong	Poster	86
Ouriadov	Alexei	Oral	188
Paish	Adam	Oral and Poster	189
Patrick	John	Oral and Poster	34
Paulin	Gregory	Oral	54

Last Name	First Name	Presentation Type	Page Number
Paulin	Gregory	Poster	53
Perruchoud	Loise	Poster	161
Peterson	Justin	Poster	162
Pike	Damien	Poster	55
Pike	Damien	Oral	56
Pike	Damien	Poster	57
Plewes	Donald	Commercialization Panel Member	10
Pop	Mihaela	Oral	105
Prior	Paul	Poster	106
Qi	Xiuling	Poster	107
Qiu	Wu	Poster	163
Quiaoit	Karina	Poster	108
Raess	Avery	Poster	190
Rajchl	Martin	Poster	128
Sadjadi	Hosseini	Poster	35
Salarian	Mehrnoush	Poster	36
Samavati	Navid	Poster	129
Sarban	Victoria	Oral and Poster	58
Seevaratnam	Subaagari	Poster	37
Seo	Minseok	Poster	164
Sethi	Benu	Poster	109
Shahedi	Maysam	Poster	130
Shapiro	Mikhail	Keynote Speaker	7
Sheikh	Khadija	Oral	131
Sheikh	Khadija	Poster	132
Sinclair	Kevin	Oral and Poster	191
Snir	Jonatan	Poster	165
So	Aaron	Oral	110
Soehl	Marie	Oral and Poster	38
Soliman	Abraam	Poster	192
Sun	Yue (Joy)	Oral and Poster	166
Sun	Cuiru	Poster	193
Svenningsen	Sarah	Oral	133
Szilagy	Gregory	Poster	87
Tavakolian	Pantea	Poster	194
Tavallaei	Ali	Oral and Poster	111
Tomaszewski	John	Keynote Speaker	8
Tremblay-Darveau	Charles	Poster	167
Tse	Justin	Oral and Poster	195
Ukwatta	Eranga	Oral and Poster	16
Umoh	Joseph	Poster	196
Ungi	Tamas	Poster	39
Ungi	Tamas	Oral	40
Walsh	Ryan	Poster	41

Last Name	First Name	Presentation Type	Page Number
Wawrzyn	Krzysztof	Poster	197
Weatherbee	Andrew	Poster	42
Weersink	Robert	Poster	134
Wong	Eugene	Poster	88
Wong	Philip	Poster	198
Wright	Trinette	Poster	89
Xia	Wenyao	Oral and Poster	90
Xu	Helen	Oral and Poster	43
Xu	Helen	Poster	44
Xu	Yiwen	Oral and Poster	45
Yang	Jun Kevin	Oral	199
Yeung	Timothy Pok Chi	Poster	168
Yohan	Darren	Poster	169
Yu	Lihai	Poster	170